Genetically Encoded Biosensors for Ketamine and Other Rapidly Acting Antidepressants in Zebrafish and Cell Culture

Thesis by

Zachary Blumenfeld

In Partial Fulfillment of the Requirements for the
Degree of
Doctor of Philosophy

Caltech

CALIFORNIA INSTITUTE OF TECHNOLOGY
Pasadena, California

2023
Defended May 5, 2023

ACKNOWLEDGEMENTS

A PhD dissertation is written by one person, but its pages do not provide adequate testimony to those who made the research it describes possible. Each graduate student represents an investment of time, money, resources, and attention, and I have been extremely fortunate to have received all of these gifts from a wonderful group of people during my time at Caltech. I have been placed in a position to succeed; I therefore take ownership of all failures and gladly share in any successes.

I would first like to thank my co-advisors, **Prof. Henry Lester** and **Prof. David Prober**. I joined Henry's lab after an uneven first year, and he agreed to take me on, mostly sight unseen — for this faith and safe harbor, I will be forever grateful. His vast knowledge and ability to recall papers written many decades ago will always impress me, but so too will his curiosity, his dedicated mentorship (particularly of Caltech's impressive undergraduates), and his wit. I will also take with me many 'Henry-isms,' and will henceforth never use 'big' or 'small' when actual quantities will do, nor will I ever try to "show off my dog, my kids, or my software." Three years into my tenure in the Lester lab, I began working in the Prober lab and, from the start, David has helped to make it a second home for me. He has provided sound and practical guidance in our weekly meetings over the past few years, helping me swiftly acclimate to a research program in which I had no prior experience. Since members of the lab are not permitted to make these sorts of comments while active, I can now say in hindsight that things went 'swimmingly,' and that 'fishing' for interesting findings with the group was a great experience.

My day-to-day life in both labs has been greatly enhanced through the contributions made by its members. In joining the Lester lab, I was fortunate to have Henry agree to accept me, but I was perhaps as or more fortunate to be paired with a fantastic mentor, **Dr. Aaron Nichols**. Having virtually no prior practical experience in molecular biology techniques, Aaron taught me everything from scratch, often spending extra time to explain the concepts behind the experiments and the tools we were using to complete them. We have published two articles (and counting) together, of which we are certainly proud, but we have also shared a bunch of laughs, insightful conversations, and great memories. As he will hopefully be running a lab of his own someday soon, I can say without reservation that Aaron will make a great principal investigator and an even better mentor to his future students. I would also like to thank: **Purnima**

Deshpande, lab manager extraordinaire, for keeping the lab running efficiently, for successfully juggling the support of many disparate projects, and for always having a quick comeback ready; **Dr. Bruce Cohen**, for his keen insights into a wide variety of subjects (including quantum physics), for his uncanny ability to ask interesting questions, and for talking with me about books we've read (even 'lending' me some along the way); **Anand Muthusamy**, for his intellectual curiosity and breadth of interests, for setting an example of how a graduate student at Caltech should be, and for finally getting an iPhone so that we could name our group chat; **Dr. Kallol Bera**, for his enthusiasm in sharing his time and hard-won experimental results with me and for having a seemingly indefatigable work ethic, even after becoming the great dad that he is; **Charlene Kim** and **Jonathan Wang**, for their unceasing support and guidance in all lab functions; **Dr. Hailey Knox** and **Dr. Chris Marotta**, our collaborators in the Dougherty lab, for their consistent help; and **Dr. Stephen Grant**, **Elaine Lin**, **Eve Fine**, **Zoe Beatty**, and **Helena Ambrosino**, for being great lab mates and collaborators.

When I joined the Prober lab, my acclimation process was greatly accelerated by the training provided by **Altyn Rymbek** and the superb support from **Tasha Cammidge**. Altyn helped train me in several techniques not too long after she had learned them, and she quickly showed herself to be the sort of person who would stop what she is doing to help a lab mate with a question or provide hands-on assistance. (Plus she always brings us presents after she goes on trips!) Tasha has been helpful in every aspect of my work in the Prober lab, and I cannot thank her enough for helping me learn new techniques, develop improved protocols for genotyping pesky mutant fish, and always asking if there is more she can do — she sets a standard for work ethic and interpersonal skills that I strive to match. I would also like to thank**:** **Dr. Andrey Andreev**, for his willingness to spend long hours in the basement microscope room with me, for his advice and mentorship, and for not making me feel bad that I don't squat; **Sophie Miller**, for being a great collaborator on exciting new research, for her impressive array of skills and curiosity, and for sorting by far the most number of embryos on a given day of anyone in the lab; **Dr. Grigorios Oikonomou**, for his willingness to answer questions and for finally reading <u>The Brothers Karamazov</u>; **Alex Mack**, for being such a vital teammate in the fish facility and for turning me into more of a soccer fan; **Brianna Garcia**, for helping me with many tasks around the lab and for laughing at (most of) my jokes; **Dr. Chanpreet Singh**, for providing crucial help in preparing our plasmids for use in fish and for taking it easy on Kallol in their cricket games;

Dr. Amina Kinkhabwala, for helping me with behavior experiments and for never taking "Mikey" out for a joy ride; **Desiderio Ascencio**, for his interest in developing new analyses of imaging data and for flexing on everyone by putting a giant monitor on his desk; **Dr. Ulrich Herget**, for helping me learn how to use the confocal microscope and for memorizing the pronunciation for the longest-named town in the world; **Marina Lecoeuche**, for being a great lab mate and for not being a bad sport about me transferring my leg injury bad luck to her; **Dr. Jin Xu**, **Dr. Steve Tran**, **Andrew Hill**, and **Jasmine Emtage**, for their great examples and making the lab a fun place to work; and **Axel Dominguez**, **Barbara Orozco**, and **Caressa Wong**, for helping to run the fish facility and providing us with the crucial support which makes our experiments possible.

Including my two co-advisors, I have had the privilege of working with and learning from a startling array of talent among the professors, staff, and fellow students at both Caltech and USC. I would especially like to thank: **Prof. Justin Bois**, for being such a great teacher and lecturer — I took three of his courses, all of which were challenging, fun, and designed to make us into Python advocates (for good reason); **Dr. Andres Collazo**, for always taking an interest in his students' work and for providing me with an enthusiasm for microscopes I didn't know I could have; **Dr. Giada Spigolon**, for her guidance and assistance every time the Nikon had problems; **Nicole McMillan**, for helping me handle controlled substances and always being available when I needed her; **Prof. Dennis Dougherty**, for helpful comments during group meetings; **Prof. Michael Roukes** and **Prof. Richard Andersen**, for allowing me to rotate in their labs; my USC-Caltech mentors, **Prof. Brian Lee**, **Prof. Spencer Kellis**, and **Prof. Daniel Kramer**; **Liz Ayala**, **Raina Beaven**, **Roland Rapanot**, and everyone else involved in the USC-Caltech MD/PhD program, for their support and desire to make all aspects of my training as enjoyable as possible; the other two members of my thesis committee, **Prof. Ralph Adolphs** and **Prof. Betty Hong**, for being great examples of how scientists can achieve excellence in scholarship, teaching, and mentorship; all of my fellow Bi 150 TAs who worked with me to help Henry and Ralph introduce four years' worth of students to neuroscience; and **Dr. Laurent Moreaux** and **Dr. Niki Kovats**, for being awesome mentors, great listeners, and true friends.

A life is perhaps lived by oneself (even if there are reasons and persons to consider), but it contains many ingredients and inputs from others — those who share our lives now, those who once shared them but are no more, those predecessors who remind us constantly that we are not our own. Sometimes I feel as though my life is like a painting-in-progress, and it has been my great privilege to have a palette with so many colors handy in my quest to craft something filled with meaning and beauty.

To begin at the beginning, I want to thank: my mother, **Teri**, for giving me life, for her unconditional love and support, for always seeing me as the person I hope to be, and for putting up with my sarcastic comments (including a great deal of dinner criticism); my father, **Andrew**, who has been a constant source of support, stability, humor, and an example of perseverance in my life – plus, I've received most of whatever athletic talent I have from him, so it's been a good deal; my older brother, **Josh**, for always looking out for me (even to this day), for traveling the world with me, and for beating me up so much when we were younger that I started doing combat sports (seeing Josh become a dad to my niece **Elleanna** has been perhaps my favorite development during my time at Caltech, and I hope to one day have the opportunity to be as good of a parent as he is); my maternal grandmother, **Pauline**, AKA "Tata," who passed away in 2015 and who provided me with an example of what total devotion to family looks like; my paternal grandmother **Sondre**, AKA "Safta," who passed away in 2018, and her husband, **Ned**, for welcoming us over countless Thanksgivings and for being two of the most naturally funny people I've ever met; my aunt **Wendy**, her partner **Memy**, and my cousins **Roni** and **Ori**, my overseas family, for giving me a home away from home; and all of my other aunts, uncles, and cousins, for being a part of my life.

I have been blessed to have so many great friends over the years. My grade school friends are a truly remarkable (and remarkably funny) group of people, many of whom are (finally) getting married. My college friends witnessed my transition out of childhood, and our shenanigans inspired countless inside jokes during our years together. My medical school friends helped me feel like I had a freshman year 2.0 during Year 1 of our program; they are a talented group of practitioners who are now almost all done with their residencies (of which fact they definitely don't remind me ever). My jiu jitsu friends have helped provide a wonderful escape for me during these long years of training, and, despite feeling like my body has aged twenty years (and now having a second cauliflower ear to match the one I had from wrestling), I have found an addicting hobby that I can do with an awesome group of people.

Throughout my time at Caltech, I have striven to cultivate a deeper appreciation for the humanities, and I have had the good fortune to participate in three different reading groups, all focused on different topics and texts. I would like to especially thank **Peter**, **George**, **Marty**, **Gabe**, **Ahmed**, **Patrick**, **Chris**, and **Max** for several years' worth of excellent conversations which helped me sharpen my claws.

Finally, I would like to thank some of my previous mentors and coworkers, including **Prof. Tom Gordon**, **Dr. Stephanie Slinski**, **Prof. Joy Geng**, **Prof. Helen Bronte-Stewart**, **Dr. Mandy Miller Koop**, **Dr. Bruce Hill**, **Dr. Tom Prieto**, **Anca Velisar**, **Dr. Lauren Shreve**, **Emma Quinn**, **Dr. Megan Trager**, **Leanel Liwanag**, **Judy Syrkin-Nikolau**, **Dr. Talora Martin**, **Carlos Rodriguez**, **Russell Mendonca**, **Scott Stanslaski**, **Duane Bourget**, and everyone else at UC Davis, Stanford, Medtronic, and USC with whom I've had the privilege to work.

PRELUDE: A PERSONAL AFFIRMATION AND THE POSSIBILITY OF EVEN GREATER HEALTH BEYOND THE FOURFOLD

"Homo sum, humani nihil a me alienum puto." – *Publius Terentius Afer's Heauton Timorumenos 77*

"No, no, no life! / Why should a dog, a horse, a rat, have life, / and thou no breath at all? Thou'lt come no more, / never, never, never, never, never!" – *William Shakespeare's King Lear, Act V Scene 3*

"I should have been a pair of ragged claws / Scuttling across the floors of silent seas." – *T.S. Eliot's The Love Song of J. Alfred Prufrock*

"Le silence éternel de ces espaces infinis m'effraie." – *Blaise Pascal's Pensées, sec. 2 no. 206*

"The horror! The horror!" – *Joseph Conrad's Heart of Darkness*

ABSTRACT

Over the past century, the development and use of treatments for depression has been one of the most important projects in both neuroscience and medicine. Not only is relatively little known about the underlying pathophysiology of major depressive disorder (MDD), a mechanistic understanding of the ways in which common antidepressants — such as selective serotonin reuptake inhibitors (SSRIs) — contribute to symptomatic relief remains elusive. Furthermore, the delay until typical antidepressant treatments take effect (a ‘therapeutic lag’ of weeks to months) presents a series of challenges to researchers in chemistry, neuroscience, pharmacology, and medicine, as the connection between apparent physiological changes and clinical benefit has yet to be established. The recent advent of a new class of drugs — rapidly acting antidepressants (RAADs), including the multi-purpose compound ketamine — which ameliorate symptoms within hours to days provides a crucial (if perplexing) perspective on the treatment of MDD and neuropsychiatric disorders more broadly. To answer questions concerning how various kinds of antidepressants might exert their effects, where those interactions take place, and what sorts of physiological changes drive clinical response, we have designed genetically encoded **drug**-specific **i**ntensity-based **s**e**n**sing **f**luorescent **r**eporters (iDrugSnFRs) which are engineered to detect drugs of interest in both *in vitro* and *in vivo* applications. We have successfully evolved iDrugSnFRs for an array of RAADs (iRAADSnFRs) which detect pharmacologically relevant concentrations of their target drugs sensitively and specifically in both cell culture as well as in the nervous tissue of larval zebrafish. Another set of iDrugSnFRs for SSRIs has provided novel insights into the potential reasons for the aforementioned ‘therapeutic lag’ as well as side effects, while yet another set has provided a pharmacokinetic basis for the evaluation of smoking cessation drugs. In all, our findings lead us to posit that iDrugSnFRs can aid in the elucidation of mechanisms by which a wide variety of orally active pharmaceutical compounds operate as well as provide a crucial basis for the development of better medicines.

PUBLISHED CONTENT AND CONTRIBUTIONS

A version of **Chapter 3** originally appeared as:

Selective Serotonin Reuptake Inhibitors within Cells: Temporal Resolution in Cytoplasm, Endoplasmic Reticulum, and Membrane

Aaron L. Nichols*, **Zack Blumenfeld***, Laura Luebbert, Hailey J. Knox, Anand K. Muthusamy, Jonathan S. Marvin, Charlene H. Kim, Stephen N. Grant, David P. Walton, Bruce N. Cohen, Rebekkah Hammar, Loren L. Looger, Per Artursson, Dennis A. Dougherty, Henry A. Lester; Journal of Neuroscience 3 March 2023, JN-RM-1519-22; doi: https://doi.org/10.1523/JNEUROSCI.1519-22.2022

Z.B. (co-first author) helped to design the *in vitro* experiments; performed the *in vitro* experiments; analyzed the dose-response imaging data, the stopped-flow and ITC data, and the spinning disk confocal imaging data; and helped write the manuscript.

A version of **Chapter 4** originally appeared as:

Fluorescence Activation Mechanism and Imaging of Drug Permeation with New Sensors for Smoking-Cessation Ligands

Aaron L. Nichols*, **Zack Blumenfeld***, Chengcheng Fan*, Laura Luebbert*, Annet E.M. Blom, Bruce N. Cohen, Jonathan S. Marvin, Philip M. Borden, Charlene H. Kim, Anand K. Muthusamy, Amol V. Shivange, Hailey J. Knox, Hugo Rego Campello, Jonathan H. Wang, Dennis A. Dougherty, Loren L. Looger, Timothy Gallagher, Douglas C. Rees, Henry A. Lester; *eLife* **11**:e74648; doi: https://doi.org/10.7554/eLife.74648

Z.B. (co-first author) helped to design the *in vitro* experiments; performed the *in vitro* experiments; analyzed the dose-response imaging data, the stopped-flow and ITC data, and the spinning disk confocal imaging data; and helped write the manuscript.

TABLE OF CONTENTS

LIST OF FIGURES AND TABLES

CHAPTER 1: INTRODUCTION

1.1. Depression: Diagnosis, History, Treatment, Mechanism

Major depressive disorder (MDD) is estimated to affect 3.8% of the global population [1]. In the United States, depression is the second-leading cause of disability [2], and one out of every six Americans will experience an episode of MDD during their lifetime [3]. Depression is currently diagnosed clinically based on whether patients experience five out of the nine possible symptoms every day for at least two weeks (one of which must be depressed mood or loss of interest/pleasure [4]). For MDD, episodes must be recurring but separated by at least two months. Other related diagnoses include: persistent depressive disorder (dysthymia), which presents with less severe symptoms than MDD but over at least a two-year period; bipolar depression (BPD), in which depressive episodes alternate with episodes of mania; seasonal affective disorder; postpartum depression; and depression arising from a primary medical condition (e.g. schizophrenia, long-term illness) [5]. Various scales can be used to assess depression subtype or suicidality, and major efforts are underway to establish more finely tuned diagnostic criteria such that potential underlying physiological causes can be more effectively targeted with specific treatments [5,6]. Over the past several decades, many studies have attempted to characterize pathophysiology at the genetic [7-10], epigenetic [8], *in utero* [9,11,12], early childhood development [9], socioeconomic [9,13,14], and environmental exposure levels [9,15], with the eventual goal of establishing biomarkers to use as more effective diagnostic criteria for, and provide a potential inroad in the treatment of, MDD.

MDD has been used as a clinical diagnosis since the 1970s and was officially added to the Third Edition of the Diagnostic and Statistical Manual (DSM-III) in 1980. However, the history of classifying depression stretches back into ancient history, with diagnoses such as ‘melancholia’ arising in the time of Hippocrates. Until the 1950s, no standardized medication regimens existed to treat the cluster of depressive disorders. A major revolution in psychiatric care occurred with the serendipitous discovery of iproniazid’s antidepressant effects. Originally developed to treat tuberculosis, clinicians noticed that patients treated with iproniazid experienced mood elevation [16]. Iproniazid, a monoamine oxidase inhibitor (MAOI), was found to induce high levels of hepatotoxicity [17], and was soon replaced by other MAOIs, including isocarboxazid, tranylcypromine, and phenelzine for the treatment of depression [18]. However, owing to their inhibition of both MAO-A and MAO-B enzymes, these MAOIs resulted in serious side effects, including hypertensive crises, particularly when administered concomitantly with sympathomimetics or, interestingly, after the consumption of certain cheeses [19]. The subsequent class of antidepressant drugs, tricyclic antidepressants (TCAs), owes its provenance to the first clinically approved antipsychotic, chlorpromazine. One such derivative, imipramine, did not exert any antipsychotic effects, but it did alleviate symptoms of depression among schizophrenic patients with depressive symptoms [20]. Yet, while TCAs proved to be effective at relieving the symptoms of depression [21], they too caused a set of unwanted side effects, owing to their promiscuous interaction with cholinergic/monoaminergic receptors and transporters [22]. Side effects included not only classic anticholinergic symptoms (e.g. confusion, dry mouth, blurred vision) and anti-adrenergic symptoms (e.g. dizziness) but also fatal overdoses due to heart block [23], particularly in MDD patients suffering from cardiac abnormalities [24]. With such a dangerous risk profile, researchers turned their attention to other potential treatments. Because of previous investigations which indicated the importance of serotonin (5-HT) to depression and suicidality [25], the serotonergic system became a target of interest for therapeutic intervention. Increases in 5-HT are common to both MAOIs and TCAs, which motivated the development of compounds to increase synaptic 5-HT reuptake inhibition. The selective serotonin reuptake inhibitors (SSRIs) are considered the first rationally designed neuropsychiatric medication; instead of relying on chance efficacy, researchers began to propose mechanisms by which depression and other disorders affected neurophysiology. The first compound in this class, fluoxetine (Prozac®), was developed in the 1970s [26,27], and demonstrated selective inhibition of the 5-HT reuptake transporter (SERT), which helps recycle 5-HT released at serotonergic synapses. By 1987, fluoxetine was approved for clinical use in the Unites States [28,29] with much broader tolerability and fewer dangerous side effects than the TCAs or MAOIs. In all, six total SSRIs have been approved for the treatment of unipolar depression (fluoxetine, sertraline, paroxetine, fluvoxamine, citalopram, escitalopram) and are currently considered the first-line treatment for MDD (SSRIs have also been approved for the treatment of anxiety disorders). However, these compounds are not without their side effects, the most vexing of which are sexual dysfunction, nausea, changes in appetite leading to weight gain, and insomnia [30-32]; in addition, perhaps the most troubling aspect of prescribing SSRIs to patients with MDD is the time to clinical efficacy, which can be anywhere from a few weeks to a few months [33].

There are multiple theories regarding the pathophysiology of depression, some of which have been influenced by the way each new class of therapeutics is purported to exert its effects. The monoamine hypothesis first gained currency owing to findings in the 1950s and 1960s that the antihypertensive agent reserpine apparently caused depression in some patients [34,35]; this was later corroborated in various animal studies [36-38]. *In vitro* data demonstrated that reserpine's mechanism of action involves inhibition of the vesicular monoamine intra-neuronal transporter, which impacts the reuptake of monoamines such as 5-HT, dopamine (DA), and norepinephrine (NE) into presynaptic vesicles [39,40]. Additional support for the monoamine hypothesis concerns the putative mechanisms by which MAOIs, TCAs, and SSRIs exert their antidepressant effects; the common pro-monoaminergic outcome of each class (either in total or in part) led to the presumption that increased monoaminergic activity at the synapse relieves depression. Various studies in both animals and humans have highlighted the important role that monoamines play in the manifestation of symptoms linked to depression [41-45], and the effectiveness of both 5-HT-NE reuptake inhibitors (SNRIs) and bupropion (thought to act as a DA-NE reuptake inhibitor) for the treatment of MDD in certain patients has added further supporting evidence. However, more recent work has undermined this narrative. Intentional depletion of monoamines in human subjects was not found to cause depression in typical patients [46] nor in MDD patients off medication [47,48]. In addition, although 5-HT levels in the synaptic cleft and extra-synaptic regions can reach steady-state levels within days after SSRI administration [49], medication must be continued during the ‘therapeutic lag’ of 2-6 weeks before patients report benefit [33,50]. The fact that all classic antidepressants appear to affect monoamine activity suggests that any theory concerning the pathophysiology of depression must take such evidence into account, yet monoamines are by no means the only appropriate target for which new antidepressant medications should be developed [33,50].

Hypothalamic-pituitary axis (HPA) dysfunction is another potential causal factor in the pathogenesis of depression. While not relying strictly on clinical results from products of rational drug design or their putative mechanisms, this theory centers on the well-characterized role of cortisol in mediating the stress response in humans. The two main stress hormone receptors —

type I, the mineralocorticoid receptor (MR); and type II, the glucocorticoid receptor (GR) — bind to the glucocorticoid cortisol, the final downstream product of the HPA axis which upregulates production in response to stressful stimuli, with the MRs (which mediate the induction of the stress response) having higher affinity for cortisol than the GRs (which mediate its termination) [51]. The GR-cortisol complex transits to the nucleus where it interacts with glucocorticoid response elements to function as a promoter for the regulation of transcription eventuating in changes across a variety of organs, including the brain [52]. Increased glucocorticoid production is proposed to be intrinsic to both animal and human responses to chronic stress; indeed, increased levels of cortisol can be found among patients with MDD [33,53-55], and overall HPA axis dysfunction in this population is thought to result from inappropriately high levels of corticotrophin-releasing hormone (CRH) [56,57] (which induces cortisol release), though the degree to which this is a product of impaired negative feedback from cortisol is not clear [53]. Additionally, higher CRH and cortisol levels among MDD patients are associated with a greater risk of relapse [58,59]. Interestingly, fluoxetine has been shown to normalize high CRH levels in patients with MDD [60], providing a potential link between the elevation of synaptic 5-HT and regulation of cortisol. However, cortisol is a generic indicator of stress, and, although one population-wide study has linked glucocorticoid receptor function to the prevalence of depression [61], the HPA axis does not yet appear to be a fruitful target for the development of future therapeutics [62].

Animal models provide another pathway by which to explore the effects of stressors on the development of depression. Several behavioral paradigms attempt to mimic stressful life events among MDD patients, including maternal deprivation stress (MDS) [63-65], chronic unpredictable stress (CUS) [66-69], and learned helplessness (LH) [70-72]. In terms of genes, while there are genetic loci associated with the heritability of depression [7,8], and there is a threefold risk of developing MDD among first-degree relatives [33], investigations of epigenetic signatures could eventually prove more insightful due to the undoubtedly complex interplay between genes and environment [8,73]. The pathophysiology of depression is likely complicated and patient-specific, so future work focusing on tailored pharmacogenomic approaches may prove most useful in both understanding potential pathophysiology as well as developing effective treatments.

The hypothesis that has become the most compelling recently concerns the role of glutamate. Glutamate is the most common neurotransmitter and is of particular importance in the forebrain, where over 30% of neurons are glutamatergic [74]. It is the major excitatory neural compound, with glutamatergic function being essential to nearly every brain region implicated in depressive states [75]. Glutamate metabolism differs between MDD patients and healthy controls [76], and antidepressant treatment can ameliorate this dysfunction [77]. Abnormalities in glial glutamate regulation have been demonstrated in postmortem analyses of the brains of MDD patients [78], and MDD patients have lower levels of glutamate in the basal ganglia [79] and cortical areas [80] as measured by magnetic resonance spectroscopy. In rodents, changes in the level of cortical glutamate are correlated with depression-like symptoms [81-83]. In all, while changes in glutamate have been associated with depression, unlike the monoaminergic hypothesis, the glutamatergic hypothesis has lacked candidate compounds which treated the symptoms of depression through a putatively glutamatergic mechanism. However, there has been renewed interest in this neural subsystem over the past few decades following the finding that ketamine, a multi-purpose drug known to the medical community for half a century, can exert antidepressant effects on a much faster timescale than SSRIs. Approved for the treatment of MDD by the Food and Drug Administration (FDA) in 2019, this compound, both intriguing and beguiling, will ultimately prove crucial to the next phase of pharmaceutical development for neuropsychiatric disorders.

1.2. Ketamine in the Clinic

Ketamine is an arylcyclohexylamine derivative originally developed in the 1960s as an alternative to phencyclidine (PCP), used initially as a surgical anesthetic due to its lack of respiratory depression [84,85] but was found to cause psychotomimetic side effects and have high abuse potential [85]. Both PCP and ketamine act on the glutamatergic system, noncompetitively binding to the N-methyl-D-aspartate (NMDA) receptor at the same site inside the channel pore [86,87]. NMDA receptors (NMDARs) are ionotropic channels ubiquitously expressed throughout the brain which play a crucial role in learning, memory, and neuroplasticity [88,89]. Postsynaptic NMDAR channels' permeability to calcium (Ca^{2+}) underlies their importance to phenomena mediating neuroplasticity, such as long-term potentiation (LTP) [90]. While ketamine has a lower side effect profile than PCP, it is likewise a dissociative anesthetic [91-93], thought to be caused by its NMDA antagonism [94]. However, it remains a popular option for pre-operative sedation of children, particularly those with cardiopulmonary problems [95,96], as it has a shorter half-life in this population than in adults [97]. Once administered, ketamine is eliminated quickly (within 2-4 h across different routes of administration [98-100]). Ketamine is metabolized by liver enzymes [101-104] and plasma levels are greatly diminished within a day of administration [100,105]; however, its metabolites are both metabolized and eliminated over longer time scales [105]. As an anesthetic, ketamine is administered both intravenously (IV) and intramuscularly (IM), with sedation achieved in adult patients using 1-2.2 mg/kg administered IV [106-108] and 11 mg/kg administered IM [107], leading to plasma concentrations around 9.3 μM [106]. Ketamine is also used as an analgesic, commonly for post-operative pain [109]. Analgesia is achieved in patients at lower concentrations than those required for sedation (0.15–0.25 mg/kg when administered IV [110-112] or 0.5 mg/kg when administered IM [113], leading to analgesic plasma concentrations between 0.29–0.67 μM [98,114-116]). As a pre-/peri-surgical anti-inflammatory treatment, ketamine can lower levels of pro-inflammatory cytokines [117,118] as well as be used to manage alcohol withdrawal symptoms [119], lessening the chance of relapse behaviors in alcohol use disorders [120].

Ketamine has a chiral center at the second carbon of its cyclohexanone ring and exists as a 50:50 racemic mixture of the optically active enantiomers S(+)-ketamine (esketamine) and R(-)-ketamine (arketamine) (**Fig. 1.1**). Esketamine binds to the PCP site of the NMDAR approximately four times more strongly than arketamine (esketamine: K_i = 0.3-0.69 μM; arketamine: K_i = 1.4-2.57 μM [94,122,123]), which appears to explain why esketamine is more potent than either arketamine or racemic ketamine as an anesthetic [99,124] and analgesic [94,125]. There is evidence that esketamine and arketamine have different side effect profiles, as arketamine was associated with fewer

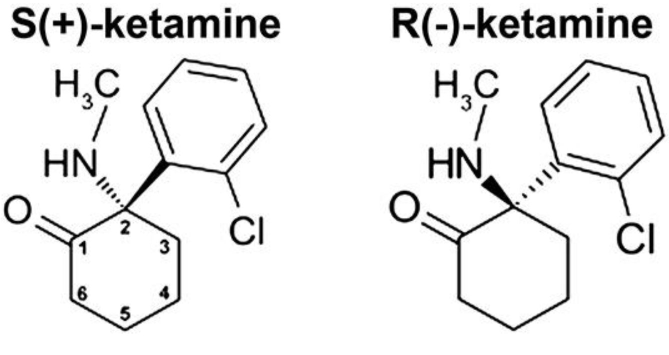

Figure 1.1. Ketamine has a chiral center at the second carbon of the cyclohexanone ring, attached to chlorobenzene and methylamine groups. (Adapted from Fig. 1 of [121].)

psychotomimetic events in both an analgesic regimen [125] and among healthy controls [94,99,126]. Ketamine metabolism is also stereospecific [116], and all metabolites likewise retain chiral centers; the enantiomers do not interconvert *in vivo* [127]. All these features allow for the independent study of each enantiomer and its effects on human physiology.

1.3. Ketamine as a Rapidly Acting Antidepressant (RAAD)

Ketamine was first shown to exert antidepressant effects in a rodent model with depression-like symptoms induced by administration of reserpine [128]. Subsequently, other rodent studies assessing the antidepressant action of various NMDA antagonists demonstrated amelioration of depression-like behavior [129-132]. There was an indication that ketamine had antidepressant effects on humans, first noticed in a general population of psychiatric patients [133], but it was only in 2000 that the first placebo-controlled trial of ketamine was conducted for patients with MDD [134]. In this small study, patients receiving 0.5 mg/kg of IV ketamine over a 40 min period experienced changes in self-reported symptoms within a day of treatment, with effects extending out to several days post-infusion. A later double-blind placebo-controlled randomized trial among patients with treatment-resistant depression (TRD; patients who fail to receive therapeutic relief from two or more SSRI compounds) confirmed the rapid relief of symptoms after the same treatment regimen as implemented in the previous study [135]. Self-reported symptoms were relieved within hours of infusion, and over a third of the treatment group experienced remission or greater than 50% response up to a week afterward (**Fig. 1.2**). Further studies have replicated these findings using the same infusion parameters, accounting for ketamine’s nonspecific sensory effects by administering midazolam to controls [136], extending the utility of ketamine to treat patients with BPD [137], using ketamine to treat acute suicidal ideation [138,139], and exploring the effect of repeated doses on mood as well as side effects [140,141]. Other follow-up studies have investigated clinical dose-response outcomes [142-144], and several meta-analyses have confirmed that ketamine infusion exerts rapid and long-lasting antidepressant effects on MDD patients [145,146]. Compared with plasma concentrations among patients receiving IV ketamine for anesthesia and analgesia, antidepressant doses result in plasma concentrations an order of magnitude lower than the former but similar to the latter (0.32-0.78 μM [116,144,147]).

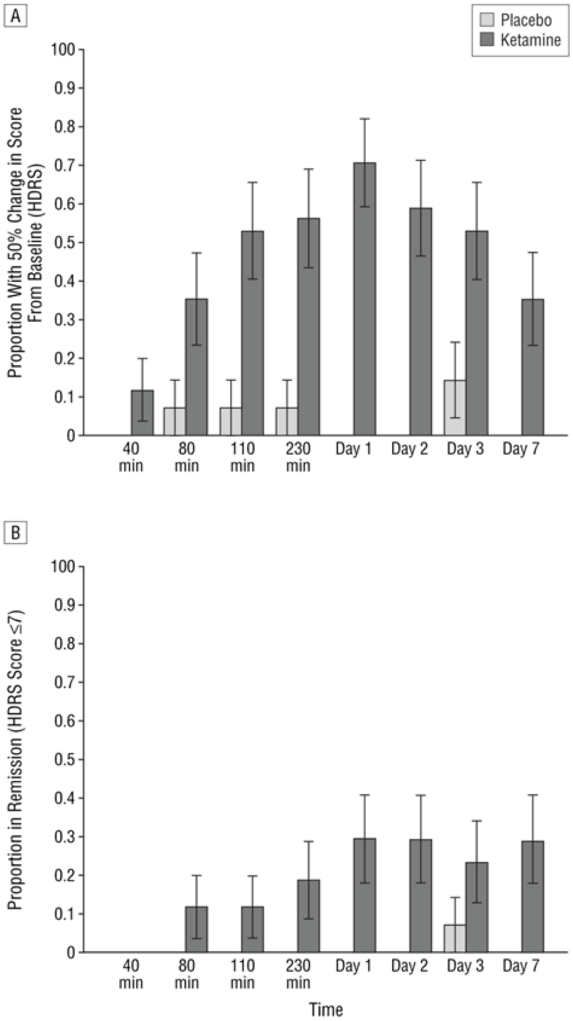

Figure 1.2. ***(A)*** Proportion of responders to ketamine or placebo treatment with greater than 50% clinical response (as measured by the Hamilton Depression Rating Scale (HDRS)) over time. ***(B)*** Proportion of responders to ketamine or placebo treatment in clinical remission (HDRS ≤ 7) over time. (The graphs display mean values and SEM; adapted from Fig. 3 of [135].)

Ketamine infusion is the most common mode of administration because of the rapidity with which plasma levels reach target concentrations, but this route of administration may present challenges to clinics with fewer resources as well as incur additional risks for patients seeking treatment. IM injections have high bioavailability in adults [98] but present similar structural barriers as the IV route, and oral administration can only achieve a bioavailability of 24% [148] due to efficient metabolism by liver enzymes [116]. In contrast, intranasal (IN) administration has proved efficacious across ketamine's various applications as well as easier to implement in the clinic. IN bioavailability is higher than from oral administration (45%) [100], due in part to rapid entry into plasma through the nasal mucosa and from bypassing first-pass metabolism by the liver [116]. A placebo-controlled study administering antidepressant doses of ketamine to patients with MDD demonstrated significant relief of depression symptoms within a day [149], and, overall, there appears to be little difference in short-term antidepressant efficacy between the IV and IN routes [150].

As mentioned, esketamine has a higher affinity for the PCP site of the NMDAR than does arketamine [94,122,123]. Because the NMDAR has been proposed as the main target through which the antidepressant effects of ketamine are mediated, esketamine became the focus of ensuing studies which aimed to increase the potency of the antidepressant response while limiting side effects. Esketamine has since demonstrated efficacy across various clinical trials [151-154], though it might be less efficacious among the elderly [155] and all of the studies demonstrating clinical efficacy had patients on both esketamine nasal spray as well as an oral antidepressant (such as an SSRI). Indeed, this latter regimen is the basis for the 2019 approval by the FDA of the intranasal esketamine formulation Spravato® (Janssen Pharmaceuticals) for the treatment of TRD. Currently, ketamine monotherapy in any formulation is not approved for the treatment of MDD, though ketamine clinics which dispense IV racemate off-label have become popular over the last several years [156].

Although ketamine provides clinical benefit to many types of patients, it has also been used as a drug of abuse by people seeking to experience its dissociative and hallucinatory effects [157-159]. Indeed, these are among the major side effects of clinically administered esketamine [160], which is one of the main reasons that it is given under the supervision of a healthcare professional. For the treatment of TRD, esketamine is administered semimonthly after a four-week loading phase, and, after each administration, patients are monitored for 2 h [161]; these practices are based on the initial landmark randomized double-blind placebo-controlled clinical trial [135]. The side effects of IN esketamine are typically transient [161] and occur within the 2 h mandatory post-administration monitoring period; for example, dissociation (as measured by Clinician-Administered Dissociative States Scale, or CADSS) tends to peak 40 min post-administration but resolves within 2 h [151]. Other common side effects of antidepressant doses of IN esketamine include altered gustation, dizziness, hallucinations, euphoria, nausea and vomiting, paresthesias, and headache [161]. Long-term ketamine abuse is associated with decreases in brain volume as well as cognitive deficits [162], though there is as yet no evidence of any long-term side effects from ketamine or esketamine administered for the treatment of MDD.

1.4. Other RAADs

Since the repurposing of esketamine for use as a RAAD, interest has arisen in evaluating other compounds which may also rapidly relieve the symptoms of MDD. The most obvious candidate compound is arketamine, which was initially less compelling than esketamine owing to its fourfold lower potency for the PCP site of the NMDAR and the hypothesis that NMDA inhibition was the main mechanism by which ketamine relieves depression. However, arketamine's lower side effect profile [94,125,126] and lower sedative potency [99] was cause for reevaluation of its role as a viable treatment for MDD.

The first dedicated study investigating the antidepressant potential of arketamine in a rodent model of depression, induced by neonatal dexamethasone exposure, found that while 10 mg/kg IP injections of esketamine or arketamine significantly lowered immobility times in the tail suspension test (TST) and forced swim test (FST) — classic tests of futility behavior used in the development of classic antidepressants [163,164] — and significantly increased sucrose preference (a proxy for anhedonia [165]) in the sucrose preference test (SPT) compared to controls [166]. Interestingly, one week after the initial dose of es- or arketamine, rodents treated with arketamine showed persistent effects, whereas rodents treated with esketamine did not [166]. A follow-up study using two different rodent models of behavior-induced depression, LH [167] and social defeat stress (SDS) [168] (treated with IP injections of es- or arketamine at 20 mg/kg), found that arketamine more potently lowered immobility time in the TST and FST for SDS rodents than esketamine as well as significantly increased anti-anhedonic effects in the SPT compared to esketamine within one day of injection [169] (**Fig. 1.3A-C**); these effects also persisted for almost a week post-treatment, with both enantiomers demonstrating continued antidepressant effects but with arketamine demonstrating greater efficacy than esketamine (**Fig. 1.3D-F**). In the LH model, only arketamine significantly reduced escape failures as well as escape latency versus controls, while esketamine did not; these effects likewise persisted for nearly a week [169] (**Fig. 1.3G**). Additionally, esketamine caused hyperlocomotion, increased pre-pulse inhibition, and increased conditioned place preference (CPP; a test of addiction behavior [170]) compared to arketamine, suggesting that esketamine is associated with greater psychomimetic side effects and addictive behavior than arketamine [169], with both effects corroborated by evidence from a non-human primate (NHP) PET study which showed that esketamine, but not arketamine, caused striatal DA release [171], a marker of addiction. A subsequent experiment using a treatment-refractory rodent model of depression (induced with repeated injections of corticosterone [172], the rodent equivalent of cortisol) found that, while IP injections of 10 mg/kg of either es- or arketamine administered both 1 d and 30 min prior to testing significantly reduced immobility time in the FST, only arketamine reduced immobility time when a single injection was given 1 d prior; additionally, brain concentrations of the two enantiomers were not significantly different, suggesting that any differences in the antidepressant

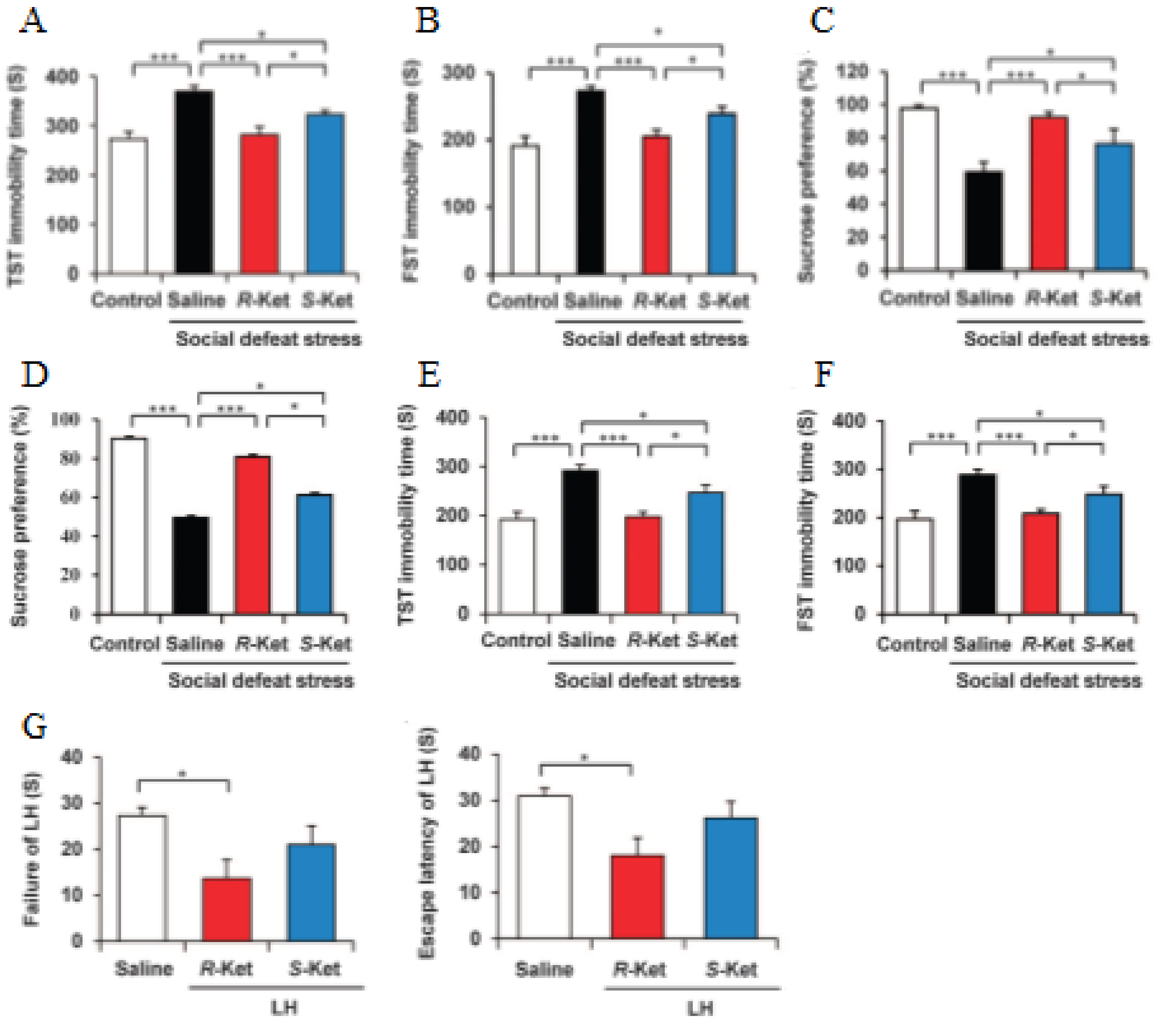

Figure 1.3. TST (***A***), FST (***B***), and SPT with 1% solution ***(C)*** performed on male adult C57BL/6 mice 1 d after the administration of saline, arketamine (10 mg/kg), or esketamine (10 mg/kg) injected IP. ***(D)***, ***(E)***, and ***(F)*** show the same tests performed one week later. ***(G)*** Male Sprague Dawley rats performed a LH task 5 d after the administration of saline, arketamine (20 mg/kg), or esketamine (20 mg/kg) injected IP, with escape failures (*left*) and escape latency *(right*) quantified. (Graphs show mean values plus SEM; *P < 0.05, **P < 0.01, ***P < 0.001; adapted from Fig. 1 of [169].)

effects of the two enantiomers is not a result of unequal pharmacokinetics [173]. Additional findings include verification of the potent and long-lasting antidepressant effects of arketamine (and its pharmacokinetic similarity to esketamine) [174] in rodent models of depression [175], the possibility that esketamine — but not arketamine — causes loss of parvalbumin-positive

(PV+) neurons (associated with psychosis [176]) in several brain regions in rodents [169,177], that direct administration of arketamine into several brain regions can reduce escape failures in LH model rodents [178], and that arketamine may stabilize the levels of gut microbes contributing to SDS-induced behavior [179]. These results suggest that, across various rodent models of depression, arketamine exerts more potent antidepressant effects, raising questions as to whether NMDAR antagonism is the chief mechanism by which ketamine relieves the symptoms of MDD [180]. To date, several clinical trials are underway to assess arketamine as an antidepressant in an IV formulation [181,182], with one trial showing significant reduction in clinical depression scores 1 d post-infusion without a concomitant increase in clinical dissociation scores [181].

Even more recently, RAAD research has expanded to consider several primary and secondary metabolites of ketamine. Within the major metabolic pathways, racemic or (R,S)-ketamine is metabolized stereospecifically by CYP liver enzymes into (R,S)-norketamine (NK), and then further into the secondary metabolites (R,S)-dehydroxynorketamine (DHNK) and various (R,S)-hydroxynorketamine (HNK) subtypes [116,183] (**Fig. 1.4**). In the latter group, all molecules retain the chiral site at the sixth position while another is added at the 2nd, 4th, or 5th positions of the cyclohexanone ring [116]. Minor pathways produce 4- and 6-hydroxyketamine (HK) as well as (2R,6R;2S,6S)-HK primary metabolites [116]. These metabolites can appear as early as 40 min after the end of IV infusion [105,147] and reach peak plasma levels within 4 h [105], with the eventual ratio of (S)-metabolites to (R)-metabolites always less than one [105,184]. In rodents, both the parent compounds and metabolites accumulate in the brain within 10 min post-infusion [185-188], with at least one study reporting higher concentrations of (S)-metabolites than (R)-metabolites in the brain [186], though with no appreciable difference in

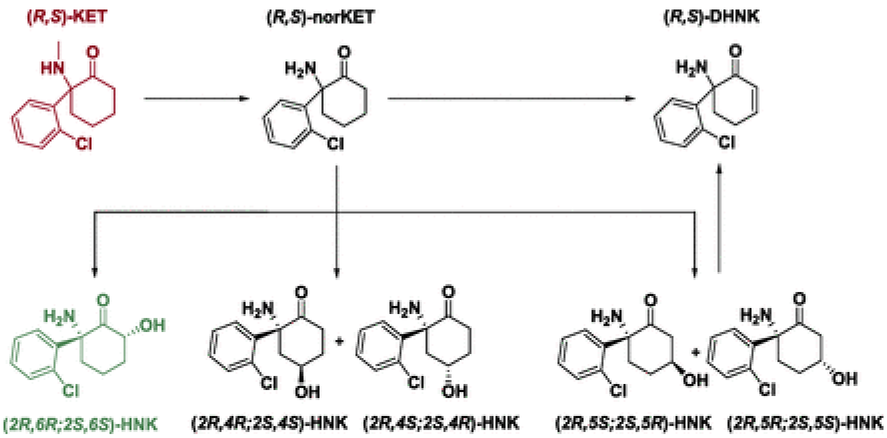

Figure 1.4. The major metabolic pathways of ketamine. (Adapted from Fig.1 of [116].)

the brain-to-plasma ratio of either set of enantiomers indicative of enantioselective uptake [116]; additionally, all metabolites cross the blood-brain barrier (BBB) less effectively than the parent compound [174]. In humans, while ketamine in plasma drops below detection within one day of an IV antidepressant dose (0.5 mg/kg over 40 mins), DHNK and the HNKs can be detected at 3 d post-infusion in patients suffering from chronic pain [184] and in BPD patients [105]. Interest in the potential antidepressant effects of ketamine metabolites was generated from studies which raised questions about the relationship between ketamine metabolism and therapeutic relief [105,147], and there was even an indication that the metabolism of ketamine was correlated with both better clinical response as well as side effects [147]. Earlier studies had considered (R,S)-ketamine and (R,S)-NK to be the active compounds in achieving anesthetic effects [186], while the various HNKs were thought to be inactive by-products [123]. Because the former two compounds act primarily on NMDARs, this was considered ketamine's main antidepressant mechanism. However, once subanesthetic doses began to show promise for treating MDD, the picture regarding the activity of the various metabolites became more complex. Indeed, unlike the parent racemate or (R,S)-NK, (2R,6R;2S,6S)-HNK inhibited α7 nicotinic acetylcholine receptors (nAChRs) at sub-micromolar levels while not inhibiting NDMARs at physiologically relevant concentrations [123,189]. However, inhibition of α7 nAChRs may in fact drive inhibition of NMDARs due to downstream attenuation of serine racemase which causes a decrease in the production of serine, a co-agonist of the NMDAR [188,190]. Initially, (2S,6S)-HNK was proposed as a candidate antidepressant owing to its sub-nanomolar potency in phosphorylating mTOR [187], a key target for antidepressants [191] (see Chapter 1.7), leading to the hypothesis that (2S,6S)-HNK mediates its antidepressant effects through downstream mechanisms ultimately culminating in indirect NMDAR inhibition via regulation of serine racemase while avoiding some of the side effects which direct inhibition of NMDARs can elicit. Yet it was in fact (2R,6R)-HNK which demonstrated stronger antidepressant effects in an important study investigating the antidepressant activity of ketamine metabolites in rodent models of depression [174]. Owing to evidence that (2R,6R;2S,6S)-HNK is the major ketamine metabolite in human plasma during the hours after administration of antidepressant doses [147], this study investigated the antidepressant potential of both of these metabolites in further detail using mice undergoing SDS induction of depression as well as mice injected repeatedly with corticosterone to induce anhedonia. Ketamine was deuterated at the C6 carbon to slow its metabolism into (2R,6R;2S,6S)-HNK without changing its pharmacological properties [192], and while the parent compound’s binding affinity to NDMARs was not affected, metabolism was slowed such that brain levels of the secondary metabolites were lowered substantially post-administration of racemic ketamine (**Fig. 1.5A-C**); this altered metabolism led to a lack of reduction in immobility time in the FST test 1 d (but not 1 h) post-administration compared to racemic ketamine and a lack of reduction in escape failures on a LH task with the same post-

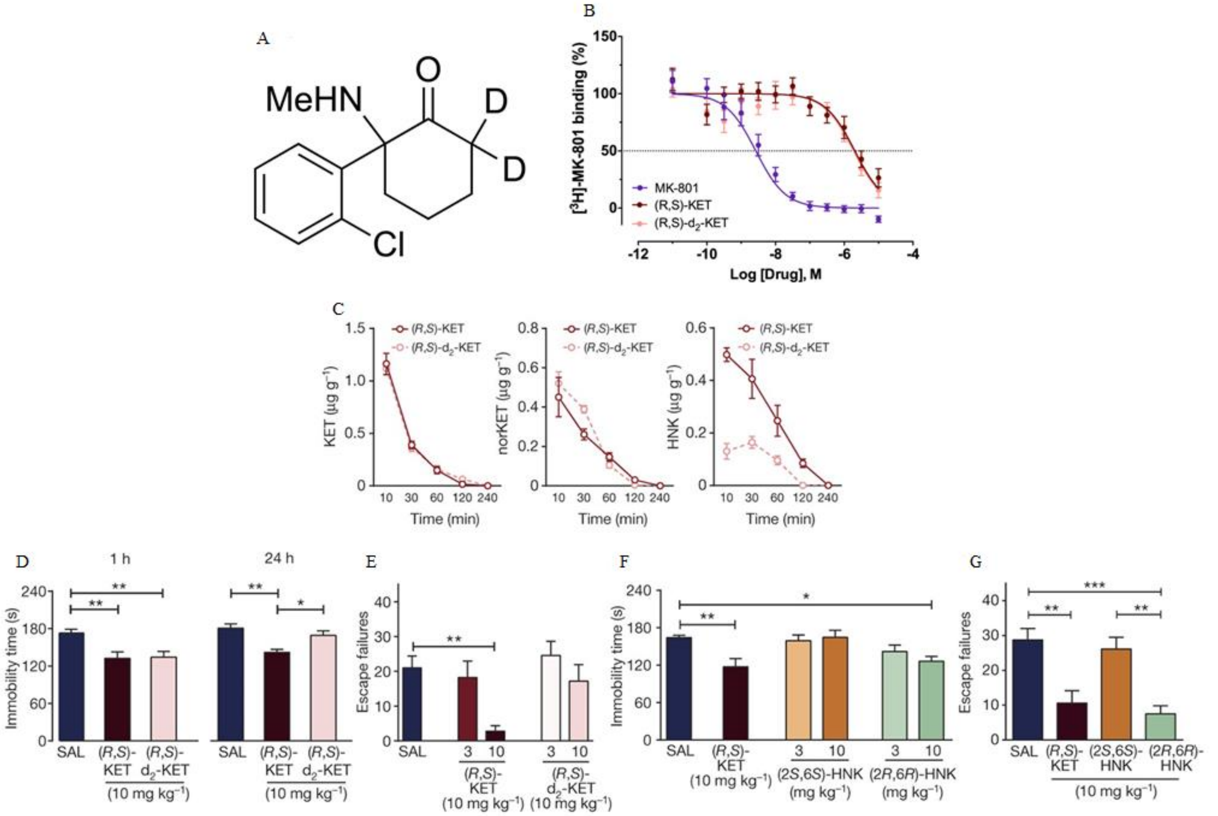

Figure 1.5. ***(A)*** The structure of 6,6-dideuteroketamine (d_2-KET) with deuteration at the C6 carbon). ***(B)*** Both (R,S)-KET (*red*) and (R,S)-d_2-KET (*orange*) have the same NMDAR binding affinity. ***(C)*** Brain levels of KET (*left*), (R,S)-NK (*middle*), and (R,S)-HNK (*right*) after administration of (R,S)-KET (*red*) or (R,S)-d_2-KET (*pink*). ***(D)*** Administration of both (R,S)-KET (*red*) or (R,S)-d_2-KET (*pink*) at 10 mg/kg improves immobility time in the FST 1 h post-treatment over saline-treated rodents (*blue*), but only (R,S)-KET (*red*) demonstrates a comparable reduction after 24 h. ***(E)*** In a LH task 24 h after treatment, 10 mg/kg (*dark red*) — but not 3 mg/kg (*red*) — (R,S)-KET reduces escape failures while no amount of (R,S)-d_2-KET (*white* and *pink*) does. ***(F and G)*** 24 h before the FST and LH task, various doses of (R,S)-KET, (S)-HNK, and (R)-HNK are administered; whereas no dose of (S)-HNK has significant effects versus saline treatment (*blue*), 10 mg/kg of (R)-HNK decreases immobility time on the FST ***(F)*** and decreases escape failures in the LH task ***(G)***. (Adapted from Fig. 1 and Extended Data Fig. 5 of [174].)

treatment latency [174] (**Fig. 1.5D-E**). Then, to compare between the two HNK enantiomers, each was administered separately 1 d before the FST and LH task to rodents, and it was found that (2R,6R)-HNK exerted more potent antidepressant effects than (2S,6S)-HNK (**Fig. 1.5F-G**), extending out to 3 d and demonstrating dose-dependency while not resulting in higher brain levels of either compound versus its enantiomer [174]. Additionally, the side effects induced by direct administration of (2R,6R)-HNK were virtually nonexistent (unlike with racemic ketamine), including lack of hyperlocomotion and addiction behavior [174]. These results spurred renewed interest in investigating the therapeutic potential of other RAAD candidates, generating questions regarding the putative antidepressant mechanism of ketamine. Follow-up studies have since complicated the picture regarding (2R,6R)-HNK's antidepressant effects, with a direct comparison of arketamine to (2R,6R)-HNK in two rodent models of depression finding that FST and TST immobility time were lowered from administration of the former but not the latter and that SPT percentage was not appreciably increased, which persisted out to one week post-administration [175]. Indeed, the authors suggest that, since direct administration of arketamine to certain brain regions corresponded with antidepressants effects in a rodent LH model, arketamine itself can exert antidepressant actions [178]. These findings were corroborated in a follow-up study from the same group in a rodent LH model [193]. Conversely, another follow-up study found that both IP and intra-cortical injections — into the medial prefrontal cortex (mPFC) — in WT mice induced significant increases in swimming duration from both racemic ketamine as well as (2R,6R)-HNK; additionally, both compounds induced increases in extracellular 5-HT in the mPFC via both routes of administration [194]. A comment on the Zanos et al., 2016 study [174] noted that (2R,6R)-HNK can in fact inhibit NMDARs to a significant degree [195], but this high of a concentration is not relevant to the doses of (2R,6R)-HNK used in the referenced study wherein (2R,6R)-HNK IP at 10 mg/kg was injected, reaching a final brain concentration of 10.69 μM [174,196]. Furthermore, another follow-up study reported rapid and sustained antidepressant effects of (2R,6R)-HNK in a rodent LH model compared to control on both the FST and SPT which also corresponded with normalization of neural activity in the ventrolateral periaqueductal gray (vlPAG) from both IP and intra-vlPAG injections [197], while yet another demonstrated the antidepressant effects of 10 mg/kg IP injections of (2R,6R)-HNK in control rodents assessed via FST as well as the novelty-suppressed feeding test (NSF) (which assesses fear induced by novel environs [198]) as well as confirmed that (2R,6R)-HNK inhibits NMDARs at concentrations well above those relevant to administered amounts requisite to induce antidepressant responses (e.g. ~8 μM extracellular concentrations in the hippocampus (HC) [199]). Possible explanations for the discrepant results include the lack of a direct comparison of arketamine to (2R,6R)-HNK [174,194,197,199], differences among the various depression models used, and sex-specific differences in rodent behavior and responses to antidepressant compounds [174]. Besides having a potentially lower side effect profile than ketamine [174,200], an advantage of using (2R,6R)-HNK is that its oral bioavailability is 46-52% in mice and 42% in rats [200] (similar to that seen with (2S,6S)-HNK in rats [188]), far higher than racemic ketamine (24% [148]); crucially, the oral route of administration would present fewer challenges to patients in need of treatment. Currently, at least one clinical trial [201] is underway to assess the safety and efficacy of IV (2R,6R)-HNK. In a study examining the antidepressant and side effects of both (R)-NK and (S)-NK in two rodent models of depression, (S)-NK was found to significantly decrease FST and TST immobility time over controls, whereas (R)-NK did not, though both did significantly improve anhedonia in the SPT as well as attenuated stress-induced reductions in dendritic spine density in both the mPFC and dentate gyrus [202]. Additionally, (S)-NK did not cause pre-pulse inhibition deficits, a marker of psychomimetic dysfunction [203] nor increased CPP scores; and PV+ spine density in the mPFC was decreased by esketamine but not by (S)-NK, implying the former’s psychomimetic potential [202]. In all, these results suggest that several primary and secondary ketamine metabolites potentially offer RAAD treatment of MDD symptoms but with a lower side effect profile.

Several other new/repurposed compounds have shown the potential to act as RAADs. A class of designer drugs based on ketamine has garnered attention over the past decade based initially on anecdotal reports suggesting relief of symptomatic depression [204-207]. The first drug from this class to offer intriguing results is methoxetamine (MXE), a ketamine analog, synthesized for recreational use in 2010 to mimic the dissociative effects of ketamine at lower concentrations while mitigating against ketamine’s urotoxicity [208] (though chronic MXE use may indeed lead to bladder and renal toxicity [209]). Like ketamine, MXE is thought to act as a noncompetitive NMDAR antagonist, with slightly higher affinity (K_i = 0.259 μM) than ketamine (K_i = 0.659 μM) for the same PCP site [210]; it was also shown to inhibit SERT at low concentrations (K_i = 0.481 μM [210] and IC_{50} = 2 μM [211]), unlike ketamine and more potently than PCP (K_i = 2.234 μM [210]), and it can also inhibit the NE transporter (NET; IC_{50}= 20 μM) and the DA transporter (DAT; IC_{50}= 33 μM) [211], unlike ketamine [210]. In a rodent study, MXE was found to fully generalize to ketamine in an operant conditioning task assessing psychomimesis in a dose-dependent manner, indicating similar subjective effects [212], and it also demonstrates the typical dose-dependent ketamine profile of inducing anxiogenic effects at lower doses while acting as a dissociative anesthetic at higher doses [213,214]. MXE's effects endure for longer than those of ketamine in rodents [213,215], consistent with case reports and testimony from users [204,205], reaching peak concentration in the brain slower than ketamine (30 min [213] versus within 10 min [185-188]) but at a higher maximal concentration (~17 μM [213] versus ~9 μM [215]) as well as being undetectable after 6 h [213] (as opposed to within 2 h with ketamine [215]). MXE also appears to undergo far less extensive hepatic metabolism than ketamine, with 75% of MXE injected into rodents extracted unchanged after one day [213]. A study of the antidepressant effects of MXE on WT rodents indicates that it can rapidly decrease immobility time in the TST and FST as well as decrease anhedonia in the SPT in a dose-dependent manner, similar to ketamine with perhaps more potent effects [216]. MXE is a racemic compound with the same chiral site as ketamine, but, unlike ketamine, (S)-MXE has a lower binding affinity for the PCP site of the NMDAR (K_i = 0.633 μM) than (R)-MXE (K_i = 0.481 μM); there does not appear to be much of a difference with respect to SERT binding between the two (IC_{50} = ~2 μM [217]). The racemate and both enantiomers produced both rapid (30 min) and sustained (1 d) antidepressant effects in a CUS rodent model, but (R)-MXE produces less anxiogenic side effects than either the racemate or (S)-MXE, similar to the relationship between the ketamine enantiomers [217]. To date, no clinical trials have been conducted or are underway assessing MXE as an antidepressant for human use. Side effects among users include dissociation, dizziness, altered sensorium, and nausea, similar to ketamine [204,218,219]. However, MXE has also been linked to seizures, hyponatremia, bradycardia, acute cerebellar toxicity, and even death [213]. Other ketamine-like designer drugs such as the deschloroketamine family [220] and MXE analogs [221] have potential antidepressant effects which remain to be studied further, based both on case reports from human users as well as on pharmacological and pharmacokinetic profiles characterized in rodents.

A surprising and chemically distinct RAAD is the muscarinic antagonist scopolamine. Scopolamine (also called hyoscine) is a tropane alkaloid derived from plants of the *Solanaceae* family [222]. It is an anticholinergic with both peripheral and central effects used to treat motion sickness and postoperative nausea but which can also induce the classic anticholinergic symptoms of tachycardia, hypertension, agitation, sweating, mydriasis, dry mouth, and abdominal symptoms, as well as inducing dizziness, restlessness, excitement, hallucinations, stupor, coma, and even death at higher doses [222]. It is optically active, and the relevant isomer is S-(-)-scopolamine [222,223]. Scopolamine has limited oral bioavailability (13%), so it is administered transdermally for the treatment of motion sickness owing to the relatively high risk of side effects (0.5 mg is released over a period of 3 d [223]). Oral and IM administration lead to maximum plasma levels within 30 min, and its half-life is 8 h; additionally, scopolamine is thought to penetrate the brain more readily than other antimuscarinics because it is a weak base [224], similar to other RAADs (see Chapter 1.5). The use of antimuscarinics for depression stretches back to the advent of TCAs (which likewise induce anticholinergic side effects [225]), and it was originally thought that their antimuscarinic actions were features which later antidepressants should avoid [226]. However, an early theory postulated that an imbalance between cholinergic and adrenergic function in limbic nuclei contributes to the pathogenesis of affective disorders, with hypercholinergic action inducing symptoms of depression and hyperadrenergic action leading to mania [225]. Reserpine, which has been shown to induce depression-like effects in both humans [34,35] and animals [36-38], also has cholinomimetic effects on human patients [227,228]. Furthermore, physostigmine, an acetylcholinesterase inhibitor, has also been found to exacerbate the symptoms of depression in MDD patients [229,230], and responses to cholinomimetics among MDD patients are exaggerated [231]. One of the first compelling findings demonstrating scopolamine's potential as an antidepressant was a sleep study which reported that MDD patients experienced some relief of depression 1 d after an IM injection of 0.4 mg scopolamine [232], though the size of the doses used were likely too low to induce a consistent effect [224]. The first evidence collected in an RCT among both MDD and BPD patients demonstrated that scopolamine can induce a significant reduction of symptoms in as little as 3 d (**Fig. 1.6**); at a concentration of 4 μg/kg, the treatment was tolerated well by patients receiving 15 min infusions 3-4 d apart across three total sessions, with no serious adverse effects reported and most minor side effects resolving within 4 h [231]. Another arm of the study indicated that scopolamine relieved symptoms in a dose-dependent manner, confirming that the amount administered is crucial to determining the therapeutic window [231,232]. These

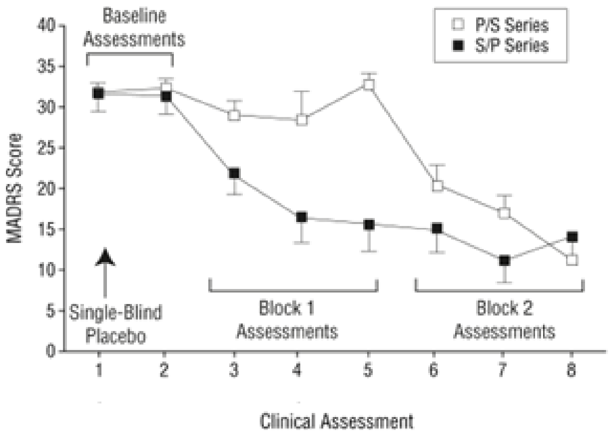

Figure 1.6. Mean Montgomery-Asberg Depression Rating Scale (MADRS) scores for the placebo/scopolamine (P/S) group and the scopolamine/placebo (S/P) group across eight assessments (3-4 d apart). Two baseline, three Block 1 (P or S), and 3 Block 2 (S or P) assessments are shown. (Graphs are mean values with SEM; all differences across time points are $P < 0.001$; adapted from Fig. 3 of [231].)

findings were replicated in a study of MDD patients only, and the effects were seen to persist for two weeks or more after the last infusion session [233], indicating a potential role for other mechanisms apart from nonspecific muscarinic acetylcholine receptor (mAChR) blockade [234]. The broad-spectrum antimuscarinic activity of scopolamine can be compared to another antimuscarinic antidepressant candidate, biperiden, which is selective for the M_1 mAChR and was found to not significantly relieve depression compared to the central nervous system (CNS)-excluded anticholinergic glycopyrrolate [235], suggesting that scopolamine's nonspecific activity is crucial to its antidepressant effect [234]. Another follow-up study reported that the antidepressant response to scopolamine was stronger in women than men [236], corroborating previous findings demonstrating that HPA responses to cholinergic stimulation are more pronounced in premenopausal women with MDD [237,238] and that variation in the *CHRM2* gene, which encodes for the M_2 mAChR, was associated with the prevalence of MDD in women but not men [239]. Additional analyses confirmed that BPD patients benefited as significantly and as rapidly as MDD patients in the previous studies from scopolamine administration [240] and that patients can be classified using baseline clinical rating scales in order to predict who will benefit from treatment with scopolamine [241]. However, results from several studies published subsequently have complicated the picture regarding the efficacy of scopolamine as an antidepressant. First, an attempt to replicate previous results using the same trial design — two blocks of three 15 min infusion days (one for placebo treatment and one for scopolamine infusion) with 3 d in between [231] — failed to find an antidepressant effect from scopolamine [242]. The patient population in this study appeared to have been more severely depressed on average as well as included a higher proportion of TRD patients than previous studies, of interest because treatment-naïve patients may respond more strongly to scopolamine infusion [231,233,242,243]; notably, patients with TRD were previously found to benefit from scopolamine infusion [243]. Thus, it might be that there is more variation among more severe (in terms of degree of symptoms as well as lack of treatment response) patients in their response to scopolamine infusion. A recent clinical trial in which scopolamine was delivered via IM injection to patients receiving oral escitalopram treatment found that there was no significant difference in short-term or long-term response rates among treatment groups (high-dose scopolamine, low-dose scopolamine, and placebo) [244], which could indicate that methods other than IV administration will face challenges in terms of clinical efficacy or that scopolamine works best as a monotherapy for a population of predominantly treatment-naïve MDD patients. A more recent trial from New Zealand comparing patients receiving a single infusion of scopolamine to patients receiving a single infusion of glycopyrrolate found that both groups experienced significant decreases in MDD symptoms by 3 d post-treatment but that there was no significant difference between treatment with either drug, including in terms of adverse effects [245]. Possible explanations for these results include the importance of blinding patients to the effects of treatment versus placebo by using another medication as a control [231,233,235,245], the involvement of the peripheral nervous system in the antidepressant effects of scopolamine (and potentially other antimuscarinics) [235], and the failure to consider different MDD etiologies between the sexes [236]. Overall, while compelling, scopolamine as a RAAD is potentially limited by group-specific effects as well as a higher barrier to entry for use due to IV administration.

Other RAAD candidates encompass a broad array of putative physiological mechanisms. Two of the more interesting and unique compounds are rapastinel, part of a larger class of NMDAR modulators, and allopregnanolone, a naturally occurring metabolite of progesterone. Rapastinel is derived from the monoclonal antibody B6B21 [246] and appears to act as an agonist at the glycine site of the NMDAR, enhancing the ability of NMDA antagonists to bind to the channel pore [247]. It has been shown to both enhance cognitive function [248-251] as well as to have antidepressant effects similar in magnitude and rapidity to ketamine (within 1 d post-administration) [251,252] in rodents. Rapastinel has shown promise in treating MDD by inducing antidepressant effects within 1 d of IV administration in two different Phase II clinical trials [253,254], but in 2019 it failed to differentiate from placebo during Phase III clinical trials as a weekly IV adjunct to oral antidepressant treatment [255]. The derivative compounds apimostinel and zelquistinel are more potent agonists of the NMDAR glycine site [256,257], with the former in both Phase I [258] and Phase II [259] clinical trials (both having completed recruitment without yet posting results) and the latter demonstrating antidepressant effects in rodent models of depression [257]. The second unique RAAD compound, allopregnanolone, is a neurosteroid which has activity both in peripheral targets like the adrenal glands and gonads as well as in the brain [260]. It is synthesized from progesterone in a two-step process via the enzymes 5α-reductase and 3α-hydroxysteroid-dehydrogenase [260]. Neural allopregnanolone is produced independently of peripheral glands in response to acute stress [261] in both glutamatergic and GABAergic neurons across several brain areas [262]. Its main function in the brain is as a positive allosteric modulator of $GABA_A$ neurons (similar to benzodiazepines but with an order of magnitude higher potency), potentiating Cl^- flux at concentrations as low as 10 nM [263]; interestingly, unlike benzodiazepines, which bind only intra-synaptically, allopregnanolone also binds to GABAergic neurons at other sites [264]. Rodents experiencing chronic stress were found to have downregulated allopregnanolone production in brain regions involved with anxiety and depression [265,266]; in humans, MDD severity is correlated with decreased allopregnanolone production [267]. Typically, plasma levels of allopregnanolone rise throughout pregnancy [268] before decreasing after childbirth [269], and serum allopregnanolone has been found to be lower in some women experiencing symptoms of postpartum depression (PPD) [269]. The development of a treatment paradigm for patients accounted for allopregnanolone's low plasma solubility, low oral bioavailability, and rapid metabolism [270] in a soluble proprietary form, brexanolone, synthesized for IV administration. Current protocols involve infusing brexanolone (30-60 μg/kg) for 60 h during inpatient care, with infusion rate adjusted to account for tolerability and side effects [270]. Both Phase II and Phase III trials have demonstrated that brexanolone significantly reduces the symptoms of PPD versus placebo after the 60 h treatment period, and these effects persisted out to one month post-treatment with few side effects [270,271]. Brexanolone has since been approved for treating PPD by the FDA in 2019. Owing to its rapid effects and good safety profile, coupled with a desire to decrease the barriers for patients to receive treatment, an oral formulation, SAGE-17, has shown promise in a Phase II clinical trial for the treatment of MDD, with relief of symptoms within two weeks [272].

The most compelling aspect of the therapeutic potential of RAADs is how fast they exert their effects compared to SSRIs (within a day versus weeks to months). The reasons why are as yet unclear, so we must first explore the various properties which these compounds might share in common, with an eye to what contribution each makes to their distinctive efficacy.

1.5. General Properties of Antidepressants

Two important properties of biochemical compounds have significant effects on a drug's ability to cross membranes, a crucial indicator of therapeutic potential. The acid dissociation constant, pK_a, measures the tendency of a chemical species to gain or lose hydrogen ions (H^+) in aqueous solution at a specific pH. An important implication of this concerns physiological pH (7.4): if the pK_a is higher, more molecules will exist in their protonated form; and if lower, then more will exist in their deprotonated form. Owing to the composition of the plasma membrane (PM), uncharged molecules can much more easily diffuse across than their charged counterparts (given roughly equivalent molecular charge distribution and steric interactions). For several RAADs, such as ketamine (pK_a = 7.5 [183]), (2S,6S;2R,6R)-HNK (pK_a = 6.89, predicted from Chemicalize), MXE (pK_a = 7.83, predicted from Chemicalize), and scopolamine (pK_a = 7.55-7.81 [273]), ~50% of the compound in solution will be deprotonated, meaning that a significant percentage can cross through the lipid membranes of cells as well as into intracellular compartments. In the aforementioned RAADs, protonation occurs at the nitrogen in their amino group (**Fig. 1.7**). The second property is described by the partition coefficient, LogP, which measures solubility in two immiscible solvents (octanol and water) at room temperature; LogP is then a ratio between lipophilicity and hydrophilicity. Compounds which are more lipophilic (LogP > 0) can more easily cross nonpolar lipid membranes, whereas more hydrophilic compounds (LogP < 0) will not, owing to interactions with phospholipid head groups. Thus, LogP can determine the availability of potential neuropsychiatric compounds in the brain, as crossing the BBB is necessary for any psychoactive molecule to exert its effects. However, a limitation of LogP is that only un-ionized molecules are included in the solubility measurements; because of the ionizing effects of physiological pH, particularly on weak bases (e.g. RAADs), a significant percentage of molecules will remain excluded from the calculation. Thus, LogD, the distribution coefficient, is necessary for understanding the actions of brain-permeant weak bases, as it accounts for ionized molecules in each solvent as well (accounting for the solubility of *all* species — charged and uncharged — of a particular compound in octanol versus water). For LogD measurements, the pH is buffered to a specific value so that the introduction of the compound does not cause it to fluctuate; for medications, this is typically pH = 7.4. Thus, when expressing the LogD for a candidate pharmaceutical, it is rendered as $\text{LogD}_{\text{pH7.4}}$. It should be noted that pH can vary throughout the body, with both intracellular compartments as well as parts of the digestive tract maintaining a lower pH, thereby influencing both ionization and lipophilicity, particularly for ingested compounds.

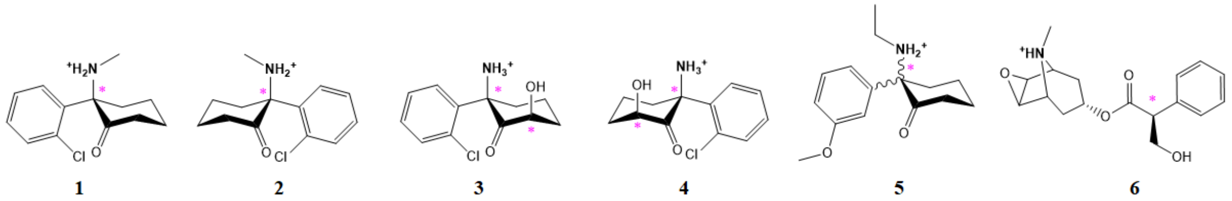

Figure 1.7. Chemical structures of arketamine (*1*), esketamine (*2*), (2R,6R)-HNK (*3*), (2S,6S)-HNK (*4*), MXE (*5*), and scopolamine (*6*). (Pink stars indicate chiral sites.)

To assess the solubility and permeability of pharmaceutical compounds to carry forward into clinical trials development so as to make the medication discovery process more efficient, a set of rules assembled by Lipinski et al. [274] based on successful Phase II trial compounds can be useful. The criteria for good oral bioavailability are: molecular weight (MW) < 500 g/mol; LogP < 5; fewer than five H-bond donors, calculated by counting amine (NH) and hydroxyl (OH) groups; and fewer than 10 H-bond acceptors, calculated by totaling nitrogen and oxygen atoms. Failure of two or more rules will drastically increase the chances of poor oral absorption, and compounds which act as substrates for biological transporters (e.g. antibiotics, antifungals, vitamins, cardiac glycosides) prove to be the vast majority of the exceptions to these rules [274]. (All reported LogP values below are calculated from Chemicalize.) For ketamine, all four criteria are met (MW = 270 g/mol, LogP = 3.35, one H-bond donor, two H-bond acceptors), which suggests that it has good oral bioavailability; however, this does not appear to bear out in clinical studies (peak oral F = 24% [148]) due to efficient metabolism by liver enzymes [116] which can prevent substantial crossing into the brain. (2S,6S;2R,6R)-HNK also appears to meet all four criteria (MW = 239.7 g/mol, LogP = 2.04, two H-bond donors, three H-bond acceptors) and does appear to have higher oral bioavailability than its parent compound (46-52% in mice and 42-46% in rats [188,200]. MXE likewise meets all criteria (MW = 247.33 g/mol, LogP = 2.94, one H-bond donor, three H-bond acceptors); as no data is available concerning its oral bioavailability, we might assume it would be somewhat higher than ketamine, owing to far less extensive hepatic metabolism (75% of MXE injected into rodents is extracted unchanged after one day [213]). Scopolamine, while comprising a much different set of functional groups than the aforementioned ketamine-class compounds, also meets all four criteria (MW = 303.35 g/mol, LogP = 0.89, one H-bond donor, five H-bond acceptors), and is known to cross into the brain more easily than most anticholinergics; however, it has limited oral bioavailability (13%), which could be due to extensive first-pass hepatic metabolism [223]. In all, these RAADs appear to differ in their oral bioavailability because of their metabolic profiles rather than intrinsic chemical properties. Meeting these criteria is not proof that a drug will be effective if administered orally, but such an assessment functions more as a means of narrowing down candidate compounds prior to investing time and money into their development. One potential interesting point of contrast exists between these RAADs and the commonly prescribed SSRIs fluoxetine and escitalopram (Lexapro®), which meet all four criteria; thus, the difference in time to therapeutic effect likely results from other factors not captured by these rules, such as receptor targets within the brain (see Chapter 1.6.1) or partitioning into membrane compartments (see Chapter 1.6.5). An update to the criteria should include reference to $\mathrm{LogD}_{\mathrm{pH7.4}}$, which could increase the chances of correctly identifying compounds likely to have high oral bioavailability. Indeed, switching to a LogD-based filter can improve the success rate of identifying medications from among compounds with the requisite lipophilicity [275].

Another key aspect of assessing the efficacy of neuropsychiatric medications is volume of distribution (V_d), a theoretical value which estimates the propensity of a drug to accumulate in extravascular compartments [276]. Because it is calculated as the ratio between the amount of drug given and the measured concentration in plasma, drugs with lower V_d (higher plasma concentration) tend to remain in the plasma, while drugs with higher V_d (lower plasma concentration) tend to extravasate into other compartments. Weak bases, such as the aforementioned RAADs and SSRIs, will tend to have higher V_d due to interactions between positively charged nitrogen atoms and negatively charged phospholipid head groups; in addition, higher lipophilicity (as measured by LogD) will also result in a higher V_d, since a higher lipophilicity will cause drugs to move out of the aqueous phase (plasma) into the membrane phase [276]. V_d is also related to the free unbound drug concentration, which can give an estimate of the amount of drug in a given dose interacting with both target and off-target receptor populations. This relationship is represented by the equation,

$$V_d = V_p + V_t \times \frac{fu_p}{fu_t},$$

where V_p is plasma volume, V_t is tissue volume, fu_p is fraction unbound in plasma, and fu_t is fraction unbound in tissue. Thus, a higher V_d corresponds to a higher fraction of unbound drug in plasma compared to unbound drug in tissue. These factors play a role in the effective dose of antidepressants; for example, the antidepressants escitalopram (20 L/kg [277]), fluoxetine (11-88 L/kg [278]), and various TCAs (10-50 L/kg [279]) have a higher V_d than ketamine (3-5 L/kg [280]), (2S,6S;2R,6R)-HNK (7.3 L/kg [188]), and scopolamine (1.4 L/kg [281]), which indicates that a lower percentage of the administered RAADs remain unbound in plasma compared to SSRIs and TCAs. Higher V_d may thus play a role in determining the time course over which antidepressant effects ensue from treatment with classic antidepressants versus RAADs.

1.6. Potential Targets for Ketamine's Antidepressant Action

Because of its importance to the entire paradigm of RAADs, focusing research efforts on ketamine will hopefully provide a starting point from which evaluations of other candidates can be performed delineating their pharmacological, physiological, and molecular properties. Ketamine has been used for disparate applications in medicine, but, unlike in its more traditional roles, its mechanism of action with respect to its antidepressant properties remains largely mysterious. The following sections will thus present a survey of the current literature concerning what ketamine might be interacting with, where those interactions take place, and how ketamine arrives there.

1.6.1. Receptors

The first discovered pharmacologic effect of ketamine was its potent NMDA antagonism [86], which is thought to underlie both its anesthetic and analgesic effects (see Chapter 1.2). The wide distribution of NMDARs across the cortex and their importance to cognition help explain how higher doses of ketamine produce loss of consciousness, as ketamine acts as a noncompetitive open channel blocker [282] which can remain in the pore even after the channel closes [283]. After administration of subanesthetic doses in either rodents or humans, resulting in brain concentrations likely in the low micromolar range [284], ketamine blocks around 30% of the available NMDARs [285], in contrast to anesthetic doses which block a much higher percentage [286]. Abnormalities of NMDAR development are implicated in the pathogenesis of various psychiatric disorders, including schizophrenia [287-289]. Indeed, a hypothesis concerning the genesis of schizophrenia involves altered glutamatergic signaling mediated by subpopulations of NMDARs on GABAergic cortical interneurons [290]; bolus dosing of ketamine in healthy patients can result in psychomimetic symptoms resembling psychosis [291], and the more potent NMDAR antagonism by PCP leads to known psychomimetic effects [85], lending further credence to the notion that NMDARs are involved in schizophrenia. NMDARs are tetramers, typically composed of two GluN1 subunits and two GluN2 subunits (GluN3 subunits exist as well, albeit more rarely, in humans [292]); while there is only one type of N1 subunit, there are four types of N2 subunits (A-D), with GluN2A and GluN2B being most common in the forebrain [293]. Ketamine has been shown to bind with roughly threefold higher affinity to Glu1/GluN2C NMDARs than other combinations [294] (with Glu1/GluN2C expressed disproportionately in GABAergic interneurons [295]), but since these results hold only in solution with the NMDA pore-blocking ion Mg^{2+}, this apparent affinity is likely not intrinsic to the relationship between GluN2C subunits and ketamine [284]. GluN2C-KO mice treated with ketamine display muted side effect profiles with no reduction in antidepressant efficacy [296], buttressing the aforementioned theory regarding schizophrenia’s pathogenesis [290]. In recombinant NMDARs in the absence of Mg^{2+}, ketamine has higher affinity for GluN2B subunits, with potency decreasing for GluN2C, GluN2D, and GluN2A subunits, respectively [297]. Deletion of GluN2B subunits in a subpopulation of cortical neurons decreased despair in a rodent model, mimicking ketamine treatment of control animals [298], suggesting that antagonism of these subunits is paramount in the antidepressant actions of ketamine; indeed, there is some evidence that specific GluN2B blockers can relieve the symptoms of depression in rodent models [299,300] and humans [301]. While esketamine has a roughly fourfold greater affinity for the PCP site than arketamine [94,122,123], there is little evidence of subunit preferences between the enantiomers (esketamine may have relatively higher affinity for GluN2C and GluN2D subunits while arketamine may have relatively higher affinity for GluN2A and GluN2B subunits [297]). The

GluN2D subunit might be necessary for the sustained antidepressant effects of arketamine but not esketamine [302] as well as the induction of cognitive impairment from arketamine [303]. Other antidepressant drugs with putative mechanisms independent of glutamatergic signaling appear to interact with NMDARs at physiologically relevant concentrations, including TCAs [304-306] and SSRIs [306] at locations distinct from the PCP binding site [307]; additionally, scopolamine may modulate NMDAR expression [308,309], suggesting that NMDAR activity may be involved in the mechanism of action of antidepressants which are not putative NMDA antagonists. Complicating the picture regarding the involvement of NMDARs in mediating antidepressant responses, direct modulation of the NMDAR glycine binding site can produce antidepressant effects in some MDD patients [254,310,311], but specific NMDA antagonists, such as memantine [145,312], MK-0657 [313], and AZD6765 [145,146], fail to demonstrate antidepressant effects in humans, suggesting that NMDAR modulation is certainly not sufficient to explain ketamine’s effects. Of interest, higher anesthetic doses of ketamine are not associated with antidepressant effects in rodents [286] nor changes in glutamate release in the PFC [314] despite blocking more NMDARs, indicating that ketamine’s effects on receptor subpopulations (possibly of various classes) are part of its antidepressant mechanism.

As alluded to above, the actions of ketamine on GABAergic neurons are thought to be crucial to its antidepressant effects. GABARs are divided into three subtypes, $GABA_A$, $GABA_B$, and $GABA_C$, the first and last of which are ionotropic receptors and the middle of which is metabotropic. Of the three, the $GABA_A$R has been most well-characterized for its role in the etiology of depression as well as its potential role in the antidepressant effects of ketamine [116]; interestingly, compounds targeting the $GABA_A$R have become of interest as antipsychotics [284], in line with the NMDA-GABA hypothesis of schizophrenia outlined previously [290]. Mice with defects in $GABA_A$Rs causing postsynaptic hyperexcitability exhibit symptoms of depression-like behavior [315] which chronic treatment with typical antidepressants can ameliorate [316]; generally, mice exposed to CUS exhibit functional changes in GABAergic activity leading to eventual deficits in glutamatergic signaling [317]. Indeed, such imbalances between glutamatergic and GABAergic tone are seen in MDD patients, who generally evince decreases in GABAergic activity [315,317]. With respect to the response to ketamine, $GABA_A$R-mutant mice (who display both molecular and behavioral markers of depression) exhibit potentiation of cortical GABAergic synapses by ketamine [318], and mice subjected to CUS showed decreases in GABAergic proteins in layer V mPFC neurons associated with depression-like behavior which can both be rescued by single doses of ketamine [319]. Evidence for the potential mechanism of action for ketamine's antidepressant effects involving release of GABAergic inhibition on excitatory pyramidal cells by targeting NMDARs on interneurons includes the finding that subanesthetic doses of ketamine perfused into rodent brain slices leads to activation of cortical pyramidal cells [300,320] as well as reduction of GABAergic tone [300], though the initial burst of glutamate engendered by GABAergic NMDAR inhibition may cause a transient increase in the release of GABA [321,322]; this hypothesis is corroborated in MDD patients receiving ketamine treatment, in whom there is a negative relationship between ketamine and GABA plasma concentrations [323]. Further supporting the importance of $GABA_A$Rs for ketamine's antidepressant effects, an experiment using a sub-antidepressant (0.1 mg/kg) dose of ketamine and a $GABA_A$R agonist 30 min later produced a significant and rapid reduction in immobility time in the TST [324]; however, intra-cerebral injections of the same $GABA_A$R agonist into mPFC abolished ketamine's longer-term (1 d) antidepressant effects on rodent behavior [325], perhaps explicable due to region-specific effects of the interaction between ketamine and GABAergic NMDARs [116]. In humans, ketamine binding to $GABA_A$Rs has been shown to occur at doses much higher than circulating levels in the brains of patients receiving antidepressant treatment [326], yet ketamine has been shown to have clear effects on GABAergic signaling, suggesting that it may indirectly impact GABA release [116]. Future investigations must focus on both the potential mechanisms by which ketamine interacts with GABAergic signaling as well as whether these mechanisms are causal or consequential to the antidepressant response in MDD patients.

Monoamine receptors and transporters are of interest when assessing ketamine's antidepressant mechanism, as the putative means by which typical antidepressants exert their effects are thought to involve their regulation (see Chapter 1.1). Of the monoamines, studies probing the relationship between the catecholamine DA and the indolamine 5-HT with ketamine have provided the most compelling results. There are five types of DA (D_1-D_5) and seven types of 5-HT (5-$HT_{1\text{-}7}$) receptors, with multiple subtypes for 5-HT_1, 5-HT_2, and 5-HT_5; all are metabotropic receptors except for the 5-HT_3 receptor, which is ionotropic [327], and all are present in the mammalian CNS, with some also presenting in locations such as the gut [328] and urinary tract [329]. Additionally, reuptake transporters — DAT, and SERT, the main target of

SSRIs (see Chapter 1.1) — help sequester recently released synaptic DA and 5-HT. Regarding direct ketamine binding to dopaminergic receptors, a few studies indicate that subanesthetic doses have partial agonist activity at the D_2R (the target of most antipsychotic drugs thought to mediate their effects [330]) with affinities in the range of 55-1000 nM [331,332] and esketamine exhibiting about three times more potent binding than the racemate [331]; this direct binding activity may drive some of ketamine's psychomimetic side effects [331-333]. Notably, these results have since been challenged by a report that there is no agonist activity at any of the DA receptors for physiologically relevant concentrations (up to 10 μM) of ketamine *in vitro* [334], though in rodents, repeated IP injections of ketamine do increase ventral tegmental area (VTA) dopaminergic tone [335], and a single IP dose can increase cortical DA [322], suggesting that *in vivo* analyses show a less direct but clearer relationship between ketamine administration and DA release. With respect to differences between the enantiomers, IP injections of esketamine in both WT and depression model mice produced a greater acute spike in extracellular DA release in the PFC than from arketamine [336], perhaps explaining esketamine's relatively stronger psychomimetic effects [169]. In healthy human subjects, subanesthetic doses of IV ketamine have been shown to increase levels of striatal DA [337-339] which has been correlated with increased psychomimetic side effects from D_2R binding [337,339]; however, several subsequent studies demonstrated no changes in striatal DA binding to D_2R [340,341], and administration of a D_2R antagonist subsequent to a subanesthetic dose of IV ketamine did not alter acute psychomimetic side effects [342]. Possible reasons for these discrepancies could be differences in the healthy controls used, the PET imaging parameters, the quantification of D_2R binding, tracer administration, and the regimens of ketamine treatment given [340,343]. Ketamine binding to DAT has been shown to occur only at concentrations above physiological relevance [334,344], which essentially rules out any direct contribution of ketamine to the recycling of synaptic DA. Overall, the literature suggesting that ketamine administration increases DA in the rodent brain is much clearer than studies suggesting the same in humans [343]. Regarding 5-HT, ketamine has not been found to bind to any of the receptor types at subanesthetic concentrations [345-348], though perhaps at analgesic concentrations [331]. While direct interactions are unlikely, ketamine's antidepressant effects may require 5-HT activity: in WT rodents, artificial depletion of neural 5-HT using a tryptophan hydroxylase inhibitor as a pretreatment before ketamine administration abolished the longer-term (1 d) but not short-term (30-60 min) reduction in immobility time on the FST [349,350], which was corroborated in genetic models of anxiety and depression [351,352]; furthermore, increased extracellular 5-HT in the cortex was associated with ketamine-induced decreases in FST immobility time as well as increased firing of dorsal raphe nucleus (DRN) neurons [352]. With respect to differences between the enantiomers, IP injections of arketamine induce greater acute extracellular 5-HT release than esketamine in both WT and depression model mice with dose-dependent effects, and direct PFC infusion of arketamine caused a significant acute release of 5-HT compared to esketamine [336], perhaps indicating that each enantiomer mediates its antidepressant effects through somewhat different mechanisms. The most intriguing recent studies looked at the effects of ketamine on 5-HT$_{1B}$ receptors, which have been shown in positron emission tomography (PET) studies to have

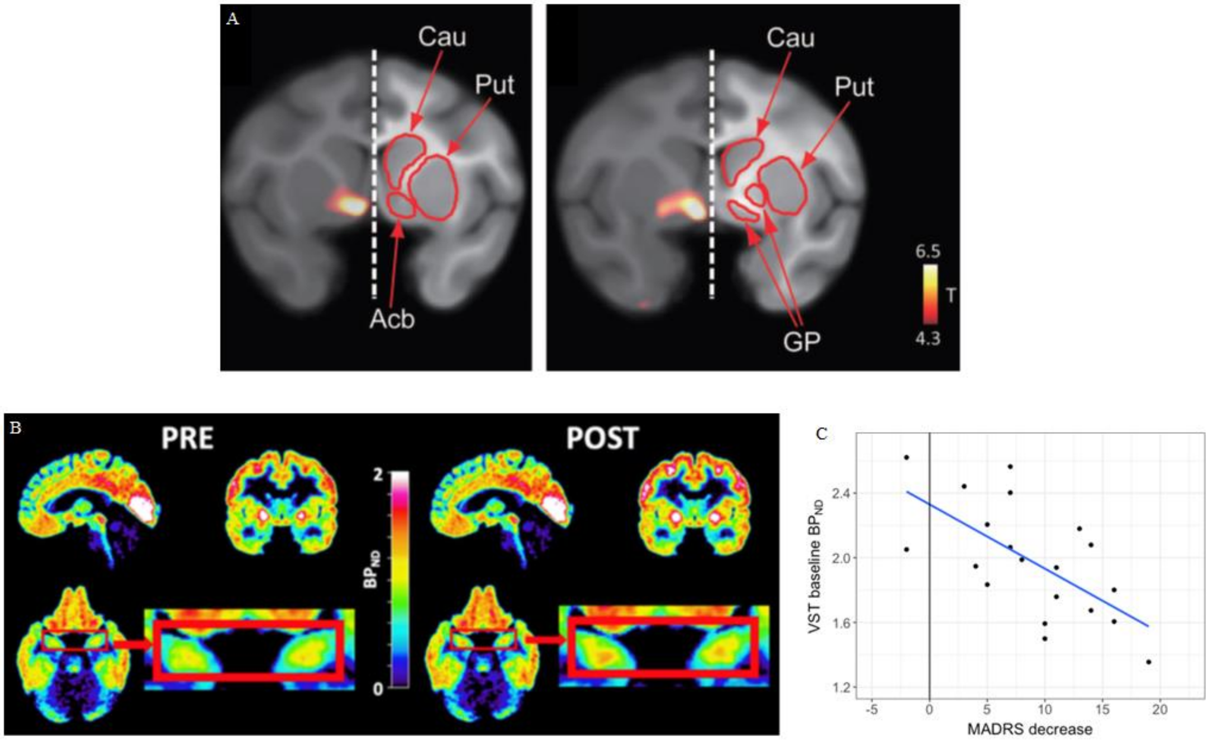

Figure 1.8. ***(A)*** The binding potential of a radioligand specific to the 5-HT$_{1B}$ receptor compared between ketamine treatment vs. control in two different coronal slices of a normalized rhesus monkey brain demonstrate significant increases in the VST (nucleus accumbens (Acb) and ventral globus pallidus (GP)) as well as the thalamus (Cau = caudate, Put = putamen; statistical threshold = $P < 0.001$ uncorrected; T-value > 4.3; adapted from Fig. 2 of [353]). ***(B)*** Binding of the same radioligand before (PRE) and after (POST) administration of ketamine in normalized human brains, with the zoomed-in area of the axial slice showing the increased binding in the HC (BP$_{ND}$ = regional binding potential for non-displaceable binding; significant differences measured via repeated measures ANOVA). ***(C)*** The correlation between decreases in MADRS scores and higher baseline ketamine binding in the VST ($r = -0.426$, $P = 0.019$ measured via Pearson's correlation method). (***B*** and ***C*** adapted from Figs. 1 and 2 of [354].)

increased binding after IV ketamine administration in the ventral striatum (VST) of NHPs [353] as well as in the HC of patients with TRD for whom reductions in the symptoms of MDD were inversely correlated with baseline 5-HT$_{1B}$ binding in the VST [354] (**Fig. 1.8A-C**). SERT, an attractive target for investigation given its involvement in the action of SSRIs, does not appear to be inhibited by ketamine *in vitro* at physiologically relevant concentrations [334,344,355], which was corroborated in a PET study of healthy human subjects [356]. However, in NHPs, ketamine infusion has been shown to decrease SERT activity in both the midbrain and PFC [357] as well as the VST [353], and a recent study in WT rodents found that ketamine inhibited 5-HT clearance in the HC which was lost in SERT-deficient mice as well as that SERT was necessary to produce ketamine's antidepressant effects on the FST [358], all of which might suggest indirect effects of ketamine on SERT activity at antidepressant doses. In sum, ketamine's likely indirect actions on the serotonergic system appear to be involved in its antidepressant mechanism, though to what degree and to what specific ends remains unknown.

Opioid receptors (ORs) are logical candidates to investigate as sites of ketamine binding, as their main function is to produce analgesia in response to noxious environmental stimuli [359] and ketamine is used to reduce pain among post-operative patients [109]; additionally, concentrations of plasma ketamine from induction of analgesia are roughly similar to those resulting from administration of antidepressant doses (analgesia: 0.29-0.67 μM [98,114-116]; antidepressant: 0.32-0.78 μM) [116,144,147]). There are three types of ORs, expressed throughout the CNS as well as the periphery, all of which are G protein-coupled: μ (MOR), δ (DOR), and κ (KOR) [359]; apart from mediating analgesia, they are also involved in the regulation of emotional and behavioral states [360]. *In vitro*, ketamine was found to bind to MORs (K_i = 42.1 μM), KORs (K_i = 28.1 μM), and DORs (K_i = 272 μM) ORs [361], with noticeable enantioselectivity of esketamine (MOR: K_i = 11-29 μM; KOR: K_i = 25-28 μM; DOR: K_i = 130-205 μM) over arketamine (MOR: K_i = 28-84 μM; KOR: K_i = 60-100 μM; DOR: K_i = 130-286 μM) [361-363]; these results align with esketamine's higher potency for inducing analgesia [94,116,124,125], though because of the high concentrations at which significant binding occurs *in vitro*, other mechanisms may contribute to ketamine's analgesic effects in patients [362]. In a rodent study assessing cognitive function, ketamine was determined to have agonist activity (K_i = 25 μM) at KORs, and ketamine-induced perceptual deficits are partially blocked via pretreatment with a KOR antagonist [363]; whereas in human subjects, coadministration of a non-perception-altering dose of IV ketamine with the longer-acting nonselective MOR antagonist naltrexone increased feelings of dissociation [364], suggesting that ketamine may differentially regulate OR subtypes to produce side effects. In a rodent behavioral model of depression, ketamine's antidepressant effects were blocked by pretreatment with naltrexone, but the MOR agonist morphine did not act as an antidepressant, suggesting that part of ketamine's antidepressant action requires OR activation but that such activation in itself is not sufficient to mediate antidepressant activity [365]. With respect to ketamine's abuse potential, rodents preferentially self-administered esketamine over arketamine, which may be MOR-dependent [366] (though this has been questioned [367]). Corroborating the results in rodents, ketamine administered IV to MDD patients had antidepressant and anti-suicidality effects which were abolished by pretreatment with naltrexone without diminishing ketamine-induced dissociation [368,369], confirming that OR signaling is necessary for ketamine's antidepressant efficacy in patients. Interestingly, other antidepressants can induce analgesia [370], with at least one, venlafaxine, potentially dependent on MORs for this effect [371]; furthermore, the opioid tramadol, also a regulator of glutamatergic and serotonergic signaling, has shown antidepressant effects in mouse models [370]. Future investigations will help determine the necessity of altering OR activity for relieving the symptoms of MDD from a wider array of medications as well as the relationship between ketamine and ORs in mediating its specific effects.

The mAChRs are metabotropic receptors categorized into five subtypes (M_1-M_5) which primarily act through G proteins [116]. *In vitro,* ketamine inhibits the M_1 receptor at a physiologically relevant range ($IC_{50} = 5.7\ \mu M$) [372], and in a non-specific mAChR binding assay, esketamine ($K_i = 20\ \mu M$) exhibited higher affinity than arketamine ($K_i = 37\ \mu M$) [362], though a follow-up study reported lower *in vitro* potencies at the M_1 ($K_i = 45\ \mu M$), M_2 ($K_i = 294\ \mu M$), and M_3 ($K_i = 246\ \mu M$) receptors [373]. Ketamine's activity at mAChRs should be considered further in light of the antidepressant effects of the nonselective muscarinic antagonist scopolamine (see Chapter 1.4) as well as because of the association of the M_2 and M_4 receptors with MDD [239,374,375]. The ionotropic nAChRs comprise a broad array of subtypes, as their pentameric structure arranged from a pool of ten α and four β subunits produce receptors with a wide variety of pharmacological and physiological functions [376]. *In vitro*, ketamine has been shown to inhibit various nAChRs, some at physiologically relevant concentrations, including $\alpha_2\beta_2$ ($IC_{50} = 92\ \mu M$ [347]), $\alpha_2\beta_4$ ($IC_{50} = 29\ \mu M$ [347]), $\alpha_3\beta_2$ ($IC_{50} = 50\ \mu M$ [347]), $\alpha_3\beta_4$ ($IC_{50} = 9.5$

μM [347] and 3.1 μM [123]), $\alpha_4\beta_2$ (IC_{50} = 72 μM [347] and 50 μM [377]), $\alpha_4\beta_4$ (IC_{50} = 0.24 μM [378] and 18 μM [347]), and α_7 (IC_{50} = 20 μM [377]); additionally, much like its action on NMDARs, ketamine was a more effective antagonist when the nAChR channel was open [378]. Perhaps of more interest is the effect of certain ketamine metabolites on nAChRs. Most notably, (2R,6R;2S,6S)-HNK, (R,S)-DHNK, and (R,S)-NK potently inhibited α_7 nAChRs at concentrations less than 1 μM while exhibiting far less potency for NMDARs [123], suggesting that these breakdown products, to the extent that they exert an antidepressant effect independent of the parent compound, require nAChR signaling. The potential antidepressant effects of (2R,6R)-HNK in rodent models of depression, coupled with its lower side effect profile [174] make the α_7 nAChR an attractive target for further investigations into the physiology underlying responses to antidepressants; indeed, α_7 nAChR modulators have already been demonstrated to have antidepressant effects in rodent models of depression [379,380].

Ketamine has also been demonstrated to affect signaling through metabotropic glutamate receptors (mGluRs), hyperpolarization-activated cyclic nucleotide (HCN) channels (also known as pacemaker channels), voltage-gated Na^+ channels, σ receptors, and voltage-dependent Ca^{2+}channels (VDCCs), as well as to modulate NE transmission [116]. These interactions are all thought to be of potential importance in the physiological instantiation of depression [75,116,284,381,382], and future work may uncover more significant involvement each has with both the antidepressant as well as side effects of ketamine.

1.6.2. Region-Specific Activity

As demonstrated in the previous subsection, ketamine interacts with a wide variety of receptors, some of which are expressed across the brain, suggesting that ketamine likely depends on multiple regions and networks to mediate its antidepressant effects. Three regions in particular are of interest with respect to identifying underlying physiological bases for depression as well as regions where ketamine acts: the PFC, HC, and lateral habenula (LHb).

The PFC is an important region whose deficits underlie many of the symptoms of depression, though the translation from preclinical studies performed in rodents to understanding the pathophysiology in patients remains to be discerned [383]; nevertheless, compelling parallels are apparent. In rodents, chronic stress can lead to the loss of apical dendrites and spines in the PFC [384-387] which is reversible in younger [386] (but less so in older [388]) animals, similar to the pathology observed in MDD patients [383]. Chronic stress in rodents can also induce cognitive dysfunction as measured across a variety of behavioral tasks [387,389-391], which is again corroborated by the remarkable cognitive deficits experienced by patients during depressive episodes [392]. In MDD patients, PFC volume is reduced as assessed in postmortem analyses [393], and synaptic-function-related gene expression as well as overall synapse count is decreased in the PFC [394]. Based on the ubiquity of glutamatergic transmission in the PFC, a decreased number of synapses implicates glutamatergic dysfunction in the pathogenesis of depression, with decreased glutamate found in several PFC regions among MDD patients [395], providing further evidence for the theory that ketamine's NMDAR antagonism — particularly on GABAergic interneurons [290], whose inhibition by ketamine has been shown to increase glutamatergic transmission [300,320] — is the mechanism by which it ameliorates symptoms. Indeed, in rodents, a single dose of ketamine administered to chronically stressed animals rapidly increased (within hours) the number of synapses in mPFC pyramidal neurons [286,299], which may occur via an increase in PFC glutamatergic signaling [314,396]. Direct infusion of arketamine into a subregion of the mPFC caused antidepressant effects [178], while repeated IP injections of esketamine led to the loss of PV+ neurons (a marker of psychosis [176]) in the PFC [177]. In imaging studies, MDD patients had reduced functional connectivity in the PFC compared to controls, which deficit was repaired from ketamine infusion after one day [397,398] and more significantly in patients who were clinical responders to ketamine versus those that were non-responders [397]; additionally, a glutamate release inhibitor abolished the reparative effects of ketamine [398], supporting a role for glutamate transmission in ketamine's normalization of PFC dysfunction. PET scans taken 2 h after ketamine administration in TRD patients showed decreased metabolism in the PFC, possibly a marker of increased synaptic plasticity [399], which suggests a mechanism underlying the aforementioned rapid restructuring of functional connectivity abnormalities seen in MDD patients [397,398]. In all, the PFC is crucial to both the pathogenesis of MDD as well as a key region involved in its relief through ketamine-induced functional changes, a phenomenon that will continue to be investigated in the development of future RAADs.

The HC is of great interest as a target for antidepressant effects, considering that its dysfunction is implicated in the pathogenesis of many neuropsychiatric disorders, including MDD [400]. While GRs are expressed throughout the brain, MRs are located in only a few areas, including the HC [401], highlighting the HC as an area of interest for studying the effects of stress on the brain. Much like in the PFC, in rodents, chronic stress leads to HC neuronal apoptosis [402] and fewer synapses [403-405] as well as decreased LTP [406] and neurogenesis [407]. Corroborating these results, imaging studies demonstrate clear loss of HC volume (4-10%) in MDD patients versus healthy controls [408], and MDD patients have been shown to have significantly reduced HC neuropil on postmortem analysis [409], indicative of dendritic loss. Ketamine has been demonstrated to rapidly reverse synaptic dysfunction in the HC in chronic stress model rodents [410-413] which is associated with antidepressant response [411-413]. Direct infusion of arketamine into a subregion of the mPFC demonstrated antidepressant effects [178], while IP injection of esketamine (but not arketamine) caused a loss of PV+ neurons in the HC [177]. In MDD patients undergoing MRI, those receiving ketamine infusion had increased HC volumes within one day, including patients with smaller HC volumes who are known to be more resistant to antidepressant treatment [414], and these changes were correlated with improved clinical response [415]; additionally, decreases in anhedonia post-ketamine administration were correlated with increased HC metabolism [416], and the connectivity of several other brain regions with the HC was reduced following application of ketamine which may reveal previously unknown functional patterns associated with both the pathogenesis of MDD as well as ketamine’s effects [417]. Many studies have implicated HC activity as intrinsic to the antidepressant mechanism of SSRIs [418,419], so the foregoing results regarding changes to HC structure and function concomitant with ketamine’s antidepressant effects indicate that the HC may be part of a common pathway by which the symptoms of depression are relieved in both animal models and MDD patients.

An area that has recently generated interest with regard to both the pathophysiology of depression as well as the antidepressant actions of ketamine is the LHb. In mammals, the habenula is a bilateral symmetric structure of the epithalamus divided into medial and lateral nuclei [420]. The LHb is implicated in depression because it can inhibit the output of monoaminergic nuclei (e.g. DRN, VTA, LC) as a means of encoding punishment signals [421-423] mediated by activation of GABAergic interneurons which project to each nucleus from the rostromedial tegmental nucleus of the VTA [424]. In rodents, both LH and MDS models of depression show increased LHb activity [425] which correlates with the degree of behavioral deficit [64,65,70,71,365]. LH has been associated specifically with increased bursting of LHb neurons in rodents, and this activity is dependent on NMDARs as well as transient-type (T-type) VDCCs; upregulation and normalization of this bursting activity exacerbates or ameliorates, respectively, behavioral deficits [426] (**Fig. 1.9A-D**), suggesting that the mode in which LHb neurons proportionally fire is implicated in the physiology of depression. Interestingly, upregulation of the Kir4.1 potassium (K^+) channel in LHb astrocytes, seen among LH model rodents, helps determine the aforementioned bursting of nearby neurons and correlates with depression-like behavior [427], further implicating the activity of the LHb in the manifestation of depressive symptoms. In humans, postmortem analysis of the LHb found a significantly decreased volume and neuronal cell count in MDD patients versus healthy controls [428], though these results are complicated by other findings in imaging studies which report either the same [429,430] or larger LHb volume among MDD patients [431,432]; reasons for these discrepancies include difficulty in determining the delineation of the nucleus due to variations in the field strength among the MRIs used [433], assessment of patients at different stages of treatment [429,431,432], inclusion of patients with BPD [428,429], differences between the sexes [429,431], and limited sample power [429,433]. Of more interest might be the positive correlation between symptoms of MDD and LHb volume [430,432], which would more definitively link clinical severity with underlying physiological changes. Functionally, the LHb has been shown to respond to on-line changes in the value encoded by negative stimuli [422] which is dysregulated in MDD patients [434], though perhaps the fact that the LHb of MDD patients is hypoactive, not hyperactive, in response to aversive stimuli compared to controls recalls the complex relationship between symptoms and treatment suggested in the aforementioned volumetric analyses; an inability to avoid negative cues causing increased perseveration is a possible explanation [433]. Given its demonstrated ability to suppress LHb neuronal activity in a rodent model of LH which was correlated with a recovery of behavioral deficits [64], deep brain stimulation (DBS) of the LHb in a TRD patient significantly decreased symptoms while on, with symptoms recurring during an unplanned stoppage of stimulation [435], suggesting that the LHb could present an attractive target for the treatment of TRD.

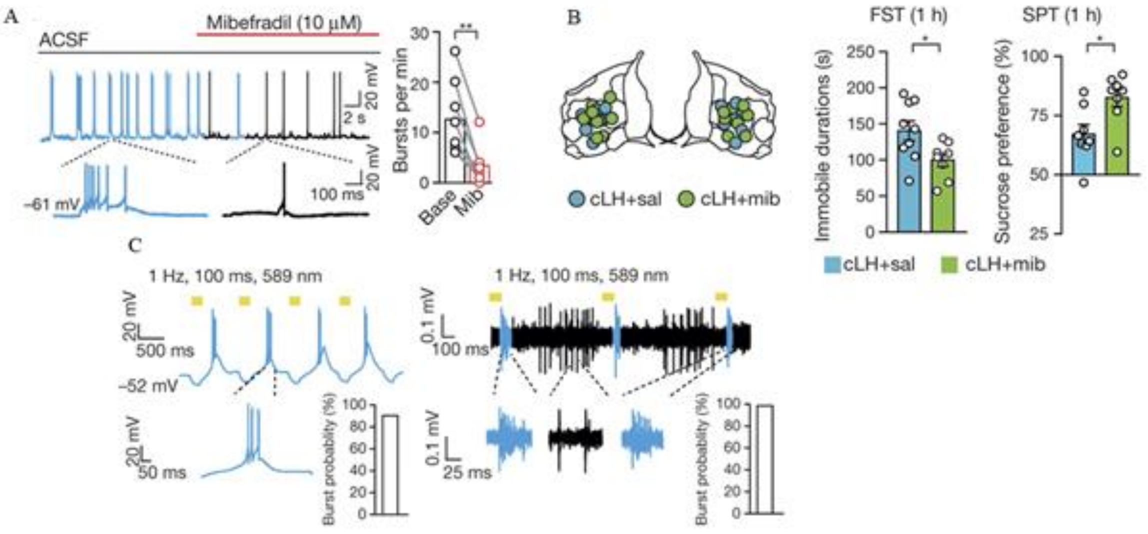

Figure 1.9. ***(A)*** *Ex vivo* recording of LHb bursting from LH rodents which application of the T-type Ca2+ channel blocker mibefradil (mib) acted to reduce (with the amount of bursting suppressed vs. baseline quantified in the bar graph on the right; ACSF = artificial CSF). ***(B)*** Bilateral injections of saline (sal; *blue*) or mibefradil (*green*) in the habenulae of LH rodents (*left*) and the quantification of the behavioral changes thereof on the FST (*middle*) and SPT (*right*) performed 1 h after treatment (*P < 0.05). ***(C)*** Rebound bursts (*green*) demonstrated both *ex vivo* (*left*) and *in vivo* (*right*) from the LHb of LH rodents expressing a viral-mediated halorhodopsin variant which causes hyperpolarization when activated by light (yellow light: 589 nm at 1 Hz for 100 ms) shone through an implanted fiber optic (*in vivo*). Burst probability reports the reliability of light stimulation eliciting bursts. (Adapted from Figs. 4 and 5 of [426].)

Currently, trials are underway to investigate this intervention further, with mixed results thus far, though most studies are still in the early stages and results so far inconclusive [436]. As for ketamine's effects, a single dose was able to reverse both the behavioral deficits in rodent models of depression as well as re-normalize intrinsic LHb firing [65,365,426]. More specifically, the degree to which ketamine suppressed the burst firing of LHb neurons was correlated with the amelioration of behavioral deficits [426] (**Fig. 1.10A-C**), suggesting that ketamine mediates its antidepressant effects in part by acting upon aberrant LHb physiology. In a PET imaging experiment, TRD patients receiving a single subanesthetic dose of IV ketamine showed decreased metabolism in the right Hb compared to baseline after 2 h correlated with decreases in the symptoms of depression [399], and an fMRI study found that LHb connectivity to PFC regions was altered one day after ketamine infusion and correlated with clinical improvement

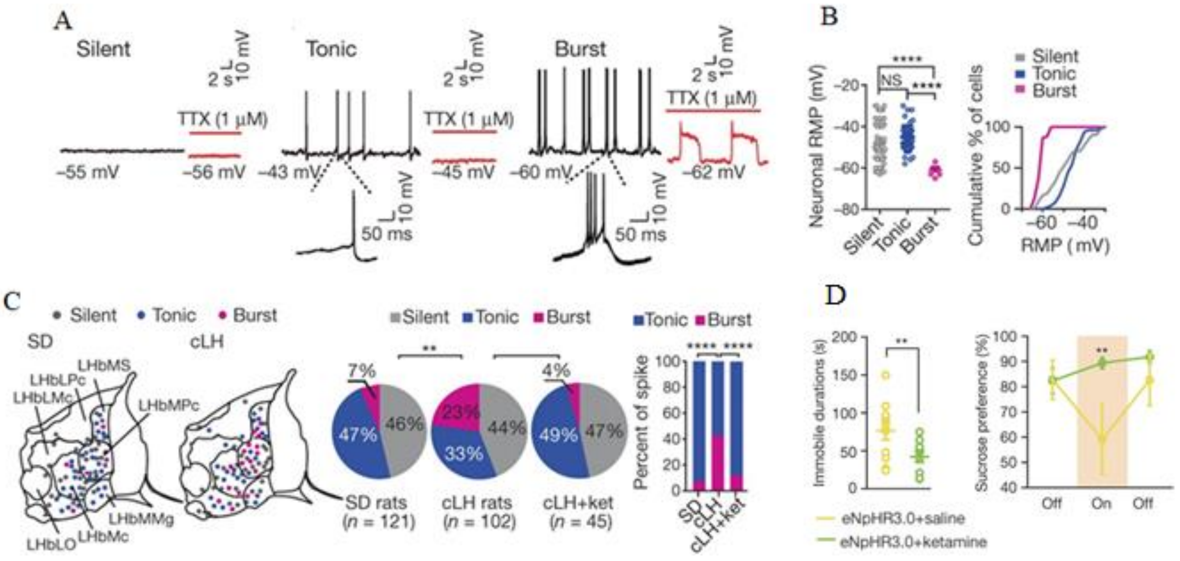

Figure 1.10. ***(A)*** Traces showing activity of the three different LHb neuron types: silent (*left*), tonic (*middle*), and burst (*right*) as well as their responses to tetrodotoxin (TTX). ***(B)*** Resting membrane potential (RMP) differences between the three neuron types (*left*) and the distribution of RMPs among the three groups (*right*) (****P < 0.0001; NS = not significant). ***(C)*** *Left*, various subregions of the LHb in both WT (SD, *left*) and LH (cLH, *right*) rodents demonstrating the recording sites from which electrophysiology was recorded and which sites produced each neuronal subtype (LHbLMc = magnocellular part of the lateral division of LHb, LHbLPc = parvocellular part of the lateral division of LHb , LHbMS = superior part of the medial division of LHb, LHbMPc = parvocellular part of the medial division of LHb, LHbMMg = marginal part of the medial division of LHb, LHbMc = central part of the medial division of LHb, LHbLO = oval part of the lateral division of LHb). *Right*, pie charts show the abundances of the three different neuron types in WT (*left*), LH (*middle*), and LH treated with ketamine (*right*) rodents demonstrating normalization of abundances from ketamine treatment while the bar graph shows the percent of all spikes recorded that had tonic or burst characteristics. ***(D)*** For both the FST (*left*) and the SPT (*right*), rodents expressing LHb halorhodopsin treated with saline (*yellow*) or ketamine (*green*) demonstrate behavioral deficits driven by light-induced (see Fig. 1.9C for details) bursting behavior ameliorated more by treatment with ketamine. (**P < 0.01). (Adapted from Figs. 2 and 5 of [426].)

[437], suggesting that the ketamine-induced normalization of LHb activity seen in rodent models of depression is corroborated in functional analysis of physiological changes among patients. The LHb has been demonstrated to be an important node in both the pathophysiology of depression as well as in the response to ketamine, and future therapies to treat MDD, particularly interventions such as DBS, will provide fascinating additional mechanistic insights into both domains.

1.6.3. The Role of Glia

The role of neurons in the pathophysiology of MDD has understandably received a great deal of attention from the research and clinical community, as neuronal transmission is both well-studied and undoubtedly crucial to any underlying aberrant processes. However, other cells in the brain have more recently received interest: glia. The role of glial cells in maintaining physiologic homeostasis among the neurons they support — and dysfunctions in that regulation — has engendered speculation that glia act as both a cause of depression as well as a target of engagement for antidepressants, including ketamine.

The number of glial cells in the mammalian brain is roughly equivalent to the number of neurons [438,439]. There are several types of glia which serve crucial roles in the CNS, with the three most common being astrocytes, oligodendrocytes, and microglia. Astrocytes are the most numerous of the three, playing a crucial role in the maintenance of synapses [440] as well as assisting the development of the CNS, forming the BBB by contributing foot processes, mediating neuroplasticity, regulating the levels of synaptic neurotransmitter, and buffering K^+ [441-444]. Oligodendrocytes are the CNS analog to Schwann cells in the periphery, ensheathing axons in myelin to allow for faster signal transduction; they also contribute to the regulation of neurotransmission [440]. Microglia are primarily immune cells which surveil the brain parenchyma for immune markers, modulating their activity in response to infection, toxicity, or damage [440-443].

While all glial functions (or their dysfunction) could contribute to the pathogenesis of depression, perhaps the most obvious and well-studied is the regulation of glutamate, a property implicated in the activity of ketamine. Glutamate is the most common excitatory neurotransmitter in the CNS and is involved in both the pathogenesis of depression (see Chapter 1.1) as well as the antidepressant effects of ketamine (see Chapter 1.6.1). While neuronal glutamate release and reuptake is critical to both of these mechanisms, the role played by glial cells has more recently generated interest. Astrocyte processes encircle glutamatergic synapses, providing rapid reuptake of synaptic glutamate through GLT-1 in rodents and the analogous EAAT-2 in humans [440,441,445,446]. Because prolonged exposure to extracellular glutamate can trigger apoptosis, astrocytic glutamate regulation is essential to maintaining neuronal health by preventing ‘spillover’ outside of synapses [440,447-450]. Synaptic release of glutamate produces a superabundance of neurotransmitter which astrocytes buffer due to the sequential binding of glutamate to EAAT-2 transporters such that more can be taken up across the membrane over time [451]. Once inside, the astrocyte-specific enzyme glutamine synthetase converts glutamate to glutamine [441], rendering the molecule electrochemically neutral before being released from astrocytes for reuptake by neurons [440]. Once inside, neurons reconvert the glutamine to glutamate via the enzyme glutaminase [452] before packaging it into synaptic vesicles for further transmission events [440]. Astrocytic foot processes also help regulate glutamatergic activity; one of the key constituents of the BBB, foot processes are the only endogenous CNS source of D-serine, a potent agonist of the NMDAR glycine site [453-455]. By regulating the release of D-serine, astrocytes can thus contribute to the activity and potentiation of NMDARs as crucial players in the encoding of information in neural circuits [454]. Oligodendrocytes also have EAAT-2 transporters and are themselves vulnerable to glutamate-induced excitotoxicity [440]; furthermore, immature oligodendrocytes in the HC receive glutamatergic transmission from nearby neurons [456] while mature cells have glutamate receptors [457], indicating that oligodendrocytes are involved with glutamatergic regulation and signaling.

Many analyses of postmortem tissue from patients with MDD and BPD indicate significant decreases in glial cell count as well as density, particularly in subregions of the PFC, cingulate cortex, and limbic areas [393,458-460], while increases in HC glial cell density may indicate loss of neuronal volume and glial processes [409,441]. Additionally, several studies report increases in the overall size of glial cells among MDD patients [393,461] (though this may be region- and cell-type-specific [393,409,460]), perhaps indicating a compensatory mechanism by which remaining glial cells expand to meet the metabolic demands of nearby neurons [441]. Astrocytes are particularly subject to these sorts of changes, undergoing hypertrophy [462] as well as decreased glial fibrillary acidic protein (GFAP) expression [442,463,464] (particularly among younger MDD patients [465,466]) in the PFC [463] and the HC [467]. MDD patients also exhibit reduced EAAT-2 and glutamine synthetase gene expression [468] as well as increased levels of s100β, an astrocyte marker of excitotoxicity [469]. In rodents, chemical destruction of glia in the PFC [470] or inhibition of normal astrocyte function [442] leads to the manifestation of depression-like behavior, and animals experiencing CUS demonstrate reduced levels of GFAP in the HC [471,472] and the PFC [470,473] as well as reduced neurogenesis and cytogenesis, respectively, in these regions [474]; additionally, D-serine and ATP, both regulated by glia, were reduced in the brains of depression-model rodents [475,476]. Myelin loss as well as smaller oligodendrocyte somata have been found in the brains of patients with MDD [477] as well as abnormal callosal tracts [478]; in rodents, chronic stress caused reversible abnormal oligodendrocyte arborization [479] while also compromising myelin in the corpus callosum [478]. Furthermore, oligodendrocyte precursor cells are lost in both the PFC and the HC after SDS, and genetic knockout likewise contributed to a depression-like phenotype [480]. With respect to proposed etiologies of MDD, inflammation has been reliably linked to its pathogenesis [442], and microglia are a key mediator of pro-inflammatory markers entering the CNS [481]. One possible mechanism by which inflammation could be increased in MDD patients is from breakdown of the BBB due to a paucity of astrocyte foot processes, allowing for more pro-inflammatory markers and cells to enter the brain [482]. Microglial morphology is different in the PFC and limbic regions among MDD patients [483], particularly for those who have completed suicide [484-486], a finding which is corroborated in analyses of rodent models of depression [487-489].

The antidepressant effects of ketamine are associated with the function of glia in both rodents and fish. In rodents, the astrocytic K^+ channel, Kir4.1, was examined with regard to its potential role in both the manifestation of behavioral deficits in a rodent LH model as well as the underlying pathophysiology in LHb neurons and glia [427]. This study builds on previous work demonstrating that ketamine suppresses burst firing in LHb neurons which increases normal tonic activity associated with the remediation of behavioral deficits in two rodent depression models [426] (see **Figs. 1.9** and **1.10**). The authors suggest that depression may be encoded via upregulation of Kir4.1 channels on astrocytes surrounding LHb synapses which leads to increased buffering of K^+ causing neuronal hyperpolarization; this can then de-inactivate T-type VDCCs leading to potentiation of NMDARs, ultimately causing a pathophysiological bursting behavior in LHb neurons. In this model, ketamine treatment regularizes LHb neuronal firing by blocking NDMARs, thereby accomplishing a similar reduction in both bursting activity and depression-like behavior as with Kir4.1 knockout rodents [427] (**Fig. 1.11A**). In zebrafish, ketamine induced antidepressant effects during a behavioral task of futility-induced passivity (FIP) [490] (**Fig. 1.11B-D**); this task had previously been shown to elicit FIP associated with the accumulation of Ca^{2+} inside brainstem radial astrocytes driven by NE signaling to thereby suppress swimming [491]. The current study found that ketamine treatment induced Ca^{2+} accumulation within radial astrocytes of the hindbrain in much larger and longer-lasting waves than seen during FIP, with the former sufficient to suppress passive behavior and the latter occurring during passive behaviors; thus, the degree to which accumulation of Ca^{2+} in astrocytes occurs drives either passivity or its overcoming, providing a subtle yet robust marker of ketamine's effects on zebrafish behavior (**Fig. 1.11E-F**). Interestingly, the behavioral effects of ketamine were not blunted by blocking associated neuronal activity, suggesting a neuron-independent mechanism by which ketamine encodes its antidepressant effects [490]. These results indicate that ketamine may alter the function of astrocytes as a means of rescuing behavioral deficits; indeed, esketamine administration has been shown to alleviate behavioral deficits in a rodent model of depression while also enlarging HC astrocytes [410]. Furthermore, ketamine has been shown to affect many functions of astroglia, including upregulating membrane cholesterol density to mediate increased neuroplasticity [492]; in turn, astroglia may help mitigate ketamine's potentially excitotoxic effects at subanesthetic doses [493]. While SSRIs were not shown to affect passivity or Ca^{2+} signaling in astrocytes in the aforementioned zebrafish assay [490], there is evidence that they can rescue astrocyte dysfunction in a rodent model of depression [474] as well as in MDD patients (correlated with relief of symptoms) [469] and may even depend on astrocytic functions to exert their effects [494]. Conversely, MXE may not depend on astrocytes and mediate its effects solely through neurons [211], though these findings have been demonstrated only *in vitro*. In all, ketamine's effects on astrocytes across species may distinguish its antidepressant mechanism from other medications and may provide the key to understanding the phenomenon of its rapid relief of symptoms in MDD patients.

1.6.4. Neuronal Anatomy

Another question regarding ketamine's antidepressant efficacy concerns the specific portions of the neuron on which it exerts its effects. Different parts of the neuron contain varying densities

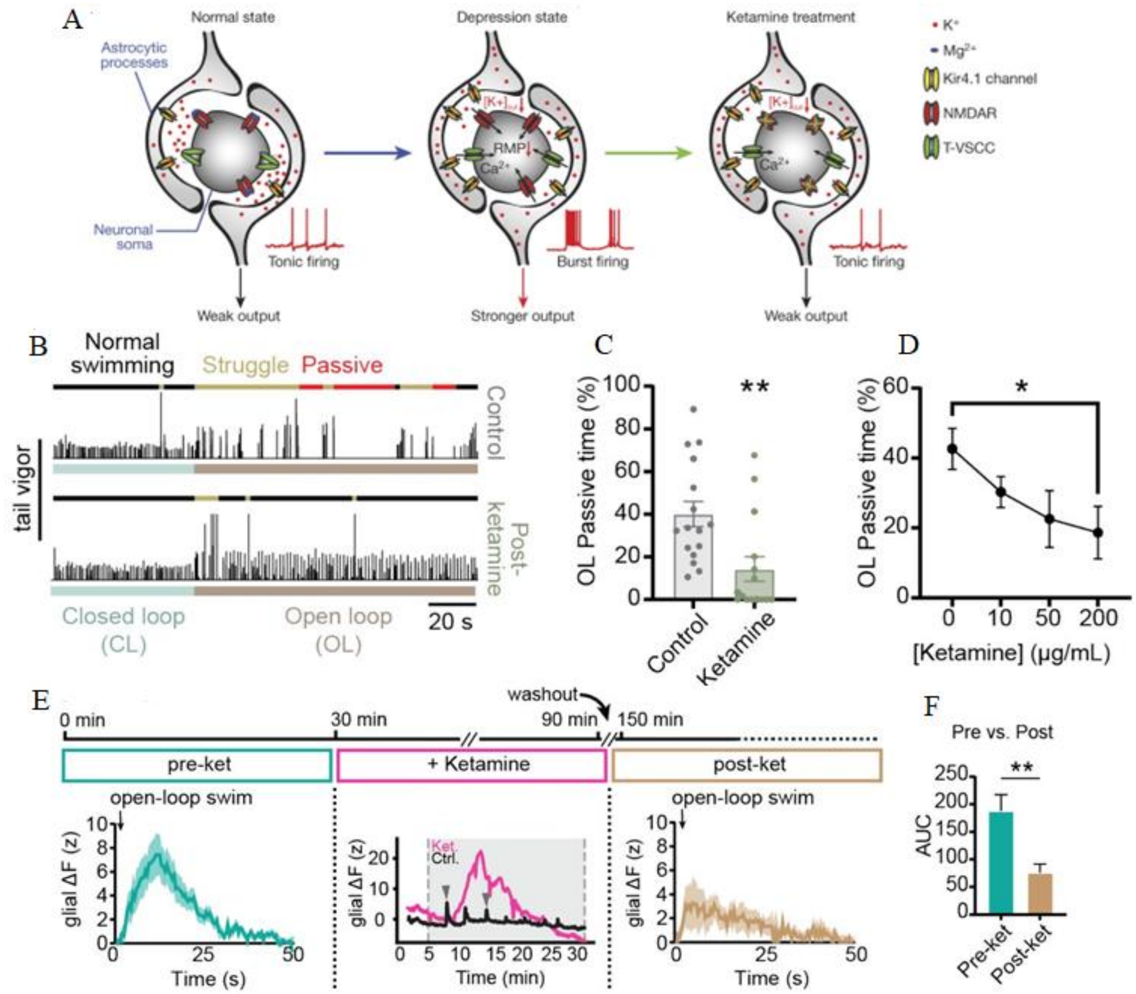

Figure 1.11. ***(A)*** In this model, normal tonic output of LHb neurons (*left*) can be altered to burst firing in the depression state (*middle*) via upregulation of Kir4.1 channels on astrocytes which causes enhanced K^+ sequestration and therefore less K^+ available for the neuron to release during an action potential leading to hyperpolarization. This can then cause de-inactivation of T-type Ca^{2+} channels which leads to NMDAR bursts due to Ca^{2+}+ flux. Ketamine treatment (*right*) blocks NMDARs and reduces neuronal firing. (Adapted from Fig. 5 of [427].) ***(B-D)*** During closed loop (CL) swimming, restrained fish receive congruent visual feedback, while during open loop (OL) swimming, the visual feedback is incongruent. Tail movements are more vigorous and sustained during OL swimming after 1 h of ketamine exposure vs. control (***B***). The amount of passivity decreases substantially after ketamine treatment (***C***) in a dose-dependent manner (***D***). ***(E)*** Before ketamine treatment, glial Ca^{2+} physiology demonstrates a large brief peak of fluorescence corresponding with futility (*left*, peaks in *middle*); during 1 h ketamine treatment, the brief peaks are replaced by a long (~15 min) fluorescence peak corresponding to decreased passivity (*middle*, *pink*); after ketamine treatment has been washed out, further futile swimming demonstrates lower Ca^{2+} activity (*right*) corresponding to less passivity behavior during OL swimming. ***(F)*** Significant differences in the size of Ca^{2+} transients between pre- and post-ketamine-treated fish during OL swimming. (*P < 0.05, **P < 0.01; adapted from Figs. 1 and 4 of [490].)

of transporters and channels, geometries, and proximities, which could be important for discerning where and with what ketamine interacts. Two main regions deserve attention: dendrites and axons, the principal players in the formation of synapses.

Dendrites are involved with receiving and transmitting information via electrophysiological signals. Spines are small extrusions of membrane populating the terminal points of shafts, which branch out from the cell body, and almost uniformly compose the postsynaptic half of neural synapses of which the vast majority signal with excitatory neurotransmitters [495,496]. Neuroplasticity is largely the result of remodeling current spines or creating new ones [496], and changes to dendritic formations are ongoing processes occurring over the lifetime of an animal which can become dysregulated in response to negative environmental stimuli [497]. Rodent models of depression show alterations in both dendritic density and function: in both the PFC [384-387,497] and HC [403-405,497], dendritic spine atrophy occurs (while in other regions, such as the amygdala and nucleus accumbens (NAc), spine formation is more typical [497]), consistent with changes in overall neuronal density seen in these areas when animals are subjected to chronic stress. Corroborating the findings in animals, MDD patients likewise demonstrate reduced spine density as well as volume in both the PFC and HC [394,498-500]. The mechanisms by which particular regions undergo dendritic decay or formation in response to chronic stress are not well understood [497], but the fact that spine atrophy and dysfunction appear before the manifestation of symptoms in several neuropsychiatric disorders [496,501] suggests that tracking such changes could be imperative in the treatment of MDD. Ketamine can partially reverse PFC spine atrophy in rodent models of depression [318,502] as well as induce spine formation after transient application *in vitro* [503]; additionally, fluoxetine [504] as well as the psychedelic antidepressant candidates LSD [503], TBG (an ibogaine derivative) [505], and 5-MeO-DMT [506] have been shown to engender synaptogenesis, all of which may operate via common downstream signaling pathways [503] (see Chapter 1.7). Future work is required to narrow down which mechanisms are causally connected to RAADs specifically versus other antidepressants, but there is no question that dendritic remodeling and spine formation are crucial to both the underlying pathophysiology of depression as well as its amelioration via neuropsychiatric compounds.

Axons are responsible for propagating action potentials from cell bodies to terminals, the latter of which in ramified form compose the presynaptic half of most synaptic clefts. Terminals are involved with the release of neurotransmitter through vesicles and contain both reuptake transporters for the recycling of synaptic transmitter as well as repackaging architecture to allow for repeated release events. Thus, any study demonstrating a reduction or dysfunction in synaptic transmission secondary to chronic stress or the diagnosis of MDD will necessarily involve changes to axons. While axonal loss or dysfunction has not been well-studied as a cause of depression, there are studies demonstrating that degeneration of monoaminergic axons is implicated in the pathogenesis of depressive behavior; specifically, Parkinson's disease (PD) patients with depression and anxiety demonstrate reduced dopaminergic innervation of the limbic system [507-509] as well as distributed loss of serotonergic innervation throughout the midbrain, with the degree of depression and anxiety correlated with increased serotonergic lesions [509,510]. In PD patients, non-motor symptoms such as depression precede the cardinal motor signs [511], which could suggest that one manifestation of MDD occurs along a spectrum of monoaminergic innervation loss among critical midbrain structures of which the more extreme version is the development of PD motor signs. In rodent models, destruction of monoaminergic neurons using the parkinsonism-inducing compound 6-OHDA can also cause depression-like symptoms [512,513], and monoaminergic neuron damage is seen in rodents exposed to various types of chronic stress [514-516] or toxins [517], potentially providing insight into one pathophysiological mechanism by which depression can manifest. Administration of SSRIs to rodents with chemical- or behavior-induced degeneration of monoaminergic axons can mitigate these losses [518], as can TCAs [514,515,519] and atypical antidepressants [519,520]; fluoxetine seems to be unable to regenerate catecholaminergic axons [520] but can affect serotonergic neurons [518,521]. There has not been much investigation into the ability of ketamine to regenerate axons in animal models of depression, though one study demonstrated that esketamine can prevent cell death in axotomized primary HC culture neurons with effects apparent within a day [522], suggesting a possible rapid effect of ketamine on axonal regrowth, whereas chronic (three to four weeks) treatment with typical antidepressants *in vivo* was required to regenerate axons [514,521]. One possible theory regarding the difference in the time course over which SSRIs and other typical antidepressants act concerns the amount of time that axonal regeneration takes [523] (about 1 mm per day [524]), which could indicate that different pathophysiologies of MDD may manifest with similar symptoms but require separate treatment paradigms to address, as well as suggest that the relative difference in time till therapeutic benefit could be a function of the manner in which each underlying pathophysiology is addressed by its optimal therapy.

1.6.5. Distribution in Compartments

As mentioned previously (see Chapter 1.5), the effect that biochemical properties such as pK_a, $LogD_{pH7.4}$, and V_d have on the ability of neuropsychiatric drugs to achieve clinical effects is a chief consideration in the investigation and development of medication regimens. Practical aspects of RAAD development concern the potential location(s) in the CNS (both around and inside cells) at which these compounds might appear; this would more fully inform our understanding of their pharmacokinetic and pharmacodynamic profiles, allowing us insight into what is important for ketamine to achieve its antidepressant effects as well as exert off-target effects. Therefore, in this section, we will review the cellular compartments in which ketamine and other RAADs have been found as well as what might interact with ketamine; ultimately, many spaces in the body, such as subcellular compartments and synaptic clefts, can achieve drastically higher concentrations of drug, so one goal of future investigations should be to redefine the physiologically and pharmacologically relevant concentration to account for site-specific accumulation.

Plasma drug concentrations are crucial for determining effective dosing regimens to account for clearance and metabolism. As described previously, the concentration of ketamine in plasma after IV or IM administration for anesthesia is 9.3 μM [106], with awakening occurring at plasma concentrations of 2.7-4.7 μM [106,116,525]; esketamine is about three times more potent than arketamine for inducing anesthesia [116]. IV or IM administration of ketamine for analgesia results in lower concentrations (0.29-0.67 μM [98,114-116]), with both esketamine and arketamine displaying similar effective concentrations (0.84-0.95 μM [116,526]). Antidepressant doses of ketamine administered IV are achieved at plasma concentrations similar to those used for analgesia (0.32-0.78 μM [116,144,147]) and with the aforementioned differences between the potencies of arketamine and esketamine for exerting behavioral effects in animal models of depression (see Chapters 1.3 and 1.4). IN esketamine, the FDA-approved route of administration for the treatment of TRD, likely induces antidepressant effects at similar plasma concentrations to IV administration, though this has yet to be confirmed in humans [527]. Two other large compartments of the body are important for discerning the effects of RAADs. First, cerebrospinal fluid (CSF) receives ketamine from plasma through the blood-CSF barrier [528] as well as the brain once ketamine has crossed the BBB [174,528]. The continual exposure of the brain to ketamine from the CSF and the time course over which this occurs is likely different than the brain exposure to ketamine from plasma, as hepatic metabolism rapidly diminishes ketamine plasma concentration (near zero within a day of administration following subanesthetic doses [116]). Deletion of two membrane-bound efflux transporters in rats led to CSF (1.74 times) and plasma (1.93 times) concentrations higher than seen in WT [529], indicating that ketamine is a substrate for efflux transporters which would impact brain exposure. Another major compartment, the interstitial fluid, has not been evaluated as a potential reservoir following ketamine administration, but it could nevertheless serve as another internal source of ketamine after distribution into tissues has occurred.

While the interaction between a compound and a PM-bound receptor is considered to be the canonical means by which downstream intracellular cascades are initiated, the effect of molecules which can traffic intracellularly has more recently become of interest for investigating the mechanisms underlying pharmacotherapy [530-532]. ‘Inside-out’ pharmacokinetics involves drugs crossing into the intracellular space — and, further, into organelles — which at physiological pH have electrochemically neutral forms [533]; many antidepressants are weak bases [530] (see Chapter 1.5) and thus significant numbers of uncharged molecules can cross membranes without the need for transporters or channels [532]. Once inside cells, these molecules can likewise cross into the lumen of many organelles, including vesicles, endosomes, lysosomes, the endoplasmic reticulum (ER), the Golgi apparatus, and the nucleus [531]. It has been demonstrated that nicotine ($pK_a = 7.5\text{-}8.1$ [533]) can enter the ER in its uncharged form to induce the upregulation of nAChRs on the PM which has been associated with the development of addiction [532-535], indicating that other weakly basic drugs could potentially interact with targets inside organelles to exert both their main and side effects. In several membrane-bound organelles, the intra-organellar spaces are held at pH values up to several log units lower than physiological pH [531]; once acidic organelles take up the neutral form of a weakly basic drug, some large portion of those molecules become charged again, thereby preventing them from crossing back into the cytosol. In the case of antidepressants, although the empirical data for the consequences of such a concentrating effect (termed acid trapping [536]) are lacking, intra-organellar accumulation — demonstrated with weakly basic antipsychotic drugs which become ~50-100 times more concentrated within acidic vesicles [537] — could undoubtedly provide a mechanism by which everything from chaperoning of a receptor population within the ER [530,532,538] to the release of neuropsychiatric drugs as part of typical vesicular transmission [537] is explained. For membrane-less organelles that present potential intracellular targets for ketamine's antidepressant activity, such as ribosomes and the nucleolus, consideration may be given to protein phase separation, a process in which a well-mixed solution containing proteins separates into a dense phase and a dilute phase [539]. The dense phase can in certain instances function as an intracellular compartment, which could increase the concentration of certain molecules inside it to influence biochemical pathways; such compartments have diverse potential roles in cellular processes, and there is evidence that neurodegenerative diseases are associated with aberrant protein phase separation due to altered solubility [539], providing a potential paradigm in which the actions of antidepressants on underlying pathophysiology can be evaluated based on the formation, maintenance, and repair of intracellular/intra-organellar condensates. Evidence that both ketamine [540] and MXE [214] increase the phosphorylation of ribosomal protein S6 (a marker of synaptic plasticity also acting as a marker of pathophysiology in animal models [541]) indicates that interactions within phase-separated compartments could be involved in the mechanisms by which RAADs exert their effects.

Another compartment within which ketamine and other antidepressants could accumulate is the PM itself, as membrane partitioning is the other main way weakly basic drugs become trapped in cells [536]. Typical antidepressant drugs have high V_d (escitalopram: 20 L/kg [277]; fluoxetine: 11-88 L/kg [278]; TCAs: 10-50 L/kg [279]) as well as generally lipophilic behavior (see Chapter 1.5 and Chapter 3), indicating that they interact significantly with membranes. Indeed, the accumulation of both escitalopram and fluoxetine as measured *in vitro* are among the largest recorded for any drug [542,543], which indicates that both the long time course for achieving therapeutic benefit as well as undesirable phenomena such as antidepressant discontinuation syndrome are due at least in part to the high uptake by membranes. Esketamine has been shown to cross the PM and enter the ER within seconds [544], which means it can interact with membrane lipids (though likely to a far lesser extent than fluoxetine or escitalopram); additionally, the more rapid time course of its entry and exit into cellular compartments compared to the SSRIs [543] may provide some insights into the reasons why their therapeutic effects ensue over much different periods of time. The composition of PM lipids influences the accumulation of compounds in the membrane phase [542,545], and other physical properties of the PM such as curvature [546], thickness [547], and fluidity [548] all effect how drugs interact with the PM; these features may also vary across cell types or as a result of underlying pathology. Membrane fluidity is influenced by the presence of lipid rafts, which are cholesterol-, sphingomyelin-, and cytoskeleton-rich regions that stiffen the membrane and regulate cellular signaling [549]. Lipid rafts can also store $G_{S\alpha}$, the subunit of G_S that stimulates cyclic adenosine monophosphate (cAMP) to activate downstream intracellular signaling [550], where its ability to upregulate cAMP is reduced [551,552]. Interestingly, $G_{S\alpha}$ can be translocated to non-raft membrane sections after the chronic (multi-day) administration of various types of typical antidepressants, such as TCAs [553,554], SSRIs [553-555], SNRIs [554], and atypical antidepressants [554]. Recently, the interaction of ketamine with raft domains during a short (15 min) incubation was demonstrated to exert the same effects on $G_{S\alpha}$ translocation [549], indicating that this may present a common mechanism for increasing intracellular signaling in patients with MDD (who may have dysregulated cAMP signaling [551]). The degree to which ketamine and other RAADs differ from typical antidepressants in their $G_{S\alpha}$-displacing effects is as yet not well understood (though (2R,6R)-HNK likewise displaces $G_{S\alpha}$ from raft domains after transient exposure [549], indicating a potential commonality among RAADs) but may depend on their ability to access lipid raft domains only briefly, as the accumulation of typical antidepressants in rafts [556] may be sufficient but not necessary to upregulate aberrant cAMP signaling and could instead reflect the tendency of non-RAADs to stay in the membrane phase, thereby slowing their therapeutic effects [543].

1.7. Potential Common Mechanisms of Antidepressants

Thus far, we have discussed the direct effects of ketamine and other antidepressants on receptors, neuronal subpopulations, and CNS cells. However, the downstream mechanisms by which antidepressants lead to changes in underlying physiology — and therefore engender long-term changes in behavior — are critical to understanding how ketamine acts, but, more broadly, may provide explanations as to how various antidepressant drugs belonging to different classes with vastly different chemical properties can achieve similar therapeutic results.

Brain-derived neurotrophic factor (BDNF) is a neural growth factor involved in the growth of new synapses as well as neuronal maturation [557]. BDNF is produced within neuronal and glial soma where it can either travel along to axon terminals to be released into the synaptic cleft [558] or transported to dendrites where it mediates activity-dependent translation independent of transcription [559]. Because of its role in synaptic plasticity, BDNF is crucial to the induction of LTP, particularly in the HC [557,560]. Presynaptic BDNF expression is thought to contribute to the efficiency of neurotransmitter release [561] while postsynaptic BDNF helps upregulate receptor trafficking, particularly α-amino-3-hydroxy-5-methyl-4-isoxazole propionic acid receptors (AMPARs) in glutamatergic synapses [562]. BDNF binds potently to tropomyosin receptor kinase B (TrkB) [563], a receptor tyrosine kinase which mediates BDNF's neuroplastic effects both pre- and postsynaptically [557,564]. Because of the association between deficits in neuroplasticity and the pathophysiology of depression [560], BDNF-TrkB signaling has been proposed as a mechanism to explore in both animal models of depression as well as experiments assessing response to antidepressant treatment. In rodent models of depression, BDNF has been shown to be reduced in the HC [565-569] (though not always clearly so [570,571]) and PFC [568,569]; additionally, rodents with focal loss of forebrain (only among females) [572] or HC [573] BDNF expression demonstrate depression-like behavior. In MDD patients, postmortem analysis reveals that expression of BDNF-related genes from cortical samples [574] is reduced; furthermore, BDNF mRNA was lower in the amygdalae of female patients [575] as well as the HC and PFC of suicide completers [576,577], and TrkB expression was likewise reduced in cortical samples [574] as well as in the HC and PFC among suicide completers [576] (though perhaps not all [578]). Serum BDNF is lower among MDD patients than controls [579-583], though it does not consistently track depression severity [583]. Direct infusion of BDNF into the midbrain and HC bilaterally ameliorated behavioral deficits in rodent LH models [584,585] which were observed within three days of intervention and were blocked by administration of a broad-spectrum tyrosine kinase inhibitor [585], suggesting a causal connection between BDNF-TrkB signaling and antidepressant effects. Interestingly, while BDNF and TrkB deficits in the PFC and HC are typically associated with depression [586], BDNF activity in the VTA and NAc may be associated with its onset: intra-VTA infusions of BDNF in WT rodents led to the development of depression-like behaviors [587], while selective deletion of BDNF genes in the VTA abolished the behavioral deficits from SDS [588]; furthermore, blocking BDNF-TrkB — but not DA — signaling in the NAc interrupted the instantiation of depression-like behavior resulting from SDS, while optogenetic stimulation of the VTA-NAc circuit during SDS exacerbated behavioral deficits [589]. These findings have been corroborated in rodent models of depression in which increases in NAc BDNF are associated with behavioral deficits [568,569] as well as in postmortem analysis of MDD patients which demonstrated significantly increased BDNF in the NAc compared to controls [590]. As far as treatment with antidepressants is concerned, their dependence on BDNF is more well-characterized than any causal relationship between BDNF-TrkB signaling and the pathophysiology of depression [560]. The first evidence that antidepressant treatment increases BDNF expression came from a rodent study demonstrating that ECT and a variety of antidepressants administered over the course of weeks caused elevations of BDNF and TrkB mRNA in both the HC and PFC [591], commensurate with the time period in which these treatments ameliorate the symptoms of MDD [560]. Further rodent studies have corroborated these results [586], as have postmortem analyses showing increased HC BDNF expression among medicated MDD patients compared to their unmedicated counterparts [577,592] as well as consistently higher serum BDNF levels [580]. HC neurogenesis is increased by chronic administration of typical antidepressants in rodents [593,594], while TrkB mediates antidepressant-induced neurogenesis in the HC as well as improvements on the NSF and TST [595]. Chronic (multi-week) treatment with SSRIs increases dendritic spine density in the PFC [596,597] and HC [598,599] and reverses HC spine atrophy seen in rodent chronic stress models [600]. Similar to the dependence of typical antidepressants on BDNF expression, ketamine likewise alters BDNF-TrkB signaling concomitant with the amelioration of depression-like symptoms in animal models. Ketamine has been shown to increase the activation of HC TrkB within hours post-administration while also increasing BDNF protein translation there, and BDNF and TrkB KO animals were insensitive to ketamine’s antidepressant effects [601]. Infusion of a neutralizing BDNF antibody into the rodent mPFC 30 min before ketamine injection blocked its antidepressant effects [602], while co-administration with a TrkB inhibitor reduced the ability of both es- and arketamine to produce an antidepressant response in two behavior-induced rodent models of depression; furthermore, both es- and arketamine ameliorate dendritic atrophy from SDS in the HC but do not reduce dendritic arborization in the NAc [169]. In humans, ketamine infusion to treat TRD leads to a rise in plasma BDNF within hours concomitant with clinical improvement [603,604]; higher BDNF levels are found among clinical responders than among non-responders [605] and the difference is sustained out to one week post-administration [606]. In one study, the rise in BDNF was correlated with reduced resting state functional connectivity (RSFC) from the mPFC to other cortical areas [604], the connectivity of which has been found to be aberrant in MDD patients [607]; these functional changes may provide a non-invasive measurement of ketamine-mediated neuroplasticity in RSFC correlated with relief of symptoms within 1 d of treatment [604]. Although studies assessing the relationship between the Val66Met mutation — which leads to decreased synthesis of BDNF from its precursor molecule [608] — with susceptibility to depression in both mice [609,610] and patients [611] do not prove a conclusive link between the two, this genotype is nevertheless associated with a reduced response to both ketamine [609] and scopolamine [612] in rodents (which was corroborated in a small human study [613]) potentially demonstrating that a subpopulation of MDD patients may be less treatable by RAADs and providing evidence that a deeper understanding of pharmacogenomics is required for more patient-tailored antidepressant regimens. Perhaps the most interesting recent result regarding the role of BDNF-TrkB signaling in mediating the antidepressant effect of both RAADs and typical antidepressants shows that ketamine, (2R,6R)-HNK, fluoxetine, and imipramine all bind directly to the transmembrane domain of the TrkB receptor, potentially even at the same site [614]. Mutations to the transmembrane domain substantially decreased binding by all compounds while attenuating their antidepressant effects in several rodent behavioral tasks; perhaps most interestingly, all tested antidepressants facilitated upregulation of TrkB receptor expression in a cholesterol-dependent manner at clinically relevant concentrations [614] (**Fig. 1.12A-I**). These results implicate not only BDNF-TrkB signaling but also cholesterol signaling as common mechanisms by which antidepressants exert their effects; direct binding to TrkB receptors by antidepressants thus might be required for a compound to act as an antidepressant, which would help provide another necessary feature when considering the development of future therapeutics.

The mammalian target of rapamycin (mTOR) is a serine/threonine kinase found across species with a conserved set of functions, including regulation of cell growth, proliferation, motility, survival, synthesis, autophagy, and transcription [615]. mTOR is organized into two

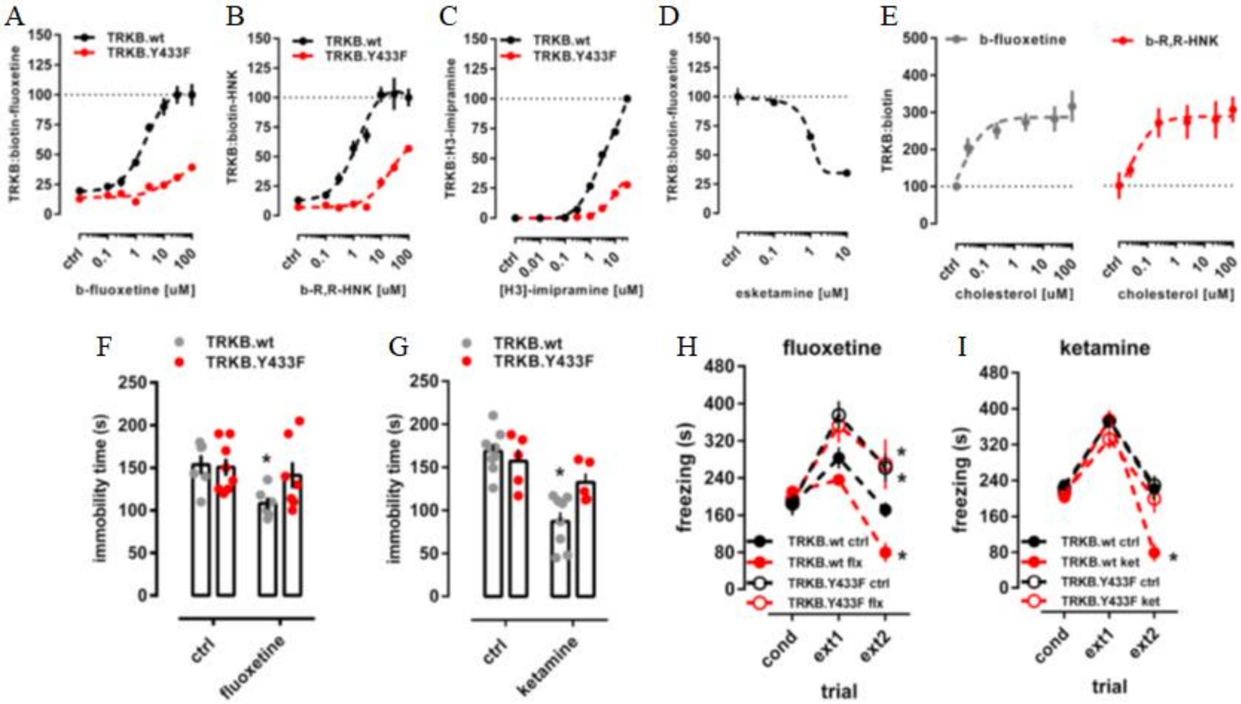

Figure 1.12. ***(A-C)*** Binding of biotinylated fluoxetine (b-fluoxetine; ***A***), biotinylated (2R,6R)-HNK (b-R,R-HNK; ***B***), and tritiated imipramine ([H3]-imipramine; ***C***) to both WT TrkB receptors (TRKB.wt; *black*) and mutant TrkB receptors (TRKB.Y433F; *red*) demonstrates that each antidepressant's binding to TrkB is significantly decreased at physiologically relevant concentrations when a binding site mutation is made. ***(D)*** Esketamine substitutes for b-fluoxetine at physiologically relevant concentrations at the TrkB receptor. ***(E)*** Both fluoxetine (*left*, *gray*) and (2R,6R)-HNK (*right*, *red*) have increased binding potency to the TrkB receptor in the presence of increasing concentrations of cholesterol. ***(F and G)*** Immobility time on the FST is decreased from fluoxetine (***F***) and ketamine (***G***) administration but only when they can bind to the WT TrkB receptor (ctrl = control). ***(H and I)*** Both fluoxetine (***H***) and ketamine (***I***) depend on the TrkB receptor to facilitate fear extinction across multiple sessions of a conditioning task (cond = conditioning, ext1 and ext2 = extinction sessions).(Graphs are mean values with SEM; *P < 0.05; adapted from Figs. 2 and 6 of [614].)

complexes with many similar functions, mTORC1 and mTORC2 (the latter of which has special function as a tyrosine kinase to activate downstream growth factors [616]). Both complexes interact with many different subcellular organelles, with mTORC1 localizing significantly to the lysosome to regulate protein catabolism [617,618]. Aberrant mTOR signaling is implicated in the pathogenesis of MDD, with reductions in pathway function found in the PFC of both MDD patients [619,620] and in rodent models of depression [621-624]. In particular, mTORC1 has been demonstrated to be a common target for neurotrophic factors such as BDNF and is therefore implicated in synaptic plasticity, a key mechanism which can be defective in neuropsychiatric disorders as well as a target for antidepressants [625]. Some SSRIs (escitalopram and paroxetine) as well as a MAOI (tranylcypromine) have been found to upregulate phosphorylation of mTOR in HC primary cultures which causes dendritic growth, while other antidepressants (fluoxetine, sertraline, and imipramine) do not; the positive effects can be blocked by either rapamycin or other mTOR inhibitors [626]. In other studies, however, imipramine has been found to inhibit mTOR in an autophagic manner in glioma cells [627], two weeks of fluoxetine (in combination with methylphenidate) administered to juvenile rodents induced mTOR activation [628], and sertraline has been shown to inhibit mTOR-dependent cell proliferative functions in cultured cells [629], suggesting that individual antidepressants interact with mTOR signaling in different ways; indeed, the antidepressant effects of the SSRI paroxetine appear to depend on HC mTOR activation in a CUS rodent model of depression [630]. The long time course over which typical antidepressants exert their therapeutic effects likely means that their interaction with mTOR signaling is necessarily more complex, while RAADs may more directly signal through mTOR to achieve neuroplasticity [631]. The most interesting findings regarding the role of mTOR in mediating antidepressant effects regard its interaction with ketamine. Working from the hypothesis that ketamine’s rapid activity involves inhibition of NMDARs on GABAergic cortical interneurons [290], the subsequent surge of glutamatergic transmission from downstream cortical neurons can lead to activation of mTOR via BDNF-mediated synaptogenesis [632]. Supporting this claim, ketamine has been shown to increase mTORC1 activity causing increased synaptogenesis in the HC [633] and the PFC [298] of rodents which correlates with antidepressant effects; rapamycin, the eponymous mTOR inhibitor, can block ketamine-induced synaptic changes [634] and its intra-cerebral administration in SDS model rodents may reveal that esketamine (but not arketamine) depends on mTOR activity to exert its antidepressant activity [635]. Interestingly, different downstream mechanisms may be involved with different phases of ketamine’s effects, with TrkB signaling required for ketamine’s initial stimulation (within 1 h) of dendritic growth while mTOR mediates longer-term (within 3 d) neuroplastic effects [503]. Ketamine may act in part as an upregulator of mTOR via its inhibition of glycogen synthase kinase 3 (GSK-3), a known inhibitor of mTOR [636,637]; indeed, a subthreshold dose of ketamine along with the GSK-3 inhibitor lithium has been shown to both activate mTORC1 as well as increase PFC spine density and exert antidepressant effects greater than from ketamine alone in rodents [637], and further evidence supports the necessity of

GSK-3 inhibition as part of ketamine's antidepressant mechanism in a rodent LH model because mice with constitutively active GSK-3 signaling are resistant to ketamine's effects [638]. Of note, in a trial of MDD patients, pre-treatment with oral rapamycin not only did not block IV ketamine's antidepressant effects but even potentiated them over a two-week period [639]. However, in a follow-up study assessing suicidality among TRD patients, pre-treatment with rapamycin did not enhance ketamine's significant antidepressant action [640]. These results may suggest that systemic rapamycin has different neuroplastic effects than the more local administration used in animal studies, but could also indicate that the underlying pathophysiology of depression in humans represents a more complex set of targets for treatment [639]. Furthermore, ketamine's general antidepressant properties may operate via different downstream pathways than its amelioration of suicidal ideation; patients with low suicidality (such as those assessed in the aforementioned study) may not demonstrate decreased risk due to floor effects [640]. Other RAADs — scopolamine [612,641] and (2R,6R)-HNK [382] (though this is not yet clear [174]) — as well as RAAD candidates — rapastinel [642-644], the mTORC1 activator NV-5138 [645], the mGluR2/3 antagonist LY 341495 [646], and the NDMAR GluN2B antagonist Ro 25-6581 [299] — may operate through the mTOR pathway as well, ensuring that its potential importance in mediating antidepressant activity per se will remain a lively subject of inquiry.

While the direct effects of ketamine at NMDARs are well-documented, investigations into the actions of ketamine on AMPARs have proved crucial to understanding the downstream mechanisms of antidepressants more broadly. AMPARs are tetramers with four different subunit types (R1-R4), with double dimers being the most common configuration [647]. Whereas the permeability of NMDARs to Ca^{2+}on the postsynaptic membrane is conditional on both presynaptic glutamate release and membrane depolarization, AMPARs are Na^+ channels that are opened simply from glutamate binding; adjacent to NDMARs on the postsynaptic membrane, AMPARs are involved in the perpetuation of neurotransmission via postsynaptic neuronal depolarization [648]. In rodents, the effect of both acute and chronic stress on AMPAR expression is unclear: while several studies report decreased expression of AMPAR subunits (particularly GluR1 in the HC), others report either no change or even increased expression [649]. Perhaps the length of the chronic stress paradigm can partially explain the discrepancies [649], as rodents subjected to 1-3 weeks of stress [650-652] had increased HC GluR1 whereas those undergoing greater than four weeks of stress [653-655] had reduced HC GluR1. Possible reasons for the overall unclear relationship include differences in stress paradigms, variation in animal age, and inconsistent GluR1 detection methods [649]. In MDD patients, the evidence for dysregulation of AMPAR activity is largely lacking, though postmortem studies have demonstrated increased AMPAR binding in the cingulate cortex [656] as well as reductions in GluR1 and GluR3 mRNA around the HC [654,657]. Much like for the association between aberrant BDNF activity and depression, the evidence for the necessity of AMPARs in antidepressants achieving their effects is clearer than any associations between AMPARs and underlying pathophysiology. AMPAR upregulation has been demonstrated in rodents treated chronically (several weeks) with TCAs and SSRIs in both HC [658-661] and cortex [596,661]. In terms of behavior, co-administration of fluoxetine with an AMPAR blocker reduced the antidepressant response in CUS rodents [662], though the AMPAR antagonist NBQX was unable to block the antidepressant effects of imipramine [649]. The connection between AMPAR activity and the antidepressant effects of ketamine are even stronger; indeed, clearer evidence supports the role of AMPAR signaling than direct NMDAR inhibition [663]. Part of ketamine’s long-lasting clinical potency is mediated by changes in AMPAR signaling [284] (including longer-term mediation of dendritic growth [503]), with ketamine upregulating AMPAR excitatory activity in the PFC [286,664] and HC [601,665,666] both *in vitro* and *in vivo*. Ketamine can specifically cause increased expression of both GluR1 and GluR2 subunits in HC synapses one day after treatment [174], providing a more direct link to previously mentioned postmortem studies indicating that both rodents and MDD patients lack GluR1 subunits in HC [653-655,657]. Most crucial to the theory that AMPARs are necessary for the antidepressant effects of ketamine is the effect of inhibition or direct stimulation of AMPARs. Administering NBQX 10 min prior to injection with ketamine abolished both the short-term (within 1 h) and longer-term (1 d) antidepressant effects of ketamine in rodents [174,633,667,668], and NBQX administration 23.5 h after ketamine injection blocked the longer-term antidepressant effects measured during the FST 30 min later [174]; perhaps unsurprisingly, arketamine’s effects are likewise blocked by NBQX [169,173,174]. AMPAR positive allosteric modulators (PAMs) [662,669-671] as well as chronic administration of AMPA itself [672] act as antidepressants in rodents, though the AMPAR PAM Org 26576 has failed to consistently relieve depression in clinical trials [673,674]; perhaps such compounds are best used as adjunctive treatments for

MDD [670,672]. In rodent models, other compounds — including RAADs such as (2R,6R)-HNK [174,197], MXE [216], and scopolamine [641]; RAAD candidates such as MXE derivatives [221]; and fluoxetine [661] — appear to depend on AMPAR activation for their effects, with the RAAD candidate (S)-NK proving a possible exception [202]. Interestingly, acute (1 h) DBS of the infralimbic cortex in a rodent model of depression leads to increased synthesis of BDNF, stimulation of mTOR, and increased transcription of GluR1 subunits [675], suggesting that therapeutic DBS may manipulate the same downstream mechanisms as antidepressant medications. In parallel, the rapid phosphorylation of mTOR by ketamine necessary for neuroplasticity is blocked by AMPAR inhibition [676], and inhibition of both in the PFC diminishes ketamine's antidepressant effects in a rodent model of depression [286], corroborated by both *in vitro* [677] and *in vivo* [633] results demonstrating that AMPAR activation upregulated mTORC1 in a BDNF-dependent manner and that both ketamine as well as direct activation of AMPARs upregulate HC mTOR expression [672]. These findings lend credence to the idea that AMPAR signaling (along with activation of mTOR and BDNF) is a common mechanism by which RAADs in particular operate to relieve depression and provide another pharmacological property for which future RAAD candidates can be evaluated.

In all, the foregoing survey demonstrates that, while there are many promising leads with respect to determining where RAADs go inside the body, how fast they arrive there, and what they might interact with to exert both their antidepressant and side effects, there are as of yet few tools developed to help address these questions. The goal of our research in the Lester and Prober labs has been to develop just such tools which can be applied both *in vitro* and *in vivo*. We have thus produced RAAD-specific genetically encoded fluorescent biosensors, targetable to both the PM as well as subcellular compartments, which allow for both classic pharmacokinetic measurements as well as provide a platform upon which to investigate brain-wide changes resulting from RAAD administration.

CHAPTER 2: GENETICALLY ENCODED SENSING FLUORESCENT REPORTERS FOR RAPIDLY ACTING ANTIDEPRESSANTS IN CELL CULTURE AND ZEBRAFISH

2.1. Development of the iDrugSnFR Paradigm

Over the past decade, a variety of genetically encoded protein-based sensing fluorescent reporters (SnFRs) have been developed, allowing for the cellular and organellar expression of biosensors responsive to both endogenous (acetylcholine [678], dopamine [679,680], GABA [681], glutamate [682], serotonin [683]) and exogenous (esketamine [544], nicotine [533], nicotinic agonists [533,684], opioids [685], SSRIs [543]) compounds; we have termed the family of sensors created for the latter group the iDrugSnFRs. These sensors permit the pharmacokinetic evaluation of pharmaceuticals and drugs of abuse in live cells to answer questions concerning how these compounds interact with as well as regulate target (and off-target) structures to produce their effects. Their ability to detect physiologically and pharmacologically relevant concentrations of drug both *in vitro* and *in vivo* marks the iDrugSnFRs as powerful tools which can inform the development of novel medicines with wider therapeutic windows.

The isolation of what is now called green fluorescent protein (GFP) from *Aequorea victoria* [686] inaugurated a paradigm shift in molecular biology. The GFP gene was successfully cloned and sequenced in 1992 [687], after which it was shown to be viable as a tag to monitor protein expression [688] before being modestly mutated to improve its fluorescence characteristics, exhibiting the now-classic excitation peak at 490 nm and emission peak at 510 nm [689]. Since then, a multitude of other fluorescent proteins (FPs) have been synthesized with the ability to emit light of many colors [690], allowing for multiplexed imaging to visualize biological material in many different applications [691] (see Chapter 7). The popularity of Ca^{2+} sensors (e.g. GCaMP [692,693]) to measure real-time physiological activity in neuronal cultures as well as in the brains of behaving animals [694,695] led to the development of additional functional FP-based sensors which can detect either endogenous or exogenous molecules in spatially discrete and temporally sensitive measurements [696]. Genetically encoding such sensors via transfection, transduction, or other transgenesis techniques allows for stable and repeatable imaging in a region-, cell-, and compartment-specific manner [697], superior to fluorescent dye-based imaging (e.g. BAPTA [698]) which is inherently less spatially precise. The initial design principle of GCaMP sensors, whereby Ca^{2+} binds to calmodulin causing a conformational change to a linked GFP (see Chapter 2.4.3), was expanded to include other proteins which likewise natively bind to molecules of interest. Bacterial periplasmic binding proteins (PBPs) from species like *Escherichia coli* were known to bind to small molecules such as amino acids (AAs) as part of their biological function; the GltI protein, which forms part of the ATP binding cassette (ABC) transporter complex, binds to both glutamate and aspartate [682], and this PBP was then incorporated to detect glutamate in both dye-based sensors [699] as well as those based on Forster resonance energy transfer (FRET) [700,701]. FRET sensors rely on energy transfer between two adjacent FPs in close (< 10 nm) proximity [702]: one FP acts as the donor, undergoing an initial conformational change when the target molecule binds to its recognition site, causing the orientation between the two FPs to shift such that the donor FP now fluoresces in response to excitation [703]. A pair of FRET FPs share spectral properties such that the emission spectrum of the donor FP overlaps significantly with the excitation spectrum of the acceptor FP [704]; as the donor FP fluoresces, it will thus excite the acceptor FP, which then emits light. While FRET sensors have several desirable features (e.g. the ability to leverage the ratiometric output of two FPs to more precisely and reliably measure intracellular concentration [705], relative ease of engineering [706]), the drawbacks are substantial, including limited multiplexing (FRET sensors have two emission spectra [706]) and insensitivity to small concentration changes [682]. In contrast, single FP sensors present distinct advantages over their FRET-based forebears, including better signal-to-noise and higher sensitivity to small target molecule concentrations [707]; while being intensiometric instead of ratiometric (thereby limiting their ability to act as precise reporters of concentration), single FPs avoid the scattering differences among wavelengths common in FRET-based imaging as well as contain a simpler set of emission and excitation spectra for users to monitor [706]. Another major innovation is the use of circularly permuted GFPs (cpGFPs); the N- and C-termini of GFP face the same direction which allows for simple connections to be made to the PBP, and circular permutation — in which the AAs at the N- and C-termini can be altered while keeping the same overall protein sequence — increases the number of possible fusion configurations such that the conformation in the absence of target molecule has a lower baseline intensity in order to increase the sensor’s dynamic range [704]. Short linker sequences (several AAs long) are then engineered to act as bridges between the two new termini of the cpGFP and sites on the PBP near the hinge region [706]; linkers allow for greater conformational mobility to help maximize GFP emission efficiency [708]. Upon binding of the target molecule, the PBP changes conformation, pulling on the cpGFP such that the chromophore is in a photoexcitable state. The foremost theory of how this occurs in iDrugSnFRs involves the action of the PBP interface with the cpGFP through the first linker which contains a cluster of three AAs with polar groups that in the unbound state can form H-bonds with the chromophore to quench its fluorescence and in the bound state moves away from the chromophore to allow its fluorescence [684,706] (see Chapter 3 for more details).

The first SnFR developed, iGluSnFR, demonstrated both *in vitro* and *in vivo* viability [682]. It senses glutamate during physiological events on the PM, with a half-maximal response (EC_{50}) of 4 μM in mammalian cells [682], well within physiologically relevant limits for extracellular release [709]. Since then, the Lester lab has used iGluSnFR as a springboard for the development of numerous iDrugSnFRs to detect exogenous compounds at (sub-)micromolar concentrations *in vitro* and *in vivo*. Using the OpuBC protein from *T. spX513* as the PBP (which has natural affinity for choline and betaine), our group has developed iDrugSnFRs for nicotine [533], esketamine [544], nicotinic agonists [684], opioids [685], and SSRIs [543], created by modifying the AAs in the binding pocket [710] such that specific and sensitive binding to the compound of choice is achieved (see Chapter 2.2.1 and Chapter 2.2.2). OpuBC is part of the Cluster F class of PBPs which includes a hinge region connecting two domains that both move upon ligand binding [711] (**Fig. 2.1**). One linker occurs before the new

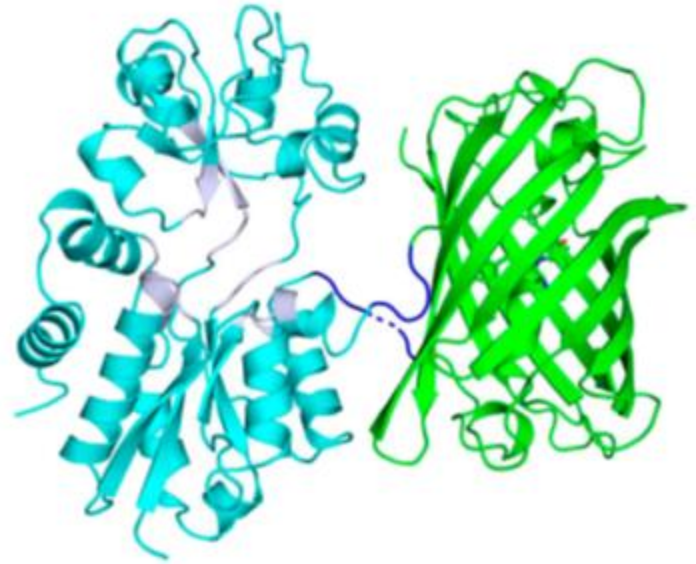

Figure 2.1. Cartoon X-ray crystallographic structure of iNicSnFR1 in the presence of nicotine (not shown). The PBP (*cyan*) is connected to the superfolder cpGFP β-barrel (*green*) via two linkers (*dark blue*) selected for their ability to produce maximal fluorescence response over baseline. Over 12,000 mutants were screened to optimize the binding site (partially obscured residues are shown in *gray*); other sensitive and specific iDrugSnFRs are constructed using similar methods (see Chapter 2.2). (Adapted from Fig. 2 of [533].)

N-terminus of the cpGFP while another occurs after the new C-terminus; each linker is four AAs long [712] (**Fig. 2.1**). The cpGFP is a 'superfolder' version which has dramatically improved robustness of fluorescent labeling allowing for reliable expression even when fused to poorly folding proteins [713]; additionally, this variant expresses well in the ER [714], a crucial feature for applications to subcellular pharmacokinetics (see Chapter 2.2.5). While the sensors have been customized to detect a wide variety of pharmaceutical compounds, of most interest are weak bases which at physiological pH will thus have a significant portion of their molecules uncharged and therefore able to cross membranes more easily (see Chapter 1.5 and Chapter 1.6.5). Thus far, of the compounds for which iDrugSnFRs have been developed, nicotine is the most well-documented and is known to operate via the inside-out pathway (**Fig. 2.2**) because it exerts its pharmacological effects in part via interactions in the ER [715], possibly a property of other weakly basic compounds [530,531]. Indeed, in the ER, nicotine not only helps chaperone nascent

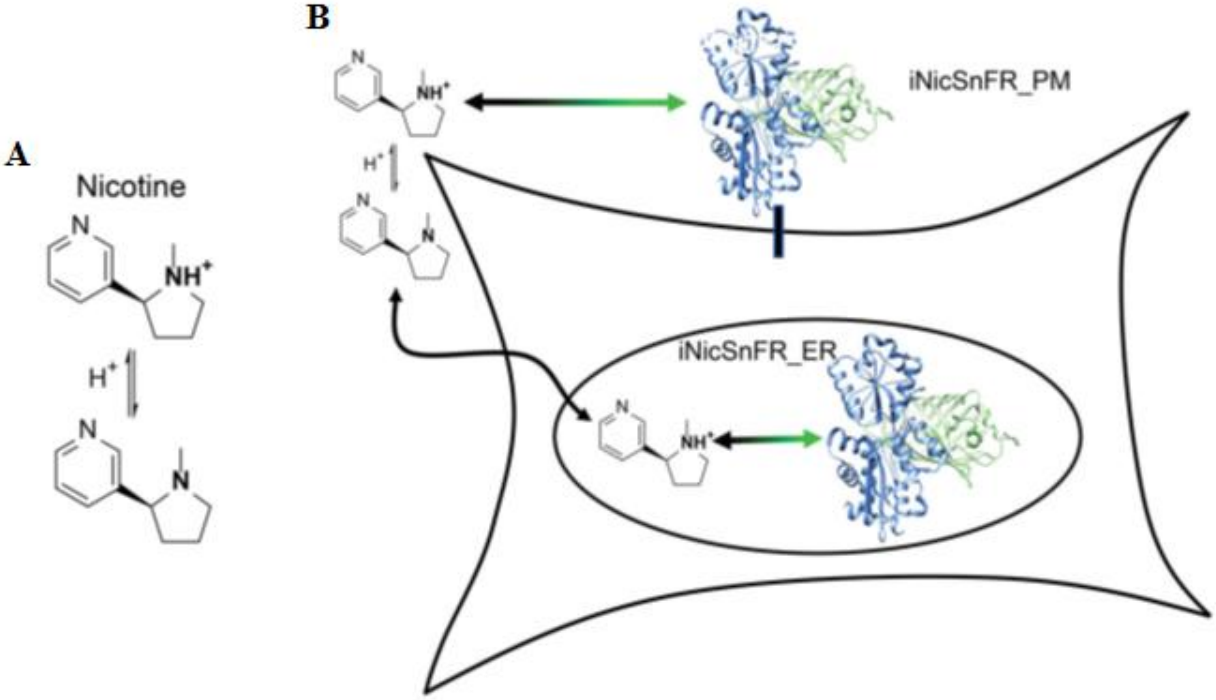

Figure 2.2. ***(A)*** Chemical structures of nicotine demonstrating its protonated (*top*) and deprotonated (*bottom*) forms (the tertiary amine of the pyrrolidine ring becomes quaternized). ***(B)*** Diagram showing the interaction of nicotine with both the PM and ER-targeted versions of iNicSnFR. Both deprotonated and protonated nicotine molecules can interact with the PM sensor (shown on the outer part of the PM) while only the deprotonated form can cross the multiple membranes required to interact with the sensor population targeted to the ER (shown inside the smaller compartment within the cartoon cell). (Adapted from Fig. 1 of [533].)

α4β2 nAChRs [534,535] but also acts on the unfolded protein response (UPR), which is responsible for managing misfolded proteins by halting translation or, if sustained, triggering cellular apoptosis [716]; by upregulating ER export of nAChRs, nicotine can reduce the UPR, leading to neuroprotective effects [532] (potentially explaining the association between tobacco use and diagnosis of PD [717]). Others of the drugs mentioned have been shown to interact with intracellular receptor populations, such as several opioid agonists with MORs in the Golgi apparatus [718] and varenicline with the same α4β2 nAChRs as nicotine [719]. Thus, developing iDrugSnFRs expressed on the PM or in subcellular compartments can allow for a greater understanding of where drugs of interest may traffic and what they might operate on to exert their (main and side) effects.

2.2. Methods for Producing SnFRs for RAADs

The following methods were used to develop the family of iRAADSnFRs (detecting esketamine, arketamine, (2S,6S)-HNK, (2R,6R)-HNK, MXE, and scopolamine) but the protocols described are generalizable to the entire family of SnFRs previously described [533,720].

2.2.1. Creating a New iDrugSnFR

The ligand binding site lies at the interdomain interface of the PBP, and mutations in this pocket are engendered to increase the sensitivity and specificity of the sensor for the drug of interest (DOI). The initial screening protocol involves using several different existing iDrugSnFRs versus a panel of drugs from a pharmaceutical class of interest for which we wish to develop sensors; these are typically weak bases (see Chapter 1.5 and Chapter 1.6.5) with $6 < \mathrm{p}K_a < 10$ with an amine group and molecular weight < 500 g/mol [720]. For a fully developed iDrugSnFR, the two factors evaluated are the change of fluorescence over baseline ($\Delta F/F_0$, unitless) and the half-maximal effective concentration (EC_{50}, in μM); the former indicates the potential dynamic range over which the sensor reports varying concentrations of DOI while the latter measures the ability of the sensor to detect the DOI at pharmacologically relevant concentrations. Their ratio,

$$\text{S-slope} = \frac{\Delta F/F_0}{EC_{50}}, \text{ in } \mu\mathrm{M}^{-1},$$

reports the sensitivity of the sensor at low (sub-micromolar) concentrations and allows for easy comparisons among candidates with different maximal $\Delta F/F_0$ ($\Delta F_{max}/F_0$) values [544]. The goal of the iDrugSnFR development process is to generate a concentration-response curve which can be fitted to the Hill equation,

$$F = \frac{[A^n]}{EC_{50}^n + [A^n]},$$

where F is the fluorescence response, A is the ligand concentration, EC_{50} is as described above, and n is the Hill coefficient (measuring cooperativity among multiple binding events); after normalizing the fluorescence values, the maximal F value reports $\Delta F_{max}/F_0$, thus providing estimates for both $\Delta F_{max}/F_0$ and EC_{50} of the particular DOI-sensor interaction *in vitro*. The concentration range of each DOI tested during development encompasses pharmacologically relevant concentrations that span ~5 orders of magnitude within the range of 1 nM to 1 mM (following roughly the range of concentrations of transmitter in the synaptic cleft [721]). Because the eventual mixture of lysate or protein with DOI will halve the effective concentration of each, the DOI solutions must be made such that all concentrations are twice the desired final concentrations.

To begin the process of screening for drug-sensor 'hit pairs' (defined as $\Delta F/F_0 > 1$) [720], we first create a drug plate containing 1 mL of up to 93 DOIs in a 96-well storage plate (2.2 mL square-well storage plate, Thermo Fisher Scientific). Each DOI is solvated in 3x PBS, pH 7.0 to a concentration of 2 mM with appropriate accounting for pH adjustment; three wells are filled with pure PBS to act as controls to monitor for cross-contamination [720]. Next, purified protein (see Chapter 2.2.3) of several candidate iDrugSnFRs from which site-saturated mutagenesis (SSM; see Chapter 2.2.2) to construct the new targeted sensor will be performed is thawed on ice at room temperature (RT) and diluted in 3x PBS, pH 7.0 to 111 nM to account for the dilution from mixing with drug (the final sensor concentration in each well will be 100 nM); enough sensor solution is made so that 100 μL can be added to each well of a 96-well assay plate (Costar, Corning) along with 11 μL of each DOI using an automatic pipetting system (ePMotion 5075, Eppendorf) [720]. Once all wells in the assay plate are filled, it is placed inside an automated 96-well plate reader (Spark M10, Tecan) where it is first shaken to mix the contents of each well before the reader (excitation: 480 nm; emission 535 nm) measures DOI-induced fluorescence; the resulting fluorescence values are then scaled and normalized using the equation

$$\Delta F/_{F_0} = \frac{(DOI - Biosensor\ F) - (Baseline\ iDrugSnFR\ F) - (Baseline\ DOI\ F)}{(Baseline\ iDrugSnFR\ F)},$$

where (Drug – Biosensor F) is the measured DOI-induced fluorescence, (Baseline iDrugSnFR F) is reported from the three wells containing just sensor added to PBS, and (Baseline DOI F) is the fluorescence response of just the DOI (measured separately by adding 11 µL of each DOI to 100 µL of 3x PBS, pH 7.0 in an assay plate using the same automated pipetting program and plate reader sequence) [720]. Hit pairs are identified and the best DOI-iDrugSnFR combinations are carried forward for further sensor development.

Once candidate starting iDrugSnFRs have been chosen for one of the DOIs, 600 ng of the bacterial vector sensor plasmid is transformed into TOP10 *E. coli* cells for amplification on ampicillin selection plates; the plasmids encode the ampicillin resistance gene *amp* [722] which helps prevent growth of invasive microorganisms. After transformation via electroporation [723], the TOP10 is added to 750 µL of SOC autoinduction media (Thermo Fisher Scientific); the mixture is then incubated in a 37ºC water bath for 1 h before 50-100 µL is spread over an ampicillin selection plate using sterilized glass beads. The plates are left with the lid facing down (to prevent condensation) overnight for ~18 h in a 37ºC incubator before being retrieved the next morning. One colony from each plate is picked and grown in 5 mL of Luria-Bertani (LB) growth medium (which increases bacterial yield [724]) along with 5 µL of 50 µg/mL ampicillin; these tubes are then placed in an incubator shaker set to 37ºC and 250 rpm for ~24 hours. The next day, the tubes are spun down in a centrifuge at 4000 rpm and 4ºC for 15 min after which the supernatant is removed; the pellet is then resuspended in 5 mL of 3x PBS, pH 7.0. The resuspended pellet is flash frozen in liquid nitrogen and then thawed at RT, after which the process is repeated twice more to extract as much sensor protein as possible in the lysate.

To perform a lysate screen with measurements made in triplicate, we first make a 2 mM stock solution of the DOI in 3x PBS, pH 7.0 with an appropriate pH correction which is pipetted into the first three rows of the first column of a 96-well storage plate, after which the automatic pipetting system is used to perform √10 dilutions in 3x PBS, pH 7.0 across the next ten columns, with the last column filled with 3x PBS, pH 7.0 as a control. The DOI plate is stored at -4ºC and thawed at RT before use. When ready to perform a concentration-response experiment, all wells in the first three rows of a 96-well assay plate are filled with 50 µL of lysate. Next, the automatic pipetting system is used to add 50 µL of DOI to each of the first three rows of the lysate plate in the corresponding wells. The plate is then placed in the automated 96-well plate reader where it is first shaken to mix the contents of each well before the reader measures DOI-induced fluorescence as described above. The data can now be exported as an Excel file for offline analysis in graphing software (Origin 2018, OriginLab) to generate estimates of $\Delta F_{max}/F_0$ and EC_{50} for the ligand-sensor pair as described above. A small correction to the typical Hill equation fitting function must be made to account for ligand depletion, a phenomenon which arises when the concentration of sensor is more than 10% of the ligand's K_d [725]; with several low concentrations of DOI (e.g. 10 nM, 100 nM) compared to sensor concentration (100 nM), we fit the data instead to a modified Hill equation [726,727]. After assessing the $\Delta F_{max}/F_0$ and EC_{50} values among the various DOI-iDrugSnFR pairs, the one with the highest S-slope ratio is carried forward as the template upon which subsequent SSM is performed.

2.2.2. Iterative Site-Saturated Mutagenesis

Once this initial survey is completed, the next step is to locate AA residues in the PBP binding pocket which can be mutated to increase DOI-iDrugSnFR sensitivity and specificity. Mutagenesis can be performed in parallel on multiple sites at the same time, allowing for faster development of the final sensor construct. The resolved crystal structure of iNicSnFR3a both with and without the addition of 10 mM varenicline [684] has been used to determine which residues are better candidates to mutate for engendering higher binding fidelity; the structure can be rendered in a molecular visualization software program (PyMol, Schrödinger) to allow for more informed choices (we currently lack computational methods to help predict which sites can be favorably mutated, though these tools are in development). Residues which have been mutated to develop past iDrugSnFRs are likely candidates upon which to perform additional mutagenesis. These often make cation-π bonds: first-shell residues with aromatic rings within seven angstroms of the binding pocket [533] (tryptophan, phenylalanine, tyrosine) have negative charge densities (π-bonds) which can make noncovalent bonds with nearby cations [728], such as the methylamine on nicotine's pyrrolidine ring which exists in a charged form ~50% of the time at physiological pH (**Fig. 2.2A**; see Chapter 1.5 and Chapter 1.6.5). Other important sites at which mutations can improve fluorescence response include three Linker2 residues. Overall, the various iDrugSnFRs differ among at least 16 first- and second-shell residues, while 10 residues have been found to be either crucial to SnFR function or unimportant; in both cases, they remain unchanged across the various sensors.

SSM is a method whereby differential fluorescence response can be evaluated across all 20 canonical AAs at a particular residue [729]. This directed evolution technique can be accomplished via a 22-codon approach [710] which allows for minimal redundancy and can generate > 95% AA coverage using a single 96-well plate assay. It relies on the use of two sets of degenerate primers, NDT and VHG, plus TGG (tryptophan) mixed in a 12:9:1 ratio, respectively, to represent the proportion of the codon space they each represent [710]. We design three sets of forward primers and one reverse primer per desired SSM location which are synthesized (Integrated DNA Technologies) and then concentrated via butanol precipitation (to filter out shorter abortive segments) as pellets before being resuspended in nuclease-free water. We then use a spectrophotometer (NanoDrop ND-1000 UV-Vis, Thermo Fisher Scientific) to measure the concentration of each primer solution, after which the three forward primers for a particular site are diluted to a concentration of 100 µM. These are then mixed in a 12:9:1 (in µL) ratio after which this mixture is diluted to a final concentration of 5 µM, the same as the reverse primer. To perform the polymerase chain reaction (PCR) amplification, a PCR master mix is first made, containing 1 µL of parent iDrugSnFR plasmid at 60 ng/µL, 10 µL of buffer (Phusion 5X HF Buffer, New England Biolabs), 1 µL of free DNA bases (dNTPs; dNTP Solution Mix, NEB), and 33.5 µL of nuclease-free water. Next, 46 µL of the master mix is split into 1.5 mL microcentrifuge tubes (Eppendorf) to which is added 2 µL of forward primer mix. Each 48 µL mix is now split into PCR tubes (USA Scientific) with two tubes (24 µL) for every SSM site. For this first PCR, the denaturation temperature is 98ºC (50 s), the annealing temperature is 57ºC (30 s), and the extension temperature is 72ºC (5 min) run over four total cycles. After the PCR plate warms to its denaturation temperature, the program is paused to add polymerase (0.25 µL per tube; Phusion HF DNA Polymerase, NEB) as the plate temperature now exceeds the specific primer annealing temperature (usually 55-60ºC); this ‘hot start’ method helps to prevent nonspecific primer extension at lower temperatures [730]. After polymerase is added, the four cycles with just the forward primer mix are run to bias the final PCR product towards mutant sequences over parent sequences. Next, the two tubes for each SSM are combined and 2 µL of reverse primer is added which will allow for completion of the preferentially amplified mutated plasmids. PCR is then performed with the same conditions as above except that the denaturation time is 40 s and there are 16 total cycles. After the second PCR is completed, the two tubes for each SSM are recombined and run on a 0.8% agarose gel with ethidium bromide (EtBr) dye (to visualize the DNA) in Tris-acetic acid-EDTA (TAE) buffer against a 1 kilobase pair (kbp) ladder. The ~4.4 kbp fragments are then excised and the DNA purified following a gel extraction protocol (QIAquick Gel Extraction Kit, Qiagen). After measuring the concentration of the resuspended plasmid DNA, we perform an overnight digest in a 37ºC incubator using DpnI (NEB) which digests methylated DNA (thereby selectively targeting parent sequences as newly formed DNA is not methylated [731]). The next day, the DpnI-digested SSM is eluted via PCR clean-up (QIAquick PCR Purification Kit, Qiagen) to remove the enzyme and other digestion by-products. The SSM mix then undergoes electroporation transformation into TOP10 cells as previously described and plated for overnight growth as before. The next day, five colonies per SSM plate are picked and each grown in 5 mL of LB with 5 µL of ampicillin at 37ºC overnight for ~18 h, after which the cultures are spun down, the supernatant is pulled off, and the pellets miniprepped (QIAprep Spin Miniprep Kit, Qiagen) before being sent for sequencing (Laragen) to confirm that there is not a high proportion (zero or one out of five) of parent AAs at the SSM site among the picked colonies. Once confirmed, the plate is washed with 5-10 mL of LB (combining all of the individual colonies into one suspension), after which that solution is miniprepped as described previously; after reading the concentration via spectrophotometry, 300 ng of the plasmid miniprep mix is next transformed into chemically competent BL21(DE3) *E. coli* cells via a 30 s heat shock at 42 ºC, incubated in a 37ºC water bath for 1 h, and plated as previously described for overnight growth in a 37ºC incubator. The next day, colonies are picked from the plate with one placed into each well of a 96 well deep-well plate with 800 µL of ZYP-5052 media (to improve yield via unblocking *lacZ* [732]); the plate is then covered in cheese cloth and placed in an incubator shaker set to 30ºC and 250 rpm for 24 h. The next day, a replica plate is made by pipetting 50-80 µL of each culture into the corresponding well of a 96-well assay plate which is covered and placed in a -80ºC freezer to be thawed when a promising candidate mutation has been identified; the original SSM plate is spun down as described previously, the supernatant is pulled off, and the pellets are stored in a -80ºC freezer. When ready, the original SSM plate is thawed at RT and the pellets resuspended in 800-1000 µL of 1x PBS, pH 7.0. The plate is then subjected to one round of the previously described liquid nitrogen freeze thaw, after which it is spun down as described above. Next, 200 µL of supernatant is withdrawn from each well, with 100 µL dispensed to test DOI-induced fluorescence in the corresponding well of one 96-well assay plate and 100 µL dispensed to test choline-induced fluorescence (choline is a natural ligand for this PBP; see Chapter 2.1) in the corresponding well of another 96-well assay plate. Two stock solutions of both the DOI and choline are made in 3x PBS, pH 7.0 with appropriate pH adjustments; solutions are made such that when 10 µL of DOI or choline solution are pipetted into each well with 100 µL of lysate, the final concentration of each will be equal to the concentration at which a $\Delta F/F_0$ of 1 was achieved against the parent plasmid for both compounds. The DOI solution is loaded into the injector of the automated 96-well plate reader; 10 µL of DOI is then added automatically to each well, the plate is shaken, and fluorescence measurements are taken as described previously. The injector is then rinsed and the process repeated for the choline solution added to a second lysate plate. After the data is exported, the ratio of the DOI-induced fluorescence to the choline-induced fluorescence of each corresponding well is calculated. After assessing the ratios, the best mutants ($\Delta F/F_0 > 1.3$, or a 30% increase over choline [533]) are then selected for further analysis, the first step of which is sequencing to confirm that the candidates are not identical to the parent plasmid. Each non-parent mutant is then inoculated from the corresponding replica plate well, with 1.5 µL pipetted into 10 mL LB with 10 µL ampicillin and grown in a 37ºC incubator shaker for ~18 h as previously described. The next day, the cultures are miniprepped and the resuspended DNA is quantified via spectrophotometry to check if the concentrations are high enough (> ~15 ng/µL) before being sent out for sequencing. Once the absence of the parent sequence is again confirmed, 100 ng of mutant DNA is transformed into BL21(DE3) *E. coli* cells and plated for overnight growth in a 37ºC incubator as before. The next day, the mutants are pelleted and lysed as described above, then assessed with full concentration-response curves against the DOI and choline plates as previously described. After the best-performing mutant (highest S-slope) has been identified, this mutant is carried forward into the next round of SSM; additional rounds following the protocols specified herein are performed until the EC_{50} in lysate is within the pharmacologically relevant concentration range; the $\Delta F_{max}/F_0$ value is typically 2-8, with higher values preferred due to the decrease in maximal fluorescence when the sensor is transfected or transduced into cells/neuronal cultures (see Chapter 2.2.5).

2.2.3. Purifying iDrugSnFR Protein

After we have settled on a new iDrugSnFR sequence, we next generate purified protein for use in further characterization protocols [720]. Compared to lysate, purified protein contains fewer contaminants and more faithfully reports the performance of the sensor in response to the DOI. First, the new iDrugSnFR plasmid is transformed into BL21(DE3) cells, incubated, and plated overnight as previously described. The next day, one colony is picked for growth in 100 mL of LB along with ampicillin, $MgSO_4$ (for stabilization of DNA [733]), ZYP-5052 media, and extra salts; the flask is loosely covered to allow for aeration and placed in a 30ºC incubator shaker (250 rpm) for 24-30 h. Once ready, the contents should appear greenish-yellow; the mixture is then transferred to two 50 mL tubes to be spun down in a centrifuge as previously described. The supernatant is pulled off and the pellets gently rinsed several times using 1x PBS, pH 7.0 before being placed in a -80ºC freezer overnight (or for long-term storage).

When beginning the purification process, the frozen pellets are thawed on ice and resuspended in 5 mL of 1x PBS, pH 7.4. The cells are then sonicated (13% amplitude, 0.7 s time-on, 0.2 s time-off, 30 s total) 3-6 times with 3 min in between on ice to increase lysis efficiency [720]. After another round of centrifugation, the supernatant is pulled off and passed through a 0.2 μm filter (Syringe Filter, VWR) to remove additional debris and unlysed bacteria before being injected onto a pre-washed Ni-NTA column in a fast protein liquid chromatography (FPLC) system (ÄKTA Start, Cytiva). The SnFR protein is eluted into glass vials using an imidazole gradient (20-200 mM in 1x PBS, pH 7.4 solution) [720]; the bacterial expression vector contains a His6 tag, which interacts with the Ni^{2+} ions on the column at lower concentrations of imidazole and is washed off at higher concentrations [734]. To make sure the purity of the protein fractions is high (> 95%) and that the molecular weight of the protein eluted is correct, we dilute 7.5 μL samples of representative fractions from across the ~25 generated (usually 11 total) in 7.5 μL of glycerol-based buffer (4x Laemmli Sample Buffer, Bio-Rad) mixed with β-mercaptoethanol (BME) [720]. After denaturing the proteins at 95ºC for 5 min, we inject each into separate lanes of a gel in Tris-glycine buffer alongside a ladder (10-250 kD, Precision Plus Protein Dual Color Standards, Bio-Rad); the glycerol buffer helps weigh down the proteins to decrease loss of protein during electrophoresis. After ~30 min at 200 V, we remove the gel and place it inside of a chamber filled with dye (Coomassie brilliant blue, Bio-Rad) on a shaker table overnight for staining. After rinsing the gel in deionized water several times the next morning, we examine the purity of the fractions (**Fig. 2.3**); once purity is confirmed, all fractions (excluding the first fraction) with significant protein content are combined and concentrated via centrifugation (8 minutes at 2000 rpm and 4ºC) in a filter unit (Amicon Ultra-15, 30 kD cutoff, Millipore). Once concentrated to approximately 500 uL, the protein is buffer exchanged into 3x PBS, pH 7.0 before being read on a spectrophotometer to determine its A_{280} (which measures UV absorbance of AAs with aromatic side chains). The final concentration (C, in M) is determined via Beer's Law,

$$A = C\varepsilon l,$$

where A is the A_{280}, ε is the molar attenuation coefficient (specific to each protein, in units of $M^{-1}cm^{-1}$), and l is the path length (equal to 1 cm). The final step involves testing the purified protein against the aforementioned DOI plate. The first three rows of a 96 well assay plate are filled with 50 uL of 200 nM purified protein using the automatic pipette system which is then used to create a mixture between sensor and ligand from the DOI plate as previously described. The plate is then placed in the automatic plate reader and the DOI-induced fluorescence response measured as previously described. Concentration-response curves are generated as before. All concentration-response experiments using purified iDrugSnFR protein are performed in triplicate and the standard deviation is calculated for each concentration.

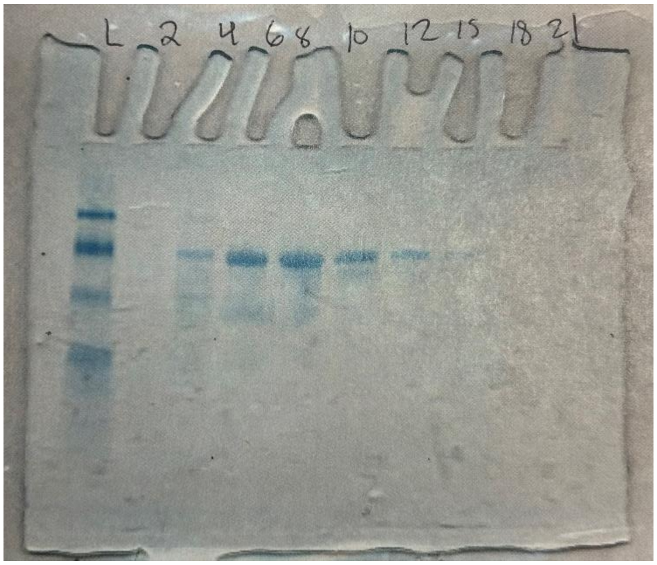

Figure 2.3. Picture of fractions (with the lanes labeled at the top denoting the fraction number) from iDrugSnFR protein purified via FPLC. The ladder (*left*) is used to measure the size of the proteins (in this case, approximately 62 kD). The presence of extra bands in a fraction or less-resolved bands disqualifies it from inclusion in the pool of protein later used for *in vitro* concentration-response experiments. (Image and annotations courtesy of Aaron L. Nichols.)

2.2.4. Characterizing iDrugSnFR Protein

Isothermal titration calorimetry (ITC) is a method of characterizing a receptor-ligand binding interaction by evaluating its thermodynamic properties [735]. The technique involves automatically injecting small volumes (~100 uL total, in increments of 1-2 uL) of ligand into a sample cell containing the receptor next to a reference cell in water, with both cells contained inside an adiabatic jacket to precisely control heat evolution. Changes to enthalpy (ΔH) are measured which determine if the interaction is exothermic (negative) or endothermic (positive). The injection peaks (in units of µcal/mol) are integrated to generate a plot of molar ratio (between moles of receptor and moles of ligand) versus ΔH which can then be fitted to the Hill-Langmuir equation (similar to the Hill equation described in Chapter 2.2.1 but concerned only with binding [736]) to generate K_d (dissociation constant) and n (occupancy number) values for the reaction which can then be compared to those generated from the aforementioned concentration-response experiments; we accept at most a 50% difference between K_d and EC_{50} [684]. To perform ITC experiments, we prepare two solutions, both in 3x PBS, pH 7.0: iDrugSnFR at a concentration at least 10 times the purified protein EC_{50}; and DOI at a concentration 10 times above the SnFR concentration [684]. These solutions are then carefully injected into the injection syringe and sample cell, respectively, of the ITC system (Affinity ITC, TA). The volume of each injection is held constant and is chosen based on estimation protocols within the proprietary software (NanoAnalyze, TA). The experiment is run at RT and both the syringe as well as the cell are carefully rinsed in 3x PBS, pH 7.0 before and after the experiment is performed. All solutions are degassed and inspected to prevent bubbles forming in the cell which can disrupt measurements. Experiments are performed in triplicate and the standard error of the mean (SEM) is calculated for each thermodynamic parameter (see **Fig. 3.2** and **Fig. 4.5**).

Stopped-flow spectrometry can determine reaction kinetics of a ligand-fluorescent receptor pair [737]. The reaction order informs our understanding of how the underlying binding mechanism affects the speed of fluorescence dynamics *in vitro* and *in vivo*. Among the iDrugSnFRs developed, both first-order (the rate of fluorescence change increases proportional to the concentration) and pseudo-first-order reactions have been observed; additionally, multiple phases (represented by double exponential fits) have likewise been observed, suggesting that at least some iDrugSnFRs have an intermediate state or states representing additional conformations required for ligand-induced fluorescence [683,684]. Stopped-flow involves the rapid mixing of two solutions (one with a FP) in a chamber which can be read via fluorescence spectroscopy within milliseconds; each solution is injected via syringe pumps equipped with baffles to ensure turbulent flow and thereby faster mixing. The injection occurs over a certain time course preset by the experimenter, as is the rate at which fluorescence is measured. Each apparatus has a dead time, the delay before the solutions are mixed but after the syringes have been plunged, which must be accounted for in subsequent analyses. In our experiments, we use an apparatus (Applied Photophysics SX20, Surrey, UK) equipped with a fluorimeter (490 nm LED excitation and 510 nm long-pass filter) designed for measuring the fluorescence response of GFPs. Concentrations ranging from 4 μM to 2 mM of DOI are mixed with 200 μM of iDrugSnFR (all in 3x PBS, pH 7.0) at RT with results averaged across five trials in 1 s experiments and collected only once in 100 s experiments. To account for instrument dead time as well as any mixing abnormalities, the first 3 ms of data are discarded [684]. Kinetics traces are fitted to single and double exponentials (based on goodness of fit) in analysis software (KaleidaGraph, Synergy Software; and Origin 2018) to determine time constants and maximal fluorescence. The observed apparent rate constant (k_{obs}) for the 1 s data is generated by inverting the time constants for each concentration; the values are plotted against concentration and then fitted by a Michaelis-Menten curve to generate V_{max} (the reaction rate when all binding has stopped) and K_d (the dissociation constant) values for the ligand-receptor interaction (see **Fig. 3.2** and **Fig. 4.6**).

2.2.5. Targeting iDrugSnFRs to Mammalian Cells and Primary Culture

The ultimate goal of developing the iDrugSnFRs is to use them both *in vitro* and *in vivo* to investigate the pharmacokinetics of pharmaceutical compounds as they transit into subcellular compartments. Thus, the sensors must be cloned into an expression vector which can be used to transfect mammalian cell culture while also separately packaged into viruses for transduction into primary rodent neuronal cultures as well as *in vivo* tissue. Currently, only one set of iDrugSnFRs — the iOpioidSnFRs — have been successfully transduced into live mouse neurons (data not yet published), so the following sections will describe only transduction of mouse primary HC culture (PHC).

For expression in mammalian cells, the iDrugSnFR recombinant plasmids are cloned into pCMV(MinDis), a variant of pDisplay (Thermo Fisher Scientific) [533,682]. This plasmid is suited for expression on the PM, as it contains a C-terminal Myc tag (to help detection of recombinant proteins [738]), an N-terminal immunoglobulin kappa light chain (IgK) leader sequence (to target the SnFR to the secretory pathway [739]), and a C-terminal platelet-derived growth factor receptor (PDGFR) tag (to help anchor the SnFR to the PM facing outward [682]); a hemagglutinin (HA) tag is removed, as it interferes with the overall fluorescence response [682]). To target the ER, the Myc tag is removed and the 14 C-terminus AAs are replaced with an ER retention motif (QTAEKDEL) [533]. To synthesize both the PM- and ER-targeted versions, we employ circular polymerase extension cloning, which relies on engineering overlapping regions at the termini of both an insert sequence and a vector sequence; each uses the other as a template for extension during PCR, with leftover nicks repaired during bacterial transformation [740]. First, we use PCR to extend the new recombinant plasmid sensor (the insert) to include overlapping regions with a vector sequence which will be harvested from the backbone of an already-functional mammalian plasmid (the backbone) targeted to either the ER or the PM. This requires a master mix for four total PCRs (insert for ER, insert for PM, vector for ER, vector for PM) composed of 35.5 μL of nuclease-free water, 10 μL of buffer, and 1 μL of dNTPs which is then split into 46.5 μL aliquots. Next, specific primers are added (1 μL each of forward and reverse) to every reaction to either engineer overlapping regions (the two inserts have separate forward primers and the same reverse primer) or to remove an old iDrugSnFR sequence to amplify the mammalian vector (the two backbones have the same forward primer and separate reverse primers) with identical overlapping regions. The insert plasmid (1 μL) is then added to the two aliquots with primers for extending the insert; the ER vector plasmid (1 μL) is added to the aliquot with primers to harvest the ER backbone and the PM vector plasmid (1 μL) is added to the aliquot with primers to harvest the PM backbone. The total volume in each aliquot is then split between two PCR tubes for each of the four aforementioned reactions before polymerase is added during a ’hot start’ as described previously and run for 20 cycles using PCR conditions described previously. Once the run is completed, the four PCRs are added to the wells of an agarose gel as described previously, after which the proper bands (inserts: ~1.8 kbp, backbones: ~3.5 kbp) are cut out, the DNA is eluted via gel extraction, and the four PCRs are digested overnight with DpnI as described before. The next day, we perform a PCR clean-up as described previously and quantify the concentrations using a spectrophotometer as described previously before preparing for the CPEC reaction (we expect 20-50 ng/μL). We thus prepare two PCR mixtures: 10 μL insert (either ER or PM), 10 μL backbone (either ER or PM, matched to the insert), 1 μL dNTPs, 10 μL buffer, and 18.5 μL nuclease-free water. The mixtures are split into PCR tubes and polymerase is added via 'hot start' again; the PCR is run using settings described previously. Once the PCR is completed, we perform another PCR clean-up to elute each of the two completed plasmids (iDrugSnFR_ER and iDrugSnFR_PM) which are then transformed into TOP10 via electroporation as described previously and added to ampicillin plates which are incubated overnight at 37ºC for 18 h. The next day, we pick five colonies per plate to grow in 5 mL LB and 5 μL ampicillin overnight in an incubator shaker at 37ºC and 250 rpm for 24 h. The following day, we centrifuge the 10 total cultures before miniprepping each of them for sequence analysis. Once the sequences have been confirmed, the plasmids are ready for use in mammalian cells.

We can synthesize a series of additional mammalian vector plasmids targeted to various subcellular compartments by using specific primers to add and delete the sequences listed below; all PCR conditions are as described previously. Except for the cytosol-targeted constructs (which we also designed for two iSSRISnFRs [543]), only the iRAADSnFRs have been modified to target these other subcellular compartments. To make iRAADSnFRs targeting the cytosol and the nucleus, we remove the ER retention motif from the ER-targeted plasmid as well as the N- and C-terminal tags via PCR. For cytosolic expression, we use PCR to add a nuclear exclusion signal (NES; DIDELALKFAGLDL) at the N-terminus [741] after the start codon. To localize the iRAADSnFR to the nucleus, we use PCR to add a nuclear localization signal (NLS) (PKKKRKV) [742] appended to the C-terminus. Next, we make additional changes and apply other techniques to localize iRAADSnFRs to the peroxisome and mitochondria. For targeting the peroxisome, we use PCR to insert a peroxisome localization sequence (SKL) [743] at the C-terminus of the cytosol-targeted construct. For targeting the mitochondria, we add the COX-VIII tag to the cytosol-targeted plasmid right after the NES; COX-VIII is a duplicated mitochondrial localization sequence derived from the VIII subunit precursor of human cytochrome c oxidase [744] (which we ordered as a synthetic gene; IDT). Finally, to target the remaining compartments of interest, we use Gibson assembly [745], an approach which leverages the presence of overlapping ends shared by at least two (but sometimes several) DNA fragments to perform an exonuclease-mediated single-step ligation. An exonuclease, a polymerase, and a ligase are added to a reaction mixture containing 0.02-0.5 pmol of total fragments and 10 μL of master mix (NEB); in a single 30 min step at 50ºC, the exonuclease removes bases from the 5' end, the fragments anneal along their overlapping regions, the polymerase fills in remaining gaps, and the ligase joins the segments together. To make the common starting sequence for the remaining plasmids, we first digest a cytosol-targeted iRAADSnFR construct using the restriction enzymes EcoRI and BglII overnight in a 37ºC incubator. We then run the double-digest product on a gel and purify using gel extraction as described previously. For targeting the Golgi apparatus, we purchased the synthetic fragment [IgK]-[B4GALT1]-[KDPPVAT] (B4GALT1: β-1,4-galactosyltransferase 1) with overhanging ends (Twist Bioscience); the IgK leader sequence targets the secretory pathway as mentioned previously and B4GALT1 has an N-terminal sequence which localizes the protein to the Golgi [746]; the last sequence is a linker. After PCR amplification of the synthetic fragment, we use Gibson assembly to ligate the synthetic gene with the double-digested backbone as described previously which comprises the final Golgi-targeted construct. The same strategy is employed to assemble the constructs targeted to the autophagosome, with the only difference being the middle targeting sequence (microtubule-associated protein light chain 3; LC3 [747]). For F-actin localization, we likewise purchase a synthetic fragment containing [NES]-[Lifeact], the second sequence being a small peptide tag for actin [748]; this is PCR amplified for Gibson assembly with the same backbone as described above. For targeting focal adhesions and the nucleolus, we purchase mRuby-Zyxin-6 (AddGene #55887) and mPlum-Fibrillarin-7 (AddGene #55969) to PCR amplify with correct overhanging sequences each of the targeting sequences from them without the red FP before performing Gibson assembly with the same backbone as described previously. (An example plasmid map is shown in **Fig. 2.4**.)

We use three different mammalian cell lines for our *in vitro* experiments: HeLa cells, Neuro2a cells, and SH-SY5Y cells. HeLa is an immortalized cell line derived from cervical cancer cells taken from a human patient [749] which means that the manner in which transgenes are expressed in this line has obvious applications to human medicine; the main disadvantage is that HeLa cells are not neurons. They have a doubling time of 33-35 h [750] and are thus advantageous for performing experiments on a shorter time scale. HeLa cells have a flat polygonal structure (average diameter = ~16 μm [751]), forming a monolayer at the bottom of the dish. Neuro2a is an immortalized cell line derived from mouse neuroblastoma [752] possessing neuronal features, which is advantageous for neuroscience research; their main disadvantage is that they are not human derived. They have a doubling time of approximately 10 h [753] and grow as a monolayer of round loosely attached cells (average diameter = 16 µm [754]). SH-SY5Y is an immortalized cell line derived from human neuroblastoma cells [755] which has the advantage of being both human-derived as well as brain-derived. These cells have a doubling time of 27-67 h [756,757] and grow smaller as confluence increases (from a 43 µm to 17 µm diameter [757]).

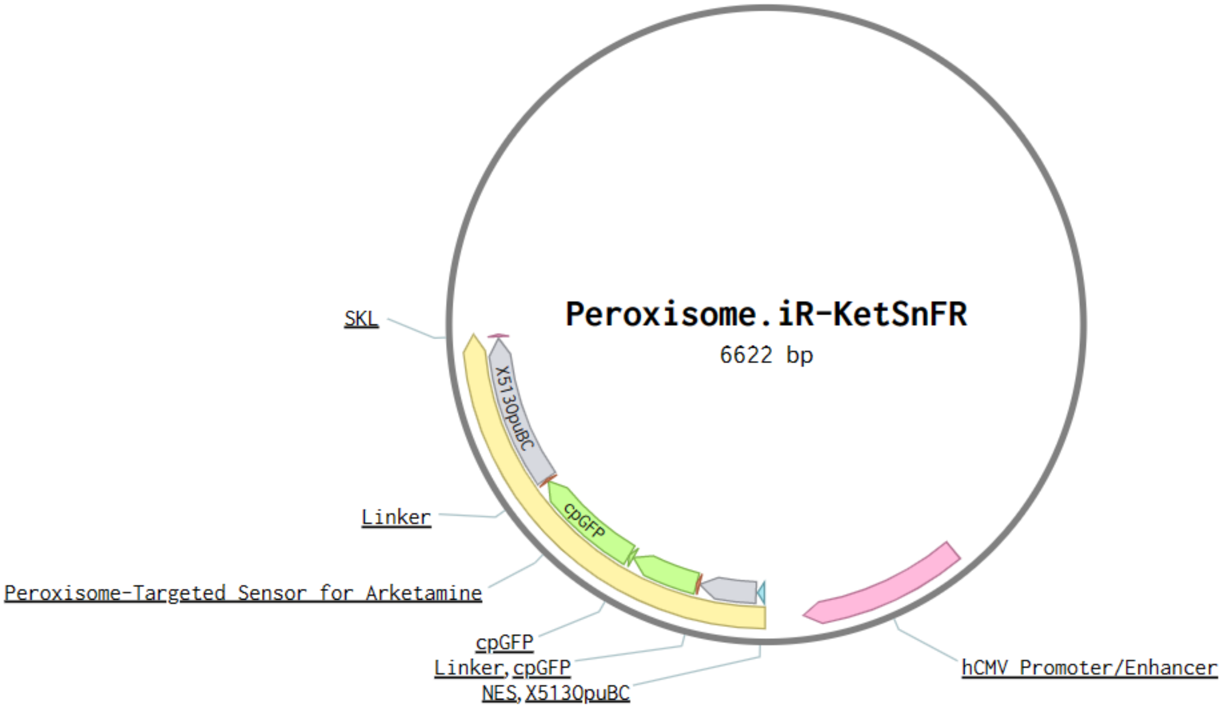

Figure 2.4. Example map of Peroxisome.iR-KetSnFR showing the general construction of the mammalian-targeted plasmids. The hCMV promoter/enhancer (*pink*) is carried over from the pCMV(MinDis) backbone. The entire iDrugSnFR sequence (Peroxisome-Targeted Sensor for Arketamine; *yellow*) comprises the N-terminal NES (*cyan*), the first part of the PBP (X513OpuBC, *gray*), Linker1 (*orange*), the cpGFP (*green segments*), Linker2 (*orange*), the second part of the PBP (X513OpuBC, *gray*), and the peroxisome targeting sequence (*SKL; brown*). (Map courtesy of Kallol Bera.)

To begin a cell culture, a vial of cells (ATCC) is thawed and passaged three times using suggested practices (ATCC). We use Eagle's minimal essential medium (EMEM) (Thermo Fisher Scientific) (HeLa and SH-SY5Y) or Dulbecco's modified Eagle's medium (DMEM) (Neuro2a) supplemented with 10% fetal bovine serum (FBS) (Thermo Fisher Scientific) and 1% penicillin-streptomycin (Thermo Fisher Scientific) as media. Trypsin (ATCC) is used to lift the cells during passaging, which is performed every 3-5 days; after ≤ 20 passages [758], the cells are bleached and a new line is initiated. Cells are stored in an incubator set at 37ºC with 5% CO_2 in 35 mm dishes with a 14 mm coverslip (MatTek). For transfection of mammalian cells, we use Lipofectamine 3000 (Invitrogen), a mixture of lipids forming a liposome around plasmids; the cationic charges of the spheres contact the negatively charged PM which allows for transfer of plasmid inside the cell [759]. To prepare for imaging experiments, either ~100,000 (HeLa) or ~50,000 (Neuro2a and SH-SY5Y) cells are plated on 35 mm dishes and incubated for 24 h in the aforementioned conditions. The cells are then transfected with a mixture of 0.25-1 μL of plasmid at 500 ng/μL, twice that volume of P3000 (which aids the transfer of plasmid across the PM; Invitrogen) and three times that volume of Lipofectamine 3000; Opti-MEM media (Thermo Fisher Scientific) is added to bring the total mixture volume to ~0.5 mL. This is then added to the dishes along with 1.5 mL of Opti-MEM. Transfection occurs within 24 h, after which the dishes are either used for imaging or swapped into EMEM for an additional 24 h of growth.

Creating recombinant viruses is a standard method for introducing transgenes into *in vivo* tissue for focused protein expression [760]. One of the most common viral vectors is adeno-associated virus (AAV), which has a number of advantages over other common strains used for transduction (e.g. lentivirus, adenovirus), including a lack of pathogenicity to humans (AAV can only infect tissue when aided by another virus), the ability to target a variety of tissue types, minimal immunogenesis, and robust and persistent expression [760]. The main drawback is the size of the DNA fragment that can be packaged, as the AAV genome is 4.7 kbp [761] and the maximal transgene size is 5 kbp [760]. For our purposes, we want to create iDrugSnFR viruses which are capable of transducing rodent cell cultures and are compatible with expression in the rodent brain *in vivo*. Assessing pharmacokinetic properties of DOIs in mammalian cell culture versus in primary neuronal cultures can demonstrate key differences [543], which suggests that important dynamics of iDrugSnFR activity can be missed if experiments are performed in only one type of cell. Thus far, we have produced AAVs for ER, PM, and cytosol-targeted iDrugSnFRs [543,684]. We begin by synthesizing an AAV-compatible plasmid which we partially harvest from a previous viral vector (pAAV.hSyn.iGluSnFR.WPRE.SV40, AddGene #98929) used previously to transduce iGluSnFR in mouse brain [682]. The human synapsin (hSyn) promoter is generic for mammalian neurons and allows for broad expression across various subtypes [762] while woodchuck hepatitis virus posttranscriptional regulatory element

(WPRE) in the 3’ untranslated region helps expression of recombinant virus proteins by increasing mRNA levels [763] and Simian virus 40 (SV40) is a polyadenylation signal which helps terminate transcription and stabilize mRNA [764]. We first perform a double digest for two hours at 37ºC with the restriction enzymes EcoRI (NEB) and HindIII (NEB) to remove the iGluSnFR sequence as well as the IgK leader sequence and the 3’ PDGFR sequence after which we purify the digest using both PCR clean-up and gel extraction as described previously; the band cut out from the gel (backbone) is ~4.5 kbp long. Next, we digest the backbone with Antarctic phosphatase (NEB), an enzyme which dephosphorylates 5’ ends after a digest to prevent self-ligation, for 2 h at 37ºC; the backbone is then heated to 80ºC for two minutes to inactivate the enzyme before the concentration is quantified on a spectrophotometer. The ER inserts are prepared by first performing PCR on the ER-targeted mammalian vector plasmid version of the iDrugSnFR (e.g. pCMV(MinDis)-iDianiSnFR_ER; AddGene #177750) to amplify the entire sequence using a melting temperature of 62ºC over 15 cycles with other settings as described previously. Next, the PCR product is run on a gel and extracted as described before, with the ~1.8 kbp ER insert fragments excised for elution. The ER inserts are then double digested with EcoRI and HindIII overnight at 37ºC to make compatible ends for ligation to the backbone before being purified using PCR clean-up as described previously the next morning. The PM inserts are prepared by first performing a double digest overnight at 37ºC on the PM-targeted mammalian vector plasmid version of the SnFR (e.g. pCMV(MinDis)-iCytSnFR_PM; AddGene #177743) with EcoRI and NotI (NEB) to remove the iDrugSnFR_PM sequence. The next day, the PM insert is purified via PCR clean-up followed by gel extraction as described previously; the ~1.8 kbp bands are excised for elution and quantified with spectrophotometry. Next, the PM inserts are PCR amplified using a melting temperature of 60ºC over 16 cycles with other settings as described previously. To increase the yield of PM insert DNA, we precipitate them overnight in 95% ethanol before spinning down the DNA pellets and using a vacuum rotor to dry them; the pellets are re-suspended in elution buffer (Qiagen) and quantified via spectrophotometry. We then run the inserts on a gel and extract the ~1.8 kbp band to elute the PM insert as described previously. This PM insert is then digested overnight at 37ºC with EcoRI and HindIII (both added during the PCR) with the ends now ready for ligation to the backbone. The next morning, we perform PCR clean-up on the digested PM insert and quantify with spectrophotometry as described previously. The fragments targeting cytoplasm (cyto inserts) are prepared by performing an EcoRI and HindIII double digest as described previously except the starting plasmid is the cytoplasm-targeted mammalian vector plasmid version of the SnFR (including the NES) and the backbone was prepared from an already-completed AAV plasmid (e.g. pAAV9-hSyn-iEscSnFR_ER, AddGene #182818) via the EcoRI and HindIII double digest described above. Ligation is performed using T4 DNA ligase (NEB) which can quickly ligate both blunt and sticky ends of DNA fragments across many conditions [765]. For ligations, we found that a molar excess of > 50:1 (insert:backbone) gave best results. We added the required volumes of insert and backbone into a mixture with T4 ligase and corresponding buffer (NEB), letting the reaction proceed for 20 min at RT before transforming the ligation product (pAAV_hSyn) into chemically competent NEB Stable *E. coli* via a 30 s heat shock at 42ºC; we then add 900 μL of NEB Stable media (NEB) to the transformation which is then incubated in a 30ºC shaker for 1 h and plated for overnight growth in a 30ºC incubator for at least 24 h. The next day, we pick five colonies which are grown in 5 mL of the nutrient-rich 2x yeast-tryptone (2xYT) media (which aids with production of the more delicate ligation product [766] and 5 μL of ampicillin in a 30ºC shaker for 24 h. We then miniprep the cultures as described previously and digest 1 μL of DNA from each miniprepped ligation with the enzyme SmaI (NEB) at RT for two hours before running on a gel beside 1 μL of undigested ligation; the presence of two smaller bands between 2-3 kbp in the digest lane confirms the proper plasmid assembly [767] (**Fig. 2.5**); the ligation products which pass this check are then sequenced and minipreps which share common correct sequences are combined.

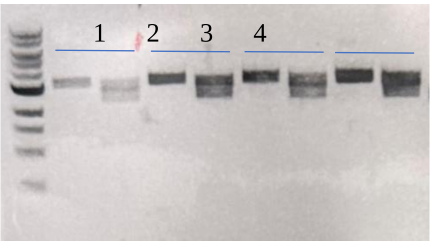

Figure 2.5. Gel with EtBr gradient run in TAE showing four different miniprepped ligation products (numbered *1*-*4*) with both un-digested (*left lanes*) and SmaI-digested (*right lanes*) helping to demonstrate that each has been correctly constructed (the two 2-3 kbp bands in the digest lanes confirm the proper ligation).

To produce viruses for transduction, we followed two different protocols: the ER- and PM-targeted AAV plasmids (pAAV-ER and pAAV-PM) were produced using the AAVpro Purification Kit (Takara Bio) while the cytoplasm-targeted AAV plasmids (pAAV-cyto) were produced using the protocol developed in the Gradinaru lab at Caltech to generate viral vectors for *in vivo* transduction [768]. We used the former protocol to make pAAV-ER and -PM because the process is less time-consuming even though the final product is less pure and less concentrated; this was not an issue because we did not plan to use these to transduce rodent neurons *in vivo*. However, we did plan to use the pAAV-cyto constructs for that purpose, so we followed the latter protocol because of the increased purity and higher concentration of the final product. Both protocols rely on the production of AAV and helper virus by mammalian cells which help package an added recombinant plasmid into the AAV capsid, after which the virus is purified, quantified, and stored at -80ºC for long-term use. We chose to use AAV9 (a gift from the Gradinaru lab) as our viral vector owing to its well-studied efficacy in rodent neuronal tissue [769]; AAV-PHP, a newer series of capsids capable of more efficiently crossing the BBB [768], presented no distinct advantages because we wish to transduce neurons with iDrugSnFR via direct infection (either *in vitro* or *in vivo*). The cell line chosen for viral replication is human embryonic kidney cell 293 T-antigen (HEK293T [768]) because these cells possess both adenoviral genes which aid in viral production as well as the SV40 T-antigen which interacts with the SV40 sequence of the recombinant plasmid to increase replication [770,771]. We followed the instructions for preparation of HEK293T cell preparation and seeding as described in the Caltech protocol [768], after which we used the protocol's 'Transfection calculator' to determine the mixture of AAV9 capsid DNA, pAAV-ER/-PM/-cyto, and pHelper plasmid (AAV Helper-Free System, Agilent; pHelper encodes several adenoviral genes necessary for AAV infection [768]). Transfection and handling of media changes are performed as described in Steps 2-4 of the Caltech protocol [768]. While transfection and production proceed in the same manner in both protocols, each relies on different methods of releasing and then purifying the recombinant viruses. In the AAVpro protocol, virus is released from cells in a series of steps: citric acid buffer (pH = 5) is used to lyse HEK293T cell membranes [772], the supernatant is treated with Tris-HCl to stabilize the pH, unincorporated RNA and DNA is degraded with an endonuclease (Cryonase Cold-Active Nuclease, Takara Bio), sodium deoxycholate [773] and another volume of citric acid are added sequentially to further aid cell lysis to increase virus yield, and the precipitate is filtered using a filter unit (Amicon Ultra-15, 100 kD cutoff, Millipore) several times. The final virus product is then stored at 4ºC until quantified. In the Caltech protocol, virus is released from cells in a different series of steps: salt-active nuclease (HL-SAN, ArcticZymes) with extra salts is added to the spun-down HEK293T pellet to lyse the cells [768] and the supernatant is treated with polyethylene glycol (PEG; Sigma-Aldrich) to precipitate virus [773] so as to increase final yield before treatment with HL-SAN; these products are then combined and carefully pipetted on top of an iodixanol density gradient (OptiPREP, Cosmo Bio) which is spun in an ultracentrifuge (the inert and nontoxic iodixanol helps separate lysis by-products from the pure virus); the pure virus forms a clear layer above the 60% iodixanol stratum and below the separated cell protein debris which is carefully extracted using a syringe; the virus is then purified in DPBS (Thermo Fisher Scientific) via filtration through a filter unit (Amicon Ultra-15, 100 kD cutoff) and stored at 4ºC until quantified. Viruses made using the AAVpro protocol have a shorter shelf life (typically 3-6 months) than viruses made using the Caltech protocol (up to one year for viruses stored at -80ºC) due to the higher purity of the latter preparation. All viruses were quantified according to Steps 32-42 of the Caltech protocol [768] using quantitative PCR (qPCR; qTOWER^3, Analytic Jena) running a program developed in the Gradinaru lab. This method of qPCR relies on the addition of a dye (SYBR Green, Thermo Fisher Scientific) which binds to double-stranded DNA as it is amplified [774]. The recombinant plasmid is harvested from a small volume of virus by first digesting unincorporated DNA using DNase (Roche Diagnostics) and then digesting the viral capsid using Proteinase K (Roche Diagnostics); a master mix containing dye (SYBR Green) and primers (targeting a conserved sequence of the open reading frame such as the WPRE gene [768]) is then added to the released viral plasmid as well as to a series of dilutions of a DNA standard known to contain the target sequence. After quantification, viruses were distributed into 5-10 µL aliquots for long-term storage at -80ºC; when the titer was higher than 1 x 10^{14} viral genomes per mL (vg/mL), the virus was diluted and re-titered to prevent unwanted aggregation during storage [768]. We transduced PHC neurons harvested from mouse pups removed in utero from a pregnant female [533]. To prepare PHC dishes for transduction, the female is euthanized at embryonic day 16, after which the uterine sac is removed and the pups inside decapitated. The brain is carefully removed and sliced down the midline, after which the striatum is moved aside to reveal the HC which is removed; HC from several pups can be combined [775]. These HC are then digested in papain (Thermo Fisher Scientific) for 15 min to dissociate neurons [776] after which DNase is added to degrade extracellular DNA and enzymes. The cells are then added to Hank’s balanced salt solution (HBSS; GIBCO, ThermoFisher Scientific) containing 5% equine serum and triturated via glass pipette after which the neurons are spun down in solution containing 4% bovine serum albumin [533]; the sera are added to provide additional nutrients and other factors which support cell growth [777]. The pellet is resuspended in plating media

(Neurobasal, Thermo Fisher Scientific) before being plated at a density of 70,000 neurons onto 35 mm dishes coated with poly-D-lysine, poly-L-ornithine, and laminin [533] to improve neuronal adherence; after one hour, 3 mL of plating media is added. Three days later, half of the media is changed [533] and the dishes are infected with the desired pAAV (from an aliquot thawed at 4ºC the night before) at a multiplicity of infection (MOI, the ratio between virions and neurons) between 0.05-1 x 10^5; the neurons are imaged 2-3 weeks later [543].

2.2.6. Imaging Live Cells Expressing iDrugSnFR

To image both transfected mammalian cell cultures as well as transduced mouse PHC while performing concentration-response experiments, we use the same apparatus and conditions as described for our experiments with iNicSnFR [533]. Dishes are placed in a perfusion ring (DH-40i, Harvard Apparatus) supported by a stage adapter (SA-TS100, Warner Instruments) under an inverted widefield epifluorescence microscope (IX-81, Olympus) equipped with an oil immersion objective (40X, NA = 1.0). Images are captured with a back-illuminated EMCCD camera (iXon DU-897, Andor) through proprietary software (Andor IQ2, Andor) at 3-4 frames per second. We installed two light-emitting diodes (LEDs), 470 nm and 400 nm (LZ1-10DB00, LED Engin), using currents from 40-800 mA and a 40 nm bandpass filter centered at 480 nm (ET 470/40X, Chroma Technology). Solutions are flowed via gravity into the dish using elevated reservoirs controlled by solenoid valves (Automate Scientific) which enter a common manifold at rates of 5-6 mL/min. All drug solutions are made in HBSS buffer to mitigate against pH change which can substantially increase the F_0 of iDrugSnFRs [533] and thereby artificially constrain DOI-induced fluorescence changes; we use Teflon tubing (Versilon, McMaster-Carr) with a fluorinated ethylene propylene lining for the same purpose. Solution inflow and outflow is through stainless steel tubes 4 mm apart with a vacuum aspirator connected to a trap pulling solution across the monolayer to create laminar flow.

Imaging data is analyzed offline using the ImageJ ‘Time Series Analyzer’ plug-in. The brightest cells — those which often saturate pixels even at baseline — are excluded as their fluorescence response exceeds the dynamic range of the detection. Regions of interest (ROIs) are selected based on which construct has been imaged; for iDrugSnFRs targeted to intracellular compartments (e.g. ER, peroxisome), the ROI is drawn around the entire fluorescent region, whereas for iDrugSnFRs targeted to membranes (e.g. PM, F-actin), ROIs are drawn only around the perimeter of the cell. $\Delta F/F_0$ time-series traces are produced by first subtracting the background (extracellular) before taking the difference between the beginning 3 s of the time-series data and all ensuing frames. We then use analysis software (Origin 2018) to plot the traces, correcting for any baseline drift using a spline toolbox. Traces for a minimum of five cells (across at least two fields of view, FOVs) are averaged and shown with standard error of the mean (SEM) as semi-transparent shrouds around them.

Visualizing the details of iDrugSnFR expression in subcellular compartments or on the PM requires a degree of resolution not available under the 40X objective described above. Thus, we also image compartment-targeted sensors under a motorized spinning disk laser scanning confocal inverted microscope (Eclipse Ti-E, Nikon) with a 100X oil immersion objective (numerical aperture, NA = 1.49; working distance, WD = 120 um) using a 488 nm laser at 15% power [543,684]. The micro-lensing of the spinning disk as well as the IMCCD camera allows for low light imaging, mitigating photobleaching and extending the duration of viable data collection. Imaging occurs within a custom incubator (Okolab) held at 37º C and 5% CO_2. Initial images are captured with the cells in HBSS only; to induce fluorescence, we double the bath volume by adding DOI dissolved in HBSS using a hand-held pipette at a concentration approximately equal to the purified protein EC_{50} [684]. We also perform colocalization experiments to validate that the expression of the compartment-targeted iDrugSnFR is in the desired organelle. This technique relies on using a red fluorescent probe (e.g. DsRed2: excitation = 561 nm, emission = 587 nm; mCherry: excitation = 587 nm, emission = 610 nm; mPlum: excitation = 590 nm, emission = 649 nm; mRuby: excitation = 558 nm, emission = 605 nm) known to target the compartment or membrane of interest and co-transfecting mammalian cells with both the probe and the compartment-specific iDrugSnFR. To assess co-localization, transfection of Neuro2a cells was as previously described (see Chapter 2.2.5) with the addition of 0.5 μg of red FP complementary DNA (cDNA) to the transfection mix. We have previously demonstrated proper localization of our ER-targeted constructs using the plasmid DsRed2-ER-5 (AddGene #55836; we can also use mCherry-ER-3, AddGene #55041) in HeLa cells [533]. For the PM-targeted constructs, we were satisfied with images showing intense peripheral fluorescence with little to no internal signal in HeLa cells [533]; for nucleus-targeted constructs, clear labeling of the large nuclei of Neuro2a cells with iRAADSnFR which excludes the rest of

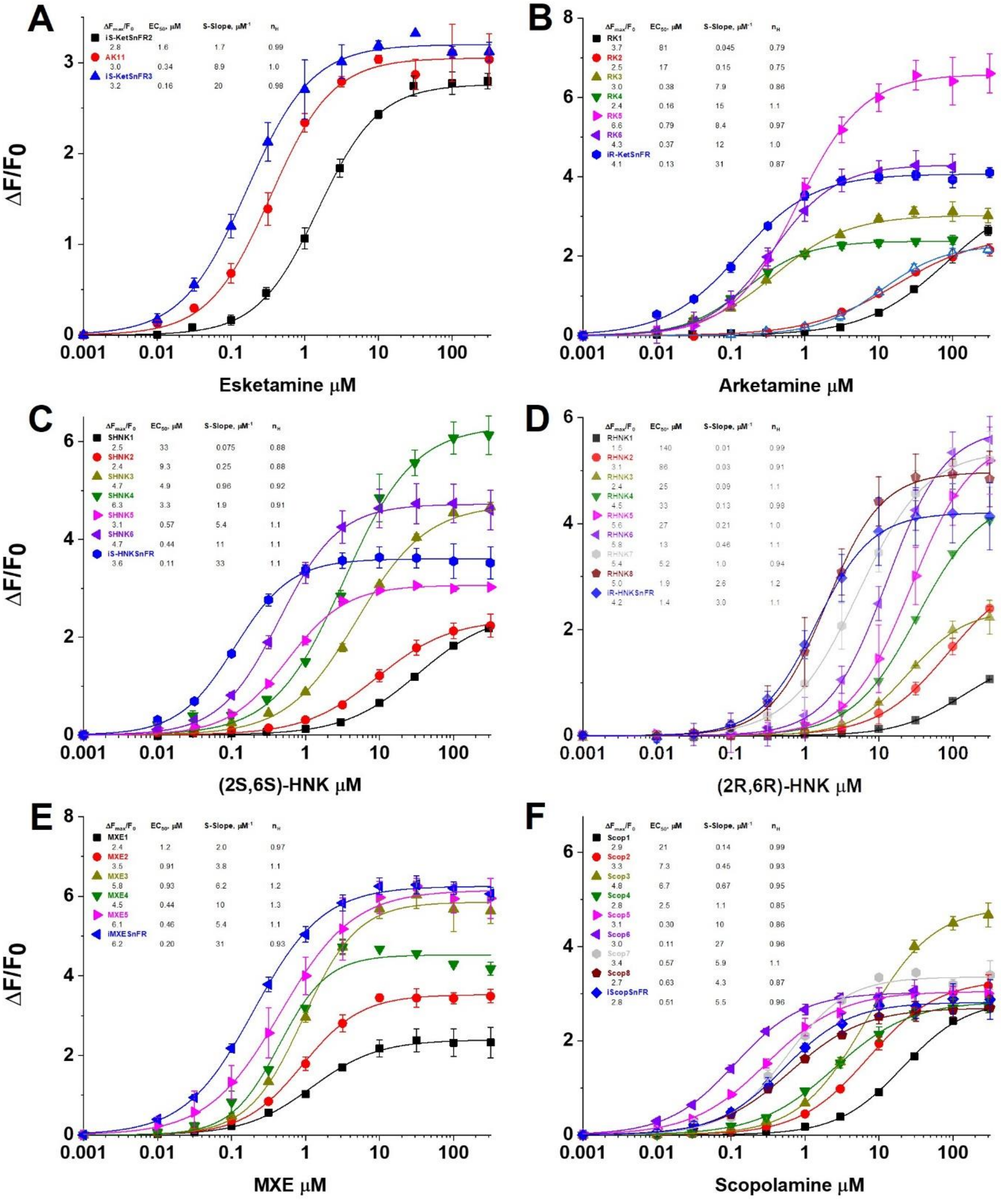

Figure 2.6. Lysate development of the six iRAADSnFRs – iS-KetSnFR3.0 (***A***), iR-KetSnFR (***B***), iS-HNKSnFR (***C***), iR-HNKSnFR (***D***), iMXESnFR (***E***), and iScopSnFR (***F***) – showing both intermediate constructs as well as the final versions (*blue*). Sensors were evaluated against concentrations of their target drug from 1 nM to 316 μM and fitted to the Hill equation; $\Delta F_{max}/F_0$, EC_{50}, S-slope, and n_H are reported in the table inset for each set of constructs. (Images provided by Kallol Bera and Elaine Lin.)

the soma was sufficient to conclude robust nuclear labeling; and for cytoplasm-targeted constructs, there is clear exclusion from the nucleus with iRAADSnFR appearing in both soma and dendrites [543]. Among the new iRAADSnFR constructs, we use mCherry-Peroxisomes-2 (AddGene #54520) to co-label peroxisomes, mCherry-Mito-7 (AddGene #55102) to co-label mitochondria, mCherry-Golgi-2 (AddGene #55052) to co-label Golgi, mCherry-hLC3B-pcDNA3.1 (AddGene #40827) to co-label autophagosomes, mCherry-Actin-C-18 (AddGene #54967) to co-label F-actin, mRuby-Zyxin-6 (AddGene #55887) to target focal adhesions, and mPlum-Fibrillarin-7 (AddGene #55969) to target nucleoli.

2.3. Results: *iRAADSnFRs* In Vitro

2.3.1. iRAADSnFR Development in Lysate and Protein

Based on the most compelling RAAD compounds/candidates, we developed iDrugSnFRs for esketamine (iS-KetSnFR3, a newer version of a previously published sensor [544]), arketamine (iR-KetSnFR), (2S,6S)-HNK (iS-HNKSnFR), (2R,6R)-HNK (iR-HNKSnFR), MXE (iMXESnFR), and scopolamine (iScopSnFR). These sensors were developed using SSM in lysate (see Chapter 2.2.2) (**Fig. 2.6**); we then transformed the cDNA into BL21(DE3) *E.* coli to harvest iRAADSnFR purified protein in order to perform more accurate concentration-response experiments for each RAAD-iRAADSnFR pair (see Chapter 2.2.3). The purified protein concentration-response relations for the optimized iRAADSnFRs are: iS-KetSnFR3 – EC$_{50}$ = 180 nM, $\Delta F_{max}/F_0$ = 3.0, S-slope = 17 μM^{-1}; iR-KetSnFR – EC$_{50}$ = 150 nM, $\Delta F_{max}/F_0$ = 3.3, S-slope = 21 μM^{-1}; iS-HNKSnFR – EC$_{50}$ = 1.4 μM, $\Delta F_{max}/F_0$ = 4.2, S-slope = 3.0 μM^{-1}; iR-HNKSnFR – EC$_{50}$ = 1.4 μM, $\Delta F_{max}/F_0$ = 4.2, S-slope = 3.0 μM^{-1}; iMXESnFR – EC$_{50}$ = 200 nM, $\Delta F_{max}/F_0$ = 6.3, S-slope = 32 μM^{-1}; iScopSnFR – EC$_{50}$ = 510 nM, $\Delta F_{max}/F_0$ = 2.8 , S-slope = 5.5 μM^{-1} (**Table 2.1**). We also performed concentration-response

iRAADSnFR	**EC$_{50}$, μM**	**$\Delta F_{max}/F_0$, unitless**	**S-slope, μM^{-1}**
iS-KetSnFR3	0.180	3.0	17
iR-KetSnFR	0.150	3.3	21
iS-HNKSnFR	1.4	4.2	3.0
iR-HNKSnFR	1.4	4.2	3.0
iMXESnFR	0.20	6.3	32
iScopSnFR	0.51	2.8	5.5

Table 2.1. EC$_{50}$, $\Delta F_{max}/F_0$, and S-slope values for the iRAADSnFRs in purified protein generated from fits to the Hill equation.

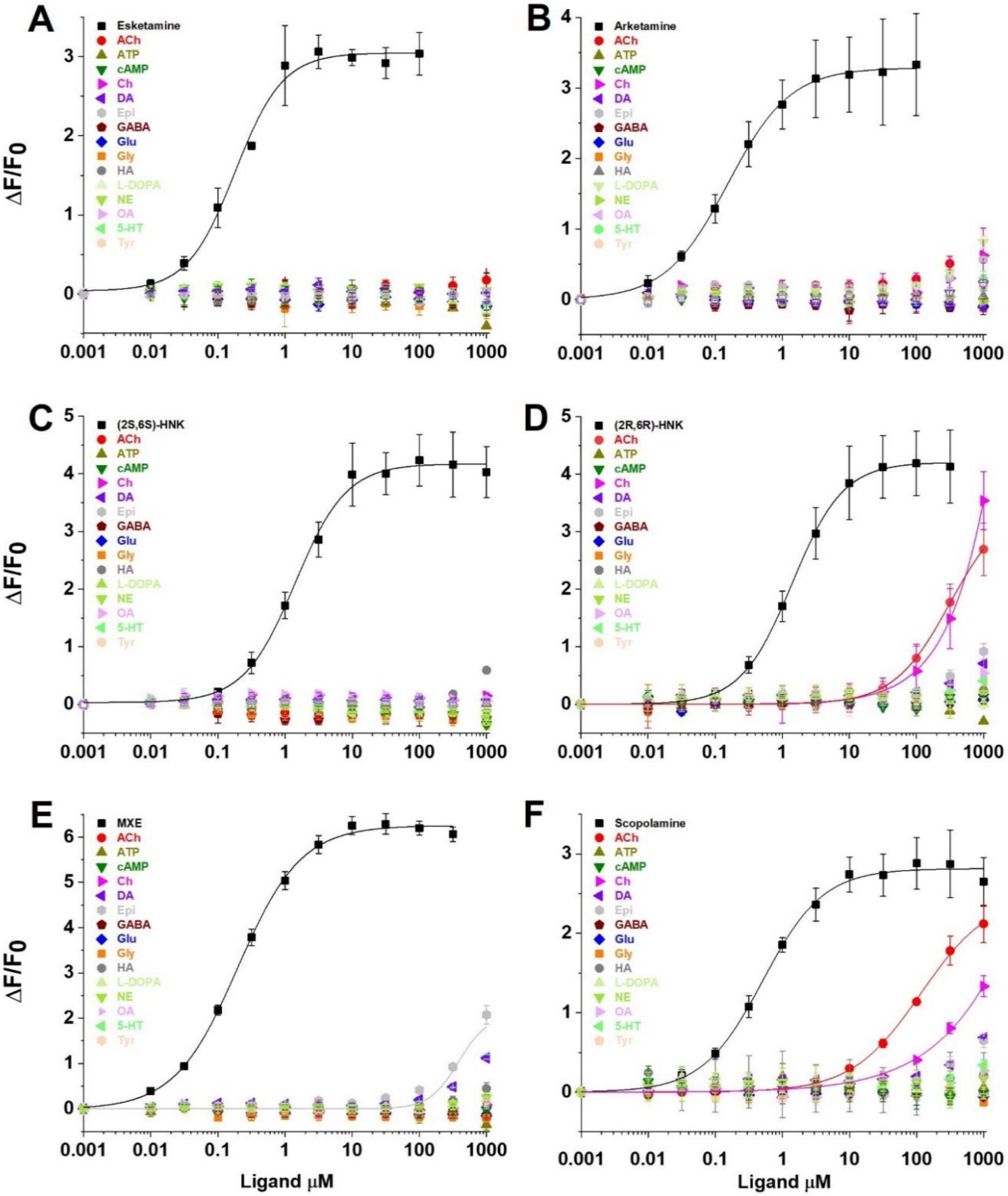

Figure 2.7. Endogenous compounds and their precursors versus the iRAADSnFRs — iS-KetSnFR (***A***), iR-KetSnFR (***B***), iS-HNKSnFR (***C***). iR-HNKSnFR (***D***), iMXESnFR (***E***), and iScopSnFR (***F***) — in purified protein (50 nM). Almost every compound vs. iRAADSnFR concentration-response curve is unable to be fit to the Hill equation save for five: ACh vs. iR-HNKSnFR, choline vs. iR-HNKSnFR, epinephrine vs. iMXESnFR, ACh vs. iScopSnFR, and choline vs. iScopSnFR. (cAMP = cyclic AMP; Ch = choline; Epi = epinephrine; Glu = glutamate; Gly = glycine; HA = histamine; L-DOPA = levodopa; OA = octopamine; Tyr = tyramine; SEM are shown for concentration-response curves fit to the Hill equation.) (Images provided by Kallol Bera.)

experiments with all six iRAADSnFRs against a panel of 15 endogenous molecules and their precursors to validate their selectivity for their target compounds both *in vitro* and *in vivo* (**Fig. 2.7**). None of the iRAADSnFRs interact with any molecules at physiologically relevant concentrations; both iR-HNKSnFR (**Fig. 2.7D**) and iScopSnFR (**Fig. 2.7F**) bind to ACh (EC_{50}: iR-HNKSnFR – 310 µM; iScopSnFR – 120 µM) and choline (EC_{50}: iR-HNKSnFR – 14 mM; iScopSnFR – 18 mM) but very weakly, while iMXESnFR (**Fig. 2.7E**) binds to epinephrine (EC_{50}: 1.2 mM) at similarly irrelevant levels.

2.3.2. Characterization of iRAADSnFRs

To examine the thermodynamics of the iRAADSnFR-RAAD interaction, we conducted ITC experiments (see Chapter 2.2.4) (**Fig. 2.8**). The experimentally determined K_d of iS-KetSnFR3, 296 ± 27 nM, was within a factor of two of the experimentally determined EC_{50} in purified protein, 180 nM; for iR-KetSnFR, the experimentally determined K_d, 120 ± 5.0 nM, was nearly identical to the experimentally determined EC_{50} in purified protein, 150 nM; for iS-HNKSnFR, the experimentally determined K_d, 249 ± 14 nM, was about an order of magnitude lower than the experimentally determined EC_{50} in purified protein, 1.4 µM; for iMXESnFR, the experimentally determined K_d, 522 ± 104 nM, was within a factor of three of the experimentally determined EC_{50} in purified protein, 200 nM; and for iScopSnFR, the experimentally determined K_d, 616 ± 97 nM, was within a factor of 1.5 of the experimentally determined EC_{50} in purified protein, 510 nM; we have not yet performed ITC experiments for iR-HNKSnFR (**Table 2.2**). The ITC data demonstrate different reaction thermodynamics across the iRAADSnFR-RAAD interactions: for iS-KetSnFR-esketamine, the reaction is exothermic (negative ΔH) and entropically favorable

Biosensor	**K_D (µM)**	**n**	**ΔH (kcal/mol)**	**-TΔS (kcal/mol)**	**ΔG (kcal/mol)**
iS-KetSnFR3	0.296 ± 0.027	0.960 ± 0.138	-3.04 ± 0.815	-5.86 ± 0.805	-8.90 ± 0.055
iR-KetSnFR	0.120 ± 0.005	0.747 ± 0.024	-5.84 ± 1.94	-3.31 ± 1.81	-9.15 ± 0.14
iS-HNKSnFR	0.249 ± 0.014	1.21 ± 0.041	-16.5 ± 0.501	7.29 ± 0.663	-9.25 ± 0.163
iR-HNKSnFR	-	-	-	-	-
iMXESnFR	0.522 ± 0.104	0.804 ± 0.098	5.76 ± 0.725	-14.3 ± 0.611	-8.57 ± 0.154
iScopSnFR	0.616 ± 0.097	0.747 ± 0.024	3.13 ± 0.699	-11.6 ± 0.814	-8.51 ± 0.142

Table 2.2. Affinity, occupancy number, and thermodynamic data calculated from ITC.

(positive entropy, ΔS), leading to an overall exergonic reaction (negative ΔG); for iR-KetSnFR-arketamine, the reaction is also exothermic and entropically favorable (though the enthalpic component is larger than the entropic component, the opposite of iS-KetSnFR-esketamine), leading to an overall exergonic reaction; for iS-HNKSnFR-(2S,6S)-HNK, the reaction is dominated by its exothermic component even though it is entropically unfavorable (positive ΔS), leading to an overall exergonic reaction; for both iMXESnFR-MXE and iScopSnFR-scopolamine, the reactions are endothermic (positive ΔH) but each reaction is dominated by its entropic favorability which leads to an overall exergonic reaction (**Fig. 2.8** and **Table 2.2**).

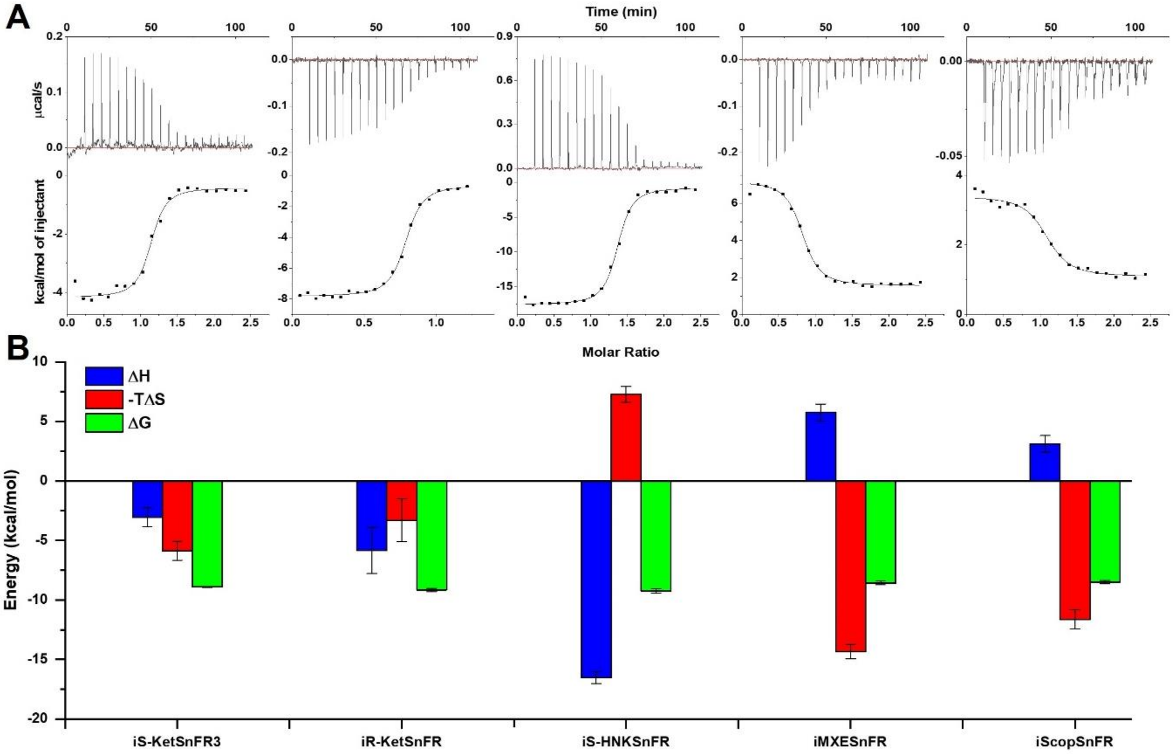

Figure 2.8. ITC traces, fits, and thermodynamic data. ***(A)*** *(Top row*) Exemplar heat traces of iS-KetSnFR, iR-KetSnFR, iS-HNKSnFR, iMXESnFR, and iScopSnFR paired with their drug partners. The heats for iS-KetSnFR, iR-KetSnFR, and iS-HNKSnFR were exothermic, while those for iMXESnFR and iScopSnFR were endothermic. (*Bottom row*) The resulting fits for each iDrugSnFR:drug pair from the integrated heats comprising each series of injections. ***(B)*** Energy calculations. All iDrugSnFRs show exergonic reactions, but the relative enthalpic and entropic contributions vary among them. (Images provided by Kallol Bera and Elaine Lin.)

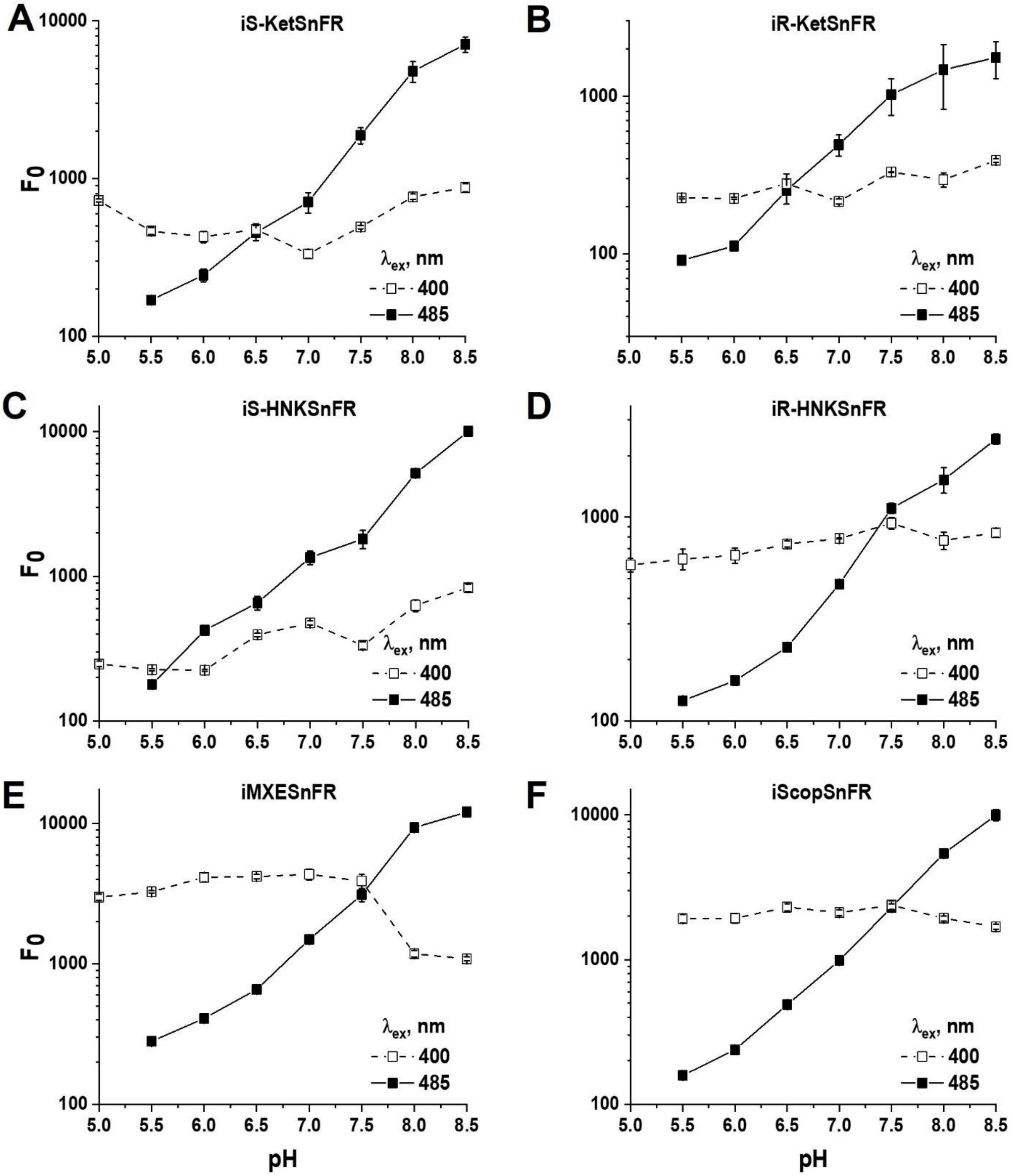

Figure 2.9. Plots of pH (from 5.0 to 8.5) vs. F_0 (in arbitrary units measured at 535 nm emission) for all six iRAADSnFRs — iS-KetSnFR (***A***), iR-KetSnFR (***B***), iS-HNKSnFR (***C***), iR-HNKSnFR (***D***), iMXESnFR (***E***), and iScopSnFR (***F***) — in purified protein (50 nM) for both 400 nm (*white boxes with dotted lines*) and 485 nm (*black boxes with solid lines*) excitation. (Images provided by Kallol Bera and Elaine Lin.)

We also investigated the pH dependence of the iRAADSnFRs. Similarly to previous characterizations of iNicSnFR [533], we compared pH-dependent F_0 values for both 400 nm and 485 nm excitation from pH 5.5 to 9, as the former wavelength (thought to be close to the isosbestic point for cpGFP-based sensors [778]) was shown to induce a consistent value across the pH range tested while the latter varied by up to three orders of magnitude [533]. In purified protein from pH 5.0 to 8.5, the iRAADSnFRs demonstrated a similar relationship, whereby excitation with 400 nm light induced F_0 variation well within one order of magnitude while excitation with 485 nm light induced F_0 variation from at least one order of magnitude (iR-KetSnFR, iR-HNKSnFR, iMXESnFR) to approximately two (iS-KetSnFR, iS-HNKSnFR, iScopSnFR) (**Fig. 2.9**). We also performed concentration-response experiments for each iRAADSnFR-RAAD across the aforementioned pH range (**Fig. 2.10**) with concentrations centered around the EC_{50} values previously determined in purified protein (**Table 2.1**) and found that $\Delta F_{max}/F_0$ was highest at pH 7.5 for only iS-KetSnFR (**Fig. 2.10A**), while for four sensors — iR-KetSnFR (**Fig. 2.10B**), iS-HNKSnFR (**Fig. 2.10C**), iMXESnFR (**Fig. 2.10E**), and iScopSnFR (**Fig. 2.10F**) — $\Delta F_{max}/F_0$ was highest at pH 7.0 and for iR-HNKSnFR it was highest at pH 6.5 (**Fig. 2.10C**). Interestingly, while the pH giving the lowest EC_{50} value tracked the highest $\Delta F_{max}/F_0$ for several sensors (iR-KetSnFR, iS-HNKSnFR), this was not true for the majority of the iRAADSnFRs (iS-KetSnFR, iR-HNKSnFR, iMXESnFR, and iScopSnFR). These results may indicate that the iRAADSnFRs display more pH tolerance than at least iNicSnFR [533], especially in weakly acidic environments such as the nucleus, ER, and Golgi [531].

Characterizing the reaction kinetics of each RAAD-iRAADSnFR pair will be performed using stopped-flow (see Chapter 2.2.4); however, we have yet to conduct these experiments.

2.3.3. Concentration-Response Experiments with Compartment-Targeted iRAADSnFRs in Mammalian Cells

We synthesized a broad array of iRAADSnFRs targeted to the aforementioned organelles/membranes in mammalian cells (see Chapter 2.2.5). Our nomenclature involved appending a compartment-specific prefix to the name of the sensor (**Table 2.3**); as we have yet to perform full sets of experiments with either focal adhesion-targeted or nucleolus-targeted iRAADSnFRs, we exclude those from further analysis. To ensure that our constructs are

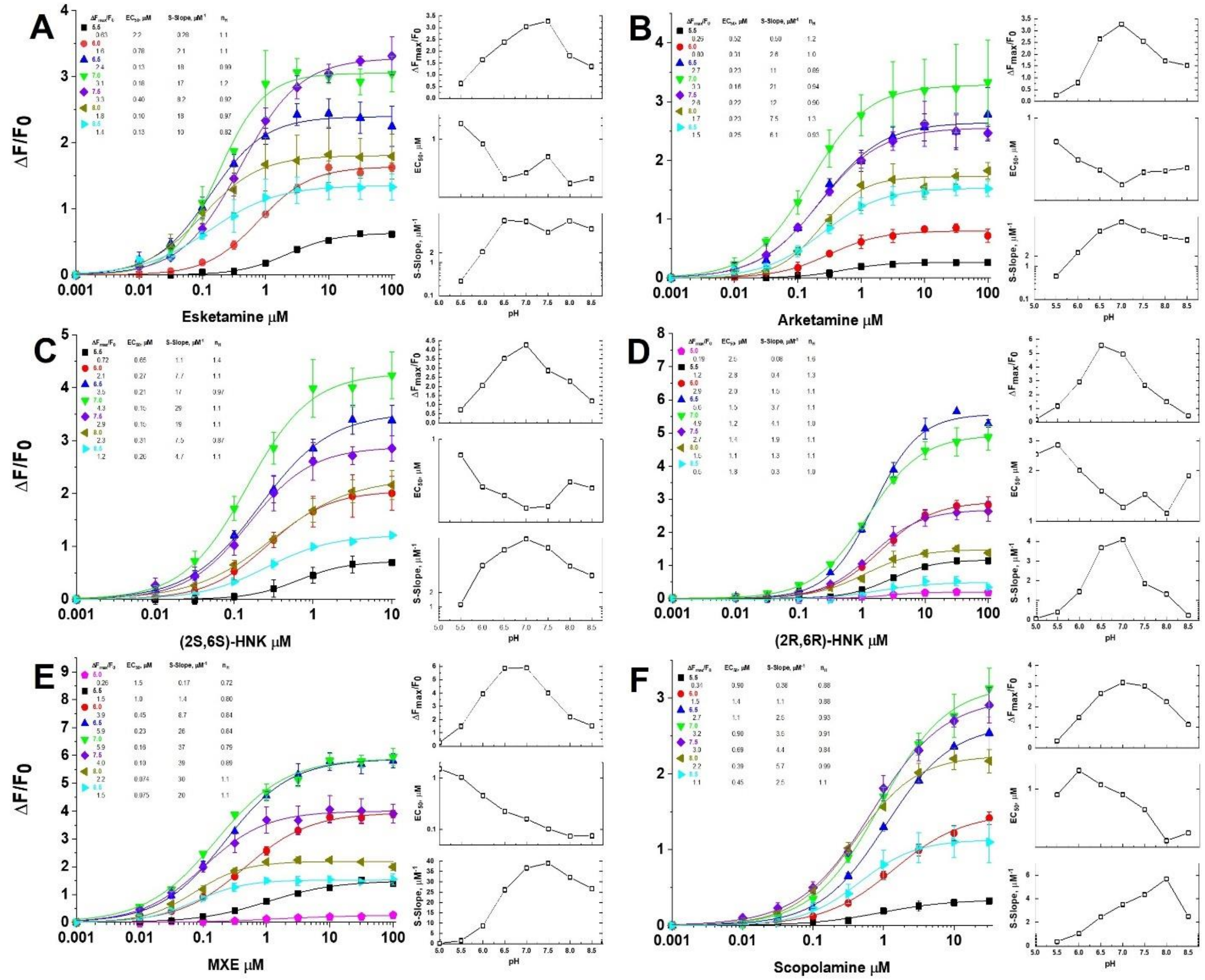

A

	$\Delta F_{max}/F_0$	EC_{50}, μM	S-Slope, μM^{-1}	n_H
5.5	0.63	2.2	0.28	1.1
6.0	1.6	0.78	2.1	1.1
6.5	2.4	0.13	18	0.99
7.0	3.1	0.16	17	1.2
7.5	3.3	0.40	8.2	0.92
8.0	1.8	0.10	18	0.97
8.5	1.4	0.13	10	0.82

B

	$\Delta F_{max}/F_0$	EC_{50}, μM	S-Slope, μM^{-1}	n_H
5.5	0.26	0.52	0.50	1.2
6.0	0.80	0.31	2.6	1.0
6.5	2.7	0.23	11	0.89
7.0	3.3	0.16	21	0.94
7.5	2.6	0.22	12	0.90
8.0	1.7	0.23	7.5	1.3
8.5	1.5	0.25	6.1	0.93

C

	$\Delta F_{max}/F_0$	EC_{50}, μM	S-Slope, μM^{-1}	n_H
5.5	0.72	0.65	1.1	1.4
6.0	2.1	0.27	7.7	1.1
6.5	3.5	0.21	17	0.97
7.0	4.3	0.15	29	1.1
7.5	2.9	0.15	19	1.1
8.0	2.3	0.31	7.5	0.87
8.5	1.2	0.26	4.7	1.1

D

	$\Delta F_{max}/F_0$	EC_{50}, μM	S-Slope, μM^{-1}	n_H
5.0	0.19	2.5	0.08	1.6
5.5	1.2	2.8	0.4	1.3
6.0	2.9	2.0	1.5	1.1
6.5	5.6	1.5	3.7	1.1
7.0	4.9	1.2	4.1	1.0
7.5	2.7	1.4	1.9	1.1
8.0	1.5	1.1	1.3	1.1
8.5	0.5	1.8	0.3	1.0

E

	$\Delta F_{max}/F_0$	EC_{50}, μM	S-Slope, μM^{-1}	n_H
5.0	0.26	1.5	0.17	0.72
5.5	1.5	1.0	1.4	0.80
6.0	3.9	0.45	6.7	0.84
6.5	5.9	0.23	26	0.84
7.0	5.9	0.16	37	0.79
7.5	4.0	0.10	39	0.89
8.0	2.2	0.074	30	1.1
8.5	1.5	0.075	20	1.1

F

	$\Delta F_{max}/F_0$	EC_{50}, μM	S-Slope, μM^{-1}	n_H
5.5	0.34	0.90	0.38	0.88
6.0	1.5	1.4	1.1	0.88
6.5	2.7	1.1	2.5	0.93
7.0	3.2	0.90	3.5	0.91
7.5	3.0	0.69	4.4	0.84
8.0	2.2	0.39	5.7	0.99
8.5	1.1	0.45	2.5	1.1

Figure 2.10. ***(A-F)*** Concentration-response traces (*left*) and trendlines for iRAADSnFR-RAAD fluorescence characteristics (*right*: $\Delta F_{max}/F_0$, *top*; EC_{50}, *middle*, S-slope, *bottom*) across pH 5.0 to 8.5 in purified protein. The values comprising the pH-dependent fluorescence characteristics are also displayed in tabular form (*upper left*) along with n_H (*right column*) which corresponds to the Hill coefficient as reported from the fits to the Hill equation (see Chapter 2.2.1). (Images provided by Kallol Bera and Elaine Lin.)

expressed in the desired compartments, we performed co-localization experiments for six out of the nine compartments using spinning disk confocal microscopy (**Fig. 2.11**) (see Chapter 2.2.6). We found that all six double-transfected Neuro2a cells displayed correct localization of the compartment-targeted iRAADSnFRs (**Fig. 2.11A-F**) and that the three constructs (PM, cytoplasm, and nucleus) transfected with iRAADSnFR only likewise showed dispositive labeling of the appropriate structures as we have seen in previous studies [533,543] (**Fig. 2.11H-I**) (see Chapter 3.3.6).

Sensor	ER	PM	Cytoplasm	Nucleus	Mitochondria	Golgi	Peroxisomes	F-Actin	Autophagosomes
iS-KetSnFR	ER.iS-KetSnFR	PM.iS-KetSnFR	Cyto.iS-KetSnFR	Nuc.iS-KetSnFR	Mito.iS-KetSnFR	Golgi.iS-KetSnFR	Per.iS-KetSnFR	Act.iS-KetSnFR	AP.iS-KetSnFR
iR-KetSnFR	ER.iR-KetSnFR	PM.iR-KetSnFR	Cyto.iR-KetSnFR	Nuc.iR-KetSnFR	Mito.iR-KetSnFR	Golgi.iR-KetSnFR	Per.iR-KetSnFR	Act.iR-KetSnFR	AP.iR-KetSnFR
iS-HNKSnFR	ER.iS-HNKSnFR	PM.iS-HNKSnFR	Cyto.iS-HNKSnFR	Nuc.iS-HNKSnFR	Mito.iS-HNKSnFR	Golgi.iS-HNKSnFR	Per.iS-HNKSnFR	Act.iS-HNKSnFR	AP.iS-HNKSnFR
iR-HNKSnFR	ER.iR-HNKSnFR	PM.iR-HNKSnFR	Cyto.iR-HNKSnFR	Nuc.iR-HNKSnFR	Mito.iR-HNKSnFR	Golgi.iR-HNKSnFR	Per.iR-HNKSnFR	Act.iR-HNKSnFR	AP.iR-HNKSnFR
iMXESnFR	ER.iMXESnFR	PM.iMXESnFR	Cyto.iMXESnFR	Nuc.iMXESnFR	Mito.iMXESnFR	Golgi.iMXESnFR	Per.iMXESnFR	Act.iMXESnFR	AP.iMXESnFR
iScopSnFR	ER.iScopSnFR	PM.iScopSnFR	Cyto.iScopSnFR	Nuc.iScopSnFR	Mito.iScopSnFR	Golgi.iScopSnFR	Per.iScopSnFR	Act.iScopSnFR	AP.iScopSnFR

Table 2.3. List of all compartment-targeted iRAADSnFRs synthesized for expression in mammalian cells.

We next performed concentration-response experiments with all nine compartment-targeted iRAADSnFRs in Neuro2a cells (see Chapter 2.2.5 and Chapter 2.2.6) over concentration ranges appropriate for the EC_{50} of each iRAADSnFR (as determined in purified protein; **Table 2.1**). For certain traces, we corrected the baseline period before the first concentration was administered to establish a consistent comparison point for subsequent washout periods. For the PM.iRAADSnFRs, we expect to have a) stronger overall signal since the RAAD molecules have the least amount of cellular material to traverse, and b) faster kinetics for the same reason, while for the constructs targeted to intracellular organelles with membranes (ER, mitochondria, Golgi, nucleus, peroxisomes, autophagosomes) as well as without (F-actin and cytoplasm), we expect lower overall fluorescence response and slower dynamics. For the PM-targeted constructs (**Fig. 2.12**), we see a fluorescence plateau reached within seconds as well as rapid returns to baseline between administered concentrations for the ketamine compounds even after only 20 s of washout (**Fig. 2.12A-D**); however, for MXE, the return to baseline is never complete after the administration of any dose (though if the washout period was extended for even 10 s, baseline would likely be recaptured) (**Fig. 2.12E**). Perhaps the most notable dynamic is how rapidly scopolamine-induced fluorescence occurs across all tested concentrations (**Fig. 2.12E**), which contrasts with scopolamine's transit time into and out of the various targeted organelles (see below). Notably, scopolamine is the only compound among the six RAADs tested which matched our prediction that PM-targeted sensors would demonstrate the highest maximal fluorescence; this may be due to scopolamine's relative lipophilicity (see Chapter 1.5 and Chapter 2.6.3) compared to the ketamine-class compounds, all of which have LogP values around two orders of magnitude higher. Thus, for PM.iRAADSnFRs, the overall fluorescence

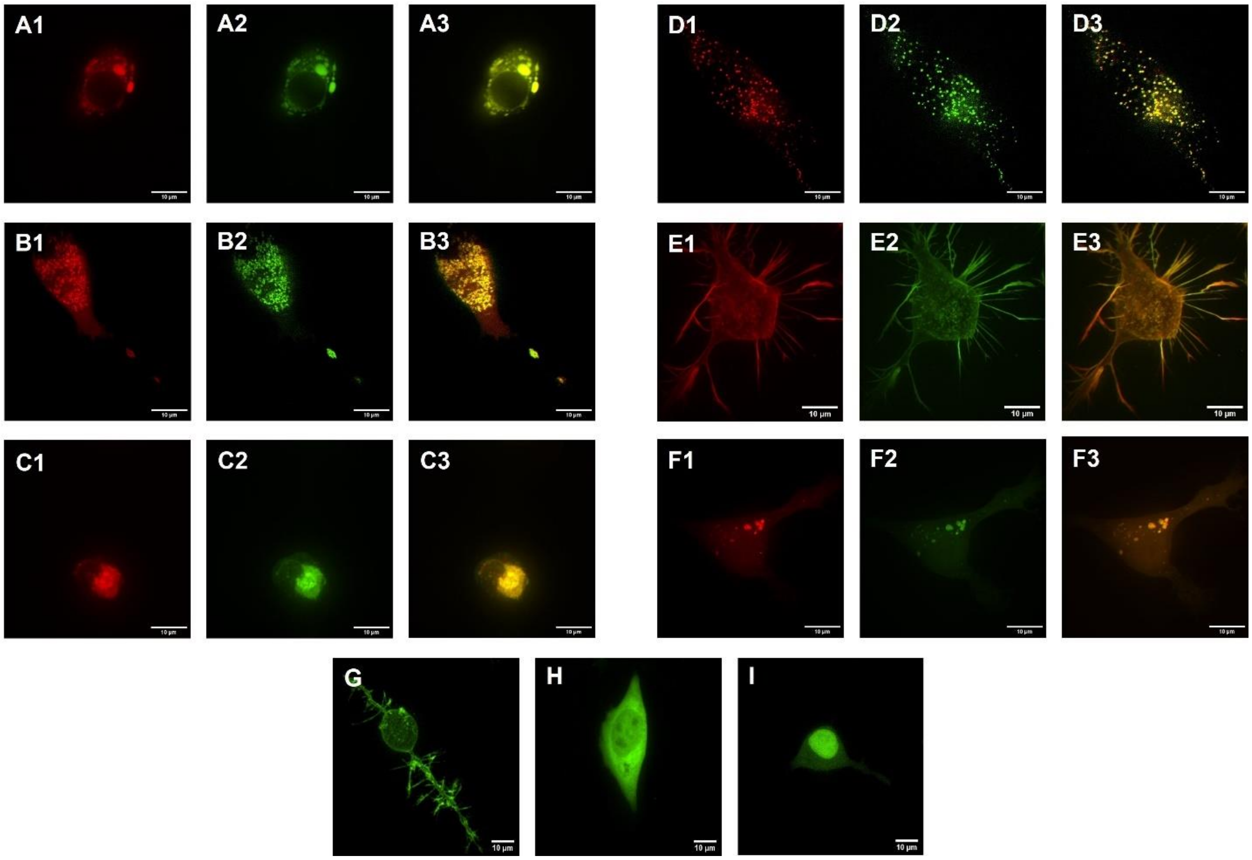

Figure 2.11. ***(A-F)*** Representative spinning disk confocal images of co-transfected Neuro2a cells showing red-shifted compartment-specific probes (***1***, *left*), GFP-based compartment-targeted iRAADSnFRs (***2***, *middle*), and merged images of the two (***3***, *right*) for six of the nine constructs synthesized — iRAADSnFRs in the ER (***A1-A3***), mitochondria (***B1-B3***), Golgi (***C1-C3***), peroxisomes (***D1-D3***), F-actin (***E1-E3***), and autophagosomes (***F1-F3***) — demonstrating appropriate labeling of the targeted structures. ***(H-J)*** iRAADSnFR-labeled Neuroa2a cells showing appropriate labeling of the PM (***H***), cytoplasm (***I***), and the nucleus (***J***) based on previous characterizations performed in mammalian cells (see Chapter 3.3.6). (Images provided by Kallol Bera and Elaine Lin.)

maxima reached per concentration for the ketamine-class compounds is no higher (and, in the case of MXE, far lower) than those observed in experiments using organelle-targeted constructs (see below).

Turning to the intracellular-targeted constructs, we see for the iRAADSnFRs localized to the ER (**Fig. 2.13**) that the pharmacokinetics appear slower compared to the PM.iRAADSnFR traces, though not appreciably so, as all of the ketamine drugs wash out fully over the same respective time scales (see **Fig. 2.12**). Interestingly, MXE induces higher fluorescence values interacting with ER-targeted iMXESnFR than with PM-targeted iMXESnFR (**Fig. 2.13E**) and

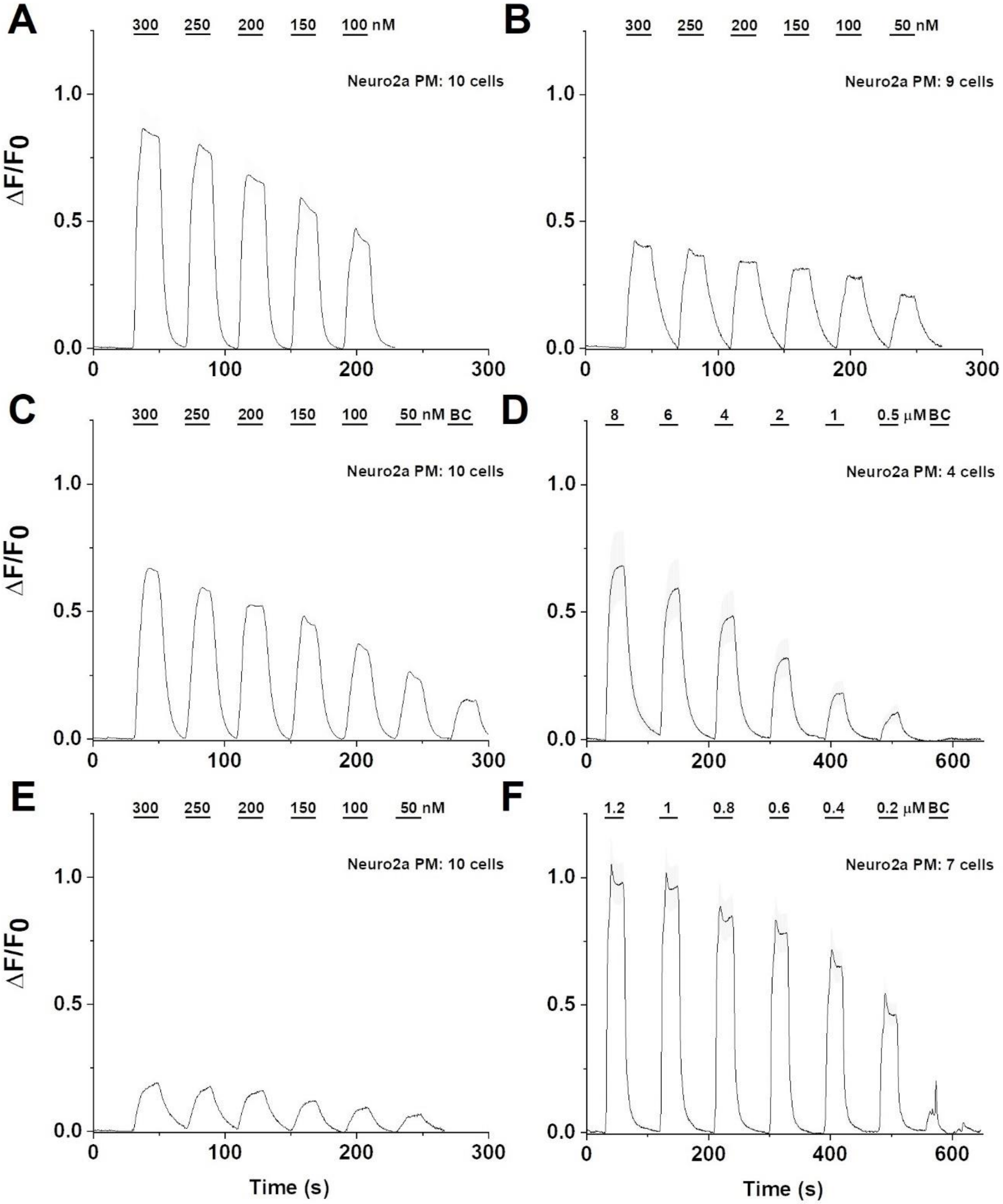

Figure 2.12. iRAADSnFRs targeted to the PM showing concentration-response traces for esketamine (***A***), arketamine (***B***), (2S,6S)-HNK (***C***), (2R,6R)-HNK (***D***), MXE (***E***), and scopolamine (***F***). Administration and washout periods are 20 s and 20 s, respectively (***A***, ***B***, ***C***, ***E***) and 40 s and 40 s (***D***, ***F***), respectively. Baseline periods have been normalized to ~ 0% $\Delta F/F_0$. (SEM is as described previously.) (Images provided by Kallol Bera and Elaine Lin.)

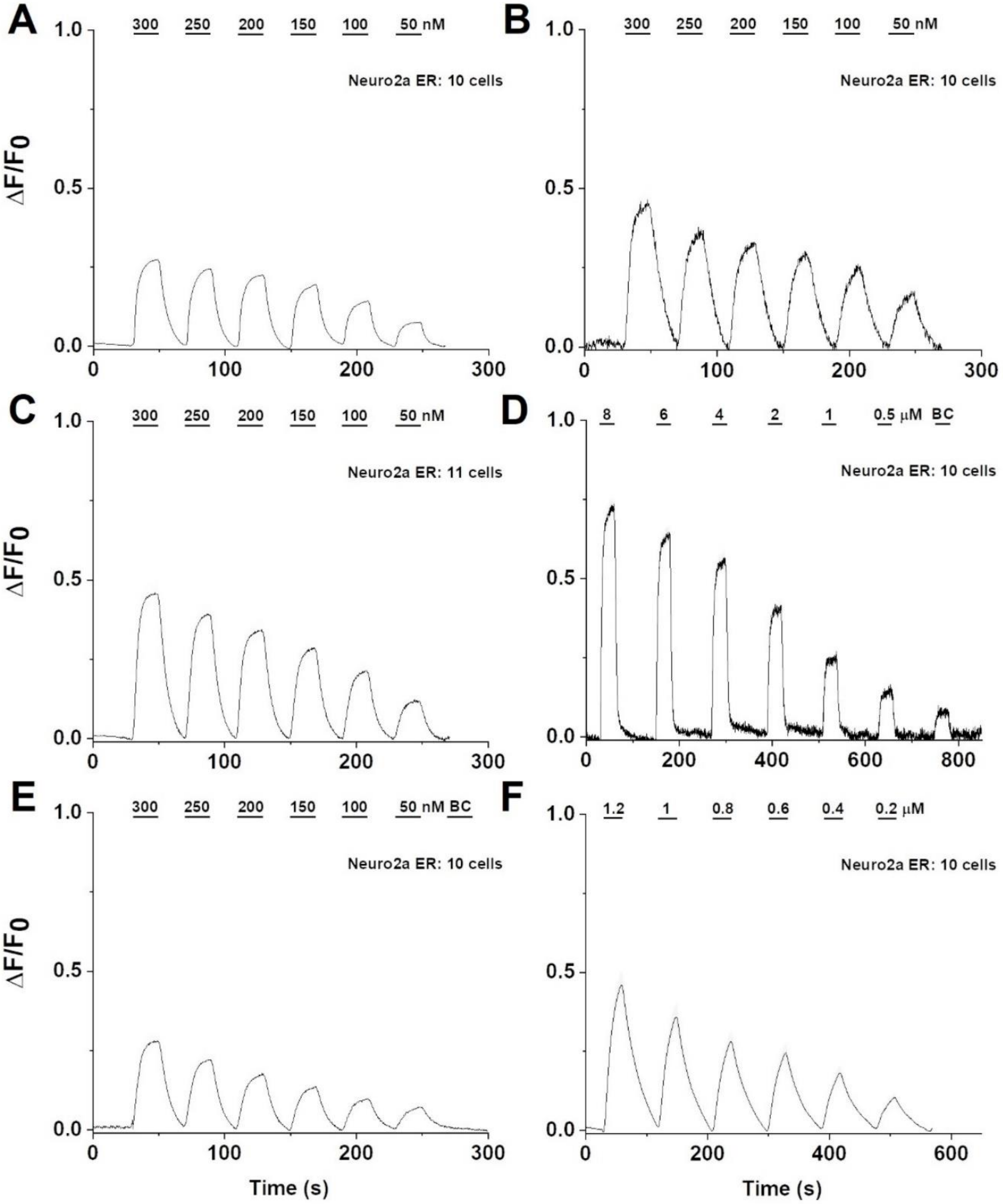

Figure 2.13. iRAADSnFRs targeted to the ER showing concentration-response traces for esketamine (***A***), arketamine (***B***), (2S,6S)-HNK (***C***), (2R,6R)-HNK (***D***), MXE (***E***), and scopolamine (***F***). Administration and washout periods are 20 s and 20 s, respectively (***A***, ***B***, ***C***, ***E***), 30 s and 90 s, respectively (***D***) and 40 s and 40 s (***F***), respectively. Baseline periods have been normalized to ~ 0% $\Delta F/F_0$. (SEM is as described previously.) (Images provided by Kallol Bera and Elaine Lin.)

also has faster kinetics (only a few of the later lower concentration traces fail to washout), a phenomenon we have not encountered before in our *in vitro* experiments. As noted above, scopolamine enters and exits the ER roughly an order of magnitude slower than the PM (tens of seconds versus seconds; **Fig. 2.13F**). Overall, however, all six constructs targeted to the ER demonstrate washout periods for which the fluorescence does return to zero, indicating that, while the dynamics show some variation, the overall behavior of the RAADs resembles most of the weakly basic drugs we have assessed for entry into the ER in mammalian cells (nicotine [533], 9-bromo-10-ethylcytisine and dianicline [684], S-methadone [685], escitalopram and fluoxetine [543]). For the cytoplasm-targeted constructs, all four of the ketamine compounds appear to reach maximum fluorescence responses across all concentrations used (**Fig. 2.14A-D**), suggesting that the entry of these compounds into cells is nearly limited by solution changes. The waveforms for scopolamine and especially MXE, however, do not appear to level off during any of the concentrations used, with MXE eliciting distinctive wash-in waveforms reminiscent of other compounds which enter cells on a slower timescale (e.g. cytisine [684]) (**Fig. 2.14E-F**). Additionally, the maximal fluorescence response for (2R,6R)-HNK is approximately four times higher than that of scopolamine and about three times higher than arketamine, (2S,6S)-HNK, or scopolamine (**Fig. 2.14D**). For iRAADSnFRs targeted to the nucleus, we observed similar fluorescence dynamics as for the cytoplasm-targeted constructs, with MXE and scopolamine evincing slower wash-in kinetics than the ketamine-class drugs; however, both arketamine and (2S,6S)-HNK display a trend towards slower kinetics as well, with both responses across all concentrations failing to reach a stable $\Delta F/F_0$ (**Fig. 2.15**); this may reflect slower transit across the two nuclear membranes. Again, the maximal response to (2R,6R)-HNK is the highest among the six iRAADSnFRs (**Fig. 2.15D**), though the relative discrepancies between it and the other five RAADs are less pronounced. Overall, the six constructs demonstrate complete washout between concentrations, recapitulating the dynamics observed for the cytoplasm-targeted constructs. iRAADSnFRs targeted to the mitochondria (**Fig. 2.16**) demonstrate similar behavior to those targeted to the nucleus, with the exception that the waveforms in response to MXE (and, to an extent, for (2S,6S)-HNK) demonstrate an odd biphasic washout with a small local maximum during the last 10 s or so of the periods (**Fig. 2.16CE**), a phenomenon we have seen only during incomplete washout from the ER (e.g. 10-fluorocytisine, see **Fig. 4.9B**). The RAADs interacting with Golgi.iRAADSnFRs (**Fig. 2.17**) showed overall slower kinetics than virtually all

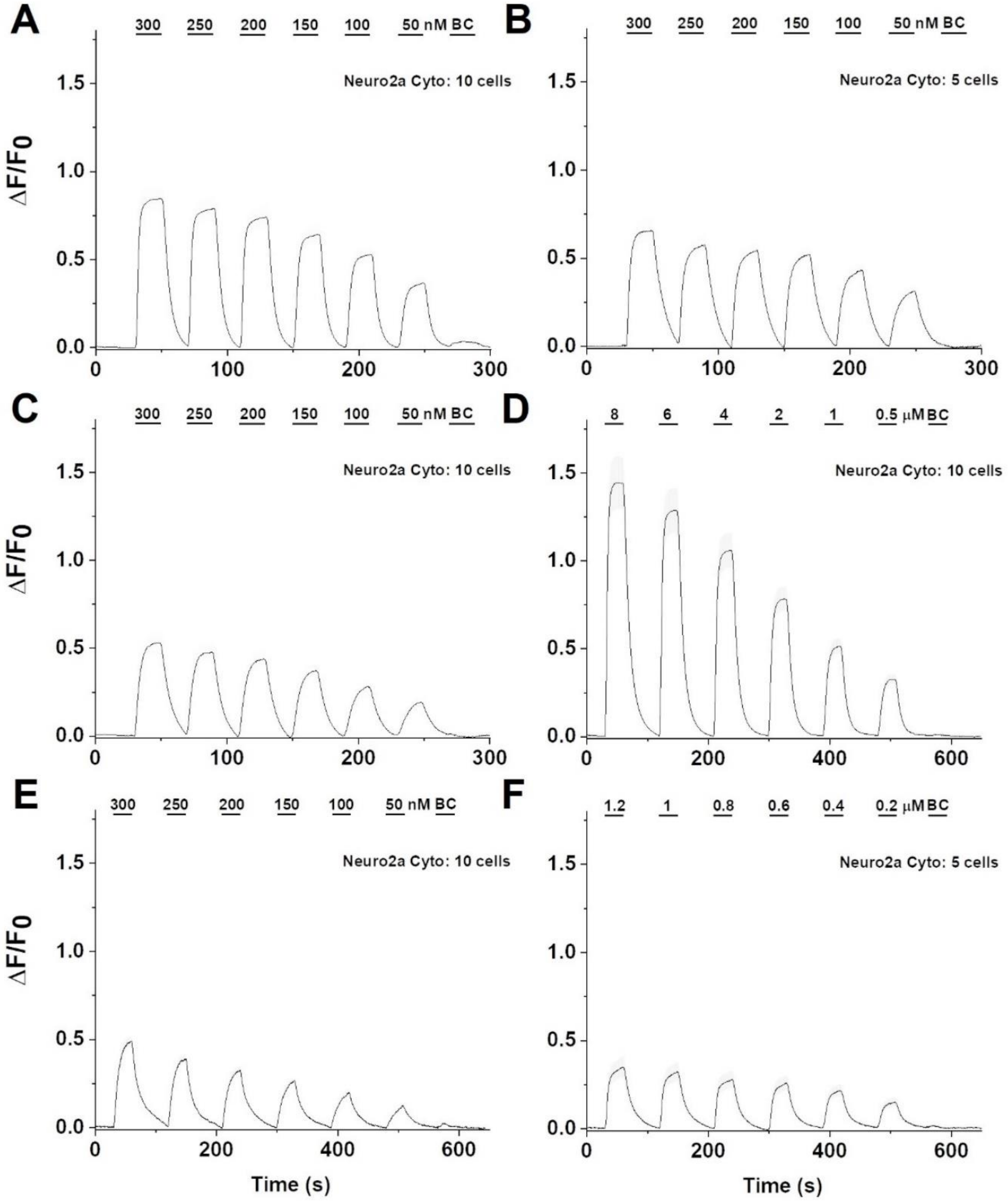

Figure 2.14. iRAADSnFRs targeted to the cytoplasm showing concentration-response traces for esketamine (***A***), arketamine (***B***), (2S,6S)-HNK (***C***), (2R,6R)-HNK (***D***), MXE (***E***), and scopolamine (***F***). Administration and washout periods are 20 s and 20 s, respectively (***A***, ***B***, ***C***) and 40 s and 40 s (***D***, ***E***, ***F***), respectively. Baseline periods have been normalized to ~ 0% $\Delta F/F_0$. (SEM is as described previously.) (Images provided by Kallol Bera and Elaine Lin.)

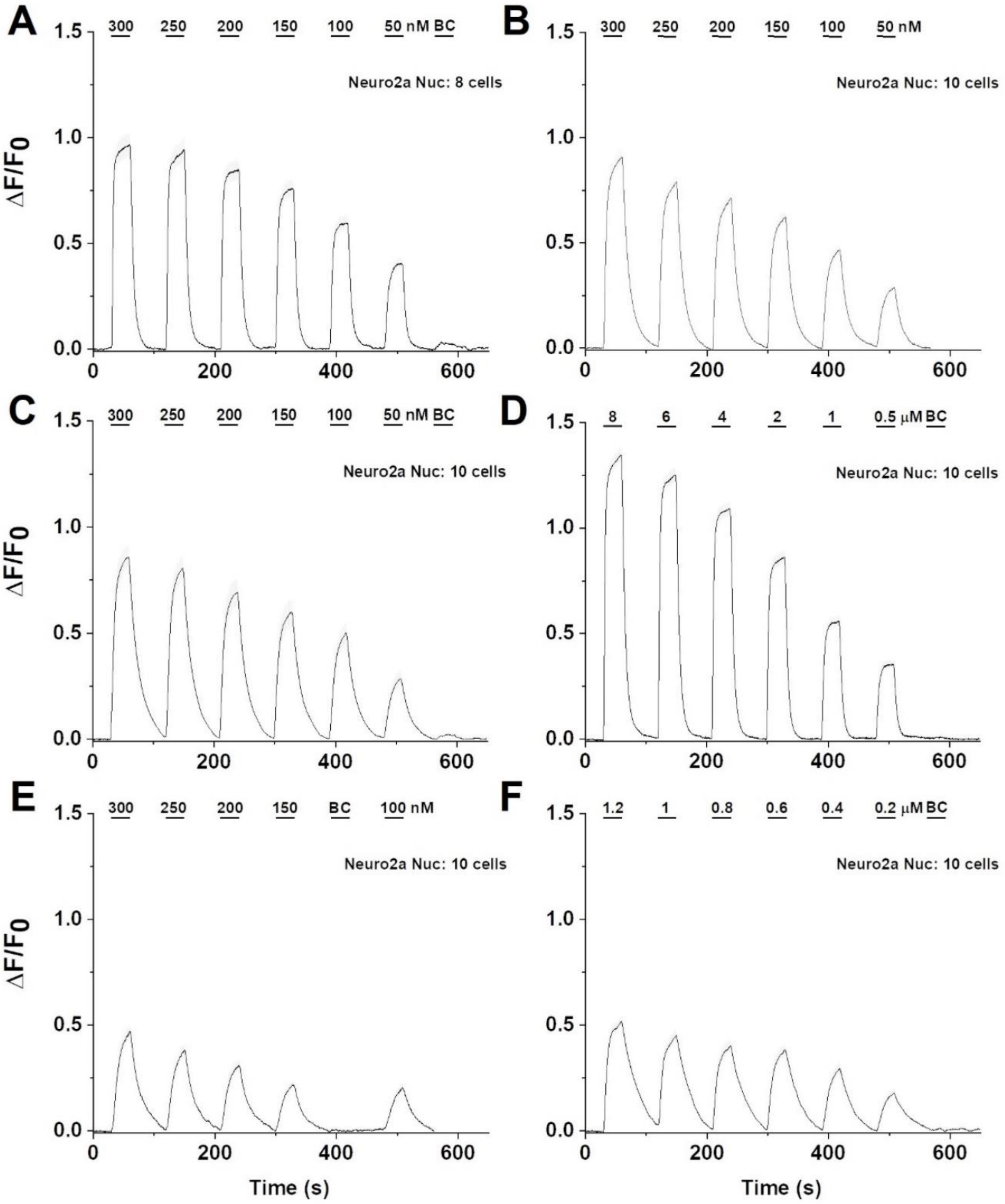

Figure 2.15. iRAADSnFRs targeted to the nucleus showing concentration-response traces for esketamine (***A***), arketamine (***B***), (2S,6S)-HNK (***C***), (2R,6R)-HNK (***D***), MXE (***E***), and scopolamine (***F***). Administration and washout periods are 40 s and 40 s, respectively. Baseline periods have been normalized to ~ 0% $\Delta F/F_0$. (SEM is as described previously.) (Images provided by Kallol Bera and Elaine Lin.)

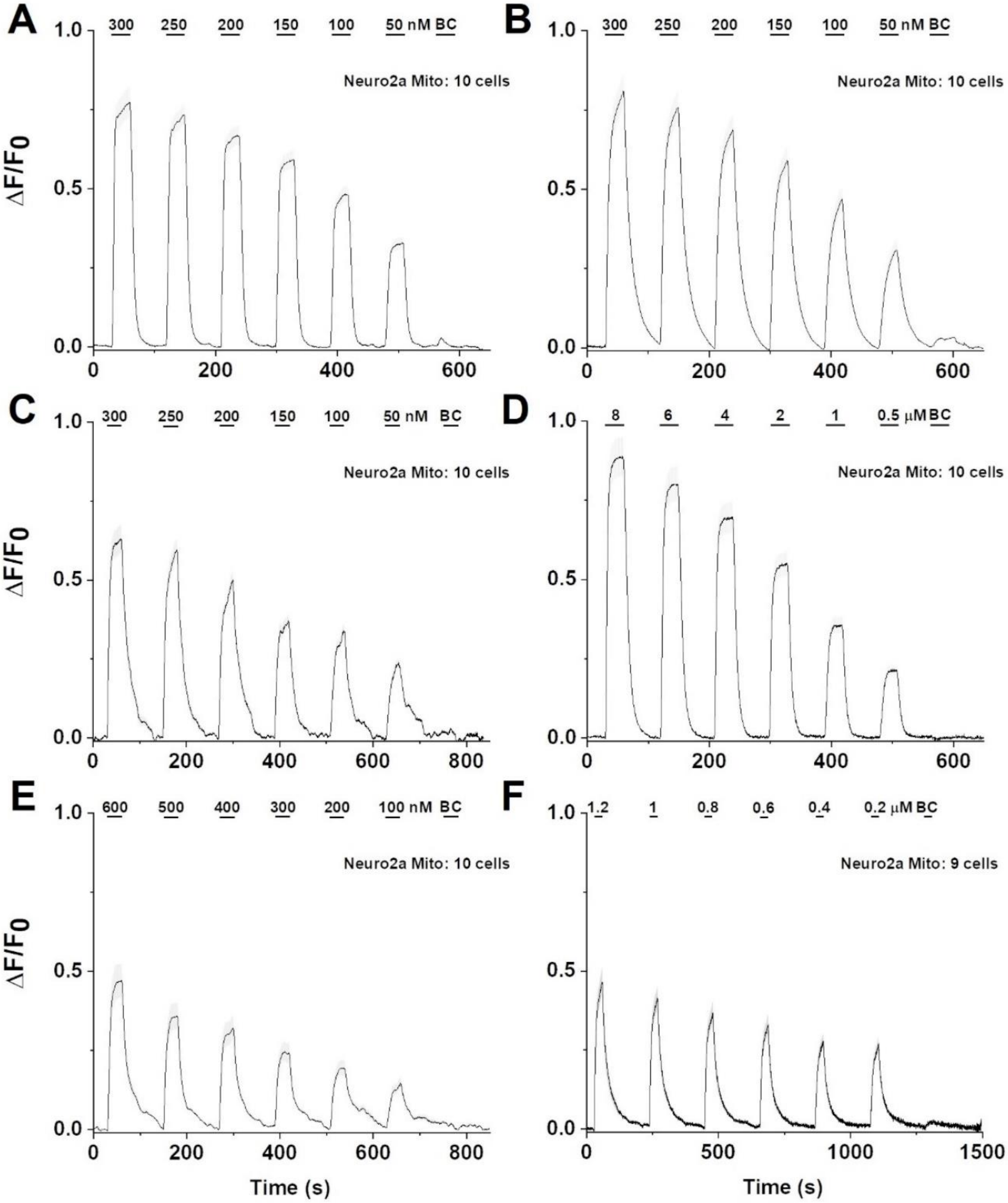

Figure 2.16. iRAADSnFRs targeted to the mitochondria showing concentration-response traces for esketamine (***A***), arketamine (***B***), (2S,6S)-HNK (***C***), (2R,6R)-HNK (***D***), MXE (***E***), and scopolamine (***F***). Administration and washout periods are 40 s and 40 s, respectively (***A***, ***B***, ***D***), 30 s and 90 s (***C***, ***E***), respectively, and 30 s and 180 s (***F***). Baseline periods have been normalized to ~ 0% $\Delta F/F_0$. (SEM is as described previously.) (Images provided by Kallol Bera and Elaine Lin.)

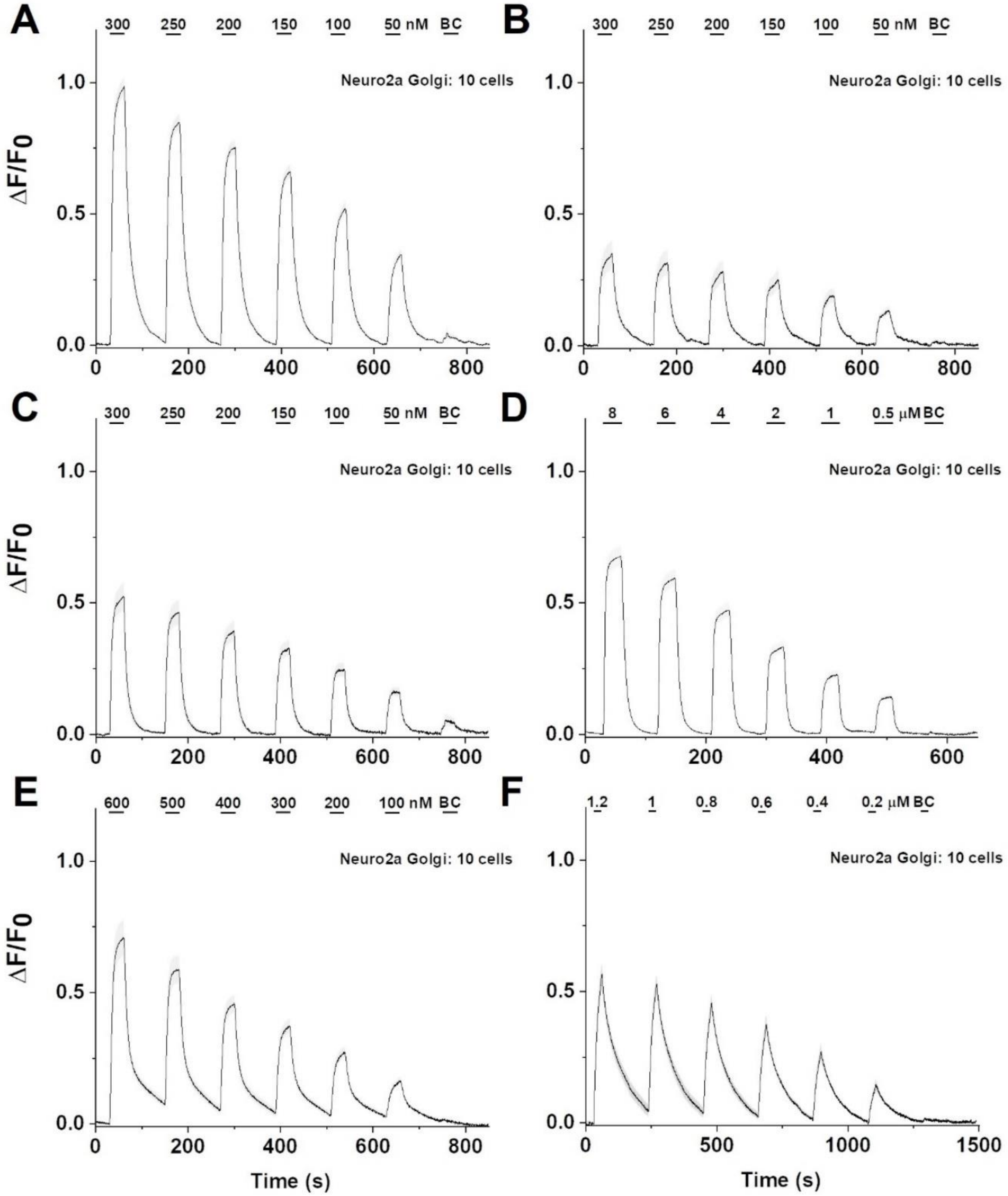

Figure 2.17. iRAADSnFRs targeted to the Golgi showing concentration-response traces for esketamine (***A***), arketamine (***B***), (2S,6S)-HNK (***C***), (2R,6R)-HNK (***D***), MXE (***E***), and scopolamine (***F***). Administration and washout periods are 30 s and 90 s, respectively (***A***, ***B***, ***C***, ***E***), 40 s and 40 s (***D***), respectively, and 30 s and 180 s, respectively (***F***). Baseline periods have been normalized to ~ 0% $\Delta F/F_0$. (SEM is as described previously.) (Images provided by Kallol Bera and Elaine Lin.)

other compartments, as no RAAD other than (2R,6R)-HNK appeared to display fluorescence responses limited by solution changes; furthermore, both MXE and scopolamine exhibit incomplete washout (no return to baseline fluorescence) after the higher concentrations, and scopolamine in particular is not close to reaching a fluorescence plateau during the wash-in periods (**Fig. 2.17F**). Perhaps the unique membrane architecture of this organelle — where folds of membrane are stacked on top of one another — contributes to the observed pharmacokinetic phenomena. RAAD binding to Per.iRAADSnFRs (**Fig. 2.18**) shows similar behavior to the Cyto.iRAADSnFRs, with the ketamine compounds inducing fluorescence responses nearly limited by solution changes, while MXE and particularly scopolamine show slightly slower kinetics, including the triangular waveforms indicating slow entry into the targeted organelle (**Fig. 2.18EF**); however, all washout periods induce a return to baseline between concentrations. Sensors targeted to F-actin (**Fig. 2.19**) demonstrate lower overall maximal fluorescence (with the exception of (2R,6R)-HNK) than virtually all other organelles targeted — possibly a reflection of the minimal amount of actin-based structure in which iRAADSnFRs can be expressed, resulting in a smaller sensor population — but the waveforms likewise appear to demonstrate faster kinetics than virtually any other set of *in vitro* experiments detailed in this section, likely due to actin existing across the cell as well as not being contained within a secondary membrane. iRAADSnFRs targeted to autophagosomes (**Fig. 2.20**) show slow kinetics similar to Golgi.iRAADSnFRs (**Fig. 2.17**) which could result from their double-membrane structure. Of interest, the maximal fluorescence reached for (2S,6S)-HNK is the lowest among all of the targeted compartments (**Fig. 2.20C**), and compared to (2R,6R)-HNK it induced a maximal fluorescence response about three times lower (**Fig. 2.20D**). All six RAADs washout from autophagosomes completely across the tested concentrations.

2.3.4. Serendipitous Discovery of iR-HNKSnFR Sensitivity for TCAs

When we were seeking to develop iDrugSnFRs for TCAs, we discovered that iR-HNKSnFR had substantial sensitivity to all five tested drugs (amitriptyline, dosulepin, doxepin, imipramine, protriptyline) (**Fig. 2.21A**). All had EC_{50} values within one order of magnitude (0.485 μM for doxepin to 4.068 μM for protriptyline) with a $\Delta F_{max}/F_0$ greater than 3 and an S-slope greater than 1.8 (**Fig. 2.21B**), making the iR-HNKSnFR a sensitive (if nonspecific) reporter for TCAs.

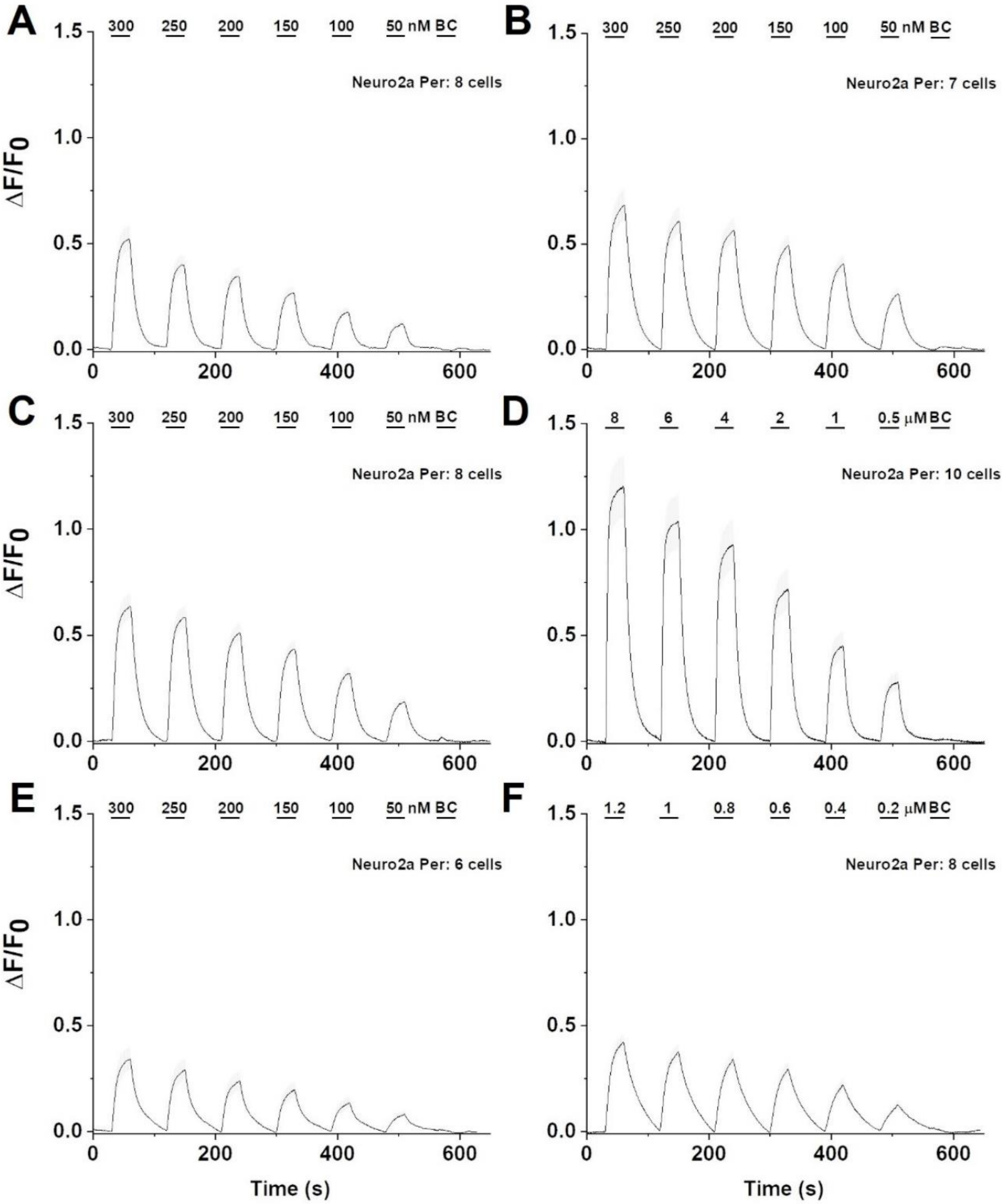

Figure 2.18. iRAADSnFRs targeted to peroxisomes showing concentration-response traces for esketamine (***A***), arketamine (***B***), (2S,6S)-HNK (***C***), (2R,6R)-HNK (***D***), MXE (***E***), and scopolamine (***F***). Administration and washout periods are 40 s and 40 s, respectively. Baseline periods have been normalized to ~ 0% $\Delta F/F_0$. (SEM is as described previously.) (Images provided by Kallol Bera and Elaine Lin.)

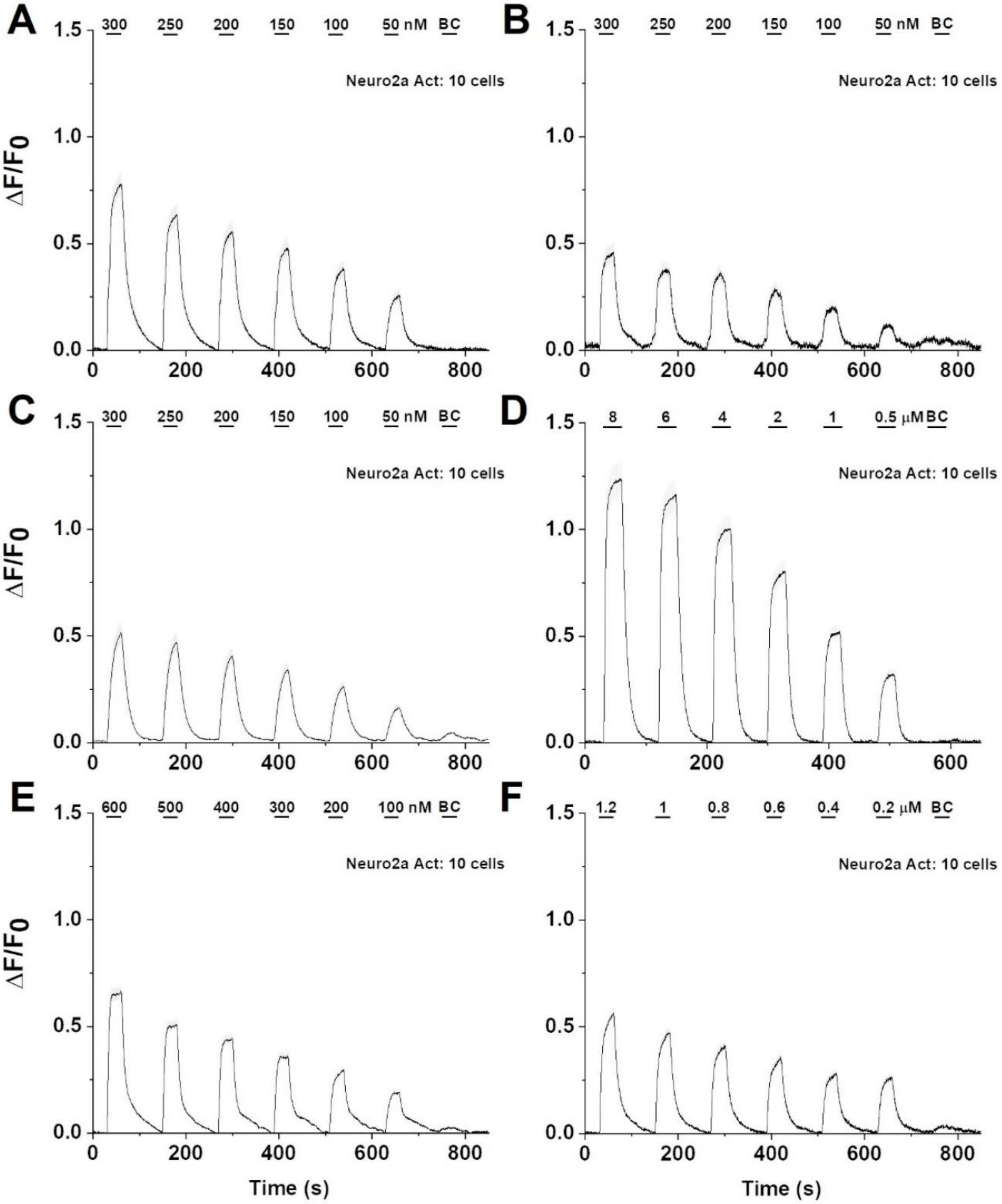

Figure 2.19. iRAADSnFRs targeted to F-actin showing concentration-response traces for esketamine (***A***), arketamine (***B***), (2S,6S)-HNK (***C***), (2R,6R)-HNK (***D***), MXE (***E***), and scopolamine (***F***). Administration and washout periods are 30 s and 90 s, respectively (***A***, ***B***, ***C***, ***E***, ***F***) and 40 s and 40 s (***D***), respectively. Baseline periods have been normalized to ~ 0% $\Delta F/F_0$. (SEM is as described previously.) (Images provided by Kallol Bera and Elaine Lin.)

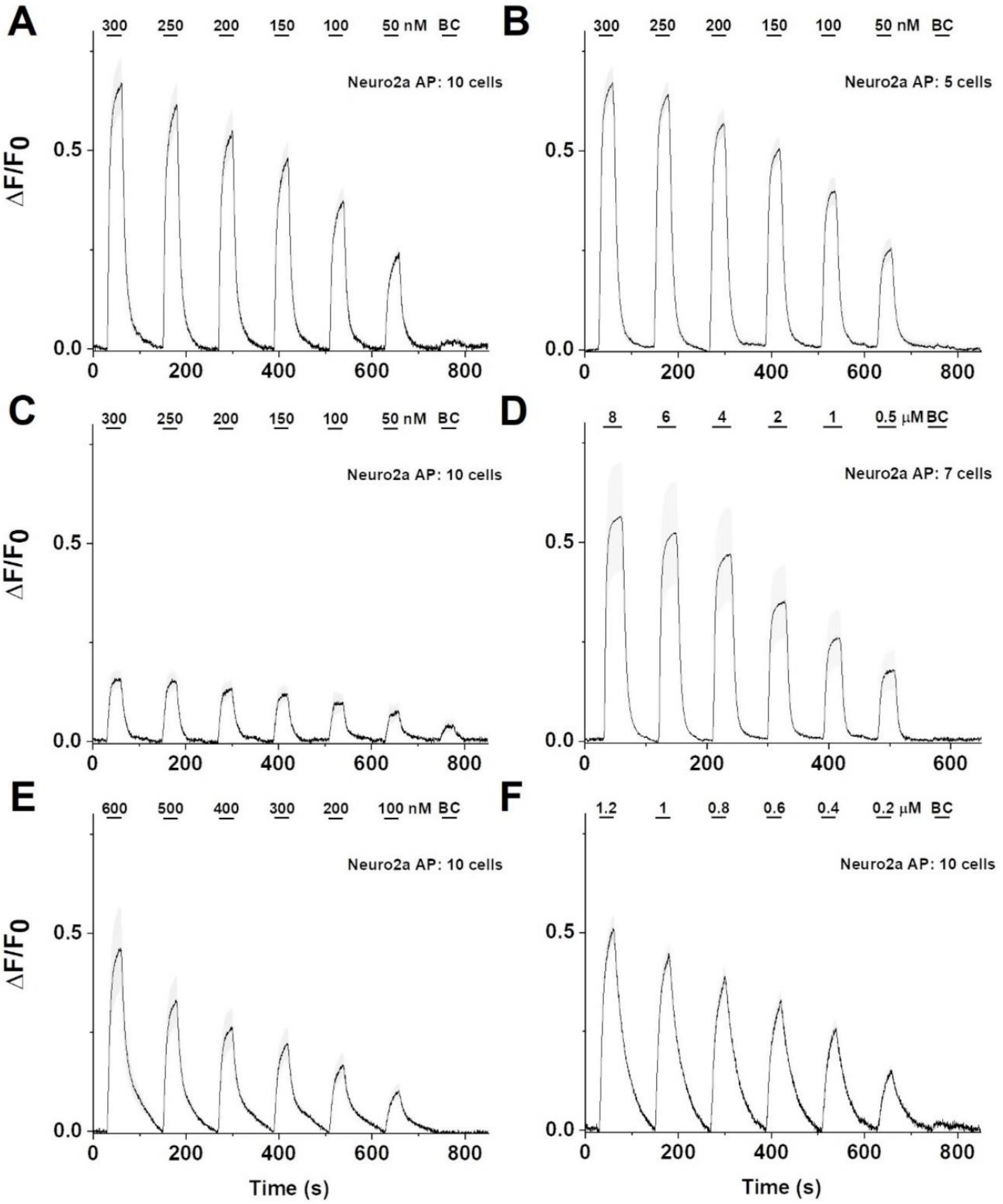

Figure 2.20. iRAADSnFRs targeted to autophagosomes showing concentration-response traces for esketamine (***A***), arketamine (***B***), (2S,6S)-HNK (***C***), (2R,6R)-HNK (***D***), MXE (***E***), and scopolamine (***F*** Administration and washout periods are 30 s and 90 s, respectively (***A***, ***B***, ***C***, ***E***, ***F***) and 40 s and 40 s (***D***), respectively. Baseline periods have been normalized to ~ 0% $\Delta F/F_0$. (SEM is as described previously.) (Images provided by Kallol Bera and Elaine Lin.)

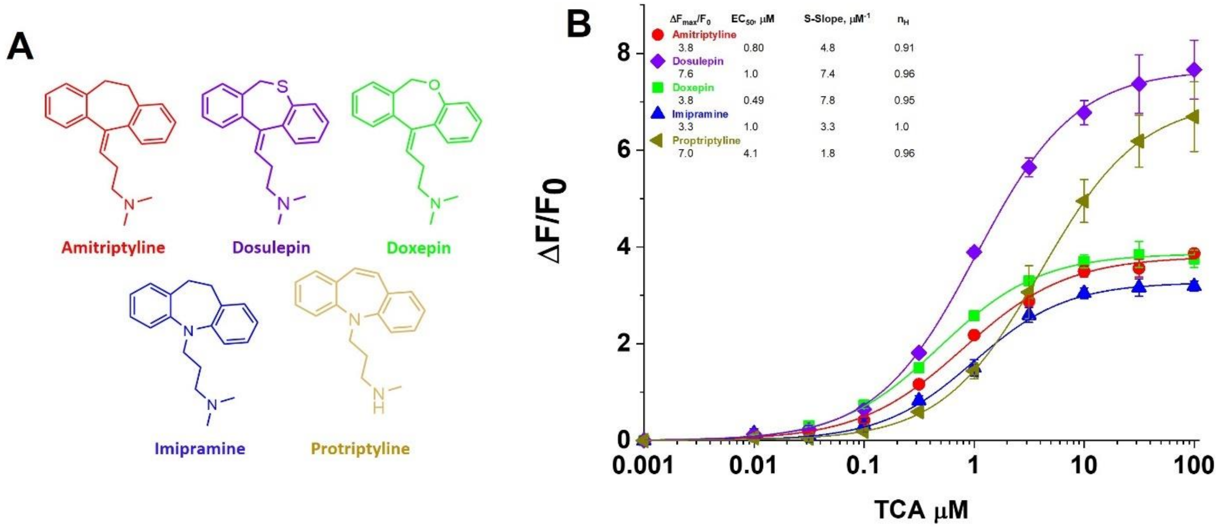

Figure 2.21. (***A***) Structures of the TCAs demonstrating their similarity; the secondary amine of protriptyline appears to decrease the affinity of iR-HNKSnFR for this TCA compared to the other four which contain tertiary amines, while the ether in doxepin confers greater affinity than the sulfide in dosulepin. (***B***) Concentration-response curves for the TCAs demonstrate sensitive (nanomolar to micromolar EC_{50}) detection by iR-HNKSnFR. (Images provided by Kallol Bera and Elaine Lin.)

Neuro2a cells transfected with Cyto.iR-HNKSnFR versus the TCAs in both Neuro2a as well as SH-SY5Y cells (**Fig. 2.22**) demonstrates slightly slower kinetics than for the target compound (see **Fig. 2.14D**), with all five TCAs exhibiting incomplete wash-in dynamics coupled with slower returns to baseline during extended washout periods. The performance of the iRAADSnFRs in detecting the TCAs was nearly identical in both cell types except for iR-HNKSnFR in Neuro2a cells detecting doxepin, which showed both slower kinetics as well as around six times lower maximal fluorescence than in SH-SY5Y cells (**Fig. 2.22C**).

2.3.5. *Summary of* In Vitro *Results and Next Steps*

Our *in vitro* experiments demonstrate that iRAADSnFRs can be successfully leveraged for detecting RAADs in various cellular compartments with apparently minimal effects on fluorescence due to the pH of the various locations (ranging from 6.5 in the Golgi to 7.4 in extracellular solution [531]); however, a further characterization of compartment-specific F_0 values is warranted which will provide a useful comparison to the data already gathered in purified protein (**Fig. 2.9**), especially because more acidic organelles such as the Golgi may also

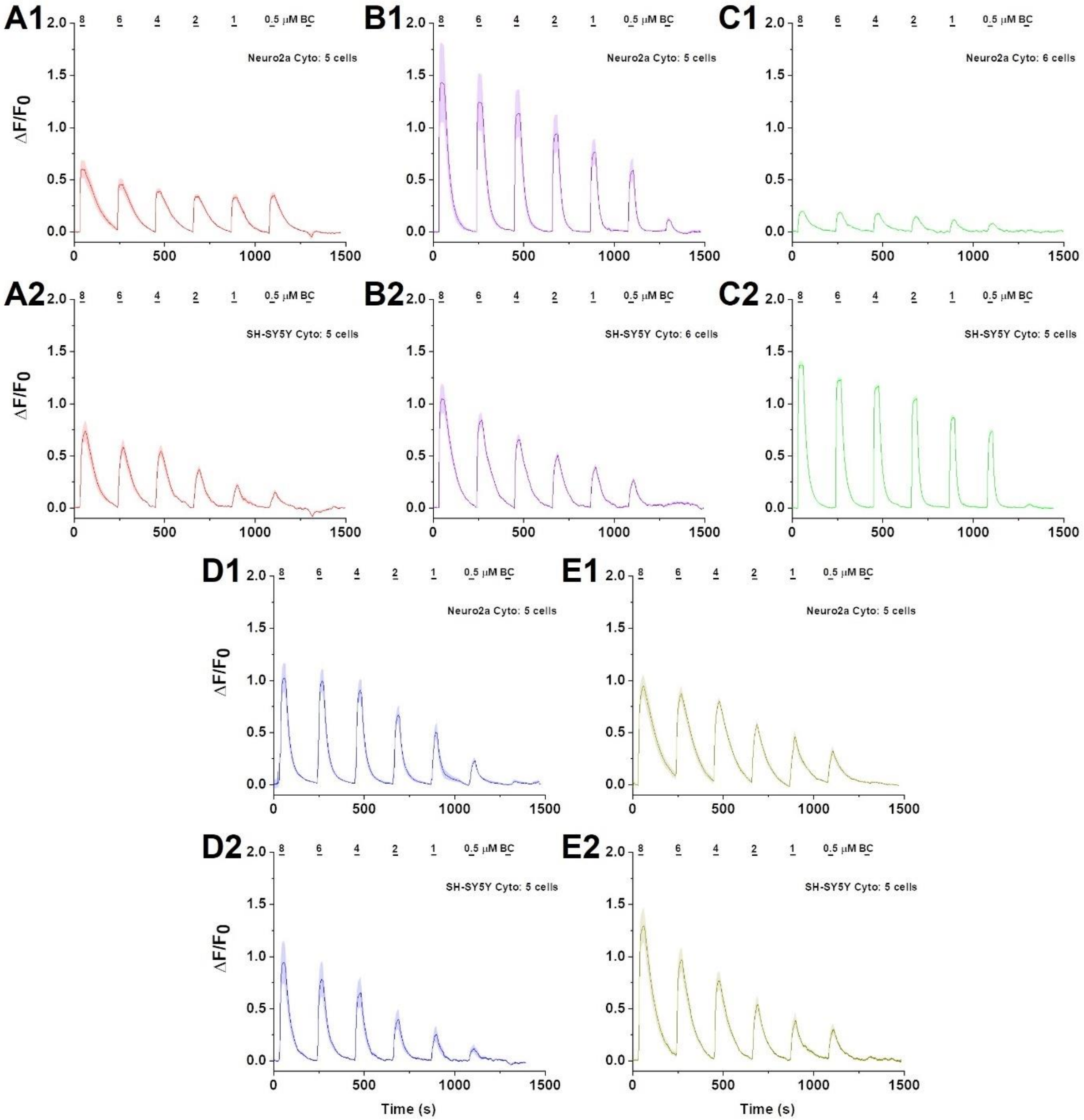

Figure 2.22. ***(A-E)*** Concentration-response experiments (30 s drug followed by 180 s washout with HBSS) in both Neuro2a (***1***) and SH-SY5Y (***2***) cells across the same concentration range for all five TCAs — (***A)*** amitriptyline, *red*; (***B)*** dosulepin, *blue*; (***C)*** doxepin, *green*; (***D)*** imipramine, *blue*; (***E)*** protriptyline, *gold*) — detected at pharmacologically relevant levels by iR-HNKSnFR. Both the maximal fluorescence — with amitriptyline (***A1***) demonstrating the lowest $\Delta F/F_0$ values and dosulepin (***B1***) the highest — and pharmacokinetics — with protriptyline (***E1***) the slowest and doxepin (***C2***) the fastest — were similar across all five TCAs as well as between cell types, with the exception of the notable discrepancy in detecting doxepin in Neuro2a (***C1***) versus SH-SY5Y (***C2***) cells. (Images provided by Kallol Bera and Elaine Lin.)

cause more acid trapping [685] and thereby increase the fluorescence response. The various RAADs transit into and out of these compartments with similar pharmacokinetics (with some exceptions which do not indicate drastically different behavior such as has been seen with nicotinic agonists [684] or with SSRIs in PHC [543]) and induce appreciable fluorescence responses such that pharmacologically relevant concentrations can be detected discretely. Additionally, we have demonstrated once again the ability of a relatively small number of RAADs to detect an abundance of DOIs [684], as we discovered that iR-HNKSnFR can detect a panoply of TCAs for which it was not specifically engineered. Because the location(s) in which RAADs may in part exert their antidepressant effects within the cell are unknown (see Chapter 1.6.5), the implementation of compartment-targeted iRAADSnFRs can provide a first step in the investigation of RAAD activity.

In order to study these sensors in a more ethologically relevant manner, we decided to explore their implementation in an *in vivo* model. To this end, we chose to work with zebrafish (*Danio rerio*), which we had access to through our collaboration with the Prober lab. The following sections will cover the most recent experimentation that we have performed using transgenic zebrafish expressing the six iRAADSnFRs pan-neuronally heretofore validated and characterized *in vitro*.

2.4. Larval Zebrafish as a Model for Depression

2.4.1. Zebrafish Basics

Zebrafish have been a part of the animal research repertoire since the 1970s. They were among the first vertebrate species to be cloned [779] and have become a popular model organism used to investigate a broad array of topics related to human medicine, from cancer to developmental biology. However, it is their role in neuroscience, particularly the study of neuropsychiatric disease, which makes them a compelling option for investigating the iRAADSnFRs *in vivo*: we have developed transgenic zebrafish lines — one for each of the six aforementioned iRAADSnFRs — that show expression of sensor throughout the brain which can be imaged using microscopy before and during the administration of DOI.

The features of zebrafish conducive to neuroscience research are: easy maintenance and breeding, small size, low cost, ease with which genes can be manipulated, and the ability to image the whole brain of larvae through translucent skin [780,781]. Zebrafish embryos are fertilized externally, with females releasing unfertilized eggs which are fertilized by sperm from the male. Embryos develop quickly, and hatching occurs between 48-72 h post-fertilization at 28ºC; full morphogenesis does not occur until 3 days post-fertilization (dpf) [782]. Because zebrafish larvae are viable without food up to around 7 dpf [783], and because we have noticed that feeding can affect skin transparency, the optimal age range within which to image is 4-7 dpf. To improve optical transparency, various mutants with less pigmentation have been developed, such as *nacre* [784] and *casper* [785]; additionally, WT larvae can be treated with 1-phenyl-2-thiourea (PTU), a depigmenting agent [786]. Larvae at this stage have brains composed of approximately 100,000 neurons, with approximate dimensions of 400 x 800 x 250 μm^3 [787]; their neural complexity thus lies between insects and rodents, yet their small brain volume allows for a unique insight into the neural dynamics of an intact behaving organism.

2.4.2. Depression in Zebrafish?

Modeling something as complex and overdetermined as a human neuropsychiatric disorder in an animal species is a daunting task, and models derived from species further down the phylogenetic ladder present even greater challenges owing to their evolutionary remove (for instance, rodents share a common ancestor with humans from ~125 million years ago [788], whereas zebrafish share a common ancestor with humans from ~450 million years ago [789]). However, while manifestations in patients are undoubtedly species-specific, certain of the common symptoms of neuropsychiatric disorders — as well as potential causes, varied and additive as they may be — can be approximated in animal behavior. In the context of depression, the rodent literature is replete with both etiological models and behavioral assays seeking to model and assess its causes, each with varying levels of validity based on our knowledge of the pathophysiology and symptoms of MDD [790]. In zebrafish, modeling depression is relatively new and exploratory: the sophistication of the rodent brain in comparison to that of the zebrafish necessarily further constrains the latter's usefulness [69]; however, there is reason to believe that zebrafish brains share many commonalities with that of the mammalian (and, specifically, primate), supported by studies demonstrating neuroanatomical and neurophysiological homology (e.g. [791-795]). Over 70% of zebrafish genes are highly similar to mammalian orthologs [796]; additionally, 70% have a human ortholog and 47% of human genes are directly comparable with those specific to zebrafish [797]. In practice, zebrafish models of MDD symptoms such as anhedonia, changes in appetite, changes in locomotion, changes in sleep, and social deficits have been designed and tested [69,798], suggesting that findings in such studies can broaden our understanding of depression at the level of physiology. Construct validity — the comparison between known human etiologies and their recapitulation in other species — is a useful criterion by which to judge animal models with respect to their relevance to human disease [790], and so experimenters have used CUS [799-801], mutations of neural GRs [802,803], and exposure to reserpine [37,38,804] to mimic known etiologies of MDD (stress beyond physiological response capacity is a major contributor to the development of affective disorders [805], dysregulated cortisol signaling via GRs contributes to the development of depression [806], and observations regarding the depressive effects of reserpine among patients were crucial to the development of the monoamine theory of depression [34]) (see Chapter 1.1). Further evidence is needed with respect to the behavioral and physiological effects induced by any model regardless of its construct validity, but the fact that, for example, elevated cortisol levels are seen in pharmacologically-induced [37,38], mutagenesis-induced [802], and stress-induced [799,807,808] zebrafish models of depression suggests that such interventions which produce depression-like behavior through different etiologies could provide a strong basis for concluding that the resulting findings will help in understanding common pathophysiology.

Although investigations so far are promising, as with any animal experimentation, unforeseen challenges have arisen in the interpretation of the behavior displayed by depression-model zebrafish. There is ongoing discussion as to the reasons why symptoms of depression and anxiety seem linked in these models [798] to a degree not seen in humans, though anxiety is indeed a known comorbidity found among MDD patients [809,810]; it is yet to be determined if this reflects the particular neurobiology of zebrafish or if this is an artifact of unrefined behavioral assays [69,798]. One possible means by which specific behaviors associated with depression could be parsed out is to assess the effects of typical anxiolytic drugs (e.g. benzodiazepines) versus typical antidepressants (e.g. SSRIs) in terms of the behavioral deficits ameliorated after administration of each [798]. Predictive validity — demonstrating that compounds which relieve the symptoms of a human disease/disorder can successfully treat the same types of symptoms when modeled in an animal — has been assessed in several zebrafish models of depression using both classes of compounds [69,780]. After treatment with a benzodiazepine, WT larvae exhibit reduced thigmotaxis (the tendency to swim around the edges of an environment) [811] while adults exposed to both acute stress [812] and CUS [813] can recover exploratory behavior. As for SSRIs, WT adults given fluoxetine chronically (over two weeks) exhibited less anxiety-like behavior upon exposure to a novel environment [814]; fish subjected to acute stress responded to a single dose of fluoxetine with normalization of locomotion [812], while fish exposed to CUS treated with fluoxetine for 7-21 days demonstrated reduced levels of anxiety-like and depression-like behavior [815] with a trend towards reducing stress-elevated cortisol [68,813]. Additionally, adult zebrafish with a point mutation in the *nr3c1* gene (which encodes the GR) show increased freezing behavior rescued by both acute administration of diazepam as well as chronic administration of fluoxetine, the latter of which also significantly reduced the elevated whole-body cortisol found among homozygous mutants [803]. Thus far, the main limitation in teasing out anxiety-related versus depression-related behaviors concerns the sensitivity of the tests as well as the lack of a deeper understanding of zebrafish affect, both of which continue to be areas of active research.

As for ketamine, its most common use in zebrafish has been to investigate neural development (zebrafish nervous systems gain functionality at 4-5 dpf) [816], as ketamine acts as a teratogen and neurotoxin in human infants [817-819]. Studies using embryonic zebrafish have recapitulated these findings [820-824], though there is no evidence that exposure to ketamine during the larval stage is associated with any developmental deficits or neurotoxicity [820,825]. More recently, ketamine has been studied for its effects on zebrafish affect, specifically related to aggression, anxiety, and depression. Ketamine can cause psychomimetic side effects at subanesthetic antidepressant doses [291,342,826] and sedation at higher doses [106-108] among patients; in rodents and zebrafish, ketamine exerts biphasic effects on aggressive behavior, whereby lower doses increase and higher doses decrease aggression [827-829], providing an analog to the aforementioned dose-dependent effects on affect in humans. Subanesthetic doses administered to WT adults can also have anxiolytic effects: exposing fish to higher (84 μM, 168 μM, and 252 μM) but not lower (8.4 μM) concentrations of ketamine for 20 min caused anxiolytic behavior in a dose-dependent manner [830,831] concomitant with decreased whole-body cortisol [832]. However, whole-body cortisol was found later to be increased at 168 μM but decreased at 84 μM [831] while 84 μM ketamine combined with fluoxetine likewise increased cortisol [833] and no significant anxiolytic effects of acute ketamine exposure were found 24 h later or after repeated exposure (20 min per day over seven days) [831], suggesting that the connection between behavior and hormone responses is perhaps difficult to assess. Studies have also reported increased stereotyped behavior [831,832,834] which corroborates previous results in rodents [835]. More recently, larval zebrafish exposed to 212 μM ketamine for 20 min were found to have prolonged coping behavior in response to an aversive stimulus [836] while futility behavior among larval zebrafish in a virtual environment was found to decrease in response to ketamine in a dose-dependent manner (from 42 μM to 800 μM) [490]. In all, these results demonstrate that, while the study of anxiety- and depression-like behavior in zebrafish is in its nascent stages, initial findings are encouraging enough to motivate the discovery of more robust behavioral paradigms which can serve as reliable methods with which to test the effects of RAADs.

2.4.3. Imaging Larval Zebrafish

Single-plane illumination microscopy (SPIM) (also known as light sheet microscopy) is a technique whereby a single plane of laser light is deflected across a sample to produce a z-stack which can be resolved as a volumetric image within a short (seconds-long) time frame [837]. When employed for imaging live larval zebrafish, SPIM allows for whole-brain near-simultaneous time-series recordings, providing an unprecedented level of access to the CNS of a complex organism [838]. Creating a light sheet involves passing a collimated laser beam through a cylindrical lens into an objective which can generate a fluorescent response from a thin (several microns thick) optical section, thereby mitigating photobleaching and out of plane illumination (see Chapter 2.5). Use of two light sheets is common, with some orientations comprising bilateral light sheets on either side of the sample while others involve a front light sheet coupled with a lateral light sheet; each is deflected in tandem to produce higher-quality emission. The detection objective is positioned perpendicularly to the illumination objective(s) such that the full view of each optical section is captured. Compared with confocal microscopy, which samples one point in a FOV at a time, SPIM's planar illumination scheme allows for much faster and more comprehensive whole-brain imaging.

Imaging live larvae has typically been in furtherance of examining physiological responses to DOIs or environmental stimuli (e.g. [491,795,839]), with fish lines expressing GCaMP in neuronal subpopulations or across the entire brain. As mentioned previously (see Chapter 2.1), GCaMP is a genetically-encoded Ca^{2+} indicator which consists of calmodulin, a second-messenger effector with native binding to Ca^{2+} [840], bound to a halved GFP molecule via a peptide sequence from myosin light chain kinase (M13). When Ca^{2+} binds to the Ca^{2+}-calmodulin binding domain, the GFP halves dimerize, causing a conformational change such that the chromophore of the GFP can fluoresce in response to incident light in the GFP excitation spectrum [841]. Ca^{2+} concentration is tightly controlled inside the cell (existing at concentrations around 100 nM at rest [842]), and cells use minor changes to signal myriad events. Because one of the most important functions of Ca^{2+} inside cells is to trigger neurotransmitter release via synaptic vesicles, intracellular Ca^{2+} changes can be used as a proxy for neuronal activity. The tools now available for leveraging brain-wide Ca^{2+} imaging allow for access to neuronal network dynamics correlated with behavior [839]; whole-brain GCaMP imaging at single-neuron resolution [843] can be performed on larval zebrafish engaging in a virtual environment while paralyzed [491] as well as during free swimming [844]. GCaMP-based physiology can also be analyzed in response to neuropsychiatric medications; a study investigating brain-wide physiology in *nr3c1* GR mutants found that fluoxetine and ketamine each normalized different functional imaging parameters (as measured by graph analysis) that are aberrant in mutant larvae compared to WT [845]. Additionally, GCaMP targeted to glia has been used to demonstrate that futility behavior is encoded by increased Ca^{2+} accumulation in radial astrocytes [491] which is reversed by ketamine-mediated inhibition [490], expanding the scope of what is possible to measure with Ca^{2+}-based imaging. In terms of iDrugSnFR-based imaging in zebrafish, iGluSnFR in the optic tectum (OT) [682], iGABASnFR in the cerebellum [681], and iAChSnFR in spinal motor neurons [678] can report physiological activity *in vivo*, suggesting that the expansion of additional iDrugSnFRs — including the iRAADSnFRS — into zebrafish is feasible and promises to yield interesting findings.

2.5. Methods for Creating Transgenic Zebrafish Expressing iRAADSnFRs

We decided that using cytoplasm-targeted iRAADSnFRs (iRAADSnFR_cyto) *in vivo* would allow for the most robust labeling of neurons, as we thought PM targeting might provide too faint of a signal while targeting intracellular compartments might provide too localized of a signal and might be of more interest once the paradigm has been established. As for where to express the iRAADSnFR_cyto constructs, we decided to target neurons (though targeting glia is a compelling option for future experiments [490,491]); because we are agnostic about which areas might be of most importance with respect to the mechanism of action of RAADs, we thus created transgenic lines with whole-brain neuronal iRAADSnFR_cyto expression. The promoter best suited for whole-brain neuronal expression is *elavl3*/*HuC*, an RNA-binding protein orthologous to a human gene of the same name which is expressed in all neurons and has a role in neurogenesis [846]. The *elavl3* promoter has been shown to successfully mediate pan-neuronal expression of other transgenes in multiple zebrafish lines (e.g. [839,845,847,848]).

The first step in developing a plasmid for expression in zebrafish is codon optimization. Because the genetic code is degenerate (64 codons encode 20 AAs), multiple codons correspond to each AA (except for methionine and tryptophan, which are encoded by one codon each). Codon usage bias refers to the specific types of tRNAs available in a species and reflects higher or lower usage of particular codons for their corresponding AAs [849]. Thus, in designing a plasmid synthesized for expression in mammalian cell lines which now will be used in zebrafish, the usage bias must be accounted for in a process called codon optimization. We used CodonZ (National Institute of Child Health and Human Development) which increases functional protein expression by changing the codon usage rates of the input sequence to match those of the desired species [850]. CodonZ has codon usage libraries for both mice and zebrafish, the latter of which was used to optimize the iRAADSnFR_cyto sequences.

After optimization, we purchased each iRAADSnFR_cyto sequence (with a NES immediately upstream [741]) as a gene fragment (Twist Bioscience) of roughly 1.8 kbp. Next, we found a suitable backbone for the fragment by using a previous plasmid engineered for whole-brain neuronal expression — *Tol2-elavl3-MTS-IRES-mKate2* (**Fig. 2.23**) — which was synthesized from *Tol2-elavl3-H2B-GCaMP6s* (AddGene #59530) [851] using the same protocol as described below. *Tol2* sequences are added to the left (200 bp) and right (150 bp) ends of a cassette of interest (in this case, *elavl3-MTS-IRES-mKate2*) such that the Tol2 transposase enzyme can excise the desired sequence and mediate its integration into host DNA [852,853]. To prepare the backbone, we performed a digestion using AgeI, as there are compatible sites immediately preceding and following the *MT-IRES-mKate2* sequence (**Fig. 2.23**). We then gel purified the larger (~12 kbp) band before treating it with calf intestinal phosphatase (CIP) (Quick CIP, NEB) which nonspecifically catalyzes the dephosphorylation of 5’ and 3’ ends of DNA and RNA phosphomonoesters to prevent self-ligation [855]. Next, we used PCR to both amplify the iRAADSnFR fragment as well as engineer 15 bp overhangs on either end to match sequences at

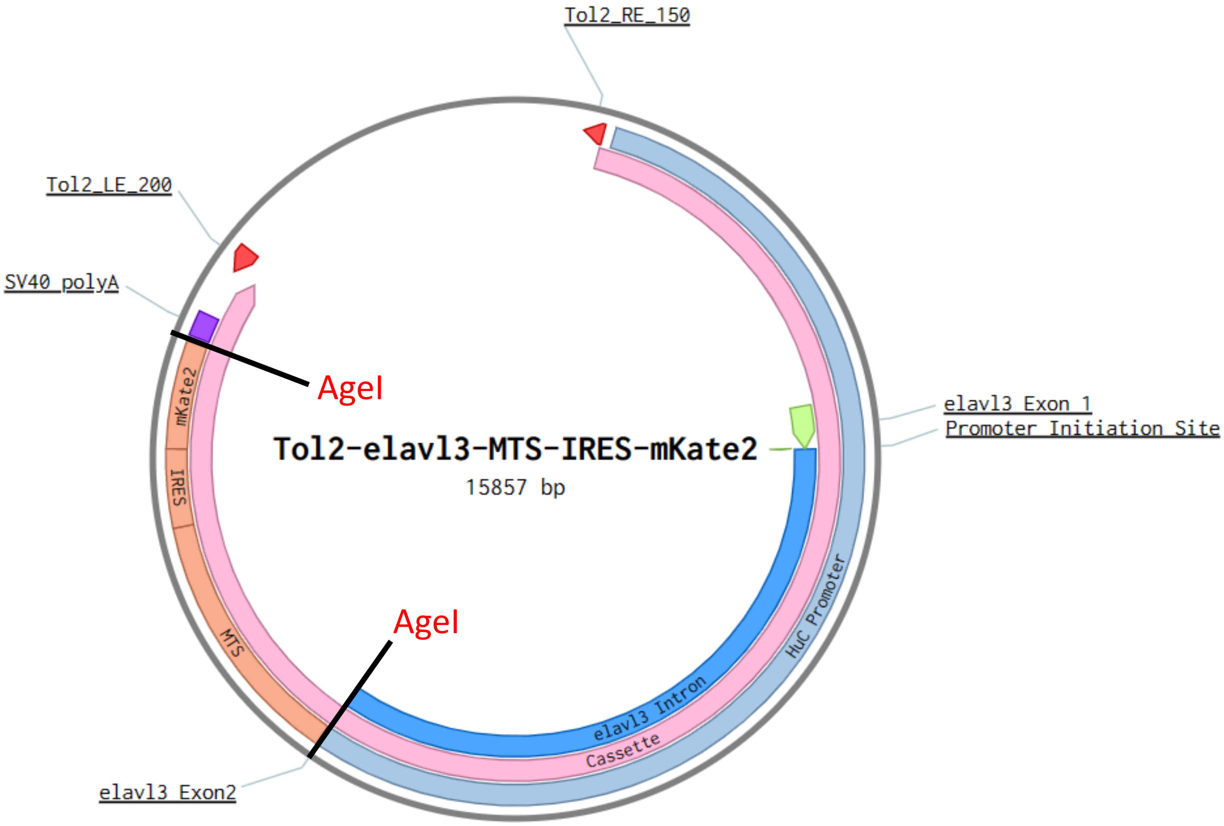

Figure 2.23. Plasmid map for *Tol2-elavl3-MTS-IRES-mKate2*. The cassette in this case codes for a GFP-based melatonin sensor (MTS; MT-Sensor, *orange*) co-expressed with the constitutively active red fluorescent protein mKate2 (*orange*) separated by an internal ribosome entry site (IRES; *orange*) sequence (which mediates internal ribosome binding [854]). The two Tol2 enzyme binding sites (Tol2_LE_200 and Tol2_RE_150; *red*) flank the cassette (*pink*) to be transposed. Within the HuC Promoter (*light blue*), the *elavl3* intron (*blue*) is shown separately from its promoter and exons (*green*). A polyadenylation signal from SV40 (SV40 polyA; *purple*) [764] follows the mKate2 sequence. AgeI enzyme cut sites (*black*) were used to linearize the plasmid. (Map courtesy of Chanpreet Singh.)

the 5’ and 3’ ends of the backbone. Finally, we used Gibson assembly [745] (see Chapter 2.2.5) to construct the final plasmid; we then performed ethanol precipitation (see Chapter 2.2.5) to generate a concentrated pellet which was resuspended in nuclease-free water. To verify the success of the synthesis, we inspected the entire sequence (~15 kbp) using a whole-plasmid sequencing service (Primordium Labs) (see **Fig. 2.24** for an example).

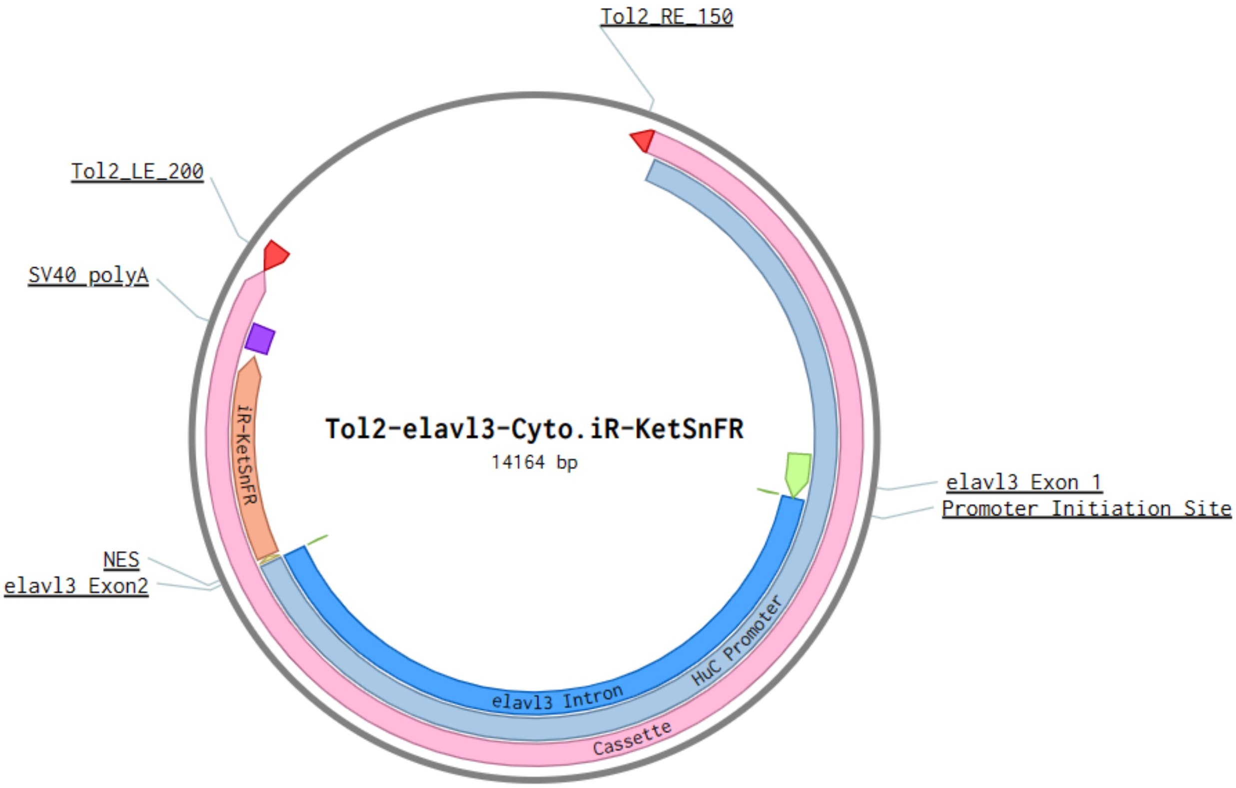

Figure 2.24. Plasmid map for *Tol2-elavl3-Cyto.iR-KetSnFR*. The cassette in this case codes for the NES (*yellow*) and the codon-optimized Cyto-iR-KetSnFR (*orange*). As in **Fig. 2.23**, the two Tol2 enzyme binding sites (Tol2_LE_200 and Tol2_RE_150; *red*) flank the cassette (*pink*) to be transposed. Within the HuC Promoter (*light blue*), the *elavl3* intron (*blue*) is shown separately from its promoter and exons (*green*). A polyadenylation signal from SV40 (SV40 polyA; *purple*) follows the iR-KetSnFR sequence. (Map courtesy of Kallol Bera.)

The California Institute of Technology's Office of Laboratory Animal Resources supervised animal care, and all zebrafish experiments were carried out in accordance with the Institutional Animal Care and Use Committee regulations (Protocol #1836). To generate transgenic lines, embryos from in-crossed WT zebrafish were injected at the one-cell stage with a mixture of intact plasmid and *Tol2* transposase mRNA [856]; as the transposase is translated quickly, it can act on the co-injected transgenic plasmid to excise the *elavl3-NES-iRAADSnFR* sequence, after which it integrates into host DNA at random sites (sometimes several times). To prepare the injection mix, 1 μL of plasmid at 125 ng/μL was mixed with 1 μL *Tol2* mRNA, 0.5 μL of phenol red (for visualization), and 7.5 μL of nuclease-free water. The mixture was allowed to sit on ice during further preparations. Next, a microinjection pump (PV 820 Pneumatic PicoPump, WPI) operated by a foot pedal and connected to a micromanipulator (M-152, Narishige) attached at an angle to a magnetized post was positioned under a stereoscope (10X magnification; Stemi 2000, Zeiss) illuminated with a lamp (EKE Illuminator, Kramer Scientific). A pre-pulled glass pipette (long-taper, WPI) was loaded with 2 μL of injection mix and inserted into a gasket and cap attachment on the micromanipulator. The pipette tip was guided into a 50 mL dish filled with deionized water and the tip was broken to a diameter of ~1 mm. Next, the hold pressure was set to 1-3 psi and the ejection pressure set to ~20 psi; the injection mix was ejected into oil under the stereoscope such that a ~1 nL bubble formed (as measured by grating marks underneath). The needle was kept in oil between successive rounds of injections to prevent leaking. WT zebrafish (age 3-12 months) kept on a 14:10 constant light-dark cycle and housed in 1.4 L tanks (ZT140, Aquaneering) containing no more than six same-sex fish were paired in breeding tanks overnight separated by a plastic divider; at the beginning of the light period (after the injection setup described above), the dividers were removed and the fish were allowed to mate (see Chapter 2.4.1). Embryos were collected within 15 min of fertilization, caught with a strainer, and washed into E3 medium (containing salts for maintaining proper pH) [857] mixed with 1% methylene blue (blue E3) as an antifungal/antiparasitic measure [858]. Embryos were then pulled up with a glass pipette and gently transferred to a 2% agarose dish with preset grooves (~0.5 μm) to restrict movement and rolling. The micromanipulator was positioned so that the needle could access the embryos; the preferred target for injection is the cell (though the yolk sac was chosen if access was impeded). Successful injection into the embryo was confirmed by visualization of the dyed mixture in the cell. After a round of injections was completed, embryos were washed into 50 mL dishes filled with blue E3 at a density of 50 embryos per dish and stored in a 28ºC incubator (on a 14:10 light-dark cycle) overnight. Additional rounds of matings and injections were repeated as necessary. The following day, 1 dpf larvae were cleaned by removing cellular debris and dead eggs. The larvae were then swapped into clean E3 and placed back in the 28ºC incubator. After the larvae hatch between 2-3 dpf, we screened the fish on 3 dpf for expression of iRAADSnFR in the whole brain with the larvae temporarily paralyzed by a 4% solution of the Na^+-channel-blocker tricaine (Sigma-Aldrich) using an epifluorescence microscope (M205 C, Leica) equipped with a filter wheel (Em01-R488/568-25, Semrock) which passes blue light at 470 nm; larvae with the brightest baseline expression (founders of the transgenic line, F0) were stored in E3 in groups of no more than 50 per dish in the 28ºC incubator. On one of the following several days (4-7 dpf), F0s were swapped into egg water (deionized water with sea salts) in 0.8 L tanks (ZT080, Aquaneering) with 10-25 larvae per tank (depending on the results of the fluorescent screening) and rotifer feed was commenced [859]. At 15 dpf, the tanks began receiving circulating system water, and at approximately six weeks, juvenile fish were swapped into 1.4 L tanks also in system water with no more than six fish per tank receiving juvenile feed. At around two months of age, the fish were sorted by sex into separate tanks (zebrafish do not begin to differentiate by sex until 20-25 dpf [860]). Once sorted, the F0s were able to mate at 2.5-3 months old [860] and were outcrossed to WT fish. First, we collected and cleaned the embryos before adding them to blue E3 up to 50 embryos per dish. The larvae were then handled as before: they were exchanged into E3 at 1 dpf and screened for baseline fluorescence at 3 dpf, with the brightest F1 larvae stored in larval water between 4-7 dpf under the same conditions as the F0s. The growth and maintenance of the F1 fish was as previously described for the F0 fish. Once of mating age, the F1 fish were outcrossed to WT fish, with the embryos collected and cleaned as previously described. On 3 dpf, the brightest larvae were selected to be the F2 final transgenic line; F2 fish are considered to have stable germline expression of the transgene [861]. Once these fish were raised (as previously described for the F0 and F1 lines), all future crosses were considered to be generative of additional F2 embryos with stable iRAADSnFR expression. For SPIM imaging experiments, F2 iRAADSnFR lines were crossed with WT fish and embryos were collected and cleaned as previously described. At 1 dpf, larvae were swapped into E3 containing 10% PTU to increase optical transparency for imaging (PTU treatment may affect eye development in larvae [862] so behavioral results should be treated with caution). At 3 dpf, larvae were screened as previously described before being swapped again into E3 containing 10% PTU and placed back in the incubator. Larvae from 4-6 dpf were used in all imaging experiments.

The SPIM imaging we performed is based on a previous design with the following details adapted [863]. Two continuous wavelength (CW) one-photon (1P) lasers at 488 nm (for excitation of GFP-based iRAADSnFRs) and 561 nm (see Chapter 7.2) are employable both singly and in tandem. Each beam is collimated and expanded to a diameter of 1.5 mm which is then passed through periscopes to raise the beams onto a 24 x 36 in.^{2} optical breadboard. Half-wave plates and polarizing beam splitters are then applied to both combine the two beams as well as split them into two paths (one for Illumination Arm 1 directed towards the left side of the sample and another for Illumination Arm 2 directed towards the front of the sample) of equivalent length. Next, all illumination beams are directed to a 2D scanning galvo mirror positioning system in which the first mirror scans the beam laterally to establish the x-y plane of the light sheet while the second mirror (conjugate with each of the back planes of the excitation objectives) translates the light sheet on the z-axis (normal to the detection plane). For scan lenses, two achromatic doublets with a 150 mm focus and 50 mm diameter (VIS-NIR 49-391, Edmund Optics) receive the light sheet which is then passed through a tube lens with a 200 mm focus and 50 mm diameter (VIS-NIR 49-391, Edmund Optics). (This scheme was chosen because the desired optical performance remained diffraction limited with no chromatic aberrations for the 488 and 561 nm beams.) The front and side excitation objectives are low magnification (5X), low NA (0.1), and have a long WD (23 mm) (LMPLN5XIR LWD M PLAN, Olympus) which completes a 4f optical system among the three lenses to avoid aberrations and tilting of the light-sheet during axial scan; the light sheets from the front and side excitation objectives are orthogonal. Total excitation light loss in the system is around 10-15% and final laser power entering the excitation objective was measured at 10 µW (488 nm). Using a 0.1 NA illumination objective allows for the generation of a thin light sheet with a gaussian waist of 3 µm. Thus, the final light sheet was created by scanning galvo mirrors allowing for single-neuron resolution across the full volume of a larval zebrafish brain with total three-dimensional FOV of 400 x 800 x 250 µm^3 [787].

Once the fluorophores in the sample are excited, the fluorescence is collected by an upright water-immersion detection lens with 20X magnification, 1.0 NA, and 2 mm WD (XLUMPLFLN-W, Olympus) arranged orthogonally to the two excitation objectives; this detection objective is chosen to maximize both resolution and light collection. The sample emissions then pass through a filter wheel (Lambda 10-B, Sutter Instruments) which blocks stray excitation light before the signal is shone onto another tube lens projecting the image onto a scientific complementary metal-oxide-semiconductor (scMOS) camera. The detection objective is scanned using an attached piezoelectric scanning collar synchronized with the second (z-axis)

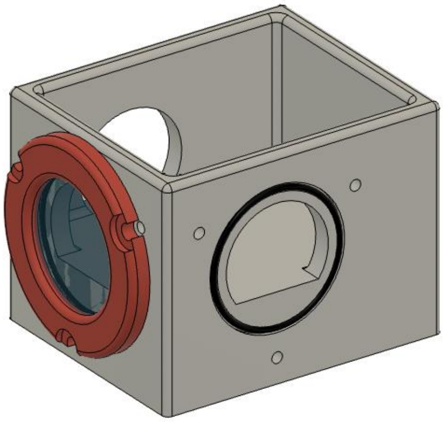

Figure 2.25. Cartoon of the sample chamber showing its three windows (the housing is shown for only the front window). (Figure courtesy of Andrey Andreev.)

galvo mirror in Illumination Arms 1 and 2; the galvo and the piezo are scanned axially across a range of ± 500 μm which allows for sequential collection along the z-axis of a larval zebrafish brain within seconds. The sample chamber was fabricated from ABS polymer using commercial CNC machining with dimensions 19 x 30 x 38 mm^3 and total volume of 21 mL (before accounting for liquid displacement by the objective and sample mounting). The chamber has three windows (round 25 mm #1 microscopy cover slips), one each for the front and side excitation beams and another to allow for heart rate monitoring (see below), and is open at the top to accommodate both the water-immersion objective as well as the mounting system for holding the larva (**Fig. 2.25**). The mounting system consists of a caddy on which the sample is mounted and a dive bar which sinks the caddy into the sample chamber below the objective, all of which can be moved using a manual 3D stage stack. The sample chamber sits on top of a 25 mm-thick copper heat block which allows for the maintenance of a constant temperature of 28ºC in the chamber; a commercial film heater and temperature sensor inserted into the copper block control the temperature through a thermostat (PID). An eye mask (cut out of black aluminum foil) is mounted on a 2D translational stage to allow for more precise coverage; the mask covers the left eye to partially block the side excitation beam which limits light scattering as well as protects the larva from ocular photodamage. We use an additional camera (CS165MU, Thorlabs) with a 780 nm bandpass filter positioned on the opposite side of the chamber from the side light sheet to monitor the heart rate throughout the experiment; a 780 nm LED illuminates the sample to provide contrast for imaging the heart.

Imaging was performed using a scMOS camera (ORCA Flash v4, Hamamatsu) with final pixel size of 0.78 µm and exposure time of 100 ms per frame for the 3 s per volume volumetric

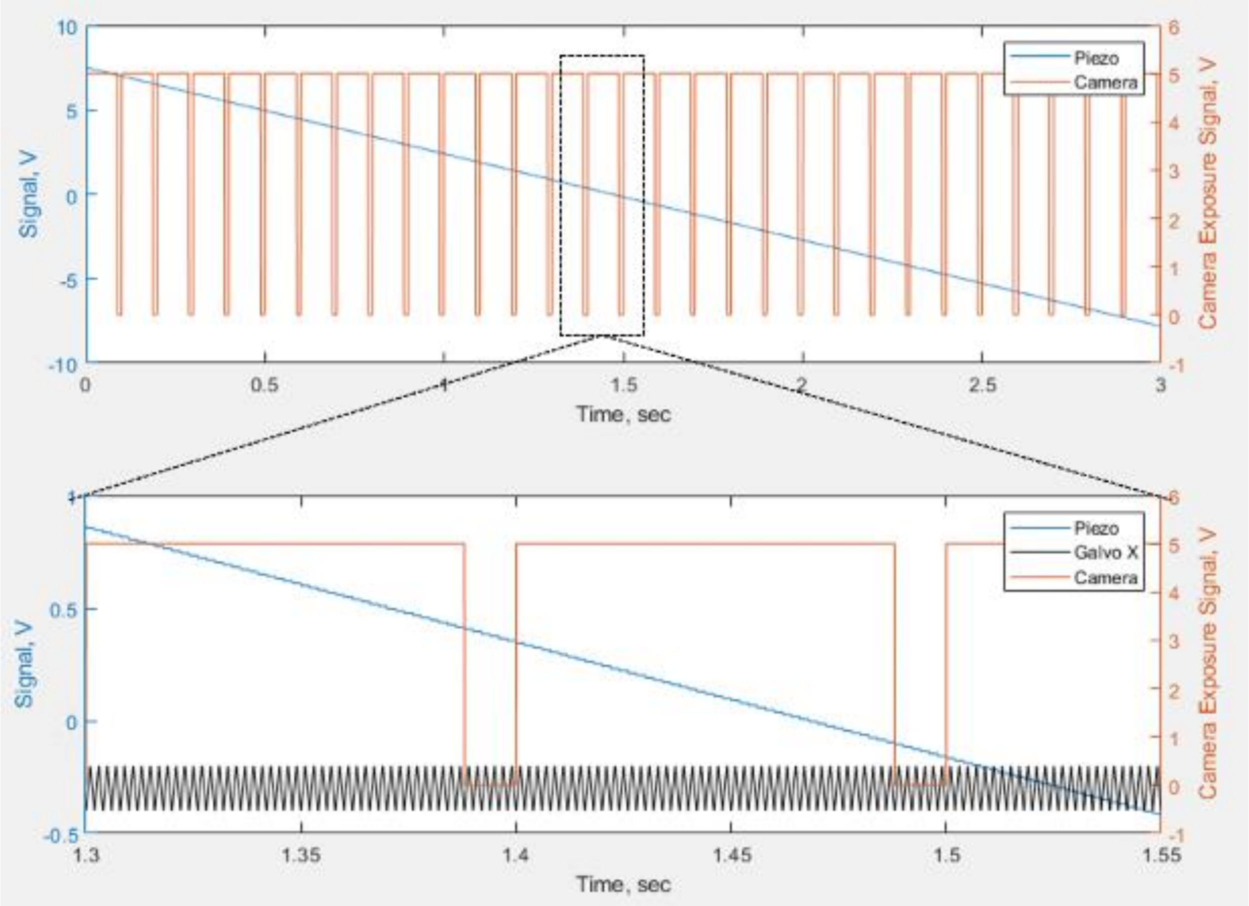

Figure 2.26. (*Top*) Voltage trace of signals for the entirety of a 3 s volumetric scan (30 z-slices) sent by custom MATLAB scripts to camera (*orange*) indicating when each image is taken (downward deflection every 100 ms) overlaid on voltage signal to piezoelectric scanning collar (Piezo, *blue*) which correlates with detection objective movement across the 300 µm z-range. (*Bottom*) Zoomed-in trace showing two images captured by camera (*orange*) again overlaid on the piezoelectric signal with the voltage trace for the 2D galvo scanning mirror in x-y (Galvo X, *black*) demonstrating the constant lateral deflection of the light sheet. (Figure courtesy of Andrey Andreev.)

scan rate and 70 ms per frame for the 2.1 s per volume rate (**Fig. 2.26**). Custom software scripts (MATLAB) were designed to provide signals that control the position of the galvos, the piezo objective collar, and the triggering of camera exposure through a digital-to-analog converter (DAQ, National Instruments). While the galvos are continuously sweeping at a 1 kHz frequency to create the light-sheet, the axial (z) position is synchronized between the galvos and piezo to allow for volumetric scanning. The exposure signals are synchronized with the z-position to ensure that frames in individual z-stacks are taken at the same physical location for each time point. Final volumetric imaging is performed over a 300 µm span (z) with 30 frames collected per z-stack. Temperature in the chamber was recorded using a custom Arduino-controlled thermometer [864] and the output data was collected alongside the imaging file.

To run an imaging experiment, the aforementioned 4-6 dpf PTU-treated larvae are paralyzed using α-bungarotoxin (~20 µL at 1 mg/mL [865]; Sigma-Aldrich) and mounted on the caddy in 1.5-2% low-melting point agarose. The caddy has a groove to constrain the larva by limiting pitch, roll, and yaw. Once the agarose has congealed, a scalpel is used to carefully remove a section near the head, which allows for direct contact between the larva and the solution in the chamber. The caddy is then attached to the dive bar and the entire mounting system is fixed to the 3D movable stage stack. For preparing DOIs, dilutions at the desired concentrations are mixed in E3. Next, we set up the same gravity flow perfusion system as previously described (see Chapter 2.2.6); solutions are flowed into a common manifold at 3-4 mL/min which descends into the sample chamber while the bath solution is withdrawn using a peristaltic pump (MP II, Harvard Apparatus) with the outflow tube positioned 2 mm above the surface of the solution to ensure the detection objective remains submerged and that solution does not overflow the chamber. The larva is then positioned using the 3D stage stack and a baseline z-stack time series is recorded for approximately 10 min to characterize baseline fluorescence. Imaging experiments from 1-4.5 hours duration are then conducted, with the DOI at various concentrations applied over 20-30 minutes followed by 30-180 minutes of E3 as washout.

Data are analyzed offline to: sort the images, adjust the brightness/contrast, choose ROIs, and generate time-series data for z-slices of interest (FIJI); generate time-frequency spectrograms for the heart rate traces and align ROIs with a standardized atlas (Python and MATLAB); and create plots of the ROI traces (Origin 2018. We used an open-source library (ANTsPy) to correct for any drift and to register data to a standardized atlas of zebrafish brain regions (Z-Brain Atlas [866]).

2.6. Results: iRAADSnFRs In Vivo

2.6.1. Concentration-Response Experiments in Awake Zebrafish

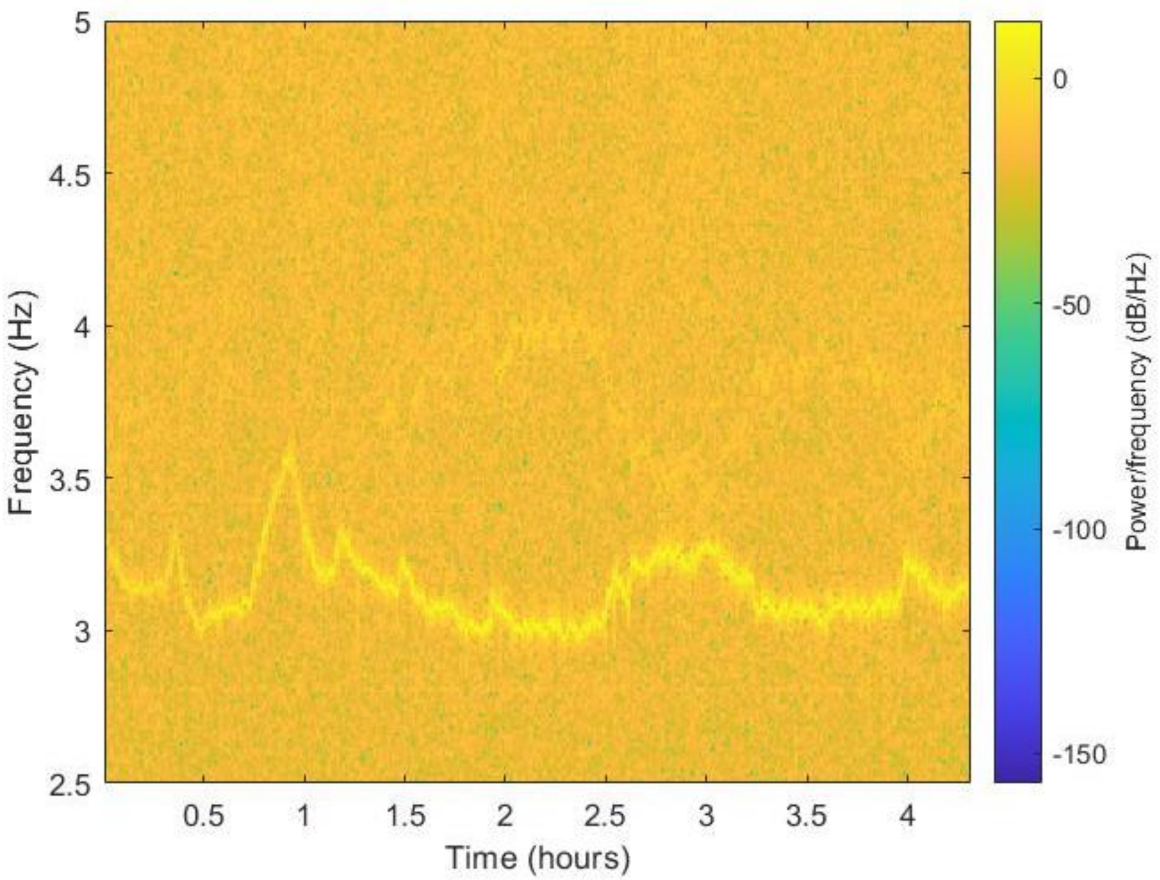

Figure 2.27. Time-frequency spectrogram (short-time Fourier transform with window = 1000, 50% overlap, sampled at 100 ms) of heart rate data from a single larval zebrafish over the course of the 260 min experiment. The heart rate shows normal variation around a typical larval zebrafish rate of ~3-3.5 Hz [867] with no significant drop-off from beginning to end.

We performed concentration-response experiments in larval zebrafish using a protocol (20 min baseline with E3 followed by three 20 min drug plus 60 min washout with E3 sequences) which privileges the return to baseline fluorescence during washout periods. These parameters were chosen after initial experiments demonstrated that the time course over which fluorescence changes occur in our setup occur is roughly two orders of magnitude slower than the dynamics observed during *in vitro* experiments (see Chapter 2.6.4). We also chose the same three concentrations (1 µM, 2 µM, 3 µM) across all experiments; despite the low (nanomolar to low micromolar) EC_{50} values determined for iRAADSnFRs in purified protein (see Chapter 2.3.1), some iDrugSnFRs exhibit ‘right-shifted’ (higher) EC_{50} values when implemented in mammalian cells and transduced neurons (e.g. dianicline [684]), so we wanted to choose concentrations which would still a) have pharmacological relevance based on concentrations determined in clinical studies (see Chapter 1.3 and Chapter 1.4), and b) would induce robust fluorescence responses. Lastly, we chose to perform experiments in which we administer only three concentrations because of time considerations; while we verified that the larvae exhibit no noticeable changes in health over the course of the 260 min experiment using heart rate recordings (**Fig. 2.27**), we worried that longer-term experiments would compromise larval health. Although we did observe definite health deficits after overnight paralysis (data not shown), longer term paralysis may indeed be feasible [868], which makes possible further experimentation encompassing a wider concentration range with more doses.

We have thus far completed the aforementioned concentration-response experiments for three different transgenic lines: *Tg(HuC:iR-KetSnFR)*, *Tg(HuC: iS-HNKSnFR)*, and *Tg(HuC:iMXESnFR)*. To allow for further standardization when comparing across different experiments and fish lines, we focus on the fluorescence response of neurons in the hindbrain using the z-slice for a given image stack in which this region has maximum cross-sectional area, as the hindbrain is large, easy to identify, and has low F_0. In the *Tg(HuC:iR-KetSnFR)* experiment (**Fig. 2.28**), we see a large (> 100%) $\Delta F/F_0$ response to the 1 μM dose which is then

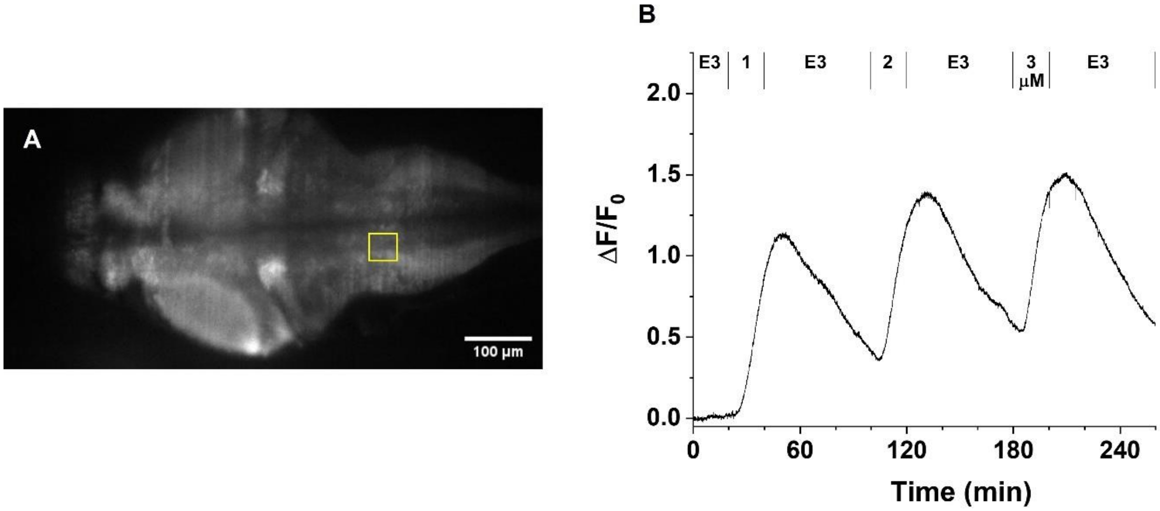

Figure 2.28. ***(A)*** Gray-scale single image of a larval zebrafish brain (z = 20/30) expressing *HuC:iR-KetSnFR* showing the ROI (*yellow*) in the hindbrain which is tracked over the course of the continuous flow experiment. ***(B)*** Fluorescence trace for the ROI drawn in (***A***) showing the responses to 20 min of arketamine administration (1/2/3 μM) as well as during 1 h washout periods (E3). (*Black lines* denote the beginning and end of each period of the protocol.)

washed out after a delay of approximately 10 min all the way to about 30% of the peak at the end of the 1 h period. The dynamics and peak fluorescence of the 2 μM dose appear nearly identical to those induced by the 1 μM dose while the washout appears to be slightly more delayed, with a slightly steeper slope resulting in a roughly 90% decrease from the starting fluorescence. Finally, the 3 μM dose induces a similarly sized (though slightly smaller) fluorescence increase with an even steeper washout such that the fluorescence nearly returns to its value before the dose was administered. In the *Tg(HuC:iS-HNKSnFR)* experiment (**Fig. 2.29**), the overall fluorescence increase from each dose administered is less than for the *Tg(HuC:iR-KetSnFR)* experiment, with each dose inducing elevations of less than 50% $\Delta F/F_0$. However, of more interest is the much slower kinetics of drug entry and exit: the fluorescence barely begins to rise during the three (2S,6S)-HNK administration periods, with nearly all of the fluorescence increase occurring during the washout periods, only appearing to level off about 40-50 min after each dose ends. There is no apparent negative slope to the fluorescence traces, suggesting that at no time during the experiment did the DOI ever exit neurons to any significant extent. The slopes of the fluorescence trace during the delayed post-administration rises do appear to increase with increasing dose, as the amount of fluorescence elevation per dose is not constant (1 μM: ~30%; 2 μM: ~40%; 3 μM: ~50%). In the *Tg(HuC:iMXESnFR)* experiment (**Fig. 2.30**), the

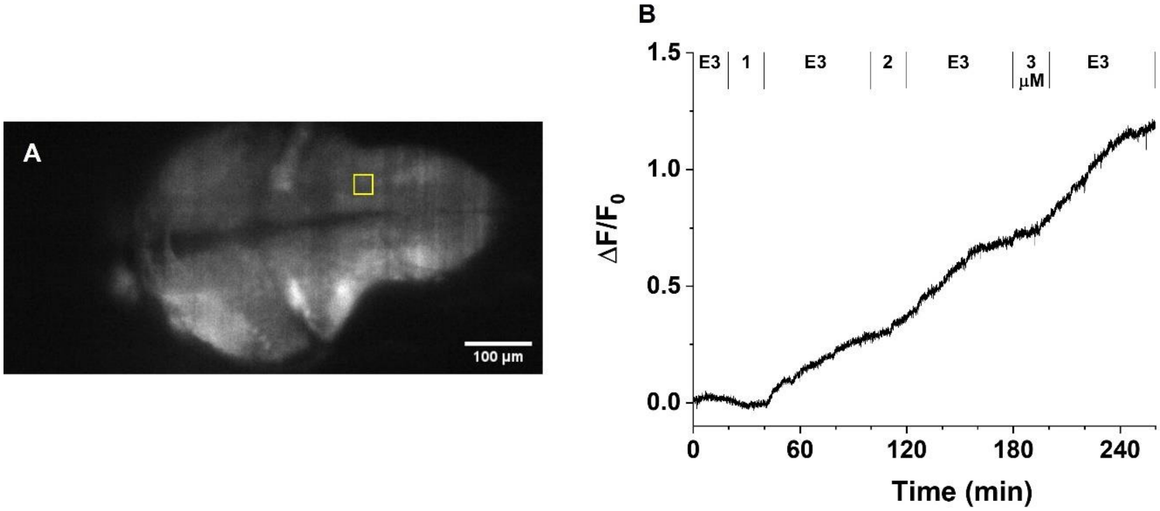

Figure 2.29. ***(A)*** Gray-scale single image of a larval zebrafish brain (z = 21/30) expressing *HuC:iS-HNKSnFR* showing the ROI (*yellow*) in the hindbrain which is tracked over the course of the continuous flow experiment. ***(B)*** Fluorescence trace for the ROI drawn in (***A***) showing the responses to 20 min of (2S,6S)-HNK administration (1/2/3 μM) as well as during 1 h washout periods (E3). (*Black lines* denote the beginning and end of each period of the protocol.)

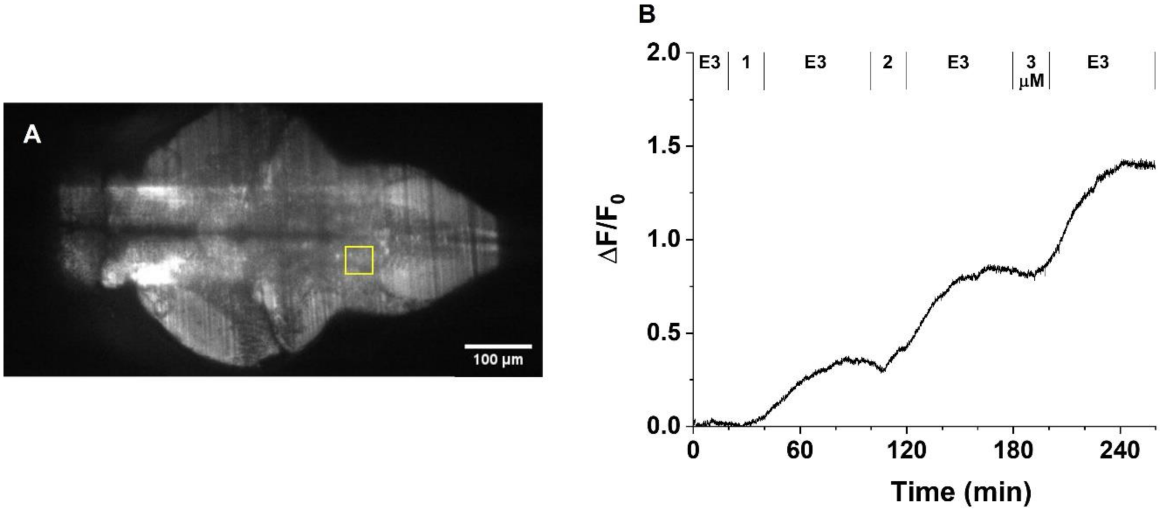

Figure 2.30. ***(A)*** Gray-scale single image of a larval zebrafish brain (z = 21/30) expressing *HuC:iMXESnFR* showing the ROI (*yellow*) in the hindbrain which is tracked over the course of the continuous flow experiment. ***(B)*** Fluorescence trace for the ROI drawn in (***A***) showing the responses to 20 min of MXE administration (1/2/3 µM) as well as during 1 h washout periods (E3). (*Black lines* denote the beginning and end of each period of the protocol.)

fluorescence dynamics display features intermediate between those determined in the previous two lines. There is a delay of about 10 min during the administration of 1 µM MXE before the fluorescence begins to rise; once the first washout period starts, the fluorescence continues to rise for an additional 40 min before leveling off, decreasing by approximately 5% $\Delta F/F_0$ from the peak value when the 2 µM dose is administered. Each of the remaining administration-washout sequences results in dynamics as described for the first, with the main difference concerning the slope of the fluorescence rise (as with the *Tg(HuC:iS-HNKSnFR)* experiment); the rise in fluorescence increases with increasing doses (1 µM: ~35%; 2 µM: ~55%; 3 µM: ~65%). As in the first washout, the last 20 min of the subsequent washout periods demonstrates a decrease in fluorescence, though this appears to remain constant regardless of the concentration administered.

2.6.2. Single-Concentration Extended Washout Experiments

A striking feature of the data from the concentration-response experiments is that we have little indication as to the time course over which the fluorescence increase from a continuously administered concentration of the DOI would reach a peak value; in the *in vitro* data (see Chapter

2.3), this typically takes place within tens of seconds. However, we have characterized the *in vitro* imaging dynamics well enough such that we designed the experimental conditions around these features. With the *in vivo* imaging experiments using larval zebrafish, we have demonstrated that 20 min — approximately two orders of magnitude greater than the administration periods used in *in vitro* experiments — is insufficient to induce a peak fluorescence value, even for the DOI with the most rapid entry into neurons, arketamine (see **Fig. 2.28**). However, as these experiments also show, we never observed a return to baseline (or even pre-dose) levels during the 1 h washout periods; yet we do see that, for at least two of the larval zebrafish lines — *Tg(HuC:iR-KetSnFR)* and *Tg(HuC:iMXESnFR)* — there is the possibility of a calculable time course estimating when the fluorescence would return to baseline/pre-dose levels, as both fluorescence traces demonstrate decreases at some point during the washout periods (with the washout for arketamine occurring faster than for MXE; **Fig. 2.28** and **Fig. 2.30**). We thus decided to design experiments in which the washout period after a single dose would be extended such that we could either better extrapolate the time course over which a return to baseline/pre-dose levels would occur or observe the return to those levels. These experiments consist of a 20 min baseline period with E3 followed by 20 min of DOI with a 180 min washout period with E3. We chose 2 μM as our concentration across experiments so that we could induce a robust fluorescent response to compare among the different zebrafish lines.

We performed extended washout experiments with the three lines for which we completed the concentration-response experiments. In the *Tg(HuC:iR-KetSnFR)* experiment (**Fig. 2.31**), we see a robust $\Delta F/F_0$ response to the 2 μM dose (~200%) which again appears with a delay of ~10 min after administration and decreases after 10-15 min of washout. Interestingly, over the course of the washout, we observe a return to baseline fluorescence in the last ~30 min of the experiment. This demonstrates that, compared to the *in vitro* fluorescence dynamics in mammalian cells, the washout of arketamine *in vivo* takes approximately three orders of magnitude longer (~10 s vs. ~10,000 s). In the *Tg(HuC:iS-HNKSnFR)* experiment (**Fig. 2.32**), we see minimal fluorescence response during the 20 min (2S,6S)-HNK administration period followed by ~140 min of increasing $\Delta F/F_0$ (up to ~60%) before the fluorescence begins to decrease. While there is not much of a decrease, when the negatively sloping portion of the washout period (the last ~30 min) is fit to a linear function, we find that a return to baseline would take an additional 330 min of washout with E3

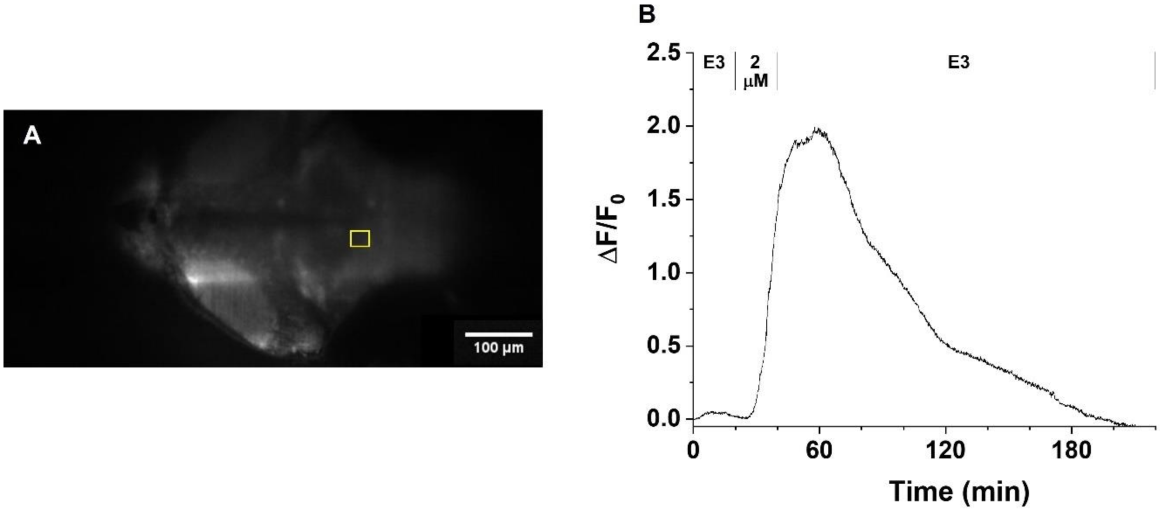

Figure 2.31. ***(A)*** Gray-scale single image of a larval zebrafish brain (z = 22/30) expressing *HuC:iR-KetSnFR* showing the ROI (*yellow*) in the hindbrain which is tracked over the course of the continuous flow experiment. ***(B)*** Fluorescence trace for the ROI drawn in (***A***) showing the responses to 20 min of arketamine administration (2 µM) as well as during the 3 h washout period (E3). (*Black lines* denote the beginning and end of each period of the protocol.)

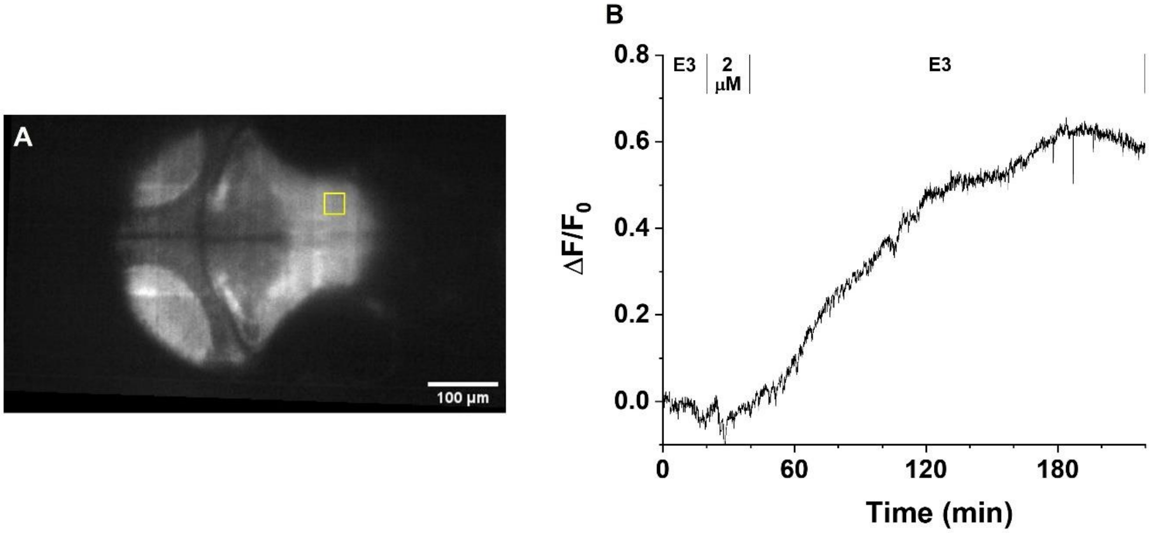

Figure 2.32. ***(A)*** Gray-scale single image of a larval zebrafish brain (z = 18/30) expressing *HuC:iS-HNKSnFR* showing the ROI (*yellow*) in the hindbrain which is tracked over the course of the continuous flow experiment. ***(B)*** Fluorescence trace for the ROI drawn in (***A***) showing the responses to 20 min of (2S,6S)-HNK administration (2 µM) as well as during the 3 h washout period (E3). (*Black lines* denote the beginning and end of each period of the protocol.)

(data not shown). In the *Tg(HuC:iMXESnFR)* experiment (**Fig. 2.33**), we corrected the baseline fluorescence as there was a slight movement during the experiment causing an aberrant increase. We see a robust $\Delta F/F_0$ response to the 2 μM dose (> 150%) which ensues ~10 min into the dosing period, levels off approximately 40 min into the washout, and begins to decrease about 20 min later. The decrease occurs in a linear manner which, when fitted to a simple linear curve, demonstrates that a return to baseline would take an additional 200 min of washout with E3 (data not shown).

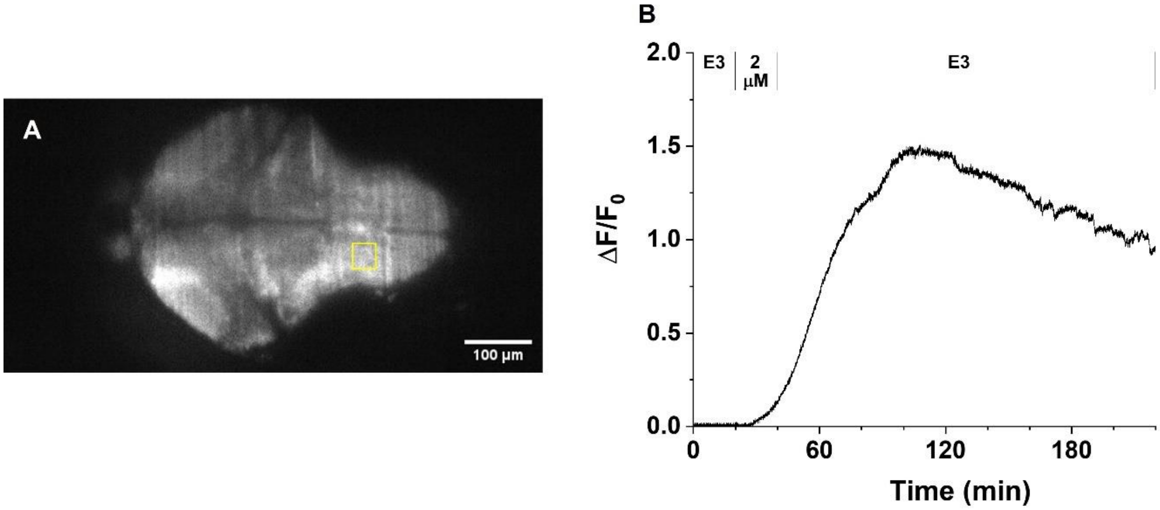

Figure 2.33. ***(A)*** Gray-scale single image of a larval zebrafish brain (z = 21/30) expressing *HuC:iMXESnFR* showing the ROI (*yellow*) in the hindbrain which is tracked over the course of the continuous flow experiment. ***(B)*** Fluorescence trace for the ROI drawn in (***A***) showing the responses to 20 min of MXE administration (2 μM) as well as during the 3 h washout period (E3). (*Black lines* denote the beginning and end of each period of the protocol.)

2.6.3. Preliminary Imaging Data: The Other iRAADSnFRs

While we have yet to perform the pair of experiments described above for the other three iRAADSnFR zebrafish lines, we have collected data to preliminarily characterize each of them *in vivo*. For *HuC:iS-KetSnFR3,* we performed a concentration-response experiment using the same temporal parameters as described in Chapter 2.6.1, but we used lower concentrations (100 nM, 250 nM, 500 nM) because we wanted to evaluate the sensor against depression-relevant concentrations of esketamine (in the sub-micromolar range in humans; see Chapter 1.3). However, we observed small rises in fluorescence upon administration of these concentrations

(**Fig. 2.34**), with the clearest rise observed after the 100 nM dose (~20% $\Delta F/F_0$) but with the return to baseline during the washout period noisy; the subsequent administration-washout cycles demonstrate < 10% changes in fluorescence along with a lack of a return to baseline. This experiment suggests that higher concentrations of esketamine induce a more robust fluorescence response, though the pharmacokinetics — especially in comparison with arketamine (see **Fig. 2.28** and **Fig. 2.31**) — are yet to be determined. For *HuC:iR-HNKSnFR*, we performed an experiment in which we administered a single dose (3 µM) followed by a 1 h washout (though the last half of the washout was corrupted by movement artifact and was excised). Both in the hindbrain (**Fig. 2.35**) as well as across other regions of the brain (data not shown), we saw negligible changes in fluorescence (< 5% $\Delta F/F_0$) suggesting that this concentration is not high enough for *in vivo* imaging with this sensor; indeed, iR-HNKSnFR had the highest EC_{50} of any iRAADSnFR in purified protein (2.5 µM; **Table 2.1**), and any right-shifting (see Chapter 2.6.1) *in vivo* would require higher concentrations of (2R,6R)-HNK to induce a robust response. For *HuC:iScopSnFR*, we performed an experiment in which we administered a single dose (4 µM) via bath perfusion for 1 h. As with the (2R,6R)-HNK experiment, we do not see an appreciable increase in fluorescence over the course of the 1 h experiment (< 5% $\Delta F/F_0$; **Fig. 2.36**) which could indicate all or some of the following: a) constant flow is necessary for more rapid transit of

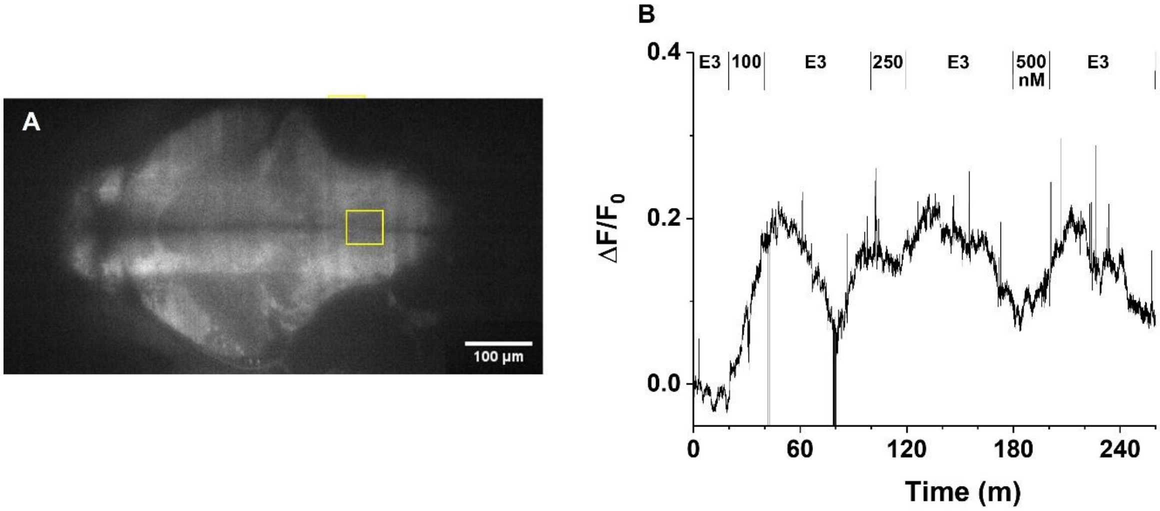

Figure 2.34. ***(A)*** Gray-scale single image of a larval zebrafish brain (z = 18/30) expressing *HuC:iS-KetSnFR* showing the ROI (*yellow*) in the hindbrain which is tracked over the course of the continuous flow experiment. ***(B)*** Fluorescence trace for the ROI drawn in (***A***) showing the responses to 20 min of esketamine administration (100/200/300 nM) as well as during 1 h washout periods (E3). (*Black lines* denote the beginning and end of each period of the protocol.)

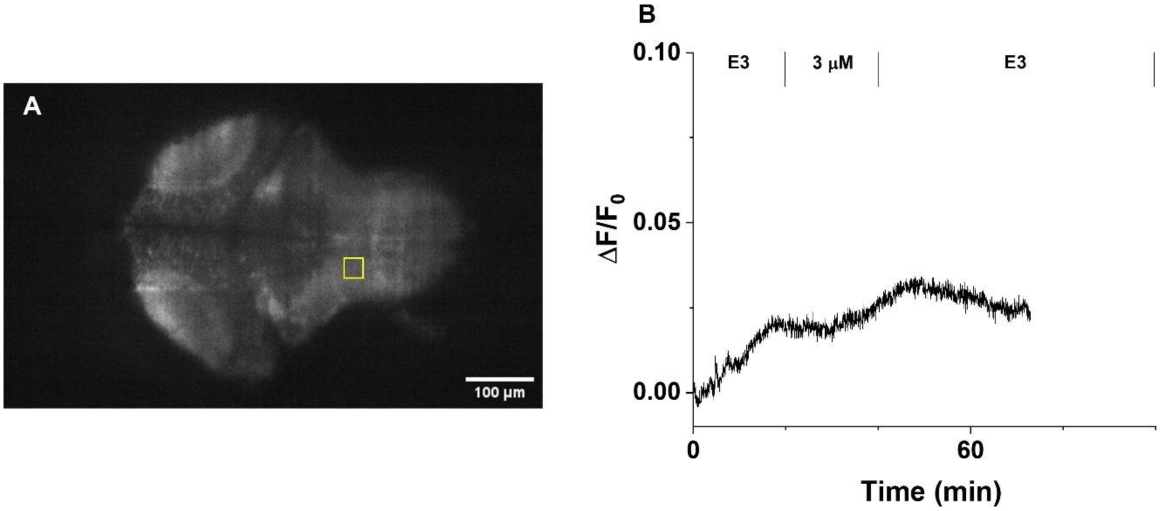

Figure 2.35. ***(A)*** Gray-scale single image of a larval zebrafish brain (z = 17/30) expressing *HuC:iR-HNKSnFR* showing the ROI (*yellow*) in the hindbrain which is tracked over the course of the continuous flow experiment. ***(B)*** Fluorescence trace for the ROI drawn in (***A***) showing the responses to 20 min of (2R,6R)-HNK administration (3 µM) as well as during the 1 h washout period (E3) (the trace was truncated due to movement artifact). (*Black lines* denote the beginning and end of each period of the protocol.)

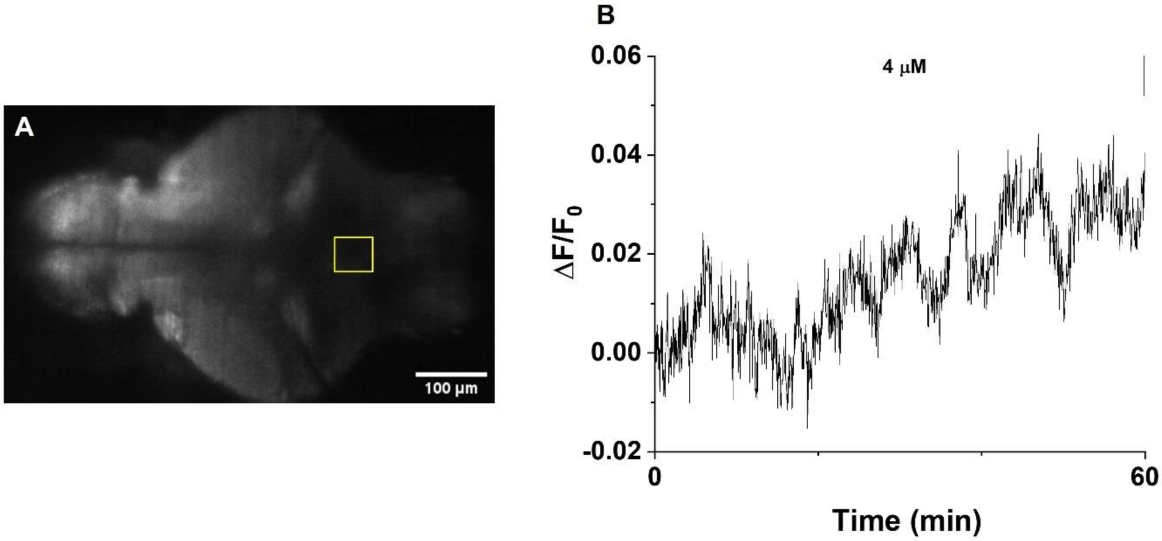

Figure 2.36. ***(A)*** Gray-scale single image of a larval zebrafish brain (z = 20/30) expressing *HuC:iScopSnFR* showing the ROI (*yellow*) in the hindbrain which is tracked over the course of the bath perfusion experiment. ***(B)*** Fluorescence trace for the ROI drawn in (***A***) showing the responses to 60 min of scopolamine administration (4 µM). (*Black lines* denote the beginning and end of each period of the protocol.)

RAADs into neurons; b) the concentration used was too low – the EC_{50} of iScopSnFR in purified protein is 510 nM (**Table 2.1**), so the *in vivo* result could indicate even more substantial right-shifting for this sensor than for iR-HNKSnFR; c) the solubility of scopolamine in E3 is lower than for the other compounds, as its LogP is 0.89, roughly two orders of magnitude lower than the ketamine-class compounds, could indicate that scopolamine does not cross into intact brain as quickly (see Chapter 1.5). In all, future concentration-response experiments will be performed with all three of these RAAD-iRAADSnFRs using concentrations approximately an order of magnitude higher (and, in the case of scopolamine, perhaps with the addition of a 0.1% volume-by-volume addition of DMSO to increase solubility; while DMSO can increase F_0 in iDrugSnFRs [720], such a small amount would have a negligible effect) to elicit fluorescence responses on par with the results observed in experiments using the other three sensors (see Chapter 2.6.1 and Chapter 2.6.2).

2.6.4. Summary of In Vivo *Results and Next Steps*

Our results from SPIM imaging of awake larval zebrafish expressing iRAADSnFRs pan-neuronally demonstrate that these sensors can detect the presence of pharmacologically relevant concentrations of RAADs in intact neural tissue over the course of hours in a dose-dependent manner. While we have yet to characterize all of the sensors (see Chapter 2.6.3), we are confident that the performance of the iRAADSnFRs *in vivo* indicates their usefulness for studying the pharmacokinetics of RAADs.

Perhaps the most interesting general result from these experiments concerns the time course over which the RAADs apparently enter and exit neurons: on the order of tens of minutes to hours, much slower than what was observed *in vitro* (see Chapter 2.3). As we have seen with the SSRI fluoxetine (see Chapter 3), drugs can interact with membranes differently in PHC compared to mammalian cells; as the intact zebrafish brain has even more cellular complexity than PHC, the potential exists for pharmacokinetic properties of RAADs to vary depending on the cell type into which they transit. Nevertheless, the rate at which an antidepressant enters inside cells does not necessarily indicate the speed with which it exerts its effects; at least in mammalian cells, both RAADs (see Chapter 2.3) and SSRIs (see Chapter 3) — compounds which produce clinical benefit on drastically different time scales — enter and exit cells within seconds. Notably, the LogP values for the SSRIs — 4.1 for fluoxetine and 3.2 for escitalopram (see Chapter 3) — are approximately within an order of magnitude of the ketamine-class compounds (see Chapter 1.5), suggesting that the putative interaction with membranes causing the slow washout of fluoxetine could conceivably occur for any or all of the RAADs as well. Characterization of the iRAADSnFRs in PHC using viral vectors would aid in understanding RAAD pharmacokinetics, as will further experiments *in vivo* with awake zebrafish. Other possible reasons involve the longer turnover time of the chamber solution (~4-5 min *in vivo* vs. seconds *in vitro*), the role of blood flow and metabolism in an intact animal, the (in)ability of RAADs to move across skin [869], and sequestration in glia [427,490].

For the three sensors in which concentration-response experiments have been performed, follow-up studies will focus on titrating the concentration range (perhaps expanding it to cover an order of magnitude) to assess potential dose-dependent effects on pharmacokinetics. In particular, the concentrations of arketamine used (**Fig. 2.28**) appear to induce similar fluorescence responses, suggesting this sensor is sensitive to lower (sub-micromolar) concentrations which may help elucidate the pharmacokinetics of antidepressant-relevant levels (see Chapter 1.3). In any case, our results suggest that such concentrations of arketamine will be detectable by iR-KetSnFR; as these doses are unlikely to induce anesthesia (see Chapter 1.2 and Chapter 5), we can further investigate the claim that anesthetic doses (800 μM) are necessary to induce antidepressant effects in larval zebrafish in a neuron-independent manner [490], as our setup allows for the simultaneous recording of physiology and pharmacokinetics (see Chapter 7) as well as (in principle) a behavioral readout (e.g. tail movement). The further development of transgenic zebrafish lines expressing iRAADSnFRs in various intracellular compartments as well as the PM (see Chapter 2.3) is also an option for assessing real-time pharmacokinetic properties of RAADs as they enter and exit organelles of interest. Finally, studies implicating glia in the mediation of ketamine's antidepressant effects [427,490] have demonstrated compelling results such that experiments on larvae co-expressing either neuron- or glia-targeted iRAADSnFRs along with a red-shifted glia-targeted Ca^{2+} sensor would be of interest to explore further using SPIM.

CHAPTER 3: SENSING FLUORESCENT REPORTERS FOR SELECTIVE SEROTONIN REUPTAKE INHIBITORS

3.1. Introduction

Theories on the pathogenesis of depression are varied, and no single etiology has proved dispositive of the clinical manifestations (see Chapter 1.1). Indeed, any explanation of underlying pathophysiology must account for the likelihood that symptoms and states of MDD are overdetermined and can arise from multiple mechanisms acting both in concert and singly. Additionally, while the pathways through which antidepressants appear to exert their main effects has inspired several of the most compelling explanations of depression's causes, these initial surmises are complicated by investigation into potential common targets for pharmaceuticals which relieve symptoms (see Chapter 1.7); furthermore, much like other successful interventions for neuropsychiatric diseases and disorders (e.g. DBS for the treatment of motor signs in PD), understanding how a treatment works does not entail understanding of pathophysiology.

With respect to one of the most common systems implicated in both depression and its treatment, the role of 5-HT in the regulation of motivation and cognition has been demonstrated across various animal species, including mammals [870]. The link between 5-HT and MDD has been investigated for over fifty years, with the putative mechanisms of several early antidepressants (MAOIs and TCAs) implying that the induced increase in synaptic 5-HT means aberrant 5-HT signaling is a biomarker of clinical symptoms. As mentioned previously (see Chapter 1.1), this finding motivated the development of SSRIs to treat MDD, as their designed function is to inhibit the reuptake of synaptic 5-HT to increase serotonergic tone. The proliferation of SSRIs subsequent to the FDA-approval of fluoxetine (Prozac®) in the mid-1980s has led many clinicians and researchers to presume the importance of 5-HT in the pathogenesis of MDD. However, more recent findings regarding both the rapid antidepressant effects of ketamine (see Chapter 1.3) as well as evidence that dysregulation of 5-HT may not be as directly related to MDD as previously considered [871] have led to a paradigm shift in the study of antidepressants; while some novel theories still posit a role for 5-HT [872], overwhelming evidence indicates that any mechanistic understanding of either MDD or antidepressants must comprise a more expansive view of neurophysiological dynamics rather than focus on one neurotransmitter, brain area, or neuronal subtype.

In our estimation, investigations into the potential antidepressant mechanisms of SSRIs aim at addressing four non-mutually exclusive domains. The first is the most basic and touches on the designed purpose of SSRIs: inhibition of SERT. In this telling, while inhibition of SERT leads to increased extracellular 5-HT within days [49], it is only after a period of 2-6 weeks [33,50] that underlying physiology is altered sufficiently such that patients experience symptom relief. A second proposal involves the build-up of SSRIs themselves in the extracellular fluid to drive the physiological changes, as SSRIs are known to accumulate substantially in tissues (as measured by V_d [277,278]) and have lipophilic properties (as measured by $LogD_{pH7.4}$; see Chapter 1.5), both of which impact accumulation near PM-anchored SERT. A third mechanism implicates the recently postulated ‘inside-out- phenomenon whereby weakly basic drugs (of which a substantial population has no charge at physiological pH) can cross both the PM as well as subcellular membranes to exert effects on their targets [530] (see Chapter 1.6.5). In contrast to the first mechanism, which postulates a so-called ‘outside-in’ interaction between an SSRI and the extracellular SERT, inside-out activity implicates subcellular compartments involved with the assembly of SERT (paralleling nicotine binding to $\alpha_4\beta_2$ nAChRs in the ER [531-534] and, more broadly, any compartment which maintains a lower pH can induce protonation and thus accumulation of the SSRI via acid-trapping [530,537]). Fourth, SSRIs operate via supplementary or entirely different mechanisms besides SERT inhibition to improve MDD symptoms. Preliminary evidence suggests that interactions with both TrkB [614] and lipid rafts [873] could be involved in the antidepressant effect of SSRIs, which motivates the evaluation of the necessity and sufficiency of these mechanisms.

Thus, investigating where SSRIs transit in and around neurons, as well as how fast they arrive, is crucial to evaluating the evidence for each of the aforementioned mechanisms. We thus identified two SSRIs, escitalopram and fluoxetine (both weak bases with pK_a values ~9.8) and evolved existing iDrugSnFRs to generate sensitive and specific iSSRISnFRs: iEscSnFR and iFluoxSnFR. These sensors were targeted to several parts of both mammalian cells and PHC — the ER, the PM, and the cytoplasm — which have relevance to the inside-out pathway (SERT is synthesized in the ER, trafficked through the cytosol, and anchored on the PM [874]). We recorded both iSSRISnFR as well as human SERT (hSERT) responses to pharmacologically relevant concentrations of the two SSRIs as well as to quaternary-amine derivatives (escitalopram: N-escitalopram; fluoxetine: N,N-dimethylfluoxetine) with a permanent positive charge; this allows for separate assessments of the outside-in and inside-out pathways (as these derivatives cannot cross the PM). Lastly, we used both simulations as well as lipid bead assays to explore the reasons for the observed slow pharmacokinetics of both SSRIs in PHC, particularly fluoxetine. In all, we believe that our results provide compelling evidence that several unusual properties of SSRIs may contribute to their slow therapeutic dynamics.

3.2. Methods

3.2.1. Development of iSSRISnFRs and Experiments Using Purified Protein

We screened previous iDrugSnFR proteins for fluorescence response to both escitalopram and fluoxetine as described in Chapter 2.2.1. Once completed, we began evolving sensors from different starting constructs: for the escitalopram sensor (iEscSnFR), iNicSnFR3b [533]; for the fluoxetine sensor (iFluoxSnFR), iAChSnFR [678]. SSM was performed as described in Chapter 2.2.2, with one round of SSM sufficient to produce iEscSnFR and three rounds for iFluoxSnFR (**Fig. 3.1A**). After concentration-response profiles were established for each iSSRISnFR in lysate (see Chapter 2.2.2), we used FPLC to purify each sensor as described in Chapter 2.2.3 after which we performed both stopped-flow and ITC as described in Chapter 2.2.4. For ITC, 450 µM escitalopram (Tocris) was titrated into 45 µM iEscSnFR, and 700 µM N,N-dimethylfluoxetine was titrated into 140 µM iFluoxSnFR; the latter drug-sensor pair was used because we found fluoxetine to be insoluble at high concentrations which affected the performance of the ITC instrument, particularly the precisely controlled injection into the sample cell. Analysis, including correction for changes in enthalpy generated from the dilution of the ligands into the sample cell during the experimental titration, was performed using a single-site binding model in NanoAnalyze as described in Chapter 2.2.4.

3.2.2. Synthesis of Quaternary SSRIs

Synthesis of N-methylescitalopram was as previously described, with escitalopram replacing citalopram as the starting reagent [875]. To generate N,N-dimethylfluoxetine, 60 mg/0.174 mmol of fluoxetine hydrochloride (Sigma-Aldrich) was dissolved in the solvent acetonitrile (ACN; 5 mL). Triethylamine (130 μL) was added as a base, followed by methyl iodide (324 μL), which acts as the methylating agent. The reaction was stirred at room temperature for 20 min. Ethyl acetate (10 mL) was added as an extracting agent, and the resulting precipitate was removed by filtration. The filtrate was concentrated, dissolved in dichloromethane, and washed with deionized water three times. The organic layer was dried over magnesium sulfate and concentrated to give a yellow oil (44 mg, 54%). Proton nuclear magnetic resonance (400 MHz) was performed with solvation in chloroform: δ 7.46-7.29 (m, 7H), 226 6.97 (d, J = 9.05 Hz, 2H), 5.57 (dd, J = 6.32 Hz, 1H), 4.22-4.15 (m, 1H), 3.80-3.73 (m, 1H), 3.38 (s, 9H), 2.41-2.35 (m, 2H). Mass, calculated for $C_{19}H_{23}F_3NO^+$ to be 338.17 g/mol, found 338.22.

3.2.3. Fluorescence Measurements in Mammalian Cells and Primary Culture

We constructed three variants for each iSSRISnFR targeting the PM (suffix '_PM'), the ER (suffix '_ER'), and the cytoplasm (suffix '_cyto') for expression in mammalian cells as described in Chapter 2.2.5. Transfections were performed in HeLa cells as described in Chapter 2.2.5. For viral transduction of PHC, we produced AAV9-hSyn-iSSRISnFR_ER, _PM, and _cyto plasmids as described in Chapter 2.2.5, with the _ER and _PM viruses made using the AAVpro protocol and the _cyto viruses made using the Caltech protocol [768]. Mouse embryonal HC were dissected and plated then transduced after 3-4 days using MOIs as described in Chapter 2.2.5. Time-resolved concentration-response imaging was performed for both transfected mammalian cells and transduced PHC as described in Chapter 2.2.6; experiments consisted of interleaving periods of washout (60-720 s) with HBSS following administration of increasing doses of SSRI (60 s). We performed experiments in PHC with 80 nM folimycin (Sigma-Aldrich), an inhibitor of vesicular ATPase used to assess trapping of SSRI in vesicles; we incubated dishes for 10 min [537] prior to performing standard imaging. The number of cells averaged was as described in Chapter 2.2.6. Spinning disk confocal microscopy was performed as described in Chapter 2.2.6, with the final drug concentrations in both mammalian cells and PHC 10 µM of escitalopram and 10 µM of fluoxetine.

3.2.4. Electrophysiology of hSERT Inhibition

Complementary DNA (cDNA) from hSERT was transferred to the pOTV vector which is an oocyte transcription vector optimized for *in vitro* transcription of RNA [876]. The K490T mutation, which increases the amplitude of the hSERT transport-associated current (TAC) at low pH [877], was encoded using the QuikChange protocol (Agilent); the TAC is induced by uptake of 5-HT [878]. Linearization of the cDNA was accomplished via single-site NotI digestion and purified using the PCR purification kit as described in Chapter 2.2. Purified DNA was then transcribed *in vitro* using the T7 mMessage Machine kit (Ambion). Newly hatched *Xenopus laevis* oocytes were isolated, injected with complementary RNA (20 ng in 50 nL of nuclease-free water), and incubated at 19°C for three days in Ca^{2+}-free ND96 solution (composed of 96 mM sodium chloride, 2 mM potassium chloride, 1 mM magnesium chloride, and 5 mM HEPES buffer [879] titrated to pH 7.5 [880]) supplemented with 0.05 mg/mL gentamicin (Sigma-Aldrich) to prevent contamination, 2.5 mM sodium pyruvate (Acros Organics) to supplement energy for oocytes, and 0.67 mM theophylline (Sigma-Aldrich) which inhibits oocyte development [881]. Two-electrode voltage clamp electrophysiology was performed on a semi-automated recording system (OpusXpress 6000A, Molecular Devices Axon Instruments) at RT. Oocytes were impaled with borosilicate glass electrodes filled with 3 M potassium chloride (0.3–3.0 MΩ resistance) and held at -60 mV. All compound solutions were prepared using Ca^{2+}-free ND96 solution titrated to a pH of 5.5 for maximizing TAC amplitude [877]. A solution containing only SSRI or quaternary derivative (0.67 mL) was applied to oocytes for 10 s followed by a 10 s incubation, after which solution containing the same concentration of SSRI/quaternary derivative mixed with 3 μM 5-HT (1 mL) was then applied for 15 s. This process was followed by a 3.2 min washout period with running buffer (Ca^{2+}-free ND96 solution, pH 7.5) flowed at 3 mL/min (see **Fig. 3.10**). To collect electrophysiological traces in the proprietary software (Clampfit 10.3, Molecular Devices Axon Instruments), we employed a low-pass Gaussian filter at 5 Hz then subtracted the average baseline current preceding application of compound solutions in low-pH buffer. For each cell, peak currents at each concentration were normalized to the maximum TAC [878] measured by applying 3 μM 5-HT in the absence of inhibitor (see **Fig. 3.10**). Normalized currents were then averaged and fitted to the Hill equation (Prism 9, GraphPad Software) in offline analysis. Measurements of IC_{50} for escitalopram, fluoxetine, and their quaternary derivatives were from at least 10 cells, from which the SEM was calculated.

3.2.5. Simulations of Diffusion and Binding

Because of the unexpected slow washout of fluoxetine from PHC (see **Fig. 3.4C-D** and **Fig. 3.5A**), we decided to expand our analysis to investigate the membrane dynamics which could account for this unusual pharmacokinetic property using mathematical modeling. The simulation we employed approximates Fick's first law,

$$J = -D\frac{dc}{dx},$$

(where J is the flux, D is the diffusion coefficient, and the differential equation measures change in concentration as a function of the change in distance) as a sequence of fluxes between nested intracellular and extracellular shell compartments governed by first-order rate constants ($k_f = k_b$) [882]. Each shell is treated as a well-stirred compartment. The units and dimensions are as described previously [882], including µm, fL (µm^3), ms, and molarity (fM, µM, or M). Most shells have thickness 0.495, 0.5, or 0.505 µm; for fluxes between shells, D is the free-solution value. In classical analyses [882], the 'membrane barrier' is not a shell: it is instead infinitely thin and has zero volume. In the model, the 'membrane barrier' is located at a radius of 7.505 µm, and its permeability is represented by a single equal pair of rate constants, $k_f = k_b$, for flux between one pair of neighboring shells. The permeability of the 'membrane barrier' is calculated as though it were a shell of finite volume with a thickness of 0.01 µm, twice the value assumed in a comparable study [883] to account for membrane proteins; it is also calculated as though it were governed by free radial diffusion but reduced by two large multiplicative factors: (a) n_{pH}, which accounts for the reduced availability of the neutral form of fluoxetine (given the difference between the pK_a of fluoxetine and physiological pH), and (b) n_{accum}, the reduction caused by binding to membrane lipids [884]. The factor n_{accum} can be calculated using the ratio (lipid molarity in the shell)/(assumed fluoxetine-lipid K_d); the latter K_d is the most important adjustable parameter (see Chapter 3.3, **Fig. 3.5C**, **Fig. 3.7L**, and **Table 3.1**). Most classical analyses [882] do not consider drug accumulation within the infinitely thin 'membrane barrier' of zero volume. Therefore, we enhanced the classical simulation by including a routine that simultaneously calculates drug accumulation within a ‘membrane shell’ of finite thickness and volume. The composition, thickness, and volume are those used to compute the permeability of the ‘membrane barrier’ above; thus, the ‘membrane shell’ has the lipid molarity and fluoxetine-lipid K_d described above and has a thickness of 10 nm (inner and outer radii at 7.495 and 7.505 μm, respectively). Fluoxetine accumulation, which does not deplete the total number of drug molecules, is calculated by simply multiplying the [fluoxetine] within the ‘membrane shell’ by n_{accum}. The inward-facing border of the ‘membrane shell’ undergoes free diffusion with the next inward shell, as described for all other pairs of adjoining shells. The outer border of the ‘membrane shell’ is the ‘membrane barrier,’ whose permeability is described above. In the simulated results, the waveform of drug concentration within the ‘membrane shell’ is simultaneous with that in the cytoplasm (within ~50 ms). This conceptual scheme is valid only if the concentration source and sink lie outside the ‘membrane barrier,’ allowing accumulation within the ‘membrane shell’ to be influenced by delayed permeation through the ‘membrane barrier.’ A more complete version, also allowing sources and sinks within the cell, would include both a 5 nm thick ‘inner membrane shell’ and a 5 nm thick ‘outer membrane shell,’ flanking the ‘membrane barrier.’ The model was constructed in a graphical user interface (GUI; Simbiology, MATLAB, MathWorks). For our purposes, this interface has heuristic value; but it has the disadvantage that rate constants and shell volumes must be calculated externally. Therefore, we transferred the parameters manually to the GUI from the calculations and assumptions described above in an Excel spreadsheet (**Table 3.1**). The program then integrated the equations to produce drug molarity versus time in each spherical shell (**Fig. 3.5C** and **Fig. 3.7L**). For our purposes, the advantages of this method are: (a) it verifies consistency among the dimensions and units, and (b) it has robust routines for integrating stiff differential equations; while the disadvantages are: (a) it cannot treat surface densities in a compartment of zero volume, and (b) its dosing routines cannot jump the concentration of a source or sink; thus, the wash-in and washout phases were simulated separately (**Fig. 3.5C** and **Fig. 3.7L**).

3.2.6. Total Cellular Accumulation, Intracellular Bioavailability, and Lipid Binding

Atorvastatin Ca^{2+} salt, escitalopram oxalate, fluoxetine hydrochloride, lopinavir, and warfarin (Sigma-Aldrich) were obtained at their highest degree of purity (≥ 98%). Atorvastatin and lopinavir were selected as reference compounds (based on previous characterization) and warfarin was used as an internal standard [885]. Atorvastatin, escitalopram, fluoxetine, lopinavir,

Compartment	**Shell outer radius µm**	**Shell volume μm^3**	**pH Divisor n_{ph}**	**Binding divisor n_{accum}**	**First-order rate constants $k_f = k_b = D_{eff}$* A/thickness μm^3/ms**	**Classical permeability k = D_{eff}/thickness µm/ms**
Cytoplasmic shells	0.5	0.52	1	1	1.26	0.04
	1	3.67	1	1	5.03	0.04
	1.5	9.95	1	1	11.31	0.04
	2	19.37	1	1	20.11	0.04
	2.5	31.94	1	1	31.42	0.04
	3	47.65	1	1	45.24	0.04
	3.5	66.50	1	1	61.58	0.04
	4	88.49	1	1	80.42	0.04
	4.5	113.62	1	1	101.79	0.04
	5	141.90	1	1	125.66	0.04
	5.5	173.31	1	1	152.00	0.04
	6	207.87	1	1	181.00	0.04
	6.5	245.57	1	1	212.37	0.04
	7	286.41	1	1	246.30	0.04
	7.495	326.86	1	1	282.37	0.04
Membrane shell	7.505	7.07	230	208	0.01	8.36E-6
Membrane barrier		n/a			0.01	8.36E-6
Extracellular shells	8	373.98	1	1	324.95	0.04
	8.5	427.78	1	1	363.17	0.04
	9	481.19	1	1	407.15	0.04
	9.5	537.74	1	1	453.65	0.04
	10	597.43	1	1	502.65	0.04
	10.5	660.26	1	1	554.18	0.04
	11	726.23	1	1	608.21	0.04
	11.5	795.35	1	1	664.76	0.04
	12	867.60	1	1	723.82	0.04
	12.5	943.00	1	1	785.40	0.04
	13	1021.54	1	1	849.49	0.04
	13.5	1103.22	1	1	916.09	0.04
	14	1188.04	1	1	985.20	0.04
	14.5	1276.01	1	1	1056.83	0.04
	15	1267.12	1	1	1130.97	0.04
	15.5	1461.36	1	1	1207.63	0.04

Table 3.1. Several columns with intermediate calculations are hidden. The workbook, an .xlsx file, is available at https://github.com/lesterha/lesterlab_caltech. The lipid molarity (0.416 M) is calculated from the usual assumption that each membrane leaflet has a lipid density of 2.5 million molecules/μm^2 [886]. The assumed fluoxetine-lipid K_d is the most important adjustable parameter; for the PHC simulation, the value of 2.2 mM produces a half time of 251 s and is consistent with the measured value of "≥ 100 µM" [545]. (In the worksheet for HeLa, K_d has the value of 22 mM.) The membrane barrier comprises a set of two equal rate constants, as though it were physically located at 7.505 µm. Varying the assumed membrane shell thickness over a threefold range changed the simulated kinetics by 10% because the structure of the model has compensatory changes in several parameters.

and warfarin were made as stocks in dimethyl sulfoxide (DMSO; ≥ 2 mM). Total accumulation ratio (K_p) was measured as described previously [545] but over a series of time points. HEK293 cells were seeded at passage 14 at 6 x 10^5 cells/mL on 24-well plates (Cellbind, Corning) in DMEM with L-glutamine and 10% FBS. At confluence, each well was washed twice with HBSS and incubated with 200 µL of HBSS containing 0.5 µM of compound for 30-120 min at 100 rpm. At each time point, the outside medium was sampled before washing the cells with HBSS and extracting the intracellular compound using ACN/water (60/40) for 15 min at 500 rpm. Protein content was quantified in representative wells using a Pierce BCA assay kit (Thermo Fisher Scientific). K_p, the intracellular compound accumulation, was calculated according to

$$K_p = \frac{A_{cell}/V_{cell}}{C_{medium}},$$

where cellular volume (V_{cell}) was calculated assuming 6.5 µL/mg protein [542,545], A_{cell} is the amount of compound inside cells (in fmol), and C_{medium} is the concentration in the surrounding medium (in nM). Experiments were carried out in triplicate on three independent occasions. Compounds were quantified via UPLC-MS (Acquity UPLC 399 coupled to a Xevo TQ-S micro MS, Waters) and data were plotted using software (Prism 9). Binding to lipid-coated beads was measured with a proprietary kit (TRANSILXL Intestinal Absorption Kit, Sovicell) as outlined previously [545]. Phosphatidylcholine (PC)-coated silica beads and 5 µM drug were incubated for 12 min in an orbital shaker, after which the beads were centrifuged at 750 rpm for 10 min before the supernatant was sampled. Experiments were carried out in triplicate at three independent occasions and compounds were quantified by LC-MS/MS. The $f_{u,lipid}$ metric, representing the fraction of unbound compound, was then calculated using the equation

$$f_{u,lipid} = \frac{C_{buffer}}{C_{buffer} + C_{membrane}},$$

where C_{buffer} is the supernatant concentration and $C_{membrane}$ is calculated using the mass balance equation $C_{membrane} = (C_{buffer} \cdot V_{buffer}) / (V_{membrane})$, with lipid membrane volume equal to 90 µL [545]. D_L, an optimized dilution factor determined by minimizing the sum of the squared prediction errors (Microsoft Excel, Solver add-in), was used to scale $f_{u,lipid}$ to $f_{u,cell}$, the predicted intracellular fraction of unbound compound, according to the equation

$$f_{u,cell} = \frac{1}{D_L \cdot \left(\frac{1}{f_{u,lipid}} - 1\right) + 1} \text{ [885].}$$

Intracellular bioavailability, F_{ic}, was calculated from the experimentally determined K_p and $f_{u,cell}$ values using the equation

$$F_{ic} = K_p \cdot f_{u,cell} \text{ [887].}$$

Analysis of sampled fluids was performed using UPLC-MS. Chromatographic separation was achieved using a column measuring 2 x 50 mm (Waters 1.7 µm C18 BEH) with a gradient of 5% to 95% mobile phase B (0.1% formic acid in 100% ACN) in mobile phase A (0.1% formic acid in LC-MS grade water) over a runtime of 2 min. The flow rate was 0.7 mL/min and 7 µL of sample was injected per run. In ESI+ ionization mode, the UPLC-MS parameters listed in **Table 3.2** were used. Data were preprocessed using proprietary software (MassLynx and TargetLynx 4.2, Waters).

Compound	**Retention time (min)**	**Parent (m/z)**	**Daughter (m/z)**	**Cone voltage (V)**	**Dwell time (s)**	**Collision energy (V)**
Atorvastatin	1.54	559.3487	440.2340	14	0.164	20
Escitalopram	1.25	325.0489	108.8380	22	0.025	26
Fluoxetine	1.33	310.1700	148.0700	36	0.110	8
Lopinavir	1.59	629.5000	155.1000	22	0.025	46
Warfarin	1.50	309.1662	163.1476	34-40	0.110-0.025	15-16

Table 3.2. Mass spectrometry parameters for chemical detection of compounds used in HEK cell and lipid-coated bead assays (m/z = mass over charge ratio).

3.3. Results

3.3.1. Generation of Sensitive and Specific iSSRISnFRs

The purified protein concentration-response relations for the optimized iSSRISnFRs are: iEscSnFR – EC_{50} = 4.5 ± 0.2 µM, $\Delta F_{max}/F_0$ = 16 ± 0.3, S-slope = 3.6; iFluoxSnFR – EC_{50} = 8.7 ± 0.2 µM, $\Delta F_{max}/F_0$ = 9.2 ± 0.1, S-slope = 1.1. (**Fig. 3.1A**). Both cDNA sequences have been deposited in an online database (AddGene #182807-182808). We then characterized specificity for their respective target drugs versus a panel of related antidepressants, antidepressant metabolites, and nicotinic agonists employing the concentration-response scheme described previously (**Fig. 3.1B-C**). iEscSnFR had greater fidelity for its drug partner, binding few drugs in our panel except for choline (EC_{50} = 140 ± 20 µM, ~10-fold above endogenous levels [888-890]; **Fig. 3.1B**). In contrast, iFluoxSnFR detected several compounds with EC_{50} values between 32-

170 µM, concentrations higher than those relevant for clinical purposes. iFluoxSnFR detected norfluoxetine, the breakdown product of fluoxetine, with an EC_{50} of 63 ± 20 µM, demonstrating

A

Informal Name	iSnFRbase ID	Primary Drug of interest	$\Delta F_{max}/F_0$	EC_{50} (µM)	S-slope	Residues Mutated vs. Parent Constructs			
						391	395	436	455
iNicSnFR3b	007	nicotine/ACh	10	19	0.5	F	G	W	A
iEscSnFR	165	escitalopram	16 ± 0.3	4.5 ± 0.2	3.6	-	-	-	E
iAChSnFR	008	ACh	12	1.3	9.2	F	G	W	G
iFluoxSnFR	019	fluoxetine	9.2 ± 0.1	8.7 ± 0.2	1.1	H	S	S	-

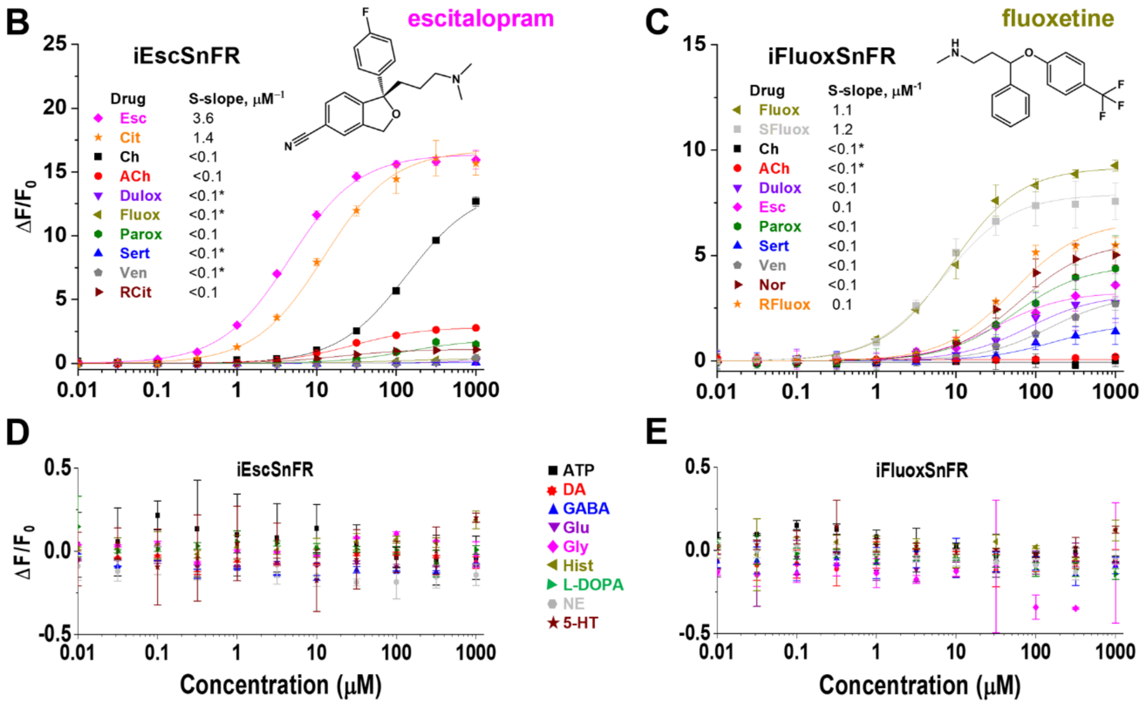

Figure 3.1. *(A)* iSSRISnFR development and concentration–response relations versus final and parent constructs. (Data for iAChSnFR from [678]; data for iNicSnFR3b from [533]). *(**B** and **C**)* Concentration-response relations of purified iEscSnFR (***B***) and iFluoxSnFR (***C***) versus a drug panel (Ch = choline, Dulox = duloxetine, Parox = paroxetine, Sert = sertraline, Ven = venlafaxine, RCit = R-(-)-citalopram, Cit = racemic citalopram, Nor = norfluoxetine; RFluox, R-(+)-fluoxetine; SFluox, S-(-)-fluoxetine; the *Insets* show relevant S-slope values for each iSSRISnFR. (Dashed lines indicate concentration–response relations that did not approach saturation for the concentration ranges tested; therefore, EC_{50} and $\Delta F_{max}/F_0$ could not be determined.) *(**D** and **E**)* iEscSnFR (***D***) and iFluoxSnFR (***E***) show little or no fluorescence response to all endogenous molecules tested (Glu = glutamate, Gly = glycine, Hist = histamine, L-DOPA = levodopa).

that iFluoxSnFR has an eight-fold preference for binding fluoxetine over its primary metabolite. iFluoxSnFR shows no binding to ACh and choline (**Fig. 3.1C**). The relative selectivity of each biosensor for its partner compound indicates a structure-function relationship that differs from that of the interaction between hSERT and SSRIs: while hSERT can bind to multiple SSRIs, each iSSRISnFR binds preferentially to only one SSRI. We also performed concentration-response experiments with iEscSnFR and iFluoxSnFR against a panel of nine endogenous molecules and their precursors (**Fig. 3.1D-E**). Neither iEscSnFR nor iFluoxSnFR showed any response to the selected compounds distinguishable from background.

3.3.2. Thermodynamics and Reaction Kinetics of iSSRISnFRs

To examine the thermodynamics of the iSSRISnFR-SSRI interaction, we conducted ITC experiments (**Fig. 3.2A**). The experimentally determined K_d of iEscSnFR, 3.4 ± 0.1 μM, was within 1.5 times of the experimentally determined EC_{50} in purified protein, 4.5 ± 0.2 μM (**Fig. 3.2B**). However, the low aqueous solubility of fluoxetine led to distortions in the evolved heats due to turbulent injections, even after multiple attempts with various solvation schemes (including the addition of 0.1% DMSO). Consequently, we performed ITC for iFluoxSnFR with N,N-dimethylfluoxetine (see Chapter 3.2.1). The experiments produced an experimentally determined K_d of 28.1 ± 3.7 μM, approximately twice the experimentally determined EC_{50} of iFluoxSnFR for N,N-dimethylfluoxetine, 14 ± 0.4 μM (see **Fig. 3.8**). The ITC data imply that the EC_{50} for fluorescence in iEscSnFR and iFluoxSnFR is dominated by the overall binding of the corresponding ligand as both are largely driven by changes in entropy (ΔS; **Fig. 3.2B**). Our stopped-flow apparatus allowed for experiments with millisecond resolution to measure the time course of fluorescent iSSRISnFR responses to various concentrations of target drug (**Fig. 3.2C-D**). These data show the trajectory of the ligand-sensor reaction as it relaxes to a new equilibrium after a sudden step up in ligand concentration, with different relaxation characteristics contingent on the concentration of drug applied. For both sensors, most of the fluorescence change occurred within the first second, with an exponential time course (**Fig. 3.2C-D**, upper left panels). An additional smaller and slower exponential fluorescence increase continued over the next 100 s (**Fig. 3.2C-D**, upper right panels). In the 1 s stopped-flow experiments, the rate constants for the fluorescence relaxation (k_{obs}) were a hyperbolic function of ligand concentration (**Fig. 3.2C-D**, lower panels). For escitalopram binding to iEscSnFR, the zero-concentration intercept was 1.8 ± 0.1 s^{-1} and k_{obs} was half-maximal at 7.7 ± 0.5 μM. We fitted the data to a three-state kinetic mechanism: the apo (no drug) state, a drug-bound nonfluorescent state, and a rate-limiting conformational change to the fluorescent state. These assumptions predicted an overall steady-

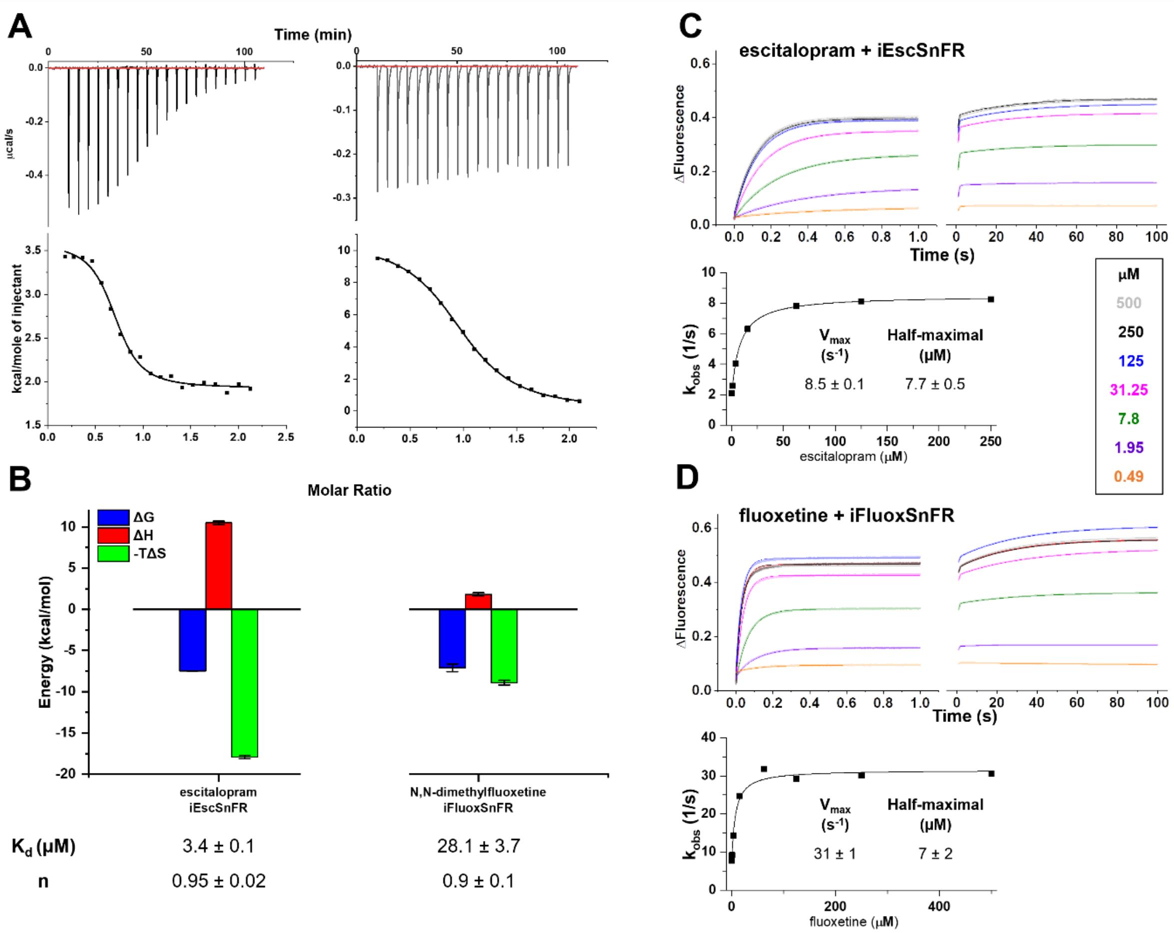

Figure 3.2. ***(A)*** Exemplar heat traces of iEscSnFR paired with escitalopram and iFluoxSnFR paired with N,N-dimethylfluoxetine as obtained by ITC (*top row*); the heats for iEscSnFR and iFluoxSnFR were endothermic. The resulting fits (*bottom row*) for each iSSRISnFR:SSRI pair from the integrated heats comprising each series of injections. ***(B)*** In energy calculations from the above ITC traces and fits, both iSSRISnFRs show exergonic reactions, but the relative enthalpic and entropic contributions differ. Affinity (K_d) and occupancy number (n) were also calculated (*bottom table*). (***C and D***) Stopped-flow fluorescence data for various concentrations of iEscSnFR (***C***) and iFluoxSnFR (***D***) recorded for periods of 1 and 100 s at sampling rates of 1 ms and 1 s, respectively. Fluorescence was activated at time 0 by mixing agonist and sensor protein as noted. iEscSnFR and iFluoxSnFR data are fit to single exponentials. Plots of the exponential rate constants (k_{obs}) versus [ligand] are shown for the 1 s data.

state EC_{50} of 1.7 ± 0.3 μM, compared to the value of 4.5 μM obtained with concentration-response experiments on iEscSnFR in purified protein (**Fig. 3.1A**). For fluoxetine binding to iFluoxSnFR, the zero-concentration intercept was 6.2 ± 1.5 s^{-1} and k_{obs} was half-maximal at 7 ± 2 µM. The three-state mechanism predicted an overall steady-state EC_{50} of 1.3 ± 0.7 µM, compared to the value of 8.7 µM obtained with concentration-response experiments on iFluoxSnFR in purified protein (**Fig. 3.1A**). The half-maximal amplitudes and rate constants for the 100 s experiments occurred at ligand concentrations in the same concentration range as those for the 1 s experiments. This observation is consistent with the suggestion that the intense excitation beam in the stopped-flow apparatus produces further photoactivation in the fluorescent state when the protein is exposed to light for long periods of time.

3.3.3. Characterization of iSSRISnFRs in Primary Culture

All AAV vector plasmid sequences have been deposited in an online database (AddGene #182818-182823). The iSSRISnFRs were targeted to the PM (iSSRISnFR_PM), the ER (iSSRISnFR _ER), or the cytoplasm (iSSRISnFR _cyto) as described in Chapter 2.2.5. Spinning-disk confocal microscopy was performed as described in Chapter 2.2.6 and showed targeting to the intended organelle or compartment (**Fig. 3.3**): ER-targeted biosensor was retained in the ER [533,544,684]; iSSRISnFR targeted to the PM showed correct localization, with sensor

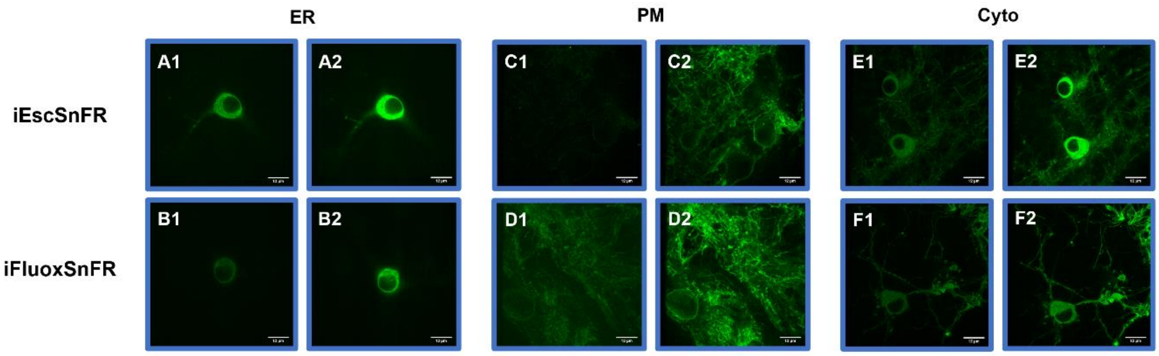

Figure 3.3. (***A-B)*** ER-targeted constructs of iEscSnFR and iFluoxSnFR are shown before (*A1*, *B1*) and during (*A2*, *B2*) exposure to each drug partner at 10 µM. ER-targeted iSSRISnFRs show the eponymous reticulated pattern, and fluorescence is excluded from the nucleus. (***C-D***) The PM-targeted versions of each are shown before (*C1*, *D1*) and during (*C2*, *D2*) drug introduction. Localization in the PM is robust, with some minimal puncta that may represent inclusion bodies or internal transport. ***(E-F)*** Cytoplasm-targeted constructs are shown before (*E1*, *F1*) and during (*E2*, *F2*) exposure to each drug partner. The cytoplasm-targeted iSSRISnFRs shows correct expression.

expression likewise seen in the cell interior but minimally so; the cytoplasm-targeted constructs was excluded from the nucleus and appeared in both soma and dendrites. We then performed concentration-response experiments in PHC as described in Chapter 2.2.6 using wide-field fluorescence imaging with each iSSRISnFR and its drug partner, sampling a range of concentrations approximately an order of magnitude above and below the EC_{50} as determined for the purified protein (**Fig. 3.4**). iEscSnFR showed a robust response to escitalopram at the PM and the ER across a range of concentrations from 0.1–31.6 µM, and the speed was nearly limited by solution changes; there was a clear return to baseline fluorescence after each drug application on the order of seconds (**Fig. 3.4A**). A $\Delta F_{max}/F_0$ value of ~2 was reached at 31.6 µM with the iEscSnFR_ER construct while the $\Delta F/F_0$ value for the _PM construct appeared ~10% lower at

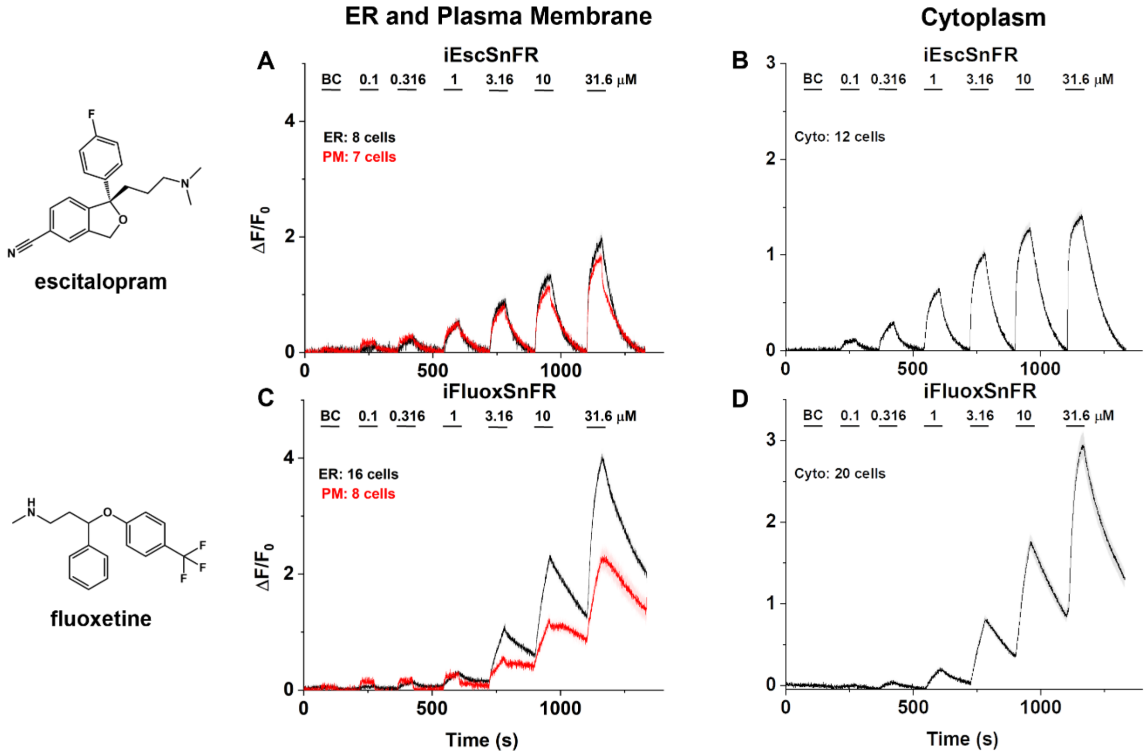

Figure 3.4. ***(A-D)*** Each iSSRISnFR detects its drug partner at the ER, PM, or cytoplasm (cyto) of PHC at the concentrations sampled; drugs were applied for 60 s pulses between 120–150 s washout intervals (BC = HBSS buffer control; SEM of data are indicated by semitransparent shrouds around traces as described in Chapter 2.2.6). ***(A-B)*** iEscSnFR fluorescence approaches a plateau during the application before returning to baseline fluorescence during the washout at all targeted locations. ***(C-D)*** iFluoxSnFR detection of fluoxetine has not yet reached a plateau during application periods and also shows an incomplete washout with no return to baseline fluorescence afterward in every targeted location.

concentrations above 1 μM, a phenomenon we had not encountered in any of our previous work (more drug should reach the outer surface of the PM than the inside of the ER). In contrast, while both the iFluoxSnFR_ER and iFluoxSnFR_PM constructs detected fluoxetine across the same concentration range, the $\Delta F/F_0$ had not begun to plateau to a maximum value even after 60 s of drug application at concentrations of 1 μM and higher (**Fig. 3.4C**), demonstrating that responses to fluoxetine wash-in and washout were much slower than solution changes for both constructs (on the order of hundreds of seconds). We also observed that the $\Delta F/F_0$ of iFluoxSnFR_ER was about twofold higher than iFluoxSnFR_PM at concentrations of 3.16 μM and higher. Concentration-response experiments in PHC with iSSRISnFR_cyto constructs demonstrated fluorescence dynamics for escitalopram and fluoxetine similar to those obtained when the sensor was targeted to the PM and ER (**Fig. 3.4B**, **D**). To further examine the slow kinetics of fluoxetine, we recorded the fluorescence waveforms at 1 μM with an extended application time of 10 min and a washout time of 12 min (**Fig. 3.5A**). For the PM, the kinetics clearly showed two components: the faster component represented ~10% of the total change and is indistinguishable from the solution change, while the slower component had time constants for both the wash-in and washout of over 250 s. After a 12 min washout, both the iFluoxSnFR_PM and _ER construct fluorescence signals neared baseline values, indicating that full washout of fluoxetine can be achieved, but on a time scale nearly a log unit slower than for drugs such as nicotine and ketamine and two times slower than cytisine [533,544,684,685]. To confirm that the iFluoxSnFR_PM and _ER constructs functioned as expected, and to ensure that the extended kinetics of fluoxetine we observed in PHC was not the result of idiosyncratic biosensor function or folding in neurons, we tested both versus escitalopram; serendipitously, iFluoxSnFR binds escitalopram in the same concentration range as fluoxetine (though right shifted and with lower $\Delta F/F_0$; **Fig. 3.1C**). We thus performed concentration-response imaging of 0.1–31.6 μM escitalopram with iFluoxSnFR_ER and _PM in PHC (**Fig. 3.5B**). These escitalopram waveforms resembled iEscSnFR detecting escitalopram in PHC (**Fig. 3.4A**), confirming that iFluoxSnFR_ER and _PM function as expected. Thus, the slower kinetics of fluoxetine arises from a property inherent to the interaction between fluoxetine and the PHC.

3.3.4. Estimating Fluoxetine Accumulation in the Neuronal Membrane

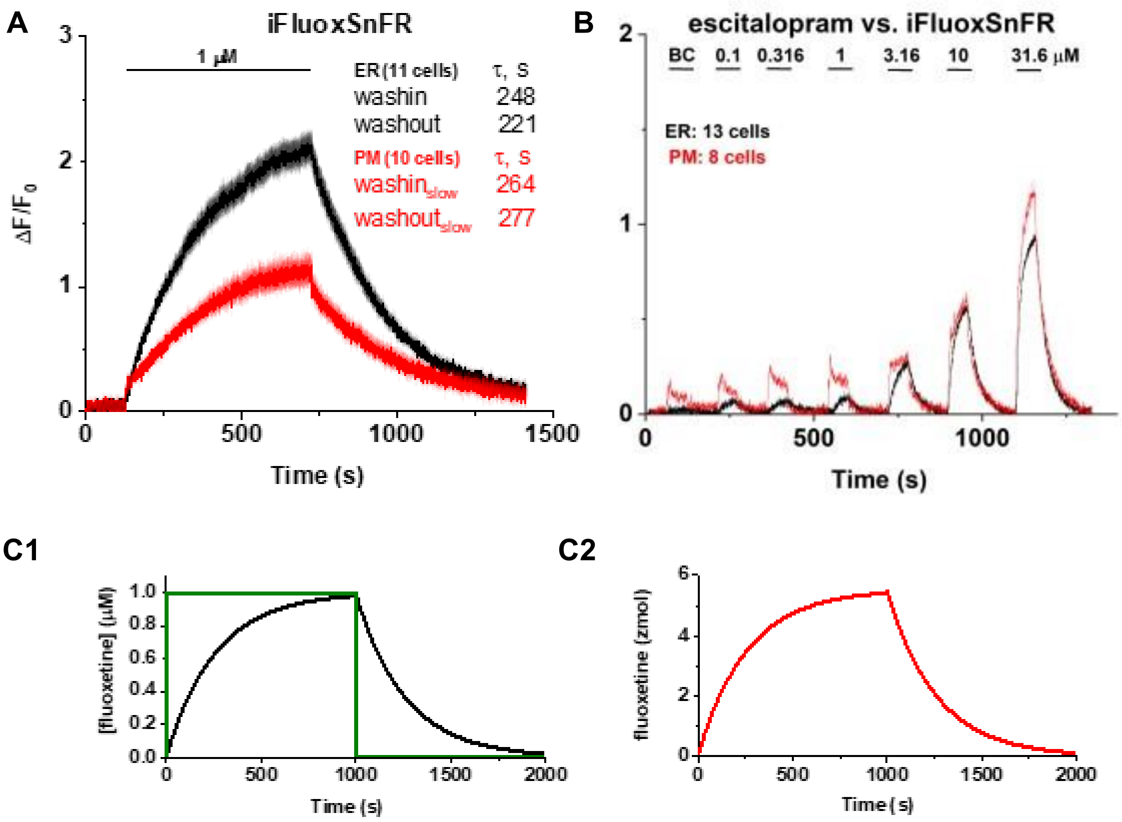

Figure 3.5. ***(A)*** A relatively long application time (600 s) of 1 µM fluoxetine allowed ER- and PM-targeted iFluoxSnFR detection of 1 µM fluoxetine to approach a maximum $\Delta F/F_0$, and a slightly longer (720 s) washout allowed a return to baseline fluorescence for both ER- and PM-targeted iFluoxSnFR. (Time constants for the slower phase are given as τ (s); SEM of data are as described previously). ***(B)*** A control experiment reporting concentration–response relations for escitalopram against iFluoxSnFR (SEM of data are as described previously). iFluoxSnFR detects escitalopram at both the PM and ER. Escitalopram enters and exits the ER with a return to baseline fluorescence during the washout, a direct contrast to the behavior of fluoxetine as detected by iFluoxSnFR. ***(C)*** Simulations of fluoxetine in the extracellular space, PM, and cytoplasm of a spherical cell. (*C1*) The green trace gives the applied (clamped) [fluoxetine] in a shell 11.5 µm from the center of the cell; the concentration is first stepped from 0 to 1 µM for 1000 s and then stepped back to zero. The concentrations in all extracellular shells (between the 11.5 µm shell and the PM shell at 7.5 µm) equilibrate within ~50 ms and are indistinguishable from the applied concentration on this time scale. The black trace gives the cytoplasmic [fluoxetine] within the shell of outer radius of 7.495 µm (10 nm below the PM). The concentrations in all other intracellular shells show a dispersion of ~50 ms and are indistinguishable from the black trace on this time scale. The intracellular [fluoxetine] resembles that of ***A***. (*C2*) Moles of fluoxetine bound within the simulated membrane shell. With the parameters given in **Table 3.1**, the time course of PM-bound fluoxetine is indistinguishable from that of intracellular [fluoxetine] and resembles that of **A**.

That the fluoxetine signals show wash-in and washout time constants of 200-300 s at both the ER and PM led us to suspect the existence of (a) local binding site(s) that delay(s) the appearance and disappearance of fluoxetine near neurons; a related phenomenon is termed ‘buffered diffusion’ [891]. While slow washout from ER-targeted constructs is not without precedent, as is the case with both cytisine and its fluorinated derivative [684] (see Chapter 4), what was surprising in our application of fluoxetine in PHC was the slow washout of drug from the PM, a phenomenon heretofore unobserved in any live-cell imaging experiments of iDrugSnFRs. We based our analysis on the unusually high pharmacokinetically defined V_d exhibited by all SSRIs (see Chapter 1.5). Basic compounds can accumulate within the body via drug partitioning into membrane lipids and acid trapping within low-pH organelles [536] (see Chapter 1.5). Because both escitalopram and fluoxetine have calculated pK_a = ~9.8, the effect caused by their protonation at physiological pH (see Chapter 1.5) is expected to decrease the effective diffusion constant (n_{pH}) by at least two orders of magnitude [882]. Recent studies show how membrane partitioning of basic molecules plays a role in some molecular and cellular bases of V_d [545,892,893]: the nitrogen interacts with the phospholipid head groups while the less polar moieties interact with the fatty acid tails [883,893]. The equilibrium parameters of such accumulation have been estimated by direct measurements on membrane-coated beads (see Chapter 3.3.9), by ITC, and by perturbation of gramicidin gating [545,883]; however, the kinetics of this accumulation are relatively unstudied and may be revealed for the first time by our measurements (**Fig. 3.4C-D** and **Fig. 3.5A**). We were able to simulate the slow wash-in and washout kinetics of fluoxetine (**Fig. 3.5C**) by assuming that the extracellular facing iFluoxSnFR_PM partially measures membrane-bound fluoxetine as it increases or decreases in response to given concentrations. We suggest that the unique signals produced by fluoxetine with iFluoxSnFR_PM arise from two facts: first, if the high V_d of fluoxetine arises from membrane accumulation, then this accumulation exceeds the aqueous concentration by orders of magnitude (we supply an estimate below); second, PBPs from bacteria and archaea are specialized to transfer ligand directly to membrane-embedded transporters that are adjacent (within just a few angstroms) to their PBP binding site [894,895], in contrast to the several μm-thick unstirred layer inferred from ITC measurements on the fluoxetine-lipid interface [883]. With the unique sensing assumption discussed above, we modeled the fluoxetine measurements by assuming that the effective diffusion coefficient is reduced further by lipid binding within the membrane [884]; **Table 3.1** gives our assumptions for the better-characterized underlying parameters. The most important adjustable parameter is the binding constant (K_d) for the lipid-fluoxetine interaction, and the only available measurement is “at least 100 μM” [885]. Because we treat membrane permeation as a single first-order process orders of magnitude slower than diffusion in the cytoplasm and extracellular solution, the simulation predicts exponential kinetics. The experimentally measured time constant of 200-300 s (**Fig. 3.5A**) was explained by a K_d of 2.2 mM. The extent of membrane accumulation is therefore equal to (lipid molarity in the shell)/(fluoxetine-lipid K_d), or 181-fold higher than the free solution value of fluoxetine.

3.3.5. Measuring Fluoxetine Accumulation in Acidic Vesicles

Acid trapping within low-pH organelles has been suggested to occur for nicotine, antipsychotics, ketamine, and other weakly basic drugs [531,537,715,719,885,896]. We simulated fluoxetine accumulation within synaptic vesicles, using a theory that includes pK_a, the LogP of the neutral and protonated forms, the diameter of the vesicle, and corrections for ionic strength (**Fig. 3.6A**) [897]. The simulations suggest that the accumulation occurs on a time scale of several hundred seconds, amounting to a ~100-fold higher concentration than the extracellular solution. Because present iDrugSnFRs do not function at pH < ~6.5 [533,544,685], we could not measure SSRIs directly within the lumen of acidic vesicles. We therefore resorted to indirect measures involving transient modification of the signals measured in other compartments. We first tested for vesicular accumulation by blocking vesicular ATPase with folimycin (see Chapter 3.2.3); we found little to no effect of such blockade (**Fig. 3.6B**). Several spinning-disk confocal microscope images revealed that the PM-targeted iSSRISnFRs had brightest signals near synapses (e.g. **Fig. 3.3D1-D2**); therefore, we sought a method to test for accumulation within synaptic vesicles. In time-resolved images with the wide-field epifluorescence microscope (see Chapter 2.2.6), we compared data from ROIs that included primarily neurites or primarily somata (**Fig. 3.6C**) and found no significant differences between the two sets of ROIs (**Fig. 3.6D**). Because the endolysosomal compartment represents only ~1% of the cytosol, drug accumulation in synaptic vesicles or other acidic vesicles is not expected to temporally distort the signals we measured. Therefore, the set of experiments to test for fluoxetine accumulation in acidic vesicles has given uninformative results.

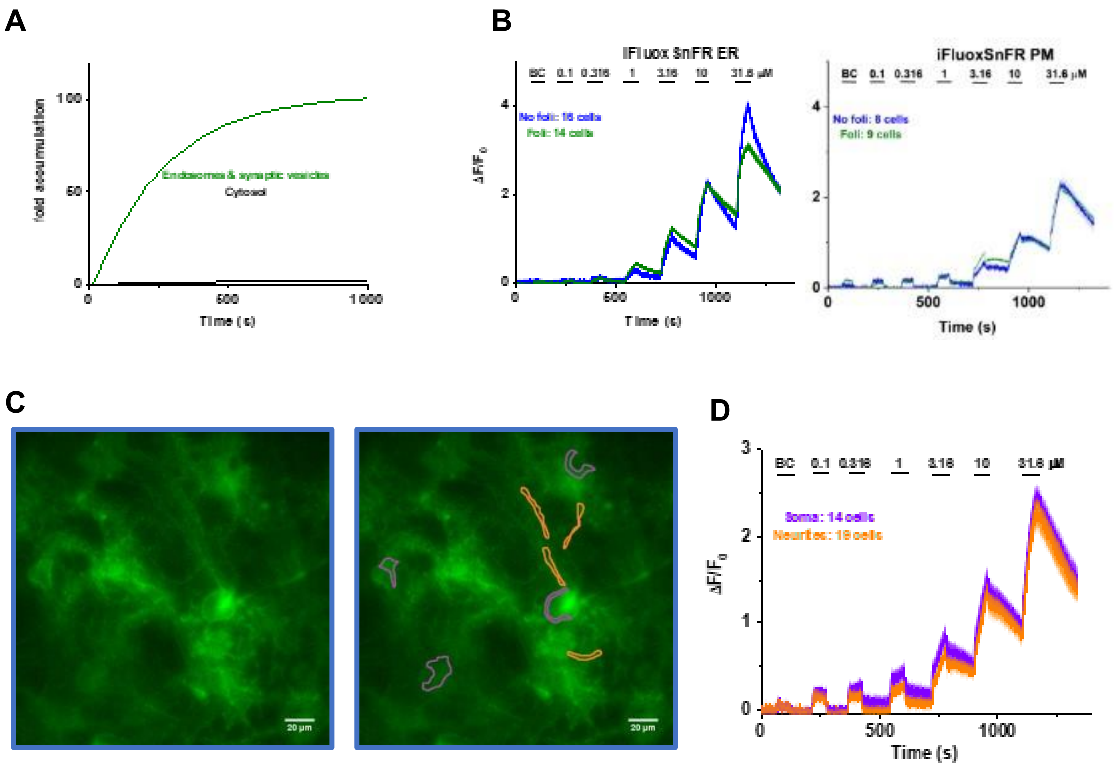

Figure 3.6. ***(A)*** Predicted accumulation of fluoxetine in synaptic vesicles and/or endosomes (green; pH 5.5) versus cytosol (black; pH 7.2). The extracellular solution has an assumed pH of 7.4. We assume the following: the cell and vesicles have a diameter of 8 µm and 100 nm, respectively; fluoxetine has a pK_a of 9.8; the neutral form has LogP of 4.1; and the charged form has a 7.5-unit-smaller LogP. (The workbook that performs the calculations is posted at https://github.com/lesterha/lesterlab_caltech.) ***(B)*** Pretreatment of PHC with 80 nM folimycin (foli) does not substantially alter the concentration–response relations or waveforms for iFluoxSnFR_ER or _PM against fluoxetine versus untreated neurons in a side-by-side experiment. ***(C)*** A typical field of PHC expressing iFluoxSnFR_PM. Orange outlines show ROIs for four neurite regions; purple lines show ROIs for four somatic regions. ***(D)*** Waveforms (mean with SEM as described previously) for all ROIs analyzed in ***C***. There was no substantial difference between neurite and somatic fluoxetine responses.

3.3.6. Characterization of iSSRISnFRs in HeLa Cells

All mammalian vector plasmid sequences have been deposited in an online database (AddGene #182812-182817). We designed iSSRISnFRs targeted to the PM, ER, and cytoplasm for expression in mammalian cells as described in Chapter 2.2.5. As with the iSSRISnFRs in PHC, we imaged transfected HeLa cell cultures using a spinning disk laser microscope (**Fig. 3.7A-C, F-H**). Localization of the biosensor resembled previously described iDrugSnFR _PM and _ER

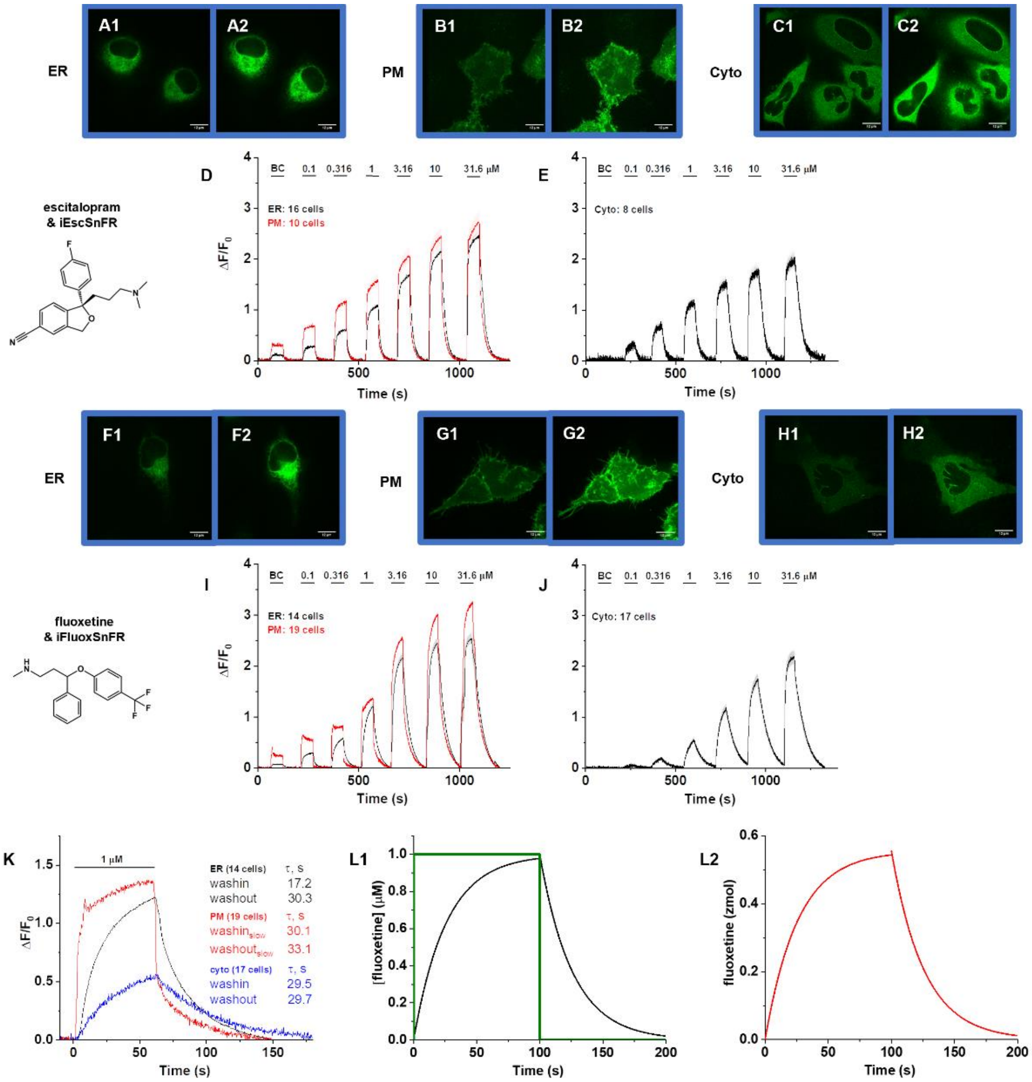

Figure 3.7. ***(A-C, F-H)***, ER-targeted (***A***, ***F***), PM-targeted (***B***, ***G***), and cytoplasm-targeted (***C***, ***H***) constructs of iEscSnFR and iFluoxSnFR are shown before (*A1*, *B1*, *C1*, *F1*, *G1*, *H1*) and during (*A2*, *B2*, *C2*, *F2*, *G2*, *H2*) exposure to 10 μM of target drug; all three demonstrate compartmental localization as in PHC (**Fig. 3**). ***(D, E, I, J)*** Drugs were applied for 60 s pulses at 90–120 s intervals. Each iSSRISnFR detects its drug partner at the PM, ER, and cytoplasm of HeLa cells at the concentrations sampled. (SEM of data is as described previously.) Both iEscSnFR (***D***, ***E***) and iFluoxSnFR (***I***, ***J***) demonstrate wash-in plateaus and return to baseline during washout for sensors targeting all three compartments. (***K***) Superimposed waveforms for a 60 s pulse of 1 μM fluoxetine vs. iFluoxSnFR targeted to the ER, PM, and cytoplasm in HeLa cells. Tabular values give the time constants (τ) of each phase for ER and cytoplasm as well as the time constants for the slower phase at the PM. (***L***) Simulations of [fluoxetine] within intracellular shells; all intracellular shells superimpose on this time scale. (*L1*) Green and black traces are the same as in the previous simulation (**Fig. 3.5C**) except that we set the fluoxetine-lipid Kd = 22 mM. (*L2*) Simulated accumulation of fluoxetine within the membrane shell, corresponding to the slower phase of ***K*** for the PM-localized sensor.

constructs [533,544,684,685] and the localization pattern of iEscSnFR and iFluoxSnFR in PHC imaging (**Fig. 3.3**). We performed concentration- response imaging experiments in HeLa cells using wide-field fluorescence imaging with each iDrugSnFR and its drug partner, applying the same concentrations as in PHC (**Fig. 3.7D-E, I-J**). Response in HeLa cell showed larger $\Delta F/F_0$ across all concentrations sampled for the _PM, _ER, and _cyto constructs compared to their performance in PHC (**Fig. 3.4**), likely because the thin HeLa cells have little endogenous fluorescence and therefore relatively smaller F_0. iEscSnFR showed a robust response to escitalopram at the PM, ER, and cytoplasm of HeLa cells across a range of concentrations from 0.1-31.6 µM and the fluorescence response was nearly limited by solution exchanges. At 31.6 µM, the PM had $\Delta F/F_0$ of ~2.75, while the ER had $\Delta F/F_0$ of ~2.5; at concentrations below this value, the ER had ~30–80% of the PM signal, a typical difference seen when a drug crosses multiple membranes (**Fig. 3.7D**). The _cyto construct had a maximal $\Delta F/F_0$ of ~2 at 31.6 µM. The iFluoxSnFR_PM construct demonstrated response across the same concentration range and a maximum $\Delta F/F_0$ of ~3.25 at 31.6 µM, while the _ER construct displayed ~50–80% of the signal seen in the PM construct (**Fig. 3.7I**). The _cyto construct had a maximal $\Delta F/F_0$ of ~2.25 at 31.6 µM. iFluoxSnFR targeted to the PM, cytoplasm, or ER in HeLa cells showed wash-in and washout kinetics characteristics that were slower than the solution changes but ~10-fold more rapid than seen in PHC. At 1 µM fluoxetine (**Fig. 3.7K**), the _ER and _cyto constructs displayed single exponential kinetics, as in the neuronal cultures. The iFluoxSnFR_PM construct showed two phases during the wash-in and washout periods, similar to the performance of the construct expressed in PHC; the faster phase was indistinguishable from the solution change, but it accounted for ~80% of the waveform, in contrast to the ~10% in PHC. We simulated the slower phase of fluoxetine kinetics in HeLa cells using the diffusion-binding model (**Fig. 3.7L**) described previously (see Chapter 3.2.5). We assumed that fluoxetine accumulation in the membrane is governed by a fluoxetine-lipid K_d of 22 mM, or ~10-fold weaker than in PHC. This assumption of weaker membrane accumulation may also explain how the iFluoxSnFR_PM signal is dominated by the [fluoxetine] in the extracellular solution, with only a small contribution from fluoxetine accumulated in the PM (as opposed to the relatively larger contribution made by PM lipid binding in PHC experiments).

3.3.7. Cellular Experiments with Impermeant Quaternary SSRI Derivatives

In solutions with purified iSSRISnFR protein, the $\Delta F_{max}/F_0$ of iEscSnFR with N-methylescitalopram and escitalopram was nearly identical at ~16, but iEscSnFR had an approximately twofold lower EC_{50} for N-methylescitalopram (4.1 ± 0.1 µM vs. 1.8 ± 0.2 µM; **Fig. 3.8A**). iFluoxSnFR detected N,N-dimethylfluoxetine with a $\Delta F_{max}/F_0$ of 5.0 ± 0.1, which

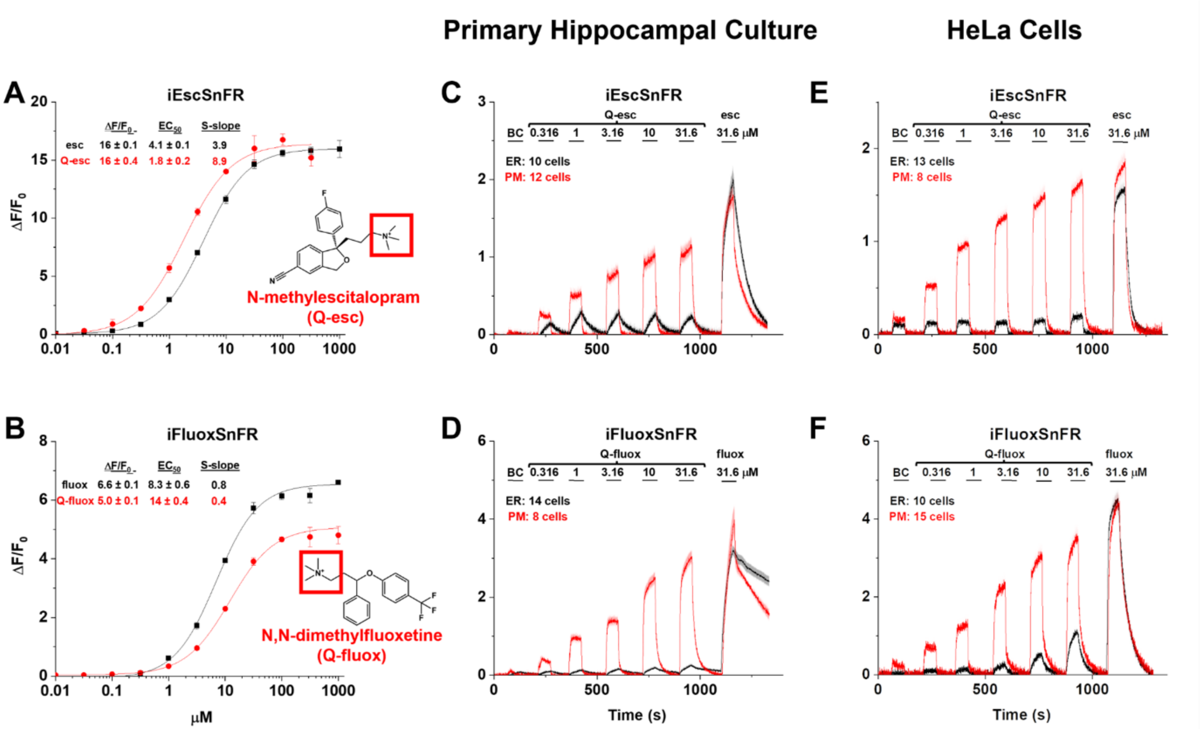

Figure 3.8. ***(A-B)*** Concentration-response relations of purified iSSRISnFRs against Q-SSRI derivatives (Q-esc = N-methylescitalopram; Q-fluox = N,N-dimethylfluoxetine). ***(C–F)*** Each iSSRISnFR detects its target Q-SSRI at the concentrations used in PHC and HeLa cells. (SEM of data as described previously.) Drugs were applied for 60 s pulses at 90–120 s intervals to cells expressing _ER or _PM constructs (***C***, ***E***). iEscSnFR_PM detects the presence of Q-esc, approaching a plateau during application before returning to baseline during the washout; in contrast, iEscSnFR_ER is unable to detect Q-esc. A control concentration of escitalopram (final application) is detected by both the PM- and ER-targeted constructs. (***D***, ***F***) iFluoxSnFR_PM detects Q-fluox, nearly approaching a plateau during application and with a return to baseline during the washout. In contrast, iFluoxSnFR_ER in PHC does not detect Q-fluox, and iFluoxSnFR_ER in HeLa cells detects Q-fluox above BC only at concentrations above 10 µM. A control concentration of fluoxetine (final application) is detected by both the PM- and ER-targeted constructs. (Application of fluoxetine in PHC reproduces the slowly increasing rising phase and the extended washout observed in **Fig. 3.4C-D**.)

was lower than that for fluoxetine (6.6 ± 0.1), while the EC_{50} of iFluoxSnFR for N,N-dimethylfluoxetine demonstrated an approximate two-fold shift in affinity (14 ± 0.4 µM vs. 8.3 ± 0.6 µM; **Fig. 3.8B**). In concentration-response imaging experiments with the quaternary SSRI (Q-SSRI) derivatives in PHC, the speed of the wash-in and washout phases was nearly limited by solution changes for both iEscSnFR_PM and iFluoxSnFR_PM (**Fig. 3.8C-D**). The application of 31.6 µM SSRI following the Q-SSRI doses (designed to act as a control) exhibited a kinetic profile resembling the equivalent concentration in previous concentration-response experiments in PHC (**Fig. 3.4A, C**). Of note, the kinetic profile of N,N-dimethylfluoxetine as detected by iFluoxSnFR_PM showed a return to baseline fluorescence within seconds after drug washout, a distinctly different result from the observed profile of fluoxetine as detected by iFluoxSnFR_PM in PHC. iEscSnFR_ER and iFluoxSnFR_ER showed little $\Delta F/F_0$ response to application of their corresponding Q-SSRI, presumably because the permanent positive charges reduce membrane crossing. We also performed concentration-response experiments with the Q-SSRIs in HeLa cells transfected with PM- and ER-targeted constructs of iEscSnFR and iFluoxSnFR (**Fig. 3.8E-F**). The PM-targeted constructs detected their respective Q-SSRI partners over the 0.1–31.6 µM range sampled, with characteristics similar to those detected in PHC (**Fig. 3.8C-D**), and the detection of Q-SSRI by the ER-targeted constructs was likewise minimal (the iFluoxSnFR_ER signal above baseline stays below ~20% of the fluorescence signal of the _PM construct and represents concentrations above clinical relevance). To examine the limits of membrane impermeability for quaternary SSRI derivatives, we tested an extended period of co-incubation (**Fig. 3.9**). We transfected the _ER and _PM constructs of both iEscSnFR and iFluoxSnFR into HeLa cells and incubated these cells with 500 nM drug (a concentration with appreciable $\Delta F/F_0$ and within a log unit of the physiologically relevant concentrations of escitalopram and fluoxetine *in vivo* [898-901]). We incubated transfected HeLa cells with either SSRI or Q-SSRI for 2.4 h (**Fig. 3.9**). After transferring the dishes to the imaging rig and allowing an equilibration period under the microscope with HBSS containing an identical concentration of the incubation drug, we started a program that included a buffer wash, a short introduction of the complementary compound (i.e. Q-SSRI if the incubation drug was SSRI or vice versa), a second buffer wash, and finally a reintroduction of the incubation compound (**Fig. 3.9**). When _ER constructs were pre-incubated with SSRI, we saw an initial fluorescence signal indicating that the SSRIs were present in the ER. Application of buffer decreased fluorescence to a new baseline. Subsequent application of Q-SSRI caused no appreciable increase in fluorescence, presumably because Q-SSRI cannot cross into the ER. A reapplication of SSRI also increased fluorescence over background in the ER, though the $\Delta F/F_0$ of the reapplication is ~50% of the signal initially observed; it is possible the $\Delta F/F_0$ would return to its maximum value if the SSRI is reapplied for longer (**Fig. 3.9**, first row). When _PM constructs were pre-incubated with SSRI, introduction of HBSS (**Fig. 3.9**, second row) produced a decrease to a new baseline. As would be predicted, application of Q-SSRI generated a reversible fluorescence increase because PM-targeted biosensor is accessible to Q-SSRI. Reapplication of SSRI once again generated fluorescence over baseline, though this signal was ~50% of the signal inferred from the end of the 2.4 h incubation (**Fig. 3.9**, second row). When _ER constructs were pre-incubated with Q-SSRI, introduction of HBSS (**Fig. 3.9**, third row) did not produce a clear decrease in fluorescence; rather, the signal continued as the existing baseline with little to no change. Upon

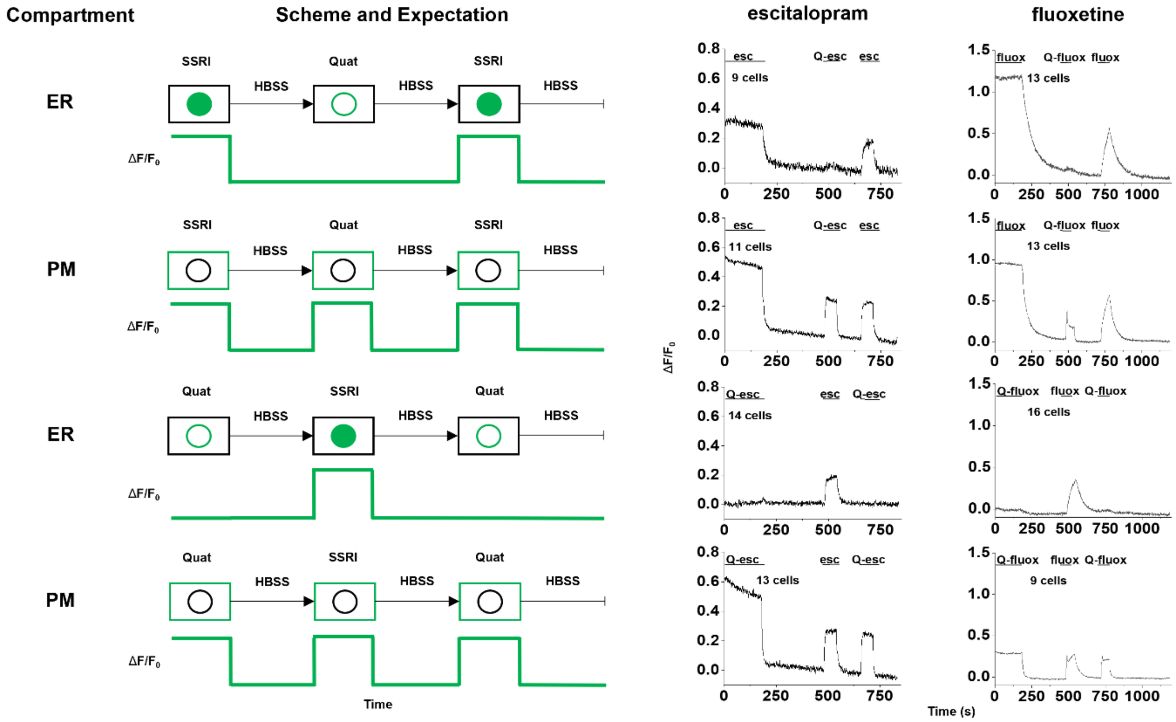

Figure 3.9. (*Left column*) Targeted compartment of the SSRI biosensor. (Middle column) Scheme and expectation of fluorescence response by biosensor based on compartment targeted and preincubated drug. Following preincubation, the drug is washed out, after which the alternate drug is washed in (i.e. when SSRI was preincubated, the quaternary derivative (Quat) was applied and vice versa). An additional washout follows, after which the preincubation drug is reapplied. (*Right columns*) Fluorescence response to escitalopram and fluoxetine after preincubation, washes, and subsequent drug reapplications, matching the scheme and prediction column.

application of SSRI, we observed a clear reversible increase in $\Delta F/F_0$ over baseline fluorescence in the ER, which indicates that SSRIs reach the ER. Reapplication of the Q-SSRI did not generate an increase in fluorescence over the existing baseline, indicating that Q-SSRI still did not cross into the ER (**Fig. 3.9**, third row). Finally, when _PM constructs were pre-incubated with Q-SSRI, fluorescent traces (**Fig. 3.9**, fourth row) resembled those obtained with the 2.4 h incubation of _PM constructs with the SSRI for the same reasons (**Fig. 3.9**, second row). When we attempted a 24 h pre-incubation with drug, we experienced a low $\Delta F/F_0$ response that was confounded by high background (data not shown).

3.3.8. SERT Inhibition by SSRIs and Quaternary SSRI Derivatives

The membrane-impermeant Q-SSRIs provided an opportunity to test the hypothesis that the potency of SSRIs for SERT arises in part because they approach their binding site from the membrane phase. To compare the results with the time scale of our fluorescence experiments, we employed temporally resolved measurements on TAC evoked by 5-HT [878] using an hSERT mutant that has unusually large TAC at low pH [902] (see Chapter 3.2.4). With membrane-bound hSERT in oocytes, we found that N,N-dimethylfluoxetine blocks hSERT with an IC_{50} ~11-fold higher than fluoxetine (**Fig. 3.10A, C**), while N-methylescitalopram blocks hSERT with an IC_{50} ~6-fold greater than escitalopram (**Fig. 3.10B, D**). In more conventional experiments using [^{3}H]serotonin flux, previous experiments found that a quaternary citalopram derivative blocks hSERT with a 10-fold higher IC_{50} than citalopram [875]. These modest differences between the SSRIs and their quaternary derivatives do not strongly support the hypothesis that fluoxetine and escitalopram approach their binding site from the membrane.

3.3.9. Measuring Free Unbound SSRI and Lipid Binding

We performed a series of binding measurements in HEK293 cells (which provide a rough approximation to brain binding [893]) to calculate: a) the ratio between the concentration of intracellular unbound (bioavailable) compound and that of the external solution (F_{ic}); and b) the total cellular drug accumulation ratio (K_p) (see Chapter 3.2.6). K_p did not fully reach equilibrium for either fluoxetine or escitalopram, with a peak reached at 30 min and a subsequent decrease over the next 90 min. For fluoxetine, at 30 and 120 min, K_p = 1590 ± 150 and 1170 ± 50 respectively (geometric mean ± SEM); the escitalopram values were 12-fold smaller (132 ± 12 and 67 ± 30, respectively). These K_p values (**Fig. 3.11A**) are among the largest measured for any drug [542]. We determined $f_{u,cell}$ (see Chapter 3.2.6) with lipid-coated beads [545]. The PC coating substitutes approximately for measurements with phospholipid mixtures from individual cell types [545] which were unavailable for these experiments. We calculated $f_{u,cell}$ to be 0.0006 for fluoxetine and 0.0085 for escitalopram, indicating that almost all of the intracellular drug is bound to lipids and that escitalopram binds less strongly than fluoxetine; this is also consistent with the idea that iSSRISnFR kinetics for escitalopram were ~10-fold faster than fluoxetine (**Fig. 3.4** and **Fig. 3.7**) because diffusion of escitalopram through the membrane is buffered less by binding within the membrane. F_{ic} ranged between 0.5 and 1.0 for both fluoxetine and escitalopram after 60 min. This result was presumably dominated by SSRI in the cytoplasm because the ER accounts for just ~10% of total intracellular volume and other organelles

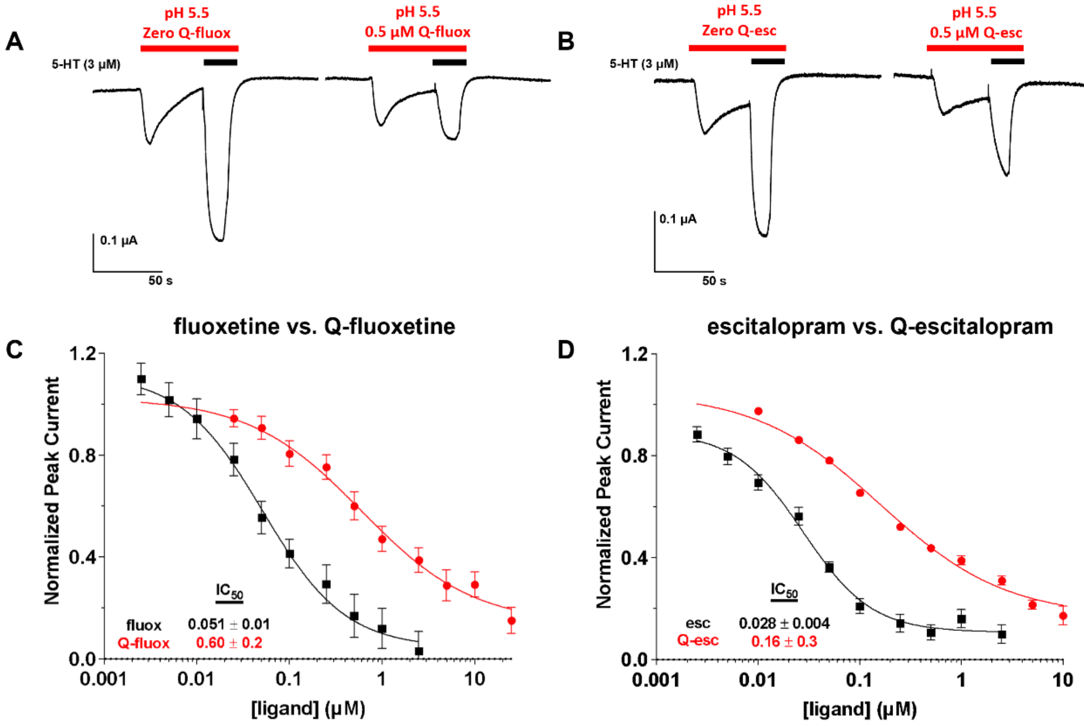

Figure 3.10. ***(A-B)*** Exemplar traces of 5-HT-induced hSERT currents in the absence and presence of Q-fluox and Q-esc respectively. ***(C-D)*** Inhibition of 5-HT-induced hSERT currents of fluoxetine vs. Q-fluox and escitalopram vs. Q-esc, respectively. The IC_{50} values and Hill coefficient were calculated from the corresponding fit. Q-fluox (n = 11) had an IC_{50} 12-fold higher than fluoxetine (n = 13) for the inhibition of hSERT TAC (***C***). Q-esc (n = 24) had an IC_{50} ~6-fold higher than escitalopram (n = 18) for the inhibition of hSERT TAC (***D***).

represent even smaller volumes; the dataset thus supports the $\Delta F/F_0$ measurements made in PHC for the iSSRISnFR_cyto constructs. Because F_{ic} is proportional to K_p, F_{ic} decreases by ~40-50% between 60 min and 120 min, but we have not systematically studied the origin of the decline, which was not observed for the two control drugs (atorvastatin and lopinavir). While the unusual kinetic properties of fluoxetine in neurons could arise from interactions with membrane cholesterol, the manufacturer does not supply beads with known or calibrated cholesterol

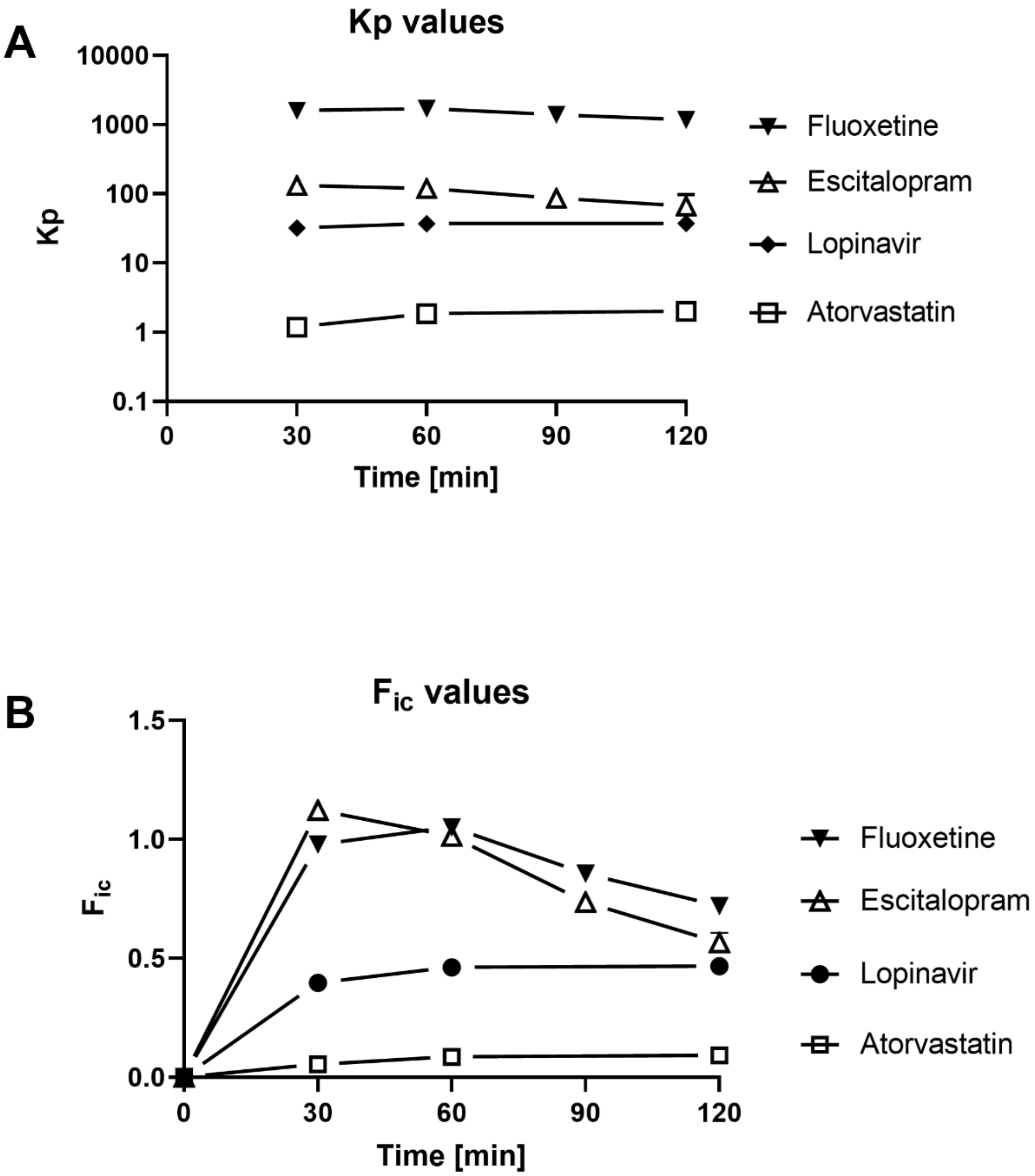

Figure 3.11. ***(A)*** K_p values, measuring total cellular accumulation in HEK293 cells after 30-120 min of incubation. **(B)** F_{ic} values measuring the ratio between unbound intracellular (mostly cytoplasmic) concentration and the external solution. (SEM values are shown where they exceed the size of data markers.)

content, so it is not yet possible to perform systematic experiments on this point. Overall, chemical determination shows that applied fluoxetine or escitalopram enters the cell within 30 min. Of the intracellular SSRI, > 99% is bound to lipids and is therefore available for interaction with membrane proteins. Although < 1% of intracellular fluoxetine or escitalopram is unbound, this concentration roughly equals that of the external solution and is also available for interaction with SERT or other molecules.

3.4. Discussion

The present data establish that fluoxetine and escitalopram, two commonly used SSRI antidepressants, enter both the cytoplasm and the ER within a few minutes of the drugs appearing outside neurons (**Fig. 3.4**) or HeLa cells (**Fig. 3.7**), and the drugs are washed out with a similar time course. That fluoxetine and escitalopram appear as unbound intracellular molecules at concentrations near the extracellular values is confirmed by detection within HEK293 cells which approximate intracellular pharmacokinetics within neurons [885], albeit with less precise temporal resolution (**Fig. 3.11**). At the same time the drugs are equilibrating within the cytoplasm and ER, they are also accumulating within the PM (**Fig. 3.5**, **Fig. 3.8**, and **Fig. 3.11**) and, presumably, other membranes (we inferred the quantitative extent of accumulation within the membrane from iSSRISnFR traces in cells). For fluoxetine detected by iFluoxSnFR during live-cell imaging, our data are consistent with concentration ratios of 180 in PHC (**Fig. 3.5**) and 18 in HeLa cells (**Fig. 3.7**); however, in pure PC membranes on beads or for ITC measurement of pure 1,2-dierucoyl-*sn*-glycero-3-phosphocholine [883], the fluoxetine accumulation ratio is 30-300 times higher. The data provide only slight support for the idea that fluoxetine and escitalopram interact with SERT more strongly when approaching from the membrane than the aqueous phase: the potency of membrane-impermeant Q-SSRIs as hSERT blockers is modestly less than the potency of the SSRIs themselves (**Fig. 3.10**).

The iSSRISnFRs developed and described herein are sensitive enough to allow detection of SSRIs within the experimentally determined (or otherwise projected) concentration in human blood and CSF [898-901]. Our previous applications of iDrugSnFRs have utilized such sensors to measure the free aqueous concentration of a drug; the present experiments show that iFluoxSnFR can also detect fluoxetine in the membrane that anchors it (even as the sensor faces the extracellular solution) during the apparent time scale of accumulation. This additional useful feature presumably arises because fluoxetine accumulates in the membrane (just a few angstroms from the binding site of iFluoxSnFR) 180-fold greater than the extracellular concentration. Similar accumulation in lipids also underlies the high V_d that generally characterizes SSRIs and TCAs (up to 88 L/kg [277-279]), while other major antidepressant classes have much lower V_d (e.g. esketamine: 3-5 L/kg [280]; venlafaxine: 6-7 L/kg [903]). More conventional measurements on SSRIs employ intracerebral microdialysis, with 10-20 min sampling intervals [904-906] to examine 5-HT (or other neurotransmitter) levels [907-910], though 5-HT levels serve only as an indirect indicator of SSRI concentration, making imaging- or photometry-based examination of the local brain concentrations of free (unbound) antidepressant in real-time less practical than using iSSRISnFRs to assess SSRI pharmacokinetics *in vivo*.

Our study exploited an important feature of the iDrugSnFR paradigm, as we can perform experiments in parallel on two therapeutic agents thought to act similarly. The iSSRISnFRs themselves differ by only eight AAs near the PBP binding site and two near the PBP-cpGFP linkers (four differences are shown in **Fig. 3.1A**, with full sequences available on AddGene #182807-182808). As the drugs themselves have similar pK_a values, we reasoned that any property governing SSRIs as a class would result in similar measurements for fluoxetine and escitalopram. In our experimental results, we found two classes of shared properties: a) entry into the cytoplasm and ER, and b) accumulation in membranes. Despite these similar properties, in clinical practice, escitalopram produces fewer adverse events than fluoxetine [911] and fluoxetine results in less frequent/severe antidepressant discontinuation syndrome [912], a clinical phenomenon affecting around 20% of patients experiencing an abrupt change in SSRI dosing and which causes flu-like symptoms, insomnia, and hyperarousal for upwards of several weeks [913]. Our experimental data are consistent with previous findings indicating that escitalopram accumulates in membrane lipids roughly an order of magnitude less than fluoxetine [883,893,914,915]. In the diffusion-bonding model, this difference explains how escitalopram enters and leaves the compartments we studied at least an order of magnitude faster than fluoxetine. The LogP and $LogD_{pH7.4}$ for escitalopram are ~0.5 units less than for fluoxetine, perhaps accounting for part of the difference in accumulation. The different accumulation of fluoxetine versus escitalopram is unlikely to arise from drug efflux pumps [916] but could arise from one or more other mechanisms, including partitioning into lipid rafts [873], lateral diffusion within the plane of the membrane, and effects on membrane elasticity/curvature [883]. We conclude that fluoxetine accumulates in membranes of PHC ~10-fold more strongly than in membranes of HeLa cells (**Fig. 3.5C1-C2** and **Fig. 3.7L1-L2**). The differences may arise from the presence of the glial layer in the former preparation as glia furnish most of the cholesterol in neuronal membranes [917] which could provide an additional sequestration target: SSRIs interact directly with cholesterol-rich membranes [556] and change their structure [918]; SSRIs alter cholesterol levels in brain; and SSRIs help TrkB to sense cholesterol [614]. As temporal and causal relations among these phenomena are not yet understood, future studies will hopefully determine whether astrocyte-supplied cholesterol underlies our observation that fluoxetine interacts for several hundred seconds with neuronal membranes; indeed, cholesterol-coated beads used in a similar assay as performed in this study would greatly inform our understanding of the role cholesterol plays in this regard.

Use of impermeant quaternary blocking drugs is an accepted paradigm in ion channel and receptor pharmacology [506,533,919,920], and we performed analogous experiments with a neurotransmitter transporter. Some data suggest that fluoxetine stabilizes SERT in a conformation that exposes the binding site to the internal solution [921], but atomic-scale structures suggest that bound escitalopram faces the external solution [922]. No previous studies address the question of whether the SSRI approaches the binding site from the membrane or from the aqueous phase, but the modest decreases in affinity for the impermeant derivatives reported herein provide little support for the membrane approach mechanism; though the protonated amine of several SSRIs makes a cation-π interaction with Tyr95 and an H-bond with Asp98 of SERT [923] and quaternization of the amine would alter the former interaction while eliminating the latter, possibly decreasing the affinity by the observed amounts. In terms of novel receptor targets, fluoxetine binds to TrkB in the deprotonated form [614], vitiating any conclusions about membrane approach from measurements on Q-SSRI derivatives at TrkB. With respect to investigating inside-out pharmacology, the impermeant derivatives provide a convenient probe to distinguish the effects of SERT blockade from the effects of intracellular SSRI-SERT interactions (for at least 2.4 h; **Fig. 3.9**); additionally, a recent study has used N-methylated tryptamines (mostly weak bases) to establish that increased compound lipophilicity correlates with increased traffic through membranes and that the interaction with intracellular 5-HT_{2A}Rs mediates their neuroplasticity which correlate with antidepressant effects [506], suggesting that the use of impermeant compounds can be applied broadly to ask questions about where crucial ligand-receptor interactions take place. Future studies may investigate the interaction between such derivatives and their putative targets to approach these questions more directly.

Returning to the four non-exclusive mechanisms summarized in Chapter 4.1, our findings allow us to comment on several of them. The first mechanism, the ‘outside-in’ interaction between SSRI and SERT, is not informed by our data, as we did not investigate SSRI-driven changes in extracellular 5-HT in this study. The second mechanism, which stipulates that SSRI levels during the therapeutic lag are governed by whole-animal or organ-level pharmacokinetic properties, is not supported by our experiments. Even if one assumes that myelin, with some 500 membranes in parallel, increases the wash-in and washout time constants for fluoxetine (300 s) by 500-fold, this extends the time to 1.5×10^4 s, or one day – enough to explain the classically measured disappearance of fluoxetine but still ~10-fold less than the time to clinical benefit. Future studies may demonstrate how membrane accumulation explains the fact that ~21 days of fluoxetine treatment are required before fluoxetine is detectable in humans via *in vivo* NMR spectroscopy [898], but what we know as of now about myelin composition precludes further speculation. The faster kinetics for escitalopram further undercut the idea that lipid accumulation can fully explain the therapeutic lag for SSRIs (though, interestingly, use of SSRIs in premenstrual syndrome is apparently not associated with delayed clinical benefit [924], and the time course of antidepressant discontinuation syndrome is also more rapid). The third mechanism, that therapeutic effects occur at least partially because of SSRI-SERT interactions in cellular compartments other than the extracellular-facing surface of the PM, is consistent with our observations. Given the dimerization and quality-control processes that transporters undergo in the ER, target engagement within the ER (including pharmacological chaperoning of nascent SERT) continues to be a suspected therapeutic mechanism of SSRIs [530]. (That fluoxetine enters the ER may also explain how fluoxetine induces cytotoxic ER stress [925].) The vast SSRI accumulation within membranes and the decreased potency of Q-SSRIs raises the possibility that SSRI-SERT engagement is enhanced because it occurs within the PM or an organellar membrane, a suggestion that broadens the meaning of the earlier phrase ‘inside-out;’ future experiments assessing the antidepressant effects of Q-SSRIs would allow for preliminary conclusions on this question. While interactions in other subcellular compartments may provide additional insights into SSRI inside-out activity, the current generation of iDrugSnFRs cannot function in acidic organelles; indeed, the indirect and relatively insensitive experiments assessing acid trapping in vesicles (pH ~6 [530]) were uninformative (**Fig. 3.6**). Furthermore, because endolysosomal compartments account for ~1% of cellular volume [885], even the predicted ~100-fold accumulation (**Fig. 3.6A**) due to acid trapping would produce a mere twofold total accumulation of fluoxetine, several orders of magnitude lower than the directly measured K_p in HEK293 membranes (**Fig. 3.11**) (acid trapping would also occur within a few hundred seconds, too slow to explain the therapeutic lag). The fourth mechanism (regarding additional pathways by which SSRIs exert their antidepressant effects) is consistent with our experiments to the extent that we found significant accumulation of SSRIs within membranes (especially neuronal membranes), which has potential bearing on previously postulated putative therapeutic pathways such as SSRI-TrkB interactions involving PM cholesterol [614], SSRI displacement of $G_{S\alpha}$ in lipid rafts [873], or lipid-modifying enzymes [926]. The discovery of RAADs, most notably ketamine (see Chapter 1.3 and Chapter 1.4), warrants a broader survey of possible antidepressant pathways, especially in light of the non-linear relationship between extracellular 5-HT and clinical state (see Chapter 3.1). The development of the next generation of antidepressants is contingent on a more complete understanding of how the current generation function; for this reason, as well as the ubiquity and efficacy of SSRIs for treating MDD, these compounds will continue to have important uses in medicine and continue to draw interest from researchers from a broad array of disciplines.

CHAPTER 4: SENSING FLUORESCENT REPORTERS FOR OTHER DRUGS: NICOTINIC AGONISTS

4.1. Introduction

Addiction neuroscience is a field of vital importance to the treatment of substance abuse, as this behavior contributes to over 5% of disability-adjusted life years (DALYs), equivalent to the loss of one year of full health [927]. Opioid use has skyrocketed over the past several decades, reaching epidemic proportions [928], and the Lester lab has developed iDrugSnFRs for common opioids to both understand their pharmacokinetics [685] as well as to combat overdose by sampling biofluids (data not yet published). But perhaps the most prominent addictive substance over the past century is nicotine, ubiquitous in popular culture and public discourse owing to its ingestion via combustible cigarettes, chewing tobacco, and most recently electronic nicotine delivery systems (ENDs, also known as 'vaping'). While programs to combat the use of combustible cigarettes and other tobacco products have been successful [929], the proliferation of ENDs among a new generation of nicotine users [930] is cause for both concern as well as renewed investigation of strategies to lessen the burden of tobacco-related disease.

Developing strategies to encourage smoking cessation is an important goal which will help decrease both the individual and societal risk for deleterious health outcomes from tobacco use. Nicotine, the addictive alkaloid present in tobacco products, remains available to users (via transdermal patches and other devices) attempting to quit smoking; however, these nicotine replacement therapies (NRTs) have distressingly low rates of success (increasing quit rates from 10% receiving placebo to 17% receiving NRT [931]. Therefore, investigations have been undergone to develop alternative ligands of nAChRs with improved clinical effect. Prior work suggests that partial agonists with lower efficacy than nicotine could serve as effective smoking-cessation drugs [932], and efforts continue in that direction [933]. Another plant alkaloid, (-)-cytisine (also called cytisinicline and Tabex®), an α4β2 nAChR partial agonist, served as a basis for the synthesis of analogs, most of which have not yet proved clinically effective [934-940]. Varenicline (Chantix®), one such derivative, has four ringed functional groups (two more than nicotine or cytisine) and is currently the only FDA-approved smoking-cessation drug; however, the modest quit rate of ~18% at 12 months [941,942] necessitates further improvement of the currently available smoking cessation therapies. Assessment of dianicline, another tetracyclic nicotinic agonist, has been discontinued following unfavorable Phase III clinical trials [943,944]. To be a candidate smoking cessation drug, a nicotinic ligand must satisfy at least three criteria [945,946]. First, it must enter the brain, where the most nicotine-sensitive nAChRs (α4β2) are contained. Second, the ligand must also activate those α4β2 nAChRs with an EC_{50} sufficient to reduce cravings and withdrawal (about 1-2 μM, also the concentration of nicotine in the plasma and CSF of a smoker [533]). Finally, it must block nicotine binding to reduce the sensation of pleasure associated with acute (minutes) nicotine ingestion. Varenicline meets these requirements, while cytisine (low brain penetration) and dianicline (EC_{50} = 18 μM) each fail one of the criteria [945].

Membrane permeation is important for investigating and treating nicotine addiction in at least two ways. Firstly, as alluded to in the first criterion above, weak bases are of special interest; most orally available neural drugs are weakly basic and thus have a fraction of their population which exists in uncharged form at physiological pH (see Chapter 1.5). Enhancing the membrane permeability of cytisine analogs and probing their nAChR subtype selectivity was addressed via direct functionalization of cytisine within the pyridone ring [947], with two of the resulting derivatives, 10-fluorocytisine and 9-bromo-10-ethylcytisine, possessing cytisine-like EC_{50} values for the α4β2 nAChRs but more positive calculated $\text{LogD}_{\text{pH7.4}}$ values than the parent compound, suggesting greater membrane permeability in the blood, brain, and cytoplasm where a significant fraction of drug exists in an unprotonated neutral form [948]. While informative for comparison purposes, estimates of $\text{LogD}_{\text{pH7.4}}$ are inexact, extrapolated, or rely on algorithmic calculations whose results can vary by over two log units for individual molecules [949]. Furthermore, these estimates have unknown applicability to biological membranes, especially at $\text{LogD}_{\text{pH7.4}}$ values < 0 (indicating lipophobicity) characteristic of varenicline, dianicline, and the cytisine analogs. Secondly, nicotine dependence involves one or more inside-out mechanisms. Nicotine itself ($\text{LogD}_{\text{pH7.4}} = 0.99$) enters the ER, binds to nascent nAChRs, becomes a pharmacological chaperone for the nAChRs, and eventually causes selective upregulation of these receptors on the PM of neurons [532] (see Chapter 1.6.5). For this reason, it is especially important to understand permeation into the ER for any candidate smoking cessation drug.

These two neuroscience aspects of nicotinic ligands — their pharmacological activity and the implications thereof for behavior — can be addressed via direct measurements of drugs within cells and their compartments. We previously explored the subcellular pharmacokinetics of nicotine and varenicline in mammalian cells and cultured neurons using the iDrugSnFRs iNicSnFR3a and iNicSnFR3b to show that these nicotinic agonists enter the ER within seconds of drug application and exit equally rapidly during washout periods [533]. That nicotine rapidly diffuses across cellular membranes has been suspected for decades; indeed, nicotine crosses six PMs to enter the brain within 20 s to cause its acute effects. Acid trapping of varenicline in subcellular compartments (such as the ER) indicates appreciable membrane permeation but may also underlie unwanted effects [719,950]. We sought to generate additional iDrugSnFRs for the candidate smoking-cessation drugs dianicline, cytisine, 10-fluorocytisine, and 9-bromo-10-ethylcytisine. We hypothesized that these targeted sensors would enable quantifiable fluorescence signals that compare the differences in permeation among these compounds as a means of assessing their candidacy as smoking cessation compounds as well as to inform the development of future compounds which address the shortcomings of each.

4.2. Methods

4.2.1. Crystallography

The gene encoding the full-length biosensor iNicSnFR3a was previously cloned into a bacterial expression vector [533] as described in Chapter 2.2.5. To improve crystallization, we deleted the N-terminal HA tag and the N-terminal Myc tag, creating constructs with the suffix ‘dt.’ These deletions were accomplished using site-directed mutagenesis (Q5 Site-Directed Mutagenesis Kit, NEB). All proteins were expressed in BL21(DE3) cells in ZYM-5052 media [732]. Cells were collected by centrifugation and stored at –80°C. For purification, frozen cell pellets were resuspended in lysis buffer containing 100 mM NaCl (to provide salts); 20 mM Tris, pH 7.5 (to buffer lysate pH); 20 mM imidazole, pH 7.5 (for elution); 5 mM BME (to deactivate RNase); lysozyme (to degrade membranes); DNase (to reduce viscosity caused by free DNA); and protease inhibitor (Pierce Protease Inhibitor Tablets, Thermo Fisher Scientific). The resuspended cells were lysed using liquid nitrogen as described in Chapter 2.2.1. The pellet of intact cells and cell debris were removed after centrifugation at 20,000 rcf for 40 min at 4°C and the supernatant was loaded onto an Ni-NTA column with wash buffer (100 mM NaCl; 20 mM Tris, pH 7.5; 30 mM imidazole, pH 7.5; and 5 mM BME). Elution was achieved in an imidazole gradient (see Chapter 2.2.3) using wash buffer but with 300 mM imidazole, pH 7.5. The eluted sample was further purified by size-exclusion chromatography (HiLoad 16/60 Superdex 200, Cytiva) in the same buffer without imidazole and BME. Fractions were collected and concentrated to ~50 mg/mL using a filter with a 10 kDa cutoff (Amicon Ultra 15, MilliporeSigma). For all constructs, initial crystallization screening was carried out with 40 mg/mL protein in the presence and absence of 10 mM nicotine or varenicline. iNicSnFR3adt was crystallized separately with 10 mM nicotine and 10 mM varenicline in condition #96 of a PEG/ion/pH screening kit (PACT premier, Molecular Dimensions) with 0.2 M sodium malonate dibasic monohydrate (SMDB; for cryoprotection and stabilization [951]); 0.1 M bis-tris propane (BTP), pH 8.5 (as a buffer); and 20% PEG 3350 (to prevent unwanted salt aggregation) at 20°C. Crystals of iNicSnFR3adt grew within two weeks of crystallization in a hexagonal rod shape (dimensions: 80 µm × 80 µm × 300 µm). Crystals were harvested and cryo-protected in 25% ethylene glycol; 0.2 M SMDB; 0.1 M BTP, pH 8.5; and 20% PEG 3350. Phase information was obtained through soaking with potassium iodide (KI) before cryo-protection. The unliganded iNicSnFR3adt was crystallized in condition #92 of a protein crystallization screen (Morpheus, Molecular Dimensions) with 2.5% PEG 1000; 12.5% PEG 3350; 12.5% 2-methyl-2,4-pentanediol (for crystallization [952]); 0.02 M of each AA; and 0.1 M MOPS/HEPES-Na, pH 7.5 (as a buffer [953]) at 23°C with no further optimization. X-ray datasets were collected at Stanford Synchrotron Radiation Laboratory Beam Line 12-2 and the Lawrence Berkeley National Laboratory Advanced Light Source Beamline 5.0.2 with hybrid photon counting detectors (Pilatus 6M, Dectris). Datasets were processed as rotation images (XDS [954]) and scaled (AIMLESS [955]). For iNicSnFR3adt, molecular replacement was carried out using domains of the unliganded structure (PDB ID 6EFR) with automated software (Phaser in Phenix [956]). The experimental phase information of KI-soaked crystals of iNicSnFR3adt was obtained with molecular replacement single-wavelength anomalous diffraction (MR-SAD, a technique for resolving the protein phase) using automated software (AutoSol in Phenix [956]). Molecular replacements of the remaining structures were carried out with the refined model of iNicSnFR3adt. Iterative refinement and model building cycles for all structures were carried out separately with automated software (phenix.refine [956] and Coot [957] in Phenix).

4.2.2. Directed Evolution and Measurements of iDrugSnFR Proteins

Starting with iAChSnFR and intermediate constructs of that sensor, we constructed and optimized iDrugSnFRs for each drug partner during iterative rounds of SSM as described in

Chapter 2.2.2 to create sensors for cytisine (iCytSnFR), 10-fluorocytisine (iCyt_F_SnFR), 9-bromo-10-ethyl-cytisine (iCyt_BrEt_SnFR), and dianicline (iDianiSnFR). Sensors selected for further study were purified as proteins using a His6 sequence as described in Chapter 2.2.3. Performance of protein quantification and dose–response relations for drug-sensor partners was also as previously described in Chapter 2.2.4, correcting for ligand depletion when appropriate as described in Chapter 2.2.1. We performed ITC experiments as described in Chapter 2.2.4: 800 μM cytisine (Sigma-Aldrich) was titrated into 80 μM iCytSnFR, 160 μM 10-fluorocytisine was titrated into 16 μM iCyt_F_SnFR, 470 μM 9-bromo-10-ethylcytisine was titrated into 47 μM iCyt_BrEt_SnFR, and 1.5 mM dianicline (Tocris) was titrated into 150 μM iDianiSnFR. Analysis was performed as previously described in Chapter 2.2.4 in NanoAnalyze software. Stopped-flow experiments were as described in Chapter 2.2.4. Data were plotted and time courses were fitted, when possible, to a single exponential, and kobs was plotted as a function of [ligand]; when the time course did not fit well to a single rising exponential, it was fitted to the sum of two increasing exponentials.

4.2.3. *Expressing iDrugSnFRs in Mammalian Cells and Primary Culture*

We constructed two variants of each iDrugSnFR for expression in mammalian cells, targeting the PM (iDrugSnFR_PM) or the ER (iDrugSnFR_ER) using techniques as described in Chapter 2.2.5. We transfected HeLa cells as described in Chapter 2.2.5. For assembly of iDrugSnFR AAV plasmid assembly, we followed the protocol described in Chapter 2.2.5 and packaged the virus using the AAVpro method as described in Chapter 2.2.5. Neurons were transduced as described in Chapter 2.2.5, the _ER construct at an MOI of 0.5-5 × 10^4 and the _PM construct at an MOI of 0.5-1 × 105. Neurons were imaged ~2-3 weeks post-transduction.

4.2.4. *Imaging iDrugSnFRs in Mammalian Cells and Primary Culture*

We performed time-resolved concentration-response imaging using the protocol as described in Chapter 2.2.6 under the setup described in Chapter 2.2.6. Data was analyzed using the processing pipeline outlined in Chapter 2.2.6. For high-resolution imaging, we used the spinning disk confocal microscope under the conditions described in Chapter 2.2.6. The final drug concentrations were: dianicline, 15 μM; cytisine, 10 μM; 10-fluorocytisine, 10 μM; and 9-bromo-10-ethylcytisine, 7.5 μM.

4.2.5. Millisecond Timescale Microperfusion

Microperfusion allows for the near-instantaneous change of solution in a small-volume chamber for the purpose of measuring millisecond-scale responses in electrophysiology and/or fluorescence. We had previously applied micro-iontophoresis techniques for delivering nicotine to transfected cells [533]; however, the major drawback of this delivery system is that the ligand concentration is unknown. Thus, to discern rapid changes in fluorescence, we applied nicotinic agonists with a laminar-flow microperfusion system (SS-77B Perfusion Fast-Step, Warner Instruments) to HEK293T cells transfected with the iCytSnFR_PM construct after 24-72 h of incubation as described in Chapter 2.2.5; the high level of protein expression in this cell line improves fluorescence response. Cells were imaged under an epifluorescence microscope (DIAPHOT 300, Nikon) with a 488 nm LED using a 63X objective (NA = 1.5). Immediately prior to imaging, we rinsed the dishes with HBSS (warmed to 37°C) three times before removing the coverslip which was then resealed to the bottom of the perfusion chamber (RC-25, Warner Instruments) with silicone grease. In an array of three square glass capillaries (internal diameter = 600 μm), we loaded the center capillary with drug dissolved in HBSS and the two outer capillaries with HBSS only; HBSS (18°C) connected to a gravity flow bath perfusion system was used to continuously oxygenate the cells. Solution was flowed for 5-30 s, and exchange (performed via 700 μm translation on the microscope stage), measured by loading the center capillary with dye, had a time constant of 90 ± 20 ms (n = 6 trials). Timing of ligand application (Clampex v.9) and image acquisition initiation (Digidata 1200) were controlled by software (Molecular Dynamics), and camera operation was controlled via software on a second PC (HCImage v3.0) at 1-8.9 Hz. For offline analysis, we fit the rise and decay of the iCytSnFR_PM drug response to the sum of one or two exponential components (FIJI and Origin 2018). An F-test determined whether two exponential components fit the data significantly better than 1 ($p < 0.05$), and statistical comparisons among groups were carried out using ANOVA.

4.3. Results

4.3.1. Generation of iDrugSnFRs for Nicotinic Agonists: Structural Tactic

Using a ‘structure-based’ tactic, we obtained the first structural data for OpuBC-based SnFRs bound by nicotinic ligands (nicotine and varenicline). Crystals of iNicSnFR3adt in the presence of 10 mM nicotine diffracted to 2.95 angstrom resolution (PDB 7S7U). Overall, the liganded

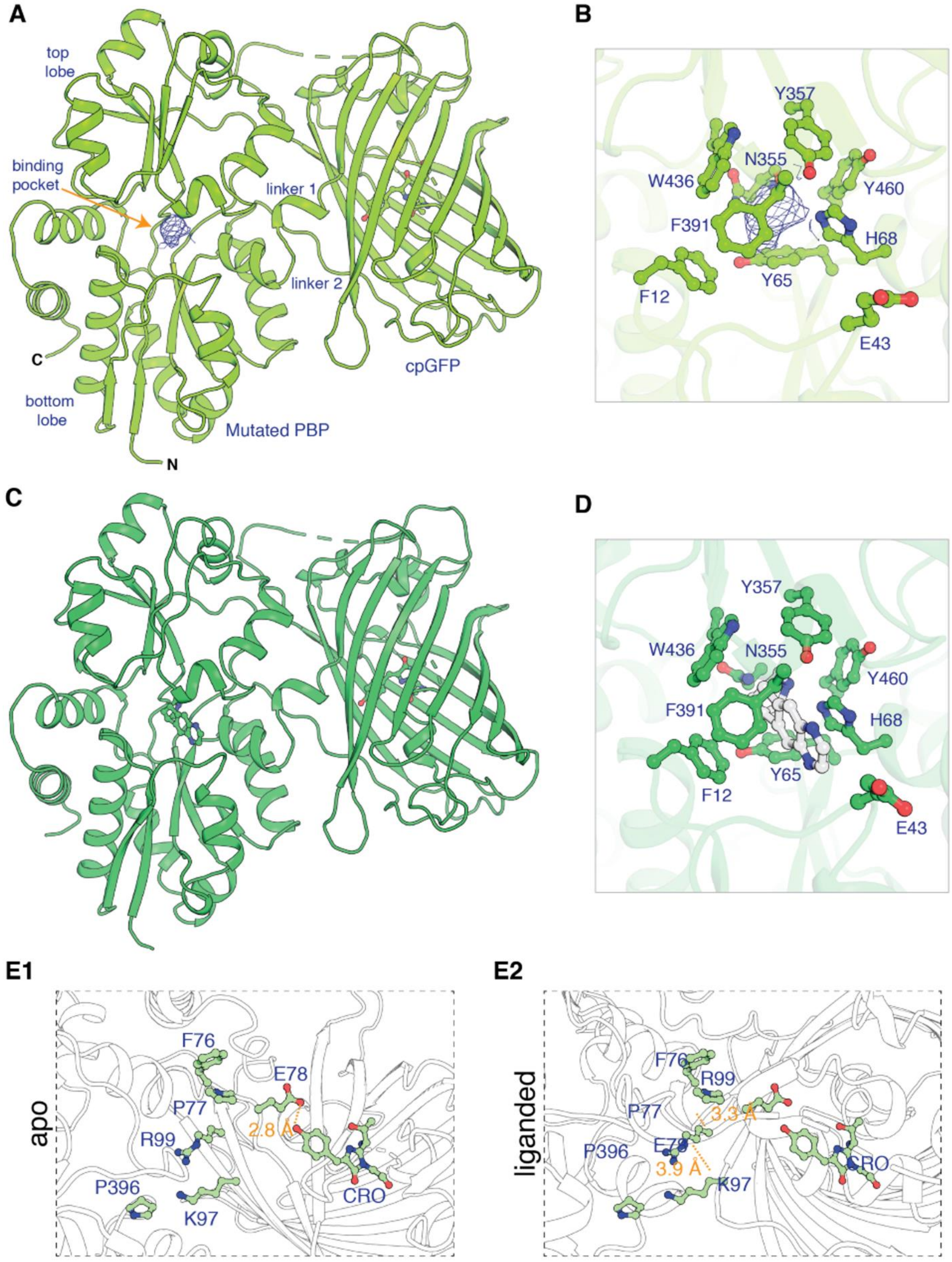
A
top lobe
binding pocket
linker 1
linker 2
C
bottom lobe
N
Mutated PBP
cpGFP
B
Y357
N355
W436
Y460
F391
H68
F12
Y65
E43
C
D
Y357
W436
N355
Y460
F391
H68
F12
Y65
E43
E1
apo
F76
E78
P77
2.8 Å
R99
P396
K97
CRO
E2
liganded
F76
R99
P77
3.3 Å
E78
P396
3.9 Å
K97
CRO

Figure 4.1. ***(A)*** Overall conformation of iNicSnFR3adt crystallized with nicotine; an electron density appears at the nicotine binding site. ***(B)*** iNicSnFR3adt binding site residues with unresolved electron density in binding site. ***(C)*** Overall conformation of iNicSnFR3adt with varenicline bound. ***(D)*** iNicSnFR3adt binding site with varenicline present. ***(E)*** Aspects of the PBP-Linker1-cpGFP interface, emphasizing contacts that change upon ligand binding. The Phe76-Pro77-Glu78 cluster (in Linker1) lies 11–16 angstroms from position 43, which defines the outer rim of the ligand site (***B***); therefore, the cluster makes no direct contact with the ligand site. (*E1*) In the apo conformation, Glu78 acts as a candle snuffer that prevents fluorescence by the chromophore. (*E2*) In the liganded conformation, the Phe76-Pro77-Glu78 cluster moves Glu78 at least 14 angstroms away

PBP domain of iNicSnFR3adt adopts a closed conformation (**Fig. 4.1A**). In the binding pocket between the top and bottom lobes of the PBP, we observed an ‘avocado’-shaped electron density in the nicotine binding site, enclosed by several aromatic residues (**Fig. 4.1B**); the combination of protonation/deprotonation and the rotatable bond of nicotine [958] vitiate unambiguously localizing it within the binding pocket. We obtained an unambiguous ligand placement for iNicSnFR3adt in the presence of 10 mM varenicline in the same crystallization condition (**Fig. 4.1C**): crystals of iNicSnFR3adt with varenicline bound were isomorphous to those of the nicotine-bound crystals and diffracted to 3.2 angstrom resolution (PDB 7S7T). While the protein structure with varenicline (**Fig. 4.1D**) is identical to that of the nicotine-bound structure (**Fig. 4.1B),** the rigidity and additional ring of varenicline allowed us to unambiguously localize it in the binding pocket. Varenicline is enclosed by the same aromatic residues as nicotine, forming cation-π interactions with Tyr65 and Tyr357, in addition to other nearby residues (**Fig. 4.1D**). In the apo state, the Glu78 in Linker1 approaches within ~2.5 angstroms of the oxygen of the tyrosine fluorophore (**Fig. 4.1E**; PDB 7S7V); we provide structural details confirming the hypothesis [706,778] that in the liganded state Glu78 has moved away from this oxygen, presumably allowing the fluorescent tyrosinate to form (see **Fig. 4.1** legend). The data confirm that similar ligand-induced conformational changes occur in the PBPs for nicotine, varenicline, ACh [678], and choline [959]; these changes resemble those for other OpuBC PBPs [960].

4.3.2. Generation of iDrugSnFRs for Nicotinic Agonists: Mutational Tactic

We screened each of the four nicotinic agonists against a panel of biosensors including iNicSnFR3a, iNicSnFR3b, and iAChSnFR as well as intermediate constructs from their developments as described in Chapter 2.2.1. SSM was performed (see Chapter 2.2.2) and the fluorescence characteristics of each iDrugSnFR were evaluated in lysate (**Table 4.1** and **Fig. 4.2**): iDianiSnFR – EC$_{50}$ = 6.7 ± 0.3 μM, $\Delta F_{max}/F_0$ = 7.4 ± 0.1, S-slope = 1.1; iCytSnFR – EC$_{50}$ = 9.4 ± 0.8 μM, $\Delta F_{max}/F_0$ = 5.0 ± 0.2, S-slope = 0.5; iCyt_F_SnFR – EC$_{50}$ = 1.4 ± 0.04 μM, $\Delta F_{max}/F_0$ = 7.9 ± 0.1, S-slope = 5.6; and iCyt_BrEt_SnFR – EC$_{50}$ = 5.7 ± 0.1 μM, $\Delta F_{max}/F_0$ = 4.0 ± 0.03, S-slope = 0.7. We deposited cDNA sequences in an online database (AddGene #177738-177741).

		$\Delta F/F_0$		**EC$_{50}$ (μM)**		**S-slope**		**Residues Mutated vs. Parent**							
Informal Name	**Drug of Interest**	**L**	**P**	**L**	**P**	**L**	**P**	**11**	**43**	**44**	**68**	**324**	**360**	**391**	**395**
iNicSnFR3b	*nicotine*	*ND*	*10*	*ND*	*19*	*ND*	*0.5*	*E*	*E*	*N*	*H*	*S*	*T*	*F*	*G*
iDianiSnFR	dianicline	7.4 ± 0.1	4.7 ± 0.2	6.7 ± 0.3	15 ± 1	1.1	0.3	D	R	-	S	N	G	-	N
iAChSnFR	*ACh*	*ND*	*12*	*ND*	*1.3*	*ND*	*9.2*	*I*	*V*	*N*	*H*	*A*	*T*	*F*	*G*
iCytSnFR	cytisine	5.0 ± 0.2	7.3 ± 0.4	9.4 ± 0.8	11 ± 1	0.5	0.7	-	Y	-	-	-	-	W	-
iCyt_F_SnFR	10-fluorocytisine	7.9 ± 0.1	2.3 ± 0.1	1.4 ± 0.04	1.6 ± 0.3	5.6	1.4	-	N	G	-	-	-	W	-
iCyt_BrEt_SnFR	9-bromo-10-ethylcytisine	4.0 ± 0.03	3.6 ± 0.03	5.7 ± 0.1	4.2 ± 0.2	0.7	0.9	-	Q	G	-	-	-	W	-

Table 4.1. iDrugSnFR naming, concentration-response relations, and residues mutated. Parent construct information is italicized. Measurements in *E. coli* lysates (L) or with purified protein (P). (ND =not determined; data for iAChSnFR from [678] and data for iNicSnFR3b from [533].

4.3.3. Specificity and Thermodynamics of iDrugSnFRs for Nicotinic Agonists

We characterized the specificity of purified iDrugSnFRs for their drug partners versus a panel of related nicotinic agonists (**Table 4.2**, **Fig. 4.3**). iDianiSnFR had the greatest fidelity for its drug partner but also showed an increased EC$_{50}$ (15 μM) as a purified protein versus in lysate (6.7 μM), possibly indicating decreased stability in a purified form. iCytSnFR, iCyt_F_SnFR, and iCyt_BrEt_SnFR showed a greater level of promiscuity for other compounds; of note, iCytSnFR, iCyt_F_SnFR, and iCyt_BrEt_SnFR have an exceptionally low (60–90 nM) EC$_{50}$ for varenicline. The newly developed iDrugSnFRs showed negligible binding to choline or ACh, suggesting minimal endogenous interference during *in vivo* experiments. We also performed dose–response experiments with iDianiSnFR, iCytSnFR, iCyt_F_SnFR, and iCyt_BrEt_SnFR against a panel of nine endogenous molecules, including neurotransmitters (**Fig. 4.4**). iDianiSnFR showed no response to any of the nine selected compounds above background; iCytSnFR, iCyt_F_SnFR, and iCyt_BrEt_SnFR showed no response above background for seven of the compounds but exhibited $\Delta F/F_0$ of 0.25-0.8 to DA at 316 µM/1 mM and $\Delta F/F_0$ of 0.8-1.5 to 5-HT at 316 µM/1 mM. Overall, the SnFRs are at least 250-fold more sensitive to their eponymous partners than to

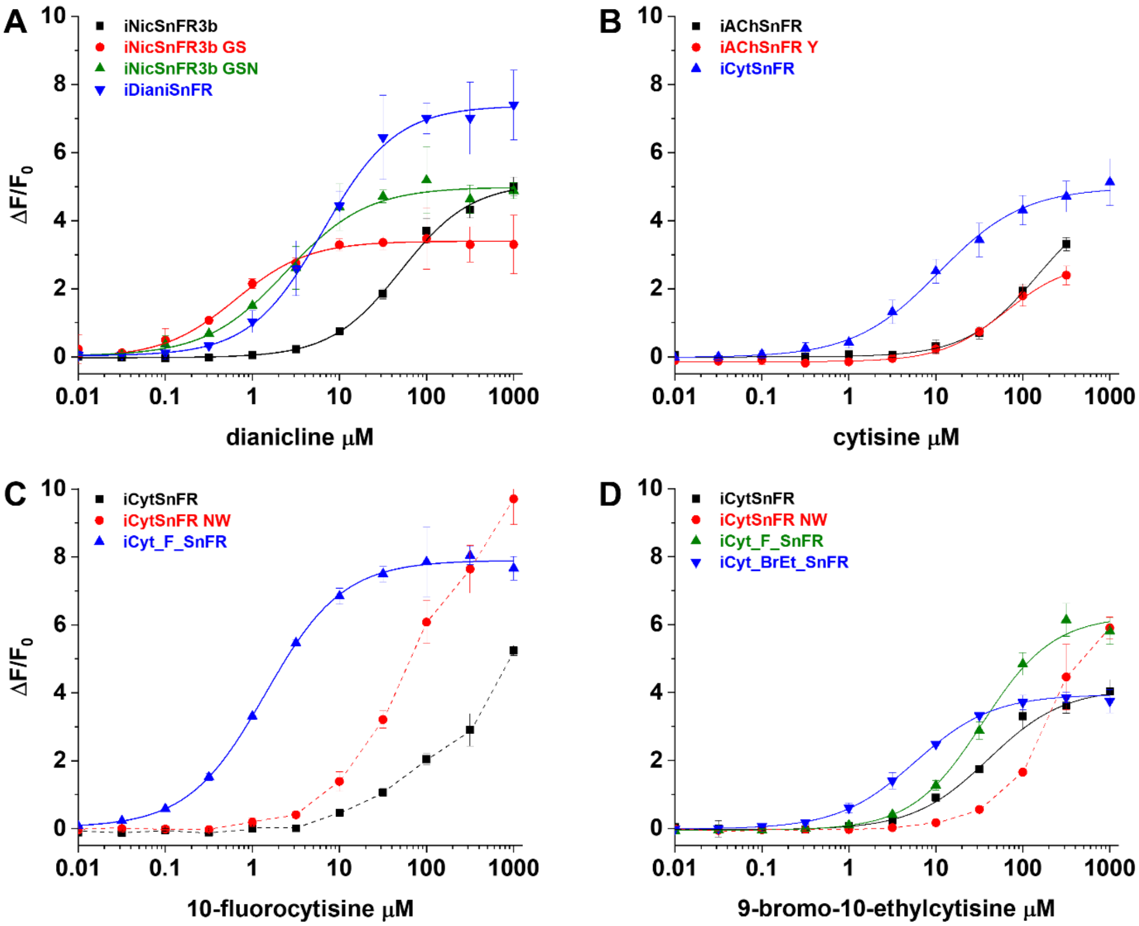

Figure 4.2. Nicotinic agonist iDrugSnFR development. Concentration-response relations on intermediate constructs using *E. coli* lysate were performed with respective drug partners to identify SSM winners. The progenitor biosensor is listed in black. Dashed lines indicate data that did not reach saturation at the concentrations tested; therefore, EC_{50} and $\Delta F_{max}/F_0$ could not be determined (see **Table 4.2**). The graphs show the development of (***A***) iDianiSnFR, (***B***) iCytSnFR, (***C***) iCyt_F_SnFR, and (***D***) iCyt_BrEt_SnFR.

other molecules we have tested (as measured by S-slope). To examine the thermodynamics of the ligand-iDrugSnFR interaction, we conducted ITC experiments (**Fig. 4.5**) as described in Chapter 2.2.4. The experimentally determined K_d of each pair was within a factor of 2 of the experimentally determined EC_{50} for fluorescence in purified protein (**Table 4.3**): iDianiSnFR – K_d = 7.6 ± 1.4 µM, EC_{50} = 15 ± 1 µM; iCytSnFR – K_d = 13.7 ± 1.1 µM, EC_{50} = 11 ± 1 µM; iCyt_F_SnFR – K_d = 1.8 ± 0.5 µM, EC_{50} = 1.6 ± 0.3 µM; iCyt_BrEt_SnFR – K_d = 5.4 ± 0.8 µM, EC_{50} = 4.2 ± 0.2 µM. We infer that the EC_{50} for fluorescence is dominated by the overall binding of the ligand for all the iDrugSnFRs; interestingly, the binding of dianicline to iDianiSnFR is endothermic but the overall reaction is still exergonic due to the large decrease in entropy.

	iDianiSnFR			**iCytSnFR**			**iCyt_F_SnFR**			**iCyt_BrEt_SnFR**		
Drug Name	**$\Delta F/F_0$**	**EC_{50} (μM)**	**S-slope**	**$\Delta F/F_0$**	**EC_{50} (μM)**	**S-slope**	**$\Delta F/F_0$**	**EC_{50} (μM)**	**S-slope**	**$\Delta F/F_0$**	**EC_{50} (μM)**	**S-slope**
choline	2.0 ± 0.1	84 ± 20	< 0.1	5.8 ± 0.2	240 ± 30	< 0.1	2.6 ± 0.1	18 ± 1	0.1	2.6 ± 0.1	12 ± 1	0.2
ACh	7.4 ± 1.0	660 ± 80	< 0.1	2.9 ± 0.1	35 ± 3	< 0.1	4.4 ± 0.3	222 ± 50	< 0.1	2.5 ± 0.2	73 ± 6	< 0.1
cytisine	-	-	< 0.1*	7.3 ± 0.4	11 ± 1	0.7	4.4 ± 0.1	2.6 ± 0.3	1.7	4.7 ± 0.1	3.5 ± 0.2	1.3
dianicline	4.7 ± 0.2	15 ± 1	0.3	6.5 ± 0.4	34 ± 4	0.2	2.3 ± 0.3	43 ± 6	< 0.1	4–6	> 100	< 0.1**
nicotine	2.2 ± 0.1	440 ± 100	< 0.1	6.4 ± 0.2	14 ± 2	0.5	4.7 ± 0.1	3.8 ± 0.2	1.2	4.8 ± 0.1	5.5 ± 0.2	0.9
varenicline	2.4 ± 2.0	1200 ± 500	< 0.1	6.5 ± 0.1	0.06 ± 0.01	110	7.1 ± 0.2	0.09 ± 0.02	79	5.3 ± 0.1	0.06 ± 0.01	88
10-fluorocytisine	ND	ND	ND	ND	ND	ND	2.3 ± 0.1	1.6 ± 0.3	1.4	3.0 ± 0.1	4.7 ± 0.3	0.6
9-bromo-10-ethylcytisine	ND	ND	ND	ND	ND	ND	3.1 ± 0.1	31 ± 2	0.1	3.6 ± 0.1	4.2 ± 0.2	0.9

Table 4.2. iDrugSnFR concentration-response relations versus a selected panel of nicotinic agonists. (ND, not determined; -/*/**: EC_{50} and $\Delta F_{max}/F_0$ could not be determined from the data (**Fig. 4.3**); therefore, the upper limit to the S-slope is estimated from the data at the foot of the concentration-response relation.

4.3.4. Stopped-Flow Kinetics of iDrugSnFRs

We measured the fluorescence changes of iDrugSnFRs in a stopped-flow apparatus with millisecond resolution during multiple 1 s trials and an independent 100 s trial. The stopped-flow data revealed that iDrugSnFRs do not have pseudo-first-order kinetic behaviors (i.e. the observed rate of fluorescence change is nearly linear with drug concentration) typical of two-state binding interactions. Time courses of iDianiSnFR (both 1 s and 100 s) were best fitted by double exponential equations, with most of the fluorescence change occurring within the first 0.1 s of mixing (**Fig. 4.6A**), with only a minor additional increase at the end of each trial. Changes in fluorescence from iCytSnFR during the first 1 s of mixing fit well to a single exponential (**Fig. 4.6B**) and have close to pseudo-first-order kinetics. As with iDianiSnFR, most of the fluorescence change occurs within the first 0.1 s, with additional fluorescent increase continuing over the remainder of the period. Like iDianiSnFR, iCyt_F_SnFR fluorescence changes are best fit by a double exponential (**Fig. 4.6C**), but the time course of fluorescence change is significantly slower: fluorescence gradually increases throughout the recording period and beyond (this information was considered in later *in vitro* experiments). iCyt_BrEt_SnFR fits well

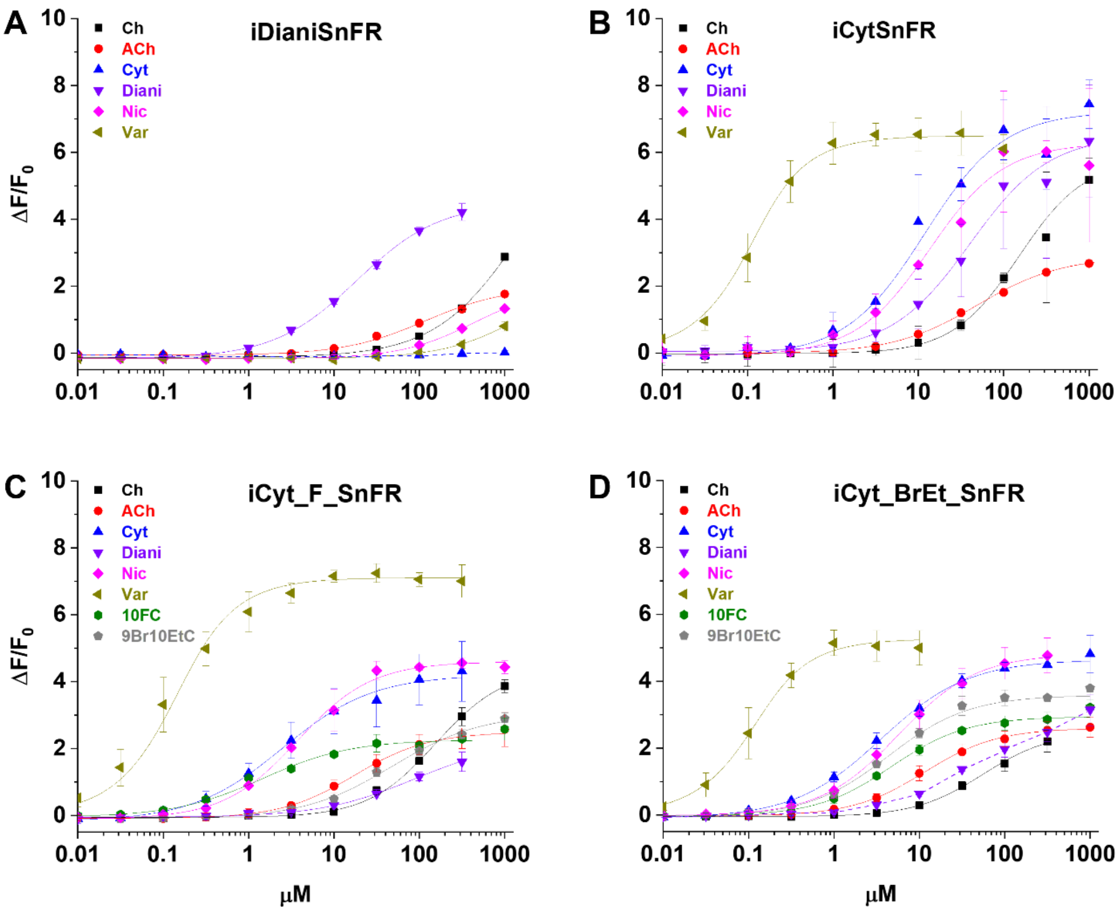

Figure 4.3. ***(A-D)*** Relevant EC_{50} values for each iDrugSnFR are listed in **Table 4.2**. Dashed lines indicate concentration-response relations that did not approach saturation for the concentration ranges tested; therefore, EC_{50} and $\Delta F_{max}/F_0$ could not be determined. (***A***) iDianiSnFR shows preference for dianicline, with some promiscuity for other nicotinic agonists. (***B***) iCytSnFR, (***C***) iCyt_F_SnFR, and (***D***) iCyt_BrEt_SnFR bind their drug partners but also respond to other nicotinic agonists. (Cyt = cytisine, Diani = dianicline, Nic = nicotine, Var = varenicline, 10FC = 10-fluorocytisine, 9Br10EtC = 9-bromo-10-ethylcytisine.)

to a single exponential (**Fig. 4.6D**) for the first 1 s of data collection, but like the other sensors, continues to increase its fluorescence over longer periods. We plotted the k_{obs} values obtained in the 1 s stopped-flow experiments versus concentration (**Fig. 4.6E–H**). Our stopped-flow experiments reinforced previous observations [683] that the kinetics of iDrugSnFR binding involve complexities beyond a simple first-order kinetic model governing two binding partners.

4.3.5. Millisecond Microperfusion Kinetics of iDrugSnFRs

We studied iCytSnFR_PM expressed in HEK293T cells during fluorescence responses to ACh, cytisine, or varenicline in a microperfusion apparatus that exchanged solutions near the cell on a

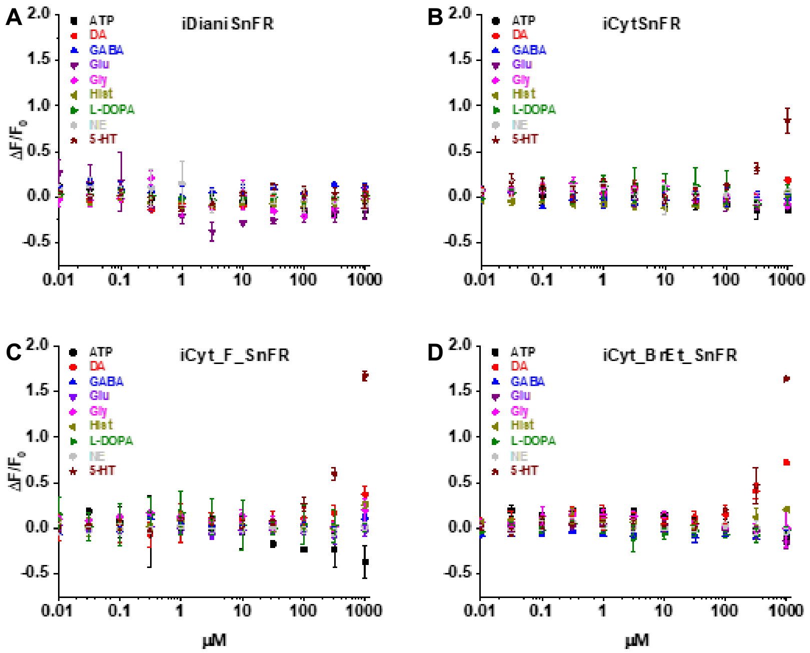

Figure 4.4. (***A***) iDianiSnFR shows no fluorescent response to any of the selected endogenous molecules. (***B***) iCytSnFR, (***C***) iCyt_F_SnFR, and (***D***) iCyt_BrEt_SnFR show no response to any of the selected endogenous molecules except 5-HT and DA at concentrations above 100 µM. (Abbreviations are the same as Fig. 3.1D-E.)

millisecond time scale (see Chapter 4.2.5); this system directly measures the decay of the response when ligand is suddenly removed. The rank order of iCytSnFR sensitivity is varenicline > cytisine > ACh; the time constant for decay decreased with increasing EC_{50} of the ligands (as measured by response in purified protein; **Fig. 4.3**), as though more tightly binding ligands dissociate more slowly (**Fig. 4.7A**). We measured the decay waveforms after drug pulses at concentrations greater than the purified protein EC_{50} to maximize the $\Delta F/F_0$ response over background (**Fig. 4.7**). Because the decay phases are measured after [ligand] has been stepped to zero, we expect that the decay rate constant(s) (k_{off}) for an iDrugSnFR do(es) not depend on the pulsed ligand concentration. Decay of the ACh response followed a single exponential time course (**Fig. 4.7B**), and the values of the k_{off} for 30, 100, and 200 µM ACh did not differ significantly (ANOVA, $p = 0.62$, df = 2, 20); thus, we pooled them to obtain a mean k_{off} of 1.9 ± 0.1 s^{-1} (n = 23). The corresponding time constant (τ_{off}) was 530 ± 30 ms, meaning that the temporal resolution of the iCytSnFR_PM sensor for changes in the ACh concentration was in the sub-second range. The decay of the cytisine and varenicline response was biphasic (**Fig. 4.7C-D**): two exponential decay terms with an additional constant component fitted the cytisine decay significantly better than a single exponential term (F-test, $p < 0.05$). As expected, neither the faster decay rate constants (kf_{off}; ANOVA, $p = 0.30$, df = 3, 32) nor the slower decay rate constants (ks_{off}; ANOVA, $p = 0.54$, df = 3, 31) differed among the tested cytisine concentrations (5–15 µM) – $kf_{off} = 0.61 \pm 0.04$ s^{-1} (n = 36) and $kf_{off} = 0.146 \pm 0.006$ s^{-1} (n = 35) with corresponding decay

Biosensor	KD (μM)	n	ΔH (kcal/mol)	-TΔS (kcal/mol)	ΔG (kcal/mol)
iCytSnFR	13.7 ± 1.1	0.84 ± 0.05	–2.1 ± 0.1	–4.6 ± 0.2	–6.6 ± 0.1
iCyt_F_SnFR	1.8 ± 0.5	0.83 ± 0.02	–5.5 ± 0.1	–2.4 ± 0.2	–7.9 ± 0.1
iCyt_BrEt_SnFR	5.4 ± 0.8	0.69 ± 0.09	–1.12 ± 0.03	6.1 ± 0.1	–7.2 ± 0.1
iDianiSnFR	7.6 ± 1.4	0.92 ± 0.02	3.2 ± 0.5	10.1 ± 0.4	–7.0 ± 0.2

Table 4.3. Affinity, occupancy number, and thermodynamic data calculated from ITC.

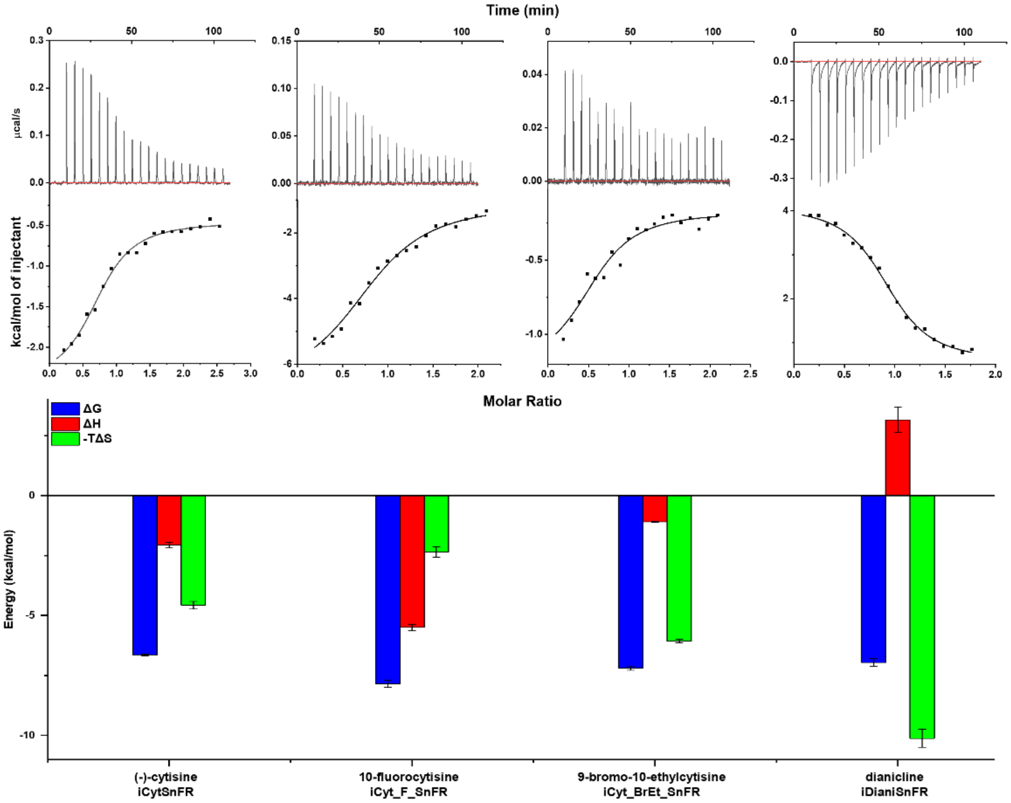

Figure 4.5. ITC traces, fits, and thermodynamic data. *(Top row*) Exemplar heat traces of iCytSnFR, iCyt_F_SnFR, iCyt_BrEt_SnFR, and iDianiSnFR paired with their drug partners. The heats for iCytSnFR, iCyt_F_SnFR, and iCyt_BrEt_SnFR were exothermic, while that for iDianiSnFR was endothermic. (*Middle row*) The resulting fits for each iDrugSnFR:drug pair from the integrated heats comprising each series of injections. (*Bottom row*) Energy calculations. All iDrugSnFRs show exergonic reactions, but the relative enthalpic and entropic contributions vary among them.

time constants (τf_{off}, τs_{off}) of 1.8 ± 0.1 s and 6.9 ± 0.2 s, respectively – meaning the temporal resolution of iCytSnFR_PM sensor for cytisine was < 10 s (sufficient for the temporal resolution of the live-cell experiments). We pulsed 2 μM varenicline, two orders of magnitude higher than the EC_{50} of the purified protein (60 ± 10 nM) (**Fig. 4.7D**). The values for kf_{off} and ks_{off} were 0.9 ± 0.2 s^{-1} and 0.0065 ± 0.0002 s^{-1}, respectively (n = 4), with the slower component dominating the decay phase (fractional amplitude = 85% ± 1%). Thus, the temporal resolution of the

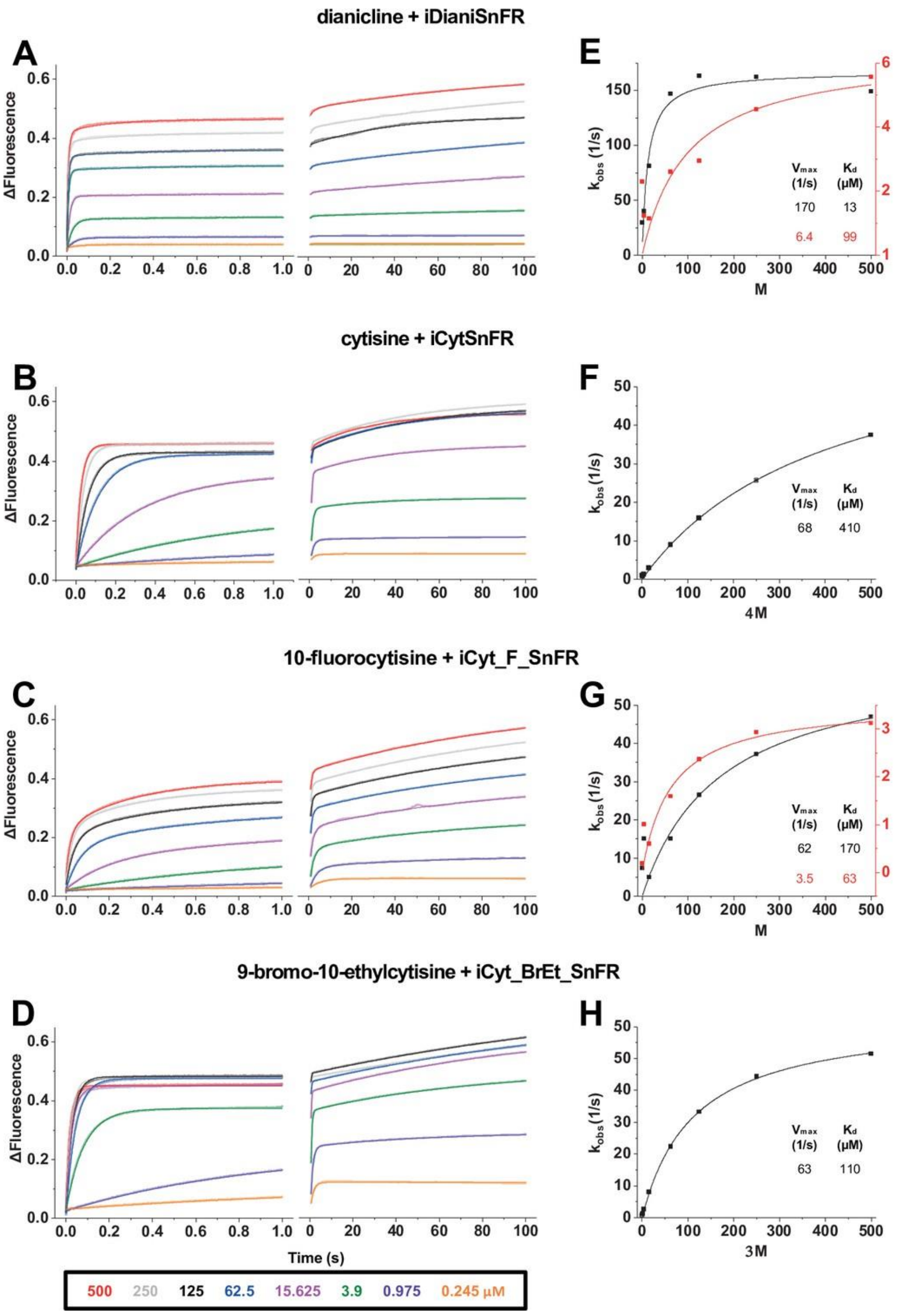

Figure 4.6. Stopped-flow fluorescence kinetic data for (***A***) iDianiSnFR, (***B***) iCytSnFR, (***C***) iCyt_F_SnFR, and (***D***) iCyt_BrEt_SnFR over 1 s and 100 s. Stopped-flow data shows a departure from first-order kinetics for this set of iDrugSnFRs. iDianiSnFR and iCyt_F_SnFR are fit to a double exponential; iCytSnFR and iCyt_BrEt_SnFR are fit to a single exponential. (***E-H***) Plots of the observed apparent rate constant against [agonist] for the 1 s data obtained in (***A-D***).

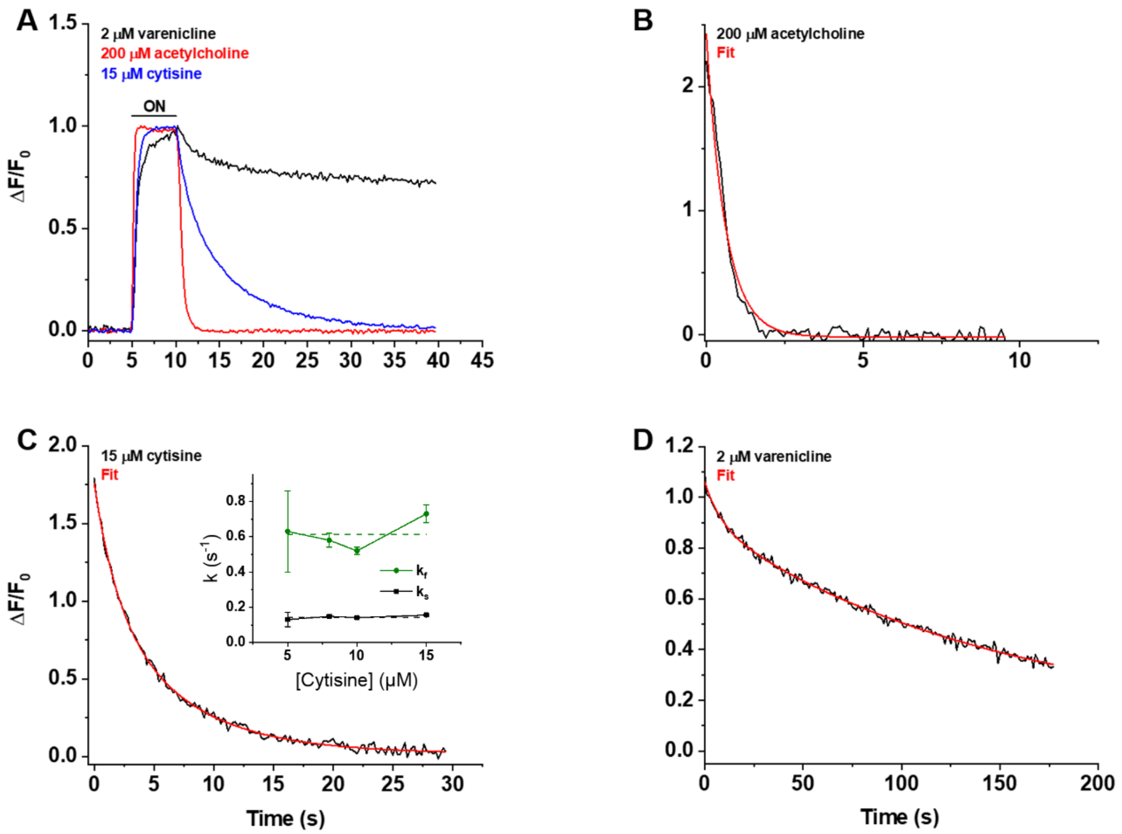

Figure 4.7. (***A***) The red, blue, and black traces are mean $\Delta F/F_0$ values for the ACh (200 µM), cytisine (15 µM), and varenicline (2 µM) responses as a function of time (n = 4–10 areas per ligand). $\Delta F/F_0$ was normalized to the peak response for each ligand. Ligand was applied for 5 s (*black horizontal bar*). ***(B–D)*** Decay phase of the response to ACh, cytisine, and varenicline in individual areas (*black traces*). (***B***) Decay of the ACh response (n = 1 area, 3 cells) was monophasic with a single time constant (τ_{off}) of 0.61 ± 0.02 s (n = 86 frames); the red line is a fit to the sum of a negative exponential component ($R^2 = 0.98$). (***C***) Decay of the cytisine response (n = 1 area, 4 cells) was biphasic with time constants (τf_{off}, τs_{off}) of 1.9 ± 0.2 and 6.6 ± 0.5 s (n = 149 frames); the red line is a fit to the sum of two negative exponential components and a constant ($R^2 = 0.996$), significantly better than the sum of a single negative exponential term and a constant (F-test, $p < 0.05$). The relative amplitude of the slower (A_s) to the faster decay component amplitude (A_f) was 61%. (*Inset*) Neither rate constant changed significantly over the [cytisine] range from 5 to 15 µM; dashed lines give the average over this range. (***D***) Decay of the varenicline response (n = 1 area, three cells) was also biphasic with a τf_{off} and τs_{off} of 9 ± 1 s and 150 ± 10 s (n = 178 frames). The red line is a fit to the sum of two negative exponential terms and a constant ($R^2 = 0.994$), and it was significantly better than the sum of a single negative exponential term and a constant (F-test, $p < 0.05$). The A_s:A_f ratio was 83%.

iCytSnFR_PM sensor for varenicline was in the minute range (too slow for resolving differences in live cell imaging).

4.3.6. iDrugSnFRs in Mammalian Cells and Primary Culture

We deposited all mammalian vector plasmids (AddGene #177742-177747, #177750-177751) and all AAV plasmids (AddGene #177752-177759) in an online database. We performed concentration-response experiments using wide-field epifluorescence imaging with each iDrugSnFR and its drug partner, sampling a range of concentrations covering a log scale

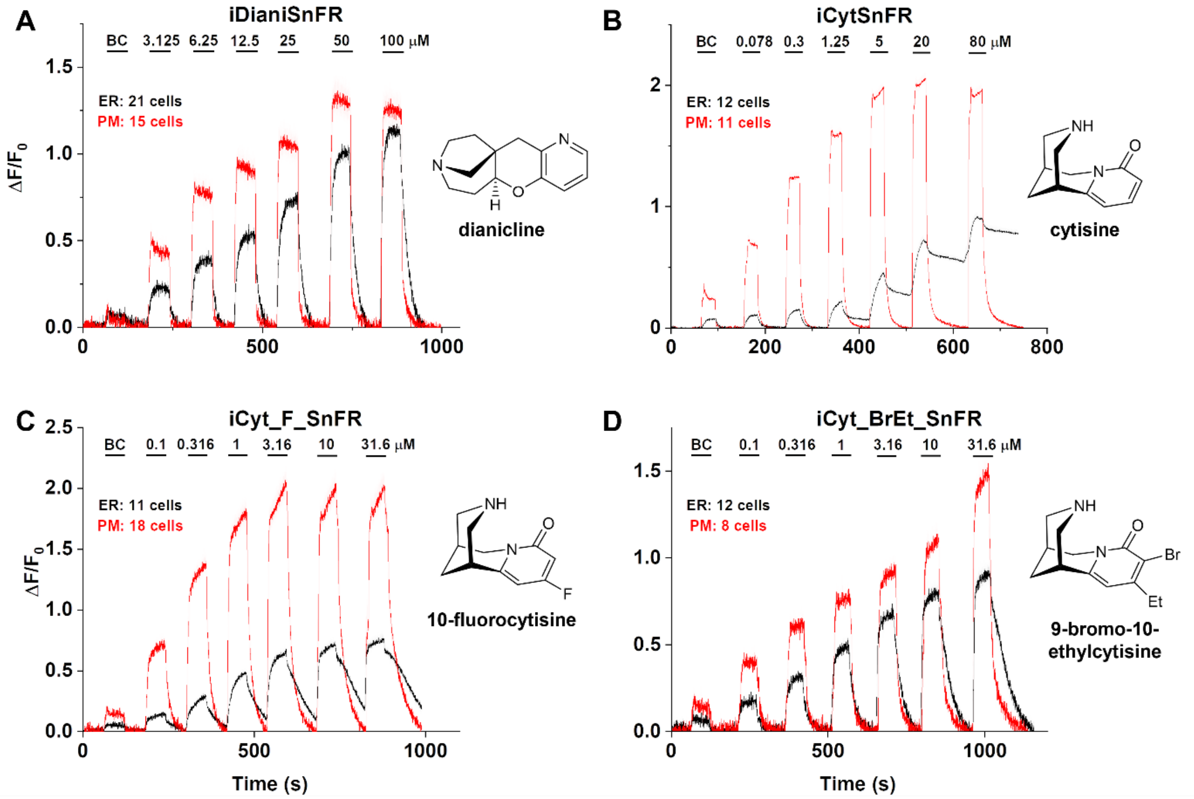

Figure 4.8. ***(A–D)*** Each iDrugSnFR detects its drug partner at the PM and ER of HeLa cells at the concentrations sampled. (SEM of data are as described previously.) (***A***) iDianiSnFR detects dianicline with a return to baseline fluorescence between drug applications. (***B***) iCytSnFR detection at the PM returns to baseline fluorescence between applications, while detection at the ER shows incomplete wash-in and washout. (***C***) iCyt_F_SnFR fluorescence response to 10-fluorocytisine in the ER also shows an incomplete washout between applications. (***D***) iCyt_BrEt_SnFR detects 9-bromo-10-ethylcytisine with wash-in and washout fluorescence similar to the pattern seen in iDianiSnFR.

surrounding the EC_{50} as determined for the purified protein (**Fig. 4.8** and **Fig. 4.9**) as described in Chapter 2.2.6. iDianiSnFR showed robust fluorescence to dianicline at the PM and the ER in HeLa cells across a range of concentrations (3.125-100 μM), and the response speed was nearly limited by solution changes, with a clear return to baseline fluorescence upon washout on the order of seconds after each drug application. At 100 μM, the PM and ER have a $\Delta F/F_0$ of ~1.2,

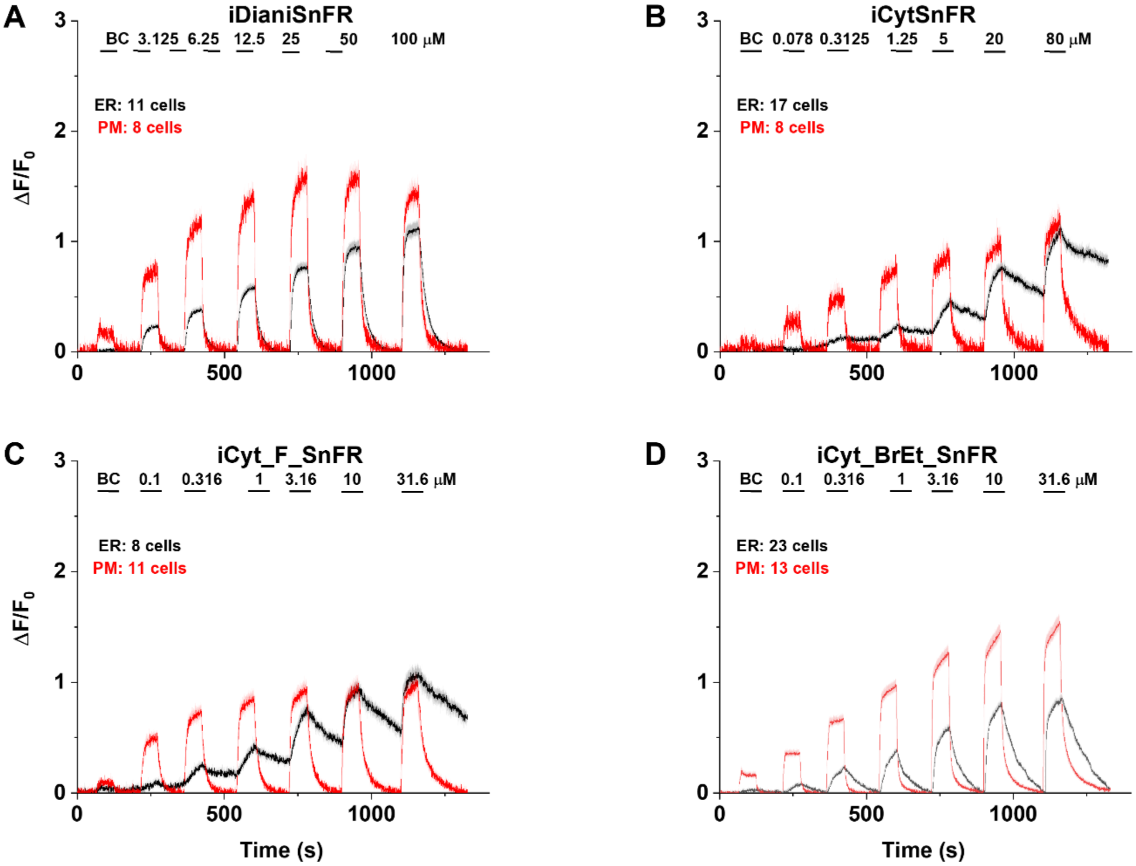

Figure 4.9. ***(A–D)*** Each iDrugSnFR detects its drug partner at the PM and ER over the concentrations sampled. (SEM of data are as described previously.) (***A***) iDianiSnFR detects dianicline with a return to baseline fluorescence between drug applications. (***B***) iCytSnFR detection at the PM returns to baseline fluorescence between applications, while detection at the ER shows an incomplete washout. (***C***) iCyt_F_SnFR fluorescence response to 10-fluorocytisine in the ER also shows an incomplete washout between applications. (***D***) iCyt_BrEt_SnFR_ER detects 9-bromo-10-ethylcytisine with a wash-in and decay intermediate between iDianiSnFR and the other two cytisine derivatives.

but at lower concentrations, the ER displayed 30–75% of the signal detected at the PM, which may indicate a difference in membrane crossing (**Fig. 4.8A**); imaging in PHC demonstrated similar trends as in HeLa cells (**Fig. 4.9A**). The iCytSnFR_PM construct detected cytisine at concentrations from 0.078 to 80 μM and demonstrated a return to baseline fluorescence upon washout on the order of seconds after each drug application, reaching a maximum ΔF/F$_0$ of ~2 at concentrations above 5 μM (**Fig. 4.8B**). In contrast to the _PM construct, the iCytSnFR_ER construct showed that cytisine exhibited slower entry into and exit from the ER of HeLa cells than other compounds we have tested [533,543,544,685], demonstrating a ΔF/F$_0$ above the

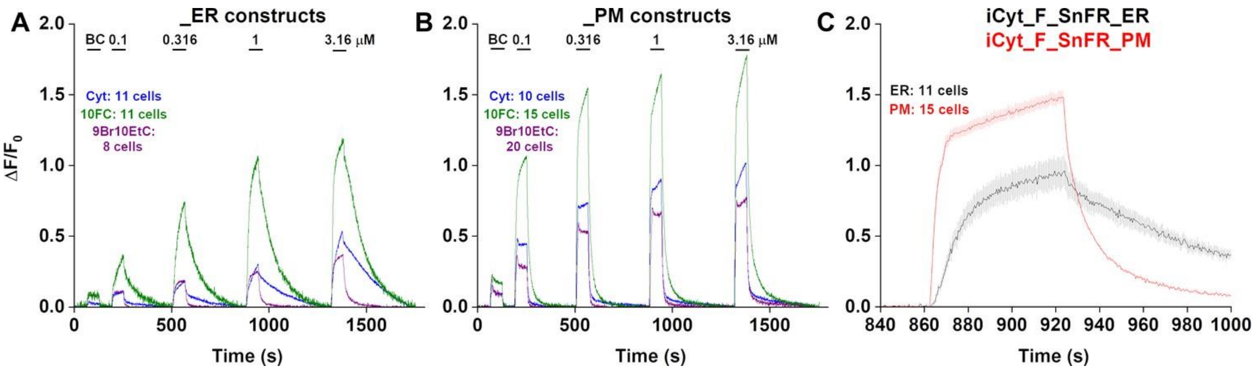

Figure 4.10. ***(A-C)*** Traces of fluorescence responses during time-resolved low-concentration dose–response relations for nicotinic agonists in HeLa cells: cytisine (Cyt) in cells expressing iCytSnFR_ER (***A***) or iCytSnFR_PM (***B***); 10-fluorocytisine (10FC) in cells expressing iCyt_F_SnFR_ER (***A***) or iCyt_F_SnFR_PM (***B***); 9-bromo-10-ethylcytisine (9Br10EtC) in cells expressing iCyt_BrEt_SnFR_ER (***A***) or iCyt_BrEt_SnFR_PM (***B***). Relatively long (300 s) washout periods between drug applications allowed a return to baseline fluorescence for the (***A***) ER and (***B***) PM. (***C***) A zoomed-in exemplar comparison of the ER and PM for a pulse of 1 μM 10-fluorocytisine shows a distinct lag in the decrease of the fluorescent signal in the ER as compared to the PM. (SEM of data as described previously.)

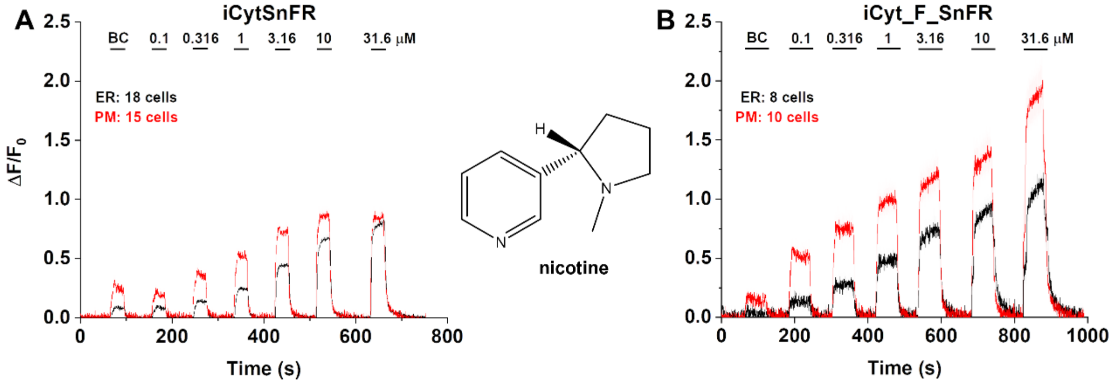

Figure 4.11. (***A***) iCytSnFR and (***B***) iCyt_F_SnFR detect nicotine at both the PM and ER. Nicotine enters and exits the ER rapidly over seconds, a direct contrast to the behavior of cytisine and 10-fluorocytisine as detected by their respective iDrugSnFR partners.

buffer control in the range of concentrations from 1.25 to 80 μM which was 25–50% of the maximum $\Delta F/F_0$ detected at the PM. Most notably, within the range of detectable concentrations of cytisine, the washout of cytisine was much slower than solution changes (**Fig. 4.8B**) with an incomplete washout persisting even after several minutes; this corroborates previous suggestions that cytisine has low membrane permeability, as evidenced by its low brain penetration [945]. In PHC, iCytSnFR detection of cytisine exhibited the same kinetic trends seen in HeLa cell experiments (**Fig. 4.9B**). During cytisine application, iCytSnFR_PM fluorescence nearly reached

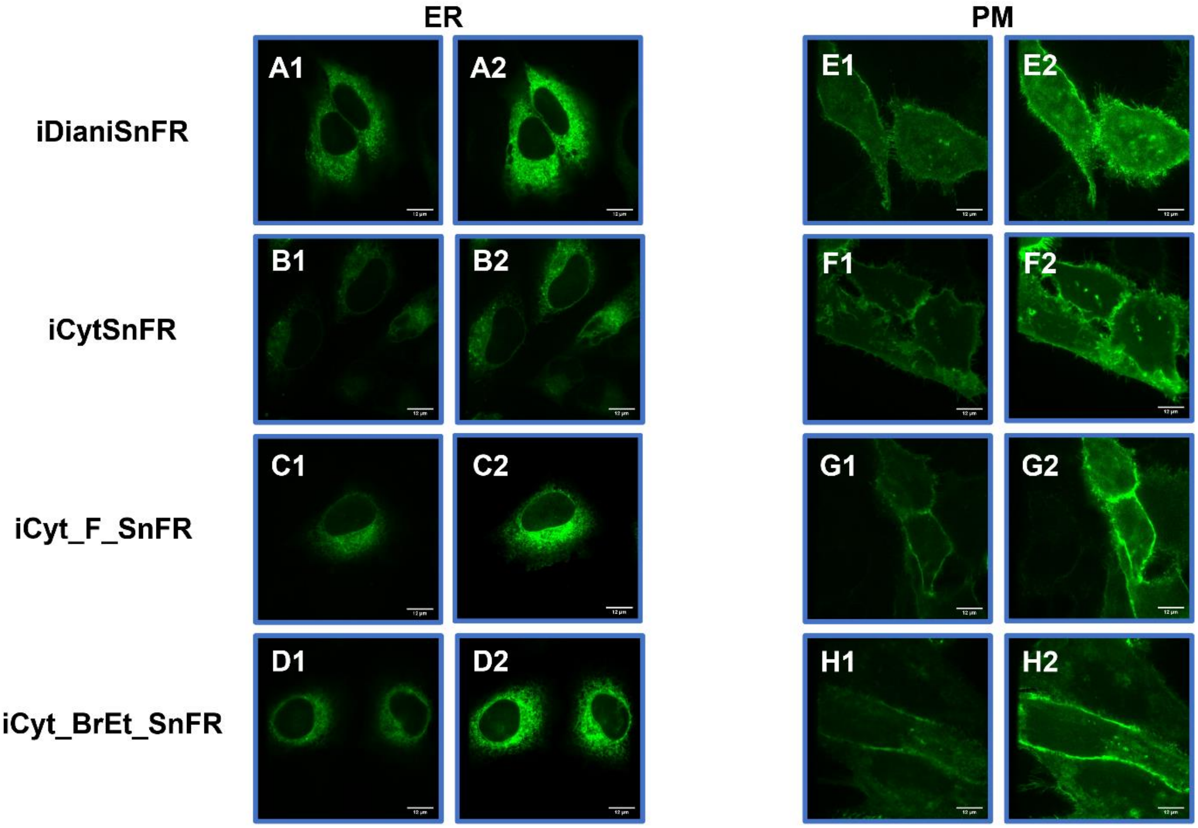

Figure 4.12. ***(A-H)*** ER-targeted constructs of iDianiSnFR, iCytSnFR, iCyt_F_SnFR, and iCyt_BrEt_SnFR are shown before (*A1*, *B1*, *C1*, *D1*) and during (*A2*, *B2*, *C2*, *D2*) exposure to each drug partner. ER-targeted iDrugSnFRs show the reticulated ER pattern and dark ovals corresponding to the nucleus. PM-targeted constructs of the same iDrugSnFRs are shown before (*E1*, *F1*, *G1*, *H1*) and during (*E2*, *F2*, *G2*, *H2*) drug introduction. Localization to the PM is robust, with some minimal puncta that may represent inclusion bodies or internal transport.

a plateau, and during the washout periods, fluorescence decreased back to baseline (though the rate slowed with higher concentrations), reaching a maximum $\Delta F/F_0$ of ~1.25 at 80 μM (approx. 60% of the observed signal in HeLa cells). The iCytSnFR_ER construct detection of cytisine in the ER reflected the trends seen in HeLa cells, with incomplete cytisine wash-in phases and prolonged cytisine washout phases; interestingly, the maximum $\Delta F/F_0$ of iCytSnFR_ER reached a similar maximum to that of iCytSnFR_PM in neurons (~1.25), which was not observed in HeLa cells (**Fig. 4.8B**). Of note, in preliminary HeLa cell imaging of varenicline applied to iCytSnFR, we found much slower kinetics that differed little between the _ER and _PM constructs (data not shown); these findings, which vitiated the use of the iCytSnFR-varenicline pair in cellular experiments, are buttressed by the microperfusion experiments demonstrating

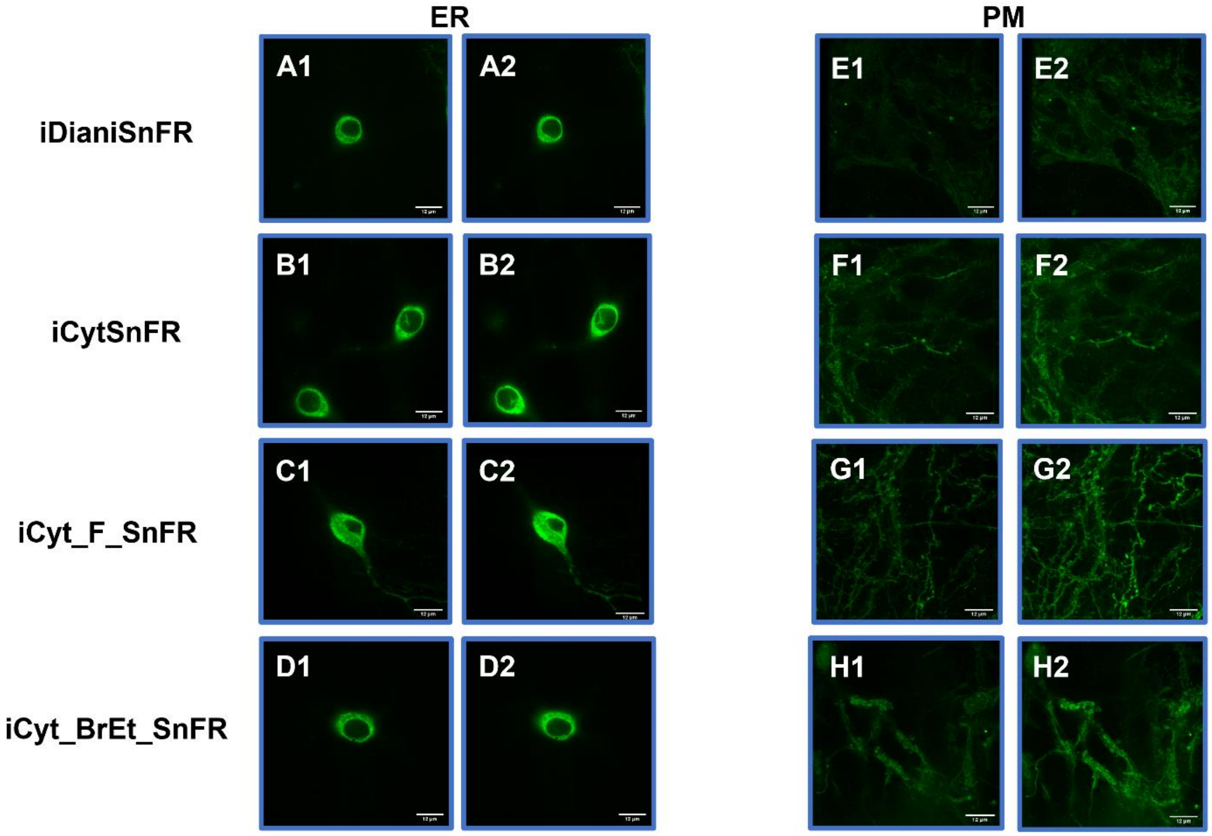

Figure 4.13. ER-targeted constructs of iDianiSnFR, iCytSnFR, iCyt_F_SnFR, and iCyt_BrEt_SnFR are shown before (*A1, B1, C1, D1*) and during (*A2, B2, C2, D2*) exposure to each drug partner. ER-targeted iDrugSnFRs show the reticulated ER pattern and dark ovals corresponding to the nucleus. PM-targeted constructs of the same iDrugSnFRs are shown before (*E1, F1, G1, H1*) and after (*E2, F2, G2, H2*) drug introduction. Localization to the PM is robust, with some minimal puncta that may represent inclusion bodies or internal transport.

markedly slow kinetics of varenicline-iCytSnFR interactions (**Fig. 4.7A, D**). In HeLa cells, iCyt_F_SnFR targeted to the PM and ER showed characteristics similar to iCytSnFR. The _PM construct detected 10-fluorocytisine across a range of concentrations with a return to baseline fluorescence between applications, while the _ER construct detected 10-fluorocytisine with $\Delta F/F_0$ values that were only 25–33% of those detected at the PM (**Fig. 4.8C**). Similar to iCytSnFR_ER detection of cytisine, iCyt_F_SnFR_ER detection of 10-fluorocytisine was much slower than solution changes and did not return to baseline between applications, though the washout occurs on the order of minutes, rather than tens of minutes (**Fig. 4.8C**). In PHC, the detection of 10-fluorocytisine by iCyt_F_SnFR resembled HeLa cell data; nevertheless, there were distinct differences (**Fig. 4.9C**), such as a decreased maximum $\Delta F/F_0$ with the iCyt_F_SnFR_PM construct and a similar maximum $\Delta F/F_0$ of ~1 for both the _ER and _PM constructs (additionally, the decay of the iCyt_F_SnFR responses lasted tens of minutes, resembling the iCytSnFR_ER data in PHC more than the iCyt_F_SnFR_ER data in HeLa cells). The other cytisine derivative, 9-bromo-10-ethylcytisine, showed a kinetic profile resembling dianicline in HeLa cells (**Fig. 4.8D**). Both iCyt_BrEt_SnFR_PM and iCyt_BrEt_SnFR_ER responses to 9-bromo-10-ethylcytisine (0.1–31.6 μM) were nearly limited by solution changes, with a return to baseline fluorescence on the order of seconds and a maximum $\Delta F/F_0$ difference of 50-75%, all of which indicated that 9-bromo-10-ethylcytisine crossed into and out of HeLa cells readily (**Fig. 4.8D**); imaging in PHC revealed the same trend (**Fig. 4.9D**). To examine the differences more fully in ER crossing among cytisine and its derivatives, we recorded fluorescence waveforms for all three at concentrations between 0.1 and 3.16 μM with much longer application and washout times than in the above experiments (**Fig. 4.10**). With these conditions, the fluorescence signals suggested complete washout of each nicotinic agonist from the ER of HeLa cells. However, it is noteworthy that even when applied at concentrations as low as 0.1 μM and 0.316 μM, cytisine and 10-fluorocytisine require washout times of several minutes from the ER, while the _PM constructs of each show a rapid return to baseline after drug application (**Fig. 4.10C**). We performed additional experiments to ensure that our observations of drug entry and exit from the ER were not the result of idiosyncratic biosensor function or folding in the ER. iCytSnFR and iCyt_F_SnFR both bind nicotine in the same concentration range as cytisine (**Fig. 4.3**), though with lower $\Delta F/F_0$. After transfection of _PM and _ER constructs for each sensor into HeLa cells (see Chapter 2.2.5), we performed concentration-response imaging of 0.1–31.6 μM nicotine (**Fig. 4.11**). These nicotine waveforms resembled those already published with iNicSnFR3a and iNicSnFR3b [533], confirming that iCytSnFR_ER functions as expected when detecting a more permeant nicotinic drug; thus, the slower kinetics for iCytSnFR_ER with cytisine and iCyt_F_SnFR_ER with 10-fluorocytisine arise because these drugs cross membranes more slowly. To examine localization of the _PM and _ER constructs at higher optical resolution, we imaged HeLa cells and PHC using a spinning disk laser scanning inverted confocal microscope as described Chapter 2.2.6. As previously observed [533,543,544,685], ER-targeted iDrugSnFR was retained in the ER (**Fig. 4.12A-D** and **Fig. 4.13A-D**). The iDrugSnFR constructs targeted to the PM showed correct localization, with some iDrugSnFR observed in the cell interior (most likely as part of the cellular membrane trafficking system; **Fig. 4.12E-H** and **Fig. 4.13E-H**).

4.4. Discussion

These experiments show, to our knowledge, the first time-resolved measurements of membrane permeation for candidate pharmaceutical drugs with LogD$_{pH7.4}$ less than -1; most orally available drugs have LogD$_{pH7.4}$ values between 2 and 4 [536], but cytisine, varenicline, dianicline, and the cytisine analogs studied here have calculated membrane partition coefficients some 3-6 orders of magnitude lower. These values and their order vary according to the algorithm, partially because of uncertainties in predicting pK$_a$ [949]; here, we provide values calculated by Chemicalize: 10-fluorocytisine = -2.70; cytisine = -2.64; dianicline = -1.29; varenicline = -1.27; 9-bromo-10-ethylcytisine = -1.13. It is remarkable that drugs with such low calculated partition coefficients cross membranes within seconds (9-bromo-10-ethylcytisine, varenicline, dianicline) to minutes (10-fluorocytisine, cytisine). According to some (but not all) algorithms, the calculated LogD$_{pH7.4}$ values suggest the two aforementioned time scales of membrane crossing; indeed, 10-fluorocytisine and cytisine cross more slowly while having LogD$_{pH7.4}$ < -2. These observations support previous work suggesting that differences among the chemical properties of nicotinic partial agonists correlate with drug permeation into the CSF after peripheral administration in mice [945].

The iDrugSnFRs for nicotinic agonists are sensitive enough to allow detection of their target compounds near experimentally determined (or otherwise projected) concentrations in the human blood and CSF [945,961,962]. These sensors have the advantage that they measure free aqueous ligand concentration (the same as sensed by nAChRs) and can be targeted to a variety of intracellular compartments (see Chapter 2.2.5). For drugs that bind at orthosteric cholinergic sites (both nicotinic and muscarinic), we anticipate that a collection of tens of iDrugSnFRs will suffice to detect all present and future ligands; for example, none of the biosensors in **Table 4.1** were evolved to bind varenicline, yet it binds to some iDrugSnFRs with nanomolar EC$_{50}$ (only iDianiSnFR, which lacks His68 in its binding site, binds varenicline with EC$_{50}$ > 10 μM). The cellular experiments described here cannot use iDrugSnFR pairs with dissociation rate constants less than ~0.1 s^{-1}, corresponding to an EC$_{50}$ of < ~100 nM; however, all known neural drugs leave the human body and brain much more slowly, with rates determined primarily by metabolism (even ‘fast’ nicotine metabolizers clear nicotine with decay time constants of ~1200 s [963]). Thus, iDrugSnFRs can be used in studies of personal pharmacokinetics in human biofluids as they are highly sensitive and simple to prepare.

This study shows that the amine group of nicotinic ligands makes equidistant cation-π interactions with two tyrosine residues (Tyr65, Tyr357) which is confirmed by higher-resolution (1.5–1.7 angstroms) structures of varenicline, ACh, and choline crystallized with isolated PBP moieties (PDB 7S7X, SV1R, 7S7Z, respectively; see also 3R6U, 6EYQ, and 3PPQ). Cation-π interactions also occur for cholinergic and/or nicotinic ligands in nAChRs [964,965], the ACh binding protein [966], PBPs [960], and mAChRs [967]; additionally, we observe that the protonated amine of varenicline makes an H-bond to a backbone carbonyl group, another similar theme in ACh binding protein [966] and nAChRs [968]. This study presents a general step forward in understanding the structure-function relations of iDrugSnFRs: the chromophore in the cpGFP moiety of most present iDrugSnFRs [533,543,544,682,685] contains a tyrosine in an extended π system [969,970] and its photophysics depend strongly on the surrounding water molecules and side chains [970,971]. We found that Glu78 in Linker1 changes its orientation: in the liganded state, it interacts with two positively charged residues (Lys97 and Arg99) on the surface of the cpGFP; and in the apo state, Glu78 has moved ~14 angstroms to form an H-bond with the tyrosine moiety of the chromophore (**Fig. 4.1E**; see Chapter 2.2.1). Presumably the liganded state of iNicSnFR3adt allows for a water molecule to H-bond with the hydroxy group of the chromophore, promoting its fluorescence; but this water molecule is replaced by protonated Glu78 in the unliganded state, which leads to the nonfluorescent state of cpGFP [706]. While we cannot resolve the protonation-deprotonation event, the available functional data show good support for its occurrence: a) the apo form of the iDrugSnFR increases its F_0 by 10-fold per pH unit [533], as though when deprotonated Glu78 leaves the quenching position and moves to make the salt bridges with Lys97 and Arg99; b) the EC_{50} for the ligand decreases by 10-fold per pH unit [533], as though the conformation of the linker that forms the salt bridges is also the ligand-bound fluorescent form of the PBP; c) only glutamate functions in position 78 of iSeroSnFR [683]; and d) the mTurquoise variant in iGluSnFR, which has a tryptophan chromophore, requires entirely different linkers [712].

Our sub-second data with cytisine at iCytSnFR are the most complete, comprising both stopped-flow and HEK293T cell microperfusion measurements. Recent literature on the kinetics of PBPs emphasizes a modified induced-fit model with the additional possibility that the apo PBP can also undergo spontaneous activation (termed the closed state in the SBP literature [972,973]). Such a scheme (**Fig. 4.14**) resembles the three-state model we and colleagues developed to account for iSeroSnFR [683]; notably, the three-state model predicts the experimental observation that the rate constant of the slower component of the kinetics decreases as the ligand concentration increases. For the cytisine-iCytSnFR case reported in this paper, we conclude that the apo fluorescent state is less bright than the bound-fluorescent state (shown by the different colors of the cpGFP moiety in **Fig. 4.14**). Interestingly, the three-state model fitted the kinetic data best if we assumed that there is a population of higher-sensitivity iDrugSnFRs in HEK293T cells with an EC_{50} at least 10 times less than we observed with the stopped-flow and HeLa cell data. The fragmentary kinetic data for ACh interacting with iCytSnFR_PM suggest equilibrium and rate constants in the same broad range as for cytisine; however, the kinetic data for varenicline suggest that ligand unbinding dominates the decay phase, with a rate constant < 0.01 s^{-1}. As a caution, recent data show that binding mechanisms at PBPs can change fundamentally with even a single mutation [895]; we therefore wish to avoid generalizing past the single iDrugSnFR (iCytSnFR) we consider here.

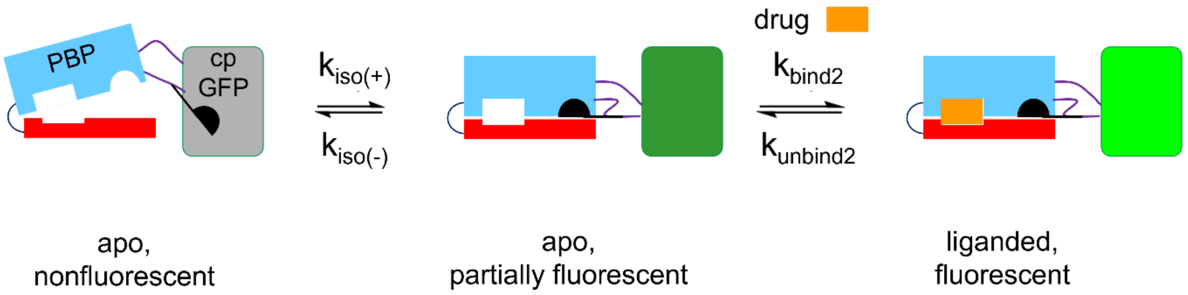

Figure 4.14. The diagram contains cartoons of the PBP moiety (*blue* and *red*), the linkers (*black* lines), the Glu78 ‘candle snuffer’ attached to Linker1 (*black*), and the cpGFP moiety (*gray*, *dark green*, or *green*). We postulate that the iDrugSnFR has both an apo nonfluorescent state and an apo fluorescent state; these states interconvert with time constants of tens of seconds ($k_{iso(+)}$ and $k_{iso(-)}$). Cytisine (‘drug,’ *yellow*) binds to the apo fluorescent state (k_{bind2}), inducing an additional fluorescent state on a briefer time scale. The initial fluorescence increase represents the binding-induced increase, and the slower increase is governed by partial re-equilibration of the two apo states. Upon removal of cytisine after just a few seconds of perfusion (**Fig. 4.7**), the fluorescence decay represents the dissociation of cytisine ($k_{unbind2}$).

Our measurements show two implications for future smoking-cessation drugs: first, α4β2 agonists that enter the ER (e.g. nicotine and varenicline) upregulate nAChRs [974], which may be necessary and sufficient to instantiate addiction [532] (indeed, maintenance of upregulation by varenicline may help to explain its suboptimal quit rate); second, ligands that do not cross into the ER well are also unlikely to enter the brain and therefore unlikely to be useful for smoking cessation [945]. Smoking-cessation drugs must also contend with other ER-based processes: most drug metabolism takes place in the ER; and upregulation occurs at a sustained agonist concentration in the ER some hundredfold lower (e.g. ~5 nM nicotine) than the extracellular concentrations (e.g. 500 nM nicotine) which transiently activate α4β2 nAChRs [534]. Given these challenges, the iDrugSnFRs present a paradigm to measure cellular and subcellular pharmacokinetics of pharmacological compounds at physiologically relevant concentrations. iDrugSnFRs can be used as a potential drug development tool to aid in the screening of compounds with poorer entry into the subcellular compartments which mediate their effects. Thus, in lieu of costly animal studies or imprecise calculations, these sensors present an appealing option for determining the potential efficacy of most weakly basic orally active candidate pharmaceuticals.

CHAPTER 5*:* HIGH-THROUGHPUT ZEBRAFISH BEHAVIORAL ASSAYS FOR ASSESSING RESPONSES TO RAPIDLY ACTING ANTIDEPRESSANTS

5.1. Background

As outlined in Chapter 2.4.2, zebrafish models of depression promise an array of advantages and disadvantages compared with other common laboratory research animals which are important to consider when designing an investigational protocol. For example, researchers assessing the efficacy of antidepressants must account for the route of administration in zebrafish, which is primarily bath perfusion (whereas for rodents the routes of administration are more varied, though IP injection is most common [975]). Additionally, the zebrafish behavioral repertoire is less varied than for rodents owing to the relative simplicity of the former's brain [69], and there are fewer tasks which have been validated for assessing affect. However, because MDD is more than mere physiological disruption (it involves an experiential component affecting consciousness [976], impossible to even approximate in another species), animal models should be leveraged not on the basis of their ancestral similarity to humans but instead on the specific feature or potential etiology of depression under consideration.

In terms of practicality, zebrafish offer a low-cost high-throughput means of testing candidate medications as well as behavior. While the causes of depression in humans are undoubtedly varied and its classification overdetermined, more straightforward single-factor etiologies (e.g. LH [977], hormonal dysfunction [802,803], or exposure to toxins [978]) can be used to answer targeted questions about physiological changes correlated with specific behavioral deficits. In addition, as with rodent models, exposure of zebrafish to antidepressants can aid in understanding their putative mechanisms even if the underlying pathophysiology of the disorder continues to elude apprehension. With the novelty of RAADs as potential paradigm-shifting medications for the treatment of MDD, zebrafish present an attractive option in large part owing to the ease with which both high-throughput behavior as well as whole-brain imaging can be performed (see Chapter 2.4 and Chapter 2.5).

With this in mind, we attempted to investigate the effects of RAADs on a genetic zebrafish model of depression. The *nr3c1* null mutant has significantly higher whole-body cortisol [802,803,979] corresponding to increased anxiety- and depression-like behavior in both larvae [802] and adult fish [803] as well as a predictively valid response to SSRIs [802,803]. We decided to adapt a behavioral challenge protocol (developed for use with WT larvae) which showed improvements to passivity caused by electrical shocks from a single dose of ketamine [836], modifying the stressor to suit our high-throughput behavioral assay to assess the stress response and recovery of *nr3c1* null mutants.

5.2. Methods

The Prober lab uses commercially available software and hardware for the quantification of movement in larval zebrafish housed in separate wells of a 96-well plate in 4-7 dpf larvae over the course of several consecutive light-dark cycles (primarily to study sleep) [848,980-983]. The most common method of quantifying larval movement is with video tracking [984], and the video tracker used in the Prober lab (ZebraBox, ViewPoint Life Sciences) is the most well-documented in the literature [983]. The video tracker consists of a monochrome camera (for reliable tracking in low-light conditions) with a fixed-angle mega-pixel lens equipped with an IR filter (to allow for detection in darkness) [983]. A 96-well plate (7701-1651, GE Healthcare Life Sciences) containing larvae (see below) is secured inside of a bath chamber filled with circulating water which is pumped (MJ-500, Maxi-Jet) from a 10 L tank below the apparatus at 1.3 mL/min [981] heated to 28.5ºC (HT100, Tetra). The light-dark cycle is held at 14:10 consistently with lights on 9am-11pm, and illumination is achieved via several white LEDs positioned below the plate; IR LEDs placed alongside allow for detection of movement throughout the experimental protocol [983]. The proprietary software (ZebraLab, VPLS) uses a frame rate background subtraction method which relies on changes in pixel intensity from frame-to-frame, with a programmable detection threshold allowing the user to set a cutoff for how many pixels must change to count as a movement; the typical detection threshold is set to 15 [983]. Frames are captured at 15 Hz with quantification of movement within 1 min bins (the amount of time in seconds that movement occurs within each bin is the output value) and the data can be exported as a spreadsheet (Excel) for offline analysis (MATLAB) using custom scripts which bin movement averaged across specified groups/genotypes present into 1-, 10, or 60-min periods as separate traces with 95% confidence intervals [983].

We adapted an aforementioned behavioral challenge [836] which consists of exposing one 10-15 dpf WT larva to 212 μM ketamine in a 50 mL dish for 20 min before transfer to a plastic tank (24 x 48 x 11 mm external and 21.2 x 46.5 mm internal, TAP Plastics) and exposure to stress in the form of electrical shocks (50 ms at 1 Hz for 30-60 min); behavior was tracked before, during, and after the shock period using an overhead camera (Manta G125B, Allied Vision Technology) at 15 Hz illuminated by IR LEDs positioned below the tank, similar to our setup. The interesting result from this experiment was that larvae treated with ketamine displayed a significantly longer period of active coping (i.e. struggling or moving after the initiation of the electrical shock stimulus) before transitioning to passive coping (i.e. moving less than pre-shock periods), with active coping persisting for upwards of 10-20 min longer among ketamine-treated fish [836]. We decided to capitalize on our high-throughput setup to increase the number of larvae assessed for changes in coping behavior from ketamine exposure. We also changed the stressor protocol to accommodate the video tracker apparatus; we decided to employ heat-shock stress over the course of 60 min because it is an easier protocol to implement and is known to have robust behavioral effects [985]. The optimal temperature for zebrafish is 27-28.5ºC, and in the wild regular temperature fluctuations of 5ºC are common [986], but zebrafish can demonstrate distinct anxiety-like behavioral phenotypes in response to larger temperature increases (up to 38ºC) including thigmotaxis [987] and dark avoidance [985]. We used a precision heating element (Sous Vide 10, American Outdoor Brands) to heat the tank such that, after compensating for the loss of heat as the water is circulated up to the bath chamber, we could achieve the desired heat shock temperature for the larvae in the plate.

We first needed to raise a breeding population of *nr3c1* heterozygotes (hets) and *nr3c1* null mutants (nulls). The mutation is of a single base pair (from C to T) at position 1692 of the cDNA which changes the AA from an arginine to a cysteine. We adapted a strategy [803] of site-directed mutagenesis to engender a point mutation at position 1680 which introduces a cut site for the DrdI enzyme; in this scheme, DNA from WT fish will be cut to give bands of approximately 100 bp and 30 bp while DNA from fish with at least one point mutation will have an uncut band at 130 bp. We used For – 5’-CAAAATCCGCCGGAAGAACTG*A*CCTGCCTG-3’, Rev – 5’-GGGAGGGGGGAATTGGGATAAGTT-3’ as our primers (the italicization in the forward primer introduces the point mutation at position 1680). To raise fish, we first in-crossed known hets (a gift from the Engert lab) to generate a population of nulls, hets, and WT embryos which we sterilized with both 0.05% bleach and Ovadine (an iodine-based disinfectant) after which larvae were raised for approximately two months (see Chapter 2.5). We then anesthetized fish with tricaine and performed fin clips using a razor blade to cut a small piece from the tail fin [988], with each clip placed separately in a labeled 96-well plate (24-300 non-skirted PCR Plate, Olympus Plastics) in 100 μL of lysis buffer consisting of: deionized water; Tris buffer, pH 8.5 (to regulate lysis pH for DNA stabilization); Triton buffer (to lyse cells); EDTA (to inactivate nucleases); and Proteinase K (to digest contaminating proteins). This lysis plate is placed in a 37ºC incubator overnight and then boiled the next morning at 98ºC (to inactivate the enzymes) before being prepared for PCR. We add 1 μL of DNA from each well to a 25 μL PCR mix including: deionized water; PCR Master Mix (salts, Tris, dNTPs, gelatin, and albumin); the forward and reverse primers (20 μM); and DNA polymerase (AmpliTaq, Thermo Fisher Scientific); PCR conditions are: melting temperature = 95ºC, annealing temperature = 58ºC, extension time = 30 s, number of cycles = 45. Once the run is complete, we add 5 μL of DrdI enzyme mix to each well and incubate for 1 h before adding the contents to a 4% gel with EtBr dye in TAE against a 100 bp DNA ladder. During UV visualization, the null genotype appears as a single higher band (~130 bp), hets appear as two bands in close proximity near ~100 bp, and WT appears as a single lower band (~100 bp) (**Fig. 5.1**). Hets and nulls are then identified in their tanks and housed separately; they are ready to mate after approximately 10 days of recovery from the fin clip procedure.

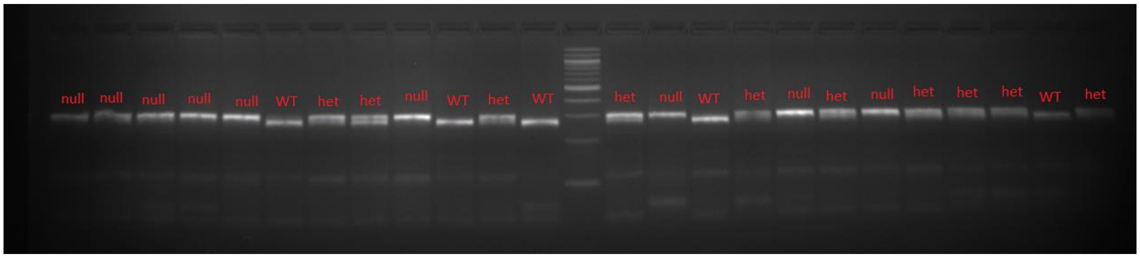

Figure 5.1. Exemplar row from a gel demonstrating the three different genotypes (annotations above each lane): the null band is noticeably higher (~130 bp) than the WT band (~100 bp) while the het genotype displays two bands distinct from each other.

The experimental protocol involved outcrossing *nr3c1* null mutants to WT zebrafish to make het larvae as well as in-crossing nulls to generate more nulls. We settled on this strategy because hets have similar behavior profiles to WTs, with both exhibiting significantly different behavior than null mutants [803]; this also simplified the genotyping process. Crosses were set up and embryos collected/cleaned as described in Chapter 2.5, and 4 dpf larvae were housed in the fish facility as described in Chapter 2.5. At 12pm on the day of the experiment (we normalized for time to account for circadian changes in cortisol [989]), age-matched groups of larvae (approx. 100 of each genotype between 10-15 dpf) were removed from the fish facility and placed into each ~650 µL well of a custom 3D-printed 96-well mesh-bottom plate which allows for exposure to solution added to a shallow plastic dish below. After two plates were filled, 50 mL of either 107 µM arketamine or 53.5 µM arketamine solution in E3 (equivalent to or half of the amount of arketamine in the racemate used in the original study [836]) with 0.1% DMSO was poured into another shallow plastic dish while E3 in 0.1% DMSO was poured into a fourth shallow plastic dish; once these transfer dishes were prepared, both mesh plates were quickly lifted and placed in the experimental solutions for 20 min at RT. After the exposure period ended, we briefly rinsed the bottom of the mesh plates in E3 before transferring them to another set of shallow plastic dishes filled with E3. The custom mesh plate apparatuses were then placed inside a pair of video trackers as described above; we allowed the larvae to acclimate for 1-2 h before switching the circulating water to draw from a tank with heat shock-temperature circulating water for 1 h, after which the circulation was changed back to the normal 28.5°C bath for the remainder of the day and overnight. The next morning, the plates were taken out and scored (wells with dead, obviously sick, or otherwise malformed fish were discounted), after which the video tracker file was exported and analyzed as described above.

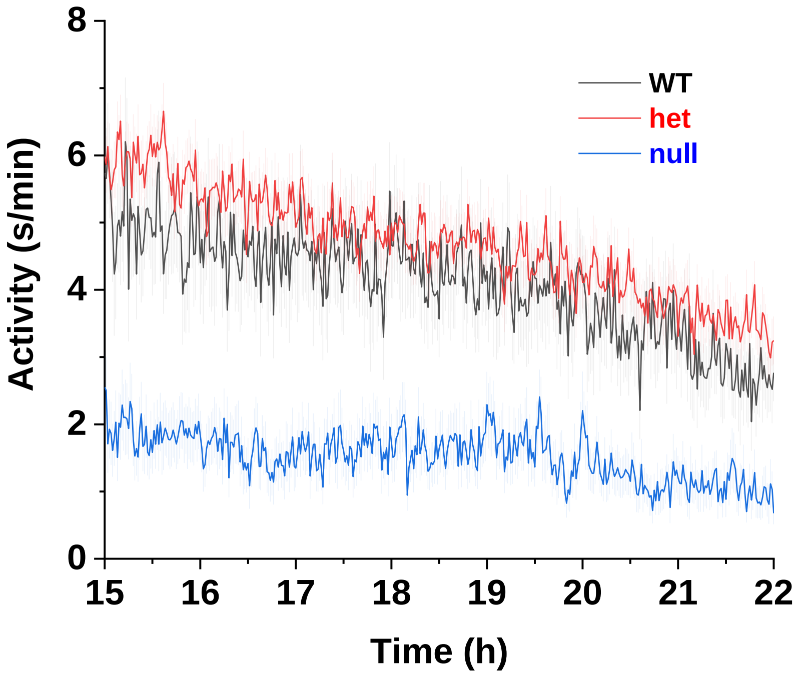

Figure 5.2. Portion of waking period demonstrating significant overall differences between the WT (*black*) and het (*red*) genotypes versus nulls (*blue*) in terms of average activity (data presented in 1 min bins; SEM is as described previously).

5.3. Results and Next Steps

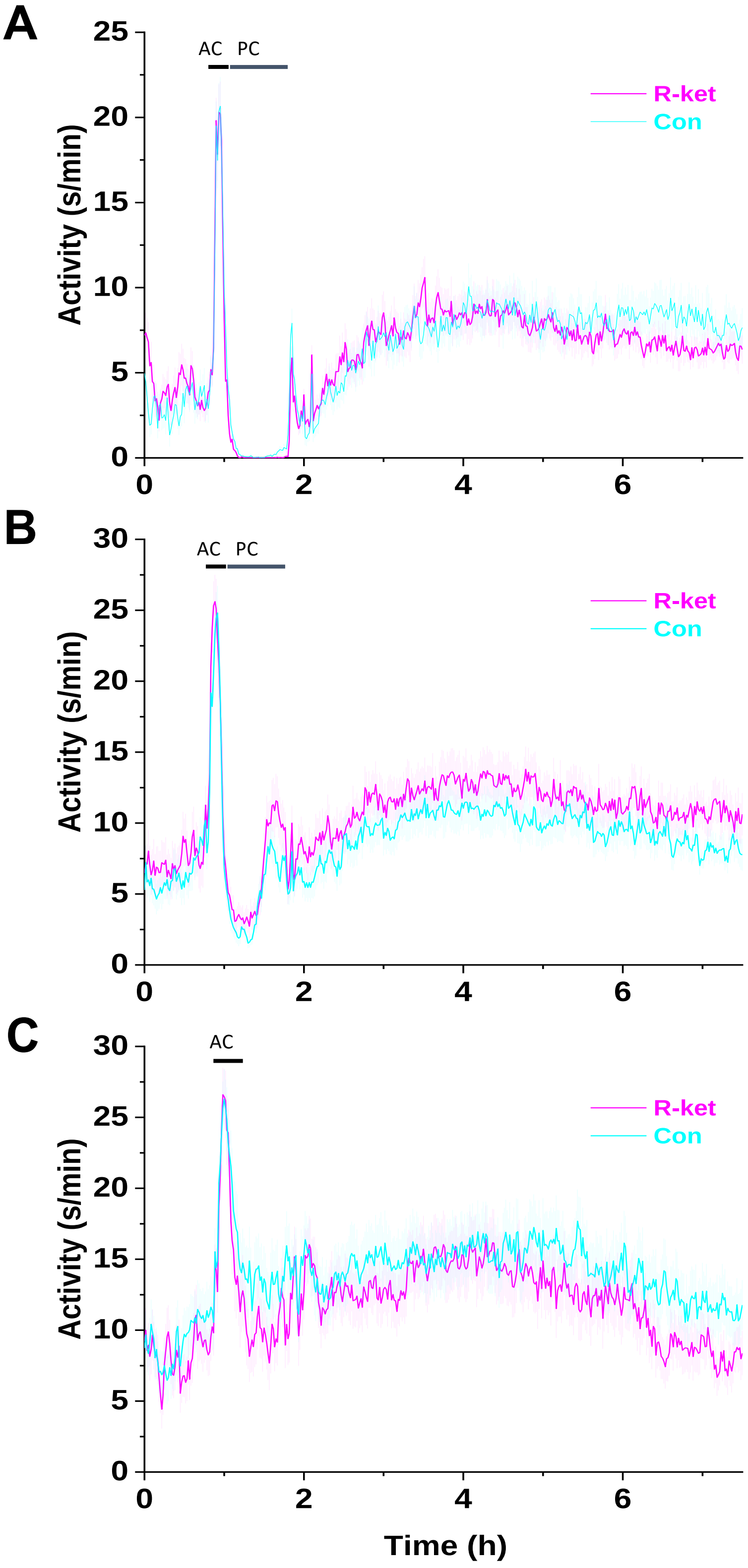

Figure 5.3. (***A***) The heat shock temperature of 37ºC produced a robust active coping (AC; *black bar*) response (20-30 min) as well as a passive coping (PC; *blue bar*) response (30-40 min) in both groups with little distinction between them. During the PC period, activity dropped to nearly 0 s/min, suggesting that this temperature is too high for characterizing a sensitive behavioral assay. (***B***) The heat shock temperature of 36ºC also produced a robust AC response as well as a PC response; both were of similar magnitude and duration as in (***A***), but neither group's activity level dropped to 0 s/min during the PC period. There was a slight increase in average activity after the heat shock among arketamine (R-ket)-treated larvae compared to controls (Con). (***C***) The heat shock temperature of 35ºC produced a robust AC period but no PC response. This demonstrates that 36ºC is the threshold at which PC can be elicited. In (**C**), Con activity after the heat shock period is higher than R-ket; such phenomena were common throughout the set of experiments we performed. (For all traces, SEM is as described previously.)

We first confirmed that null larvae have lower overall spontaneous activity while hets and WT do not show any appreciable differences from one another [803]. We found that, among 4 dpf larvae generated from *nr3c1* het in-crosses, nulls demonstrated on average a lower level of activity compared to hets and WT, both of which exhibited average activity levels (~3-6 s/min) typical of normal larvae behavior (**Fig. 5.2**).

After several rounds of preliminary tests using 10-15 dpf WT larvae comparing arketamine-treatment activity with controls, we found that the optimal bath temperature for eliciting a robust behavioral response was 36ºC (**Fig. 5.3B**). Our evaluation was based on the lowest temperature at which the active coping response (larvae motion significantly increased above resting levels) was still elicited so as to stress the larvae without causing additional unwanted side effects (**Fig. 5.3**). We then ran several iterations of the adapted heat shock protocol using 10-15 dpf hets and nulls, with one plate treated with arketamine and the other with E3 (**Fig 5.4** is exemplary of the overall trends exhibited across datasets and is discussed in detail). We noticed that, even with half of the concentration of arketamine as was present in the initial protocol (and a quarter of the concentration of total ketamine) [836], all larvae exhibit some degree of sedation during the pre-shock rest period; of interest, the null larvae in the control condition also appear to have lower spontaneous activity than the hets (20-35 s/min vs. 15-25 s/min) but exposure to arketamine appears to affect the hets more than the nulls such that both drop to similar levels of activity (15-25

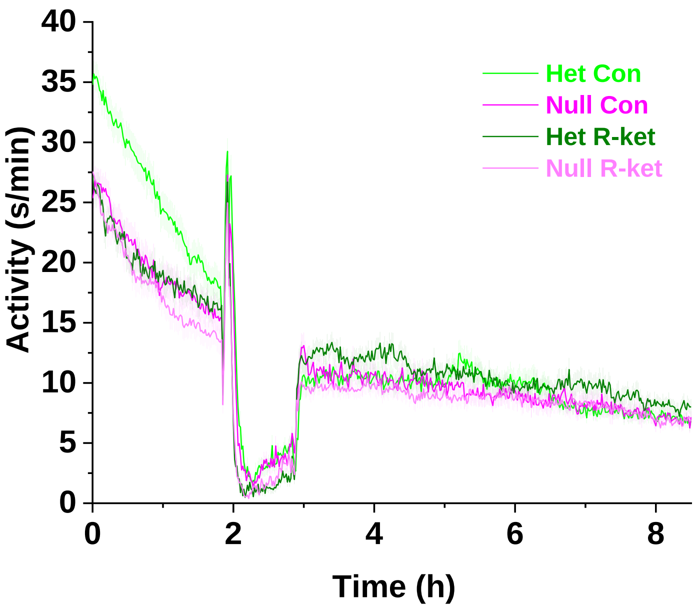

Figure 5.4. Optimized experiments demonstrating both active coping and passive coping among all four groups assessed in these experiments (het controls, *bright green*; null controls, *magenta*; het arketamine-treated larvae, *dark green*; null arketamine-treated larvae, *pink*). While the het control fish demonstrate higher baseline activity than the other three groups, there are no meaningful distinctions among any groups in the heat shock nor recovery periods.

s/min). During the heat shock stress, the first 20-30 min comprise the active coping period wherein the larvae respond by increasing their activity over baseline (~60% increase); the last 30-40 min comprise the passive coping period in which the larvae display futility behavior, with their average activity dropping below baseline levels (< 5 s/min). During these two periods, we did not notice any significant differences between the nulls and hets in either the length of the active coping period or the vigorousness of the response to the stress; both groups also demonstrate activity levels during the passive coping period that are nearly zero (with perhaps a slightly stronger effect from arketamine treatment than among the control-treated larvae). During the rest of the day after the stress period, there were no appreciable differences in the recovery period between hets and nulls, though nulls treated with arketamine appear to have slightly lower overall activity (~2 s/min difference).

We were thus unable to recreate the extension of active coping behavior demonstrated in the study from which our protocol was adapted [836]. Possible reasons include the smaller size of the wells (8 mm x 8 mm) in the 96-well plate versus in the customized plastic chamber (see Chapter 5.2), the difference in the stressor used, and the time of day during which the experiments took place (we do not know if they controlled for this and, if so, what time of day they chose). Additionally, we used a lower level of effective ketamine than their protocol specified, as we noticed clear sedation at the effective arketamine concentration (107 μM) used in their protocol (as well as some sedation even at the half-effective dose of 53.5 μM). Of interest, we observed that, when using the mesh plate, the pre-shock baseline activity displayed a distinctively linear character such that average activity continuously decreased over the course of the period; in previous experiments, the baseline activity was flat (e.g. **Fig. 5.3**). This could reflect the fact that the E3 medium is shared communally among the larvae in the mesh plate apparatus, as opposed to in the isolated wells of the typical plate, thereby allowing for more direct interaction among the larvae which could potentially cause unforeseen group-wide effects.

In further experiments, our goal would be to attempt to account for the differences from the original protocol. While we demonstrated that the heat shock stress response is robust and stereotyped, it may be that any small effect from arketamine exposure is overwhelmed by the force of the heat shock; under this reading, the electrical shock is perhaps less stressful, allowing for more separation in behavioral profiles between nulls and hets. Because larvae in our mesh plate apparatus share communal solution, we could use one device to administer shocks to the entire chamber. Another change we could make is to increase the size of the wells; we could instead use customized mesh plates with 48, 24, or 12 wells, each with larger volumes, thereby allowing the larvae more room to maneuver and perhaps display more nuanced behavioral characteristics (e.g. thigmotaxis). Under these circumstances, we would have fewer larvae which would reduce statistical power but might perhaps ensure the collection of higher-quality data. Finally, we could try the experiment at different times throughout the day (early morning, late morning, etc.) to account for changes in cortisol release (see Chapter 5.2). In all, we have demonstrated that our experimental protocol elicits a robust behavioral response over 1 h, and future experiments can elaborate on these findings to develop a reliable high-throughput test of futility behavior that will be crucial for establishing zebrafish as an organism in which depression-like behavior can be modeled and treated with RAADs.

CHAPTER 6: TIME-RESOLVED PROTEOMICS FOR INVESTIGATING THE MECHANISMS OF SELECTIVE SEROTONIN REUPTAKE INHIBITORS

6.1. Background

As discussed throughout Chapter 1, the mechanisms by which both classic antidepressants and RAADs exert their effects are not well understood despite decades' worth of investigations. With regard to SSRIs, designed specifically as SERT blockers to increase extracellular 5-HT levels [26,27], the antidepressant mechanism appears more complex than this intended function, as 5-HT levels in the synaptic cleft reach a steady-state within days of initiating SSRI treatment [49] yet the therapeutic lag until clinical benefit is much longer [33,50]; additionally, the artificial depletion of endogenous 5-HT in healthy subjects does not cause a depressive episode [46]. Indeed, more recent evidence points towards the importance of AMPARs [663], the displacement of $G_{S\alpha}$ subunits from lipid rafts [873], and interactions with TrkB [614] as potential supplementary or even primary mechanisms by which SSRIs exert their effects. Furthermore, questions concerning the location(s) in which SSRIs engage their targets — SERT or otherwise — have arisen owing to the weakly basic nature of several common drugs in this class (see Chapter 1.5 and Chapter 1.6.5), as other drugs with such properties have been shown to cross membranes at physiological pH to interact with intracellular receptor populations (e.g. nicotine [534,535]), and more recent work has demonstrated the ability of many other drug classes (esketamine [544], nicotinic agonists [533,684], opioids [685], SSRIs [543]) to enter intracellular compartments *in vitro* within seconds to minutes. These interactions, deemed part of the inside-out pathway [530-532] (see Chapter 1.6.5), provide an important perspective on the potential means by which various neuroactive compounds cause behavioral effects such as addiction [533-535,684,685] and relief of depression [543,544]. Synthesizing two Q-SSRIs, unable to cross into the cytoplasm (validated in mammalian cells and PHC [543]; see Chapter 3), has provided tools to explore differences between typical ligand-receptor interactions on the PM and inside-out pathway activity.

Several techniques can help elucidate the pathways — both suspected and unknown — which mediate SSRI activity to construct a more detailed picture of the molecular changes pursuant to the inception of clinical treatment. Proteomic analysis allows for the identification and relative quantification of proteins present in biological samples exposed to various kinds of environmental stimuli; unlike genomics, which focuses on the underlying genetic sequences, or transcriptomics, which focuses on transcribed mRNA, proteomics provides functional information about the response of an organism to its environment [990]. With respect to the effects of SSRIs on protein expression, most studies have used fluoxetine to investigate chronic treatment effects on peripheral blood mononuclear cells [991] as well as brain samples obtained *in vivo* [992,993]. However, these experiments chronicled effects after long-term (four weeks) administration, providing only a single time point assessing proteomic changes and thereby ignoring potentially crucial structural changes which begin to manifest during the therapeutic lag period. Additionally, the methods used — 2D gel electrophoresis followed by mass spectroscopy — identify only a small number of proteins (on the order of dozens) compared to the thousands of proteins that can be detected using newer techniques such as liquid chromatography-tandem mass spectrometry (LC-MS/MS); all traditional shotgun proteomics methods lack temporal resolution, which makes it impossible to distinguish between pre-existing and newly synthesized proteins in response to treatment.

We thus decided to explore changes in protein expression from SSRI treatment during the therapeutic lag period using both SSRIs and Q-SSRIs as a means of determining if intracellular interactions are crucial to the early stages of the antidepressant response. We propose to use state-of-the-art bioorthogonal noncanonical AA tagging (BONCAT) proteomics (developed in the Tirrell lab at Caltech) which allows for the generation of time-resolved expression profiles measuring only newly synthesized proteins. BONCAT involves the one-time addition of a noncanonical AA (e.g. azidohomoalanine, or AHA, a methionine analog containing an azido moiety in place of the *S*-methyl thioester on the amino acid side chain [994]) which competes with methionine (the starting AA in all proteins) for methionyl-tRNA synthetase-based incorporation into nascent peptides; labeled proteins can be enriched via covalent attachment to dibenzocyclooctyne-functionalized agarose beads in copper-free click chemistry, which can subsequently be collected using on-bead digestion with trypsin and Lys-C proteases. The resulting protein mixture is quantified via LC-MS/MS [995]; this scheme restricts protein labeling to a time interval of interest (hours to days) which has allowed researchers to precisely identify protein expression subsequent to a perturbation of interest across a variety of organisms and cell types [996-1000]. In collaboration with Sophie Miller in the Tirrell lab, our goal was to investigate the SSRI- and Q-SSRI-induced changes in proteomic signatures during the early stages of treatment (e.g. Week 1), when SSRIs increase 5-HT levels but do not yet alleviate symptoms of MDD, as well as after prolonged treatment (e.g. Week 3), at the early stages of

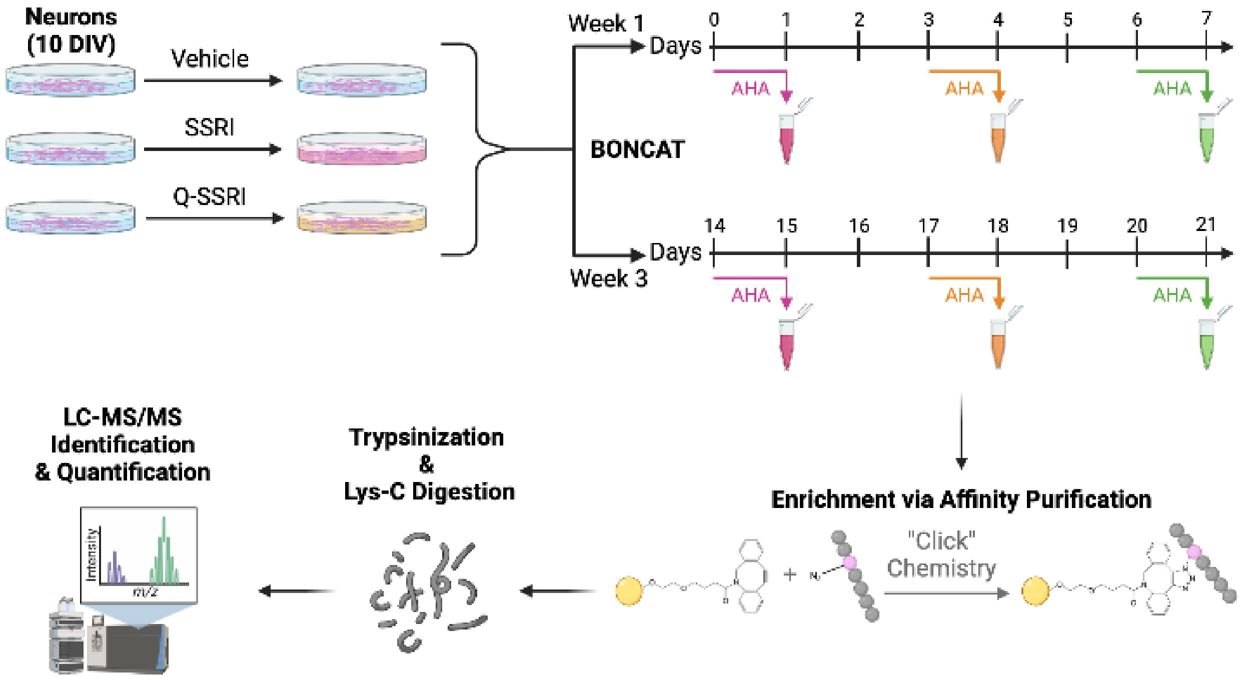

Figure 6.1. Proposed timeline of BONCAT experiments. Sets of separate dishes of PCC at 10 DIV are treated with SSRI, Q-SSRI, or pure medium (vehicle; early experiments will concern varying the concentration of drug to explore the clinically relevant range of 50-1000 nM [900,901,1001-1003]); during Week 1 (10-17 DIV) and Week 3 (24-31 DIV), several dishes from each treatment group will be dosed with AHA at the start of each 24 h interval of interest (e.g. Days 0, 3, and 6 during Week 1). After completion of the AHA-treatment period, cells will be enriched and purified via click chemistry [1004] before being processed for LC-MS/MS quantification [997]. (Figure courtesy of Sophie E. Miller.)

6.2. Methods

While proteomic signatures collected after pharmacological interventions in animals (e.g. mice or zebrafish) would be compelling, we chose the *in vitro* model because it allows for more controlled treatment conditions (including direct administration of drug to the culture dish). To survey a representative sample of neuronal subtypes, we decided to use primary cortical neuronal cultures (PCC) obtained from mouse embryos (embryonic day 18) prepared, dissociated, and shipped to us by an online retailer (BrainBits). Neurons were then plated at a density of 4,000,000 on culture dishes (100 mm focus, MatTek) coated with poly-D-lysine with 10 mL of

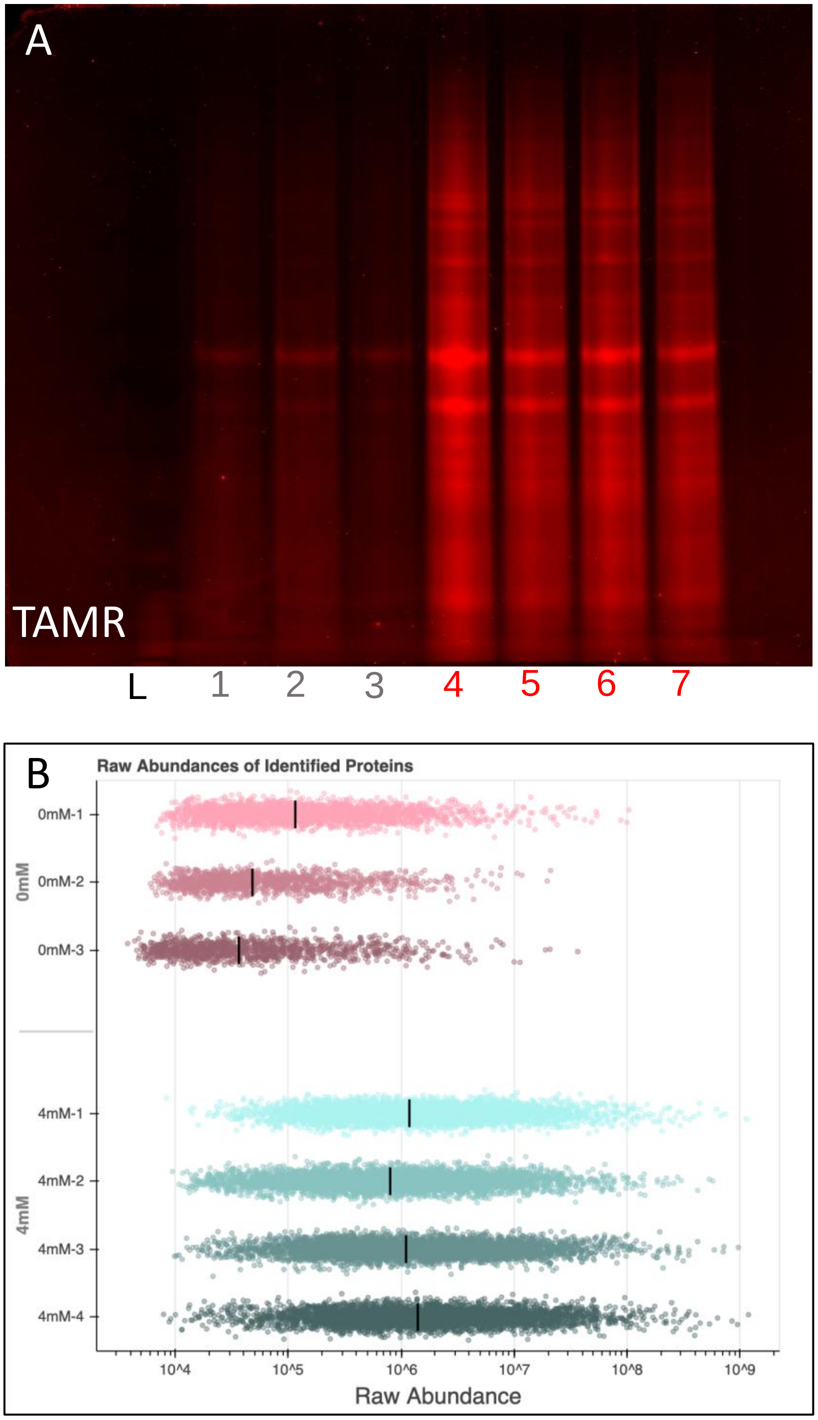

Figure 6.2. We collected four million neurons (yielding ~100 µg of total protein in lysate) from each dish and normalized the total protein concentration before enrichment. ***(A)*** Tetramethylrhodamine (TAMRA) alkyne was used to ‘click’ on to the azide in 4 mM AHA-labeled proteins after a 24 h treatment (*4-7*) which showed significantly brighter labeling than control (*1-3*) dishes (treated with 0 mM AHA for 0 h). (*L* is a ladder standard.) ***(B)*** The raw abundances of the proteins identified from subsequent enrichment demonstrates ~100 times greater raw abundance among the 4 mM AHA-labeled dishes (*blues*) than the control dishes (*reds*). Each *dot* represents a uniquely identified protein while the *black bars* show average abundances for each dish. (Figures courtesy of Sophie E. Miller.)

media (NB4activ, BrainBits) and placed in an incubator (37ºC, 5% CO_2) to mature. We first validated that we could successfully label newly synthesized proteins in our PCC dishes after a 24 h treatment with AHA (**Fig. 6.2A**) and that we could successfully enrich AHA-labeled proteins compared to unlabeled controls (**Fig. 6.2B**). Although cultured neurons can be viable past 20 days *in vitro* (DIV; [997,1005]), we were unable to maintain cell health past ~10 DIV, at which point dendritic blebbing and the presence of vacuoles in cell soma was observed; possible reasons for this lack of persistence include differences in oxygenation and the absence of a glial cell layer.

After changing the media at 4 DIV (we removed 7 mL and added 7 mL of fresh media), on 7 DIV, we again removed 7 mL of media and added 6 mL of drug dissolved in media at 1.67 times the final desired concentration as well as 1 mL of AHA at 10 times the final desired concentration (4 mM [997]). The plates were then placed back in the incubator for 24 h. The next day, we aspirated the media, rinsed the cells with 20 mL total of 1x PBS containing protease inhibitors (cOmplete, mini, EDTA-free, Roche), and scraped the cells into 15 mL tubes (Falcon); the tubes were then centrifuged at 5000 rcf for 5 min at 4ºC, after which the supernatant was discarded and the pellets stored at -80 ºC.

LC-MS/MS analysis was performed using an ultra-high performance liquid chromatography apparatus (EASY-nLC 1200, Thermo Fisher Scientific) coupled to a mass spectrometer (Orbitrap Eclipse Tribrid, Thermo Fisher Scientific). Peptides were separated on an analytic column (500 mm x 75 μm, 2 μm C18, ES903, Thermo Fisher Scientific) heated to 50°C with a trap column (20 mm x 75 μm, Acclaim PepMap 164535, Thermo Fisher Scientific). The LC gradient flow rate was 0.3 μL/min for 85 min with ionization achieved at 1.6 kV using an electronic ionization source in the positive ion mode (EASY-Spray, Thermo Fisher Scientific). The gradient was composed of 6% solvent B (80% ACN and 0.2% formic acid; 3.5 min), 6-25% solvent B (34.5 min), 25-40% solvent B (25 min), 40-98% solvent B (1 min), and 98% solvent B (21 min). Scans during the first round of MS (MS1) were acquired at a resolution of 120,000 from 375 to 1,600 m/z, an automatic gain control target of 1,000,000, and a maximum injection time of 50 ms. Scans during the second round of MS (MS2) were acquired in the ion trap using a fast scan rate on precursors with 2-6 charge states in quadrupole isolation mode (isolation window: 0.7 m/z) with the higher-energy collisional dissociation (30%) activation type; dynamic exclusion was set to 30 s, and the temperature of the ion transfer tube was 300°C while the S-lens radio frequency level was set to 30. MS2 fragmentation spectra were searched with proprietary software (Proteome Discoverer SEQUEST 3.0, Thermo Fisher Scientific) against an online database (UP000002494, an *in silico* tryptic digested Uniprot *Rattus norvegicus* proteome; or UP000000437, a *Danio rerio* proteome). The maximum for missed cleavages was set to 2. Dynamic modifications were set to oxidation on methionine (M, +15.995 Da), protein N-terminal acetylation (+42.011 Da) and Met-loss (-131.040 Da). Carbamidomethylation on cysteine residues (C, +57.021 Da) was set as a fixed modification. The maximum parental mass error was set to 10 parts per million, and the MS2 mass tolerance was set to 0.6 Da. The false discovery threshold was set to 0.01 using a web application (Percolator node). The relative abundance of parental peptides was calculated by integrating the area under the curve of the MS1 peaks using a second web application (Minora LFQ node). Protein abundances were normalized, and statistical analysis was performed using an online software repository (Tidyproteomics package, https://jeffsocal.github.io/tidyproteomics/; The R Project for Statistical Computing).

BONCAT enrichment of labeled proteins, bead washing, peptide elution, and LC-MS/MS sample preparation were performed by Sophie Miller as described in a previous study [997]; LC-MS/MS injection and protein identification and quantification were performed by Dr. Ting-Yu Wang and Dr. Baiyi Quan at the Caltech Proteome Exploration Laboratory (PEL); and proteomic data analysis was performed by Sophie Miller and Dr. Jeff Jones at the PEL.

6.3. Results and Next Steps

We treated four dishes each with 100 nM final concentrations of escitalopram and fluoxetine (based on effective CSF concentration [901]) as well as four control dishes, all of which were simultaneously treated with 4 mM AHA and harvested after 24 h. Among these dishes, we identified 6,794 proteins after BONCAT enrichment and quantification, though only a small proportion were specific to each treatment condition (**Fig. 6.3**). When we examined the covariance of the labeled protein abundances among the 12 dishes, we found that one of the 100 nM escitalopram treatment dishes had significantly lower raw protein abundances than the other three treatment dishes as measured by principal component analysis (PCA; data not shown), and

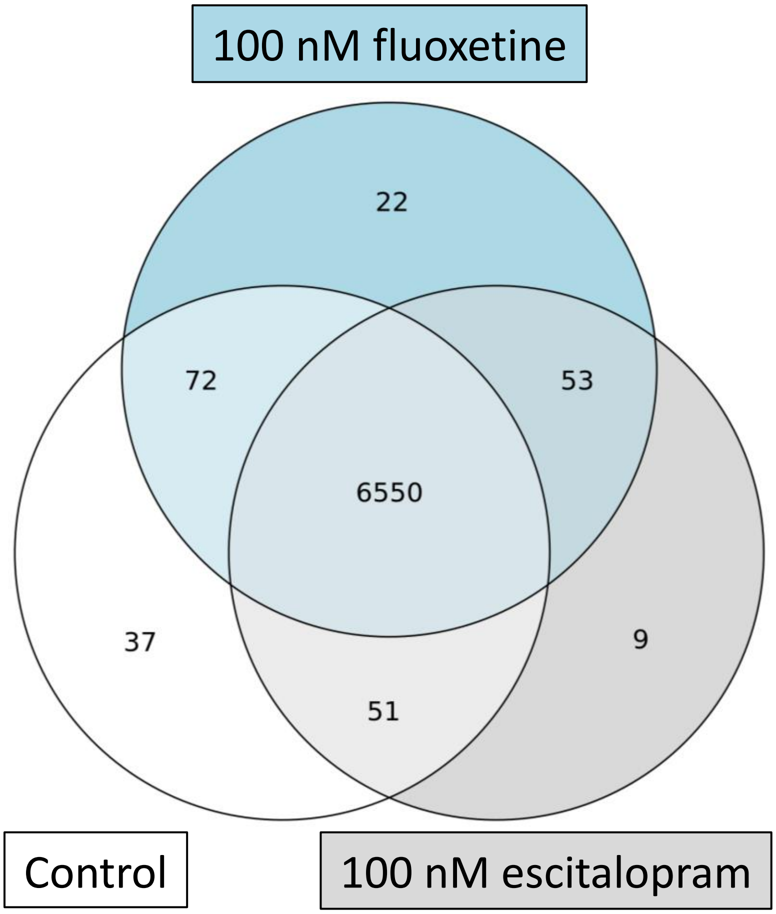

Figure 6.3. Venn diagram showing the distributions of the 6,794 unique proteins identified across all three treatment conditions. The control (*white*) condition had the most unique proteins, while the 100 nM escitalopram (*gray*) condition had the least. In total, the SSRI treatments contained 53 unique proteins between them. (Figure courtesy of Sophie E. Miller.)

thus we decided to exclude it from further analysis. In all, PCA did not demonstrate significant grouping by treatment, which is often a benchmark used for discerning the differences among treatments (e.g. [1006]). Next, we normalized the abundances using a random forest algorithm [1007], with a twofold change as the threshold for significant up- or down-regulation, and plotted these for 100 nM escitalopram vs. control, 100 nM fluoxetine vs. control, and 100 nM fluoxetine vs. 100 nM escitalopram (**Fig. 6.4**). After correcting for multiple hypothesis testing (see Chapter 6.2), we found that there were six proteins upregulated by 100 nM escitalopram versus control, four by 100 nM fluoxetine versus control, and five by 100 nM escitalopram versus 100 nM fluoxetine. Of these, several proteins stand out as potentially involved with the antidepressant effects of SSRIs. Both 100 nM escitalopram and 100 nM fluoxetine versus control caused a significant upregulation of CHRM4, the M_4 mAChR. The closely related M_2 mAChR has a polymorphism associated with MDD [374], particularly among women [239], while both MDD and BPD patients show decreased frontal cortex binding to the M_2 mAChR in the frontal cortex as assessed by PET [375]; however, no evidence implicates the M_4 subtype in the pathogenesis of affective disorders [375]. Of note, the broad-spectrum antimuscarinic scopolamine has been shown to act as a RAAD in MDD patients (see Chapter

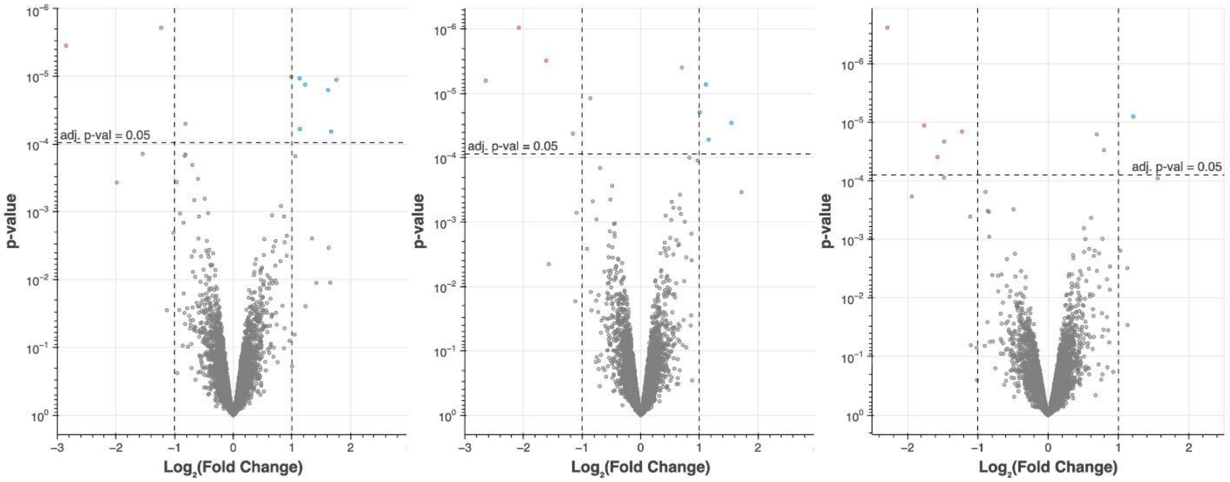

Figure 6.4. Volcano plots generated using normalized abundances of BONCAT-enriched proteins in 100 nM escitalopram vs. control (*left*), 100 nM fluoxetine vs. control (*middle*), and 100 nM fluoxetine vs. 100 nM escitalopram (*right*) comparisons showing Log_2 fold changes (with *dotted lines* at -1 and 1 representing half and twice as much protein as in the comparison condition, respectively) against p-values (with a *dotted line* at the p-value corresponding to an adjusted p-value of 0.05). Points in the *upper-left quadrants* show proteins that are significantly downregulated by the first treatment in comparison to the second while points in the *upper-right quadrants* show proteins that are significantly upregulated by the first treatment in comparison to the second treatment. (Figure courtesy of Sophie E. Miller.)

1.4), potentially implicating the mAChR population in the response to other antidepressants. Another protein, CLSTN3, was upregulated by 100 nM escitalopram versus control and by 100 nM escitalopram versus both control as well as 100 nM fluoxetine. This protein enables Ca^{2+} binding activity as well as upregulates synaptic formation and transmission [1008]; as synaptic remodeling and plasticity is intrinsic to the action of many antidepressants (see Chapter 1.6.4 and Chapter 1.7), this could be representative of the sorts of underlying physiological changes which an SSRI like escitalopram induces even in the short-term to eventually achieve its clinical effects. Additionally, *CLSTN3* KO mice demonstrate reduced body mass [1009] while the gene was also found to be associated with adipose fat with a polymorphism associated with obesity risk [1010], perhaps helping to explain in part the association between SSRI use and weight gain [32]. Fibroblast growth factor 13 (FGF13) was found to be downregulated by 100 nM fluoxetine treatment versus control. The FGF family of growth factors are involved with the development and maintenance of brain function [1011], and various subtypes have been found to be both up- and downregulated across various areas of the brain in MDD patients [1012]. While FGF13 has not been specifically implicated in the pathogenesis of depression, similar to CLSTN3, its inclusion here could reflect broader neuroplastic changes undergone during the pre-therapeutic period.

Although the results obtained in our initial experiments were unpromising in terms of providing definitive proteomic signatures corresponding to the pre-therapeutic phase of SSRI treatment, we have several options for follow-up investigations. Developing a protocol such that neuronal health is robust out to several weeks will allow us to assess temporal effects of chronic SSRI treatment during the therapeutic lag phase as we had originally planned (**Fig. 6.1**). We can also explore dose-dependent effects, challenging neurons with both sub-therapeutic, therapeutic, and supra-therapeutic concentrations; because we know that Q-SSRIs interact with hSERT more weakly than SSRIs [543], we can account for this difference by scaling the Q-SSRI-matched concentrations appropriately. Lastly, we have performed initial experiments using es- and arketamine, drugs which may be more amenable to a 24 h assessment owing to their known rapid clinical effects; indeed, future BONCAT studies performed by Sophie Miller in the Tirrell lab will focus on RAADs both *in vitro* as well as their effects on zebrafish (data not published).

CHAPTER 7: SINGLE-NEURON PHYSIOLOGY AND PHARMACOKINETICS IN LARVAL ZEBRAFISH

7.1. Background

As discussed in Chapter 2.4.3, whole-brain GCaMP imaging in larval zebrafish has allowed for unprecedented access to neuronal network dynamics at single-neuron resolution during behavioral tasks [843,844] as well as in response to DOIs [491,795,839]. The robustness of GCaMP reporting in zebrafish using SPIM (see Chapter 2.5) suggests that other fluorescent proteins with different spectral dynamics are viable for *in vivo* imaging; indeed, red-shifted Ca^{2+} sensors (e.g. jRGECO1a) have been validated *in vivo* with larvae [1013]. While sensors such as jRGECO1a possess potential advantages over GFP-based Ca^{2+} sensors, including the ability to penetrate deeper into brain tissue [1014], their main application is in multiplexed imaging whereby neuronal populations labeled with both GFP- and RFP-based sensors are imaged simultaneously to investigate complex physiological dynamics (e.g. different responses of DA receptor subtypes to DOIs [1015]). While our iRAADSnFR experiments using larval zebrafish are still in their nascent stages (see Chapter 2.6), we have a unique opportunity to leverage two-color imaging to assess real-time pharmacokinetics of exogenous drugs (GFP-based RAAD sensors) coupled with physiological signals from red-shifted Ca^{2+} sensors (jRGECO1a). The goal of this study is to collect whole-brain data from both channels to correlate changes in neuronal RAAD concentration with physiological activity across the CNS, providing the first demonstration of the real-time effects of RAADs with single-neuron resolution.

7.2. Methods

The SPIM setup used for this project is as described previously, with the main difference being that both CW lasers (488 nm and 561 nm, the latter for excitation of red-shifted jRGECO1a) operate simultaneously (see Chapter 2.5 for more details). Our strategy involved spectral separation using dichroic mirrors to project two images onto the single scMOS camera chip (total field of view 800 μm x 800 μm). Images from the ‘green’ and ‘red’ channels are spatially separated so that a set of signals from each fluorescent protein can be quantified. The spectral

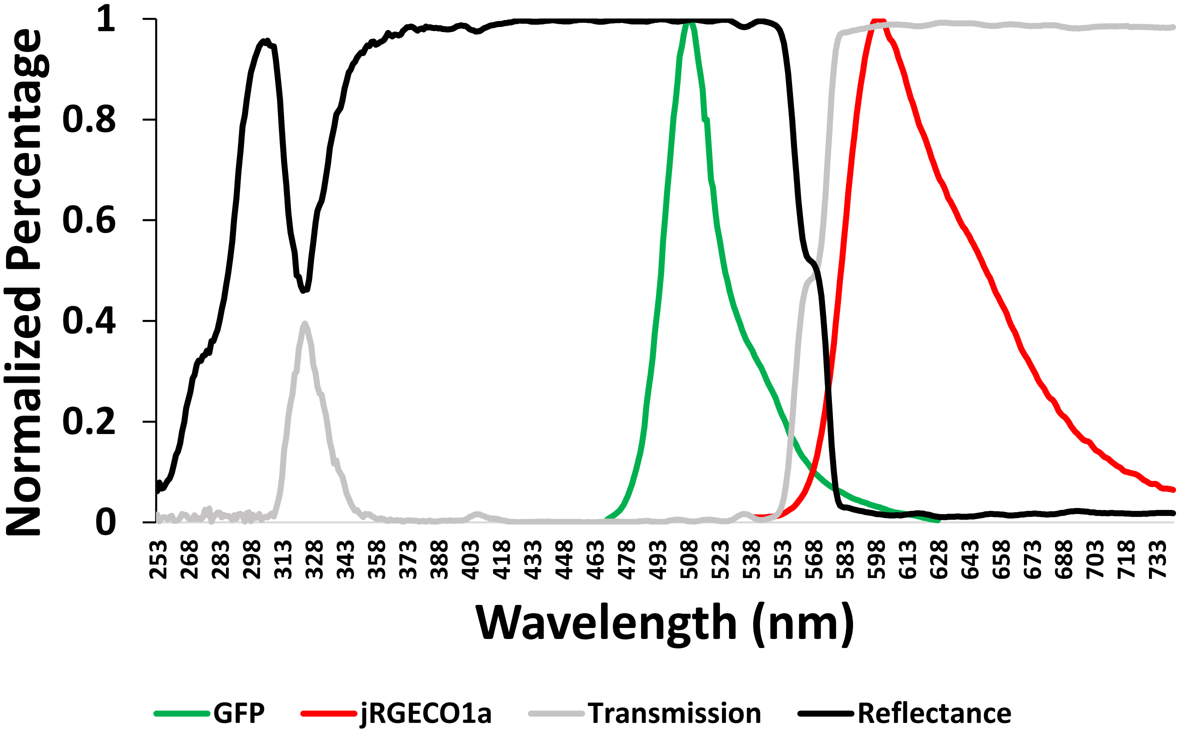

Figure 7.1. Emission spectra for iRAADSnFR (GFP, *green*) and jrGECO1a (*red*) plotted as normalized percentages of their maximum values (GFP: 510 nm; jRGECO1a: 600 nm) along with the transmission (*grey*) and reflectance (*black*) spectra for the 567 nm long-pass dichroic mirrors demonstrating that nearly all (> 90%) of the green light will be reflected while nearly all (> 90%) red light will be passed through.

dynamics of the iRAADSnFR GFP are as described previously (excitation = 488 nm, emission = 510 nm; see Chapter 2.1); the excitation peak of jRGECO1a is 562 nm and the emission peak is 600 nm. To separate these signals, we used a custom-made beam splitter comprising dichroic and silver mirrors to separate the incoming emission beams from the sample. The beam splitter consists of two long-pass dichroic mirrors with 567 nm cut-on wavelengths (DLMP567, ThorLabs) mounted in filter cubes (CM1-DCH, ThorLabs) and two elliptical aluminum-coated mirrors (PFE10-G01) housed in mirror mounts (KCB1E, ThorLabs). The 567 nm limit was chosen because this wavelength lies near the higher edge of the GFP emission spectrum as well as near the lower edge of the jRGECO1a emission spectrum; the amount of GFP signal that would be passed through is under 10% while the amount of jRGECO1a signal that would be blocked is also under 10% (**Fig. 7.1**). The optical parts are arranged such that both beams of light will be deflected 90° from their original light path (**Fig. 7.2**). Mixed light from the sample first passes through a dichroic mirror at a 45° angle where it is refracted via thin film interference;

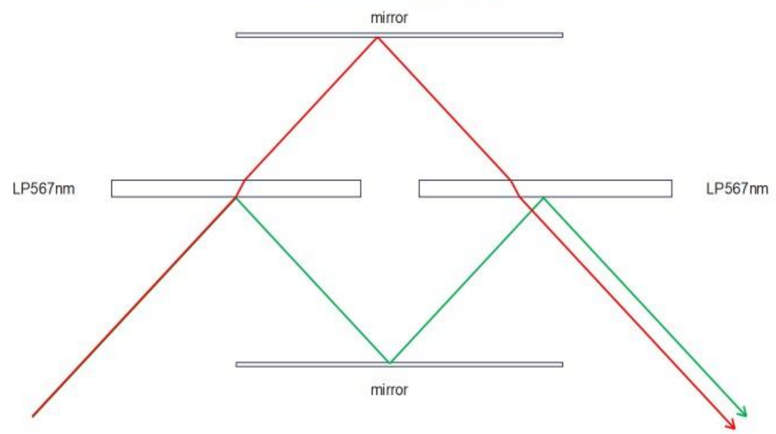

Figure 7.2. Cartoon of the light path among the components of the custom-made beam splitter showing the trajectory of each image (*red* and *green*) interacting with both the elliptical mirrors (*mirror*) as well as the dichroic mirrors (*LP567nm*).

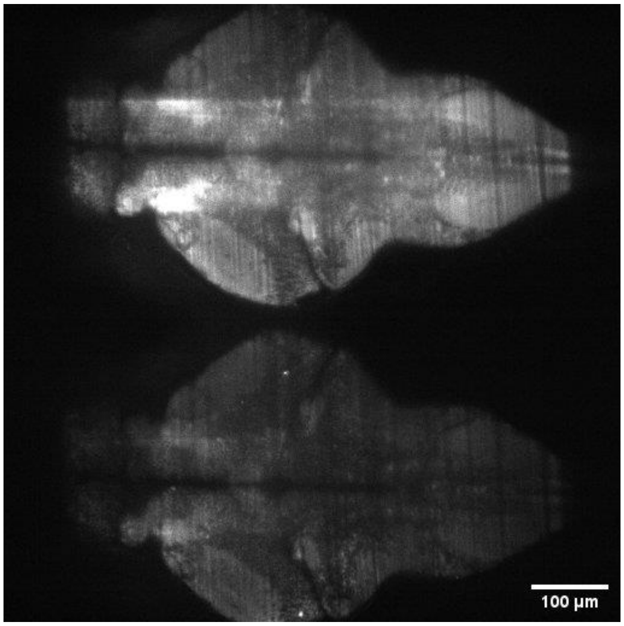

Figure 7.3. Gray-scale images projected onto the scMOS camera, with the 'green' image (*top*) slightly brighter than the 'red' image (*bottom*) because of a) differences in the laser power used and b) intensity-based activation of the GFP by the administered RAAD. Future experiments will include an optimization process to balance the baseline fluorescence between the two FPs.

incident red light is then deflected by an elliptical mirror at a 45º angle through a second dichroic mirror (which refracts the red light once more) onto the camera sensor. The position of the 'red' image on the sensor is controlled by the angle of the elliptical mirror. The incident green light is reflected by the first dichroic, reflected again at a 45º angle by a second elliptical mirror, and finally reflected by the second dichroic to achieve the same direction as the 'red' light beam (**Fig. 7.2**). The position of the 'green' image is controlled by deflection of the second elliptical mirror which allows for spectral separation on the scMOS camera.

To create transgenic fish for two-color imaging experiments, we crossed iRAADSnFR fish with a *Tg(HuC:jRGECO1a;nacre +/-;casper +/-;+RED x TLAB)* line which has cytosol-targeted pan-neuronal expression of jRGECO1a, a red-shifted Ca^{2+} sensor [1013]. Collection and cleaning are as described in Chapter 2.5; for fluorescent screening, 3 dpf larvae were paralyzed with 4% tricaine and viewed under an epifluorescence microscope equipped with a filter wheel which can pass blue light at 470 nm and green light at 560 nm (Em01-R488/568-25). Larvae with whole-brain expression of both the iRAADSnFR GFP and jRGECO1a are separated and stored in a 28ºC incubator. Treatment with PTU before and after fluorescent screening is as previously described. Larvae are prepared and imaged at 4-6 dpf as described in Chapter 2.5.

7.3. Preliminary Results and Analysis Goals

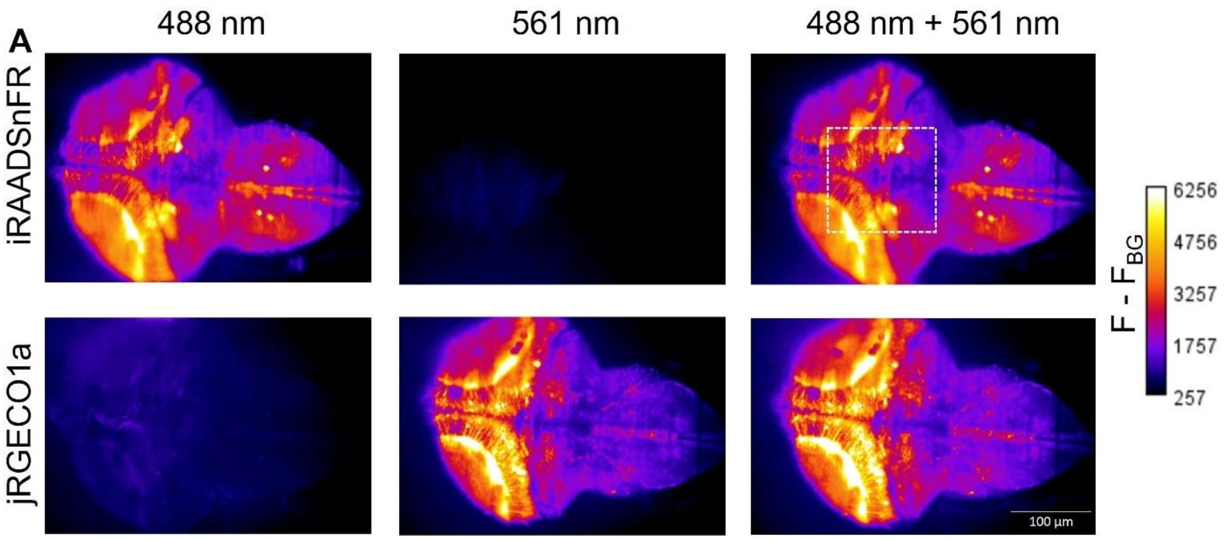

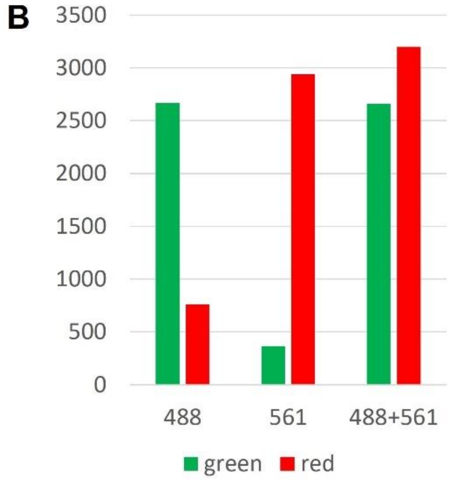

Figure 7.4. ***(A)*** Fluorescence signal above background (BG; quantified using the *F-F_{BG}* fluorescence counts color bar, *far right*) from 488 nm (*left*), 561 nm (*middle*), or excitation from both (*right*) for the iRAADSnFR GFP (*top*) and jRGECO1a FP (*bottom*) showing cross-excitation from both lasers, particularly from the 488 nm laser in the 'red' channel. ***(B)*** Quantification of fluorescence counts from 488 nm (*left*), 561 nm (*middle*), and 488 + 561 nm excitation (*right*) in both the 'green' and the 'red' images. The amount of 'bleed-through' from 488 nm excitation of the RFP is under 10% (compare the heights of the red bars in the *middle* and *right* pairs). Figures courtesy of Andrey Andreev.)

The optics scheme described in the previous subsection successfully renders two images, with the 'green' image on top of the 'red' image (**Fig. 7.3**); there does not appear to be a difference in resolution between the images as single neurons are resolvable in each. With respect to cross-excitation between the channels (**Fig. 7.4**), the 488 nm laser significantly activates the

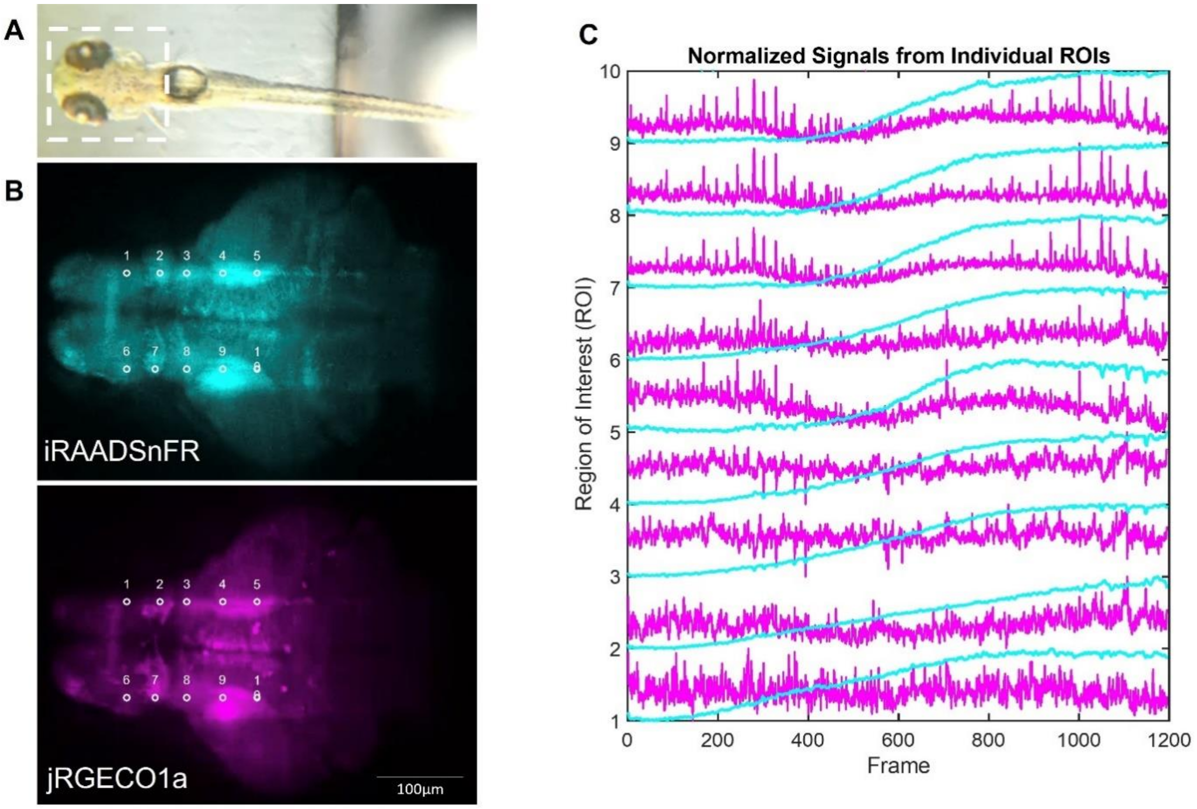

Figure 7.5. ***(A)*** Image of 5 dpf larva embedded in agarose in the mounting system; the head is highlighted (*white dashed lines*). ***(B)*** The iRAADSnFR (*cyan, top*) and jRGECO1a (*magenta, bottom*) images from the same larva with 10 ROIs (*white circles*) labeled. ***(C)*** Both 'green' (*cyan*) and 'red' (*magenta*) image traces from the 10 ROIs specified in (**B)** normalized to background fluorescence demonstrating the heterogeneous rates of RAAD accumulation across regions of the brain; spiking activity is less obviously correlated with increased intracellular RAAD but can be quantified using several standard neurophysiological metrics. (Figures courtesy of Andrey Andreev.)

jRGECO1a RFP, which emits a signal ~25% as strong as the iRAADSnFR GFP, while the 561 nm laser excites the GFP < 5% as much as the RFP; however, the cumulative additional excitation of the RFP is ~10% (**Fig. 7.4B**), within the expected range based on each FP's excitation and emission spectra (see **Fig. 7.1**).

To analyze two-color datasets, we employed simple intensity-based processing. Ten ROIs representing regions of approximately 5 x 5 neurons were chosen with time-series data from each channel in a given region plotted together (**Fig. 7.5**). The fluorescence dynamics of RAAD entry into neurons as measured by the GFP appear to vary in each ROI, suggesting that there may be differences among neurons and brain regions in terms of the dynamics of RAAD uptake which could depend on proximity to blood vessels or the skin. In comparison, the physiological activity reported by the jRGECO1a FP can be analyzed based on metrics such as firing frequency and inter-spike intervals to determine if changes in these features correlate with accumulation of intracellular RAAD.

Future analyses will depend on our ability to collect high-resolution volumetric images to allow for single-neuron segmentation. Several protocols for delineating individual neurons [787,845] and their connections [1016,1017] are available, and ready-made customizable software programs (e.g. suite2p [1018], CaImAn [1019]) can simplify the identification and segmentation process. We are currently exploring machine learning regression algorithms which can help assess the potential causal relationship between RAAD pharmacokinetics and Ca^{2+}-based physiology using our multimodal datasets.

REFERENCES

1 Exchange. IoHMaEGHD. 2021. http://ghdx.healthdata.org/gbd-results-tool?params=gbd-api-2019-permalink/d780dffbe8a381b25e1416884959e88b. Accessed 9 January 2023.

2 Murray CJ, Lopez AD. Measuring the global burden of disease. N Engl J Med. 2013;369(5):448-57.

3 Kessler RC, Berglund P, Demler O, Jin R, Merikangas KR, Walters EE. Lifetime prevalence and age-of-onset distributions of DSM-IV disorders in the National Comorbidity Survey Replication. Arch Gen Psychiatry. 2005;62(6):593-602.

4 NIMH. Depression. 2021. https://www.nimh.nih.gov/health/publications/depression. Accessed 9 January 2023.

5 Association AP. Diagnostic and Statistical Manual of Mental Disorders. 2022.

6 Musil R, Seemüller F, Meyer S, Spellmann I, Adli M, Bauer M, et al. Subtypes of depression and their overlap in a naturalistic inpatient sample of major depressive disorder. Int J Methods Psychiatr Res. 2018;27(1).

7 Shadrina M, Bondarenko EA, Slominsky PA. Genetics Factors in Major Depression Disease. Front Psychiatry. 2018;9:334.

8 Alshaya DS. Genetic and epigenetic factors associated with depression: An updated overview. Saudi J Biol Sci. 2022;29(8):103311.

9 Kwong ASF, López-López JA, Hammerton G, Manley D, Timpson NJ, Leckie G, et al. Genetic and Environmental Risk Factors Associated With Trajectories of Depression Symptoms From Adolescence to Young Adulthood. JAMA Netw Open. 2019;2(6):e196587.

10 Ormel J, Hartman CA, Snieder H. The genetics of depression: successful genome-wide association studies introduce new challenges. Translational psychiatry. 2019;9(1):114.

11 Kinsella MT, Monk C. Impact of maternal stress, depression and anxiety on fetal neurobehavioral development. Clin Obstet Gynecol. 2009;52(3):425-40.

12 Nomura Y, Davey K, Pehme PM, Finik J, Glover V, Zhang W, et al. Influence of in utero exposure to maternal depression and natural disaster-related stress on infant temperament at 6 months: The children of Superstorm Sandy. Infant Ment Health J. 2019;40(2):204-16.

13 Freeman A, Tyrovolas S, Koyanagi A, Chatterji S, Leonardi M, Ayuso-Mateos JL, et al. The role of socio-economic status in depression: results from the COURAGE (aging survey in Europe). BMC Public Health. 2016;16(1):1098.

14 Schlax J, Jünger C, Beutel ME, Münzel T, Pfeiffer N, Wild P, et al. Income and education predict elevated depressive symptoms in the general population: results from the Gutenberg health study. BMC Public Health. 2019;19(1):430.

15 van den Bosch M, Meyer-Lindenberg A. Environmental Exposures and Depression: Biological Mechanisms and Epidemiological Evidence. Annu Rev Public Health. 2019;40:239-59.

16 Loomer HP, Saunders JC, Kline NS. A clinical and pharmacodynamic evaluation of iproniazid as a psychic energizer. Psychiatric Research Reports. 1957;8:129-41.

17 Nelson SD, Mitchell JR, Snodgrass WR, Timbrell JA. Hepatotoxicity and metabolism of iproniazid and isopropylhydrazine. J Pharmacol Exp Ther. 1978;206(3):574-85.

18 Ramachandraih CT, Subramanyam N, Bar KJ, Baker G, Yeragani VK. Antidepressants: From MAOIs to SSRIs and more. Indian J Psychiatry. 2011;53(2):180-2.

19 Horwitz D, Lovenberg W, Engelman K, Sjoerdsma A. Monoamine Oxidase Inhibitors, Tyramine, and Cheese. JAMA. 1964;188(13):1108-10.
20 Kuhn R. The treatment of depressive states with G 22355 (imipramine hydrochloride). Am J Psychiatry. 1958;115(5):459-64.
21 Arroll B, Macgillivray S, Ogston S, Reid I, Sullivan F, Williams B, et al. Efficacy and tolerability of tricyclic antidepressants and SSRIs compared with placebo for treatment of depression in primary care: a meta-analysis. Ann Fam Med. 2005;3(5):449-56.
22 Hillhouse TM, Porter JH. A brief history of the development of antidepressant drugs: from monoamines to glutamate. Exp Clin Psychopharmacol. 2015;23(1):1-21.
23 Williams RB, Jr., Sherter C. Cardiac complications of tricyclic antidepressant therapy. Ann Intern Med. 1971;74(3):395-8.
24 Roose SP, Glassman AH, Giardina EG, Walsh BT, Woodring S, Bigger JT. Tricyclic antidepressants in depressed patients with cardiac conduction disease. Arch Gen Psychiatry. 1987;44(3):273-5.
25 Shaw DM, Camps FE, Eccleston EG. 5-Hydroxytryptamine in the hind-brain of depressive suicides. Br J Psychiatry. 1967;113(505):1407-11.
26 Wong DT, Horng JS, Bymaster FP, Hauser KL, Molloy BB. A selective inhibitor of serotonin uptake: Lilly 110140, 3-(p-trifluoromethylphenoxy)-N-methyl-3-phenylpropylamine. Life Sci. 1974;15(3):471-9.
27 Wong DT, Bymaster FP, Horng JS, Molloy BB. A new selective inhibitor for uptake of serotonin into synaptosomes of rat brain: 3-(p-trifluoromethylphenoxy). N-methyl-3-phenylpropylamine. J Pharmacol Exp Ther. 1975;193(3):804-11.
28 Wong DT, Bymaster FP, Engleman EA. Prozac (fluoxetine, Lilly 110140), the first selective serotonin uptake inhibitor and an antidepressant drug: twenty years since its first publication. Life Sci. 1995;57(5):411-41.
29 Wong DT, Perry KW, Bymaster FP. The Discovery of Fluoxetine Hydrochloride (Prozac). Nature Reviews Drug Discovery. 2005;4(9):764-74.
30 Papakostas GI. Tolerability of modern antidepressants. J Clin Psychiatry. 2008;69 Suppl E1:8-13.
31 Moret C, Isaac M, Briley M. Problems associated with long-term treatment with selective serotonin reuptake inhibitors. Journal of psychopharmacology (Oxford, England). 2009;23(8):967-74.
32 Lee SH, Paz-Filho G, Mastronardi C, Licinio J, Wong ML. Is increased antidepressant exposure a contributory factor to the obesity pandemic? Translational psychiatry. 2016;6(3):e759.
33 Malhi GS, Mann JJ. Depression. Lancet. 2018;392(10161):2299-312.
34 Muller JC, Pryor WW, Gibbons JE, Orgain ES. Depression and anxiety occurring during Rauwolfia therapy. J Am Med Assoc. 1955;159(9):836-9.
35 Strawbridge R, Javed RR, Cave J, Jauhar S, Young AH. The effects of reserpine on depression: A systematic review. Journal of psychopharmacology (Oxford, England). 2022:2698811221115762.
36 Hirschfeld RM. History and evolution of the monoamine hypothesis of depression. J Clin Psychiatry. 2000;61 Suppl 6:4-6.
37 Kyzar E, Stewart AM, Landsman S, Collins C, Gebhardt M, Robinson K, et al. Behavioral effects of bidirectional modulators of brain monoamines reserpine and d-amphetamine in zebrafish. Brain Res. 2013;1527:108-16.

38 Li X, Liu X, Li T, Li X, Feng D, Kuang X, et al. SiO2 nanoparticles cause depression and anxiety-like behavior in adult zebrafish. RSC Advances. 2017;7(5):2953-63.

39 Kirshner N. Uptake of catecholamines by a particulate fraction of the adrenal medulla. J Biol Chem. 1962;237:2311-7.

40 Weiner N, Cloutier G, Bjur R, Pfeffer RI. Modification of norepinephrine synthesis in intact tissue dy drugs and during short-term adrenergic nerve stimulation. Pharmacol Rev. 1972;24(2):203-21.

41 Maletic V, Eramo A, Gwin K, Offord SJ, Duffy RA. The Role of Norepinephrine and Its α-Adrenergic Receptors in the Pathophysiology and Treatment of Major Depressive Disorder and Schizophrenia: A Systematic Review. Front Psychiatry. 2017;8:42.

42 Grace AA. Dysregulation of the dopamine system in the pathophysiology of schizophrenia and depression. Nature Reviews Neuroscience. 2016;17(8):524-32.

43 Stahl SM. Mechanism of action of serotonin selective reuptake inhibitors: Serotonin receptors and pathways mediate therapeutic effects and side effects. Journal of Affective Disorders. 1998;51(3):215-35.

44 Maes M. The serotonin hypothesis of major depression. Psychopharmacology: The fourth generation of progress. 1995:933-44.

45 Seo D, Patrick CJ, Kennealy PJ. Role of serotonin and dopamine system interactions in the neurobiology of impulsive aggression and its comorbidity with other clinical disorders. Aggression and violent behavior. 2008;13(5):383-95.

46 Salomon RM, Miller HL, Krystal JH, Heninger GR, Charney DS. Lack of behavioral effects of monoamine depletion in healthy subjects. Biol Psychiatry. 1997;41(1):58-64.

47 Berman RM, Sanacora G, Anand A, Roach LM, Fasula MK, Finkelstein CO, et al. Monoamine depletion in unmedicated depressed subjects. Biol Psychiatry. 2002;51(6):469-73.

48 Delgado PL, Price LH, Miller HL, Salomon RM, Aghajanian GK, Heninger GR, et al. Serotonin and the Neurobiology of Depression: Effects of Tryptophan Depletion in Drug-Free Depressed Patients. Archives of General Psychiatry. 1994;51(11):865-74.

49 Artigas F, Romero L, de Montigny C, Blier P. Acceleration of the effect of selected antidepressant drugs in major depression by 5-HT1A antagonists. Trends in Neurosciences. 1996;19(9):378-83.

50 Belmaker RH, Agam G. Major depressive disorder. N Engl J Med. 2008;358(1):55-68.

51 Kino T. Stress, glucocorticoid hormones, and hippocampal neural progenitor cells: implications to mood disorders. Frontiers in Physiology. 2015;6.

52 Kino T, Ichijo T, Amin ND, Kesavapany S, Wang Y, Kim N, et al. Cyclin-dependent kinase 5 differentially regulates the transcriptional activity of the glucocorticoid receptor through phosphorylation: clinical implications for the nervous system response to glucocorticoids and stress. Mol Endocrinol. 2007;21(7):1552-68.

53 Vreeburg SA, Hoogendijk WJG, van Pelt J, DeRijk RH, Verhagen JCM, van Dyck R, et al. Major Depressive Disorder and Hypothalamic-Pituitary-Adrenal Axis Activity: Results From a Large Cohort Study. Archives of General Psychiatry. 2009;66(6):617-26.

54 Martinac M, Babić D, Bevanda M, Vasilj I, Glibo DB, Karlović D, et al. Activity of the hypothalamic-pituitary-adrenal axis and inflammatory mediators in major depressive disorder with or without metabolic syndrome. Psychiatr Danub. 2017;29(1):39-50.

55 Gillespie CF, Nemeroff CB. Hypercortisolemia and depression. Psychosomatic medicine. 2005;67:S26-S28.

56 Nemeroff CB. The role of corticotropin-releasing factor in the pathogenesis of major depression. Pharmacopsychiatry. 1988;21(2):76-82.

57 Nemeroff CB, Widerlöv E, Bissette G, Walléus H, Karlsson I, Eklund K, et al. Elevated Concentrations of CSF Corticotropin-Releasing Factor-Like Immunoreactivity in Depressed Patients. Science. 1984;226(4680):1342-44.

58 Charles B. Nemeroff, M.D., Ph.D. Recent Findings in the Pathophysiology of Depression. Focus. 2008;6(1):3-14.

59 Ising M, Künzel HE, Binder EB, Nickel T, Modell S, Holsboer F. The combined dexamethasone/CRH test as a potential surrogate marker in depression. Progress in Neuro-Psychopharmacology and Biological Psychiatry. 2005;29(6):1085-93.

60 De Bellis MD, Gold PW, Geracioti TD, Jr., Listwak SJ, Kling MA. Association of fluoxetine treatment with reductions in CSF concentrations of corticotropin-releasing hormone and arginine vasopressin in patients with major depression. Am J Psychiatry. 1993;150(4):656-7.

61 Peng Q, Yan H, Wen Y, Lai C, Shi L. Association between NR3C1 rs41423247 polymorphism and depression: A PRISMA-compliant meta-analysis. Medicine (Baltimore). 2018;97(39):e12541.

62 Menke A. Is the HPA Axis as Target for Depression Outdated, or Is There a New Hope? Frontiers in Psychiatry. 2019;10.

63 Ramsteijn AS, Verkaik-Schakel RN, Houwing DJ, Plösch T, Olivier JDA. Perinatal exposure to fluoxetine and maternal adversity affect myelin-related gene expression and epigenetic regulation in the corticolimbic circuit of juvenile rats. Neuropsychopharmacology. 2022;47(9):1620-32.

64 Tchenio A, Lecca S, Valentinova K, Mameli M. Limiting habenular hyperactivity ameliorates maternal separation-driven depressive-like symptoms. Nature communications. 2017;8(1):1135.

65 Shepard RD, Langlois LD, Browne CA, Berenji A, Lucki I, Nugent FS. Ketamine Reverses Lateral Habenula Neuronal Dysfunction and Behavioral Immobility in the Forced Swim Test Following Maternal Deprivation in Late Adolescent Rats. Front Synaptic Neurosci. 2018;10:39.

66 Willner P. Chronic mild stress (CMS) revisited: consistency and behavioural-neurobiological concordance in the effects of CMS. Neuropsychobiology. 2005;52(2):90-110.

67 Xiao Y, Luo H, Yang WZ, Zeng Y, Shen Y, Ni X, et al. A Brain Signaling Framework for Stress-Induced Depression and Ketamine Treatment Elucidated by Phosphoproteomics. Frontiers in cellular neuroscience. 2020;14:48.

68 Song C, Liu BP, Zhang YP, Peng Z, Wang J, Collier AD, et al. Modeling consequences of prolonged strong unpredictable stress in zebrafish: Complex effects on behavior and physiology. Prog Neuropsychopharmacol Biol Psychiatry. 2018;81:384-94.

69 Nguyen M, Stewart AM, Kalueff AV. Aquatic blues: modeling depression and antidepressant action in zebrafish. Prog Neuropsychopharmacol Biol Psychiatry. 2014;55:26-39.

70 Li B, Piriz J, Mirrione M, Chung C, Proulx CD, Schulz D, et al. Synaptic potentiation onto habenula neurons in the learned helplessness model of depression. Nature. 2011;470(7335):535-9.

71 Mirrione MM, Schulz D, Lapidus KA, Zhang S, Goodman W, Henn FA. Increased metabolic activity in the septum and habenula during stress is linked to subsequent expression of learned helplessness behavior. Front Hum Neurosci. 2014;8:29.

72 Lecca S, Pelosi A, Tchenio A, Moutkine I, Lujan R, Hervé D, et al. Rescue of GABAB and GIRK function in the lateral habenula by protein phosphatase 2A inhibition ameliorates depression-like phenotypes in mice. Nat Med. 2016;22(3):254-61.

73 Klengel T, Binder EB. Epigenetics of Stress-Related Psychiatric Disorders and Gene × Environment Interactions. Neuron. 2015;86(6):1343-57.

74 Rajkowska G. Histopathology of the prefrontal cortex in major depression: what does it tell us about dysfunctional monoaminergic circuits? Prog Brain Res. 2000;126:397-412.

75 Paul IA, Skolnick P. Glutamate and depression: clinical and preclinical studies. Ann N Y Acad Sci. 2003;1003:250-72.

76 Kim JS, Schmid-Burgk W, Claus D, Kornhuber HH. Increased serum glutamate in depressed patients. Arch Psychiatr Nervenkr (1970). 1982;232(4):299-304.

77 Maes M, Verkerk R, Vandoolaeghe E, Lin A, Scharpé S. Serum levels of excitatory amino acids, serine, glycine, histidine, threonine, taurine, alanine and arginine in treatment-resistant depression: modulation by treatment with antidepressants and prediction of clinical responsivity. Acta Psychiatr Scand. 1998;97(4):302-8.

78 Kugaya A, Sanacora G. Beyond monoamines: glutamatergic function in mood disorders. CNS Spectr. 2005;10(10):808-19.

79 Yildiz-Yesiloglu A, Ankerst DP. Review of 1H magnetic resonance spectroscopy findings in major depressive disorder: A meta-analysis. Psychiatry Research: Neuroimaging. 2006;147(1):1-25.

80 Moriguchi S, Takamiya A, Noda Y, Horita N, Wada M, Tsugawa S, et al. Glutamatergic neurometabolite levels in major depressive disorder: a systematic review and meta-analysis of proton magnetic resonance spectroscopy studies. Mol Psychiatry. 2019;24(7):952-64.

81 Tordera RM, Totterdell S, Wojcik SM, Brose N, Elizalde N, Lasheras B, et al. Enhanced anxiety, depressive-like behaviour and impaired recognition memory in mice with reduced expression of the vesicular glutamate transporter 1 (VGLUT1). Eur J Neurosci. 2007;25(1):281-90.

82 Almeida RF, Thomazi AP, Godinho GF, Saute JA, Wofchuk ST, Souza DO, et al. Effects of depressive-like behavior of rats on brain glutamate uptake. Neurochem Res. 2010;35(8):1164-71.

83 Lee Y, Son H, Kim G, Kim S, Lee DH, Roh GS, et al. Glutamine deficiency in the prefrontal cortex increases depressive-like behaviours in male mice. J Psychiatry Neurosci. 2013;38(3):183-91.

84 Chen G, Ensor CR, Russell D, Bohner B. The pharmacology of 1-(1-phenylcyclohexyl) piperidine-HCl. J Pharmacol Exp Ther. 1959;127:241-50.

85 Greifenstein FE, Devault M, Yoshitake J, Gajewski JE. A study of a 1-aryl cyclo hexyl amine for anesthesia. Anesth Analg. 1958;37(5):283-94.

86 Lodge D, Anis NA, Burton NR. Effects of optical isomers of ketamine on excitation of cat and rat spinal neurones by amino acids and acetylcholine. Neurosci Lett. 1982;29(3):281-6.

87 Kohrs R, Durieux ME. Ketamine: teaching an old drug new tricks. Anesth Analg. 1998;87(5):1186-93.

88 Collingridge G. The role of NMDA receptors in learning and memory. Nature. 1987;330(6149):604-05.
89 Li F, Tsien JZ. Memory and the NMDA receptors. N Engl J Med. 2009;361(3):302-3.
90 Sumi T, Harada K. Mechanism underlying hippocampal long-term potentiation and depression based on competition between endocytosis and exocytosis of AMPA receptors. Scientific reports. 2020;10(1):14711.
91 Domino EF, Chodoff P, Corssen G. PHARMACOLOGIC EFFECTS OF CI-581, A NEW DISSOCIATIVE ANESTHETIC, IN MAN. Clin Pharmacol Ther. 1965;6:279-91.
92 Corssen G, Domino EF. Dissociative anesthesia: further pharmacologic studies and first clinical experience with the phencyclidine derivative CI-581. Anesth Analg. 1966;45(1):29-40.
93 Virtue Robert W, Alonis Joseph M, Mori M, Laforgue Robert T, Vogel John HK, Metcalf David R. An Anesthetic Agent: 2-0rthochlorophenyl, 2- Methylamino Cyclohexanone HCl (CI-581). Anesthesiology. 1967;28(5):823-33.
94 Oye I, Paulsen O, Maurset A. Effects of ketamine on sensory perception: evidence for a role of N-methyl-D-aspartate receptors. J Pharmacol Exp Ther. 1992;260(3):1209-13.
95 Jamora C, Iravani M. Unique Clinical Situations in Pediatric Patients Where Ketamine may be the Anesthetic Agent of Choice. American Journal of Therapeutics. 2010;17(5).
96 Kurdi MS, Theerth KA, Deva RS. Ketamine: Current applications in anesthesia, pain, and critical care. Anesth Essays Res. 2014;8(3):283-90.
97 Haas DA, Harper DG. Ketamine: a review of its pharmacologic properties and use in ambulatory anesthesia. Anesth Prog. 1992;39(3):61-8.
98 Clements JA, Nimmo WS, Grant IS. Bioavailability, pharmacokinetics, and analgesic activity of ketamine in humans. J Pharm Sci. 1982;71(5):539-42.
99 White PF, Schüttler J, Shafer A, Stanski DR, Horai Y, Trevor AJ. Comparative pharmacology of the ketamine isomers. Studies in volunteers. Br J Anaesth. 1985;57(2):197-203.
100 Yanagihara Y, Ohtani M, Kariya S, Uchino K, Hiraishi T, Ashizawa N, et al. Plasma concentration profiles of ketamine and norketamine after administration of various ketamine preparations to healthy Japanese volunteers. Biopharm Drug Dispos. 2003;24(1):37-43.
101 Kharasch ED, Labroo R. Metabolism of ketamine stereoisomers by human liver microsomes. Anesthesiology. 1992;77(6):1201-7.
102 Yanagihara Y, Kariya S, Ohtani M, Uchino K, Aoyama T, Yamamura Y, et al. Involvement of CYP2B6 in n-demethylation of ketamine in human liver microsomes. Drug Metab Dispos. 2001;29(6):887-90.
103 Hijazi Y, Boulieu R. Contribution of CYP3A4, CYP2B6, and CYP2C9 isoforms to N-demethylation of ketamine in human liver microsomes. Drug Metab Dispos. 2002;30(7):853-8.
104 Desta Z, Moaddel R, Ogburn ET, Xu C, Ramamoorthy A, Venkata SL, et al. Stereoselective and regiospecific hydroxylation of ketamine and norketamine. Xenobiotica. 2012;42(11):1076-87.
105 Zhao X, Venkata SL, Moaddel R, Luckenbaugh DA, Brutsche NE, Ibrahim L, et al. Simultaneous population pharmacokinetic modelling of ketamine and three major metabolites in patients with treatment-resistant bipolar depression. Br J Clin Pharmacol. 2012;74(2):304-14.

106 Idvall J, Ahlgren I, Aronsen KR, Stenberg P. Ketamine infusions: pharmacokinetics and clinical effects. Br J Anaesth. 1979;51(12):1167-73.

107 Sussman DR. A comparative evaluation of ketamine anesthesia in children and adults. Anesthesiology. 1974;40(5):459-64.

108 Green SM, Roback MG, Kennedy RM, Krauss B. Clinical Practice Guideline for Emergency Department Ketamine Dissociative Sedation: 2011 Update. Annals of Emergency Medicine. 2011;57(5):449-61.

109 Laskowski K, Stirling A, McKay WP, Lim HJ. A systematic review of intravenous ketamine for postoperative analgesia. Can J Anaesth. 2011;58(10):911-23.

110 Roytblat L, Korotkoruchko A, Katz J, Glazer M, Greemberg L, Fisher A. Postoperative pain: the effect of low-dose ketamine in addition to general anesthesia. Anesth Analg. 1993;77(6):1161-5.

111 Backonja M, Arndt G, Gombar KA, Check B, Zimmermann M. Response of chronic neuropathic pain syndromes to ketamine: a preliminary study. Pain. 1994;56(1):51-57.

112 Eide PK, Jørum E, Stubhaug A, Bremnes J, Breivik H. Relief of post-herpetic neuralgia with the N-methyl-D-aspartic acid receptor antagonist ketamine: a double-blind, cross-over comparison with morphine and placebo. Pain. 1994;58(3):347-54.

113 Hirlinger WK, Dick W. [Intramuscular ketamine analgesia in emergency patients. II. Clinical study of traumatized patients]. Anaesthesist. 1984;33(6):272-5.

114 Clements JA, Nimmo WS. Pharmacokinetics and analgesic effect of ketamine in man. Br J Anaesth. 1981;53(1):27-30.

115 Grant IS, Nimmo WS, Clements JA. Pharmacokinetics and analgesic effects of i.m. and oral ketamine. Br J Anaesth. 1981;53(8):805-10.

116 Zanos P, Moaddel R, Morris PJ, Riggs LM, Highland JN, Georgiou P, et al. Ketamine and Ketamine Metabolite Pharmacology: Insights into Therapeutic Mechanisms. Pharmacol Rev. 2018;70(3):621-60.

117 Roytblat L, Talmor D, Rachinsky M, Greemberg L, Pekar A, Appelbaum A, et al. Ketamine attenuates the interleukin-6 response after cardiopulmonary bypass. Anesth Analg. 1998;87(2):266-71.

118 Beilin B, Rusabrov Y, Shapira Y, Roytblat L, Greemberg L, Yardeni IZ, et al. Low-dose ketamine affects immune responses in humans during the early postoperative period. Br J Anaesth. 2007;99(4):522-7.

119 Shah P, McDowell M, Ebisu R, Hanif T, Toerne T. Adjunctive Use of Ketamine for Benzodiazepine-Resistant Severe Alcohol Withdrawal: a Retrospective Evaluation. J Med Toxicol. 2018;14(3):229-36.

120 Grabski M, McAndrew A, Lawn W, Marsh B, Raymen L, Stevens T, et al. Adjunctive Ketamine With Relapse Prevention-Based Psychological Therapy in the Treatment of Alcohol Use Disorder. Am J Psychiatry. 2022;179(2):152-62.

121 Willis DE, Goldstein PA. Targeting Affective Mood Disorders With Ketamine to Prevent Chronic Postsurgical Pain. Frontiers in Pain Research. 2022;3.

122 Ebert B, Mikkelsen S, Thorkildsen C, Borgbjerg FM. Norketamine, the main metabolite of ketamine, is a non-competitive NMDA receptor antagonist in the rat cortex and spinal cord. Eur J Pharmacol. 1997;333(1):99-104.

123 Moaddel R, Abdrakhmanova G, Kozak J, Jozwiak K, Toll L, Jimenez L, et al. Sub-anesthetic concentrations of (*R*,*S*)-ketamine metabolites inhibit acetylcholine-evoked currents in α7 nicotinic acetylcholine receptors. Eur J Pharmacol. 2013;698(1-3):228-34.

124 White Paul F, Ham J, Way Walter L, Trevor A. Pharmacology of Ketamine Isomers in Surgical Patients Anesthesiology. 1980;52(3):231-39.

125 Mathisen LC, Skjelbred P, Skoglund LA, Øye I. Effect of ketamine, an NMDA receptor inhibitor, in acute and chronic orofacial pain. Pain. 1995;61(2):215-20.

126 Vollenweider FX, Leenders KL, Oye I, Hell D, Angst J. Differential psychopathology and patterns of cerebral glucose utilisation produced by (S)- and (R)-ketamine in healthy volunteers using positron emission tomography (PET). Eur Neuropsychopharmacol. 1997;7(1):25-38.

127 Geisslinger G, Hering W, Thomann P, Knoll R, Kamp HD, Brune K. PHARMACOKINETICS AND PHARMACODYNAMICS OF KETAMINE ENANTIOMERS IN SURGICAL PATIENTS USING A STEREOSELECTIVE ANALYTICAL METHOD††Reported in part at the Annual Meeting of American Society of Anesthesiologists, October 17-21, 1992, New Orleans, U.S.A. British Journal of Anaesthesia. 1993;70(6):666-71.

128 Sofia RD, Harakal JJ. Evaluation of ketamine HCl for anti-depressant activity. Arch Int Pharmacodyn Ther. 1975;214(1):68-74.

129 Trullas R, Skolnick P. Functional antagonists at the NMDA receptor complex exhibit antidepressant actions. Eur J Pharmacol. 1990;185(1):1-10.

130 Moryl E, Danysz W, Quack G. Potential antidepressive properties of amantadine, memantine and bifemelane. Pharmacol Toxicol. 1993;72(6):394-7.

131 Papp M, Moryl E. Antidepressant activity of non-competitive and competitive NMDA receptor antagonists in a chronic mild stress model of depression. Eur J Pharmacol. 1994;263(1-2):1-7.

132 Przegaliński E, Tatarczyńska E, Dereń-Wesołek A, Chojnacka-Wojcik E. Antidepressant-like effects of a partial agonist at strychnine-insensitive glycine receptors and a competitive NMDA receptor antagonist. Neuropharmacology. 1997;36(1):31-7.

133 Khorramzadeh E, Lotfy AO. The use of ketamine in psychiatry. Psychosomatics. 1973;14(6):344-6.

134 Berman RM, Cappiello A, Anand A, Oren DA, Heninger GR, Charney DS, et al. Antidepressant effects of ketamine in depressed patients. Biol Psychiatry. 2000;47(4):351-4.

135 Zarate CA, Jr., Singh JB, Carlson PJ, Brutsche NE, Ameli R, Luckenbaugh DA, et al. A randomized trial of an N-methyl-D-aspartate antagonist in treatment-resistant major depression. Arch Gen Psychiatry. 2006;63(8):856-64.

136 Murrough JW, Iosifescu DV, Chang LC, Al Jurdi RK, Green CE, Perez AM, et al. Antidepressant efficacy of ketamine in treatment-resistant major depression: a two-site randomized controlled trial. Am J Psychiatry. 2013;170(10):1134-42.

137 Zarate CA, Jr., Brutsche NE, Ibrahim L, Franco-Chaves J, Diazgranados N, Cravchik A, et al. Replication of ketamine's antidepressant efficacy in bipolar depression: a randomized controlled add-on trial. Biol Psychiatry. 2012;71(11):939-46.

138 Price RB, Nock MK, Charney DS, Mathew SJ. Effects of intravenous ketamine on explicit and implicit measures of suicidality in treatment-resistant depression. Biol Psychiatry. 2009;66(5):522-6.

139 DiazGranados N, Ibrahim LA, Brutsche NE, Ameli R, Henter ID, Luckenbaugh DA, et al. Rapid resolution of suicidal ideation after a single infusion of an N-methyl-D-

aspartate antagonist in patients with treatment-resistant major depressive disorder. J Clin Psychiatry. 2010;71(12):1605-11.

140 aan het Rot M, Collins KA, Murrough JW, Perez AM, Reich DL, Charney DS, et al. Safety and efficacy of repeated-dose intravenous ketamine for treatment-resistant depression. Biol Psychiatry. 2010;67(2):139-45.

141 Singh JB, Fedgchin M, Daly EJ, De Boer P, Cooper K, Lim P, et al. A Double-Blind, Randomized, Placebo-Controlled, Dose-Frequency Study of Intravenous Ketamine in Patients With Treatment-Resistant Depression. Am J Psychiatry. 2016;173(8):816-26.

142 Su TP, Chen MH, Li CT, Lin WC, Hong CJ, Gueorguieva R, et al. Dose-Related Effects of Adjunctive Ketamine in Taiwanese Patients with Treatment-Resistant Depression. Neuropsychopharmacology. 2017;42(13):2482-92.

143 Fava M, Freeman MP, Flynn M, Judge H, Hoeppner BB, Cusin C, et al. Double-blind, placebo-controlled, dose-ranging trial of intravenous ketamine as adjunctive therapy in treatment-resistant depression (TRD). Mol Psychiatry. 2020;25(7):1592-603.

144 Loo CK, Gálvez V, O'Keefe E, Mitchell PB, Hadzi-Pavlovic D, Leyden J, et al. Placebo-controlled pilot trial testing dose titration and intravenous, intramuscular and subcutaneous routes for ketamine in depression. Acta Psychiatr Scand. 2016;134(1):48-56.

145 Newport DJ, Carpenter LL, McDonald WM, Potash JB, Tohen M, Nemeroff CB. Ketamine and Other NMDA Antagonists: Early Clinical Trials and Possible Mechanisms in Depression. Am J Psychiatry. 2015;172(10):950-66.

146 Kishimoto T, Chawla JM, Hagi K, Zarate CA, Kane JM, Bauer M, et al. Single-dose infusion ketamine and non-ketamine N-methyl-d-aspartate receptor antagonists for unipolar and bipolar depression: a meta-analysis of efficacy, safety and time trajectories. Psychol Med. 2016;46(7):1459-72.

147 Zarate CA, Jr., Brutsche N, Laje G, Luckenbaugh DA, Venkata SL, Ramamoorthy A, et al. Relationship of ketamine's plasma metabolites with response, diagnosis, and side effects in major depression. Biol Psychiatry. 2012;72(4):331-8.

148 Chong C, Schug SA, Page-Sharp M, Jenkins B, Ilett KF. Development of a sublingual/oral formulation of ketamine for use in neuropathic pain: Preliminary findings from a three-way randomized, crossover study. Clin Drug Investig. 2009;29(5):317-24.

149 Lapidus KA, Levitch CF, Perez AM, Brallier JW, Parides MK, Soleimani L, et al. A randomized controlled trial of intranasal ketamine in major depressive disorder. Biol Psychiatry. 2014;76(12):970-6.

150 McIntyre RS, Carvalho IP, Lui LMW, Majeed A, Masand PS, Gill H, et al. The effect of intravenous, intranasal, and oral ketamine in mood disorders: A meta-analysis. J Affect Disord. 2020;276:576-84.

151 Canuso CM, Singh JB, Fedgchin M, Alphs L, Lane R, Lim P, et al. Efficacy and Safety of Intranasal Esketamine for the Rapid Reduction of Symptoms of Depression and Suicidality in Patients at Imminent Risk for Suicide: Results of a Double-Blind, Randomized, Placebo-Controlled Study. Am J Psychiatry. 2018;175(7):620-30.

152 Daly EJ, Trivedi MH, Janik A, Li H, Zhang Y, Li X, et al. Efficacy of Esketamine Nasal Spray Plus Oral Antidepressant Treatment for Relapse Prevention in Patients With Treatment-Resistant Depression: A Randomized Clinical Trial. JAMA Psychiatry. 2019;76(9):893-903.

153 Popova V, Daly EJ, Trivedi M, Cooper K, Lane R, Lim P, et al. Efficacy and Safety of Flexibly Dosed Esketamine Nasal Spray Combined With a Newly Initiated Oral Antidepressant in Treatment-Resistant Depression: A Randomized Double-Blind Active-Controlled Study. Am J Psychiatry. 2019;176(6):428-38.
154 Jeon HJ, Ju PC, Sulaiman AH, Aziz SA, Paik JW, Tan W, et al. Long-term Safety and Efficacy of Esketamine Nasal Spray Plus an Oral Antidepressant in Patients with Treatment-resistant Depression- an Asian Sub-group Analysis from the SUSTAIN-2 Study. Clin Psychopharmacol Neurosci. 2022;20(1):70-86.
155 Ochs-Ross R, Daly EJ, Zhang Y, Lane R, Lim P, Morrison RL, et al. Efficacy and Safety of Esketamine Nasal Spray Plus an Oral Antidepressant in Elderly Patients With Treatment-Resistant Depression-TRANSFORM-3. Am J Geriatr Psychiatry. 2020;28(2):121-41.
156 Pai SM, Gries JM. Off-Label Use of Ketamine: A Challenging Drug Treatment Delivery Model With an Inherently Unfavorable Risk-Benefit Profile. J Clin Pharmacol. 2022;62(1):10-13.
157 Siegel RK. Phencyclidine and ketamine intoxication: a study of four populations of recreational users. NIDA Res Monogr. 1978(21):119-47.
158 Reich DL, Silvay G. Ketamine: an update on the first twenty-five years of clinical experience. Can J Anaesth. 1989;36(2):186-97.
159 Stewart CE. Ketamine as a street drug. Emerg Med Serv. 2001;30(11):30, 32, 34 passim.
160 Short B, Fong J, Galvez V, Shelker W, Loo CK. Side-effects associated with ketamine use in depression: a systematic review. Lancet Psychiatry. 2018;5(1):65-78.
161 Bahr R, Lopez A, Rey JA. Intranasal Esketamine (Spravato(TM)) for Use in Treatment-Resistant Depression In Conjunction With an Oral Antidepressant. P t. 2019;44(6):340-75.
162 Strous JFM, Weeland CJ, van der Draai FA, Daams JG, Denys D, Lok A, et al. Brain Changes Associated With Long-Term Ketamine Abuse, A Systematic Review. Frontiers in neuroanatomy. 2022;16.
163 Cryan JF, Mombereau C, Vassout A. The tail suspension test as a model for assessing antidepressant activity: review of pharmacological and genetic studies in mice. Neurosci Biobehav Rev. 2005;29(4-5):571-625.
164 Slattery DA, Cryan JF. Using the rat forced swim test to assess antidepressant-like activity in rodents. Nature Protocols. 2012;7(6):1009-14.
165 Liu M-Y, Yin C-Y, Zhu L-J, Zhu X-H, Xu C, Luo C-X, et al. Sucrose preference test for measurement of stress-induced anhedonia in mice. Nature Protocols. 2018;13(7):1686-98.
166 Zhang JC, Li SX, Hashimoto K. R (-)-ketamine shows greater potency and longer lasting antidepressant effects than S (+)-ketamine. Pharmacol Biochem Behav. 2014;116:137-41.
167 Maier SF, Seligman ME. Learned helplessness at fifty: Insights from neuroscience. Psychol Rev. 2016;123(4):349-67.
168 Hollis F, Kabbaj M. Social Defeat as an Animal Model for Depression. ILAR Journal. 2014;55(2):221-32.
169 Yang C, Shirayama Y, Zhang JC, Ren Q, Yao W, Ma M, et al. R-ketamine: a rapid-onset and sustained antidepressant without psychotomimetic side effects. Translational psychiatry. 2015;5(9):e632.

170 McKendrick G, Graziane NM. Drug-Induced Conditioned Place Preference and Its Practical Use in Substance Use Disorder Research. Frontiers in behavioral neuroscience. 2020;14:582147.
171 Hashimoto K, Kakiuchi T, Ohba H, Nishiyama S, Tsukada H. Reduction of dopamine D(2/3) receptor binding in the striatum after a single administration of esketamine, but not R-ketamine: a PET study in conscious monkeys. Eur Arch Psychiatry Clin Neurosci. 2017;267(2):173-76.
172 Iijima M, Ito A, Kurosu S, Chaki S. Pharmacological characterization of repeated corticosterone injection-induced depression model in rats. Brain Res. 2010;1359:75-80.
173 Fukumoto K, Toki H, Iijima M, Hashihayata T, Yamaguchi JI, Hashimoto K, et al. Antidepressant Potential of (R)-Ketamine in Rodent Models: Comparison with (S)-Ketamine. J Pharmacol Exp Ther. 2017;361(1):9-16.
174 Zanos P, Moaddel R, Morris PJ, Georgiou P, Fischell J, Elmer GI, et al. NMDAR inhibition-independent antidepressant actions of ketamine metabolites. Nature. 2016;533(7604):481-6.
175 Yang C, Qu Y, Abe M, Nozawa D, Chaki S, Hashimoto K. (R)-Ketamine Shows Greater Potency and Longer Lasting Antidepressant Effects Than Its Metabolite (2R,6R)-Hydroxynorketamine. Biol Psychiatry. 2017;82(5):e43-e44.
176 Gonzalez-Burgos G, Cho RY, Lewis DA. Alterations in Cortical Network Oscillations and Parvalbumin Neurons in Schizophrenia. Biological Psychiatry. 2015;77(12):1031-40.
177 Yang C, Han M, Zhang JC, Ren Q, Hashimoto K. Loss of parvalbumin-immunoreactivity in mouse brain regions after repeated intermittent administration of esketamine, but not R-ketamine. Psychiatry Res. 2016;239:281-3.
178 Shirayama Y, Hashimoto K. Effects of a single bilateral infusion of R-ketamine in the rat brain regions of a learned helplessness model of depression. Eur Arch Psychiatry Clin Neurosci. 2017;267(2):177-82.
179 Yang C, Qu Y, Fujita Y, Ren Q, Ma M, Dong C, et al. Possible role of the gut microbiota-brain axis in the antidepressant effects of (R)-ketamine in a social defeat stress model. Translational psychiatry. 2017;7(12):1294.
180 Hashimoto K. Rapid-acting antidepressant ketamine, its metabolites and other candidates: A historical overview and future perspective. Psychiatry Clin Neurosci. 2019;73(10):613-27.
181 Leal GC, Bandeira ID, Correia-Melo FS, Telles M, Mello RP, Vieira F, et al. Intravenous arketamine for treatment-resistant depression: open-label pilot study. Eur Arch Psychiatry Clin Neurosci. 2021;271(3):577-82.
182 (https://ClinicalTrials.gov/show/NCT05414422).
183 Dinis-Oliveira RJ. Metabolism and metabolomics of ketamine: a toxicological approach. Forensic Sci Res. 2017;2(1):2-10.
184 Moaddel R, Venkata SL, Tanga MJ, Bupp JE, Green CE, Iyer L, et al. A parallel chiral-achiral liquid chromatographic method for the determination of the stereoisomers of ketamine and ketamine metabolites in the plasma and urine of patients with complex regional pain syndrome. Talanta. 2010;82(5):1892-904.
185 Cohen ML, Chan SL, Way WL, Trevor AJ. Distribution in the brain and metabolism of ketamine in the rat after intravenous administration. Anesthesiology. 1973;39(4):370-6.

186 Leung LY, Baillie TA. Comparative pharmacology in the rat of ketamine and its two principal metabolites, norketamine and (Z)-6-hydroxynorketamine. J Med Chem. 1986;29(11):2396-9.

187 Paul RK, Singh NS, Khadeer M, Moaddel R, Sanghvi M, Green CE, et al. (*R*,*S*)-Ketamine metabolites (*R*,*S*)-norketamine and (*2S*,*6S*)-hydroxynorketamine increase the mammalian target of rapamycin function. Anesthesiology. 2014;121(1):149-59.

188 Moaddel R, Sanghvi M, Dossou KS, Ramamoorthy A, Green C, Bupp J, et al. The distribution and clearance of (2S,6S)-hydroxynorketamine, an active ketamine metabolite, in Wistar rats. Pharmacol Res Perspect. 2015;3(4):e00157.

189 Morris PJ, Moaddel R, Zanos P, Moore CE, Gould T, Zarate CA, Jr., et al. Synthesis and N-Methyl-d-aspartate (NMDA) Receptor Activity of Ketamine Metabolites. Organic letters. 2017;19(17):4572-75.

190 Singh NS, Paul RK, Ramamoorthy A, Torjman MC, Moaddel R, Bernier M, et al. Nicotinic acetylcholine receptor antagonists alter the function and expression of serine racemase in PC-12 and 1321N1 cells. Cell Signal. 2013;25(12):2634-45.

191 Ignácio ZM, Réus GZ, Arent CO, Abelaira HM, Pitcher MR, Quevedo J. New perspectives on the involvement of mTOR in depression as well as in the action of antidepressant drugs. Br J Clin Pharmacol. 2016;82(5):1280-90.

192 Gant TG. Using Deuterium in Drug Discovery: Leaving the Label in the Drug. Journal of Medicinal Chemistry. 2014;57(9):3595-611.

193 Shirayama Y, Hashimoto K. Lack of Antidepressant Effects of (2R,6R)-Hydroxynorketamine in a Rat Learned Helplessness Model: Comparison with (R)-Ketamine. Int J Neuropsychopharmacol. 2018;21(1):84-88.

194 Pham TH, Defaix C, Xu X, Deng SX, Fabresse N, Alvarez JC, et al. Common Neurotransmission Recruited in (R,S)-Ketamine and (2R,6R)-Hydroxynorketamine-Induced Sustained Antidepressant-like Effects. Biol Psychiatry. 2018;84(1):e3-e6.

195 Suzuki K, Nosyreva E, Hunt KW, Kavalali ET, Monteggia LM. Effects of a ketamine metabolite on synaptic NMDAR function. Nature. 2017;546(7659):E1-e3.

196 Zanos P, Moaddel R, Morris PJ, Georgiou P, Fischell J, Elmer GI, et al. Zanos et al. reply. Nature. 2017;546(7659):E4-e5.

197 Chou D, Peng HY, Lin TB, Lai CY, Hsieh MC, Wen YC, et al. (2R,6R)-hydroxynorketamine rescues chronic stress-induced depression-like behavior through its actions in the midbrain periaqueductal gray. Neuropharmacology. 2018;139:1-12.

198 Blasco-Serra A, González-Soler EM, Cervera-Ferri A, Teruel-Martí V, Valverde-Navarro AA. A standardization of the Novelty-Suppressed Feeding Test protocol in rats. Neurosci Lett. 2017;658:73-78.

199 Lumsden EW, Troppoli TA, Myers SJ, Zanos P, Aracava Y, Kehr J, et al. Antidepressant-relevant concentrations of the ketamine metabolite (2R,6R)-hydroxynorketamine do not block NMDA receptor function. Proc Natl Acad Sci U S A. 2019;116(11):5160-69.

200 Highland JN, Morris PJ, Zanos P, Lovett J, Ghosh S, Wang AQ, et al. Mouse, rat, and dog bioavailability and mouse oral antidepressant efficacy of (2R,6R)-hydroxynorketamine. Journal of psychopharmacology (Oxford, England). 2019;33(1):12-24.

201 (https://ClinicalTrials.gov/show/NCT04711005).

202 Yang C, Kobayashi S, Nakao K, Dong C, Han M, Qu Y, et al. AMPA Receptor Activation-Independent Antidepressant Actions of Ketamine Metabolite (S)-Norketamine. Biol Psychiatry. 2018;84(8):591-600.

203 Takahashi H, Hashimoto R, Iwase M, Ishii R, Kamio Y, Takeda M. Prepulse inhibition of startle response: recent advances in human studies of psychiatric disease. Clin Psychopharmacol Neurosci. 2011;9(3):102-10.

204 Corazza O, Schifano F, Simonato P, Fergus S, Assi S, Stair J, et al. Phenomenon of new drugs on the Internet: the case of ketamine derivative methoxetamine. Hum Psychopharmacol. 2012;27(2):145-9.

205 Hofer KE, Grager B, Müller DM, Rauber-Lüthy C, Kupferschmidt H, Rentsch KM, et al. Ketamine-like effects after recreational use of methoxetamine. Ann Emerg Med. 2012;60(1):97-9.

206 Kjellgren A, Jonsson K. Methoxetamine (MXE)--a phenomenological study of experiences induced by a "legal high" from the internet. J Psychoactive Drugs. 2013;45(3):276-86.

207 Striebel JM, Nelson EE, Kalapatapu RK. "Being with a Buddha": A Case Report of Methoxetamine Use in a United States Veteran with PTSD. Case Rep Psychiatry. 2017;2017:2319094.

208 Morris H, Wallach J. From PCP to MXE: a comprehensive review of the non-medical use of dissociative drugs. Drug Test Anal. 2014;6(7-8):614-32.

209 Dargan PI, Tang HC, Liang W, Wood DM, Yew DT. Three months of methoxetamine administration is associated with significant bladder and renal toxicity in mice. Clinical Toxicology. 2014;52(3):176-80.

210 Roth BL, Gibbons S, Arunotayanun W, Huang XP, Setola V, Treble R, et al. The ketamine analogue methoxetamine and 3- and 4-methoxy analogues of phencyclidine are high affinity and selective ligands for the glutamate NMDA receptor. PLoS One. 2013;8(3):e59334.

211 Hondebrink L, Kasteel EEJ, Tukker AM, Wijnolts FMJ, Verboven AHA, Westerink RHS. Neuropharmacological characterization of the new psychoactive substance methoxetamine. Neuropharmacology. 2017;123:1-9.

212 Chiamulera C, Armani F, Mutti A, Fattore L. The ketamine analogue methoxetamine generalizes to ketamine discriminative stimulus in rats. Behav Pharmacol. 2016;27(2-3 Spec Issue):204-10.

213 Horsley RR, Lhotkova E, Hajkova K, Jurasek B, Kuchar M, Palenicek T. Detailed pharmacological evaluation of methoxetamine (MXE), a novel psychoactive ketamine analogue—Behavioural, pharmacokinetic and metabolic studies in the Wistar rat. Brain Research Bulletin. 2016;126:102-10.

214 Zanda MT, Fadda P, Antinori S, Di Chio M, Fratta W, Chiamulera C, et al. Methoxetamine affects brain processing involved in emotional response in rats. Br J Pharmacol. 2017;174(19):3333-45.

215 Páleníček T, Fujáková M, Brunovský M, Balíková M, Horáček J, Gorman I, et al. Electroencephalographic spectral and coherence analysis of ketamine in rats: correlation with behavioral effects and pharmacokinetics. Neuropsychobiology. 2011;63(4):202-18.

216 Botanas CJ, Bryan de la Peña J, Custodio RJ, Joy Dela Peña I, Kim M, Woo T, et al. Methoxetamine produces rapid and sustained antidepressant effects probably via glutamatergic and serotonergic mechanisms. Neuropharmacology. 2017;126:121-27.

217 Botanas CJ, Perez Custodio RJ, Kim HJ, de la Pena JB, Sayson LV, Ortiz DM, et al. R (-)-methoxetamine exerts rapid and sustained antidepressant effects and fewer behavioral side effects relative to S (+)-methoxetamine. Neuropharmacology. 2021;193:108619.

218 Craig CL, Loeffler GH. The ketamine analog methoxetamine: a new designer drug to threaten military readiness. Mil Med. 2014;179(10):1149-57.

219 Luethi D, Liechti ME. Designer drugs: mechanism of action and adverse effects. Arch Toxicol. 2020;94(4):1085-133.

220 Štefková-Mazochová K, Danda H, Dehaen W, Jurásek B, Šíchová K, Pinterová-Leca N, et al. Pharmacokinetic, pharmacodynamic, and behavioural studies of deschloroketamine in Wistar rats. Br J Pharmacol. 2022;179(1):65-83.

221 Sayson LV, Botanas CJ, Custodio RJP, Abiero A, Kim M, Lee HJ, et al. The novel methoxetamine analogs N-ethylnorketamine hydrochloride (NENK), 2-MeO-N-ethylketamine hydrochloride (2-MeO-NEK), and 4-MeO-N-ethylketamine hydrochloride (4-MeO-NEK) elicit rapid antidepressant effects via activation of AMPA and 5-HT(2) receptors. Psychopharmacology (Berl). 2019;236(7):2201-10.

222 Lakstygal AM, Kolesnikova TO, Khatsko SL, Zabegalov KN, Volgin AD, Demin KA, et al. DARK Classics in Chemical Neuroscience: Atropine, Scopolamine, and Other Anticholinergic Deliriant Hallucinogens. ACS Chem Neurosci. 2019;10(5):2144-59.

223 Renner UD, Oertel R, Kirch W. Pharmacokinetics and pharmacodynamics in clinical use of scopolamine. Ther Drug Monit. 2005;27(5):655-65.

224 Jaffe RJ, Novakovic V, Peselow ED. Scopolamine as an antidepressant: a systematic review. Clin Neuropharmacol. 2013;36(1):24-6.

225 Janowsky DS, el-Yousef MK, Davis JM, Sekerke HJ. A cholinergic-adrenergic hypothesis of mania and depression. Lancet. 1972;2(7778):632-5.

226 Pacher P, Kecskemeti V. Trends in the Development of New Antidepressants. Is there a Light at the End of the Tunnel? Current Medicinal Chemistry. 2004;11(7):925-43.

227 DOYLE AE, MCQUEEN EG, SMIRK FH. Treatment of Hypertension with Reserpine,with Reserpine in Combination with Pentapyrrolidinium,and with Reserpine in Combination with Veratrum Alkaloids. Circulation. 1955;11(2):170-81.

228 Locket S. Oral preparations of Reuwolfia serpentina in treatment of essential hypertension. Br Med J. 1955;1(4917):809-16.

229 Janowsky DS, El-Yousef KM, Davis JM. Acetylcholine and Depression*. Psychosomatic Medicine. 1974;36(3).

230 Risch SC, Kalin NH, Janowsky DS. Cholinergic challenges in affective illness: behavioral and neuroendocrine correlates. J Clin Psychopharmacol. 1981;1(4):186-92.

231 Furey ML, Drevets WC. Antidepressant efficacy of the antimuscarinic drug scopolamine: a randomized, placebo-controlled clinical trial. Arch Gen Psychiatry. 2006;63(10):1121-9.

232 Gillin JC, Sutton L, Ruiz C, Darko D, Golshan S, Risch SC, et al. The effects of scopolamine on sleep and mood in depressed patients with a history of alcoholism and a normal comparison group. Biol Psychiatry. 1991;30(2):157-69.

233 Drevets WC, Furey ML. Replication of scopolamine's antidepressant efficacy in major depressive disorder: a randomized, placebo-controlled clinical trial. Biol Psychiatry. 2010;67(5):432-8.

234 Drevets WC, Zarate CA, Jr., Furey ML. Antidepressant effects of the muscarinic cholinergic receptor antagonist scopolamine: a review. Biol Psychiatry. 2013;73(12):1156-63.

235 Gillin JC, Lauriello J, Kelsoe JR, Rapaport M, Golshan S, Kenny WM, et al. No antidepressant effect of biperiden compared with placebo in depression: a double-blind 6-week clinical trial. Psychiatry Res. 1995;58(2):99-105.

236 Furey ML, Khanna A, Hoffman EM, Drevets WC. Scopolamine produces larger antidepressant and antianxiety effects in women than in men. Neuropsychopharmacology. 2010;35(12):2479-88.

237 Rubin RT, O'Toole SM, Rhodes ME, Sekula LK, Czambel RK. Hypothalamo-pituitary-adrenal cortical responses to low-dose physostigmine and arginine vasopressin administration: sex differences between major depressives and matched control subjects. Psychiatry Res. 1999;89(1):1-20.

238 Rubin RT, Abbasi SA, Rhodes ME, Czambel RK. Growth hormone responses to low-dose physostigmine administration: functional sex differences (sexual diergism) between major depressives and matched controls. Psychol Med. 2003;33(4):655-65.

239 Comings DE, Wu S, Rostamkhani M, McGue M, Iacono WG, MacMurray JP. Association of the muscarinic cholinergic 2 receptor (CHRM2) gene with major depression in women. Am J Med Genet. 2002;114(5):527-9.

240 Janowsky DS. Serendipity strikes again: scopolamine as an antidepressant agent in bipolar depressed patients. Curr Psychiatry Rep. 2011;13(6):443-5.

241 Furey ML, Nugent AC, Speer AM, Luckenbaugh DA, Hoffman EM, Frankel E, et al. Baseline mood-state measures as predictors of antidepressant response to scopolamine. Psychiatry Res. 2012;196(1):62-7.

242 Park L, Furey M, Nugent AC, Farmer C, Ellis J, Szczepanik J, et al. Neurophysiological Changes Associated with Antidepressant Response to Ketamine Not Observed in a Negative Trial of Scopolamine in Major Depressive Disorder. Int J Neuropsychopharmacol. 2019;22(1):10-18.

243 Ellis JS, Zarate CA, Jr., Luckenbaugh DA, Furey ML. Antidepressant treatment history as a predictor of response to scopolamine: clinical implications. J Affect Disord. 2014;162:39-42.

244 Zhou J, Yang J, Zhu X, Zghoul T, Feng L, Chen R, et al. The effects of intramuscular administration of scopolamine augmentation in moderate to severe major depressive disorder: a randomized, double-blind, placebo-controlled trial. Therapeutic Advances in Psychopharmacology. 2020;10:2045125320938556.

245 Chen JCC, Sumner RL, Naga VK, Hoeh N, Ayeni HA, Singh V, et al. A Randomized Controlled Trial of Intravenous Scopolamine Versus Active-Placebo Glycopyrrolate in Patients With Major Depressive Disorder. J Clin Psychiatry. 2022;83(5).

246 Moskal JR, Burgdorf JS, Stanton PK, Kroes RA, Disterhoft JF, Burch RM, et al. The Development of Rapastinel (Formerly GLYX-13); A Rapid Acting and Long Lasting Antidepressant. Curr Neuropharmacol. 2017;15(1):47-56.

247 Moskal JR, Yamamoto H, Colley PA. The use of antibody engineering to create novel drugs that target N-methyl-D-aspartate receptors. Curr Drug Targets. 2001;2(3):331-45.

248 Moskal JR, Kuo AG, Weiss C, Wood PL, O'Connor Hanson A, Kelso S, et al. GLYX-13: a monoclonal antibody-derived peptide that acts as an N-methyl-D-aspartate receptor modulator. Neuropharmacology. 2005;49(7):1077-87.

249 Burgdorf J, Kroes RA, Weiss C, Oh MM, Disterhoft JF, Brudzynski SM, et al. Positive emotional learning is regulated in the medial prefrontal cortex by GluN2B-containing NMDA receptors. Neuroscience. 2011;192:515-23.

250 Burgdorf J, Zhang XL, Weiss C, Matthews E, Disterhoft JF, Stanton PK, et al. The N-methyl-D-aspartate receptor modulator GLYX-13 enhances learning and memory, in young adult and learning impaired aging rats. Neurobiol Aging. 2011;32(4):698-706.

251 Burgdorf J, Zhang XL, Weiss C, Gross A, Boikess SR, Kroes RA, et al. The long-lasting antidepressant effects of rapastinel (GLYX-13) are associated with a metaplasticity process in the medial prefrontal cortex and hippocampus. Neuroscience. 2015;308:202-11.

252 Burgdorf J, Zhang XL, Nicholson KL, Balster RL, Leander JD, Stanton PK, et al. GLYX-13, a NMDA receptor glycine-site functional partial agonist, induces antidepressant-like effects without ketamine-like side effects. Neuropsychopharmacology. 2013;38(5):729-42.

253 Moskal JR, Burch R, Burgdorf JS, Kroes RA, Stanton PK, Disterhoft JF, et al. GLYX-13, an NMDA receptor glycine site functional partial agonist enhances cognition and produces antidepressant effects without the psychotomimetic side effects of NMDA receptor antagonists. Expert Opin Investig Drugs. 2014;23(2):243-54.

254 Preskorn S, Macaluso M, Mehra DO, Zammit G, Moskal JR, Burch RM. Randomized proof of concept trial of GLYX-13, an N-methyl-D-aspartate receptor glycine site partial agonist, in major depressive disorder nonresponsive to a previous antidepressant agent. J Psychiatr Pract. 2015;21(2):140-9.

255 (https://ClinicalTrials.gov/show/NCT02932943).

256 Henter ID, Park LT, Zarate CA, Jr. Novel Glutamatergic Modulators for the Treatment of Mood Disorders: Current Status. CNS Drugs. 2021;35(5):527-43.

257 Burgdorf JS, Zhang XL, Stanton PK, Moskal JR, Donello JE. Zelquistinel Is an Orally Bioavailable Novel NMDA Receptor Allosteric Modulator That Exhibits Rapid and Sustained Antidepressant-Like Effects. Int J Neuropsychopharmacol. 2022;25(12):979-91.

258 (https://ClinicalTrials.gov/show/NCT02366364).

259 (https://ClinicalTrials.gov/show/NCT02067793).

260 Kimball A, Dichtel LE, Nyer MB, Mischoulon D, Fisher LB, Cusin C, et al. The allopregnanolone to progesterone ratio across the menstrual cycle and in menopause. Psychoneuroendocrinology. 2020;112:104512.

261 Pinna G. Allopregnanolone, the Neuromodulator Turned Therapeutic Agent: Thank You, Next? Frontiers in Endocrinology. 2020;11.

262 Agís-Balboa RC, Pinna G, Zhubi A, Maloku E, Veldic M, Costa E, et al. Characterization of brain neurons that express enzymes mediating neurosteroid biosynthesis. Proceedings of the National Academy of Sciences. 2006;103(39):14602-07.

263 Morrow AL, Suzdak PD, Paul SM. Steroid hormone metabolites potentiate GABA receptor-mediated chloride ion flux with nanomolar potency. Eur J Pharmacol. 1987;142(3):483-5.

264 Martinez Botella G, Salituro FG, Harrison BL, Beresis RT, Bai Z, Blanco M-J, et al. Neuroactive Steroids. 2. 3α-Hydroxy-3β-methyl-21-(4-cyano-1H-pyrazol-1′-yl)-19-nor-5β-pregnan-20-one (SAGE-217): A Clinical Next Generation Neuroactive Steroid

Positive Allosteric Modulator of the (γ-Aminobutyric Acid)A Receptor. Journal of Medicinal Chemistry. 2017;60(18):7810-19.

265 Matsumoto K, Uzunova V, Pinna G, Taki K, Uzunov DP, Watanabe H, et al. Permissive role of brain allopregnanolone content in the regulation of pentobarbital-induced righting reflex loss. Neuropharmacology. 1999;38(7):955-63.

266 Pinna G, Dong E, Matsumoto K, Costa E, Guidotti A. In socially isolated mice, the reversal of brain allopregnanolone down-regulation mediates the anti-aggressive action of fluoxetine. Proc Natl Acad Sci U S A. 2003;100(4):2035-40.

267 Deligiannidis KM, Kroll-Desrosiers AR, Mo S, Nguyen HP, Svenson A, Jaitly N, et al. Peripartum neuroactive steroid and γ-aminobutyric acid profiles in women at-risk for postpartum depression. Psychoneuroendocrinology. 2016;70:98-107.

268 Luisi S, Petraglia F, Benedetto C, Nappi RE, Bernardi F, Fadalti M, et al. Serum allopregnanolone levels in pregnant women: changes during pregnancy, at delivery, and in hypertensive patients. J Clin Endocrinol Metab. 2000;85(7):2429-33.

269 Nappi RE, Petraglia F, Luisi S, Polatti F, Farina C, Genazzani AR. Serum allopregnanolone in women with postpartum "blues". Obstet Gynecol. 2001;97(1):77-80.

270 Kanes S, Colquhoun H, Gunduz-Bruce H, Raines S, Arnold R, Schacterle A, et al. Brexanolone (SAGE-547 injection) in post-partum depression: a randomised controlled trial. The Lancet. 2017;390(10093):480-89.

271 Meltzer-Brody S, Colquhoun H, Riesenberg R, Epperson CN, Deligiannidis KM, Rubinow DR, et al. Brexanolone injection in post-partum depression: two multicentre, double-blind, randomised, placebo-controlled, phase 3 trials. Lancet. 2018;392(10152):1058-70.

272 Gunduz-Bruce H, Silber C, Kaul I, Rothschild AJ, Riesenberg R, Sankoh AJ, et al. Trial of SAGE-217 in Patients with Major Depressive Disorder. N Engl J Med. 2019;381(10):903-11.

273 Antor MA, Uribe AA, Erminy-Falcon N, Werner JG, Candiotti KA, Pergolizzi JV, et al. The effect of transdermal scopolamine for the prevention of postoperative nausea and vomiting. Frontiers in Pharmacology. 2014;5.

274 Lipinski CA, Lombardo F, Dominy BW, Feeney PJ. Experimental and computational approaches to estimate solubility and permeability in drug discovery and development settings. Adv Drug Del Revs. 1997;23(1-3):3-25.

275 Bhal SK, Kassam K, Peirson IG, Pearl GM. The Rule of Five revisited: applying log D in place of log P in drug-likeness filters. Molecular pharmaceutics. 2007;4(4):556-60.

276 Mansoor A MN. StatPearls [Internet]. 2022.

277 Søgaard B, Mengel H, Rao N, Larsen F. The pharmacokinetics of escitalopram after oral and intravenous administration of single and multiple doses to healthy subjects. J Clin Pharmacol. 2005;45(12):1400-6.

278 Gracia R. Fluoxetine. In: Wexler P, editor Encyclopedia of Toxicology (Second Edition). New York: Elsevier; 2005. p. 347-48.

279 Gillman PK. Tricyclic antidepressant pharmacology and therapeutic drug interactions updated. Br J Pharmacol. 2007;151(6):737-48.

280 Karch SB. The pathology of drug abuse. CRC press Boca Raton; 1996.

281 Prusakov PA. Belladonna Alkaloids. In: Wexler P, editor Encyclopedia of Toxicology (Third Edition). Oxford: Academic Press; 2014. p. 399-401.

282 MacDonald JF, Miljkovic Z, Pennefather P. Use-dependent block of excitatory amino acid currents in cultured neurons by ketamine. J Neurophysiol. 1987;58(2):251-66.

283 Huettner JE, Bean BP. Block of N-methyl-D-aspartate-activated current by the anticonvulsant MK-801 - selective binding to open channels. Proceedings of the National Academy of Sciences of the United States of America. 1988;85:1307-11.

284 Zorumski CF, Izumi Y, Mennerick S. Ketamine: NMDA Receptors and Beyond. The Journal of Neuroscience. 2016;36(44):11158-64.

285 Shaffer CL, Osgood SM, Smith DL, Liu J, Trapa PE. Enhancing ketamine translational pharmacology via receptor occupancy normalization. Neuropharmacology. 2014;86:174-80.

286 Li N, Lee B, Liu RJ, Banasr M, Dwyer JM, Iwata M, et al. mTOR-dependent synapse formation underlies the rapid antidepressant effects of NMDA antagonists. Science. 2010;329(5994):959-64.

287 Mohn AR, Gainetdinov RR, Caron MG, Koller BH. Mice with reduced NMDA receptor expression display behaviors related to schizophrenia. Cell. 1999;98(4):427-36.

288 Mueller HT, Meador-Woodruff JH. NR3A NMDA receptor subunit mRNA expression in schizophrenia, depression and bipolar disorder. Schizophr Res. 2004;71(2-3):361-70.

289 Woo TU, Walsh JP, Benes FM. Density of glutamic acid decarboxylase 67 messenger RNA-containing neurons that express the N-methyl-D-aspartate receptor subunit NR2A in the anterior cingulate cortex in schizophrenia and bipolar disorder. Arch Gen Psychiatry. 2004;61(7):649-57.

290 Moghaddam B, Javitt D. From revolution to evolution: the glutamate hypothesis of schizophrenia and its implication for treatment. Neuropsychopharmacology. 2012;37(1):4-15.

291 Richardson S, Hirsch JS, Narasimhan M, Crawford JM, McGinn T, Davidson KW, et al. Presenting Characteristics, Comorbidities, and Outcomes Among 5700 Patients Hospitalized With COVID-19 in the New York City Area. Jama. 2020.

292 Pérez-Otaño I, Larsen RS, Wesseling JF. Emerging roles of GluN3-containing NMDA receptors in the CNS. Nat Rev Neurosci. 2016;17(10):623-35.

293 McKay S, Ryan TJ, McQueen J, Indersmitten T, Marwick KFM, Hasel P, et al. The Developmental Shift of NMDA Receptor Composition Proceeds Independently of GluN2 Subunit-Specific GluN2 C-Terminal Sequences. Cell reports. 2018;25(4):841-51.e4.

294 Kotermanski SE, Johnson JW. Mg2+ imparts NMDA receptor subtype selectivity to the Alzheimer's drug memantine. J Neurosci. 2009;29(9):2774-9.

295 Monyer H, Burnashev N, Laurie DJ, Sakmann B, Seeburg PH. Developmental and regional expression in the rat brain and functional properties of four NMDA receptors. Neuron. 1994;12(3):529-40.

296 Tarrés-Gatius M, Miquel-Rio L, Campa L, Artigas F, Castañé A. Involvement of NMDA receptors containing the GluN2C subunit in the psychotomimetic and antidepressant-like effects of ketamine. Translational psychiatry. 2020;10(1):427.

297 Dravid SM, Erreger K, Yuan H, Nicholson K, Le P, Lyuboslavsky P, et al. Subunit-specific mechanisms and proton sensitivity of NMDA receptor channel block. J Physiol. 2007;581(Pt 1):107-28.

298 Miller OH, Yang L, Wang CC, Hargroder EA, Zhang Y, Delpire E, et al. GluN2B-containing NMDA receptors regulate depression-like behavior and are critical for the rapid antidepressant actions of ketamine. eLife. 2014;3:e03581.

299 Li N, Liu RJ, Dwyer JM, Banasr M, Lee B, Son H, et al. Glutamate N-methyl-D-aspartate receptor antagonists rapidly reverse behavioral and synaptic deficits caused by chronic stress exposure. Biol Psychiatry. 2011;69(8):754-61.

300 Gerhard DM, Pothula S, Liu R-J, Wu M, Li X-Y, Girgenti MJ, et al. GABA interneurons are the cellular trigger for ketamine's rapid antidepressant actions. The Journal of Clinical Investigation. 2020;130(3):1336-49.

301 Preskorn SH, Baker B, Kolluri S, Menniti FS, Krams M, Landen JW. An innovative design to establish proof of concept of the antidepressant effects of the NR2B subunit selective N-methyl-D-aspartate antagonist, CP-101,606, in patients with treatment-refractory major depressive disorder. J Clin Psychopharmacol. 2008;28(6):631-7.

302 Ide S, Ikekubo Y, Mishina M, Hashimoto K, Ikeda K. Role of NMDA receptor GluN2D subunit in the antidepressant effects of enantiomers of ketamine. J Pharmacol Sci. 2017;135(3):138-40.

303 Ide S, Ikekubo Y, Mishina M, Hashimoto K, Ikeda K. Cognitive Impairment That Is Induced by (R)-Ketamine Is Abolished in NMDA GluN2D Receptor Subunit Knockout Mice. Int J Neuropsychopharmacol. 2019;22(7):449-52.

304 Reynolds IJ, Miller RJ. Tricyclic antidepressants block N-methyl-D-aspartate receptors: similarities to the action of zinc. British Journal of Pharmacology. 1988;95(1):95-102.

305 Sills MA, Loo PS. Tricyclic antidepressants and dextromethorphan bind with higher affinity to the phencyclidine receptor in the absence of magnesium and L-glutamate. Mol Pharmacol. 1989;36(1):160-5.

306 Kiss JP, Szasz BK, Fodor L, Mike A, Lenkey N, Kurkó D, et al. GluN2B-containing NMDA receptors as possible targets for the neuroprotective and antidepressant effects of fluoxetine. Neurochem Int. 2012;60(2):170-6.

307 Raabe R, Gentile L. Antidepressant interactions with the NMDA NR1-1b subunit. J Biophys. 2008;2008:474205.

308 Rami A, Ausmeir F, Winckler J, Krieglstein J. Differential effects of scopolamine on neuronal survival in ischemia and glutamate neurotoxicity: relationships to the excessive vulnerability of the dorsoseptal hippocampus. J Chem Neuroanat. 1997;13(3):201-8.

309 Liu HF, Zhou WH, Xie XH, Cao JL, Gu J, Yang GD. [Muscarinic receptors modulate the mRNA expression of NMDA receptors in brainstem and the release of glutamate in periaqueductal grey during morphine withdrawal in rats]. Sheng Li Xue Bao. 2004;56(1):95-100.

310 Crane GE. Cyloserine as an antidepressant agent. Am J Psychiatry. 1959;115(11):1025-6.

311 Heresco-Levy U, Gelfin G, Bloch B, Levin R, Edelman S, Javitt DC, et al. A randomized add-on trial of high-dose D-cycloserine for treatment-resistant depression. Int J Neuropsychopharmacol. 2013;16(3):501-6.

312 Zarate CA, Jr., Singh JB, Quiroz JA, De Jesus G, Denicoff KK, Luckenbaugh DA, et al. A double-blind, placebo-controlled study of memantine in the treatment of major depression. Am J Psychiatry. 2006;163(1):153-5.

313 Ibrahim L, Diaz Granados N, Jolkovsky L, Brutsche N, Luckenbaugh DA, Herring WJ, et al. A Randomized, placebo-controlled, crossover pilot trial of the oral selective NR2B antagonist MK-0657 in patients with treatment-resistant major depressive disorder. J Clin Psychopharmacol. 2012;32(4):551-7.

314 Moghaddam B, Adams B, Verma A, Daly D. Activation of glutamatergic neurotransmission by ketamine: a novel step in the pathway from NMDA receptor

blockade to dopaminergic and cognitive disruptions associated with the prefrontal cortex. J Neurosci. 1997;17(8):2921-7.
315 Luscher B, Fuchs T. Chapter Five - GABAergic Control of Depression-Related Brain States. In: Rudolph U, editor Advances in Pharmacology. Academic Press; 2015. p. 97-144.
316 Shen Q, Lal R, Luellen BA, Earnheart JC, Andrews AM, Luscher B. γ-Aminobutyric Acid-Type A Receptor Deficits Cause Hypothalamic-Pituitary-Adrenal Axis Hyperactivity and Antidepressant Drug Sensitivity Reminiscent of Melancholic Forms of Depression. Biological Psychiatry. 2010;68(6):512-20.
317 Luscher B, Feng M, Jefferson SJ. Antidepressant mechanisms of ketamine: Focus on GABAergic inhibition. Adv Pharmacol. 2020;89:43-78.
318 Ren Z, Pribiag H, Jefferson SJ, Shorey M, Fuchs T, Stellwagen D, et al. Bidirectional Homeostatic Regulation of a Depression-Related Brain State by Gamma-Aminobutyric Acidergic Deficits and Ketamine Treatment. Biol Psychiatry. 2016;80(6):457-68.
319 Ghosal S, Duman CH, Liu RJ, Wu M, Terwilliger R, Girgenti MJ, et al. Ketamine rapidly reverses stress-induced impairments in GABAergic transmission in the prefrontal cortex in male rodents. Neurobiol Dis. 2020;134:104669.
320 Widman AJ, McMahon LL. Disinhibition of CA1 pyramidal cells by low-dose ketamine and other antagonists with rapid antidepressant efficacy. Proc Natl Acad Sci U S A. 2018;115(13):E3007-E16.
321 Duman RS, Sanacora G, Krystal JH. Altered Connectivity in Depression: GABA and Glutamate Neurotransmitter Deficits and Reversal by Novel Treatments. Neuron. 2019;102(1):75-90.
322 Wojtas A, Bysiek A, Wawrzczak-Bargiela A, Szych Z, Majcher-Maślanka I, Herian M, et al. Effect of Psilocybin and Ketamine on Brain Neurotransmitters, Glutamate Receptors, DNA and Rat Behavior. Int J Mol Sci. 2022;23(12).
323 Milak MS, Rashid R, Dong Z, Kegeles LS, Grunebaum MF, Ogden RT, et al. Assessment of Relationship of Ketamine Dose With Magnetic Resonance Spectroscopy of Glx and GABA Responses in Adults With Major Depression: A Randomized Clinical Trial. JAMA Network Open. 2020;3(8):e2013211-e11.
324 Rosa PB, Neis VB, Ribeiro CM, Moretti M, Rodrigues AL. Antidepressant-like effects of ascorbic acid and ketamine involve modulation of GABAA and GABAB receptors. Pharmacological reports : PR. 2016;68(5):996-1001.
325 Fuchikami M, Thomas A, Liu R, Wohleb ES, Land BB, DiLeone RJ, et al. Optogenetic stimulation of infralimbic PFC reproduces ketamine’s rapid and sustained antidepressant actions. Proceedings of the National Academy of Sciences. 2015;112(26):8106-11.
326 Salmi E, Långsjö JW, Aalto S, Någren K, Metsähonkala L, Kaisti KK, et al. Subanesthetic ketamine does not affect 11C-flumazenil binding in humans. Anesthesia and analgesia. 2005;101(3):722-25.
327 Frazer A HJ. Serotonin Receptors. In: Basic Neurochemistry: Molecular, Cellular and Medical Aspects.; 1999.
328 Wood JD. Enteric nervous system, serotonin, and the irritable bowel syndrome. Curr Opin Gastroenterol. 2001;17(1):91-7.
329 Goldberg LI. Dopamine receptors and hypertension. Physiologic and pharmacologic implications. Am J Med. 1984;77(4a):37-44.

330 Howes OD, Kapur S. The dopamine hypothesis of schizophrenia: version III--the final common pathway. Schizophr Bull. 2009;35(3):549-62.

331 Kapur S, Seeman P. NMDA receptor antagonists ketamine and PCP have direct effects on the dopamine D(2) and serotonin 5-HT(2)receptors-implications for models of schizophrenia. Mol Psychiatry. 2002;7(8):837-44.

332 Seeman P, Ko F, Tallerico T. Dopamine receptor contribution to the action of PCP, LSD and ketamine psychotomimetics. Mol Psychiatry. 2005;10(9):877-83.

333 Seeman P, Kapur S. Anesthetics inhibit high-affinity states of dopamine D2 and other G-linked receptors. Synapse. 2003;50(1):35-40.

334 Can A, Zanos P, Moaddel R, Kang HJ, Dossou KS, Wainer IW, et al. Effects of Ketamine and Ketamine Metabolites on Evoked Striatal Dopamine Release, Dopamine Receptors, and Monoamine Transporters. J Pharmacol Exp Ther. 2016;359(1):159-70.

335 Iro CM, Hamati R, El Mansari M, Blier P. Repeated but Not Single Administration of Ketamine Prolongs Increases of the Firing Activity of Norepinephrine and Dopamine Neurons. Int J Neuropsychopharmacol. 2021;24(7):570-79.

336 Ago Y, Tanabe W, Higuchi M, Tsukada S, Tanaka T, Yamaguchi T, et al. (R)-Ketamine Induces a Greater Increase in Prefrontal 5-HT Release Than (S)-Ketamine and Ketamine Metabolites via an AMPA Receptor-Independent Mechanism. Int J Neuropsychopharmacol. 2019;22(10):665-74.

337 Breier A, Adler CM, Weisenfeld N, Su T-P, Elman I, Picken L, et al. Effects of NMDA antagonism on striatal dopamine release in healthy subjects: Application of a novel PET approach. Synapse. 1998;29(2):142-47.

338 Smith GS, Schloesser R, Brodie JD, Dewey SL, Logan J, Vitkun SA, et al. Glutamate modulation of dopamine measured in vivo with positron emission tomography (PET) and 11C-raclopride in normal human subjects. Neuropsychopharmacology. 1998;18(1):18-25.

339 Vollenweider FX, Vontobel P, Oye I, Hell D, Leenders KL. Effects of (S)-ketamine on striatal dopamine: a [11C]raclopride PET study of a model psychosis in humans. J Psychiatr Res. 2000;34(1):35-43.

340 Aalto S, Hirvonen J, Kajander J, Scheinin H, Någren K, Vilkman H, et al. Ketamine does not decrease striatal dopamine D2 receptor binding in man. Psychopharmacology (Berl). 2002;164(4):401-6.

341 Kegeles LS, Martinez D, Kochan LD, Hwang DR, Huang Y, Mawlawi O, et al. NMDA antagonist effects on striatal dopamine release: positron emission tomography studies in humans. Synapse. 2002;43(1):19-29.

342 Krystal JH, D'Souza DC. Comment on "Ketamine has equal affinity for NMDA receptors and the high-affinity state of the dopamine D(2) receptor". Biol Psychiatry. 2001;50(7):555-6.

343 Kokkinou M, Ashok AH, Howes OD. The effects of ketamine on dopaminergic function: meta-analysis and review of the implications for neuropsychiatric disorders. Mol Psychiatry. 2018;23(1):59-69.

344 Nishimura M, Sato K, Okada T, Yoshiya I, Schloss P, Shimada S, et al. Ketamine inhibits monoamine transporters expressed in human embryonic kidney 293 cells. Anesthesiology. 1998;88(3):768-74.

345 Martin LL, Bouchal RL, Smith DJ. Ketamine inhibits serotonin uptake in vivo. Neuropharmacology. 1982;21(2):113-8.

346 Appadu BL, Lambert DG. Interaction of i.v. anaesthetic agents with 5-HT3 receptors. Br J Anaesth. 1996;76(2):271-3.

347 Yamakura T, Chavez-Noriega LE, Harris RA. Subunit-dependent inhibition of human neuronal nicotinic acetylcholine receptors and other ligand-gated ion channels by dissociative anesthetics ketamine and dizocilpine. Anesthesiology. 2000;92(4):1144-53.

348 Ho Kenny K, Flood P. Single Amino Acid Residue in the Extracellular Portion of Transmembrane Segment 2 in the Nicotinic α7 Acetylcholine Receptor Modulates Sensitivity to Ketamine. Anesthesiology. 2004;100(3):657-62.

349 Gigliucci V, O'Dowd G, Casey S, Egan D, Gibney S, Harkin A. Ketamine elicits sustained antidepressant-like activity via a serotonin-dependent mechanism. Psychopharmacology (Berl). 2013;228(1):157-66.

350 Fukumoto K, Iijima M, Chaki S. The Antidepressant Effects of an mGlu2/3 Receptor Antagonist and Ketamine Require AMPA Receptor Stimulation in the mPFC and Subsequent Activation of the 5-HT Neurons in the DRN. Neuropsychopharmacology. 2016;41(4):1046-56.

351 du Jardin KG, Liebenberg N, Müller HK, Elfving B, Sanchez C, Wegener G. Differential interaction with the serotonin system by S-ketamine, vortioxetine, and fluoxetine in a genetic rat model of depression. Psychopharmacology (Berl). 2016;233(14):2813-25.

352 Pham TH, Mendez-David I, Defaix C, Guiard BP, Tritschler L, David DJ, et al. Ketamine treatment involves medial prefrontal cortex serotonin to induce a rapid antidepressant-like activity in BALB/cJ mice. Neuropharmacology. 2017;112(Pt A):198-209.

353 Yamanaka H, Yokoyama C, Mizuma H, Kurai S, Finnema SJ, Halldin C, et al. A possible mechanism of the nucleus accumbens and ventral pallidum 5-HT1B receptors underlying the antidepressant action of ketamine: a PET study with macaques. Translational psychiatry. 2014;4(1):e342.

354 Tiger M, Veldman ER, Ekman C-J, Halldin C, Svenningsson P, Lundberg J. A randomized placebo-controlled PET study of ketamine´s effect on serotonin1B receptor binding in patients with SSRI-resistant depression. Translational psychiatry. 2020;10(1):159.

355 Azzaro AJ, Smith DJ. The inhibitory action of ketamine HC1 on [3H]5-hydroxytryptamine accumulation by rat brain synaptosomal-rich fractions: comparison with [3H]catecholamine and [3H]gamma-aminobutyric acid uptake. Neuropharmacology. 1977;16(5):349-56.

356 Spies M, James GM, Berroterán-Infante N, Ibeschitz H, Kranz GS, Unterholzner J, et al. Assessment of Ketamine Binding of the Serotonin Transporter in Humans with Positron Emission Tomography. Int J Neuropsychopharmacol. 2018;21(2):145-53.

357 Yamamoto S, Ohba H, Nishiyama S, Harada N, Kakiuchi T, Tsukada H, et al. Subanesthetic Doses of Ketamine Transiently Decrease Serotonin Transporter Activity: A PET Study in Conscious Monkeys. Neuropsychopharmacology. 2013;38(13):2666-74.

358 Bowman MA, Vitela M, Clarke KM, Koek W, Daws LC. Serotonin Transporter and Plasma Membrane Monoamine Transporter Are Necessary for the Antidepressant-Like Effects of Ketamine in Mice. Int J Mol Sci. 2020;21(20).

359 Trescot AM, Datta S, Lee M, Hansen H. Opioid pharmacology. Pain physician. 2008;11(2 Suppl):S133-53.

360 Berrocoso E, Sánchez-Blázquez P, Garzón J, Mico JA. Opiates as antidepressants. Curr Pharm Des. 2009;15(14):1612-22.

361 Hirota K, Okawa H, Appadu BL, Grandy DK, Devi LA, Lambert DG. Stereoselective interaction of ketamine with recombinant mu, kappa, and delta opioid receptors expressed in Chinese hamster ovary cells. Anesthesiology. 1999;90(1):174-82.
362 Hustveit O, Maurset A, Oye I. Interaction of the chiral forms of ketamine with opioid, phencyclidine, sigma and muscarinic receptors. Pharmacol Toxicol. 1995;77(6):355-9.
363 Nemeth CL, Paine TA, Rittiner JE, Béguin C, Carroll FI, Roth BL, et al. Role of kappa-opioid receptors in the effects of salvinorin A and ketamine on attention in rats. Psychopharmacology (Berl). 2010;210(2):263-74.
364 Krystal JH, Madonick S, Perry E, Gueorguieva R, Brush L, Wray Y, et al. Potentiation of low dose ketamine effects by naltrexone: potential implications for the pharmacotherapy of alcoholism. Neuropsychopharmacology. 2006;31(8):1793-800.
365 Klein ME, Chandra J, Sheriff S, Malinow R. Opioid system is necessary but not sufficient for antidepressive actions of ketamine in rodents. Proc Natl Acad Sci U S A. 2020;117(5):2656-62.
366 Bonaventura J, Lam S, Carlton M, Boehm MA, Gomez JL, Solís O, et al. Pharmacological and behavioral divergence of ketamine enantiomers: implications for abuse liability. Molecular Psychiatry. 2021;26(11):6704-22.
367 Heifets BD, Bentzley BS, Williams N, Schatzberg AF. Unraveling the opioid actions of S-ketamine and R-ketamine: comment on Bonaventura et al. Molecular Psychiatry. 2021;26(11):6104-06.
368 Williams NR, Heifets BD, Blasey C, Sudheimer K, Pannu J, Pankow H, et al. Attenuation of Antidepressant Effects of Ketamine by Opioid Receptor Antagonism. Am J Psychiatry. 2018;175(12):1205-15.
369 Williams NR, Heifets BD, Bentzley BS, Blasey C, Sudheimer KD, Hawkins J, et al. Attenuation of antidepressant and antisuicidal effects of ketamine by opioid receptor antagonism. Mol Psychiatry. 2019;24(12):1779-86.
370 Barber J. Examining the use of tramadol hydrochloride as an antidepressant. Exp Clin Psychopharmacol. 2011;19(2):123-30.
371 Ide S, Fujiwara S, Fujiwara M, Sora I, Ikeda K, Minami M, et al. Antidepressant-like effect of venlafaxine is abolished in μ-opioid receptor-knockout mice. J Pharmacol Sci. 2010;114(1):107-10.
372 Durieux ME. Inhibition by ketamine of muscarinic acetylcholine receptor function. Anesth Analg. 1995;81(1):57-62.
373 Hirota K, Hashimoto Y, Lambert DG. Interaction of intravenous anesthetics with recombinant human M1-M3 muscarinic receptors expressed in chinese hamster ovary cells. Anesth Analg. 2002;95(6):1607-10, table of contents.
374 Wang JC, Hinrichs AL, Stock H, Budde J, Allen R, Bertelsen S, et al. Evidence of common and specific genetic effects: association of the muscarinic acetylcholine receptor M2 (CHRM2) gene with alcohol dependence and major depressive syndrome. Hum Mol Genet. 2004;13(17):1903-11.
375 Gibbons AS, Scarr E, McLean C, Sundram S, Dean B. Decreased muscarinic receptor binding in the frontal cortex of bipolar disorder and major depressive disorder subjects. J Affect Disord. 2009;116(3):184-91.
376 Albuquerque EX, Pereira EF, Alkondon M, Rogers SW. Mammalian nicotinic acetylcholine receptors: from structure to function. Physiol Rev. 2009;89(1):73-120.

377 Coates KM, Flood P. Ketamine and its preservative, benzethonium chloride, both inhibit human recombinant α7 and α4β2 neuronal nicotinic acetylcholine receptors in Xenopus oocytes. Br J Pharmacol. 2001;134(4):871-9.

378 Flood P, Krasowski MD. Intravenous anesthetics differentially modulate ligand-gated ion channels. Anesthesiology. 2000;92(5):1418-25.

379 Alzarea S, Rahman S. Effects of alpha-7 nicotinic allosteric modulator PNU 120596 on depressive-like behavior after lipopolysaccharide administration in mice. Progress in Neuro-Psychopharmacology and Biological Psychiatry. 2018;86:218-28.

380 Alzarea S, Rahman S. Alpha-7 nicotinic receptor allosteric modulator PNU120596 prevents lipopolysaccharide-induced anxiety, cognitive deficit and depression-like behaviors in mice. Behavioural Brain Research. 2019;366:19-28.

381 Gerhard DM, Wohleb ES, Duman RS. Emerging treatment mechanisms for depression: focus on glutamate and synaptic plasticity. Drug Discov Today. 2016;21(3):454-64.

382 Fukumoto K, Fogaça MV, Liu RJ, Duman C, Kato T, Li XY, et al. Activity-dependent brain-derived neurotrophic factor signaling is required for the antidepressant actions of (2R,6R)-hydroxynorketamine. Proc Natl Acad Sci U S A. 2019;116(1):297-302.

383 Pizzagalli DA, Roberts AC. Prefrontal cortex and depression. Neuropsychopharmacology. 2022;47(1):225-46.

384 Cook SC, Wellman CL. Chronic stress alters dendritic morphology in rat medial prefrontal cortex. J Neurobiol. 2004;60(2):236-48.

385 Radley JJ, Sisti HM, Hao J, Rocher AB, McCall T, Hof PR, et al. Chronic behavioral stress induces apical dendritic reorganization in pyramidal neurons of the medial prefrontal cortex. Neuroscience. 2004;125(1):1-6.

386 Radley JJ, Rocher AB, Janssen WG, Hof PR, McEwen BS, Morrison JH. Reversibility of apical dendritic retraction in the rat medial prefrontal cortex following repeated stress. Exp Neurol. 2005;196(1):199-203.

387 Liston C, Miller MM, Goldwater DS, Radley JJ, Rocher AB, Hof PR, et al. Stress-Induced Alterations in Prefrontal Cortical Dendritic Morphology Predict Selective Impairments in Perceptual Attentional Set-Shifting. The Journal of Neuroscience. 2006;26(30):7870.

388 Bloss EB, Janssen WG, McEwen BS, Morrison JH. Interactive effects of stress and aging on structural plasticity in the prefrontal cortex. J Neurosci. 2010;30(19):6726-31.

389 Mizoguchi K, Yuzurihara M, Ishige A, Sasaki H, Chui DH, Tabira T. Chronic stress induces impairment of spatial working memory because of prefrontal dopaminergic dysfunction. J Neurosci. 2000;20(4):1568-74.

390 Dias-Ferreira E, Sousa JC, Melo I, Morgado P, Mesquita AR, Cerqueira JJ, et al. Chronic stress causes frontostriatal reorganization and affects decision-making. Science. 2009;325(5940):621-5.

391 Lapiz-Bluhm MD, Soto-Piña AE, Hensler JG, Morilak DA. Chronic intermittent cold stress and serotonin depletion induce deficits of reversal learning in an attentional set-shifting test in rats. Psychopharmacology (Berl). 2009;202(1-3):329-41.

392 Lam RW, Kennedy SH, McLntyre RS, Khullar A. Cognitive dysfunction in major depressive disorder: effects on psychosocial functioning and implications for treatment. Can J Psychiatry. 2014;59(12):649-54.

393 Rajkowska G, Miguel-Hidalgo JJ, Wei J, Dilley G, Pittman SD, Meltzer HY, et al. Morphometric evidence for neuronal and glial prefrontal cell pathology in major depression. Biol Psychiatry. 1999;45(9):1085-98.

394 Kang HJ, Voleti B, Hajszan T, Rajkowska G, Stockmeier CA, Licznerski P, et al. Decreased expression of synapse-related genes and loss of synapses in major depressive disorder. Nat Med. 2012;18(9):1413-7.

395 Ionescu DF, Felicione JM, Gosai A, Cusin C, Shin P, Shapero BG, et al. Ketamine-Associated Brain Changes: A Review of the Neuroimaging Literature. Harv Rev Psychiatry. 2018;26(6):320-39.

396 Chowdhury GM, Zhang J, Thomas M, Banasr M, Ma X, Pittman B, et al. Transiently increased glutamate cycling in rat PFC is associated with rapid onset of antidepressant-like effects. Mol Psychiatry. 2017;22(1):120-26.

397 Abdallah CG, Averill LA, Collins KA, Geha P, Schwartz J, Averill C, et al. Ketamine Treatment and Global Brain Connectivity in Major Depression. Neuropsychopharmacology. 2017;42(6):1210-19.

398 Abdallah CG, Averill CL, Salas R, Averill LA, Baldwin PR, Krystal JH, et al. Prefrontal Connectivity and Glutamate Transmission: Relevance to Depression Pathophysiology and Ketamine Treatment. Biol Psychiatry Cogn Neurosci Neuroimaging. 2017;2(7):566-74.

399 Carlson PJ, Diazgranados N, Nugent AC, Ibrahim L, Luckenbaugh DA, Brutsche N, et al. Neural correlates of rapid antidepressant response to ketamine in treatment-resistant unipolar depression: a preliminary positron emission tomography study. Biol Psychiatry. 2013;73(12):1213-21.

400 Campbell S, Macqueen G. The role of the hippocampus in the pathophysiology of major depression. J Psychiatry Neurosci. 2004;29(6):417-26.

401 Arriza JL, Simerly RB, Swanson LW, Evans RM. The neuronal mineralocorticoid eeceptor as a mediator of glucocorticoid response. Neuron. 1988;1(9):887-900.

402 Sapolsky RM, Krey LC, McEwen BS. Prolonged glucocorticoid exposure reduces hippocampal neuron number: implications for aging. The Journal of Neuroscience. 1985;5(5):1222.

403 Watanabe Y, Gould E, McEwen BS. Stress induces atrophy of apical dendrites of hippocampal CA3 pyramidal neurons. Brain Research. 1992;588(2):341-45.

404 Lambert KG, Buckelew SK, Staffiso-Sandoz G, Gaffga S, Carpenter W, Fisher J, et al. Activity-stress induces atrophy of apical dendrites of hippocampal pyramidal neurons in male rats. Physiology & Behavior. 1998;65(1):43-49.

405 Sousa N, Lukoyanov NV, Madeira MD, Almeida OF, Paula-Barbosa MM. Reorganization of the morphology of hippocampal neurites and synapses after stress-induced damage correlates with behavioral improvement. Neuroscience. 2000;97(2):253-66.

406 Pavlides C, Nivón LG, McEwen BS. Effects of chronic stress on hippocampal long-term potentiation. Hippocampus. 2002;12(2):245-57.

407 Pham K, Nacher J, Hof PR, McEwen BS. Repeated restraint stress suppresses neurogenesis and induces biphasic PSA-NCAM expression in the adult rat dentate gyrus. Eur J Neurosci. 2003;17(4):879-86.

408 Roddy DW, Farrell C, Doolin K, Roman E, Tozzi L, Frodl T, et al. The Hippocampus in Depression: More Than the Sum of Its Parts? Advanced Hippocampal Substructure Segmentation in Depression. Biol Psychiatry. 2019;85(6):487-97.

409 Stockmeier CA, Mahajan GJ, Konick LC, Overholser JC, Jurjus GJ, Meltzer HY, et al. Cellular changes in the postmortem hippocampus in major depression. Biol Psychiatry. 2004;56(9):640-50.

410 Ardalan M, Wegener G, Rafati AH, Nyengaard JR. S-Ketamine Rapidly Reverses Synaptic and Vascular Deficits of Hippocampus in Genetic Animal Model of Depression. Int J Neuropsychopharmacol. 2017;20(3):247-56.

411 Dong C, Zhang JC, Yao W, Ren Q, Ma M, Yang C, et al. Rapid and Sustained Antidepressant Action of the mGlu2/3 Receptor Antagonist MGS0039 in the Social Defeat Stress Model: Comparison with Ketamine. Int J Neuropsychopharmacol. 2017;20(3):228-36.

412 Tornese P, Sala N, Bonini D, Bonifacino T, La Via L, Milanese M, et al. Chronic mild stress induces anhedonic behavior and changes in glutamate release, BDNF trafficking and dendrite morphology only in stress vulnerable rats. The rapid restorative action of ketamine. Neurobiol Stress. 2019;10:100160.

413 Aleksandrova LR, Wang YT, Phillips AG. Ketamine and its metabolite, (2R,6R)-HNK, restore hippocampal LTP and long-term spatial memory in the Wistar-Kyoto rat model of depression. Molecular Brain. 2020;13(1):92.

414 Abdallah CG, Salas R, Jackowski A, Baldwin P, Sato JR, Mathew SJ. Hippocampal volume and the rapid antidepressant effect of ketamine. Journal of Psychopharmacology. 2015;29(5):591-95.

415 Abdallah CG, Jackowski A, Salas R, Gupta S, Sato JR, Mao X, et al. The Nucleus Accumbens and Ketamine Treatment in Major Depressive Disorder. Neuropsychopharmacology. 2017;42(8):1739-46.

416 Lally N, Nugent AC, Luckenbaugh DA, Niciu MJ, Roiser JP, Zarate CA, Jr. Neural correlates of change in major depressive disorder anhedonia following open-label ketamine. Journal of psychopharmacology (Oxford, England). 2015;29(5):596-607.

417 Nugent AC, Robinson SE, Coppola R, Zarate CA. Preliminary differences in resting state MEG functional connectivity pre- and post-ketamine in major depressive disorder. Psychiatry Research: Neuroimaging. 2016;254:56-66.

418 Dale E, Pehrson AL, Jeyarajah T, Li Y, Leiser SC, Smagin G, et al. Effects of serotonin in the hippocampus: how SSRIs and multimodal antidepressants might regulate pyramidal cell function. CNS Spectr. 2016;21(2):143-61.

419 Segi-Nishida E. The Effect of Serotonin-Targeting Antidepressants on Neurogenesis and Neuronal Maturation of the Hippocampus Mediated via 5-HT1A and 5-HT4 Receptors. Frontiers in cellular neuroscience. 2017;11:142.

420 Zhao H, Zhang BL, Yang SJ, Rusak B. The role of lateral habenula-dorsal raphe nucleus circuits in higher brain functions and psychiatric illness. Behav Brain Res. 2015;277:89-98.

421 Lammel S, Lim BK, Ran C, Huang KW, Betley MJ, Tye KM, et al. Input-specific control of reward and aversion in the ventral tegmental area. Nature. 2012;491(7423):212-17.

422 Lawson RP, Seymour B, Loh E, Lutti A, Dolan RJ, Dayan P, et al. The habenula encodes negative motivational value associated with primary punishment in humans. Proc Natl Acad Sci U S A. 2014;111(32):11858-63.

423 Wang D, Li Y, Feng Q, Guo Q, Zhou J, Luo M. Learning shapes the aversion and reward responses of lateral habenula neurons. eLife. 2017;6:e23045.

424 Lima LB, Bueno D, Leite F, Souza S, Gonçalves L, Furigo IC, et al. Afferent and efferent connections of the interpeduncular nucleus with special reference to circuits involving the habenula and raphe nuclei. J Comp Neurol. 2017;525(10):2411-42.

425 Shumake J, Edwards E, Gonzalez-Lima F. Opposite metabolic changes in the habenula and ventral tegmental area of a genetic model of helpless behavior. Brain Res. 2003;963(1-2):274-81.

426 Yang Y, Cui Y, Sang K, Dong Y, Ni Z, Ma S, et al. Ketamine blocks bursting in the lateral habenula to rapidly relieve depression. Nature. 2018;554(7692):317-22.

427 Cui Y, Yang Y, Ni Z, Dong Y, Cai G, Foncelle A, et al. Astroglial Kir4.1 in the lateral habenula drives neuronal bursts in depression. Nature. 2018;554(7692):323-27.

428 Ranft K, Dobrowolny H, Krell D, Bielau H, Bogerts B, Bernstein HG. Evidence for structural abnormalities of the human habenular complex in affective disorders but not in schizophrenia. Psychol Med. 2010;40(4):557-67.

429 Savitz JB, Nugent AC, Bogers W, Roiser JP, Bain EE, Neumeister A, et al. Habenula volume in bipolar disorder and major depressive disorder: a high-resolution magnetic resonance imaging study. Biol Psychiatry. 2011;69(4):336-43.

430 Schmidt FM, Schindler S, Adamidis M, Strauß M, Tränkner A, Trampel R, et al. Habenula volume increases with disease severity in unmedicated major depressive disorder as revealed by 7T MRI. Eur Arch Psychiatry Clin Neurosci. 2017;267(2):107-15.

431 Carceller-Sindreu M, de Diego-Adeliño J, Serra-Blasco M, Vives-Gilabert Y, Martín-Blanco A, Puigdemont D, et al. Volumetric MRI study of the habenula in first episode, recurrent and chronic major depression. Eur Neuropsychopharmacol. 2015;25(11):2015-21.

432 Liu WH, Valton V, Wang LZ, Zhu YH, Roiser JP. Association between habenula dysfunction and motivational symptoms in unmedicated major depressive disorder. Soc Cogn Affect Neurosci. 2017;12(9):1520-33.

433 Gold PW, Kadriu B. A Major Role for the Lateral Habenula in Depressive Illness: Physiologic and Molecular Mechanisms. Front Psychiatry. 2019;10:320.

434 Lawson RP, Nord CL, Seymour B, Thomas DL, Dayan P, Pilling S, et al. Disrupted habenula function in major depression. Molecular Psychiatry. 2017;22(2):202-08.

435 Sartorius A, Kiening KL, Kirsch P, von Gall CC, Haberkorn U, Unterberg AW, et al. Remission of major depression under deep brain stimulation of the lateral habenula in a therapy-refractory patient. Biol Psychiatry. 2010;67(2):e9-e11.

436 Germann J, Mameli M, Elias GJB, Loh A, Taha A, Gouveia FV, et al. Deep Brain Stimulation of the Habenula: Systematic Review of the Literature and Clinical Trial Registries. Front Psychiatry. 2021;12:730931.

437 Rivas-Grajales AM, Salas R, Robinson ME, Qi K, Murrough JW, Mathew SJ. Habenula Connectivity and Intravenous Ketamine in Treatment-Resistant Depression. Int J Neuropsychopharmacol. 2021;24(5):383-91.

438 Hilgetag CC, Barbas H. Are there ten times more glia than neurons in the brain? Brain Structure and Function. 2009;213(4):365-66.

439 von Bartheld CS, Bahney J, Herculano-Houzel S. The search for true numbers of neurons and glial cells in the human brain: A review of 150 years of cell counting. J Comp Neurol. 2016;524(18):3865-95.

440 Haroon E, Miller AH, Sanacora G. Inflammation, Glutamate, and Glia: A Trio of Trouble in Mood Disorders. Neuropsychopharmacology. 2017;42(1):193-215.

441 Rajkowska G, Miguel-Hidalgo JJ. Gliogenesis and glial pathology in depression. CNS Neurol Disord Drug Targets. 2007;6(3):219-33.

442 Rial D, Lemos C, Pinheiro H, Duarte JM, Gonçalves FQ, Real JI, et al. Depression as a Glial-Based Synaptic Dysfunction. Frontiers in cellular neuroscience. 2015;9:521.

443 Sild M, Ruthazer ES, Booij L. Major depressive disorder and anxiety disorders from the glial perspective: Etiological mechanisms, intervention and monitoring. Neurosci Biobehav Rev. 2017;83:474-88.

444 McNeill J, Rudyk C, Hildebrand ME, Salmaso N. Ion Channels and Electrophysiological Properties of Astrocytes: Implications for Emergent Stimulation Technologies. Frontiers in cellular neuroscience. 2021;15.

445 Bezzi P, Gundersen V, Galbete JL, Seifert G, Steinhäuser C, Pilati E, et al. Astrocytes contain a vesicular compartment that is competent for regulated exocytosis of glutamate. Nat Neurosci. 2004;7(6):613-20.

446 Divito CB, Borowski JE, Glasgow NG, Gonzalez-Suarez AD, Torres-Salazar D, Johnson JW, et al. Glial and Neuronal Glutamate Transporters Differ in the Na+ Requirements for Activation of the Substrate-Independent Anion Conductance. Frontiers in Molecular Neuroscience. 2017;10.

447 Rothstein JD, Jin L, Dykes-Hoberg M, Kuncl RW. Chronic inhibition of glutamate uptake produces a model of slow neurotoxicity. Proc Natl Acad Sci U S A. 1993;90(14):6591-5.

448 Rothstein JD, Dykes-Hoberg M, Pardo CA, Bristol LA, Jin L, Kuncl RW, et al. Knockout of glutamate transporters reveals a major role for astroglial transport in excitotoxicity and clearance of glutamate. Neuron. 1996;16(3):675-86.

449 Tanaka K, Watase K, Manabe T, Yamada K, Watanabe M, Takahashi K, et al. Epilepsy and exacerbation of brain injury in mice lacking the glutamate transporter GLT-1. Science. 1997;276(5319):1699-702.

450 McCullumsmith RE, Sanacora G. Regulation of extrasynaptic glutamate levels as a pathophysiological mechanism in disorders of motivation and addiction. Neuropsychopharmacology. 2015;40(1):254-5.

451 Tzingounis AV, Wadiche JI. Glutamate transporters: confining runaway excitation by shaping synaptic transmission. Nat Rev Neurosci. 2007;8(12):935-47.

452 Hayashi MK. Structure-Function Relationship of Transporters in the Glutamate-Glutamine Cycle of the Central Nervous System. Int J Mol Sci. 2018;19(4).

453 Miyazaki J, Nakanishi S, Jingami H. Expression and characterization of a glycine-binding fragment of the N-methyl-D-aspartate receptor subunit NR1. Biochem J. 1999;340 (Pt 3)(Pt 3):687-92.

454 Wolosker H, Blackshaw S, Snyder SH. Serine racemase: a glial enzyme synthesizing D-serine to regulate glutamate-N-methyl-D-aspartate neurotransmission. Proc Natl Acad Sci U S A. 1999;96(23):13409-14.

455 Panatier A, Theodosis DT, Mothet JP, Touquet B, Pollegioni L, Poulain DA, et al. Glia-derived D-serine controls NMDA receptor activity and synaptic memory. Cell. 2006;125(4):775-84.

456 Bergles DE, Roberts JD, Somogyi P, Jahr CE. Glutamatergic synapses on oligodendrocyte precursor cells in the hippocampus. Nature. 2000;405(6783):187-91.

457 Steinhäuser C, Gallo V. News on glutamate receptors in glial cells. Trends Neurosci. 1996;19(8):339-45.

458 Ongür D, Drevets WC, Price JL. Glial reduction in the subgenual prefrontal cortex in mood disorders. Proc Natl Acad Sci U S A. 1998;95(22):13290-5.

459 Cotter D, Mackay D, Landau S, Kerwin R, Everall I. Reduced glial cell density and neuronal size in the anterior cingulate cortex in major depressive disorder. Arch Gen Psychiatry. 2001;58(6):545-53.

460 Cotter D, Mackay D, Chana G, Beasley C, Landau S, Everall IP. Reduced neuronal size and glial cell density in area 9 of the dorsolateral prefrontal cortex in subjects with major depressive disorder. Cereb Cortex. 2002;12(4):386-94.

461 Chana G, Landau S, Beasley C, Everall IP, Cotter D. Two-dimensional assessment of cytoarchitecture in the anterior cingulate cortex in major depressive disorder, bipolar disorder, and schizophrenia: evidence for decreased neuronal somal size and increased neuronal density. Biol Psychiatry. 2003;53(12):1086-98.

462 Torres-Platas SG, Hercher C, Davoli MA, Maussion G, Labonté B, Turecki G, et al. Astrocytic hypertrophy in anterior cingulate white matter of depressed suicides. Neuropsychopharmacology. 2011;36(13):2650-8.

463 Johnston-Wilson NL, Sims CD, Hofmann JP, Anderson L, Shore AD, Torrey EF, et al. Disease-specific alterations in frontal cortex brain proteins in schizophrenia, bipolar disorder, and major depressive disorder. The Stanley Neuropathology Consortium. Mol Psychiatry. 2000;5(2):142-9.

464 Torres-Platas SG, Nagy C, Wakid M, Turecki G, Mechawar N. Glial fibrillary acidic protein is differentially expressed across cortical and subcortical regions in healthy brains and downregulated in the thalamus and caudate nucleus of depressed suicides. Mol Psychiatry. 2016;21(4):509-15.

465 Miguel-Hidalgo JJ, Baucom C, Dilley G, Overholser JC, Meltzer HY, Stockmeier CA, et al. Glial fibrillary acidic protein immunoreactivity in the prefrontal cortex distinguishes younger from older adults in major depressive disorder. Biol Psychiatry. 2000;48(8):861-73.

466 Si X, Miguel-Hidalgo JJ, O'Dwyer G, Stockmeier CA, Rajkowska G. Age-dependent reductions in the level of glial fibrillary acidic protein in the prefrontal cortex in major depression. Neuropsychopharmacology. 2004;29(11):2088-96.

467 Müller MB, Lucassen PJ, Yassouridis A, Hoogendijk WJ, Holsboer F, Swaab DF. Neither major depression nor glucocorticoid treatment affects the cellular integrity of the human hippocampus. Eur J Neurosci. 2001;14(10):1603-12.

468 Choudary PV, Molnar M, Evans SJ, Tomita H, Li JZ, Vawter MP, et al. Altered cortical glutamatergic and GABAergic signal transmission with glial involvement in depression. Proc Natl Acad Sci U S A. 2005;102(43):15653-8.

469 Schroeter ML, Abdul-Khaliq H, Diefenbacher A, Blasig IE. S100B is increased in mood disorders and may be reduced by antidepressive treatment. Neuroreport. 2002;13(13):1675-8.

470 Banasr M, Duman RS. Glial loss in the prefrontal cortex is sufficient to induce depressive-like behaviors. Biol Psychiatry. 2008;64(10):863-70.

471 Araya-Callís C, Hiemke C, Abumaria N, Flugge G. Chronic psychosocial stress and citalopram modulate the expression of the glial proteins GFAP and NDRG2 in the hippocampus. Psychopharmacology. 2012;224(1):209-22.

472 Liu Q, Li B, Zhu H-Y, Wang Y-Q, Yu J, Wu G-C. Glia atrophy in the hippocampus of chronic unpredictable stress-induced depression model rats is reversed by electroacupuncture treatment. Journal of Affective Disorders. 2011;128(3):309-13.

473 Banasr M, Chowdhury GM, Terwilliger R, Newton SS, Duman RS, Behar KL, et al. Glial pathology in an animal model of depression: reversal of stress-induced cellular, metabolic and behavioral deficits by the glutamate-modulating drug riluzole. Mol Psychiatry. 2010;15(5):501-11.

474 Czéh B, Müller-Keuker JIH, Rygula R, Abumaria N, Hiemke C, Domenici E, et al. Chronic Social Stress Inhibits Cell Proliferation in the Adult Medial Prefrontal Cortex: Hemispheric Asymmetry and Reversal by Fluoxetine Treatment. Neuropsychopharmacology. 2007;32(7):1490-503.

475 Cao X, Li L-P, Wang Q, Wu Q, Hu H-H, Zhang M, et al. Astrocyte-derived ATP modulates depressive-like behaviors. Nature Medicine. 2013;19(6):773-77.

476 Gómez-Galán M, De Bundel D, Van Eeckhaut A, Smolders I, Lindskog M. Dysfunctional astrocytic regulation of glutamate transmission in a rat model of depression. Molecular Psychiatry. 2013;18(5):582-94.

477 Rajkowska G, Mahajan G, Maciag D, Sathyanesan M, Iyo AH, Moulana M, et al. Oligodendrocyte morphometry and expression of myelin - Related mRNA in ventral prefrontal white matter in major depressive disorder. J Psychiatr Res. 2015;65:53-62.

478 Miyata S, Taniguchi M, Koyama Y, Shimizu S, Tanaka T, Yasuno F, et al. Association between chronic stress-induced structural abnormalities in Ranvier nodes and reduced oligodendrocyte activity in major depression. Scientific reports. 2016;6(1):23084.

479 Miyata S, Koyama Y, Takemoto K, Yoshikawa K, Ishikawa T, Taniguchi M, et al. Plasma Corticosterone Activates SGK1 and Induces Morphological Changes in Oligodendrocytes in Corpus Callosum. PLOS ONE. 2011;6(5):e19859.

480 Birey F, Kloc M, Chavali M, Hussein I, Wilson M, Christoffel DJ, et al. Genetic and Stress-Induced Loss of NG2 Glia Triggers Emergence of Depressive-like Behaviors through Reduced Secretion of FGF2. Neuron. 2015;88(5):941-56.

481 Prinz M, Priller J. Microglia and brain macrophages in the molecular age: from origin to neuropsychiatric disease. Nature Reviews Neuroscience. 2014;15(5):300-12.

482 Shalev H, Serlin Y, Friedman A. Breaching the blood-brain barrier as a gate to psychiatric disorder. Cardiovasc Psychiatry Neurol. 2009;2009:278531.

483 Setiawan E, Wilson AA, Mizrahi R, Rusjan PM, Miler L, Rajkowska G, et al. Role of translocator protein density, a marker of neuroinflammation, in the brain during major depressive episodes. JAMA Psychiatry. 2015;72(3):268-75.

484 Steiner J, Bielau H, Brisch R, Danos P, Ullrich O, Mawrin C, et al. Immunological aspects in the neurobiology of suicide: elevated microglial density in schizophrenia and depression is associated with suicide. J Psychiatr Res. 2008;42(2):151-7.

485 Schnieder TP, Trencevska I, Rosoklija G, Stankov A, Mann JJ, Smiley J, et al. Microglia of prefrontal white matter in suicide. J Neuropathol Exp Neurol. 2014;73(9):880-90.

486 Torres-Platas SG, Cruceanu C, Chen GG, Turecki G, Mechawar N. Evidence for increased microglial priming and macrophage recruitment in the dorsal anterior cingulate white matter of depressed suicides. Brain, behavior, and immunity. 2014;42:50-9.

487 Kreisel T, Frank MG, Licht T, Reshef R, Ben-Menachem-Zidon O, Baratta MV, et al. Dynamic microglial alterations underlie stress-induced depressive-like behavior and suppressed neurogenesis. Molecular Psychiatry. 2014;19(6):699-709.

488 Ślusarczyk J, Trojan E, Głombik K, Budziszewska B, Kubera M, Lasoń W, et al. Prenatal stress is a vulnerability factor for altered morphology and biological activity of microglia cells. Frontiers in cellular neuroscience. 2015;9.

489 Milior G, Lecours C, Samson L, Bisht K, Poggini S, Pagani F, et al. Fractalkine receptor deficiency impairs microglial and neuronal responsiveness to chronic stress. Brain, behavior, and immunity. 2016;55:114-25.

490 Duque M, Chen AB, Narayan S, Olson DE, Fishman MC, Engert F, et al. Astroglial mediation of fast-acting antidepressant effect in zebrafish. bioRxiv. 2022:2022.12.29.522099.

491 Mu Y, Bennett DV, Rubinov M, Narayan S, Yang CT, Tanimoto M, et al. Glia Accumulate Evidence that Actions Are Futile and Suppress Unsuccessful Behavior. Cell. 2019;178(1):27-43.e19.

492 Stenovec M, Li B, Verkhratsky A, Zorec R. Astrocytes in rapid ketamine antidepressant action. Neuropharmacology. 2020;173:108158.

493 Zuo D, Wang C, Li Z, Lin L, Duan Z, Qi H, et al. Existence of glia mitigated ketamine-induced neurotoxicity in neuron-glia mixed cultures of neonatal rat cortex and the glia-mediated protective effect of 2-PMPA. Neurotoxicology. 2014;44:218-30.

494 Kong H, Sha L-l, Fan Y, Xiao M, Ding J-h, Wu J, et al. Requirement of AQP4 for Antidepressive Efficiency of Fluoxetine: Implication in Adult Hippocampal Neurogenesis. Neuropsychopharmacology. 2009;34(5):1263-76.

495 K M Harris a, Kater SB. Dendritic Spines: Cellular Specializations Imparting Both Stability and Flexibility to Synaptic Function. Annual Review of Neuroscience. 1994;17(1):341-71.

496 Runge K, Cardoso C, de Chevigny A. Dendritic Spine Plasticity: Function and Mechanisms. Front Synaptic Neurosci. 2020;12:36.

497 Qiao H, Li MX, Xu C, Chen HB, An SC, Ma XM. Dendritic Spines in Depression: What We Learned from Animal Models. Neural Plast. 2016;2016:8056370.

498 Hastings RS, Parsey RV, Oquendo MA, Arango V, Mann JJ. Volumetric analysis of the prefrontal cortex, amygdala, and hippocampus in major depression. Neuropsychopharmacology. 2004;29(5):952-9.

499 Malykhin NV, Carter R, Seres P, Coupland NJ. Structural changes in the hippocampus in major depressive disorder: contributions of disease and treatment. J Psychiatry Neurosci. 2010;35(5):337-43.

500 Kaul D, Smith CC, Stevens J, Fröhlich AS, Binder EB, Mechawar N, et al. Severe childhood and adulthood stress associates with neocortical layer-specific reductions of mature spines in psychiatric disorders. Neurobiology of Stress. 2020;13:100270.

501 Marín O. Developmental timing and critical windows for the treatment of psychiatric disorders. Nat Med. 2016;22(11):1229-38.

502 Moda-Sava RN, Murdock MH, Parekh PK, Fetcho RN, Huang BS, Huynh TN, et al. Sustained rescue of prefrontal circuit dysfunction by antidepressant-induced spine formation. Science. 2019;364(6436).

503 Ly C, Greb AC, Vargas MV, Duim WC, Grodzki ACG, Lein PJ, et al. Transient Stimulation with Psychoplastogens Is Sufficient to Initiate Neuronal Growth. ACS Pharmacol Transl Sci. 2021;4(2):452-60.

504 Reinés A, Cereseto M, Ferrero A, Sifonios L, Podestá MF, Wikinski S. Maintenance Treatment with Fluoxetine is Necessary to Sustain Normal Levels of Synaptic Markers in an Experimental Model of Depression: Correlation with Behavioral Response. Neuropsychopharmacology. 2008;33(8):1896-908.

505 Cameron LP, Tombari RJ, Lu J, Pell AJ, Hurley ZQ, Ehinger Y, et al. A non-hallucinogenic psychedelic analogue with therapeutic potential. Nature. 2021;589(7842):474-79.

506 Vargas MV, Dunlap LE, Dong C, Carter SJ, Tombari RJ, Jami SA, et al. Psychedelics promote neuroplasticity through the activation of intracellular 5-HT2A receptors. Science. 2023;379(6633):700-06.

507 Remy P, Doder M, Lees A, Turjanski N, Brooks D. Depression in Parkinson's disease: loss of dopamine and noradrenaline innervation in the limbic system. Brain. 2005;128(Pt 6):1314-22.

508 Grosch J, Winkler J, Kohl Z. Early Degeneration of Both Dopaminergic and Serotonergic Axons – A Common Mechanism in Parkinson’s Disease. Frontiers in cellular neuroscience. 2016;10.

509 Maillet A, Krack P, Lhommée E, Météreau E, Klinger H, Favre E, et al. The prominent role of serotonergic degeneration in apathy, anxiety and depression in de novo Parkinson's disease. Brain. 2016;139(Pt 9):2486-502.

510 Paulus W, Jellinger K. The Neuropathologic Basis of Different Clinical Subgroups of Parkinson's Disease. Journal of Neuropathology & Experimental Neurology. 1991;50(6):743-55.

511 Weintraub D, Simuni T, Caspell-Garcia C, Coffey C, Lasch S, Siderowf A, et al. Cognitive performance and neuropsychiatric symptoms in early, untreated Parkinson's disease. Movement Disorders. 2015;30(7):919-27.

512 Santiago RM, Barbieiro J, Lima MMS, Dombrowski PA, Andreatini R, Vital MABF. Depressive-like behaviors alterations induced by intranigral MPTP, 6-OHDA, LPS and rotenone models of Parkinson's disease are predominantly associated with serotonin and dopamine. Progress in Neuro-Psychopharmacology and Biological Psychiatry. 2010;34(6):1104-14.

513 Santiago RM, Barbiero J, Gradowski RW, Bochen S, Lima MMS, Da Cunha C, et al. Induction of depressive-like behavior by intranigral 6-OHDA is directly correlated with deficits in striatal dopamine and hippocampal serotonin. Behavioural Brain Research. 2014;259:70-77.

514 Kitayama I, Yaga T, Kayahara T, Nakano K, Murase S, Otani M, et al. Long-term stress degenerates, but imipramine regenerates, noradrenergic axons in the rat cerebral cortex. Biol Psychiatry. 1997;42(8):687-96.

515 Gonzalez MM, Aston-Jones G. Light deprivation damages monoamine neurons and produces a depressive behavioral phenotype in rats. Proc Natl Acad Sci U S A. 2008;105(12):4898-903.

516 Kuramochi M, Nakamura S. Effects of postnatal isolation rearing and antidepressant treatment on the density of serotonergic and noradrenergic axons and depressive behavior in rats. Neuroscience. 2009;163(1):448-55.

517 Mohideen SS, Ichihara G, Ichihara S, Nakamura S. Exposure to 1-bromopropane causes degeneration of noradrenergic axons in the rat brain. Toxicology. 2011;285(1-2):67-71.

518 Zahrai A, Vahid-Ansari F, Daigle M, Albert PR. Fluoxetine-induced recovery of serotonin and norepinephrine projections in a mouse model of post-stroke depression. Translational psychiatry. 2020;10(1):334.

519 Nakamura S. Antidepressants induce regeneration of catecholaminergic axon terminals in the rat cerebral cortex. Neurosci Lett. 1990;111(1-2):64-8.

520 Nakamura S. Effects of mianserin and fluoxetine on axonal regeneration of brain catecholamine neurons. Neuroreport. 1991;2(9):525-8.

521 Zhou L, Huang K-X, Kecojevic A, Welsh AM, Koliatsos VE. Evidence that serotonin reuptake modulators increase the density of serotonin innervation in the forebrain. Journal of Neurochemistry. 2006;96(2):396-406.

522 Himmelseher S, Pfenninger E, Georgieff M. The effects of ketamine-isomers on neuronal injury and regeneration in rat hippocampal neurons. Anesth Analg. 1996;83(3):505-12.

523 Shoji N. Perspective Chapter: Depression as a Disorder of Monoamine Axon Degeneration May Hold an Answer to Two Antidepressant Questions - Delayed Clinical Efficacy and Treatment-Resistant Depression. In: Ph DSP, Prof. Berend O, editors. COVID-19 Pandemic, Mental Health and Neuroscience - New Scenarios for Understanding and Treatment. Rijeka: IntechOpen; 2022. p. Ch. 3.

524 Giger RJ, Hollis ER, 2nd, Tuszynski MH. Guidance molecules in axon regeneration. Cold Spring Harbor perspectives in biology. 2010;2(7):a001867.

525 Little B, Chang T, Chucot L, Dill WA, Enrile LL, Glazko AJ, et al. Study of ketamine as an obstetric anesthetic agent. Am J Obstet Gynecol. 1972;113(2):247-60.

526 Goldberg ME, Torjman MC, Schwartzman RJ, Mager DE, Wainer IW. Pharmacodynamic profiles of ketamine (R)- and (S)- with 5-day inpatient infusion for the treatment of complex regional pain syndrome. Pain physician. 2010;13(4):379-87.

527 Vlerick L, Devreese M, Peremans K, Dockx R, Croubels S, Duchateau L, et al. Pharmacokinetics, absolute bioavailability and tolerability of ketamine after intranasal administration to dexmedetomidine sedated dogs. PLoS One. 2020;15(1):e0227762.

528 Theurillat R, Larenza MP, Feige K, Bettschart-Wolfensberger R, Thormann W. Development of a method for analysis of ketamine and norketamine enantiomers in equine brain and cerebrospinal fluid by capillary electrophoresis. Electrophoresis. 2014;35(19):2863-9.

529 Ganguly S, Panetta JC, Roberts JK, Schuetz EG. Ketamine Pharmacokinetics and Pharmacodynamics Are Altered by P-Glycoprotein and Breast Cancer Resistance Protein Efflux Transporters in Mice. Drug Metab Dispos. 2018;46(7):1014-22.

530 Lester HA, Miwa JM, Srinivasan R. Psychiatric Drugs Bind to Classical Targets Within Early Exocytotic Pathways: Therapeutic Effects. Biol Psychiatry. 2012;72:905-15.

531 Lester HA, Lavis LD, Dougherty DA. Ketamine Inside Neurons? Am J Psychiatry. 2015;172(11):1064-6.

532 Henderson BJ, Lester HA. Inside-out neuropharmacology of nicotinic drugs. Neuropharmacol. 2015;96(Pt B):178-93.

533 Shivange AV, Borden PM, Muthusamy AK, Nichols AL, Bera K, Bao H, et al. Determining the pharmacokinetics of nicotinic drugs in the endoplasmic reticulum using biosensors. J Gen Physiol 2019;151(4):738-57.

534 Kuryatov A, Luo J, Cooper J, Lindstrom J. Nicotine acts as a pharmacological chaperone to up-regulate human a4b2 acetylcholine receptors. Mol Pharmacol. 2005;68(6):1839-51.

535 Sallette J, Pons S, Devillers-Thiery A, Soudant M, Prado de Carvalho L, Changeux JP, et al. Nicotine upregulates its own receptors through enhanced intracellular maturation. Neuron. 2005;46(4):595-607.

536 Smith D, Allerton C, Kalgutkar A, van de Waterbeemd H, Walker D. Pharmacokinetics and Metabolism in Drug Design. 3rd ed. Wiley: Weinheim; 2012.

537 Tischbirek CH, Wenzel EM, Zheng F, Huth T, Amato D, Trapp S, et al. Use-dependent inhibition of synaptic transmission by the secretion of intravesicularly accumulated antipsychotic drugs. Neuron. 2012;74(5):830-44.

538 Srinivasan R, Henderson BJ, Lester HA, Richards CI. Pharmacological chaperoning of nAChRs: A therapeutic target for Parkinson's disease. Pharmacol Res. 2014;83C:20-29.

539 Alberti S, Dormann D. Liquid-Liquid Phase Separation in Disease. Annu Rev Genet. 2019;53:171-94.

540 Tedesco V, Ravagnani C, Bertoglio D, Chiamulera C. Acute ketamine-induced neuroplasticity: ribosomal protein S6 phosphorylation expression in drug addiction-related rat brain areas. Neuroreport. 2013;24(7):388-93.

541 Biever A, Valjent E, Puighermanal E. Ribosomal Protein S6 Phosphorylation in the Nervous System: From Regulation to Function. Frontiers in Molecular Neuroscience. 2015;8.

542 Treyer A, Mateus A, Wiśniewski JR, Boriss H, Matsson P, Artursson P. Intracellular Drug Bioavailability: Effect of Neutral Lipids and Phospholipids. Molecular pharmaceutics. 2018;15(6):2224-33.

543 Nichols AL, Blumenfeld Z, Luebbert L, Knox HJ, Muthusamy AK, Marvin JS, et al. Selective Serotonin Reuptake Inhibitors within Cells: Temporal Resolution in Cytoplasm, Endoplasmic Reticulum, and Membrane. The Journal of Neuroscience. 2023:JN-RM-1519-22.

544 Bera K, Kamajaya A, Shivange AV, Muthusamy AK, Nichols AL, Borden PM, et al. Biosensors Show the Pharmacokinetics of S-Ketamine in the Endoplasmic Reticulum. Frontiers in cellular neuroscience. 2019;13:499-99.

545 Treyer A, Walday S, Boriss H, Matsson P, Artursson P. A Cell-Free Approach Based on Phospholipid Characterization for Determination of the Cell Specific Unbound Drug Fraction (f(u,cell)). Pharmaceutical research. 2019;36(12):178.

546 Yesylevskyy S, Rivel T, Ramseyer C. Curvature increases permeability of the plasma membrane for ions, water and the anti-cancer drugs cisplatin and gemcitabine. Scientific reports. 2019;9(1):17214.

547 Frallicciardi J, Melcr J, Siginou P, Marrink SJ, Poolman B. Membrane thickness, lipid phase and sterol type are determining factors in the permeability of membranes to small solutes. Nature communications. 2022;13(1):1605.

548 Alves AC, Magarkar A, Horta M, Lima J, Bunker A, Nunes C, et al. Influence of doxorubicin on model cell membrane properties: insights from in vitro and in silico studies. Scientific reports. 2017;7(1):6343.

549 Wray NH, Schappi JM, Singh H, Senese NB, Rasenick MM. NMDAR-independent, cAMP-dependent antidepressant actions of ketamine. Mol Psychiatry. 2019;24(12):1833-43.

550 Sassone-Corsi P. The cyclic AMP pathway. Cold Spring Harbor perspectives in biology. 2012;4(12).

551 Donati RJ, Dwivedi Y, Roberts RC, Conley RR, Pandey GN, Rasenick MM. Postmortem brain tissue of depressed suicides reveals increased Gs alpha localization in lipid raft domains where it is less likely to activate adenylyl cyclase. J Neurosci. 2008;28(12):3042-50.

552 Allen JA, Yu JZ, Dave RH, Bhatnagar A, Roth BL, Rasenick MM. Caveolin-1 and Lipid Microdomains Regulate G<sub>s</sub> Trafficking and Attenuate G<sub>s</sub>/Adenylyl Cyclase Signaling. Molecular Pharmacology. 2009;76(5):1082.

553 Toki S, Donati RJ, Rasenick MM. Treatment of C6 Glioma Cells and Rats with Antidepressant Drugs Increases the Detergent Extraction of Gsα from Plasma Membrane. Journal of Neurochemistry. 1999;73(3):1114-20.

554 Czysz AH, Schappi JM, Rasenick MM. Lateral Diffusion of Gαs in the Plasma Membrane Is Decreased after Chronic but not Acute Antidepressant Treatment: Role of Lipid Raft and Non-Raft Membrane Microdomains. Neuropsychopharmacology. 2015;40(3):766-73.

555 Zhang L, Rasenick MM. Chronic treatment with escitalopram but not R-citalopram translocates Galpha(s) from lipid raft domains and potentiates adenylyl cyclase: a 5-hydroxytryptamine transporter-independent action of this antidepressant compound. J Pharmacol Exp Ther. 2010;332(3):977-84.

556 Erb SJ, Schappi JM, Rasenick MM. Antidepressants Accumulate in Lipid Rafts Independent of Monoamine Transporters to Modulate Redistribution of the G Protein, Gαs. J Biol Chem. 2016;291(38):19725-33.

557 Björkholm C, Monteggia LM. BDNF - a key transducer of antidepressant effects. Neuropharmacology. 2016;102:72-9.

558 Lessmann V, Brigadski T. Mechanisms, locations, and kinetics of synaptic BDNF secretion: an update. Neurosci Res. 2009;65(1):11-22.

559 Lau AG, Irier HA, Gu J, Tian D, Ku L, Liu G, et al. Distinct 3′UTRs differentially regulate activity-dependent translation of brain-derived neurotrophic factor (BDNF). Proceedings of the National Academy of Sciences. 2010;107(36):15945-50.

560 Yang T, Nie Z, Shu H, Kuang Y, Chen X, Cheng J, et al. The Role of BDNF on Neural Plasticity in Depression. Frontiers in cellular neuroscience. 2020;14:82.

561 Tyler WJ, Perrett SP, Pozzo-Miller LD. The Role of Neurotrophins in Neurotransmitter Release. The Neuroscientist. 2002;8(6):524-31.

562 Caldeira MV, Melo CV, Pereira DB, Carvalho R, Correia SS, Backos DS, et al. Brain-derived Neurotrophic Factor Regulates the Expression and Synaptic Delivery ofα-Amino-3-hydroxy-5-methyl-4-isoxazole Propionic Acid Receptor Subunits in Hippocampal Neurons*. Journal of Biological Chemistry. 2007;282(17):12619-28.

563 Soppet D, Escandon E, Maragos J, Middlemas DS, Reid SW, Blair J, et al. The neurotrophic factors brain-derived neurotrophic factor and neurotrophin-3 are ligands for the trkB tyrosine kinase receptor. Cell. 1991;65(5):895-903.

564 Madara JC, Levine ES. Presynaptic and Postsynaptic NMDA Receptors Mediate Distinct Effects of Brain-Derived Neurotrophic Factor on Synaptic Transmission. Journal of Neurophysiology. 2008;100(6):3175-84.

565 Smith MA, Makino S, Kvetnansky R, Post RM. Stress and glucocorticoids affect the expression of brain-derived neurotrophic factor and neurotrophin-3 mRNAs in the hippocampus. J Neurosci. 1995;15(3 Pt 1):1768-77.

566 Rasmusson AM, Shi L, Duman R. Downregulation of BDNF mRNA in the Hippocampal Dentate Gyrus after Re-exposure to Cues Previously Associated with Footshock. Neuropsychopharmacology. 2002;27(2):133-42.

567 Tsankova NM, Berton O, Renthal W, Kumar A, Neve RL, Nestler EJ. Sustained hippocampal chromatin regulation in a mouse model of depression and antidepressant action. Nat Neurosci. 2006;9(4):519-25.

568 Zhang JC, Wu J, Fujita Y, Yao W, Ren Q, Yang C, et al. Antidepressant effects of TrkB ligands on depression-like behavior and dendritic changes in mice after inflammation. Int J Neuropsychopharmacol. 2014;18(4).

569 Yang C, Shirayama Y, Zhang JC, Ren Q, Hashimoto K. Regional differences in brain-derived neurotrophic factor levels and dendritic spine density confer resilience to inescapable stress. Int J Neuropsychopharmacol. 2015;18(7):pyu121.

570 Kuroda Y, McEwen BS. Effect of chronic restraint stress and tianeptine on growth factors, growth-associated protein-43 and microtubule-associated protein 2 mRNA expression in the rat hippocampus. Brain Research: Molecular Brain Research. 1998;59(1):35-39.

571 Molteni R, Calabrese F, Cattaneo A, Mancini M, Gennarelli M, Racagni G, et al. Acute stress responsiveness of the neurotrophin BDNF in the rat hippocampus is modulated by chronic treatment with the antidepressant duloxetine. Neuropsychopharmacology. 2009;34(6):1523-32.

572 Monteggia LM, Luikart B, Barrot M, Theobold D, Malkovska I, Nef S, et al. Brain-derived neurotrophic factor conditional knockouts show gender differences in depression-related behaviors. Biol Psychiatry. 2007;61(2):187-97.

573 Taliaz D, Stall N, Dar DE, Zangen A. Knockdown of brain-derived neurotrophic factor in specific brain sites precipitates behaviors associated with depression and reduces neurogenesis. Molecular Psychiatry. 2010;15(1):80-92.

574 Adam Tripp, M.D., Ph.D. ,, Hyunjung Oh, M.S. ,, Jean-Philippe Guilloux, Ph.D. ,, Keri Martinowich, Ph.D. ,, David A. Lewis, M.D. , and, Etienne Sibille, Ph.D. Brain-Derived Neurotrophic Factor Signaling and Subgenual Anterior Cingulate Cortex Dysfunction in Major Depressive Disorder. American Journal of Psychiatry. 2012;169(11):1194-202.

575 Guilloux JP, Douillard-Guilloux G, Kota R, Wang X, Gardier AM, Martinowich K, et al. Molecular evidence for BDNF- and GABA-related dysfunctions in the amygdala of female subjects with major depression. Molecular Psychiatry. 2012;17(11):1130-42.

576 Dwivedi Y, Rizavi HS, Conley RR, Roberts RC, Tamminga CA, Pandey GN. Altered Gene Expression of Brain-Derived Neurotrophic Factor and Receptor Tyrosine Kinase B in Postmortem Brain of Suicide Subjects. Archives of General Psychiatry. 2003;60(8):804-15.

577 Karege F, Vaudan G, Schwald M, Perroud N, La Harpe R. Neurotrophin levels in postmortem brains of suicide victims and the effects of antemortem diagnosis and psychotropic drugs. Brain Research: Molecular Brain Research. 2005;136(1):29-37.

578 Ernst C, Deleva V, Deng X, Sequeira A, Pomarenski A, Klempan T, et al. Alternative Splicing, Methylation State, and Expression Profile of Tropomyosin-Related Kinase B in the Frontal Cortex of Suicide Completers. Archives of General Psychiatry. 2009;66(1):22-32.

579 Karege F, Perret G, Bondolfi G, Schwald M, Bertschy G, Aubry JM. Decreased serum brain-derived neurotrophic factor levels in major depressed patients. Psychiatry Res. 2002;109(2):143-8.

580 Sen S, Duman R, Sanacora G. Serum brain-derived neurotrophic factor, depression, and antidepressant medications: meta-analyses and implications. Biol Psychiatry. 2008;64(6):527-32.

581 Bocchio-Chiavetto L, Bagnardi V, Zanardini R, Molteni R, Gabriela Nielsen M, Placentino A, et al. Serum and plasma BDNF levels in major depression: A replication study and meta-analyses. The World Journal of Biological Psychiatry. 2010;11(6):763-73.

582 Molendijk ML, Bus BA, Spinhoven P, Penninx BW, Kenis G, Prickaerts J, et al. Serum levels of brain-derived neurotrophic factor in major depressive disorder: state-trait issues, clinical features and pharmacological treatment. Mol Psychiatry. 2011;16(11):1088-95.

583 Molendijk ML, Spinhoven P, Polak M, Bus BA, Penninx BW, Elzinga BM. Serum BDNF concentrations as peripheral manifestations of depression: evidence from a systematic review and meta-analyses on 179 associations (N=9484). Mol Psychiatry. 2014;19(7):791-800.

584 Siuciak JA, Lewis DR, Wiegand SJ, Lindsay RM. Antidepressant-like effect of brain-derived neurotrophic factor (BDNF). Pharmacol Biochem Behav. 1997;56(1):131-7.

585 Shirayama Y, Chen AC, Nakagawa S, Russell DS, Duman RS. Brain-derived neurotrophic factor produces antidepressant effects in behavioral models of depression. J Neurosci. 2002;22(8):3251-61.

586 Deyama S, Duman RS. Neurotrophic mechanisms underlying the rapid and sustained antidepressant actions of ketamine. Pharmacol Biochem Behav. 2020;188:172837.

587 Eisch AJ, Bolaños CA, de Wit J, Simonak RD, Pudiak CM, Barrot M, et al. Brain-derived neurotrophic factor in the ventral midbrain-nucleus accumbens pathway: a role in depression. Biol Psychiatry. 2003;54(10):994-1005.

588 Berton O, McClung CA, Dileone RJ, Krishnan V, Renthal W, Russo SJ, et al. Essential role of BDNF in the mesolimbic dopamine pathway in social defeat stress. Science. 2006;311(5762):864-8.

589 Wook Koo J, Labonté B, Engmann O, Calipari ES, Juarez B, Lorsch Z, et al. Essential Role of Mesolimbic Brain-Derived Neurotrophic Factor in Chronic Social Stress–Induced Depressive Behaviors. Biological Psychiatry. 2016;80(6):469-78.

590 Krishnan V, Han MH, Graham DL, Berton O, Renthal W, Russo SJ, et al. Molecular adaptations underlying susceptibility and resistance to social defeat in brain reward regions. Cell. 2007;131(2):391-404.

591 Nibuya M, Morinobu S, Duman RS. Regulation of BDNF and trkB mRNA in rat brain by chronic electroconvulsive seizure and antidepressant drug treatments. J Neurosci. 1995;15(11):7539-47.

592 Chen B, Dowlatshahi D, MacQueen GM, Wang J-F, Young LT. Increased hippocampal bdnf immunoreactivity in subjects treated with antidepressant medication. Biological Psychiatry. 2001;50(4):260-65.

593 Malberg JE, Eisch AJ, Nestler EJ, Duman RS. Chronic Antidepressant Treatment Increases Neurogenesis in Adult Rat Hippocampus. The Journal of Neuroscience. 2000;20(24):9104.

594 Santarelli L, Saxe M, Gross C, Surget A, Battaglia F, Dulawa S, et al. Requirement of hippocampal neurogenesis for the behavioral effects of antidepressants. Science. 2003;301(5634):805-9.

595 Li Y, Luikart BW, Birnbaum S, Chen J, Kwon C-H, Kernie SG, et al. TrkB Regulates Hippocampal Neurogenesis and Governs Sensitivity to Antidepressive Treatment. Neuron. 2008;59(3):399-412.

596 Ampuero E, Rubio FJ, Falcon R, Sandoval M, Diaz-Veliz G, Gonzalez RE, et al. Chronic fluoxetine treatment induces structural plasticity and selective changes in glutamate receptor subunits in the rat cerebral cortex. Neuroscience. 2010;169(1):98-108.

597 Song T, Wu H, Li R, Xu H, Rao X, Gao L, et al. Repeated fluoxetine treatment induces long-lasting neurotrophic changes in the medial prefrontal cortex of adult rats. Behavioural Brain Research. 2019;365:114-24.

598 Guilloux J-P, Mendez-David I, Pehrson A, Guiard BP, Repérant C, Orvoën S, et al. Antidepressant and anxiolytic potential of the multimodal antidepressant vortioxetine (Lu AA21004) assessed by behavioural and neurogenesis outcomes in mice. Neuropharmacology. 2013;73:147-59.

599 Chen F, du Jardin KG, Waller JA, Sanchez C, Nyengaard JR, Wegener G. Vortioxetine promotes early changes in dendritic morphology compared to fluoxetine in rat hippocampus. European Neuropsychopharmacology. 2016;26(2):234-45.

600 Dávila-Hernández A, Zamudio SR, Martínez-Mota L, González-González R, Ramírez-San Juan E. Antidepressant effects of acupoint stimulation and fluoxetine by increasing dendritic arborization and spine density in CA1 hippocampal neurons of socially isolated rats. Neuroscience Letters. 2018;675:48-53.

601 Autry AE, Adachi M, Nosyreva E, Na ES, Los MF, Cheng PF, et al. NMDA receptor blockade at rest triggers rapid behavioural antidepressant responses. Nature. 2011;475(7354):91-5.

602 Lepack AE, Fuchikami M, Dwyer JM, Banasr M, Duman RS. BDNF release is required for the behavioral actions of ketamine. Int J Neuropsychopharmacol. 2014;18(1).

603 Duncan WC, Sarasso S, Ferrarelli F, Selter J, Riedner BA, Hejazi NS, et al. Concomitant BDNF and sleep slow wave changes indicate ketamine-induced plasticity in major depressive disorder. Int J Neuropsychopharmacol. 2013;16(2):301-11.

604 Woelfer M, Li M, Colic L, Liebe T, Di X, Biswal B, et al. Ketamine-induced changes in plasma brain-derived neurotrophic factor (BDNF) levels are associated with the resting-state functional connectivity of the prefrontal cortex. World J Biol Psychiatry. 2020;21(9):696-710.

605 Haile CN, Murrough JW, Iosifescu DV, Chang LC, Al Jurdi RK, Foulkes A, et al. Plasma brain derived neurotrophic factor (BDNF) and response to ketamine in treatment-resistant depression. Int J Neuropsychopharmacol. 2014;17(2):331-6.

606 Allen AP, Naughton M, Dowling J, Walsh A, Ismail F, Shorten G, et al. Serum BDNF as a peripheral biomarker of treatment-resistant depression and the rapid antidepressant response: A comparison of ketamine and ECT. J Affect Disord. 2015;186:306-11.

607 Kaiser RH, Andrews-Hanna JR, Wager TD, Pizzagalli DA. Large-Scale Network Dysfunction in Major Depressive Disorder: A Meta-analysis of Resting-State Functional Connectivity. JAMA Psychiatry. 2015;72(6):603-11.

608 Egan MF, Kojima M, Callicott JH, Goldberg TE, Kolachana BS, Bertolino A, et al. The BDNF val66met polymorphism affects activity-dependent secretion of BDNF and human memory and hippocampal function. Cell. 2003;112(2):257-69.

609 Liu R-J, Lee FS, Li X-Y, Bambico F, Duman RS, Aghajanian GK. Brain-Derived Neurotrophic Factor Val66Met Allele Impairs Basal and Ketamine-Stimulated Synaptogenesis in Prefrontal Cortex. Biological Psychiatry. 2012;71(11):996-1005.

610 Yu H, Wang D-D, Wang Y, Liu T, Lee FS, Chen Z-Y. Variant Brain-Derived Neurotrophic Factor Val66Met Polymorphism Alters Vulnerability to Stress and Response to Antidepressants. The Journal of Neuroscience. 2012;32(12):4092.

611 Notaras M, Hill R, van den Buuse M. The BDNF gene Val66Met polymorphism as a modifier of psychiatric disorder susceptibility: progress and controversy. Molecular Psychiatry. 2015;20(8):916-30.

612 Ghosal S, Bang E, Yue W, Hare BD, Lepack AE, Girgenti MJ, et al. Activity-Dependent Brain-Derived Neurotrophic Factor Release Is Required for the Rapid Antidepressant Actions of Scopolamine. Biol Psychiatry. 2018;83(1):29-37.

613 Laje G, Lally N, Mathews D, Brutsche N, Chemerinski A, Akula N, et al. Brain-derived neurotrophic factor Val66Met polymorphism and antidepressant efficacy of ketamine in depressed patients. Biol Psychiatry. 2012;72(11):e27-8.

614 Casarotto PC, Girych M, Fred SM, Kovaleva V, Moliner R, Enkavi G, et al. Antidepressant drugs act by directly binding to TRKB neurotrophin receptors. Cell. 2021;184(5):1299-313 e19.

615 Lipton Jonathan O, Sahin M. The Neurology of mTOR. Neuron. 2014;84(2):275-91.

616 Yin Y, Hua H, Li M, Liu S, Kong Q, Shao T, et al. mTORC2 promotes type I insulin-like growth factor receptor and insulin receptor activation through the tyrosine kinase activity of mTOR. Cell Res. 2016;26(1):46-65.

617 Betz C, Hall MN. Where is mTOR and what is it doing there? Journal of Cell Biology. 2013;203(4):563-74.

618 Puertollano R. mTOR and lysosome regulation. F1000Prime Rep. 2014;6:52.

619 Karege F, Perroud N, Burkhardt S, Schwald M, Ballmann E, La Harpe R, et al. Alteration in kinase activity but not in protein levels of protein kinase B and glycogen synthase kinase-3beta in ventral prefrontal cortex of depressed suicide victims. Biol Psychiatry. 2007;61(2):240-5.

620 Jernigan CS, Goswami DB, Austin MC, Iyo AH, Chandran A, Stockmeier CA, et al. The mTOR signaling pathway in the prefrontal cortex is compromised in major depressive disorder. Prog Neuropsychopharmacol Biol Psychiatry. 2011;35(7):1774-9.

621 Chandran A, Iyo AH, Jernigan CS, Legutko B, Austin MC, Karolewicz B. Reduced phosphorylation of the mTOR signaling pathway components in the amygdala of rats exposed to chronic stress. Prog Neuropsychopharmacol Biol Psychiatry. 2013;40:240-5.

622 Zhu WL, Wang SJ, Liu MM, Shi HS, Zhang RX, Liu JF, et al. Glycine site N-methyl-D-aspartate receptor antagonist 7-CTKA produces rapid antidepressant-like effects in male rats. J Psychiatry Neurosci. 2013;38(5):306-16.

623 Ota KT, Liu RJ, Voleti B, Maldonado-Aviles JG, Duric V, Iwata M, et al. REDD1 is essential for stress-induced synaptic loss and depressive behavior. Nat Med. 2014;20(5):531-5.

624 Zhong P, Wang W, Pan B, Liu X, Zhang Z, Long JZ, et al. Monoacylglycerol lipase inhibition blocks chronic stress-induced depressive-like behaviors via activation of mTOR signaling. Neuropsychopharmacology. 2014;39(7):1763-76.

625 Duman RS, Aghajanian GK, Sanacora G, Krystal JH. Synaptic plasticity and depression: new insights from stress and rapid-acting antidepressants. Nature Medicine. 2016;22(3):238-49.

626 Park SW, Lee JG, Seo MK, Lee CH, Cho HY, Lee BJ, et al. Differential effects of antidepressant drugs on mTOR signalling in rat hippocampal neurons. Int J Neuropsychopharmacol. 2014;17(11):1831-46.

627 Jeon S-H, Kim SH, Kim Y, Kim YS, Lim Y, Lee YH, et al. The tricyclic antidepressant imipramine induces autophagic cell death in U-87MG glioma cells. Biochemical and Biophysical Research Communications. 2011;413(2):311-17.

628 Warren BL, Iñiguez SD, Alcantara LF, Wright KN, Parise EM, Weakley SK, et al. Juvenile administration of concomitant methylphenidate and fluoxetine alters behavioral reactivity to reward- and mood-related stimuli and disrupts ventral tegmental area gene expression in adulthood. J Neurosci. 2011;31(28):10347-58.

629 Lin CJ, Robert F, Sukarieh R, Michnick S, Pelletier J. The antidepressant sertraline inhibits translation initiation by curtailing mammalian target of rapamycin signaling. Cancer Res. 2010;70(8):3199-208.

630 Xu D, Sun Y, Wang C, Wang H, Wang Y, Zhao W, et al. Hippocampal mTOR signaling is required for the antidepressant effects of paroxetine. Neuropharmacology. 2018;128:181-95.

631 K V A, Mohan AS, Chakravarty S. Rapid acting antidepressants in the mTOR pathway: Current evidence. Brain Research Bulletin. 2020;163:170-77.

632 Duman RS. NEUROBIOLOGY OF STRESS, DEPRESSION, AND RAPID ACTING ANTIDEPRESSANTS: REMODELING SYNAPTIC CONNECTIONS. Depression and Anxiety. 2014;31(4):291-96.

633 Zhou W, Wang N, Yang C, Li XM, Zhou ZQ, Yang JJ. Ketamine-induced antidepressant effects are associated with AMPA receptors-mediated upregulation of mTOR and BDNF in rat hippocampus and prefrontal cortex. Eur Psychiatry. 2014;29(7):419-23.

634 Liu R-J, Ota KT, Dutheil S, Duman RS, Aghajanian GK. Ketamine Strengthens CRF-Activated Amygdala Inputs to Basal Dendrites in mPFC Layer V Pyramidal Cells in the Prelimbic but not Infralimbic Subregion, A Key Suppressor of Stress Responses. Neuropsychopharmacology. 2015;40(9):2066-75.

635 Yang C, Ren Q, Qu Y, Zhang JC, Ma M, Dong C, et al. Mechanistic Target of Rapamycin-Independent Antidepressant Effects of (R)-Ketamine in a Social Defeat Stress Model. Biol Psychiatry. 2018;83(1):18-28.

636 Zoncu R, Efeyan A, Sabatini DM. mTOR: from growth signal integration to cancer, diabetes and ageing. Nat Rev Mol Cell Biol. 2011;12(1):21-35.

637 Liu RJ, Fuchikami M, Dwyer JM, Lepack AE, Duman RS, Aghajanian GK. GSK-3 inhibition potentiates the synaptogenic and antidepressant-like effects of subthreshold doses of ketamine. Neuropsychopharmacology. 2013;38(11):2268-77.

638 Beurel E, Song L, Jope RS. Inhibition of glycogen synthase kinase-3 is necessary for the rapid antidepressant effect of ketamine in mice. Mol Psychiatry. 2011;16(11):1068-70.

639 Abdallah CG, Averill LA, Gueorguieva R, Goktas S, Purohit P, Ranganathan M, et al. Modulation of the antidepressant effects of ketamine by the mTORC1 inhibitor rapamycin. Neuropsychopharmacology. 2020;45(6):990-97.

640 Averill LA, Averill CL, Gueorguieva R, Fouda S, Sherif M, Ahn K-H, et al. mTORC1 inhibitor effects on rapid ketamine-induced reductions in suicidal ideation in patients with treatment-resistant depression. Journal of Affective Disorders. 2022;303:91-97.

641 Voleti B, Navarria A, Liu RJ, Banasr M, Li N, Terwilliger R, et al. Scopolamine rapidly increases mammalian target of rapamycin complex 1 signaling, synaptogenesis, and antidepressant behavioral responses. Biol Psychiatry. 2013;74(10):742-9.

642 Liu RJ, Duman C, Kato T, Hare B, Lopresto D, Bang E, et al. GLYX-13 Produces Rapid Antidepressant Responses with Key Synaptic and Behavioral Effects Distinct from Ketamine. Neuropsychopharmacology. 2017;42(6):1231-42.

643 Kato T, Fogaça MV, Deyama S, Li XY, Fukumoto K, Duman RS. BDNF release and signaling are required for the antidepressant actions of GLYX-13. Mol Psychiatry. 2018;23(10):2007-17.

644 Shen M, Lv D, Liu X, Wang C. ERK/mTOR signaling may underlying the antidepressant actions of rapastinel in mice. Translational psychiatry. 2022;12(1):522.

645 Kato T, Pothula S, Liu RJ, Duman CH, Terwilliger R, Vlasuk GP, et al. Sestrin modulator NV-5138 produces rapid antidepressant effects via direct mTORC1 activation. J Clin Invest. 2019;129(6):2542-54.

646 Dwyer JM, Lepack AE, Duman RS. mTOR activation is required for the antidepressant effects of mGluR$_2$/$_3$ blockade. Int J Neuropsychopharmacol. 2012;15(4):429-34.

647 Hollmann M, Heinemann S. Cloned Glutamate Receptors. Annual Review of Neuroscience. 1994;17(1):31-108.

648 Marenco S, Weinberger DR. Therapeutic potential of positive AMPA receptor modulators in the treatment of neuropsychiatric disorders. CNS Drugs. 2006;20(3):173-85.

649 Freudenberg F, Celikel T, Reif A. The role of α-amino-3-hydroxy-5-methyl-4-isoxazolepropionic acid (AMPA) receptors in depression: central mediators of pathophysiology and antidepressant activity? Neurosci Biobehav Rev. 2015;52:193-206.

650 Schwendt M, Ježová D. Gene Expression of Two Glutamate Receptor Subunits in Response to Repeated Stress Exposure in Rat Hippocampus. Cellular and Molecular Neurobiology. 2000;20(3):319-29.

651 Rosa MLNM, Guimarães FS, Pearson RCA, Del Bel EA. Effects of single or repeated restraint stress on GluR1 and GluR2 flip and flop mRNA expression in the hippocampal formation. Brain Research Bulletin. 2002;59(2):117-24.

652 Qin Y, Karst H, Joëls M. Chronic unpredictable stress alters gene expression in rat single dentate granule cells. Journal of Neurochemistry. 2004;89(2):364-74.

653 Toth E, Gersner R, Wilf-Yarkoni A, Raizel H, Dar DE, Richter-Levin G, et al. Age-dependent effects of chronic stress on brain plasticity and depressive behavior. Journal of Neurochemistry. 2008;107(2):522-32.

654 Duric V, Banasr M, Stockmeier CA, Simen AA, Newton SS, Overholser JC, et al. Altered expression of synapse and glutamate related genes in post-mortem hippocampus

of depressed subjects. International Journal of Neuropsychopharmacology. 2013;16(1):69-82.

655 Kallarackal AJ, Kvarta MD, Cammarata E, Jaberi L, Cai X, Bailey AM, et al. Chronic Stress Induces a Selective Decrease in AMPA Receptor-Mediated Synaptic Excitation at Hippocampal Temporoammonic-CA1 Synapses. The Journal of Neuroscience. 2013;33(40):15669.

656 Gibbons AS, Brooks L, Scarr E, Dean B. AMPA receptor expression is increased post-mortem samples of the anterior cingulate from subjects with major depressive disorder. Journal of Affective Disorders. 2012;136(3):1232-37.

657 Beneyto M, Kristiansen LV, Oni-Orisan A, McCullumsmith RE, Meador-Woodruff JH. Abnormal Glutamate Receptor Expression in the Medial Temporal Lobe in Schizophrenia and Mood Disorders. Neuropsychopharmacology. 2007;32(9):1888-902.

658 Martinez-Turrillas R, Frechilla D, Del Río J. Chronic antidepressant treatment increases the membrane expression of AMPA receptors in rat hippocampus. Neuropharmacology. 2002;43(8):1230-7.

659 Martínez-Turrillas R, Del Río J, Frechilla D. Sequential changes in BDNF mRNA expression and synaptic levels of AMPA receptor subunits in rat hippocampus after chronic antidepressant treatment. Neuropharmacology. 2005;49(8):1178-88.

660 Du J, Suzuki K, Wei Y, Wang Y, Blumenthal R, Chen Z, et al. The Anticonvulsants Lamotrigine, Riluzole, and Valproate Differentially Regulate AMPA Receptor Membrane Localization: Relationship to Clinical Effects in Mood Disorders. Neuropsychopharmacology. 2007;32(4):793-802.

661 Barbon A, Caracciolo L, Orlandi C, Musazzi L, Mallei A, La Via L, et al. Chronic antidepressant treatments induce a time-dependent up-regulation of AMPA receptor subunit protein levels. Neurochemistry International. 2011;59(6):896-905.

662 Farley S, Apazoglou K, Witkin JM, Giros B, Tzavara ET. Antidepressant-like effects of an AMPA receptor potentiator under a chronic mild stress paradigm. Int J Neuropsychopharmacol. 2010;13(9):1207-18.

663 Park M, Niciu MJ, Zarate CA, Jr. Novel Glutamatergic Treatments for Severe Mood Disorders. Current behavioral neuroscience reports. 2015;2(4):198-208.

664 Björkholm C, Jardemark K, Schilström B, Svensson TH. Ketamine-like effects of a combination of olanzapine and fluoxetine on AMPA and NMDA receptor-mediated transmission in the medial prefrontal cortex of the rat. Eur Neuropsychopharmacol. 2015;25(10):1842-7.

665 Nosyreva E, Szabla K, Autry AE, Ryazanov AG, Monteggia LM, Kavalali ET. Acute Suppression of Spontaneous Neurotransmission Drives Synaptic Potentiation. The Journal of Neuroscience. 2013;33(16):6990.

666 El Iskandrani KS, Oosterhof CA, El Mansari M, Blier P. Impact of subanesthetic doses of ketamine on AMPA-mediated responses in rats: An in vivo electrophysiological study on monoaminergic and glutamatergic neurons. Journal of psychopharmacology (Oxford, England). 2015;29(7):792-801.

667 Maeng S, Zarate CA, Jr., Du J, Schloesser RJ, McCammon J, Chen G, et al. Cellular mechanisms underlying the antidepressant effects of ketamine: role of alpha-amino-3-hydroxy-5-methylisoxazole-4-propionic acid receptors. Biol Psychiatry. 2008;63(4):349-52.

668 Koike H, Chaki S. Requirement of AMPA receptor stimulation for the sustained antidepressant activity of ketamine and LY341495 during the forced swim test in rats. Behav Brain Res. 2014;271:111-5.

669 Li X, Tizzano JP, Griffey K, Clay M, Lindstrom T, Skolnick P. Antidepressant-like actions of an AMPA receptor potentiator (LY392098). Neuropharmacology. 2001;40(8):1028-33.

670 Li X, Witkin JM, Need AB, Skolnick P. Enhancement of antidepressant potency by a potentiator of AMPA receptors. Cell Mol Neurobiol. 2003;23(3):419-30.

671 Lindholm JS, Autio H, Vesa L, Antila H, Lindemann L, Hoener MC, et al. The antidepressant-like effects of glutamatergic drugs ketamine and AMPA receptor potentiator LY 451646 are preserved in bdnf^{+}/$^{-}$ heterozygous null mice. Neuropharmacology. 2012;62(1):391-7.

672 Akinfiresoye L, Tizabi Y. Antidepressant effects of AMPA and ketamine combination: role of hippocampal BDNF, synapsin, and mTOR. Psychopharmacology (Berl). 2013;230(2):291-8.

673 Nations KR, Dogterom P, Bursi R, Schipper J, Greenwald S, Zraket D, et al. Examination of Org 26576, an AMPA receptor positive allosteric modulator, in patients diagnosed with major depressive disorder: an exploratory, randomized, double-blind, placebo-controlled trial. Journal of psychopharmacology (Oxford, England). 2012;26(12):1525-39.

674 Machado-Vieira R, Henter ID, Zarate CA, Jr. New targets for rapid antidepressant action. Prog Neurobiol. 2017;152:21-37.

675 Jiménez-Sánchez L, Linge R, Campa L, Valdizán EM, Pazos Á, Díaz Á, et al. Behavioral, neurochemical and molecular changes after acute deep brain stimulation of the infralimbic prefrontal cortex. Neuropharmacology. 2016;108:91-102.

676 Cavalleri L, Merlo Pich E, Millan MJ, Chiamulera C, Kunath T, Spano PF, et al. Ketamine enhances structural plasticity in mouse mesencephalic and human iPSC-derived dopaminergic neurons via AMPAR-driven BDNF and mTOR signaling. Mol Psychiatry. 2018;23(4):812-23.

677 Jourdi H, Hsu YT, Zhou M, Qin Q, Bi X, Baudry M. Positive AMPA receptor modulation rapidly stimulates BDNF release and increases dendritic mRNA translation. J Neurosci. 2009;29(27):8688-97.

678 Borden PM, Zhang P, Shivange AV, Marvin JS, Cichon J, Dan C, et al. A fast genetically encoded fluorescent sensor for faithful in vivo acetylcholine detection in mice, fish, worms and flies. bioRxiv. 2020:2020.02.07.939504.

679 Patriarchi T, Cho JR, Merten K, Howe MW, Marley A, Xiong WH, et al. Ultrafast neuronal imaging of dopamine dynamics with designed genetically encoded sensors. Science. 2018;360(6396).

680 Sun F, Zeng J, Jing M, Zhou J, Feng J, Owen SF, et al. A Genetically Encoded Fluorescent Sensor Enables Rapid and Specific Detection of Dopamine in Flies, Fish, and Mice. Cell. 2018;174(2):481-96.e19.

681 Marvin JS, Shimoda Y, Magloire V, Leite M, Kawashima T, Jensen TP, et al. A genetically encoded fluorescent sensor for in vivo imaging of GABA. Nat Methods. 2019;16(8):763-70.

682 Marvin JS, Borghuis BG, Tian L, Cichon J, Harnett MT, Akerboom J, et al. An optimized fluorescent probe for visualizing glutamate neurotransmission. Nat Methods. 2013;10(2):162-70.

683 Unger EK, Keller JP, Altermatt M, Liang R, Matsui A, Dong C, et al. Directed Evolution of a Selective and Sensitive Serotonin Sensor via Machine Learning. Cell. 2020;183(7):1986-2002.e26.

684 Nichols AL, Blumenfeld Z, Fan C, Luebbert L, Blom AEM, Cohen BN, et al. Fluorescence activation mechanism and imaging of drug permeation with new sensors for smoking-cessation ligands. eLife. 2022;11:e74648.

685 Muthusamy AK, Kim CH, Virgil SC, Knox HJ, Marvin JS, Nichols AL, et al. Three Mutations Convert the Selectivity of a Protein Sensor from Nicotinic Agonists to S-Methadone for Use in Cells, Organelles, and Biofluids. Journal of the American Chemical Society. 2022;144(19):8480-86.

686 Shimomura O, Johnson FH, Saiga Y. Extraction, purification and properties of aequorin, a bioluminescent protein from the luminous hydromedusan, Aequorea. J Cell Comp Physiol. 1962;59:223-39.

687 Prasher DC, Eckenrode VK, Ward WW, Prendergast FG, Cormier MJ. Primary structure of the Aequorea victoria green-fluorescent protein. Gene. 1992;111(2):229-33.

688 Wang S, Hazelrigg T. Implications for bcd mRNA localization from spatial distribution of exu protein in Drosophila oogenesis. Nature. 1994;369(6479):400-03.

689 Heim R, Cubitt AB, Tsien RY. Improved green fluorescence. Nature. 1995;373(6516):663-64.

690 Shaner NC, Steinbach PA, Tsien RY. A guide to choosing fluorescent proteins. Nat Methods. 2005;2(12):905-9.

691 Eng J, Bucher E, Hu Z, Zheng T, Gibbs SL, Chin K, et al. A framework for multiplex imaging optimization and reproducible analysis. Communications Biology. 2022;5(1):438.

692 Miyawaki A, Llopis J, Heim R, McCaffery JM, Adams JA, Ikura M, et al. Fluorescent indicators for Ca2+ based on green fluorescent proteins and calmodulin. Nature. 1997;388(6645):882-7.

693 Nakai J, Ohkura M, Imoto K. A high signal-to-noise Ca2+ probe composed of a single green fluorescent protein. Nature Biotechnology. 2001;19(2):137-41.

694 Tallini YN, Ohkura M, Choi BR, Ji G, Imoto K, Doran R, et al. Imaging cellular signals in the heart in vivo: Cardiac expression of the high-signal Ca2+ indicator GCaMP2. Proc Natl Acad Sci U S A. 2006;103(12):4753-8.

695 Dana H, Sun Y, Mohar B, Hulse BK, Kerlin AM, Hasseman JP, et al. High-performance calcium sensors for imaging activity in neuronal populations and microcompartments. Nature Methods. 2019;16(7):649-57.

696 Okumoto S. Imaging approach for monitoring cellular metabolites and ions using genetically encoded biosensors. Curr Opin Biotechnol. 2010;21(1):45-54.

697 Tian L, Hires SA, Mao T, Huber D, Chiappe ME, Chalasani SH, et al. Imaging neural activity in worms, flies and mice with improved GCaMP calcium indicators. Nature Methods. 2009;6(12):875-81.

698 Tsien RY. New calcium indicators and buffers with high selectivity against magnesium and protons: design, synthesis, and properties of prototype structures. Biochemistry. 1980;19:2396-404.

699 de Lorimier RM, Smith JJ, Dwyer MA, Looger LL, Sali KM, Paavola CD, et al. Construction of a fluorescent biosensor family. Protein Sci. 2002;11(11):2655-75.

700 Okumoto S, Looger LL, Micheva KD, Reimer RJ, Smith SJ, Frommer WB. Detection of glutamate release from neurons by genetically encoded surface-displayed FRET nanosensors. Proceedings of the National Academy of Sciences. 2005;102(24):8740-45.

701 Hires SA, Zhu Y, Tsien RY. Optical measurement of synaptic glutamate spillover and reuptake by linker optimized glutamate-sensitive fluorescent reporters. Proc Natl Acad Sci U S A. 2008;105(11):4411-6.

702 Förster T. Zwischenmolekulare Energiewanderung und Fluoreszenz. Annalen der Physik. 1948;437(1-2):55-75.

703 Lindenburg L, Merkx M. Engineering genetically encoded FRET sensors. Sensors (Basel). 2014;14(7):11691-713.

704 Kim H, Ju J, Lee HN, Chun H, Seong J. Genetically Encoded Biosensors Based on Fluorescent Proteins. Sensors (Basel). 2021;21(3).

705 Grynkiewicz G, Poenie M, Tsien RY. A new generation of Ca^{2+} indicators with greatly improved fluorescence properties. J Biol Chem. 1985;260:3440-50.

706 Nasu Y, Shen Y, Kramer L, Campbell RE. Structure- and mechanism-guided design of single fluorescent protein-based biosensors. Nat Chem Biol. 2021;17(5):509-18.

707 Sadoine M, Ishikawa Y, Kleist TJ, Wudick MM, Nakamura M, Grossmann G, et al. Designs, applications, and limitations of genetically encoded fluorescent sensors to explore plant biology. Plant Physiology. 2021;187(2):485-503.

708 Kostyuk AI, Demidovich AD, Kotova DA, Belousov VV, Bilan DS. Circularly Permuted Fluorescent Protein-Based Indicators: History, Principles, and Classification. Int J Mol Sci. 2019;20(17).

709 Moussawi K, Riegel A, Nair S, Kalivas PW. Extracellular glutamate: functional compartments operate in different concentration ranges. Front Syst Neurosci. 2011;5:94.

710 Kille S, Acevedo-Rocha CG, Parra LP, Zhang ZG, Opperman DJ, Reetz MT, et al. Reducing codon redundancy and screening effort of combinatorial protein libraries created by saturation mutagenesis. ACS synthetic biology. 2013;2(2):83-92.

711 Berntsson RP, Smits SH, Schmitt L, Slotboom DJ, Poolman B. A structural classification of substrate-binding proteins. FEBS Lett. 2010;584(12):2606-17.

712 Marvin JS, Scholl B, Wilson DE, Podgorski K, Kazemipour A, Muller JA, et al. Stability, affinity, and chromatic variants of the glutamate sensor iGluSnFR. Nat Methods. 2018;15(11):936-39.

713 Pédelacq JD, Cabantous S, Tran T, Terwilliger TC, Waldo GS. Engineering and characterization of a superfolder green fluorescent protein. Nat Biotechnol. 2006;24(1):79-88.

714 Aronson DE, Costantini LM, Snapp EL. Superfolder GFP is fluorescent in oxidizing environments when targeted via the Sec translocon. Traffic. 2011;12(5):543-8.

715 Lester HA, Xiao C, Srinivasan R, Son C, Miwa J, Pantoja R, et al. Nicotine is a Selective Pharmacological Chaperone of Acetylcholine Receptor Number and Stoichiometry. Implications for Drug Discovery. AAPS Journal. 2009;11:167-77.

716 Hetz C, Papa FR. The Unfolded Protein Response and Cell Fate Control. Molecular Cell. 2018;69(2):169-81.

717 Hernan MA, Takkouche B, Caamano-Isorna F, Gestal-Otero JJ. A meta-analysis of coffee drinking, cigarette smoking, and the risk of Parkinson's disease. Ann Neurol. 2002;52(3):276-84.

718 Stoeber M, Jullie D, Lobingier BT, Laeremans T, Steyaert J, Schiller PW, et al. A Genetically Encoded Biosensor Reveals Location Bias of Opioid Drug Action. Neuron. 2018;98(5):963-76.e5.

719 Govind AP, Vallejo YF, Stolz JR, Yan JZ, Swanson GT, Green WN. Selective and regulated trapping of nicotinic receptor weak base ligands and relevance to smoking cessation. eLife. 2017;6.

720 Beatty ZG, Muthusamy AK, Unger EK, Dougherty DA, Tian L, Looger LL, et al. Fluorescence Screens for Identifying Central Nervous System-Acting Drug-Biosensor Pairs for Subcellular and Supracellular Pharmacokinetics. Bio Protoc. 2022;12(22).

721 Dzubay JA, Jahr CE. The concentration of synaptically released glutamate outside of the climbing fiber-Purkinje cell synaptic cleft. J Neurosci. 1999;19(13):5265-74.

722 Sutcliffe JG. Nucleotide sequence of the ampicillin resistance gene of Escherichia coli plasmid pBR322. Proc Natl Acad Sci U S A. 1978;75(8):3737-41.

723 Dower WJ, Miller JF, Ragsdale CW. High efficiency transformation of E. coli by high voltage electroporation. Nucleic Acids Res. 1988;16(13):6127-45.

724 Sezonov G, Joseleau-Petit D, D'Ari R. Escherichia coli physiology in Luria-Bertani broth. J Bacteriol. 2007;189(23):8746-9.

725 Chang KJ, Jacobs S, Cuatrecasas P. Quantitative aspects of hormone-receptor interactions of high affinity. Effect of receptor concentration and measurement of dissociation constants of labeled and unlabeled hormones. Biochim Biophys Acta. 1975;406(2):294-303.

726 Abele R, Keinanen K, Madden DR. Agonist-induced isomerization in a glutamate receptor ligand-binding domain. A kinetic and mutagenetic analysis. J Biol Chem. 2000;275(28):21355-63.

727 Oswald C, Smits SH, Hoing M, Sohn-Bosser L, Dupont L, Le Rudulier D, et al. Crystal structures of the choline/acetylcholine substrate-binding protein ChoX from Sinorhizobium meliloti in the liganded and unliganded-closed states. J Biol Chem. 2008;283(47):32848-59.

728 Ma JC, Dougherty DA. The cation-p interaction. Chem Rev. 1997;97(5):1303-24.

729 Reetz MT, Carballeira JD. Iterative saturation mutagenesis (ISM) for rapid directed evolution of functional enzymes. Nature Protocols. 2007;2(4):891-903.

730 Paul N, Shum J, Le T. Hot Start PCR. In: King N, editor RT-PCR Protocols: Second Edition. Totowa, NJ: Humana Press; 2010. p. 301-18.

731 Lu L, Patel H, Bissler JJ. Optimizing DpnI digestion conditions to detect replicated DNA. Biotechniques. 2002;33(2):316-8.

732 Studier FW. Protein production by auto-induction in high-density shaking cultures. Protein Expression and Purification. 2005;41(1):207-34.

733 Hartwig A. Role of magnesium in genomic stability. Mutat Res. 2001;475(1-2):113-21.

734 Porath J. Immobilized metal ion affinity chromatography. Protein Expression and Purification. 1992;3(4):263-81.

735 Grolier J-PE, del Río JM. Isothermal titration calorimetry: A thermodynamic interpretation of measurements. The Journal of Chemical Thermodynamics. 2012;55:193-202.

736 Finlay DB, Duffull SB, Glass M. 100 years of modelling ligand-receptor binding and response: A focus on GPCRs. Br J Pharmacol. 2020;177(7):1472-84.

737 Chance B. Rapid and Sensitive Spectrophotometry. I. The Accelerated and Stopped-Flow Methods for the Measurement of the Reaction Kinetics and Spectra of Unstable Compounds in the Visible Region of the Spectrum. Review of Scientific Instruments. 1951;22(8):619-27.

738 Russo G, Unkauf T, Meier D, Wenzel EV, Langreder N, Schneider K-T, et al. In vitro evolution of myc-tag antibodies: in-depth specificity and affinity analysis of Myc1-9E10 and Hyper-Myc. Biological chemistry. 2022;403(5-6):479-94.

739 Wöhner M, Pinter T, Bönelt P, Hagelkruys A, Kostanova-Poliakova D, Stadlmann J, et al. The Xbp1-regulated transcription factor Mist1 restricts antibody secretion by restraining Blimp1 expression in plasma cells. Frontiers in Immunology. 2022;13.

740 Quan J, Tian J. Circular polymerase extension cloning of complex gene libraries and pathways. PLoS One. 2009;4(7):e6441.

741 Güttler T, Madl T, Neumann P, Deichsel D, Corsini L, Monecke T, et al. NES consensus redefined by structures of PKI-type and Rev-type nuclear export signals bound to CRM1. Nature structural & molecular biology. 2010;17(11):1367-76.

742 Kalderon D, Roberts BL, Richardson WD, Smith AE. A short amino acid sequence able to specify nuclear location. Cell. 1984;39(3):499-509.

743 Gould SG, Keller GA, Subramani S. Identification of a peroxisomal targeting signal at the carboxy terminus of firefly luciferase. Journal of Cell Biology. 1987;105(6):2923-31.

744 Hüttemann M, Schmidt TR, Grossman LI. A third isoform of cytochrome c oxidase subunit VIII is present in mammals. Gene. 2003;312:95-102.

745 Gibson DG, Young L, Chuang RY, Venter JC, Hutchison CA, 3rd, Smith HO. Enzymatic assembly of DNA molecules up to several hundred kilobases. Nat Methods. 2009;6(5):343-5.

746 Qasba PK, Ramakrishnan B, Boeggeman E. Structure and function of beta -1,4-galactosyltransferase. Curr Drug Targets. 2008;9(4):292-309.

747 Kuma A, Matsui M, Mizushima N. LC3, an autophagosome marker, can be incorporated into protein aggregates independent of autophagy: caution in the interpretation of LC3 localization. Autophagy. 2007;3(4):323-8.

748 Flores LR, Keeling MC, Zhang X, Sliogeryte K, Gavara N. Lifeact-TagGFP2 alters F-actin organization, cellular morphology and biophysical behaviour. Scientific reports. 2019;9(1):3241.

749 Masters JR. HeLa cells 50 years on: the good, the bad and the ugly. Nature Reviews Cancer. 2002;2(4):315-19.

750 Sato S, Rancourt A, Sato Y, Satoh MS. Single-cell lineage tracking analysis reveals that an established cell line comprises putative cancer stem cells and their heterogeneous progeny. Scientific reports. 2016;6:23328.

751 James MB, Giorgio TD. Nuclear-associated plasmid, but not cell-associated plasmid, is correlated with transgene expression in cultured mammalian cells. Mol Ther. 2000;1(4):339-46.

752 Tremblay RG, Sikorska M, Sandhu JK, Lanthier P, Ribecco-Lutkiewicz M, Bani-Yaghoub M. Differentiation of mouse Neuro 2A cells into dopamine neurons. J Neurosci Methods. 2010;186(1):60-7.

753 van Zoelen EJ, Twardzik DR, van Oostwaard TM, van der Saag PT, de Laat SW, Todaro GJ. Neuroblastoma cells produce transforming growth factors during exponential growth in a defined hormone-free medium. Proc Natl Acad Sci U S A. 1984;81(13):4085-9.

754 Lulevich V, Zimmer CC, Hong HS, Jin LW, Liu GY. Single-cell mechanics provides a sensitive and quantitative means for probing amyloid-beta peptide and neuronal cell interactions. Proc Natl Acad Sci U S A. 2010;107(31):13872-7.

755 Biedler JL, Roffler-Tarlov S, Schachner M, Freedman LS. Multiple neurotransmitter synthesis by human neuroblastoma cell lines and clones. Cancer Res. 1978;38(11 Pt 1):3751-7.

756 Kovalevich J, Langford D. Considerations for the use of SH-SY5Y neuroblastoma cells in neurobiology. Methods Mol Biol. 2013;1078:9-21.

757 Feles S, Overath C, Reichardt S, Diegeler S, Schmitz C, Kronenberg J, et al. Streamlining Culture Conditions for the Neuroblastoma Cell Line SH-SY5Y: A Prerequisite for Functional Studies. Methods Protoc. 2022;5(4).

758 Hughes P, Marshall D, Reid Y, Parkes H, Gelber C. The costs of using unauthenticated, over-passaged cell lines: how much more data do we need? Biotechniques. 2007;43(5):575, 77-8, 81-2 passim.

759 Ohki EC, Tilkins ML, Ciccarone VC, Price PJ. Improving the transfection efficiency of post-mitotic neurons. J Neurosci Methods. 2001;112(2):95-9.

760 Zinn E, Vandenberghe LH. Adeno-associated virus: fit to serve. Curr Opin Virol. 2014;8:90-7.

761 Howley PM, Knipe DM. Fields virology: Emerging viruses. Lippincott Williams & Wilkins; 2020.

762 Nathanson JL, Yanagawa Y, Obata K, Callaway EM. Preferential labeling of inhibitory and excitatory cortical neurons by endogenous tropism of adeno-associated virus and lentivirus vectors. Neuroscience. 2009;161(2):441-50.

763 Zanta-Boussif MA, Charrier S, Brice-Ouzet A, Martin S, Opolon P, Thrasher AJ, et al. Validation of a mutated PRE sequence allowing high and sustained transgene expression while abrogating WHV-X protein synthesis: application to the gene therapy of WAS. Gene Therapy. 2009;16(5):605-19.

764 Li SP, Feng JJ, Wang HG, Wang XF, Lv ZJ. [The effects of SV40 PolyA sequence and its AATAAA signal on upstream GFP gene expression and transcription termination]. Yi Chuan. 2012;34(1):113-9.

765 Tabor S. DNA Ligases. Current Protocols in Molecular Biology. 1989;8(1):3.14.1-3.14.4.

766 MILLER LK, IVEAVER F. ExPERIMENT I. JOURNAL OF APPLIED BEHAVIOR ANALYSIS. 1976;9:289-300.

767 Gray JT, Zolotukhin S. Design and construction of functional AAV vectors. Methods Mol Biol. 2011;807:25-46.

768 Challis RC, Ravindra Kumar S, Chan KY, Challis C, Beadle K, Jang MJ, et al. Systemic AAV vectors for widespread and targeted gene delivery in rodents. Nat Protoc. 2019;14(2):379-414.

769 Forsayeth JR, Bankiewicz KS. AAV9: Over the Fence and Into the Woods …. Molecular Therapy. 2011;19(6):1006-07.

770 DuBridge RB, Tang P, Hsia HC, Leong PM, Miller JH, Calos MP. Analysis of mutation in human cells by using an Epstein-Barr virus shuttle system. Mol Cell Biol. 1987;7(1):379-87.

771 Tan E, Chin CSH, Lim ZFS, Ng SK. HEK293 Cell Line as a Platform to Produce Recombinant Proteins and Viral Vectors. Front Bioeng Biotechnol. 2021;9:796991.

772 Lan WC, Lan WH, Chan CP, Hsieh CC, Chang MC, Jeng JH. The effects of extracellular citric acid acidosis on the viability, cellular adhesion capacity and protein synthesis of cultured human gingival fibroblasts. Aust Dent J. 1999;44(2):123-30.

773 Guo P, El-Gohary Y, Prasadan K, Shiota C, Xiao X, Wiersch J, et al. Rapid and simplified purification of recombinant adeno-associated virus. J Virol Methods. 2012;183(2):139-46.

774 Wittwer CT, Herrmann MG, Moss AA, Rasmussen RP. Continuous fluorescence monitoring of rapid cycle DNA amplification. Biotechniques. 1997;22(1):130-38.

775 Seibenhener ML, Wooten MW. Isolation and culture of hippocampal neurons from prenatal mice. J Vis Exp. 2012(65).

776 Oorschot D. Effect of fluorodeoxyuridine on neurons and non-neuronal cells in cerebral explants. Experimental brain research. 1989;78:132-38.

777 Francis GL. Albumin and mammalian cell culture: implications for biotechnology applications. Cytotechnology. 2010;62(1):1-16.

778 Barnett LM, Hughes TE, Drobizhev M. Deciphering the molecular mechanism responsible for GCaMP6m's Ca^{2+}-dependent change in fluorescence. PLoS One. 2017;12(2):e0170934.

779 Streisinger G, Walker C, Dower N, Knauber D, Singer F. Production of clones of homozygous diploid zebra fish (Brachydanio rerio). Nature. 1981;291(5813):293-96.

780 Fontana BD, Mezzomo NJ, Kalueff AV, Rosemberg DB. The developing utility of zebrafish models of neurological and neuropsychiatric disorders: A critical review. Exp Neurol. 2018;299(Pt A):157-71.

781 Basnet RM, Zizioli D, Taweedet S, Finazzi D, Memo M. Zebrafish Larvae as a Behavioral Model in Neuropharmacology. Biomedicines. 2019;7(1).

782 Kimmel CB, Ballard WW, Kimmel SR, Ullmann B, Schilling TF. Stages of embryonic development of the zebrafish. Dev Dyn. 1995;203(3):253-310.

783 Hernandez RE, Galitan L, Cameron J, Goodwin N, Ramakrishnan L. Delay of Initial Feeding of Zebrafish Larvae Until 8 Days Postfertilization Has No Impact on Survival or Growth Through the Juvenile Stage. Zebrafish. 2018;15(5):515-18.

784 Lister JA, Robertson CP, Lepage T, Johnson SL, Raible DW. nacre encodes a zebrafish microphthalmia-related protein that regulates neural-crest-derived pigment cell fate. Development. 1999;126(17):3757-67.

785 White RM, Sessa A, Burke C, Bowman T, LeBlanc J, Ceol C, et al. Transparent adult zebrafish as a tool for in vivo transplantation analysis. Cell stem cell. 2008;2(2):183-9.

786 Karlsson J, von Hofsten J, Olsson P-E. Generating Transparent Zebrafish: A Refined Method to Improve Detection of Gene Expression During Embryonic Development. Marine Biotechnology. 2001;3(6):522-27.

787 Bruzzone M, Chiarello E, Albanesi M, Miletto Petrazzini ME, Megighian A, Lodovichi C, et al. Whole brain functional recordings at cellular resolution in zebrafish larvae with 3D scanning multiphoton microscopy. Scientific reports. 2021;11(1):11048.

788 the mouse genome. Nature. 2002;420(6915):510-10.

789 Postlethwait JH, Woods IG, Ngo-Hazelett P, Yan YL, Kelly PD, Chu F, et al. Zebrafish comparative genomics and the origins of vertebrate chromosomes. Genome Res. 2000;10(12):1890-902.

790 Nestler EJ, Hyman SE. Animal models of neuropsychiatric disorders. Nat Neurosci. 2010;13(10):1161-9.

791 Kaslin J, Panula P. Comparative anatomy of the histaminergic and other aminergic systems in zebrafish (Danio rerio). J Comp Neurol. 2001;440(4):342-77.

792 Panula P, Sallinen V, Sundvik M, Kolehmainen J, Torkko V, Tiittula A, et al. Modulatory neurotransmitter systems and behavior: towards zebrafish models of neurodegenerative diseases. Zebrafish. 2006;3(2):235-47.

793 Amo R, Aizawa H, Takahoko M, Kobayashi M, Takahashi R, Aoki T, et al. Identification of the zebrafish ventral habenula as a homolog of the mammalian lateral habenula. J Neurosci. 2010;30(4):1566-74.

794 deCarvalho TN, Subedi A, Rock J, Harfe BD, Thisse C, Thisse B, et al. Neurotransmitter map of the asymmetric dorsal habenular nuclei of zebrafish. Genesis. 2014;52(6):636-55.

795 Oikonomou G, Altermatt M, Zhang RW, Coughlin GM, Montz C, Gradinaru V, et al. The Serotonergic Raphe Promote Sleep in Zebrafish and Mice. Neuron. 2019;103(4):686-701.e8.

796 MacRae CA, Peterson RT. Zebrafish as tools for drug discovery. Nat Rev Drug Discov. 2015;14(10):721-31.

797 Howe K, Clark MD, Torroja CF, Torrance J, Berthelot C, Muffato M, et al. The zebrafish reference genome sequence and its relationship to the human genome. Nature. 2013;496(7446):498-503.

798 de Abreu MS, Friend AJ, Demin KA, Amstislavskaya TG, Bao W, Kalueff AV. Zebrafish models: do we have valid paradigms for depression? J Pharmacol Toxicol Methods. 2018;94(Pt 2):16-22.

799 Piato Â L, Capiotti KM, Tamborski AR, Oses JP, Barcellos LJ, Bogo MR, et al. Unpredictable chronic stress model in zebrafish (Danio rerio): behavioral and physiological responses. Prog Neuropsychopharmacol Biol Psychiatry. 2011;35(2):561-7.

800 Chakravarty S, Reddy BR, Sudhakar SR, Saxena S, Das T, Meghah V, et al. Chronic unpredictable stress (CUS)-induced anxiety and related mood disorders in a zebrafish model: altered brain proteome profile implicates mitochondrial dysfunction. PLoS One. 2013;8(5):e63302.

801 Pittman JT, Lott CS. Startle response memory and hippocampal changes in adult zebrafish pharmacologically-induced to exhibit anxiety/depression-like behaviors. Physiol Behav. 2014;123:174-9.

802 Griffiths B, Schoonheim P, Ziv L, Voelker L, Baier H, Gahtan E. A zebrafish model of glucocorticoid resistance shows serotonergic modulation of the stress response. Frontiers in behavioral neuroscience. 2012;6.

803 Ziv L, Muto A, Schoonheim PJ, Meijsing SH, Strasser D, Ingraham HA, et al. An affective disorder in zebrafish with mutation of the glucocorticoid receptor. Mol Psychiatry. 2013;18(6):681-91.

804 Wang S, Duan M, Guan K, Zhou X, Zheng M, Shi X, et al. Developmental neurotoxicity of reserpine exposure in zebrafish larvae (Danio rerio). Comp Biochem Physiol C Toxicol Pharmacol. 2019;223:115-23.

805 McEwen BS. Brain on stress: how the social environment gets under the skin. Proc Natl Acad Sci U S A. 2012;109 Suppl 2(Suppl 2):17180-5.

806 de Kloet ER, Joëls M, Holsboer F. Stress and the brain: from adaptation to disease. Nat Rev Neurosci. 2005;6(6):463-75.

807 Pavlidis M, Digka N, Theodoridi A, Campo A, Barsakis K, Skouradakis G, et al. Husbandry of zebrafish, Danio rerio, and the cortisol stress response. Zebrafish. 2013;10(4):524-31.

808 Pavlidis M, Theodoridi A, Tsalafouta A. Neuroendocrine regulation of the stress response in adult zebrafish, Danio rerio. Prog Neuropsychopharmacol Biol Psychiatry. 2015;60:121-31.

809 Hirschfeld RM. The Comorbidity of Major Depression and Anxiety Disorders: Recognition and Management in Primary Care. Prim Care Companion J Clin Psychiatry. 2001;3(6):244-54.

810 Wu Z, Fang Y. Comorbidity of depressive and anxiety disorders: challenges in diagnosis and assessment. Shanghai Arch Psychiatry. 2014;26(4):227-31.

811 Schnörr SJ, Steenbergen PJ, Richardson MK, Champagne DL. Measuring thigmotaxis in larval zebrafish. Behav Brain Res. 2012;228(2):367-74.

812 Giacomini ACVV, Abreu MS, Giacomini LV, Siebel AM, Zimerman FF, Rambo CL, et al. Fluoxetine and diazepam acutely modulate stress induced-behavior. Behavioural Brain Research. 2016;296:301-10.

813 Marcon M, Herrmann AP, Mocelin R, Rambo CL, Koakoski G, Abreu MS, et al. Prevention of unpredictable chronic stress-related phenomena in zebrafish exposed to bromazepam, fluoxetine and nortriptyline. Psychopharmacology (Berl). 2016;233(21-22):3815-24.

814 Egan RJ, Bergner CL, Hart PC, Cachat JM, Canavello PR, Elegante MF, et al. Understanding behavioral and physiological phenotypes of stress and anxiety in zebrafish. Behav Brain Res. 2009;205(1):38-44.

815 Demin KA, Kolesnikova TO, Galstyan DS, Krotova NA, Ilyin NP, Derzhavina KA, et al. Modulation of behavioral and neurochemical responses of adult zebrafish by fluoxetine, eicosapentaenoic acid and lipopolysaccharide in the prolonged chronic unpredictable stress model. Scientific reports. 2021;11(1):14289.

816 Suen MF, Chan WS, Hung KW, Chen YF, Mo ZX, Yung KK. Assessments of the effects of nicotine and ketamine using tyrosine hydroxylase-green fluorescent protein transgenic zebrafish as biosensors. Biosens Bioelectron. 2013;42:177-85.

817 Mellon RD, Simone AF, Rappaport BA. Use of anesthetic agents in neonates and young children. Anesth Analg. 2007;104(3):509-20.

818 Dong C, Anand KJ. Developmental neurotoxicity of ketamine in pediatric clinical use. Toxicol Lett. 2013;220(1):53-60.

819 Yan J, Jiang H. Dual effects of ketamine: neurotoxicity versus neuroprotection in anesthesia for the developing brain. J Neurosurg Anesthesiol. 2014;26(2):155-60.

820 Kanungo J, Cuevas E, Ali SF, Paule MG. Ketamine induces motor neuron toxicity and alters neurogenic and proneural gene expression in zebrafish. J Appl Toxicol. 2013;33(6):410-7.

821 Félix LM, Antunes LM, Coimbra AM, Valentim AM. Behavioral alterations of zebrafish larvae after early embryonic exposure to ketamine. Psychopharmacology (Berl). 2017;234(4):549-58.

822 Félix LM, Vidal AM, Serafim C, Valentim AM, Antunes LM, Monteiro SM, et al. Ketamine induction of p53-dependent apoptosis and oxidative stress in zebrafish (Danio rerio) embryos. Chemosphere. 2018;201:730-39.

823 Robinson B, Dumas M, Gu Q, Kanungo J. N-acetylcysteine prevents ketamine-induced adverse effects on development, heart rate and monoaminergic neurons in zebrafish. Neurosci Lett. 2018;682:56-61.

824 Félix L, Coimbra AM, Valentim AM, Antunes L. Review on the use of zebrafish embryos to study the effects of anesthetics during early development. Crit Rev Toxicol. 2019;49(4):357-70.

825 Tombari RJ, Mundy PC, Morales KM, Dunlap LE, Olson DE, Lein PJ. Developmental Neurotoxicity Screen of Psychedelics and Other Drugs of Abuse in Larval Zebrafish (Danio rerio). ACS Chem Neurosci. 2023;14(5):875-84.

826 Bowdle TA, Radant AD, Cowley DS, Kharasch ED, Strassman RJ, Roy-Byrne PP. Psychedelic effects of ketamine in healthy volunteers: relationship to steady-state plasma concentrations. Anesthesiology. 1998;88(1):82-8.

827 Takahashi A, Miczek KA. Neurogenetics of aggressive behavior: studies in rodents. Current topics in behavioral neurosciences. 2014;17:3-44.

828 Newman EL, Terunuma M, Wang TL, Hewage N, Bicakci MB, Moss SJ, et al. A Role for Prefrontal Cortical NMDA Receptors in Murine Alcohol-Heightened Aggression. Neuropsychopharmacology. 2018;43(6):1224-34.

829 Michelotti P, Quadros VA, Pereira ME, Rosemberg DB. Ketamine modulates aggressive behavior in adult zebrafish. Neuroscience Letters. 2018;684:164-68.

830 De Campos EG, Bruni AT, De Martinis BS. Ketamine induces anxiolytic effects in adult zebrafish: A multivariate statistics approach. Behav Brain Res. 2015;292:537-46.

831 Michelotti P, Franscescon F, Müller TE, Rosemberg DB, Pereira ME. Ketamine acutely impairs memory consolidation and repeated exposure promotes stereotyped behavior without changing anxiety- and aggression-like parameters in adult zebrafish. Physiology & Behavior. 2022;247:113708.

832 Riehl R, Kyzar E, Allain A, Green J, Hook M, Monnig L, et al. Behavioral and physiological effects of acute ketamine exposure in adult zebrafish. Neurotoxicol Teratol. 2011;33(6):658-67.

833 Pittman J, Hylton A. Behavioral, endocrine, and neuronal alterations in zebrafish (Danio rerio) following sub-chronic coadministration of fluoxetine and ketamine. Pharmacol Biochem Behav. 2015;139 Pt B:158-62.

834 Zakhary SM, Ayubcha D, Ansari F, Kamran K, Karim M, Leheste JR, et al. A behavioral and molecular analysis of ketamine in zebrafish. Synapse. 2011;65(2):160-7.

835 Canever L, Oliveira L, D'Altoé de Luca R, Correa PT, de BFD, Matos MP, et al. A rodent model of schizophrenia reveals increase in creatine kinase activity with associated behavior changes. Oxid Med Cell Longev. 2010;3(6):421-7.

836 Andalman AS, Burns VM, Lovett-Barron M, Broxton M, Poole B, Yang SJ, et al. Neuronal Dynamics Regulating Brain and Behavioral State Transitions. Cell. 2019;177(4):970-85.e20.

837 Huisken J, Swoger J, Del Bene F, Wittbrodt J, Stelzer EH. Optical sectioning deep inside live embryos by selective plane illumination microscopy. Science. 2004;305(5686):1007-9.

838 Panier T, Romano S, Olive R, Pietri T, Sumbre G, Candelier R, et al. Fast functional imaging of multiple brain regions in intact zebrafish larvae using Selective Plane Illumination Microscopy. Front Neural Circuits. 2013;7.

839 Ahrens MB, Li JM, Orger MB, Robson DN, Schier AF, Engert F, et al. Brain-wide neuronal dynamics during motor adaptation in zebrafish. Nature. 2012;485(7399):471-7.

840 Stevens FC. Calmodulin: an introduction. Canadian Journal of Biochemistry and Cell Biology. 1983;61(8):906-10.

841 Akerboom J, Rivera JD, Guilbe MM, Malavé EC, Hernandez HH, Tian L, et al. Crystal structures of the GCaMP calcium sensor reveal the mechanism of fluorescence signal change and aid rational design. J Biol Chem. 2009;284(10):6455-64.

842 Bagur R, Hajnóczky G. Intracellular Ca(2+) Sensing: Its Role in Calcium Homeostasis and Signaling. Mol Cell. 2017;66(6):780-88.

843 Ahrens MB, Orger MB, Robson DN, Li JM, Keller PJ. Whole-brain functional imaging at cellular resolution using light-sheet microscopy. Nature Methods. 2013;10(5):413-20.

844 Cong L, Wang Z, Chai Y, Hang W, Shang C, Yang W, et al. Rapid whole brain imaging of neural activity in freely behaving larval zebrafish (Danio rerio). eLife. 2017;6:e28158.

845 Burgstaller J, Hindinger E, Donovan J, Dal Maschio M, Kist AM, Gesierich B, et al. Light-sheet imaging and graph analysis of antidepressant action in the larval zebrafish brain network. bioRxiv. 2019:618843.

846 Murphy M, Brown G, Wallin C, Tatusova T, Pruitt K, Murphy T, et al. Gene Help: Integrated Access to Genes of Genomes in the Reference Sequence Collection. NCBI: Bethesda, MD; 2022.

847 Park HC, Kim CH, Bae YK, Yeo SY, Kim SH, Hong SK, et al. Analysis of upstream elements in the HuC promoter leads to the establishment of transgenic zebrafish with fluorescent neurons. Dev Biol. 2000;227(2):279-93.

848 Lee DA, Andreev A, Truong TV, Chen A, Hill AJ, Oikonomou G, et al. Genetic and neuronal regulation of sleep by neuropeptide VF. eLife. 2017;6.

849 Alexaki A, Kames J, Holcomb DD, Athey J, Santana-Quintero LV, Lam PVN, et al. Codon and Codon-Pair Usage Tables (CoCoPUTs): Facilitating Genetic Variation Analyses and Recombinant Gene Design. Journal of Molecular Biology. 2019;431(13):2434-41.

850 Horstick EJ, Jordan DC, Bergeron SA, Tabor KM, Serpe M, Feldman B, et al. Increased functional protein expression using nucleotide sequence features enriched in highly expressed genes in zebrafish. Nucleic Acids Research. 2015;43(7):e48-e48.

851 Freeman J, Vladimirov N, Kawashima T, Mu Y, Sofroniew NJ, Bennett DV, et al. Mapping brain activity at scale with cluster computing. Nat Methods. 2014;11(9):941-50.

852 Kawakami K. Transposon tools and methods in zebrafish. Dev Dyn. 2005;234(2):244-54.

853 Kawakami K. Tol2: a versatile gene transfer vector in vertebrates. Genome Biology. 2007;8(1):S7.

854 Mountford PS, Smith AG. Internal ribosome entry sites and dicistronic RNAs in mammalian transgenesis. Trends in Genetics. 1995;11(5):179-84.

855 Fernley H. The Enzymes. Mammalian alkaline phosphatase. 1971;4:417-47.

856 Clark KJ, Urban MD, Skuster KJ, Ekker SC. Transgenic zebrafish using transposable elements. Methods Cell Biol. 2011;104:137-49.

857 E3 medium (for zebrafish embryos). Cold Spring Harbor protocols. 2011;2011(10):pdb.rec66449.

858 Williams SY, Renquist BJ. High Throughput Danio Rerio Energy Expenditure Assay. J Vis Exp. 2016(107):e53297.

859 Aoyama Y, Moriya N, Tanaka S, Taniguchi T, Hosokawa H, Maegawa S. A Novel Method for Rearing Zebrafish by Using Freshwater Rotifers (Brachionus calyciflorus). Zebrafish. 2015;12(4):288-95.

860 Kossack ME, Draper BW. Genetic regulation of sex determination and maintenance in zebrafish (Danio rerio). Curr Top Dev Biol. 2019;134:119-49.

861 Stuart GW, McMurray JV, Westerfield M. Replication, integration and stable germ-line transmission of foreign sequences injected into early zebrafish embryos. Development. 1988;103(2):403-12.

862 Li Z, Ptak D, Zhang L, Walls EK, Zhong W, Leung YF. Phenylthiourea specifically reduces zebrafish eye size. PLoS One. 2012;7(6):e40132.

863 Keomanee-Dizon K, Fraser SE, Truong TV. A versatile, multi-laser twin-microscope system for light-sheet imaging. Review of Scientific Instruments. 2020;91(5):053703.

864 Andreev A, Vasnarungruengkul P, Wagenaar DA, Prober DA. Open-Source Thermometer, Temperature Controller, and Light Meter for Use in Animal Facilities and During Experiments. bioRxiv. 2021:2021.05.18.444705.

865 Antinucci P, Hindges R. A crystal-clear zebrafish for in vivo imaging. Scientific reports. 2016;6(1):29490.

866 Randlett O, Wee CL, Naumann EA, Nnaemeka O, Schoppik D, Fitzgerald JE, et al. Whole-brain activity mapping onto a zebrafish brain atlas. Nat Methods. 2015;12(11):1039-46.

867 Gierten J, Pylatiuk C, Hammouda OT, Schock C, Stegmaier J, Wittbrodt J, et al. Automated high-throughput heartbeat quantification in medaka and zebrafish embryos under physiological conditions. Scientific reports. 2020;10(1):2046.

868 Swinburne IA, Mosaliganti KR, Green AA, Megason SG. Improved Long-Term Imaging of Embryos with Genetically Encoded α-Bungarotoxin. PLoS One. 2015;10(8):e0134005.

869 Kämmer N, Erdinger L, Braunbeck T. The onset of active gill respiration in post-embryonic zebrafish (Danio rerio) larvae triggers an increased sensitivity to neurotoxic compounds. Aquat Toxicol. 2022;249:106240.

870 Bacqué-Cazenave J, Bharatiya R, Barrière G, Delbecque JP, Bouguiyoud N, Di Giovanni G, et al. Serotonin in Animal Cognition and Behavior. Int J Mol Sci. 2020;21(5).

871 Moncrieff J, Cooper RE, Stockmann T, Amendola S, Hengartner MP, Horowitz MA. The serotonin theory of depression: a systematic umbrella review of the evidence. Molecular Psychiatry. 2022.

872 Sun N, Qin YJ, Xu C, Xia T, Du ZW, Zheng LP, et al. Design of fast-onset antidepressant by dissociating SERT from nNOS in the DRN. Science. 2022;378(6618):390-98.

873 Senese NB, Rasenick MM. Antidepressants produce persistent Gα_s associated signaling changes in lipid rafts following drug withdrawal. Molecular Pharmacology. 2021:MOLPHARM-AR-2020-000226.

874 Sucic S, El-Kasaby A, Kudlacek O, Sarker S, Sitte HH, Marin P, et al. The serotonin transporter is an exclusive client of the coat protein complex II (COPII) component SEC24C. J Biol Chem. 2011;286(18):16482-90.

875 Bismuth-Evenzal Y, Roz N, Gurwitz D, Rehavi M. N-methyl-citalopram: A quaternary selective serotonin reuptake inhibitor. Biochem Pharmacol. 2010;80(10):1546-52.

876 Arriza JL, Fairman WA, Wadiche JI, Murdoch GH, Kavanaugh MP, Amara SG. Functional comparisons of three glutamate transporter subtypes cloned from human motor cortex. The Journal of Neuroscience. 1994;14(9):5559-69.
877 Cao Y, Li M, Mager S, Lester HA. Amino acid residues that control pH modulation of transport-associated current in mammalian serotonin transporters. J Neurosci. 1998;18(19):7739-49.
878 Mager S, Min C, Henry DJ, Chavkin C, Hoffman BJ, Davidson N, et al. Conducting states of a mammalian serotonin transporter. Neuron. 1994;12(4):845-59.
879 Williamson JD, Cox P. Use of a New Buffer in the Culture of Animal Cells. Journal of General Virology. 1968;2(2):309-12.
880 Pike S, Matthes MS, McSteen P, Gassmann W. Using Xenopus laevis Oocytes to Functionally Characterize Plant Transporters. Curr Protoc Plant Biol. 2019;4(1):e20087.
881 O'Connor CM, Smith LD. Inhibition of oocyte maturation by theophylline: Possible mechanism of action. Developmental Biology. 1976;52(2):318-22.
882 Yu H, Dickson EJ, Jung SR, Koh DS, Hille B. High membrane permeability for melatonin. J Gen Physiol. 2016;147(1):63-76.
883 Kapoor R, Peyear TA, Koeppe RE, 2nd, Andersen OS. Antidepressants are modifiers of lipid bilayer properties. J Gen Physiol. 2019;151(3):342-56.
884 Crank J. The Mathematics of Diffusion. Clarendon Press: Oxford, UK; 1975.
885 Mateus A, Matsson P, Artursson P. Rapid Measurement of Intracellular Unbound Drug Concentrations. Molecular pharmaceutics. 2013;10(6):2467-78.
886 Alberts B, Bray D, Lewis J, Morgan D, Raff M, Roberts K, et al. The Molecular Biology of the Cell. Garland Science: New York; 2015.
887 Mateus A, Treyer A, Wegler C, Karlgren M, Matsson P, Artursson P. Intracellular drug bioavailability: a new predictor of system dependent drug disposition. Scientific reports. 2017;7:43047.
888 Zeisel SH, Epstein MF, Wurtman RJ. Elevated choline concentration in neonatal plasma. Life Sci. 1980;26(21):1827-31.
889 Schapiro MB, Atack JR, Hanin I, May C, Haxby JV, Rapoport SI. Lumbar Cerebrospinal Fluid Choline in Healthy Aging and in Down's Syndrome. Archives of Neurology. 1990;47(9):977-80.
890 Vargas HM, Jenden DJ. Elevation of cerebrospinal fluid choline levels by nicotinamide involves the enzymatic formation of N1-methylnicotinamide in brain tissue. Life Sci. 1996;58(22):1995-2002.
891 Armstrong D, Lester HA. The kinetics of tubocarine action and restricted diffusion within the synaptic cleft. Journal of Physiology. 1979;294:365-86.
892 Loryan I, Friden M, Hammarlund-Udenaes M. The brain slice method for studying drug distribution in the CNS. Fluids and barriers of the CNS. 2013;10(1):6.
893 Mateus A, Matsson P, Artursson P. A high-throughput cell-based method to predict the unbound drug fraction in the brain. J Med Chem. 2014;57(7):3005-10.
894 Scheepers GH, Lycklama ANJA, Poolman B. An updated structural classification of substrate-binding proteins. FEBS Lett. 2016;590(23):4393-401.
895 Nguyen PT, Lai JY, Lee AT, Kaiser JT, Rees DC. Noncanonical role for the binding protein in substrate uptake by the MetNI methionine ATP Binding Cassette (ABC) transporter. Proc Natl Acad Sci U S A. 2018;115(45):E10596-e604.

896 Tucker KR, Block ER, Levitan ES. Action potentials and amphetamine release antipsychotic drug from dopamine neuron synaptic VMAT vesicles. Proc Natl Acad Sci U S A. 2015;112(32):E4485-94.

897 Trapp S, Rosania GR, Horobin RW, Kornhuber J. Quantitative modeling of selective lysosomal targeting for drug design. Eur Biophys J. 2008;37(8):1317-28.

898 Karson CN, Newton JE, Mohanakrishnan P, Sprigg J, Komoroski RA. Fluoxetine and trifluoperazine in human brain: a 19F-nuclear magnetic resonance spectroscopy study. Psychiatry Res. 1992;45(2):95-104.

899 Renshaw PF, Guimaraes AR, Fava M, Rosenbaum JF, Pearlman JD, Flood JG, et al. Accumulation of fluoxetine and norfluoxetine in human brain during therapeutic administration. Am J Psychiatry. 1992;149(11):1592-4.

900 Bolo NR, Hodé Y, Nédélec JF, Lainé E, Wagner G, Macher JP. Brain pharmacokinetics and tissue distribution in vivo of fluvoxamine and fluoxetine by fluorine magnetic resonance spectroscopy. Neuropsychopharmacology. 2000;23(4):428-38.

901 Paulzen M, Lammertz SE, Gründer G, Veselinovic T, Hiemke C, Tauber SC. Measuring citalopram in blood and cerebrospinal fluid: revealing a distribution pattern that differs from other antidepressants. Int Clin Psychopharmacol. 2016;31(3):119-26.

902 Cao Y, Mager S, Lester HA. H^+ permeation and pH regulation at a mammalian serotonin transporter. J Neurosci. 1997;17(7):2257-66.

903 Ilett KF, Hackett LP, Dusci LJ, Roberts MJ, Kristensen JH, Paech M, et al. Distribution and excretion of venlafaxine and O-desmethylvenlafaxine in human milk. Br J Clin Pharmacol. 1998;45(5):459-62.

904 Fukushima T, Naka-aki E, Guo X, Li F, Vankeirsbilck T, Baeyens WRG, et al. Determination of fluoxetine and norfluoxetine in rat brain microdialysis samples following intraperitoneal fluoxetine administration. Analytica Chimica Acta. 2004;522(1):99-104.

905 Bundgaard C, Jørgensen M, Larsen F. Pharmacokinetic modelling of blood-brain barrier transport of escitalopram in rats. Biopharm Drug Dispos. 2007;28(7):349-60.

906 O'Brien FE, O'Connor RM, Clarke G, Dinan TG, Griffin BT, Cryan JF. P-glycoprotein inhibition increases the brain distribution and antidepressant-like activity of escitalopram in rodents. Neuropsychopharmacology. 2013;38(11):2209-19.

907 Cryan JF, O'Leary OF, Jin SH, Friedland JC, Ouyang M, Hirsch BR, et al. Norepinephrine-deficient mice lack responses to antidepressant drugs, including selective serotonin reuptake inhibitors. Proc Natl Acad Sci U S A. 2004;101(21):8186-91.

908 Bundgaard C, Jørgensen M, Mørk A. An integrated microdialysis rat model for multiple pharmacokinetic/pharmacodynamic investigations of serotonergic agents. J Pharmacol Toxicol Methods. 2007;55(2):214-23.

909 Deltheil T, Tanaka K, Reperant C, Hen R, David DJ, Gardier AM. Synergistic neurochemical and behavioural effects of acute intrahippocampal injection of brain-derived neurotrophic factor and antidepressants in adult mice. International Journal of Neuropsychopharmacology. 2009;12(7):905-15.

910 Gardier A. Antidepressant activity: contribution of brain microdialysis in knock-out mice to the understanding of BDNF/5-HT transporter/5-HT autoreceptor interactions. Frontiers in Pharmacology. 2013;4.

911 Kennedy SH, Andersen HF, Thase ME. Escitalopram in the treatment of major depressive disorder: a meta-analysis. Curr Med Res Opin. 2009;25(1):161-75.

912 Fava GA, Gatti A, Belaise C, Guidi J, Offidani E. Withdrawal Symptoms after Selective Serotonin Reuptake Inhibitor Discontinuation: A Systematic Review. Psychother Psychosom. 2015;84(2):72-81.

913 Gabriel M, Sharma V. Antidepressant discontinuation syndrome. Cmaj. 2017;189(21):E747.

914 Wan H, Rehngren M, Giordanetto F, Bergström F, Tunek A. High-throughput screening of drug-brain tissue binding and in silico prediction for assessment of central nervous system drug delivery. J Med Chem. 2007;50(19):4606-15.

915 Lanevskij K, Dapkunas J, Juska L, Japertas P, Didziapetris R. QSAR analysis of blood–brain distribution: The influence of plasma and brain tissue binding. J Pharm Sci. 2011;100(6):2147-60.

916 Peters EJ, Reus V, Hamilton SP. The ABCB1 transporter gene and antidepressant response. F1000 Biol Rep. 2009;1:23.

917 Pfrieger FW, Ungerer N. Cholesterol metabolism in neurons and astrocytes. Prog Lipid Res. 2011;50(4):357-71.

918 Momo F, Fabris S, Stevanato R. Interaction of fluoxetine with phosphatidylcholine liposomes. Biophys Chem. 2005;118(1):15-21.

919 Hille B. The pH-dependent rate of action of local anesthetics on the node of Ranvier. J Gen Physiol. 1977;69(4):475-96.

920 Hille B. Local anesthetics: hydrophilic and hydrophobic pathways for the drug-receptor reaction. J Gen Physiol. 1977;69:497-515.

921 Tavoulari S, Forrest LR, Rudnick G. Fluoxetine (Prozac) binding to serotonin transporter is modulated by chloride and conformational changes. J Neurosci. 2009;29(30):9635-43.

922 Coleman JA, Green EM, Gouaux E. X-ray structures and mechanism of the human serotonin transporter. Nature. 2016.

923 Coleman JA, Gouaux E. Structural basis for recognition of diverse antidepressants by the human serotonin transporter. Nature structural & molecular biology. 2018;25(2):170-75.

924 Steinberg EM, Cardoso GMP, Martinez PE, Rubinow DR, Schmidt PJ. Rapid response to fluoxetine in women with premenstrual dysphoric disorder. Depression and Anxiety. 2012;29(6):531-40.

925 Bowie M, Pilie P, Wulfkuhle J, Lem S, Hoffman A, Desai S, et al. Fluoxetine induces cytotoxic endoplasmic reticulum stress and autophagy in triple negative breast cancer. World J Clin Oncol. 2015;6(6):299-311.

926 Kornhuber J, Gulbins E. New Molecular Targets for Antidepressant Drugs. Pharmaceuticals (Basel). 2021;14(9).

927 Degenhardt L, Charlson F, Ferrari A, Santomauro D, Erskine H, Mantilla-Herrara A, et al. The global burden of disease attributable to alcohol and drug use in 195 countries and territories, 1990–2016: a systematic analysis for the Global Burden of Disease Study 2016. The Lancet Psychiatry. 2018;5(12):987-1012.

928 Strang J, Volkow ND, Degenhardt L, Hickman M, Johnson K, Koob GF, et al. Opioid use disorder. Nature Reviews Disease Primers. 2020;6(1):3.

929 Cummings KM, Proctor RN. The changing public image of smoking in the United States: 1964-2014. Cancer Epidemiol Biomarkers Prev. 2014;23(1):32-6.

930 Lavacchi D, Roviello G, Rodriquenz MG. Electronic nicotine delivery systems (ENDS): not still ready to put on END. J Thorac Dis. 2020;12(7):3857-65.

931 Stead LF, Perera R, Bullen C, Mant D, Hartmann-Boyce J, Cahill K, et al. Nicotine replacement therapy for smoking cessation. Cochrane Database Syst Rev. 2012;11:Cd000146.

932 Rose JE, Behm FM, Westman EC, Levin ED, Stein RM, Ripka GV. Mecamylamine combined with nicotine skin patch facilitates smoking cessation beyond nicotine patch treatment alone. Clin Pharmacol Ther. 1994;56(1).

933 Rollema H, Hurst RS. The contribution of agonist and antagonist activities of α4β2* nAChR ligands to smoking cessation efficacy: a quantitative analysis of literature data. Psychopharmacology. 2018;235(9):2479-505.

934 Imming P, Klaperski P, Stubbs MT, Seitz G, Gündisch D. Syntheses and evaluation of halogenated cytisine derivatives and of bioisosteric thiocytisine as potent and selective nAChR ligands. European journal of medicinal chemistry. 2001;36(4):375-88.

935 Rouden J, Ragot A, Gouault S, Cahard D, Plaquevent J-C, Lasne M-C. Regio- and diastereoselective functionalization of (−)-cytisine: an unusual N–C acyl migration. Tetrahedron: Asymmetry. 2002;13(12):1299-305.

936 Chellappan SK, Xiao Y, Tueckmantel W, Kellar KJ, Kozikowski AP. Synthesis and Pharmacological Evaluation of Novel 9- and 10-Substituted Cytisine Derivatives. Nicotinic Ligands of Enhanced Subtype Selectivity. Journal of Medicinal Chemistry. 2006;49(9):2673-76.

937 Houllier N, Gouault S, Lasne M-C, Rouden J. Regio- and diastereoselective functionalization of (−)-cytisine. Tetrahedron. 2006;62(50):11679-86.

938 Kozikowski AP, Chellappan SK, Xiao Y, Bajjuri KM, Yuan H, Kellar KJ, et al. Chemical Medicine: Novel 10-Substituted Cytisine Derivatives with Increased Selectivity for α4β2 Nicotinic Acetylcholine Receptors. ChemMedChem. 2007;2(8):1157-61.

939 Marcaurelle LA, Johannes C, Yohannes D, Tillotson BP, Mann D. Diversity-oriented synthesis of a cytisine-inspired pyridone library leading to the discovery of novel inhibitors of Bcl-2. Bioorganic & Medicinal Chemistry Letters. 2009;19(9):2500-03.

940 Philipova I, Stavrakov G, Vassilev N, Nikolova R, Shivachev B, Dimitrov V. Cytisine as a scaffold for ortho-diphenylphosphinobenzenecarboxamide ligands for Pd-catalyzed asymmetric allylic alkylation. Journal of Organometallic Chemistry. 2015;778:10-20.

941 Coe JW, Brooks PR, Vetelino MG, Wirtz MC, Arnold EP, Huang J, et al. Varenicline: an a4b2 nicotinic receptor partial agonist for smoking cessation. J Med Chem. 2005;48(10):3474-7.

942 Mills EJ, Wu P, Spurden D, Ebbert JO, Wilson K. Efficacy of pharmacotherapies for short-term smoking abstinance: A systematic review and meta-analysis. Harm Reduction Journal. 2009;6(1):25.

943 Cohen C, Bergis OE, Galli F, Lochead AW, Jegham S, Biton B, et al. SSR591813, a Novel Selective and Partial a4b2 Nicotinic Receptor Agonist with Potential as an Aid to Smoking Cessation. J Pharmacol Exp Ther. 2003;306(1):407-20.

944 Fagerström K, Balfour DJK. Neuropharmacology and potential efficacy of new treatments for tobacco dependence. Expert Opinion on Investigational Drugs. 2006;15(2):107-16.

945 Rollema H, Shrikhande A, Ward KM, Tingley FD, 3rd, Coe JW, O'Neill BT, et al. Pre-clinical properties of the α4β2 nicotinic acetylcholine receptor partial agonists varenicline, cytisine and dianicline translate to clinical efficacy for nicotine dependence. Br J Pharmacol. 2010;160(2):334-45.

946 Tashkin DP. Smoking Cessation in Chronic Obstructive Pulmonary Disease. Semin Respir Crit Care Med. 2015;36(04):491-507.

947 Rego Campello H, Del Villar SG, Honraedt A, Minguez T, Oliveira ASF, Ranaghan KE, et al. Unlocking Nicotinic Selectivity via Direct C–H Functionalization of (−)-Cytisine. Chem. 2018;4(7):1710-25.

948 Blom AEM, Campello HR, Lester HA, Gallagher T, Dougherty DA. Probing Binding Interactions of Cytisine Derivatives to the α4β2 Nicotinic Acetylcholine Receptor. J Am Chem Soc. 2019.

949 Pieńko T, Grudzień M, Taciak PP, Mazurek AP. Cytisine basicity, solvation, logP, and logD theoretical determination as tool for bioavailability prediction. Journal of Molecular Graphics and Modelling. 2016;63:15-21.

950 Le Houezec J. Role of nicotine pharmacokinetics in nicotine addiction and nicotine replacement therapy: a review. Int J Tuberc Lung Dis. 2003;7(9):811-9.

951 Holyoak T, Fenn TD, Wilson MA, Moulin AG, Ringe D, Petsko GA. Malonate: a versatile cryoprotectant and stabilizing solution for salt-grown macromolecular crystals. Acta crystallographica Section D, Biological crystallography. 2003;59(Pt 12):2356-8.

952 Anand K, Pal D, Hilgenfeld R. An overview on 2-methyl-2,4-pentanediol in crystallization and in crystals of biological macromolecules. Acta crystallographica Section D, Biological crystallography. 2002;58(Pt 10 Pt 1):1722-8.

953 Good NE, Winget GD, Winter W, Connolly T, Izawa S, Singh RMM. Hydrogen ion buffers for biological research. Biochemistry. 1966;5:467-77.

954 Kabsch W. Xds. Acta Crystallographica D Biological Crystallography. 2010;66(Pt 2):125-32.

955 Winn MD, Ballard CC, Cowtan KD, Dodson EJ, Emsley P, Evans PR, et al. Overview of the CCP4 suite and current developments. Acta Crystallographica D Biological Crystallography. 2011;67(Pt 4):235-42.

956 Adams PD, Afonine PV, Bunkoczi G, Chen VB, Davis IW, Echols N, et al. PHENIX: A comprehensive Python-based system for macromolecular structure solution. Acta Crystallographica D Biological Crystallography. 2010;66(Pt 2):213-21.

957 Emsley P, Lohkamp B, Scott WG, Cowtan K. Features and development of Coot. Acta crystallographica Section D, Biological crystallography. 2010;66(Pt 4):486-501.

958 Elmore DE, Dougherty DA. A Computational Study of Nicotine Conformations in the Gas Phase and in Water. The Journal of Organic Chemistry. 2000;65(3):742-47.

959 Fan C. in *Chemistry and Chemical Engineering* (California Institute of Technology, Pasadena, 2020).

960 Schiefner A, Breed J, Bosser L, Kneip S, Gade J, Holtmann G, et al. Cation-pi interactions as determinants for binding of the compatible solutes glycine betaine and proline betaine by the periplasmic ligand-binding protein ProX from Escherichia coli. J Biol Chem. 2004;279(7):5588-96.

961 Astroug H, Simeonova R, Kassabova L, Danchev N, Svinarov D. Pharmacokinetics of cytisine after single intravenous and oral administration in rabbits. Interdisciplinary Toxicology. 2010;3(1):15-20.

962 Jeong SH, Sheridan J, Newcombe D, Tingle M. Plasma concentrations of cytisine, a commercially available plant-based alkaloid, in healthy adult smokers taking recommended doses for smoking cessation. Xenobiotica. 2018;48(12):1245-48.

963 Dempsey D, Tutka P, Jacob P, 3rd, Allen F, Schoedel K, Tyndale RF, et al. Nicotine metabolite ratio as an index of cytochrome P450 2A6 metabolic activity. Clin Pharmacol Ther. 2004;76(1):64-72.

964 Morales-Perez CL, Noviello CM, Hibbs RE. X-ray structure of the human alpha4beta2 nicotinic receptor. Nature. 2016;538(7625):411-15.

965 Post MR, Tender GS, Lester HA, Dougherty DA. Secondary Ammonium Agonists Make Dual Cation-π Interactions in α4β2 Nicotinic Receptors. eNeuro. 2017;4(2).

966 Celie P, van Rossum-Fikkert S, Van Dyke W, Brejc K, Smit A, Sixma T. Nicotine and Carbamylcholine Binding to Nicotinic Acetylcholine Receptors as Studied in AChBP Crystal Structures. Neuron. 2004;41:907-14.

967 Haga K, Kruse AC, Asada H, Yurugi-Kobayashi T, Shiroishi M, Zhang C, et al. Structure of the human M2 muscarinic acetylcholine receptor bound to an antagonist. Nature. 2012;482(7386):547-51.

968 Xiu X, Puskar NL, Shanata JA, Lester HA, Dougherty DA. Nicotine binding to brain receptors requires a strong cation-π interaction. Nature. 2009;458(7237):534-7.

969 Ormo M, Cubitt AB, Kallio K, Gross LA, Tsien RY, Remington SJ. Crystal structure of the *Aequorea victoria* green fluorescent protein. Science. 1996;273(5280):1392-5.

970 Tsien RY. The green fluorescent protein. Annu Rev Biochem. 1998;67:509-44.

971 Brejc K, Sixma TK, Kitts PA, Kain SR, Tsien RY, Ormö M, et al. Structural basis for dual excitation and photoisomerization of the Aequorea victoria green fluorescent protein. Proc Natl Acad Sci U S A. 1997;94(6):2306-11.

972 Gouridis G, Schuurman-Wolters GK, Ploetz E, Husada F, Vietrov R, de Boer M, et al. Conformational dynamics in substrate-binding domains influences transport in the ABC importer GlnPQ. Nature structural & molecular biology. 2015;22(1):57-64.

973 de Boer M, Gouridis G, Muthahari YA, Cordes T. Single-Molecule Observation of Ligand Binding and Conformational Changes in FeuA. Biophysical Journal. 2019;117(9):1642-54.

974 Turner JR, Castellano LM, Blendy JA. Parallel anxiolytic-like effects and upregulation of neuronal nicotinic acetylcholine receptors following chronic nicotine and varenicline. Nicotine Tob Res. 2011;13(1):41-6.

975 Al Shoyaib A, Archie SR, Karamyan VT. Intraperitoneal Route of Drug Administration: Should it Be Used in Experimental Animal Studies? Pharmaceutical research. 2019;37(1):12.

976 Whiteley C. Depression as a Disorder of Consciousness. British Journal for the Philosophy of Science.

977 Nascimento G, Walsh-Monteiro A, Gouveia jr A. A Reliable Depression-Like Model in Zebrafish (Danio rerio): Learned Helplessness. Psychology & Neuroscience. 2016;9.

978 Zhang S, Liu X, Sun M, Zhang Q, Li T, Li X, et al. Reversal of reserpine-induced depression and cognitive disorder in zebrafish by sertraline and Traditional Chinese Medicine (TCM). Behav Brain Funct. 2018;14(1):13.

979 Facchinello N, Skobo T, Meneghetti G, Colletti E, Dinarello A, Tiso N, et al. nr3c1 null mutant zebrafish are viable and reveal DNA-binding-independent activities of the glucocorticoid receptor. Scientific reports. 2017;7(1):4371.

980 Prober DA, Rihel J, Onah AA, Sung RJ, Schier AF. Hypocretin/orexin overexpression induces an insomnia-like phenotype in zebrafish. J Neurosci. 2006;26(51):13400-10.

981 Chen S, Reichert S, Singh C, Oikonomou G, Rihel J, Prober DA. Light-Dependent Regulation of Sleep and Wake States by Prokineticin 2 in Zebrafish. Neuron. 2017;95(1):153-68.e6.

982 Lee DA, Liu J, Hong Y, Lane JM, Hill AJ, Hou SL, et al. Evolutionarily conserved regulation of sleep by epidermal growth factor receptor signaling. Sci Adv. 2019;5(11):eaax4249.

983 Tran S, Prober DA. Methods to Study Sleep in Zebrafish. In: Hirota T, Hatori M, Panda S, editors. Circadian Clocks. New York, NY: Springer US; 2022. p. 259-86.

984 Blaser R, Gerlai R. Behavioral phenotyping in zebrafish: comparison of three behavioral quantification methods. Behav Res Methods. 2006;38(3):456-69.

985 Bai Y, Liu H, Huang B, Wagle M, Guo S. Identification of environmental stressors and validation of light preference as a measure of anxiety in larval zebrafish. BMC Neurosci. 2016;17(1):63.

986 Feugere L, Scott VF, Rodriguez-Barucg Q, Beltran-Alvarez P, Wollenberg Valero KC. Thermal stress induces a positive phenotypic and molecular feedback loop in zebrafish embryos. J Therm Biol. 2021;102:103114.

987 Haesemeyer M, Robson DN, Li JM, Schier AF, Engert F. The structure and timescales of heat perception in larval zebrafish. Cell Syst. 2015;1(5):338-48.

988 Xing L, Quist TS, Stevenson TJ, Dahlem TJ, Bonkowsky JL. Rapid and efficient zebrafish genotyping using PCR with high-resolution melt analysis. J Vis Exp. 2014(84):e51138.

989 Yeh C-M. The Basal NPO crh Fluctuation is Sustained Under Compromised Glucocorticoid Signaling in Diurnal Zebrafish. Frontiers in Neuroscience. 2015;9.

990 Al-Amrani S, Al-Jabri Z, Al-Zaabi A, Alshekaili J, Al-Khabori M. Proteomics: Concepts and applications in human medicine. World J Biol Chem. 2021;12(5):57-69.

991 Mendez-David I, Boursier C, Domergue V, Colle R, Falissard B, Corruble E, et al. Differential Peripheral Proteomic Biosignature of Fluoxetine Response in a Mouse Model of Anxiety/Depression. Frontiers in cellular neuroscience. 2017;11:237.

992 Ruiz-Perera L, Muniz M, Vierci G, Bornia N, Baroncelli L, Sale A, et al. Fluoxetine increases plasticity and modulates the proteomic profile in the adult mouse visual cortex. Scientific reports. 2015;5:12517.

993 Guest PC. Brain Proteomic Analysis on the Effects of the Antidepressant Fluoxetine. Methods Mol Biol. 2020;2138:419-30.

994 Kiick KL, Saxon E, Tirrell DA, Bertozzi CR. Incorporation of azides into recombinant proteins for chemoselective modification by the Staudinger ligation. Proc Natl Acad Sci U S A. 2002;99(1):19-24.

995 Dieterich DC, Link AJ, Graumann J, Tirrell DA, Schuman EM. Selective identification of newly synthesized proteins in mammalian cells using bioorthogonal noncanonical amino acid tagging (BONCAT). Proceedings of the National Academy of Sciences of the United States of America. 2006;103(25):9482-7.

996 Kenney JW, Genheden M, Moon KM, Wang X, Foster LJ, Proud CG. Eukaryotic elongation factor 2 kinase regulates the synthesis of microtubule-related proteins in neurons. J Neurochem. 2016;136(2):276-84.

997 Schanzenbächer CT, Sambandan S, Langer JD, Schuman EM. Nascent Proteome Remodeling following Homeostatic Scaling at Hippocampal Synapses. Neuron. 2016;92(2):358-71.

998 Schanzenbächer CT, Langer JD, Schuman EM. Time- and polarity-dependent proteomic changes associated with homeostatic scaling at central synapses. eLife. 2018;7.

999 Alvarez-Castelao B, Tom Dieck S, Fusco CM, Donlin-Asp P, Perez JD, Schuman EM. The switch-like expression of heme-regulated kinase 1 mediates neuronal proteostasis following proteasome inhibition. eLife. 2020;9.

1000 Perez JD, Dieck ST, Alvarez-Castelao B, Tushev G, Chan IC, Schuman EM. Subcellular sequencing of single neurons reveals the dendritic transcriptome of GABAergic interneurons. eLife. 2021;10.

1001 Karson CN, Newton JE, Livingston R, Jolly JB, Cooper TB, Sprigg J, et al. Human brain fluoxetine concentrations. J Neuropsychiatry Clin Neurosci. 1993;5(3):322-9.

1002 Johnson RD, Lewis RJ, Angier MK. The distribution of fluoxetine in human fluids and tissues. J Anal Toxicol. 2007;31(7):409-14.

1003 Measuring citalopram in blood and central nervous system: revealing a distribution pattern that differs from other antidepressants: Erratum. Int Clin Psychopharmacol. 2016;31(5):300.

1004 Devaraj NK, Finn MG. Introduction: Click Chemistry. Chem Rev. 2021;121(12):6697-98.

1005 Sahu MP, Nikkilä O, Lågas S, Kolehmainen S, Castrén E. Culturing primary neurons from rat hippocampus and cortex. Neuronal Signal. 2019;3(2):Ns20180207.

1006 Wang F, Li S, Houerbi N, Chou T-F. Temporal proteomics reveal specific cell cycle oncoprotein downregulation by p97/VCP inhibition. Cell Chemical Biology. 2022;29(3):517-29.e5.

1007 Fan S, Kind T, Cajka T, Hazen SL, Tang WHW, Kaddurah-Daouk R, et al. Systematic Error Removal Using Random Forest for Normalizing Large-Scale Untargeted Lipidomics Data. Anal Chem. 2019;91(5):3590-96.

1008 CLSTN3. 2022. https://www.alliancegenome.org/gene/HGNC:18371.

1009 Kim SJ, Jeong YT, Jeong SR, Park M, Go HS, Kim MY, et al. Neural regulation of energy and bone homeostasis by the synaptic adhesion molecule Calsyntenin-3. Exp Mol Med. 2020;52(5):793-803.

1010 Bai N, Lu X, Jin L, Alimujiang M, Ma J, Hu F, et al. CLSTN3 gene variant associates with obesity risk and contributes to dysfunction in white adipose tissue. Mol Metab. 2022;63:101531.

1011 Terwisscha van Scheltinga AF, Bakker SC, Kahn RS, Kas MJ. Fibroblast growth factors in neurodevelopment and psychopathology. Neuroscientist. 2013;19(5):479-94.

1012 Deng Z, Deng S, Zhang MR, Tang MM. Fibroblast Growth Factors in Depression. Front Pharmacol. 2019;10:60.

1013 Dana H, Mohar B, Sun Y, Narayan S, Gordus A, Hasseman JP, et al. Sensitive red protein calcium indicators for imaging neural activity. eLife. 2016;5:e12727.

1014 Xu Y, Deng M, Zhang S, Yang J, Peng L, Chu J, et al. Imaging Neuronal Activity with Fast and Sensitive Red-Shifted Electrochromic FRET Indicators. ACS Chem Neurosci. 2019;10(12):4768-75.

1015 Patriarchi T, Mohebi A, Sun J, Marley A, Liang R, Dong C, et al. An expanded palette of dopamine sensors for multiplex imaging in vivo. Nature Methods. 2020;17(11):1147-55.

1016 Kunst M, Laurell E, Mokayes N, Kramer A, Kubo F, Fernandes AM, et al. A Cellular-Resolution Atlas of the Larval Zebrafish Brain. Neuron. 2019;103(1):21-38.e5.

1017 Svara F, Förster D, Kubo F, Januszewski M, dal Maschio M, Schubert PJ, et al. Automated synapse-level reconstruction of neural circuits in the larval zebrafish brain. Nature Methods. 2022;19(11):1357-66.

1018 Marius P, Carsen S, Mario D, Sylvia S, Rossi LF, Henry D, et al. Suite2p: beyond 10,000 neurons with standard two-photon microscopy. bioRxiv. 2017:061507.

1019 Giovannucci A, Friedrich J, Gunn P, Kalfon J, Brown BL, Koay SA, et al. CaImAn an open source tool for scalable calcium imaging data analysis. eLife. 2019;8:e38173.